Calculation of linelists for Chromium Hydride (CrH) & Manganese Hydride (MnH)

Maire N. Gorman
Department of Physics & Astronomy
University College London

A thesis submitted for the degree of
Doctor of Philosophy
August 31, 2016

Supervisors: Dr Sergey N. Yurchenko
&
Professor Jonathan Tennyson

I, Maire N. Gorman certify that, unless otherwise stated the work contained within this thesis is my own. I confirm that where information has been obtained from other sources this has been indicated.

To Donal, Mum & Dad.

Acknowledgements

Throughout my time as a PhD student I have felt privileged to be part of the vibrant and talented group that is ExoMol. I have always found the Department of Physics at UCL very welcoming and supportive which I am grateful for. I would like to thank my supervisors Sergey & Jonathan for giving me the challenging and unpredictable molecule of Chromium Hydride. I am really grateful for the opportunities I have had to present work at various conferences & scientific meetings throughout the UK and Europe.

I would firstly like to pay tribute to Kirsty McCabe, a former student from my school who inspired me to firstly study physics and also to apply to Oxford where I spent an enjoyable and hugely challenging 4 years prior to coming to UCL. I would like to thank my tutors at Oxford Dr Jo Ashbourn, Dr Jeff Tseng & Professor Philipp Podsiadlowski who encouraged me to apply for a PhD and have since offered inspiration me when I have visited.

I would like to thank Professor Jonathan Tennyson for offering me a place at UCL in the ExoMol group having applied to study magnetospheric physics in the astronomy department. During the lunch which the department put on for interviewees I guess I was in the right place at the right time! I fully appreciate that there were many strong candidates and thus am indebted to Jonathan for taking me on.

When I moved to London I was very fortunate to live in the Victoria League House in Bayswater for two years and then for a further year as a study duty officer. On behalf of fellow students I would like to thank the charity for providing a safe, quiet, convenient & affordable place for students to live. I thoroughly enjoyed my time as a student duty officer-thank you students for been very well behaved!

Outside of my PhD I have spent many a happy hour demonstrating in the undergraduate laboratories. I would like to thank Dr Paul Bartlett with whom I shared many helpful discussions with about research, teaching, academia and industry. Also Kirsty Dunnett, a fellow PhD student whom I demonstrated with. I would also like to thank the Brilliant Club for giving me the opportunity to teach mathematics in two primary schools. To all the pupils I had the privilege of teaching: thank you for been delightful in character and very insightful about the modern world.

Within the ExoMol group, there are several people within the group I would like to thank in particular. Lorenzo Lodi for sharing his experience about diatomic hydrides with me and also Laura McKemmish and Emma Barton for their encouragement as well as practical support & advice during this last year. Also I would like to acknowledge the support and friendliness I have received from the rest of the ExoMol group: Christian Hill, Emil Zak, Phillip Coles, Oleg Polyansky, Andrey Yachmenev,

Katie Chubb, the late Anatoly Pavlyuchko, Ahmed Al-Refaie, Renia Diamantopoulou & Clara Sousa Silva. I have thoroughly enjoyed our weekly ExoMol meetings where we have shared journal papers & also each given 20 minute presentations on our individual research on a rota basis: an invaluable exercise in itself.

I am very grateful to both Professor Andrew Evans and Professor Eleri Pryse from Aberystwyth University who have been supporting me professionally and on a personal level.

And finally I'd like to thank my first supervisor Sergey for his patience, understanding and pragmatic advice.

Abstract

New linelists (list of wavelengths with associated frequencies) for the open-shell transition metal diatomics Chromium Hydride (CrH) and Manganese Hydride (MnH) have been calculated. These linelists have been calculated from first principles making use of the Born-Oppenheimer approximation which decomposes the Schrödinger equation for a molecule into an electronic equation and rovibronic equation.

To solve the electronic Schrödinger equation and thus produce Potential Energy Curves (PECs), Dipole Moment Curves (DMCs) and all relevant couplings (transition dipole, electronic angular momentum, spin-orbit) the MRCI (Multi-Reference Configuration Interaction) method as implemented in the *ab initio* `MOLPRO` package was used. The electronic states considered were those up to 20 000 cm^{-1} as this region is of most importance to astronomers to whom we are creating the linelists for within the ExoMol project.

The construction of linelists for transition metal diatomics is very much at a developmental stage due to the myriad of low-lying electronic states of high multiplicity which couple together. Hence during the calculation of *ab initio* curves a systematic study of the CASSCF orbitals used for the proceeding MRCI calculations was undertaken for both CrH and MnH. Also the effect of changing the configuration space of electrons was found to have profound effects on the behaviour of the PECs obtained. Additionally, the variation in properties obtained by changing the number of states calculated within a single MRCI calculation was investigated.

A choice selection of these *ab initio* curves were then implemented into the in-house programme Duo to produce linelists for CrH and MnH. These linelists were refined using available experimental data.

At present, the existing linelist available for CrH in literature has 2 electronic states. Our new linelist is composed from 8 low-lying electronic states of CrH. CrH is used to classify L type dwarfs under the widely accepted classification scheme of Kirkpatrick. Additionally it has been shown theoretically that CrH could be used as a sensitive probe of magnetic fields of stars and also in the so-called "deuterium test" to probe the evolutionary history of sub-stellar objects. Due to the limited coverage of the existing linelist, a new linelist is sought after by astronomers.

At present MnH has not been discovered in outer space but due to the favourable abundance of manganese it has been speculated that it could be present in the ISM. Hence the creation of a linelist opens up the possibility of the first astronomical detection of this molecule.

Since January 2016 I have been working as a teaching fellow at Aberystwyth University. Hence preliminary work has been done on creating projects for under-

graduate students for the molecules of BeH, MgH and CaH. A summary of literature has also been created for FeH with a view to in future creating a new linelist for this molecule which is of considerable interest both from an astronomical and theoretical perspective.

Contents

List of Tables

List of Figures

Chapter 1

Astronomical Context

In this chapter the astronomical motivation for the ExoMol project will be outlined. Since the first exoplanet was discovered orbiting a main-sequence star in 1995 (Mayor & Queloz 1995, see section 1.4), a whole community of exoplanet observers has evolved which is developing increasingly novel methods to detect these far-away worlds. With the launch of the Kepler satellite in 2009, the field has literally exploded with new planetary candidates been identified every week, papers submitted to the arXiv and intellectual debates ensuing as to whether candidates can be confirmed: or indeed if what was once thought a planet is actually a planet or just an aberration in signal. Indeed, as of April 2016, there are over 200 exoplanets listed as "unconfirmed, controversial or retracted" in the Exoplanet.eu database. In detecting, and indeed confirming the existence of an exoplanet, a detailed knowledge of the host star is often paramount as often sunspots can give the illusion of an exoplanet (see Barstow et al. 2014). In this chapter, an overview of stellar evolution (section 1.1) and classification (section 1.2) is given as well as a brief introduction to the study of brown dwarf objects: CrH is an important molecule in the study of brown dwarfs (see section 3.4). With this ever-increasing population of confirmed exoplanets, statistical studies can be undertaken of properties such as planetary and stellar radii, distance to host star, effective temperature and surface gravity: these studies do indeed show the biases inherent in the various detection methods which favour large "Hot Jupiter" planets orbiting close to their host star (section 1.4). These population studies also act as crucial feedback to the protoplanetary disk formation communities: indeed questions have been now raised about the formation sequence of our very own solar system. An overview of the highly sophisticated field of exomoons is presented in section 1.5 which has in some cases, helped confirm or de-confirm exoplanetary candidates.

Now as well as actually finding exoplanets, an increasingly diverse and vibrant community characterising the atmospheres of these planets has evolved. After all, the million-dollar question is "Are we alone in the Universe?". Certain exoplanets have proved very popular with the exoplanet community (section 1.6) due to their short orbits which has allowed repeat observations to made in realistic timescales. With this increasing desire to understand the chemistry of exoplanets, the need for developments in atmospheric modelling but also for higher quality, more complete linelists applicable to higher temperatures commonly found on these exoplanets has

been invoked. It is this need for higher quality molecular data which has led to the creation of the ExoMol project. At present the ExoMol project is feeding this research community with molecular data which can be used in theoretical atmospheric models which are aiming to reproduce observed spectra.

1.1 Stellar Evolution

This section was written with reference to Philips (1999). A star is formed when a giant molecular cloud collapses under gravity: during this collapse, gravitational potential energy is released in the form of heat. Provided the mass of this protostar is greater than 0.08 $M_{\odot}$, once its' temperature reaches approximately 10×10^6 K hydrogen-burning is ignited and thus the star 'joins' the main-sequence. Classically, by equating $\frac{Q_p^2}{4\pi\epsilon_0 r^2}$ to $k_B T$ it would be expected that in order for protons to overcome their electrostatic repulsion and thus be 10^{-15} m apart (at which point the strong force becomes dominant), a temperature of 10^{10} K would be required. However, due to the phenomenon of quantum tunnelling this threshold temperature for Hydrogen burning to occur is reduced. The timescale for which a star is on the main-sequence and its' eventual fate is dependent on its mass: heavier stars have higher core temperatures and greater inner gravitational forces acting which allows hydrogen to burn (fuse) quicker. For solar-type stars, during the main-sequence part of a star's life, there is equilibrium between the inward gravitational forces and the outward thermal pressure produced by the nuclear fusion processes. For larger stars, the outward pressure is due to radiation.

As a star begins to leave the main sequence, this balance oscillates as the star goes through phases of internal contraction of the core and expansion of outer layers: the exact sequence and whether or not there is a so-called "Helium-flash" depends on the initial mass of the star. Once hydrogen in the core has been exhausted there is hence then no outward pressure acting outwards to counteract the force of gravity pulling inwards: thus gravitational collapse of the core occurs. This collapse releases heat which thus allows an outer layer of hydrogen to be ignited. This outer 'shell' then starts fusing hydrogen: the radiation pressure produced counteracts further gravitational collapse until the hydrogen in this shell is exhausted. For a star of mass between approximately 0.5-10 $M_{\odot}$ these outer shells of hydrogen burning expand thus causing the star to expand to become a red giant. As the core continues to collapse, gravitational potential energy is released and the outer layers are expelled as planetary nebula leaving behind a white dwarf. This will be the fate of our own sun which is predicted to leave the main sequence in around 5 billion years.

For more massive stars, M $>$ 10 $M_{\odot}$ if the mass of the inert core exceeds the Chandrasekhar limit, then the outward acting electron degeneracy pressure is not sufficient to withstand gravitational collapse: thus the cores collapse to become a neutron star or black hole as the outer shells are blown off. A neutron star is formed when electrons are captured by protons to create neutrons.

1.2 Stellar Classification

This section was written with reference to Gray & Corbally (2009). Stars are classified using a letter, number & roman numeral based on the temperature and density of their photosphere. For our own star, the sun, the photosphere is what we actually see in the visible with the chromosphere radiating in the infrared. The temperature of a star is classified by the under the Morgan-Keenan system as shown in table 1.1.

Spectral Class	T_e (K)	Main sequence			Fraction
		Mass ($M_\odot$)	Radius ($R_\odot$)	Luminosity ($L_\odot$)	
O	$\geqslant 30,000$	$\geqslant 16$	$\geqslant 6.6$	30, 000	0.00003%
B	10,000-30,000	2.1-16	1.8-6.6	25-30, 000	0.13%
A	7500-10,000	1.4-2.1	1.4-1.8	5-25	0.6%
F	6000-7500	1.04-1.4	1.15-1.4	1.5-5	3.0%
G	5200-6000	0.8-1.04	0.96-1.15	0.6-1.5	7.6%
K	3700-5200	0.45-0.8	0.7-0.96	0.08-0.6	12.1%
M	2400-3700	0.08-0.45	$\leqslant 0.7$	$\leqslant 0.08$	76.45%

Table 1.1: Summary of the Harvard Spectral Classification Scheme developed by Annie Jump Cannon between 1918 and 1924 as part of a team led by Edward Pickering (Cannon & Pickering 1924).

In table 1.1 the fraction is the % fraction of all main sequence stars which fall under the respective classification. Continuing on this classification after M stars there is also L, T and Y dwarfs which have approximate temperatures T_e of 1300-2400 K, 700-1300 K and $<$ 700 K respectively. Here T_e is the effective temperature which is commonly defined by fitting a Planck function to the stars atmosphere. Within each spectral class, stars are further subdivided by their photosphere temperature using the numbers 0 to 9 with 9 been the coolest within a spectral class and '0' being the hottest.

To distinguish between stars with a similar temperature profile, a Roman numeral is used to classify the stars based on absorption features within the photosphere which are dependent on the density and surface gravity of the photosphere and hence the mass of the star. The assigned Roman numerals are as follows which distinguish these luminosity classes are shown in table 1.2.

Roman Numeral	Classification
$0/Ia^+$	Hyper giants
Ia	Luminous super-giants
Iab	Intermediate luminous supergiants
Ib	Less luminous super-giants
II	Bright giants
III	regular(normal) giants
IV	sub giants
V	main sequence stars
sd	sub dwarfs
D	white dwarfs

Table 1.2: The Yerkes spectral classification developed by Morgan, Keenan and Kellman (known as MKK) for distinguishing stars of the same effective temperature but different immensities first published in 1943.

The Hertzsprung-Russell diagram shows the relation between the spectral & luminosity classes of stars: during and after its' construction it was realised that it was actually a convenient method to plot the evolution of stars. A Hertzsprung-Russell diagram is shown for reference in figure 1.1.

1.3 Brown Dwarfs

This section was written with reference to Reid & Hawley (2005). Protostars which have masses less than approximately 0.08 $M_{\odot}$ will not obtain this required core temperature to ignite hydrogen (10×10^6 K). However, if their mass is above 13 M_J (Jupiter Masses), deuterium burning can instead take place which requires a temperature of 8×10^5 K. By the IAU, a brown dwarf is defined as an object with mass between 13 M_J and 65 M_J. For objects which have mass less than 13 M_J are classified as sub brown-dwarfs.

Brown dwarfs are classified into M, L, T and Y dwarfs which is simply an extension of the Harvard Spectral Classification Scheme (see table 1.1). Broadly speaking, M dwarfs have atmospheres dominated by oxide species such as TiO, VO with L dwarfs dominated by hydride species such as CrH, FeH, CaH and T and Y dwarfs dominated by H_20 and CH_4. L dwarfs are taken to have 1400 K $\lesssim T_{eff} \lesssim$ 2000 K with T and Y dwarfs been even cooler.

The detection of brown dwarfs has mostly occurred during wide-angle field searches such as 2MASS, DENNIS & the SLOAN digital sky survey. The first L subdwarf to be discovered was 2MASS 0532+82 and the first T dwarf confirmed was T6 2MASS 0937+29. One of the first missions to detect brown dwarfs was the Wide-field Infrared Survey Explorer (WISE): the first 100 brown dwarfs discovered by this mission was composed of 6 Y dwarfs, 89 T dwarfs, 8 L dwarfs and 1 M dwarfs: over 80 of these dwarfs had an age of T6 or older (Kirkpatrick et al. 2011).

Professor Isabelle Baraffe, who is based at the University of Exeter has undertaken extensive theoretical studies of the evolution of brown dwarfs (Baraffe et al. 2003, Baraffe et al. 2002, Chabrier et al. 2000, Baraffe et al. 1998). The Met Office, which produces climate forecasts for the UK and worldwide is also based in Exeter and has benefited from her studies as the brown dwarf atmosphere characterisation community frequently pushes the boundaries of modelling. Baraffes' work includes producing theoretical colour-magnitude diagrams as well as metallicity, mass, temperature and luminosity calibrations for objects between 0.075-1 $M_{\odot}$ with solar type metallicities [M/H]=0 to 0.5: these have been found to match the observations of brown dwarf made by Henry and McCarthy (1993). Her work has mostly focused on modelling the interiors of brown dwarfs alongside initially grey atmospheres using the NEXT Gen atmospheric models of Allard and Hauschildt (1998). It was realised that there were shortcomings in the grey atmosphere models: hence these atmospheric models were then updated to become the so-called "DUSTY" and "COND" models which considered the effects of wavelength dependent opacity sources and grain formation in limiting cases. Furthermore it has been found that the magnitude of the surface gravity is important in correctly modelling convection in the atmospheres of brown dwarfs.

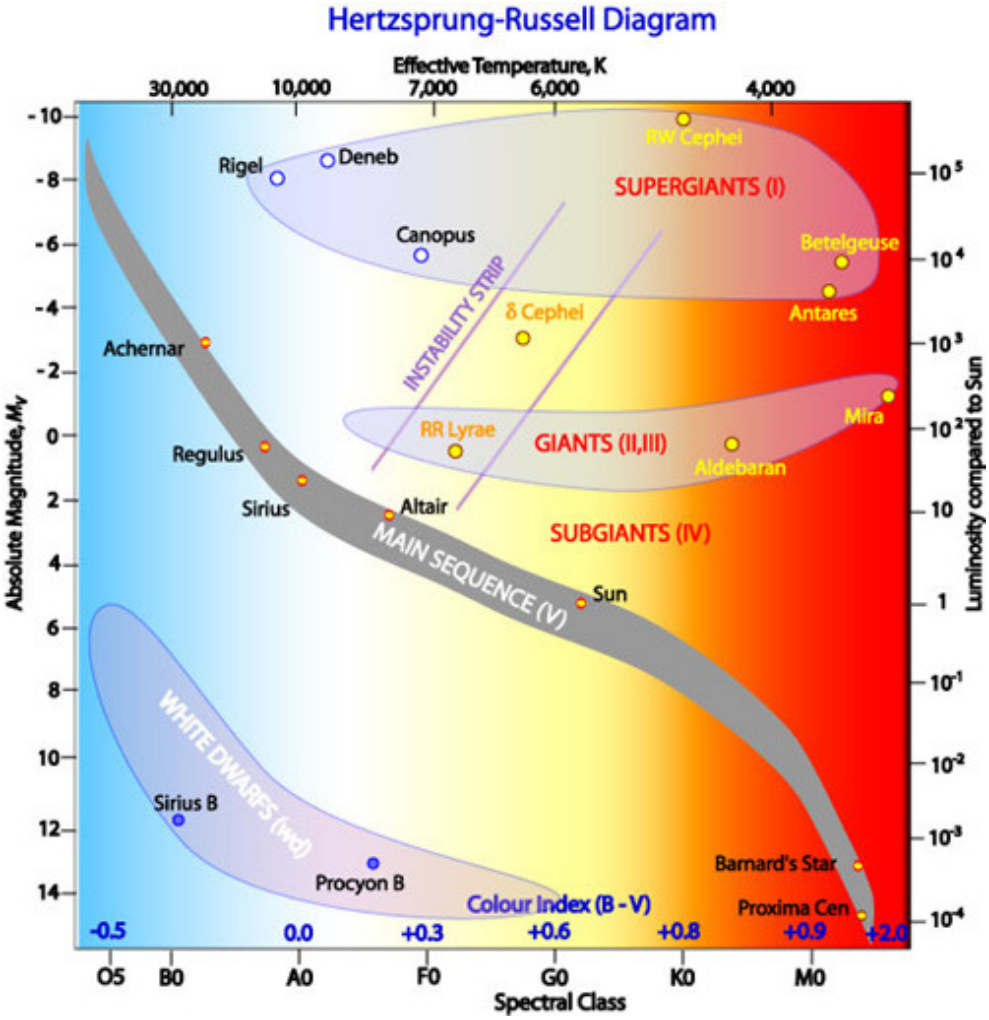

Figure 1.1: Hertzsprung-Russell diagram showing the classification and evolution of stars. Image retrieved from Australian Telescope National Facility (ATNF) webpages. For approximately 90% of a main-sequence star's lifetime, stellar evolution is driven by burning of Hydrogen in the core. The fate of any protostar is dependent upon its' initial mass. Several methods can be used to determine the distance a star is away, d such as the method of parallax and using Cepheid Variables. With this distance known and by measuring the flux, F of the star reaching Earth, the intrinsic luminosity, L of the star can be determined using $L = 4\pi d^2 F$. The mass-luminosity relationship, $\frac{L}{L_\odot} = \left(\frac{M}{M_\odot}\right)^a$ can then be applied in order to determine the mass of the star: for main-sequence stars the index a is commonly taken to be 3.5. If the spectrum emitted by the star is of the form of a Blackbody, Wein's Displacement Law, $\lambda_{\max} T = b \approx 2900 \mu m K$, can then be applied in order to determine the surface temperature T of the star. Finally, the radius of the star, R can be determined using the Luminosity and Temperature of the star, $L = 4\pi R^2 \sigma T^4$ where σ is Stefan's constant.

A project of interest within the Brown Dwarf community is the LEAP (Life, Electricity, Atmospheres, Planets) project been led by Dr. Christiane Helling at St Andrews University in Scotland. In 2012 Dr Christiana Helling published a book in German entitled “Wolken” which translates as "Cloud" and takes the reader through a journey of cloud shapes, sizes, observations of them and cloud formation processes both on our own planet and finally, objects outside our solar system. The LEAP project was a 5 year project which commenced in 2010 and was funded by the European Research Council under the title of "Charge separation, lightning and radio emission in low-mass objects". It was a collaboration between St Andrews, Glasgow, Lancaster & Oxford. One of the aims of the project was to investigate if the synthesis of early molecules essential to life could be initiated on extra-solar objects by charge process. In our earth's atmosphere, thunder & lightening storms are produced when ice grains rub against each other producing distributions of static charge within clouds which are then dissipated by lightening bolts. The project thus worked on the hypothesis that similarly, dust clouds could act as sources for lightening (discharge) events on objects outside our solar system such as brown dwarfs, M-dwarfs, exoplanets. In summary the project has an active blog and has produced to date around 60 papers studying the charge processes happening within brown dwarfs. Another leading figure in the study of Brown Dwarfs is Professor Adam Burgasser who is based at the University of California San Diego: his work is focused on brown dwarf binaries and the L/T transition. The study of brown-dwarf binaries is of paramount important in the study of galaxy & star formation. The general consensus amongst the community is that VLMs (Very Low Mass) binaries occur for approximately 10-30% of stars and that within these binaries 93% have a separation of < 20 AU with 77% having a mass ratio M_2/M_1 of $\geqq 0.8$ (Burgasser 2006). A rapid transition through the L/T boundary is observed within the observed brown dwarf population: across the transition there is complete removal of photospheric dust which may require non-equilibrium type processes. (Burgasser 2007). The temperature range of transition is around 100-200 K either side of 1200 K. The process which triggers this rapid transition is still an open question in the brown dwarf community with ideas centered around changes in cloud characteristics and structure (Marley & Cushing 2010, Saumon & Marley 2008). Table 1.3 shows the typical time evolution of brown dwarfs across the L/T boundary.

Mass	L0 to L8	L8 to T3	T3 to T8
0.05 $M_\odot$	1200 -1800 Myr	600 Myr	7 Gyr
0.03 $M_\odot$	200-300 Myr	100 Myr	3 Gyr

Table 1.3: Transition of Brown Dwarfs across the L/T boundary.

Very often L, T binaries are observed in which the primary star will dominate the spectrum and the binary will typically be 1 subclass younger in age.

1.4 Detection of Exoplanets

This section was written with reference to Pater & Lissauer (2010). The first discovery of planets outside our solar system (so called “exoplanets”) was made in 1992 by

Aleksander Wolszczan who deduced that the pulsar PSR 1257 had two planets orbiting around it. The first exoplanet to be discovered orbiting around a main-sequence star was 51 Pegasi b (Mayor & Queloz 1995) which is widely regarded as a prototype for "Hot Jupiters" and orbits its host star at a distance of approximately 0.53 AU (Mercury's orbit around our sun is 0.39 AU and that of Venus is 0.72 AU).

There are various methods by which exoplanets can be detected both directly and by indirect means. A summary of existing and possible proposed methods is shown in figure 1.2.

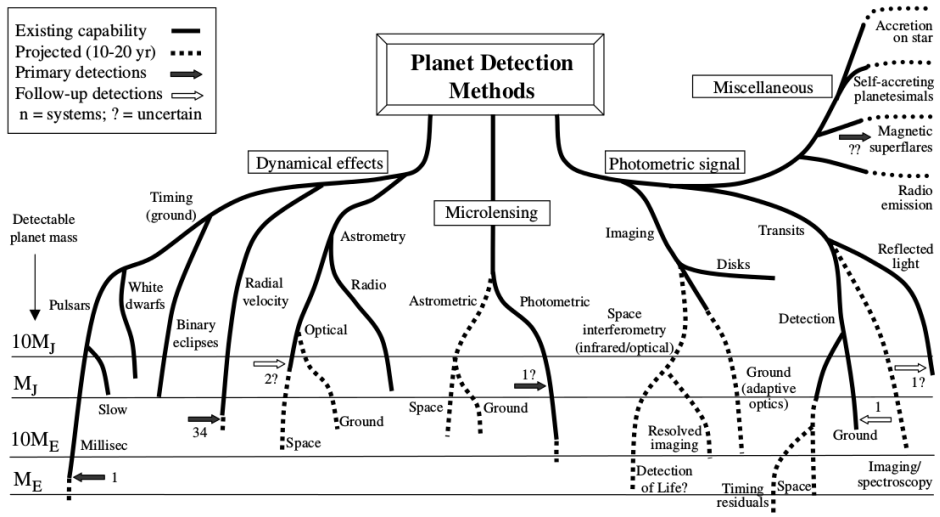

Figure 1.2: A summary of methods by which exoplanets can be detected, Perryman (2000).

As of August 2016, the Exoplanet.eu website lists a total of 2670 exoplanets confirmed using the transit method (section 1.4.1), 678 using the radial velocity method (section 1.4.2), 70 confirmed using direct imaging, 50 by microlensing and 23 using timing variations.

1.4.1 Exoplanet transit Method (Photometric Method)

The exoplanet transit method is a technique which uses photometry to study the flux output from a star-planet system over a period of time. As a planet passes in front of a star, the observed flux will decrease (primary transit). The transit technique can only detect planets which have orbits aligned edge on to the direction of viewing-thus around 98% of planets cannot be detected by this method as their orbits are not parallel to the line of sight of a telescope. The change in flux, ΔF is related to the radius of the eclipsing planet and its parent star by:

$$\frac{\Delta F}{F} = \left(\frac{R_{\text{planet}}}{R_{star}}\right)^2 \tag{1.1}$$

where F is the flux when the planet it not transiting in front of the star. This relation is derived by comparing the flux observed when the planet is away from the star and when it transits in front: the power of 2 is simply a result of flux, by definition been inversely proportional to surface area of the emitting body. The radius of Jupiter is

$\sim 0.1 R_{\odot}$. The dip in brightness of Jupiter passing front of our own star as observed by an observer outside of Jupiter's solar orbit will be $\sim 1\%$. For the earth passing in front of the sun the dip in brightness observed by an observer outside of the earths' solar orbit will be $\sim 0.01\%$. Hence the transit technique is only suited to planets which are orbiting close in to their parent star have planetary radii which are comparable to the radii of their parent star. Additionally the transit method is only suited to cases where the transit of the planet is near the line-of sight of the satellite or telescope aiming to observe it (Borucki & Summers, 1984).

1.4.2 Radial Velocity Method

51 Pegasi b was discovered using the Doppler radial velocity method using the ELODIE spectrograph on the Observatoire de Haute-Provence telescope based in south-east France. The radial velocity phase curve for 51 Pegasi is shown in figure 1.3.

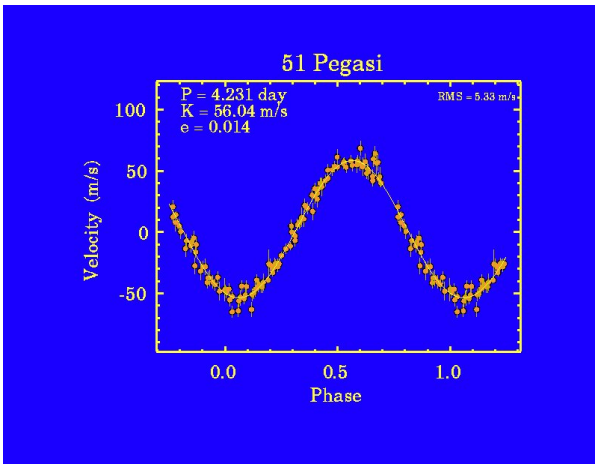

Figure 1.3: Radial Velocity Phase curve for 51 Pegasi which was used to discern the presence of 51 Pegasi b which has been widely accepted to be the first exoplanet discovered orbiting a main-sequence star. Image retrieved from exoplanets.org web-pages.

As a planet orbits around a star, the colloquially held belief is that the star is stationary-or for the purposes of calculations (particularly at school)- the star is assumed to be stationary. However, in practice both the star and planet orbit around the centre of mass of the planet-star system they form. Hence the star actually moves, aka "wobbles" as the planet orbits around. This "wobble" can be detected using the so-called "Doppler method" where the star's spectral lines are observed to be red shifted (as the star moves away from the observer) and blue-shifted (as the star moves towards the observer) in a periodic trend as the planet orbits.
For this method, in order to observe a measurable effect in the line position of spectral lines from a star the Doppler shift must be sufficiently large-this method favours large planets that have small orbits around their host stars.
Our very own sun "wobbles" by around 12.6 ms^{-1} For a Hydrogen α line, $\lambda_0 = 6563$ Å. The change in wavelength, $\Delta\lambda$ is given by:
$\delta\lambda = \lambda_0 \frac{v}{c} \sim 2.8 \times 10^{-4}$ Å where c is the speed of light.
A problem with this method is that very often wavelength of the star's spectral lines

are observed to oscillate without the presence of an exoplanet due to effects such as stellar oscillation. Hence the concept of the PLATO mission (Rauer et al. 2014) mentioned in section 1.8.3.

1.5 ExoMoons

Another interesting field of study which has developed from the search for exoplanets is the search for exomoons. This field has been pushing the boundaries of exoplanet detection by creating algorithms to thoroughly account for the systematic noise inherent in the Kepler satellite. David Kipping was a PhD student at UCL (2007-2011) who, under the direction of Professor Giovanna Tinetti developed techniques for detecting exomoons: this pioneering work won him several awards including the Royal Astronomical Society Keith Runcorn Prize (2012 and the Springer Thesis Prize for Outstanding PhD Research (2011). Since then he has worked at Harvard University, Smithsonian Institution and now Columbia University in the City of New York where he is leading the HEK (Hunt for Exomoons with Kepler) project which uses computer algorithms to search for bodies (moons) orbiting exoplanets. HEK is independently funded and has recently been able to purchase a new supercomputer (Michael Dodds Computing Facility) from donations through the science crowd funding website Petridish.org. The HEK project searches for exomoons by automatically selecting from KOIs (Kepler Objects of Interest) targets which could possibly host exomoons and then comparing their observed lightcurves to simulated lightcurves of a planet-only system and a a planet & moon system lightcurve. All of the comparisons are done within a Bayesian framework. In principle the project can detect planet binaries as well as distinct planet-moon systems (this definition is more of a continuum and can be defined in terms of position of the centre of mass of the two objects). Early pioneering work by Elser et al. (2011) of simulations of planet formation predicted that ExoMoons should form: hence with this in mind, the HEK project was created. A summary of the studies published to date by the HEK project are shown in table 1.4.

Reference	Title	Year
HEK-I	Description of a New Observational project	2012
HEK-II	Analysis of Seven Viable Satellite-hosting Planet Candidates	2013
HEK-III	The First Search for an Exomoon around a Habitable-zone Planet	2013
HEK-IV	A Search for Moons around Eight M Dwarfs	2014
HEK-V	A Survey of 41 Planetary Candidates for Exomoons	2015

Table 1.4: Summary of studies undertaken by the HEK project

Before the project started, Kipping et al. (2009) had done a test study of the Kepler data and demonstrated that moons of mass ≥ 0.2 $M_{\oplus}$ should be detectable. In contrast, the largest known moon in our solar system is Ganymede (which orbits Jupiter) which has a mass of 0.025 $M_{\oplus}$. Thus the project is searching for moons that are at least an order of magnitude larger in mass than any known in our own solar system.

HEK I discusses the TSA (Target Selection Algorithm) and TSP(Target Selec-

tion Prioritisation) algorithms developed to automatically search through the Kepler catalogue.

HEK II investigates 7 targets which were selected from 35 targets determined by the TSA from 2321 objects. The *LUNA* algorithm (Kipping et al. 2011a) was used to simulate model planet lightcurves: for each target 9 models were simulated using various parameters and constraints and *a prioris* with planet-only system, planet and moon system: additionally non-physical models were simulated. A Bayesian model selection was then undertaken and confirmation was obtained that this model selection was not favouring non-physical models (i.e. radius of moon set to zero). This model selection was looking for so-called TTVs: Transit Timing Variations which would be indicative of another mass perturbing the planet transiting in front of its' host star.

HEK III described the work undertaken in searching for an exomoon around Kepler 22b which is a planet in the so-called "Habitable zone". This target is advantageous as had previously been studied by astro-seismologists due to the low photometric noise in its' transit curve and multiple radial velocity measurements. This study utilised the CoFiAM algorithm(Cosine Filtering with Autocorrelation Minimization) to filter out various systematic effects and sources of noise as described in Kipping et al. (2013a). In summary no evidence was found for a moon larger than $0.2M_{\oplus}$ and furthermore, with the current availability and quality of lightcurve data only moons with mass greater than $1M_{\oplus}$ would theoretically be detectable.

HEK IV searched for planetary systems around 8 M dwarfs. A result of HEK IV was the discovery of the lowest mass exoplanet to date which highlights why this work is still important. It has been determined that this planet, KOI-314c has a mass of 1.0^{+4}_{-3} earth masses and a radius of $1.61^{+0.16}_{-0.15}$ earth radii.

HEK V found no evidence for exomoons in a study of 41 planetary KOIs. The authors do however note that when photodynamics is not used and instead only photometric transits alone are used, it could be incorrectly discerned that around 1 out of 4 of the KOIs could harbour exomoons due to the effects of signal noise inherent in the Kepler instruments. An ancillary result of this study is that 13 out of 41 KOIs have masquerading planet signals which are actually due to stellar variation and various systematics of the detection equipment. Hence this result helps justify the existence of the HEK project: even if no exomoons are detected, at the very least the algorithms generated have helped tease apart true planetary transit signals from false positives. In order to characterise exoplanets accurately using the transit method it is vitally important that all systematics affecting the transit curves are considered.

1.6 Characterisation of Exoplanets

Since the discovery of 51 Pegasi b in 1995 (Mayor & Queloz 1995) the field of exoplanetary science has blossomed with over 2000 exoplanets confirmed(as of February 2016) with a further 201 candidates which are classed as "controversial" as defined on the Exoplanets.eu website. Over 60% of these confirmed planets are transiting exoplanets and around 30% have been detected by the indirect radial velocity technique. This website can be used to generate histograms and scatter plots of data showing the inherent bias in the detection methods for finding large planets orbiting close-in

to their host stars. An analysis of the exoplanets detected to date can also potentially provide information on how planetary systems form and evolve in general.

However, an obvious next step for the field is to ask the question: "What do these exoplanets contain?". Is there life on other planets? In order to characterise the atmospheres of exoplanets, spectroscopy is needed as well as developments in modelling of atmospheres.

A modern description of spectroscopy is that it is the interaction between matter and radiation. However traditionally spectroscopy was thought of as the process by which visible light is split by prisms: for example the experiments on optics done by Newton. Joseph von Fraunhofer was a key player in the development of spectroscopy becoming a precise science with his development of disperse spectrometers. Today spectroscopy can be used in all areas of science to identify both atoms and molecules in samples by precise knowledge of the wavelengths that they emit or absorb.

Spectroscopy can be applied to the transit method of detection: by observing a planet orbiting its' host star changes in the transit depth at different wavelengths can be used to help deduce which molecules are in the planets' atmosphere using knowledge of which molecules absorb at particular wavelengths.

In exoplanetary modelling very often the process called "forward modelling" is used: by this we mean that a synthetic spectrum is generated using a computer programme for a whole range of model atmospheres which sample a huge range of parameters such as temperature, pressure and molecular composition. These synthetic models are then compared to real observations with the aim of hence placing constraints on what the atmosphere of the planet observed in question contains and its Temperature & pressure profiles. At present due to the lack of data covering multiple wavelength regions very often there are huge degeneracy's in the models selected. The opposite of this approach is to use "inverse modelling" in which a programme tries to "work backwards" to solve what the atmospheric profile is of an observed exoplanet. The geosciences literature contains many reviews explaining the difference between forward and inverse modelling applied to modelling scenarios such as along tectonic fault lines (Allmendinger, 1998), helioseismic modelling (Ritzwoller & Lavely, 1991) and also in understanding how light propagates through materials (Arridge & Schotland 2009).

NEMESIS (Irwin 2008), which is an acronym for "Non-linear optimal Estimator for MultivariateE spectral analysis", is an example of a program developed to create synthetic spectra for model atmospheres. It was originally developed by Professor Patrick Irwin for analysing data from the NASA Cassini spacecraft of Saturn and Titan. Since then it has been used for making predictions of exoplanetary atmospheres in the near Infra red to microwave regions.

UCL are developing a program called Tau-REx (Tau Retrieval of Exoplanets) which uses a Bayesian framework in order to select in an unbiased manner a model atmospheric composition from sampling a large sample space of input composition (Waldmann et al. 2015, 2016). Tau-REx will use all molecular data provided and make no assumptions about molecular composition or temperature thus sidestepping human bias. In order to model the (T, p) profile of a planet, Tau-Rex will combine the two commonly used approaches of writing an analytic equation for profile and

a “layer by layer” approach thus gaining the unique benefits of both methods. This programme will use linelists from the ExoMol project and is designed to make use of parallel computing so that it is fully scale-able for use in cluster computing sites. This work is described in Waldmann et al. 2015 in which the functionality of the programme is demonstrated for the cases of the Hot Jupiter WASP-76b and the SuperEarth 55 Cnc e.

To date several exoplanets have been studied intensively by astronomers wishing to characterise their atmospheres, for example, GJ 1214b, HD 189733b, HAT-P-32b & HAT-P-33b and WASP 33b. These are discussed in proceeding sections. Table 1.5 gives a summary of notable review papers in the field of the exoplanetary atmosphere characterisation.

Author(s)	Year	Title	Journal/Book
G. Laughlin, Gregory, J. J. Lissauer	2015	Exoplanetary Geophysics - An Emerging Discipline	Review chapter to appear in Treatise on Geophysics, 2nd Edition
K. Heng, A. P. Showman	2015	Atmospheric Dynamics of Hot Exoplanets	Annual Review of Earth and Planetary Sciences
K. Poppenhaeger	2014	Stellar magnetic activity and Star-Planet Interactions	Invited review for the CoRoT Symposium 3 / Kepler KASC-7 joint meeting, Toulouse, July 2014.
A. S. Burrows	2014	Spectra as windows into exoplanet atmospheres	Proceedings of the National Academy of Sciences
N. Madhusudhan, H. Knutson, J. J. Fortney & T. Barman	2014	Exoplanetary Atmospheres	Protostars and Planets VI
J. Bailey	2014	The Dawes Review 3: The Atmospheres of Extrasolar Planets and Brown Dwarfs	Publications of the Astronomical Society of Australia
A. S. Burrows	2014	Highlights in the study of exoplanet atmospheres	Nature
M. S. Marley, A. S. Ackerman, J. N. Cuzzi, D. Kitzmann	2013	Clouds and Hazes in Exoplanet Atmospheres	Comparative Climatology of Terrestrial Planets
G. Tinetti, T. Encrenaz, A. Coustenis	2013	Spectroscopy of planetary atmospheres in our Galaxy	The Astronomy and Astrophysics Review
F. Allard, D. Homeier, B. Freytag W. Schaffenberger, A. S. Rajpurohit	2013	Progress in modeling very low mass stars, brown dwarfs, and planetary mass objects.	Memorie della Societa Astronomica Italiana Supplement
F. Allard, D. Homeier, B, Freytag C. M. Sharp	2012	Atmospheres From Very Low-Mass Stars to Extrasolar Planets	EAS Publications Series
A. P. Showman, J. Y.K. Cho, K. Menou	2010	Atmospheric Circulation of Exoplanets	Exoplanets, edited by S. Seager
G. Chabrier, I. Baraffe, F. Allard & P. H. Hauschildt	2005	Review on low-mass stars and brown dwarfs	Invited review, "Resolved Stellar Populations", Cancun, april 2005

Table 1.5: Summary of Exoplanet & Brown dwarf atmospheric characterisation review papers

1.6.1 Super-Earth GJ 1214b

The "Super-Earth" GJ 1214b, originally nicknamed "The Water World" is a particular favourite of exoplanet scientists. Super-earths are commonly defined as planets with mass between 1.9 and 10 $M_{\oplus}$. GJ 1214b was found by Charbonneau et al. (2009) orbiting its host star GJ 1214 using the MEarth project which uses the technique of planetary transits to detect planets. Table 1.6 shows a sample of parameters for the planet and its' host star estimated by the authors in their original *Nature* paper assuming a thin outer envelope of hydrogen and helium with the remaining 95% of the mass of the planet been water.

Property		Estimate
Planetary	Mass	6.55 ± 0.98 $M_{\oplus}$
	Radius	2.678 ± 0.13 $R_{\oplus}$
	Gravitational Acceleration	8.93 ± 1.3 ms^{-2}
	Hydrodynamical Escape Rate	9×10^5 kg s^{-1}
	Orbital Period	1.5803925 ± 0.0000117 days
Planetary equilibrium temperature	Assuming a Bond albedo of 0	555 K
	Assuming a Bond albedo of 0.75	393 K
Stellar	Mass	0.157 ± 0.019 $M_{\odot}$
	Radius	0.2110 ± 0.0097 $R_{\odot}$
	Effective Temperature	$3{,}026 \pm 130$ K

Table 1.6: Parameters of the Super-Earth GJ 1214b and its' host star, GJ 1214 estimated by Charbonneau et al. (2009) assuming a solid core of water

Since this planet-star system is only 13 parsecs away it is accessible to be studied by spectroscopic analysis and has since been with over 130 papers as of December in the SAO/NASA Astrophysics Data System (ADS) referring to GJ 1214b. Of particular controversy is the "the flat spectrum" of GJ 1214b (Bean et al. 2010) which has sparked debate within the exoplanet community as very often any atmospheric model put forward is loaded with assumptions and at present it is difficult, if not impossible to break the degeneracies of parameters between model atmospheres.

To briefly summarise a choice selection of papers:

- Bean et al. (2010) performed a ground-bases transmission spectrum analysis between 780 and 1000 nm and concluded that, to a significance level of 4.9 σ, that the spectrum was featureless and hence must contain clouds that are obscuring any underlying features at the measured wavelengths. Furthermore a dense atmosphere of water vapour is consistent with the flat spectrum observed.

- Bean et al. (2011) put forward evidence for a metal-rich atmosphere by examining the transmission spectrum at optical and near infra-red wavelengths. They conclude from their cross-analysis of data that either GJ 1214b has an atmosphere composed of 70% H_2O(by mass) or contains optically thick clouds or haze at high altitude.

- Morley et al. (2013) have performed simulations of model atmospheres for GJ 1214b using two types of cloud cover which are physically motivated: a) clouds that are present in chemical equilibrium and b) clouds due to photochemical kinetic models. They conclude that the former type of clouds if present in the

upper-atmosphere and of enhanced metallicity can match the observations of GJ 1214b.

1.6.2 Hot Jupiter HD 189733b

The Hot Jupiter planet of HD 189733b was discovered by Bouchy et al. (2005) who were undertaking a joint photometric (transit) and radial-velocity search for exoplanets orbiting stars of high metallicity: they estimated its' mass and radius to be 1.15 ± 0.04 M_J and a radius of 1.26 ± 0.03 R_J respectively. It was the first planet to be found with visible scattered polarised light (Berdyugina et al. 2008). Since it is one of the closest transiting Hot Jupiter to earth known, and coupled with its short planetary transit of 2.219 days making it tidally locked it has thus been vigorously studied from an orbital dynamics and spectroscopic (atmospheric characterisation) perspective.

Again, to briefly summarise a choice selection of papers: Knutson et al. (2007) have constructed "a map" of the temperature and thermal transport on HD 189733b: they concluded that heat energy is effectively transported from the "dayside" to the "nightside" with a "dayside" temperature range between 973 ± 33 K and 1212 ± 11 K. In 2007, Tinetti et al. put forward the hypothesis that water vapour absorption in the atmosphere of HD 189733b was responsible for changes in effective radius when observed at infrared wavelengths of 3.6 μm, 5.8 μm and 8 μm. They also demonstrate in their paper that a so-called non-detection of water is the likely result of assuming an isothermal atmospheric temperature profile. In 2007, Swain et al. (also based at UCL) backed this claim of water detection with a resolved water band at 1.9 μm and also claimed the presence of methane in a near infra-red transmission spectrum taken of HD 189733b. The authors also note that models of Hot Jupiters predict also the presence of carbon monoxide that they were unable to observe hence potentially implying the need for new models including potentially photochemical reactions and/or horizontal chemical gradients.

1.6.3 HAT-P-32b & HAT-P-33b

The discoveries of HAT-P-32b and HAT-P-33b were reported by Hartman et al. (2011) and both orbit so called "high-jitter" stars which made their detection troublesome and hence required detailed photometric modelling of light curves. The authors noted that "both planets are among the largest radii transiting planets discovered to date". Their orbital periods were estimated by the authors to be 2.150008 ± 0.000001 days and 3.474474 ± 0.000001 days respectively. Indeed, the discovery of large Hot Jupiter planets orbiting close in to their host stars has sparked fresh debate and questioning as to the formation of our own solar system.

1.6.4 WASP-33b

Guenther et al. (2011) reported the detection of WASP-33b (also known as HD 15082b) using SuperWasp project which searches for exoplanetary transits. It orbits the A5 star of HD15082 with an estimated orbital period of 1.22 days and thus, to date is the hottest known exoplanet detected with an the initial estimated of effective

surface temperature being 2700 K. Since its' discovery, studies have been undertaken of heat distribution within its atmosphere. Ground based transit observation of Smith et al. (2011) in the 0.91 μm region of its luminosity profile indicated that it has a corresponding brightness temperature of 3620^{200}_{250} K which is consistent with a model in which there is very inefficient, if any at all distribution of heat from the tidally locked dayside to nightside of the planet. Furthermore, Haynes et al. (2015) presented spectroscopic evidence for a temperature inversion in this tidally-locked dayside which they hypothesis is due to the presence of TiO: if this is confirmed it would be the first hot Jupiter to have a thermal inversion due to this molecule.

1.7 Astrobiology

Due to the extensive efforts that have been made to characterise exoplanets a field of study which has developed is that of "Astrobiology". To quote Professor Peter Read (Oxford University) at a RAS(Royal Astronomical Society) meeting in London during March 2013 "Astrobiology can be viewed as an interesting new subject or an annoying distraction (!)."

A very notable paper uploaded to the Archive was that by Jacob Haqq-Misra(2013) who proposed a funding mechanism for searching for extra terrestrial intelligence (SETI) using a "lottery bond" for which maturity would occur when ETI was confirmed. In his paper he discusses ethical considerations and puts forward mathematical models of the funding structure. He concludes by noting that "In the best case, SETI succeeds; but even in the worst case, if SETI finds nothing, then it will at least have taught us how to think more seriously about our financial future". On a more serious note, a prominent figure in the emerging discipline of astrobiology is Professor Sara Seager who is based at MIT. Her work focuses on studying transiting exoplanets with a particular focus on modelling the photochemistry of atmospheres containing so-called "biosignatures" which are defined as gases such as methane whose simultaneous presence could possibly indicate the presence of life(Seager 2013, Seager, Bains & Hu 2013, Seager, Turner, Seager & Deming 2010, Schafer & Ford 2005).

1.8 Past, Present, Proposed and Future Satellites for Exoplanetary Study

Figure 1.4 shows a summary of present and future missions which will be used to study exoplanets. The future missions of TESS and the JWST are described below as well as the proposed missions of ARIEL and Twinkle.

1.8.1 TESS

TESS, Transiting Exoplanet Survey Satellite, selected by NASA in 2013 as an Explorer (EX) Mission, is due to launch between August 2017 and June 2018 and will be delivered into orbit by the Falcoln 9 rocket which has a track record of launching NASA and commercial satellites. TESS will be a two year survey which will monitor 50, 000 stars in the solar neighbourhood for transiting exoplanets. It is led by

Figure 1.4: Present and Future Exoplanet Missions

Dr. George Ricker and MIT and has "the principle goal" of "detecting "small planets with bright host stars in the solar neighbourhood". Since the stars surveyed will be 30-100 times brighter than those surveyed by Kepler, follow-on characterisation of atmospheres and determination of parameters such as planetary masses & radii should be enhanced. By statistical arguments, it is expected that from the 50, 000 stars surveyed, approximately 3000 transiting exoplanet candidates should be observed by TESS: in amongst these candidates it is reasonable to expect around 500 "Super-Earth" planets. The instruments onboard TESS will include 4 wide field CCS cameras which have been designed for photometric stability.

1.8.2 JWST

The James Webb Space Telescope (JWST) is, at present expected to launch in October 2018 and is a joint international effort between NAA, ESA and CAS(Canadian Space Agency). It is named after James Webb who is a former administrator of NASA. It will be a telescope operating in the infra-red (0.6 to 28.5 μm) with 4 instruments which will study over a 5-10 year lifetime a range of astrophysical environments. It is designed to be a follow-on to the Hubble space telescope(which operates in the visible and UV) with mission goals including searching for primordial galaxies formed closely after the Big Bang, tracking the evolution of galaxies and stars and also searching for life on other planets by the chemical and physical properties of exoplanetary systems. Upon been placed in an L2 orbit at approximately 1.5 million km from earth its' primary 6.5 m mirror will unfold from 18 different segments and will be protected from the damaging effects of our sun by a 5-layer sunshield the size of a tennis court. A notable tweet on twitter about the JWST is that of Dr Jo Barstow: "It'll be 15

DAYS after JWST arrives at L2 b4 telescope fully unfolded. 15 DAYS of TERROR. Every1 will be on blood pressure meds. "

Dr Jo Barstow, has undertaken work on constraining what quality of exoplanet atmosphere retrievals would theoretically be possible with the JWST: "Transit spectroscopy with JWST: Systematics, starspots and stitching", Barstow et al. (2015). This study investigates how data from the NIRSpec and MIRI-LRS instruments could be "stitched" together to help degeneracy's inherent within models of exoplanetary atmospheres provided that individual instrument noise as well as the effects of taking measurements at different times is considered. These instruments will operate at 0.6-5 μm and 5-12 μm respectively. Using the NEMESIS programme Barstow et al. (2013) created synthetic "single-slab" model atmosphere spectra for primary and secondary transits for different planetary objects shown in table 1.7 using the molecular data shown in table 1.8. For the "Earth" like planet they used a bulk composition of N_2-O_2 and for the other planets used a bulk H_2-He composition: for each of these planets they varied the concentration of the trace elements of CO_2, CO and CH_4. They then applied the expected noise levels expected from the instrument systematic on-board JWST before finally using NEMESIS to retrieve the input model atmosphere. The team then established the minimum concentrations of trace elements, as shown in table 1.9 for the various exoplanets required so that a single observation would correctly constrain the input model atmosphere within a statistical uncertainty of 2σ.

Planet	Mass(10^{24}kg)	Radius (km)
Hot Jupiter	1800	75000
Hot Neptune	180	30000
GJ 1214b	37	15355
"Earth"	6	6378

Table 1.7: Planetary objects considered by Barstow et al. (2013) considered for study by JWST.

Molecule	Source	Reference paper
H_2O	HITEMP2010	Rothman et al. (2010)
CO_2	CDSD-1000	Tashkun et al. (2003)
CO	HITRAN1995	Rothman et al. (1995)
CH_4	STDS	(Wenger & Champion (1998)
H_2/He	Borysow & Frommhold 1989; Borysow et al. 1989; Borysow & Frommhold 1990; Borysow et al. 1997; Borysow 2002	

Table 1.8: Molecular data used in the simulations of Barstow et al. (2013).

Gas	Hot Jupiter		Hot Neptune	
	Precision factor	concentration (ppmv)	Precision factor	concentration (ppmv)
H_2O	3	0.1	1.5	1
CO_2	2	0.5	3	10
CO	10	10	5	10
CH_4	3	0.1	2	0.1

Table 1.9: Minimum concentration required for trace elements in order for there to be a detection for a typical Hot Jupiter and Hot Neptune as determined by Barstow et al. (2013)

Barstow et al. have also studied how the presence of star spots observed in the primary transit may effect the orbital radius of the planet determined which is dependent on the wavelength observed. For M dwarfs with sunspots it is not appropriate to model the stellar spectrum using a Boltzmann distribution. Barstow also points out that as star spots may vary between the time of observations taken by the two instruments there is a need for a study of the time variability of individual star spots. The team also establish that the JWST could be used to distinguish between cloudy and cloud free atmospheres and the authors point out that, with the increasing characterisation work been undertaken within the research field, using cloud-free models is no longer a physically accurate interpretation. In summary the team highlight the need for planning on behalf of the exoplanet community in order that suitable targets are selected which would really make efficient use of the capabilities of the JWST. Since the JWST is not dedicated solely to exoplanetary science the community will be competing for observation time with astronomers working in competing fields.

1.8.3 The ECho Science Mission

Prior to studying the capabilities of the JWST, Barstow et al. (2013, 2014) studied what the capabilities for atmospheric retrieval of ECho would have been. ECho was a short-listed candidate mission for the M3 launch of the ESA's cosmic vision programme, PI'd by Professor Giovanna Tinetti. Again, using the technique of simulating synthetic spectra using NEMESIS, integrating in system noise (using the specially developed EChoSim programme) and then carrying out a retrieval Barstow et al. found that for planets with bulk H_2−He composition it would be possible using ECho to correctly detect the trace molecules of H_20, CO_2, CO and CH_4 within a certainty of 2σ and also retrieve the temperature profile within 200 K given the necessary data shown in table 1.10. For GJ 1214b no CO or NH_3 was included. Planets with a bulk H_2−He composition are those that lie close to their host star and thus have a composition which reflects the centre of the protoplanetary disc which they emerged from.

Planet				Host star	D	Data required
type	Mass (M_J)	Radius (R_J)	T_{eff} (K)			
Hot Jupiter	0.95	1.07	1500	G2(sun like)	35	single transit or eclipse
Warm Jupiter	0.95	1.07	650	G2	35	20 transits or eclipses
Hot Neptune	0.095	0.43	800	M dwarf	6	10 transits of eclipses
GJ 1214b	0.02	0.22	450	GJ 1214	13	30 transits

Table 1.10: Summary of deductions made about data required to successfully characterise different exoplanets by Barstow et al. (2013, 2014). Here D is the distance in pc to the system

Unfortunately ECho was not selected but instead PLATO, The PLAnetary Transits and Oscillations of stars was instead selected and is expected to launch in 2024. PLATO will search for planets orbiting in the so-called Habitable zone of their host stars as part of a survey searching for extrasolar planetary systems. PLATO will also be used to study seismic activity of stars: a very important consideration when trying to characterise exoplanets as at present it is very difficult to distinguish between host

star variability and variability in transit curves which is genuinely due to a planet passing in front of the star.

Following on from all the substantial scientific research which had been invested into ECho by the exoplanet community, two proposed missions, ARIEL and Twinkle have been created and are both been led by Prof. Tinetti.

1.8.4 ARIEL

ARIEL (Atmospheric Remote-sensing Infra-red Exoplanet Large-survey) is a proposed European Space Agency M4 mission which has been selected for further study along with THOR (Turbulence Heating ObserveR) and XIPE (X-ray Imaging Polarimetry Explorer) from 27 original proposals. From these three proposed missions, one will be selected and scheduled for launch in 2024 into the L2 orbit with a budget of around 450 million Euros. If ARIEL is selected it will study the atmospheres of around 500 planets which are orbiting close in to their parent stars within our galaxy using a 90 cm infra-red telescope. This telescope will cover the wavelength range from around 1.95 to 7.8 μm: additionally to aid the detection and characterisation of clouds there will be photometric bands in both the visible and near-IR which will also assist with the monitoring of stellar activity. Figure 1.5a shows a concept view of what ARIEL will look like if it is selected for flight.

1.8.5 TWINKLE

"Twinkle: A British Space Mission to Explore Faraway Worlds" is a proposed satellite which aims to investigate the atmospheres of target exoplanets by studying the wavelength region of approximately 0.5 to 5 μm (subject to refinement). This is a region in which molecules of significant importance to life (e.g. methane, ethane and precursors to amino acids such as ammonia and HCN) have important distinguishable features. Twinkle will observe around 100 nearby known exoplanets: by building up repeat measurements over multiple wavelengths over time of the planetary transits unprecedented information will be obtained about the atmospheres of these planets. It is been built by Surrey Satellites-a company which has a proven track record of delivering small scale, small cost missions on time and on budget. Since the satellite will be using "off the shelf" components the budget for research & development of detection technology is reduced. It will be placed in a a low-earth polar orbit 700 km above the earth's surface with a launch date been targeted within the next 4 years. Universities and Research Institutions throughout the UK are involved in the development of the payload study and science case including UCL Department of Physics and Astronomy & UCL Mullard Space Science Laboratory, Surrey Satellite Technology Ltd, Selex ES, STFC Rutherford Appleton Laboratory, STFC UK Astronomy Technology Centre, Cardiff University, Imperial College, Queen Mary University London, Royal Holloway, Open University, Oxford University, University of Hertfordshire, University of Leicester, University of East Anglia, Keele University, University of Manchester and Royal Observatory Edinburgh. Figure 1.5b shows a computer generated image of what Twinkle is designed to look like upon been built and launched into space. In terms of funding, the project has a budge of around 50

million pounds: at present the ongoing payload study is been funded by grants from various UK Universites and the European Research council. The Twinkle team is actively seeking funding from both private and public sources e.g. schemes such as crowdfunding which was a highly efficient means of raising capita for the case of the Lunar One module.

(a) (b)

Figure 1.5: Concept view of the ARIEL spacecraft, credit ESA (figure 1.5a) and a computer generated image of the Twinkle spacecraft (figure 1.5b) been built by Surrey Satellite Technology Ltd. Images retrieved from the website for the centre of planetary sciences(cps) based at UCL.

EduTwinkle

Alongside the scientific research work and money-raising efforts been undertaken to ensure that TWINKLE flies, a concerted effort is been put into developing an accompanying educational program, EduTwinkle which is been led by Dr Clara Sousa-Silva, a former PhD student of the ExoMol group. EduTwinkle covers all Key Stages with an emphasis on encouraging more girls to enter STEM careers. The IOP (Institute of Physics) undertakes a lot of research investigating why fewer girls choose to study A-Level physics ("It's different for Girls") and eventually university. EduTwinkle activities include:

- CPD (Continuing Professional Development) sessions run for Primary School teachers demonstrating how they can use the science in Twinkle to inspire their pupils.
- Twinkle's Little Stars (KS2/KS3)
- The Twinkle Challenge (KS4)-A challenge in which school pupils work as teams on activities that showcase how scientific missions are multi-disciplinary and thus how a science degree can lead to many career opportunities
- Exoplanet Explorers-AS level(KS5)-module aimed at getting pupils to understand the ethics of scientific work

- Work with the Brilliant Club which is an award-winning charity which places PhD and postdocs in state schools all over England with the aim of raising attainment
- ORBYTS (Original Research By Young Twinkle Students)-an initiative in which Year 12 and Year 13 students work with a PhD student within the ExoMol group on analyses experimental data which can then be used in the construction of new linelists

Engaging school pupils as well as the public in scientific missions is a worthwhile cause. The so-called "public" can also be potentially a substantial help in undertaking research: for example the Galaxy Zoo project. An example of a citizen science project in the field of exoplanets is that of the "Disk detectives" which asks users to examine images taken by the WISE spacecraft and determine if young stars contain dusty disks which could potentially harbour planets.

1.9 Existing Molecular Databases

Before the ExoMol project was created (Tennyson & Yurchenko 2012), there were and still are several other groups working in molecular spectroscopy on creating databases of molecular data that can be used by astronomers for characterisation purposes. The HITRAM, HITEMP and CDMS databases are discussed below. Other sources of molecular and atomic data include:

- SPECTRA, based in Tomsk
- GEISA Database
- NIST: Quantitative Infrared Database (Version 1.10), Chu, Rhoderick, Guenther & Lafferty)
- Pacific Northwest National Laboratory, Vapor phase infrared spectral library
- CHIANTI: An Atomic Database for Spectroscopic Diagnostics of Astrophysical Plasmas (Version 6)
- The University of Denver Atlas of High-Resolution IR Stratospheric Spectra
- SMPO (Spectroscopy and Molecular Properties of Ozone), Universitè de Reims, Reims, FRANCE, Institute of Atmospheric Optics, Tomsk, RUSSIA
- SpectralCalc.com, GATS, Inc.
- The Virtual Atomic and Molecular Database Consortium (VAMDC)
- Jet Propulsion Laboratory , Molecular Spectroscopy Catalog,
- Database of Bernard Plez
- The Kurucz databases
- The Submilimtetre IR experimental data recorded by the Ziury's Group based in Arizona

With all these databases available the obvious question to ask is: why is the ExoMol project needed? Put very simply these databases are typically only valid for molecules(and atoms) existing at room temperatures. As the temperature increases electrons within the molecules reach higher electronic states and molecules rotate & vibrate faster: hence new and more transitions occur between molecular states(which are a combination of electronic configuration, rotational state and vibrational state) as higher energy states are accessed. Also, often these databases only cover specific regions: in order to model the opacity of molecules within an atmosphere accurately all transitions between possible molecular states need to be known. And finally one of the key aims of the ExoMol project is high accuracy.

Prior to the creation of the ExoMol project in 2011, two of the most commonly used databases by astronomers for molecular data were the HITRAN and CDMS databases which are described in sections 1.9.1 and 1.9.2 respectively. These databases both aim to create self-consistent parameters for molecules using hybrids of all available experimental and theoretical data for each particular species.

1.9.1 HITRAN & HITEMP

The HITRAN (HIgh-resolution TRANsmission molecular absorption database) and HITEMP (HIgh-TEMPerature spectroscopic absorption parameters) projects are based at the Harvard-Smithsonian Centre for Astrophysics and led by Dr L. Rothman and Dr I. Gordon. The aim of the HITRAN projects is to produce spectroscopic parameters for molecules of interest to modelling the earths' atmosphere (180 to 300K) which are self consistent with all available experimental data. HITRAN is essentially a central database for wavelength data (measured in the vacuum) for molecules. HITEMP is the high temperature analogue and is in development: the aim of this project is to gather and compile data which can be used for exoplanets with higher atmospheric temperatures than the Earth. At present the HITRAN database (HITRAN 2012) contains data for 47 molecules(covering 120 isotopologues): a new version is due in 2016. These molecules are: H_2O, CO_2, O_3, N_2O, CO, CH_4, O_2, NO, SO_2, NO_2, NH_3, HNO_3, OH, HF, HCl, HBr, HI, ClO, OCS, H_2CO, HOCl, N_2, HCN, CH_3Cl, HOBr, C_2H_2, C_2H_6, PH_3, COF_2, SF_6, H_2S, HCOOH, HO_2, $ClONO_2$, NO^+, HOBr, C_2H_4, CH_3OH, CH_3Br, CH_3CN, CF_4, C_4H_2, HC_3N, H_2, CS and SO_3. Additionally the HITRAN project also contains cross sectional absorption data for around 38 molecules.

1.9.2 The Cologne Database for Molecular Spectroscopy (CDMS)

The CDMS database is a database of theoretical predictions of wavenumbers for both atoms and molecules which are of interest to astronomers and atmospheric scientists. As of November 2015 the database contains 788 entries. The diatomic hydride molecules and diatomic molecules found in the ISM and extragalactically contained in this database are shown in tables 1.11, 1.12 and 1.13 respectively.

Group	Molecules
1	NaH, KH
2	MgH
11	CuH, ^{65}CuH
12	^{66}ZnH, ZnH, ^{68}ZnH
13	BH, AlH
14	CH, CH^+, $^{13}CH^+$, CD^+, $^{13}CD^+$, CT^+, SiH
15	NH, ND, PH
16	OH^+, $^{18}OH^+$, OD^+, OH^-, $^{18}OH^-$, OD^-, SH, SH^+, SH^-
18	NeH^+, $^{22}NeH^+$, NeD^+, $^{36}ArH^+$, $^{40}ArH^+$

Table 1.11: Diatomic hyrides contained with the CDMS database as of November 2015.

Diatomic Hydrides	Other diatomics
H_2, HD	AlF, AlCl, KCl, NaCl
CH, CH^+, SiH?	C_2**, CN, CO, CO^+, CP, SiC, CF^+, CN
NH	PN, SiN
OH, OH^+,SH, SH^+	SiS, CS, NS
HF, HCl, HCl^+	NO, NO^+, SO, SO^+, SiO, O_2, PO, AlO
ArH^+	TiO, FeO?

Table 1.12: Diatomic molecules in the CDMS database which are commonly found in the Interstellar medium of Circumstellar Shells

Diatomic Hydrides	Other diatomics
ArH^+(2015)	CO, CO^+
H_2	CS
CH, CH^+	CN
NH	SO, SO^+
OH, OH^+	SiO
HF	NO
	NS

Table 1.13: Extragalactic diatomic molecules in the CDMS database

1.10 The ExoMol Database

The ExoMol project was created in May 2011 at UCL and is funded by a 5 year ERC Advanced Investigator fund awarded to Professor Jonathan Tennyson. The outline aims of the project are to provide linelists for molecules of astronomical importance which are of high accuracy and more complete than existing experimentally based databases (Tennyson & Yurchenko 2012). As the temperature of a molecule is increased, higher states can be reached and thus more transitions (i.e. "lines") are created.

Experimentally it is often very difficult, if not too dangerous to measure the spectra of molecules at temperatures exceeding 5000 K. As an example BeH and PH_3 are both toxic species but are of interest astronomically (Tennyson et al. 2016).

Hence why there is a need to use state-of-the are *ab initio* methods to solve the Schrödinger equation and hence produce a list of wavelengths and frequencies. Nevertheless, experimental data acts as a valuable "sanity" check and is indeed used to

refine theoretical predictions. The methane linelist, which is aptly named "10to10" as it contains 9.8 billion lines has proved very popular with the exoplanetary community due to its completeness. For example, Yurchenko et al. (2014) have applied this methane linelist to atmospheric models the T4.5 brown dwarf 2MASS 0559-14 and found that the opacities matched observations in places where previously they had either under or over-estimated the opacity. Since 2011 the expertise of the group has increased for both diatomic and triatomic and tetratomic molecules. Molecules for which linelists have been created, or are indeed in the process include: BeH, MgH, CaH, ScH, CaO, AlO, SiO, VO, TiO CS, NaCl, KCl, PH_3, H_2O_2, H_2S, SO_2, SO_3, CH_4, NH_3, HCN, HNC, nitric acid (HNO_3) and formaldehyde (H_2CO). With each conference, new molecules have been added to the "to do" list as the exoplanet community becomes more ambitious in their characterisation of far-away atmospheres. Collaborations with industry have been formed such as that with Alexander Fateev based at the Technical University of Denmark who wishes to make in-situ measurements of gases such as SO_2 and SO_3 which are a by-product of coal-based power plants. Due to the size of the linelists generated, the need to make our linelists accessible and of an appropriate format to be put into atmospheric models has been recognised and addressed with the creation of cross-sections (Hill, Yurchenko & Tennyson 2013) and also the creation of the "ExoMol Database paper", Tennyson et al. (2015).

Chapter 2

Theory and Methodology

In this chapter important concepts in molecular spectroscopy will be summarised and then hence used to explain how linelists for diatomic molecules are constructed. Before studying molecules, it is useful to understand atomic spectroscopy which is detailed in section 2.1. Molecular spectroscopy is then explained in section 2.2 with the selection rules which determine allowed transitions detailed in section 2.3. The Born-Oppenheimer approximation is outlined in section 2.4: this approximation allows the construction of linelists to be done in several distinct parts as it decouples the Schrödinger equation into an "electronic" Schrödinger equation and a rovibronic Schrödinger equation. These sections have been written in reference to Haken & Wolf(2004), Brown (1998) and Bransden & Joachain (2000). The challenges of constructing linelists for transition-metal bearing diatomics is discussed in section 2.5. Moving onto methodology, section 2.6 explains how the electronic Schrödinger equation was solved using the *ab initio* program `MOLPRO` and section 2.9 explains how the rovibronic Schrödinger equation was solved using the in-house program Duo.

2.1 Atomic Spectroscopy

Starting with the case of the Hydrogen atom, in the classical picture, electrons orbit around the nucleus (composed of a single proton) in atomic shells which can be thought of as regions of probability in which an electron can be found at any one time. These shells are labelled by their principle quantum number $n = 1, 2, 3, 4$ which describes how far away it is from the nucleus. The famous Rydberg formula describing the so-called "gross structure" of the Hydrogen atom is as follows:

$$\frac{E_n}{hc} = -R\frac{1}{n^2} \tag{2.1}$$

where $R = 1 \times 10^7$ m$^-$1 the Rydberg constant, h is the Planck constant, c is the speed of light and E_n is the energy of the shell with principle quantum number n. When an electron falls from a higher shell (n_i) into a shell lower in energy (n_f), a photon is emitted which is of energy equal to the energy gap between these two energy shells:

$$\frac{\Delta E}{hc} = -R(\frac{1}{n_i^2} - \frac{1}{n_f^2}). \tag{2.2}$$

Within each shell labelled by n there are subshells which are labelled by l, the angular momentum quantum number which describes the shape of the subshell. The value of the angular momentum quantum number l can take on any integer value from 0 to $n-1$. By historic conventions, the subshells defined by l for each shell are labelled as s, p, d, f etc with s subshells having a spherical shape and p orbitals been dumb-bell shaped: there are three of them, p_x, p_y and p_z which can be thought of as three "dumb-bell" shaped regions of space aligned along the x, y and z directions respectively.

For the case of the Hydrogen atom the subshells within a shell have the same energy. For the case of atoms larger than Hydrogen, the subshells have different energies. The idea of electron configuration refers to how electrons are arranged in these subshells within an atom. Since electrons are fermions they have to obey the Pauli Exclusion Principle which means that no two electrons can be in the same spin-subshell (refereed to as spin-orbital from herein) at the same time: i.e. two electrons both with spin up cannot occupy the same s orbital. An electron can have a spin of either "spin-up" or "spin-down". To overcome this constraint of quantum mechanics, electrons therefore "pair" up in subshells. The number of electrons which can fill a subshell is $2(2l+1)$. Hence s subshells can house two electrons, p orbitals can house 6 electrons and d orbitals can house 10 electrons etc. When filling the subshells, electrons obey the Aufbau Principle which states that they will fill subshells in order of increasing energy. For the case when electrons fill the p orbitals (and d, f orbitals etc) the electrons will typically fill each of the p_x, p_y and p_z orbitals each with spin up first as this is energetically favourable as electrons will repel each other due to both having a negative charge. As an example of describing electronic configuration, for an Argon atom the electron configuration can be given as:

$$1s^2 2s^2 2p^6 3s^2 3p^6 \tag{2.3}$$

where

- $1s^2$ indicates that there are 2 electrons occupying the s subshell of the $n=1$ shell.
- $2s^2$ indicates that there are 2 electrons occupying the s subshell of the $n=2$ shell.
- $2p^6$ indicates that there are 6 electrons occupying the three p subshells of the $n=2$ shell.
- $3s^2$ indicates that there are 2 electrons occupying the s subshell of the $n=3$ shell.
- $3p^6$ indicates that there are 6 electrons occupying the three p subshells of the $n=3$ shell.

This electronic configuration stated in terms of the Principle Quantum Number n and the angular momentum quantum number l is referred to as the "central field approximation" with corresponding Hamiltonian H_0. The atomic term value is determined

by the so-called "valence" electrons of the atom: these are the electrons which occupy unfilled shells. The notation for an atomic "Term" value is

$$^{2S+1}L \tag{2.4}$$

where S is the total spin and L is the total orbital momentum of the electrons for the respective atomic state. In standard notation, the value of L is represented by the letters S, P, D etc corresponding to $L = 0, 1, 2$ respectively. J is the total angular momentum, $L + S$ which takes integer or half-integer values from $-|L+S|$, $-|L+S| + 1$, ... $|L+S| - 1$, $|L+S|$

The "vector model" is a graphical method to illustrate how the various angular momenta within an atom or molecule couple together. It can be used to show the vectors representing various angular momenta couple together and thus precess around an axis defined through the centre of the atom or molecule. In terms of perturbation to the gross structure, residual electrostatic interactions lead to splitting of atomic terms defined by L (total angular momenta of all the electrons) and S (total spin momenta of all the electrons). As a further perturbation, spin-orbit coupling in which **L** and **S** couple together leads to energy levels defined by the quantum number **J**. Finally, an external magnetic field can split these energy levels into states defined by the quantum number M_J which can take the values $M_J = -J, -J+1, .., J-1, J$ provided it is weaker than the internal spin-orbit interaction (Zeeman Effect). The Paschen-Back effect occurs when the External magnetic field is strong enough that it breaks the coupling between L and S.

2.2 Molecular Spectroscopy

As two atoms join together to form a diatomic molecule, electrons which are in closed atomic shells will typically remain in these shells. The valence electrons will, however become distributed throughout the molecule and form molecular orbitals. As is the case of atoms, when an electron redistributes itself to another orbital a photon will be emitted when the new orbital energy is lower than the first. For a molecule, its state is not only an indication of its electron configuration: it also indicates how it is rotating and vibrating. Hence in molecules, as well as changes in electronic energy state, there are additionally two other forms of transitions of state which can occur: vibrational and rotational. For the case of a diatomic molecules, the vibrational motions can be described in terms of the vibrational quantum number ν and the rotational motion in terms of J. By conservation of energy, when a diatomic either starts vibrating slower of rotating at a slower rate, there must be energy emitted: i.e a photon. We can approximate the relative sizes of these transitions.

If we assume that the valence electrons are confined within an area of length a we can approximate that, via the Heisenberg Uncertainty Principle, the momentum of these electrons is $\approx \frac{\hbar}{a}$. Hence the electronic energy of these electrons will be of the order $E_e \approx \frac{p^2}{2m_e} = \frac{\hbar^2}{2m_e a^2}$ which, if we assume $a = 2a_0$ is $\approx 30\ 000\ \text{cm}^{-1}$. To approximate the order of magnitude of the vibronic energy of a molecule, if we assume that the vibrations follow simple harmonic motion then the vibrational energy is of

order for an inter-nuclear separation of x is $U(x) = \frac{1}{2}\mu\omega_\nu^2 x^2$ where μ is the reduced mass of the two nuclei and ω_ν is the harmonic angular frequency. It can be assumed that when a molecule dissociates (i.e. $x = a$), the vibronic energy will be of the same order as the electronic energy i.e. $U(a) \approx E_e$. Hence by simple algebra it can thus be shown that the virbonic energy of a molecule is $E_\nu = \hbar\omega_\nu = \sqrt{\frac{m}{\mu}}E_e$. Finally for the rotational energy of a molecule, if we assume that the angular momentum $L = I\omega_r$ where ω_r is the angular rotational frequency and I is the moment of inertia given by $I = \mu a^2$, is of the order $\hbar$ then it can be shown that the typical rotational energy of a molecule is of the order $E_r \approx \frac{m}{\mu}E_e$.

Hence in summary it can be expected that the separate electronic, vibrational and rotational energy level transitions occur in different regions of the electromagnetic spectrum. It should however be noted that often the vibrational and rotational transitions are coupled and hence called "rovibronic transitions".

Moving onto notation, the notation for molecular electronic states is analogous to atomic term values and is given by:

$$^{2S+1}\Lambda^{+}. \tag{2.5}$$

Here S is the electronic spin of the molecule in a given electronic molecular state-for reference its projection onto the inter-nuclear axis is Σ. Λ is the projection of the total orbital angular momentum along the inter-nuclear axis: for Σ, Π and Δ states its value is $0, 1$ and 2 respectively. In the case of atoms, spherical symmetry can be assumed. However, for the case of diatomic molecules this symmetry is "broken" by the inter-nuclear axis. Hence states with $\Lambda > 0$ are doubly-degenerate. Classically this can be explained by the fact that electrons spinning either clockwise or anti-clockwise around the axis will have the same energy hence the states been doubly degenerate. For the case of $\Lambda = 0$, Σ^+ and Σ^- states are distinct in energy. In the molecular term, $(+)$ refers only to Σ states and describes the reflection properties of the molecular orbitals through a plane containing the inter-nuclear axis. As an example of this notation, a $^6\Sigma^+$ state has $\Lambda = 0$ and total electronic spin of $\frac{5}{2}$, with projections of $(-5/2, -3/2, -1/2, 1/2, 3/2, 5/2)$ along the inter-nuclear axis. For the case of homonuclear molecules, subscripts gerade (g) and ungerade (u) which indicate if the total wavefunction of the molecule is symmetric or anti-symmetric respectively under reflection through the centre of mass of the molecule.

As is the case in an atom, molecular terms can be split by couplings of angular momenta (such as spin-orbit) and also by the presence of external magnetic and electric fields. The work that is been undertaken in understanding the splitting of molecular energy levels by external magnetic fields for astrophysics applications by the HotMol is described in sections 3.4 and 9.2. Also hyperfine splitting can occur which is the result of the interaction of the nuclear spin acting on the various electronic momenta. For the MnH molecule hyperfine splitting can be pretty significant: this was investigated experimentally by Varberg for his PhD thesis (see section 6.2). A summary of quantum numbers which are frequently used to describe the various momenta within a diatomic molecule are shown in table 2.1.

Type of Momenta	Meaning
$\mathbf{L}$	Total electronic orbital momentum
$\mathbf{S}$	Total electronic spin
$\mathbf{J_a} = \mathbf{L} + \mathbf{S}$	Total electronic momentum
$\mathbf{J}$	Total angular momentum of system
$\mathbf{N} = \mathbf{J} - \mathbf{S}$	Total angular momentum of system minus total electronic spin
$\mathbf{R} = \mathbf{N} - \mathbf{L} = \mathbf{J} - \mathbf{S} - \mathbf{L}$	Total angular momentum of nuclei

Table 2.1: Summary and Description of Angular Momentum Quantum numbers used to describe the state of a diatomic molecule.

Refer to table 2.1. By definition $\mathbf{R}$ is always perpendicular to the inter-nuclear axis. In describing diatomics, limiting idealised cases in which the different angular momenta couple in different ways are referred to as Hund's cases. Hund's cases are idealised, simplified cases where certain angular momenta coupling terms dominate over others. Each of the Hund's cases give rise to so-called "good quantum" numbers which are defined when the eigenvector of the momenta operator and its associative eigenvalue are constants of motion. Hence they can be adequately used to describe well-defined energy levels which, by Ehrenfest's Theorem, will remain constant as the Time-depedent Schrödinger equation evolves.

In Hund's case(a) the spin-orbit coupling between $\mathbf{L}$ and $\mathbf{S}$ is sufficiently weak such that they instead individually couple to the the electrostatic field produced by the two nuclear charges. $\mathbf{L}$ couples electrostatically to the internuclear axis by the electrostatic field set up by the nuclei. The projection of $\mathbf{L}$ on the inter-nuclear axis is Λ. $\mathbf{S}$ couples to the internuclear axis by the magnetic field generated by the electrons orbiting the internuclear axis: it's projection is given by Σ which can take the values of $\Sigma = -S, -S+1, -S+2....., S-2, S-1, S$. Hence, using the vector model, both L and S independently precess around the inter-nuclear axis (z) forming two "cones" which add together to form $\Omega = \Lambda + \Sigma$. (We can define Ω in this case as both Λ and Σ are constants of motion). $\mathbf{\Omega}$ then couples with $\mathbf{R}$ (total angular momentum of nuclei) to form $\mathbf{J}$(total angular momentum of system) which precesses around the axis Z. In this case the total angular momentum of the system is given by $\mathbf{J} = \mathbf{\Omega} + \mathbf{R}$ i.e. J takes the values $J = \Omega, \Omega+1, \Omega+2.....$ Taking the example of a $^3\Pi$ state, the value of $S = 1 (2S+1 = 3)$ so hence $\Sigma = -1, 0, 1$. By definition of a Π state, $\Lambda = 1$ so hence Ω can take the values of 0, 1 and 2. If a molecule contains a a nucleus with a high charge then spin-orbit coupling may be significant. For a case (a) molecule the rotational energy levels will have rotational energy levels described as $BJ(J+1)$ where B is the rotational constant.

In Hund's case (b), $\mathbf{L}$ is strongly coupled to internuclear axis (little z)-hence Λ is still a so-called "good quantum" number in this case. By definition, Σ states which have $\Lambda = 0$ obey Hund's case (b). But unlike in Hund's case (a), the S is not coupled the inter-nuclear axis. Instead $\mathbf{L}$ and $\mathbf{R}$ couple to form $\mathbf{N}$. $\mathbf{N}$ then couples with $\mathbf{S}$ to form $\mathbf{J}$ which precess around the Z axis. In this case good quantum numbers are Λ, N, S and J. For case (b) molecule the rotational energy levels will have rotational energy levels described as $BN(N+1)$ where B is the rotational constant.

In practice, usually molecules can alternate between been adequately described as obeying Hund's case (a) or (b). (It should be noted there are other cases (c), (d) and

(e) but these are less common. In general molecules that are rotating slowing are best described as Hund's case (a) and those that are rotating at a greater rate as Hund's case(b)).

2.3 Selection Rules and Transition Strengths

The probability of a transition between two molecular states is related to the transition dipole moment operator acting between them. It can be shown that when applying this operator between the wavefunctions of the two respective states, that the probability of a transition occuring can be decomposed into three parts, namely:

1. The Electronic transitional probability.
2. The Franck-Condon Factor describing the vibrational probability.
3. The Hönl-London factor which describes the probability of transitions within individual P, Q and R branches (see below).

To carry out this decomposition, it is assumed that the wavefunction describing the state of the molecule can be approximated as being decomposed into three wavefunctions describing the electronic motion, vibrational motion and rotation motion. It is assumed that both the electronic and vibrational wavefunctions only depend on the inter-nuclear distance R only with the rotational wavefunctions depending on the angular co-ordinates θ and ϕ. The key result from carrying out these integrals over the wavefunctions and transition dipole moment operator is the derivation of selection rules which govern which transitions are actually allowed to take place. The selection rules can be derived by use of "Ladder Operators" and known identities. For a diatomic molecule, it can be shown that the selection rules are as follows for transitions between different molecular states:

$$\Delta\Lambda = 0, \pm 1 \tag{2.6}$$

$$\Delta S = 0 \tag{2.7}$$

$$\Delta J = 0,\ \pm 1,\ \text{with } J = 0 \rightarrow 0 \text{ forbidden} \tag{2.8}$$

The selection rules on J, gives rise to P, Q and R branches which are defined as:

$$R : J' - J'' = +1 \tag{2.9}$$

$$Q : J' - J'' = 0 \tag{2.10}$$

$$P : J' - J'' = -1 \tag{2.11}$$

where J' refers to the upper state and J'' refers to the lower state. It should be noted that selection rule, Eq. 2.7 can break down if the nuclear charge is significant leading to so-called "forbidden transitions" e.g. singlet-triplet transitions. The Franck-Condon Factor is simply the integral over the inter-nuclear distances of the two vibrational wavefunctions of the two states in question. The Franck-Condon Principle states that

the intensity of a transition between two states will be largest where the wavefunctions overlap at the same inter-nuclear distance.

2.4 Producing a Linelist: Solving the Schrödinger Equation for a molecule

Refer to figure 2.2 which outlines the generic process employed within the ExoMol project to produce a linelist for a molecule of interest whereby the Born-Oppenheimer approximation is implicitly employed. The state of a molecule is described using the formalism of quantum mechanics by use of the Schrödinger equation,

$$\hat{H}\Psi = E\Psi \tag{2.12}$$

where $\hat{H}$ is the Hamiltonian describing the molecule and Ψ and E are the energy eigenvectors and eigenvalues respectively with Ψ describing the wavefunction of the molecule (Lodi & Tennyson 2012). For the case of a diatomic molecule with nuclei A and B the non-relativistic Hamiltonian is:

$$\hat{H} = \hat{V}_{Ae} + \hat{V}_{Be} + \hat{V}_{ee} + \hat{V}_{AB} + \hat{T}_A + \hat{T}_B + \hat{T}_e \tag{2.13}$$

where $\hat{V}$ terms represent the potential energy between nuclei and electrons (Ae and Be), between electrons (ee) and between the two nuclei (AB). The $\hat{T}$ terms represents the kinetic energy of nuclei A, B and electrons e. Figure 2.1 shows a schematic of a diatomic molecule in which the inter-nuclear distance, R is represented: it is the distance between the two nuclei which varies as the molecule vibrates and, in the case of higher-order rotation may also increase (centrifugal distortion).

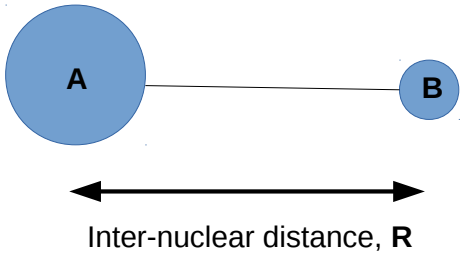

Figure 2.1: Pictorial representation of a diatomic molecule with nuclei A and nuclei B separated by an internuclear distance, R.

Written out in full, these operators are:

$$\begin{aligned}\hat{H} = &-\sum_{i=1}^{n}\frac{Z_A e^2}{4\pi\epsilon_0|\mathbf{R}_A-\mathbf{r}_i|}-\sum_{i=1}^{n}\frac{Z_B e^2}{4\pi\epsilon_0|\mathbf{R}_B-\mathbf{r}_i|}+\\ &\sum_{j<i}\sum_{i=1}^{n}\frac{e^2}{4\pi\epsilon_0|\mathbf{r}_i-\mathbf{r}_j|}+\frac{Z_A Z_B}{4\pi\epsilon_0|\mathbf{R}_A-\mathbf{R}_B|}\\ &-\frac{\hbar^2}{2M_A}\nabla_A^2-\frac{\hbar^2}{2M_B}\nabla_B{}^2-\sum_{i=1}^{n}\frac{\hbar^2}{2m_e}\nabla_i^2\end{aligned} \tag{2.14}$$

Here Z_A and Z_B refer to the charges of nuclei A and B respectively, R_A, R_B, r_i represent the position of nuclei A and B and the i$^{\text{th}}$ electron (molecule of n electrons) respectively from the origin of a chosen co-ordinate system. Referring to Eq. 2.14 it can be seen that the nuclear-nuclear ($\hat{V}_{AB}$), electron-nuclear ($\hat{V}_{Ae}+\hat{V}_{Be}$) and electron-electron ($\hat{V}_{ee}$) interaction terms are of approximately the same order. Generally speaking, a two-body problem can be solved exactly: however for any system with a greater number of particles approximations must be made. In the context of solving the Schrödinger equation for a molecule with N nuclei, the universally accepted approximation made is the Born-Oppenheimer approximation. The Born-Oppenheimer approximation exploits the fact that $m_e \ll m_p$ ie the mass of an electron, $m_e = 9.11 \times 10^{-31}$kg is of order 10^{-4} that of the mass of the proton, $m_p = 1.67 \times 10^{-27}$ kg. Hence it can be assumed that electrons will respond instantaneously to any changes of position of the nuclei which are composed of both protons and neutrons with $m_p \approx m_n$ where m_n is the mass of a neutron. For the case of a diatomic nuclei, changes in the position of the nuclei need only be described by one parameter, the inter-nuclear distance R.

The key result of the Born-Oppenheimer approximation is that the Schrödinger equation describing the state of a molecule, $\hat{H}\Psi = E\Psi$ can be decoupled into two equations, namely the electronic equation

$$\hat{H}_e(\mathbf{r},\mathbf{R})\chi(\mathbf{r},\mathbf{R}) = E_e\chi(\mathbf{r},\mathbf{R}), \tag{2.15}$$

and the nuclear (rovibronic) equation

$$[\hat{T}_n + E_e(\mathbf{R})]\phi(\mathbf{R}) = E\phi(\mathbf{R}). \tag{2.16}$$

It should be noted that in the literature there is some ambiguity over exactly what the approximation is: however on a simplistic level, the decoupling of the Schrödinger equation into an electronic and rovibronic equation is pragmatically the most important result. The Born-Oppenheimer approximation assumes that nuclear motion is very slow compared to electron motion and that the nuclei are effectively stationary when an electronic transition takes place. The result of solving the electronic Schrödinger equation, Eq. 2.15, is a set of potential energy curves (PEC), dipole moment curves (DMC) describing electronic states along with the electronic angular momenta couplings ($\hat{l}_x, \hat{l}_y, \hat{l}_z$) and spin-orbit couplings ($\hat{H}_{\text{SO}}$) between them. For the case of a diatomic molecule, a PEC and DMC describes how the electronic energy, given by E_e and total dipole moment of a molecule in a specific electron configura-

tion (state) changes with inter-nuclear distance R. In the electronic Schrödinger, Eq. 2.15, $\chi(\mathbf{r}, \mathbf{R})$ represents the electronic wavefunctions which are a function of both the inter-nuclear distance $\mathbf{R}$ and the position of the electrons represented by the quantity $\mathbf{r}$. More generally for triatomic or larger molecules, these functions are replaced by a surface which is simply the energy or dipole moment plotted against two co-ordinates describing the position of nuclei using a convenient co-ordinate framework. Within the Born-Oppenheimer framework, for each PEC (i.e. list of E_e values for range of inter-nuclear distances $\mathbf{R}$) generated by solving the electronic Schrödinger, 2.15, the nuclear Schrödinger equation, Eq. 2.16 is then solved.

Applying the Born-Oppenheimer framework to the case of CrH, the electronic Schrödinger equation, given by Eq. 2.15 is solved by use of *ab initio* methods implemented in the quantum chemistry package `MOLPRO` (Werner and Knowles 2012) and the nuclear Schrödinger equation, Eq. 2.16 is solved by use of the in-house programme Duo (Yurchenko et al. (2016). The programme Duo has been developed specifically for solving the nuclear equation for transition-metal diatomics using the programme TROVE (Yurchenko, Thiel, Jensen 2007) as guidance.

For CrH (or indeed any transition metal hydride) it would not be appropriate to use the nuclear programme LEVEL (Le Roy 2007) due to the high spin (multiplicity 6) of the ground state $^6\Sigma^+$ and also due to the nature of electronic structure i.e. manifolds of low-lying coupled electronic states.

Using the PECs calculated in `MOLPRO`, Duo calculates rovibronic energy levels. These are then matched to experimental data and thus the PECs are then semi-empirically refined. Typically, experimental data is in the form of a list of transition frequencies with assigned quantum numbers-Duo can fit to this or alternatively, to a set of energies generated from the experimental frequencies using the programme MARVEL (Furtenbacher, Csàszàr, and Tennyson 2007).

Duo performs a variational calculation whereby the sum of squares residual for the *ab initio* data to the experimental data and to a functional form is minimised. Using these fitted functional forms (e.g. Morse potential) for each PEC along with the respective dipole moment curves, Duo then calculates rovibronic wavefunctions and intensities for transitions in the form of Einstein A coefficients. Hence combining the list of rovibronic energy levels with the respective Einstein A-coefficients, a list of transition energies and frequencies, ie a linelist is thus produced.

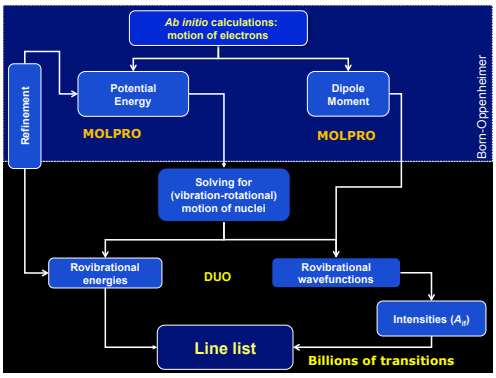

Figure 2.2: Overall process to produce a linelist.

2.5 Producing a Linelist for Open-shell transition metal diatomic hydrides

It should be noted that the production of linelists for transition-metal bearing diatomics is still very much at the developmental stage compared to that of triatomic and tetratomic molecules. At present there are no routine procedures for solving both the electronic Schrödinger equation and rovibronic Schrödinger equation for transition metal containing molecules. In larger molecules containing elements such as H, O, N, C, S, P very often there is typically one low-lying electronic ground state with many excited states high up in energy and non-interacting. Solving the electronic Schrödinger equation for these molecules for the ground state PEC is thus usually reasonably straightforward: the tricky and computationally challenging part is solving the rovibronic Schrödinger equation which typically involves undertaking a transformation of co-ordinates, expanding a kinetic energy operator within a basis set and diagonalising matrices of the order 10^6. For transition-metal bearing diatomics, the situation is the reverse. Due to the myriad of low-lying electronic states within these molecules which couple together via angular momenta and spin-orbit coupling, solving the electronic Schrödinger equation is often the most challenging part. Indeed studies talk about transition metals been an interesting "theoretical playground". In terms of solving the rovibronic Schrödinger equation, the in-house program Duo (section 2.9) had to be created as there was no such program which could deal with coupled electronic states of high multiplicity.

2.6 Solving the Electronic Schrödinger equation

For any electronic calculation, in general there are two factors which affect the accuracy of the result namely the level of theory (e.g. HF, MP2, CCSD (T), MRCI) used and the size of the basis set used. The basis set used act as the "building blocks" for constructing the electronic wavefunctions: as the size of the basis set is expanded the answer obtained will converge to what is called the "complete basis set limit (CBSL)". These two factors can be conveniently plotted on a so-called 'Pople' diagram. In the limit of infinte basis set and higher-order theory, the solution obtained should converge to the exact solution. John A. Pople was a recipient of the Nobel Prize for Chemistry in 1998 for his work on computational methods in quantum chemistry: he shared the prize with Walter John who was awarded it for his work on developing density functional theory, DFT. Figure 2.3 shows a typical Pople diagram for reference.

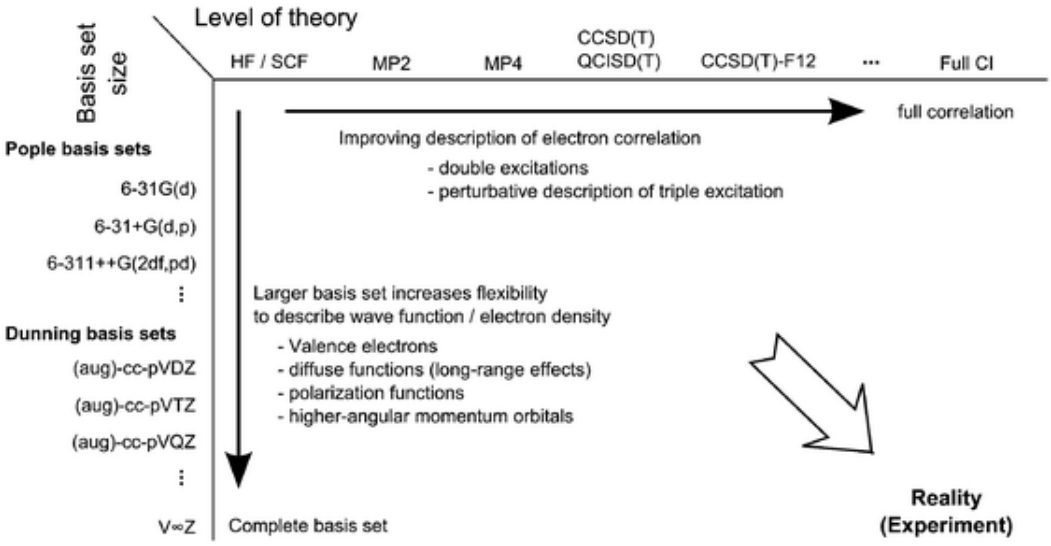

Figure 2.3: An example of a Pople Diagram the concept of which was introduced by John A. Pople who was the joint recipient of the Nobel Prize for Chemistry in 1998.

The Pople diagram can be used to extrapolate results in 2 dimensions: if the effect of changing a basis set at one level of theory is known and the effect of changing method for a single basis set is known then a prediction can be made about upgrading both a basis set and level of theory simultaneously without the need to run expensive calculations.

2.6.1 Electronic Basis sets

For a given *ab initio* method, the level of accuracy obtained is dependent on the size of the basis set employed. The basis set is simply a series of basis functions which are used to generate wavefunctions i.e. act as building blocks. Gaussian functions are typically used as basis functions owing to their desirable integral qualities which is paramount in determining the speed of *ab initio* calculations as most *ab initio* methods make frequent use of Gaussian integrals. The most simplest type of Gaussian Basis sets used is the $STO-nG$ family where n is an integer. The most popular Gaussian basis sets which are used are:

- Pople basis sets such as 6-31G
- Dunning family of basis sets, cc-pVNZ which are optimized for MP2 calculations
- Jensen Basis sets of the form pc-n which are optimized for DFT calculations

In this work a correlation-consistent basis sets of the form cc-pVNZ developed by Dunning et al. was used where "N" denotes the size of the basis set. Here the "cc-p" is an abbreviation for "correlation-consistent polarized". These are also "valence-only" basis functions which is signified by the "V". The progressive series of basis sets within this family are denoted cc-pVDZ, cc-pVTZ, cc-pVQZ, cc-PV5Z, etc where "D", "T", "Q" and "5" represent "double", "triple", "quadruple" and "5" respectively. These define the number of separate functions used for describing the valence region of electrons. These basis sets are designed such that as the size of the set is increased, the CBSL is

converged to. However, it should be noted that when "moving up" a basis set within a family towards towards the CBSL, more flexibility is introduced in the orbitals hence there is more likely to be problems with convergence. Typically these basis functions are used to solve problems involving organic chemistry which is typically concerned with the study of large molecules: for these molecules there is typically a low-lying ground state with any excited states relatively high up in energy such that they are of less significance for the study. Hence these basis functions have thus been optimised for use in studying low-lying ground states of large molecules. For the application of diatomic transition metal hydrides which have many low-lying excited states, these basis functions can be "augmented" by adding so-called "diffuse' functions to thus create the family of aug-cc-pVNZ basis functions.

2.6.2 Level of Theory

There is a myriad of quantum chemistry *ab initio* methods which can be used to solve the electronic Schrödinger equation. As was stated in section 2.4 to solve any problem with more than two particles, approximations must be used. Generally speaking, for the case of solving the electronic Schrödinger equation for a molecule, various *ab initio* methods are available. Discretion is needed as to which method is most appropriate for the given molecule of interest and the level of accuracy desired or, more prudently which is feasible given the computational resources available. The various *ab initio* quantum chemistry methods have been implemented into various quantum chemistry packages such as Gaussian, QChem, GAMESS, TURBOMOLE, MOLPRO, MOLCAS, NWChem, Dalton and CFOUR. It should be noted that this is by no means an exhaustive list. Each quantum chemistry package available, either commercially or through open source has its own speciality/(ies). Throughout this project `MOLPRO` (H.J. Werner and P. J. Knowles, 2012) was used as the MRCI method has been developed significantly within this package.

It should be noted that whichever method or package is used to solve a problem, the Variational Principle will always apply:

$$E_{\text{ground state}} \leq E_{\text{guess from method}}. \tag{2.17}$$

Hence, as a consequence of the Variational Principle, a calculation will never compute an energy which is lower than the true value. When the size of the basis set used is increased, the energy calculated will get lower and approach the true value as you reach the CBSL. The derivation of the Variational Theorem can be found in any standard quantum physics textbooks: the derivation involves taking derivative of wavefunctions to find a minimum by varying the coefficients of the functions used to describe the total wavefunction.

Slater Determinants, Hartree-Fock, CASSCF and MRCI theory

One of the most simplest type of calculation which can be performed is the variational method of Hartree-Fock. However, this method is only applicable to the ground state of molecules and as we are interested in the ground but also excited states for CrH & MnH, Hartree-Fock is not adequate. Hence higher-order methods are required:

in this project Multi-Reference Configuration Interaction (MRCI) calculations were undertaken.

The Hartree-Fock method is one, if not the simplest method which can be used to solve for the motion of electrons orbiting within atoms or molecules. The key features of the Hartree-Fock method are:

- It is a Variational method using the Self-Consistent Field (SCF) method.
- A single Slater Determinant is used.
- No relativistic effects are included.
- No electron correlation (as defined within the chemistry community) is incorporated.

For the case of a molecule which has n electrons with positions denoted by $\mathbf{r}_1$, $\mathbf{r}_2$,....$\mathbf{r}_n$ each occupying an orbital denoted ϕ_i, a wavefunction, Ψ of the simplest form which can be used to describe them is:

$$\Psi(\mathbf{r}_1, \mathbf{r}_2, ...\mathbf{r}_n) = \phi_1(\mathbf{r}_1)\phi_2(\mathbf{r}_2).....\phi_n(\mathbf{r}_n) \tag{2.18}$$

Here electrons are each positioned in a unique "spin" orbital. Note each "space" orbital can occupy two electrons. Since electrons are classified as indistinguishable particles, the total electronic wavefunction must obey the Pauli Exclusion Principle. As a consequence, the total wavefunction must be anti-symmetric with respect to the swapping of two electrons, i.e. the sign of the total wavefunction must change upon exchanging two electrons. In the above notation, placing electron 1 in orbital 2 is denoted by $\phi_2(\mathbf{r}_1)$.

For the example of a two electron system, a very simple way to make the total wavefunction antisymmetric with respect to exchange of electrons is to expand simple wavefunction as follows:

$$\Psi(\mathbf{r}_1, \mathbf{r}_2, ...\mathbf{r}_n) = \phi_1(\mathbf{r}_1)\phi_2(\mathbf{r}_2) - \phi_1(\mathbf{r}_2)\phi_2(\mathbf{r}_1) \tag{2.19}$$

For the case of a larger system, the Pauli Exclusion Principle can be satisfied by introducing the antisymmetric operator such that the total wavefunction becomes:

$$\Psi = \hat{A}[\phi_1(\mathbf{r}_1)\phi_2(\mathbf{r}_2).....\phi_n(\mathbf{r}_n)] \tag{2.20}$$

This is known as a Slater Determinant. A determinant matrix has the essential required property for this application that if you swap a pair of rows or columns, the determinant is left unchanged. The Hartree-Fock method uses a single Slater Determinant. The starting Ansatz (guess) for a Hartree-Fock solution is:

$$\phi_i = \sum_k^N c_{ik}\chi_k \tag{2.21}$$

where χ_k = is a basis function and c_{ik} are the coefficients of the Basis functions to be used in the orbital i. Thus c_{ik} is a matrix of coefficients. It should be noted that the basis functions within a basis set are not always ortho-normal. If basis functions

are orthogonal then the inner product of any two different basis functions is zero i.e. $\langle \chi_i \chi_k \rangle = 0$ for all i, k where $i \neq k$. If the basis functions are ortho-normal then there exists no linear dependence between between basis functions i.e. it is not possible to write one basis function as linear sum of the others and the inner product of a single basis function is unity. As an example of non-orthogonal basis functions, diffuse basis functions will often have some inherent linear dependence between them as they are describing the physics of dissociation.

Molecular orbitals, ϕ_i on the other hand are always defined to be ortho-normal.

In Hartree-Fock theory the total wavefunction Ψ_{total} is simply one single Slater Determinant which is a product of molecular orbitals ϕ_i. In Hartree-Fock theory these molecular orbitals are varied by varying the coefficients c_{ik}. In MCSCF and MRCI theory, the total wavefunction Ψ_{total} is a linear sum of Slater Determinants each denoted by Ψ_j. The total wavefunction is thus given by $\Psi_{\text{total}} = \sum_j C_j \Psi_j(\phi(k))$. In MCSCF theory both the coefficient C_j and c_{ik} are varied. In CI theory, the molecular orbitals ϕ_i are kept constant (i.e. c_{ik} are not varied) but the coefficients of each Slater Determinant C_j is varied.

For further reading on the MCSCF method the following resources should be consulted:

H. J. Werner and W. Meyer, J. Chem. Phys. 73, 2342 (1980)
H. J. Werner and W. Meyer, J. Chem. Phys. 74, 5794 (1981)
H. J. Werner and P. J. Knowles, J. Chem. Phys. 82, 5053 (1985)
P. J. Knowles and H. J. Werner, Chem. Phys. Lett. 115, 259 (1985)

and for the MRCI method:

H. J. Werner and E.A. Reinsch, J. Chem. Phys. 76, 3144 (1982)
H. J. Werner and P.J. Knowles, J. Chem. Phys. 89, 5803 (1988)
P. J. Knowles and H. J. Werner, Chem. Phys. Lett. 145, 514 (1988)

2.7 Calculation of *Ab initio* Curves in MOLPRO

Ab initio calculations for the electronic Schrödinger equation, given by Eq. (2.15) were performed using the quantum chemistry package MOLPRO for the diatomics of CrH and MnH. The result of these calculations are potential energy curves, dipole moment curves and coupling curves for the various interactions. These curves are calculated by calculating the relevant parameter (i.e. energy for the case of PEC, dipole moment for the case of DMC) at a set inter-nuclear point R. The matrix of inter-nuclear points used in this project is outlined in section 2.7.1. For any calculation of molecular states, knowledge of atomic and molecular term values is required: this is presented in sections 2.1 and 2.2 respectively. The C_{2v} symmetry point group framework that is utilised in MOLPRO is then described, along with its ramifications in section 2.7.2. In order to deduce what molecular states are of interest below a pre-defined energy level, knowledge of atomic dissociation limits for the hydrogen and relevant transition metal atom are needed. The process for deducing which molecular states are to be calculated for each molecule is described in section 2.7.3. Sections 2.7.4 and 2.7.7 then outline the molecular states of interest for CrH and MnH respec-

tively along with full description of their implementation into a MOLPRO calculation.

2.7.1 Grid of inter-nuclear points

For each calculation run during the project a matrix of inter-nuclear distances, R, consisting of 88 points ranging from 0.70 to 10.0 Å was used. A summary of this matrix is shown in table 2.2 which shows how the points were distributed from R = 0.7 Å to R= 6.20 Å. The remaining points were 6.50, 6.70, 7.00, 7.20, 7.40, 7.50, 7.70, 8.00, 8.50, 9.00 and 10.00 Å.

Range (Å)	Spacing (Å)
$0.70 \leq R \geq 1.20$	0.10
$1.20 \leq R \geq 1.65$	0.05
intermediate point	1.66
$1.68 \leq R \geq 1.76$	0.01
intermediate point	1.78
$1.80 \leq R \geq 3.00$	0.05
$3.0 \leq R \geq 5.00$	0.10
$5.0 \leq R \geq 6.20$	0.20

Table 2.2: Summary of matrix of inter-nuclear distances used in calculations throughout the project.

Table 2.2 shows how the R values were distributed such that more points were calculated between 1.65 and 1.80 Å as this is the region of the minima for the majority of PECs for both CrH and MnH. Indeed for both molecules it was found that most of the PECs important behaviour was between approximately 0.90 and 4.00 Å with most PECs reaching their respective dissociation limits by R=5.00 Å.

2.7.2 Description of the C_{2v} framework

To aid efficiency of calculations, MOLPRO makes use of symmetry point groups: for our case of diatomic metal hydrides, the relevant point group is C_{2v} symmetry which has 4 symmetry components namely A_1, B_1, B_2 and A_2. Hereafter, in line with MOLPRO notation these will be referred to as symmetries 1,2,3, and 4 respectively. Naturally, the point group which a diatomic molecule belongs to is $C_{2\infty}$. However, for the purposes of computation this is a non-Albelian group (i.e. rules of commutation do not apply) so hence for this reason the makers of MOLPRO set up the code using the reduced C_{2v} point group.
Mathematically speaking, a symmetry point group is simply a collection of symmetry components which together as a group obey the axioms required to be a point group. Each symmetry component is defined to have certain properties relating to reflections, denoted by σ and rotations about the principle axis, X, Y, Z. For the C_{2v} symmetry point group these properties are shown in table 2.3.

SYM	SYM	$\sigma_\nu(xy)$	$\sigma_\nu(yz)$	Linear functions (Rotations)	Quadratic functions	Cubic functions
A_1	1	+1	+1	z	x^2, y^2, z^2	z^3, x^2y, y^2x
B_1	2	+1	-1	X,R_y	xz	xz^2, x^3, xy^2
B_2	3	-1	+1	Y, R_x	yz	yz^2,y^3,x^2y
A_2	4	-1	-1	R_z	xy	xyz

Table 2.3: Definition of C_{2v} symmetry (Willock 2009).

For practical purposes, the consequences of working within the MOLPRO C_{2v} symmetry framework is that atomic orbital (e.g. s, p, d orbitals) and molecular states (e.g. Σ^+, Σ^-, Π and Δ) belong to the four symmetry components, irrespective of their spin(multiplicity). Table 2.4 demonstrates how s, p and d atomic orbitals are assigned to the 4 symmetries within the C_{2v} framework and hence table 2.5 then summarises how the different components of the p and d orbitals add. Table 2.6 lists out which molecular states have components in the 4 symmetries.

Atomic Orbital	E	$C2(z)$	$\sigma_\nu(xz)$	$\sigma_\nu(yz)$	Symmetry
s	+1	+1	+1	+1	1
p_x	+1	-1	+1	-1	2
p_y	+1	-1	-1	+1	3
p_z	+1	+1	+1	+1	1
d_{xy}	+1	+1	-1	-1	4
d_{xz}	+1	-1	+1	-1	2
d_{yz}	+1	-1	-1	+1	3
$d_{x^2-y^2}$	+1	+1	+1	+1	1
d_{z^2}	+1	+1	+1	+1	1

Table 2.4: Assignment of atomic electron configuration orbitals to symmetries 1, 2, 3 & 4 within the C_{2v} framework

orbital	sym1	sym2	sym3	sym4
s	1	0	0	0
p	1	1	1	0
d	2	1	1	1

Table 2.5: Atomic s, p, d electron configuration orbitals symmetry assignments within the C_{2v} symmetry framework

Symmetry	Molecular states
1	Σ^+, Δ, Γ, ...
2	Π, Φ, ...
3	Π, Φ, ...
4	Σ^-, Δ, Γ, ...

Table 2.6: MOLPRO C_{2v} framework: electronic state classification

Hence the main consequence of using this framework is that, as an example for a Π molecular state, a calculation for both a symmetry 2 state and a state of symmetry 3 need to be performed. Theoretically the values of properties such as energy and dipole moment produced by these calculations should be numerically the same within

the convergence thresholds selected. Also for a Δ molecular state a calculation for both symmetry 1 and symmetry 4 needs to be undertaken.

2.7.3 Deduction of Molecular states to be calculated for diatomic hydrides

Before any *ab initio* calculations can be undertaken, we first need to establish which molecular electronic states are expected to be of greatest interest and important ie determine a list of electronic states which are theoretically expected to be present up to a pre-defined energy limit. For the purpose of this project, it was agreed that we focus on molecular states that converge to atomic dissociation limits below approximately 20 000 cm^{-1} were of primary concern. This limit was chosen as it corresponds to an astronomical range beginning at 0.5 μm heading into the infrared which is most concern to astromers studying L type dwards in which CrH has been detected (see section 3.4). Also, it can be shown that energy levels of 20 000 cm^{-1} have a corresponding Boltzmann factor of 2×10^{-7} at a typical L dwarf temperature of 2000 K so hence are unlikely to be populated. Table 2.7 shows the lowest lying atomic term values for the hydrogen atom.

Configuration	Term	J	Energy (cm^{-1})
$1s$	^2S	1/2	0.00000 00000
$2p$	$^2P^0$	1/2	82 259.9191133
		3/2	92 259.2850014

Table 2.7: H atom dissociation energy limits

Hence referring to table 2.7, it can be assumed that for the diatomic metal hydride molecules studied, the electron associated with the Hydrogen nucleus will have a configuration of $1s$.

2.7.4 Deduction of Molecular states to be calculated for CrH

Using data from the NIST website, the lowest lying atomic-dissociation limits with respective atomic term values and atomic electronic configurations for the Hydrogen and Chromium atom are presented in tables 2.7 and 2.8 respectively.

Configuration	Term	J	E_J (cm^{-1})	E_0 (cm^{-1})	Molecular States	
$[Ar]3d^5(^6S)4s$	a^7S	3	0.0000	0.0000	$X^6\Sigma^+$	$^8\Sigma^+$
$[Ar]3d^5(^6S)4s$	a^5S	2	7 593.1484	7 593.1484	$A^6\Sigma^+$	$^4\Sigma^+$
$[Ar]3d^44s^2$	a^5D	0	7 750.7465	8 090.1903	$^6\Sigma^+(III)$	$^4\Sigma^+(II)$
		1	7 810.7795		$^6\Pi$	$^4\Pi$
		2	7 927.4410		$^6\Delta$	$^4\Delta$
		3	8 095.1842			
		4	8 307.5753			
$[Ar]3d^5(^4G)4s$	a^5G	2	20 517.4222	20521.4036	$^6\Sigma^+(IV)$	$^4\Sigma^+(III)$
		6	20 519.5515		$^6\Pi(II)$	$^4\Pi(II)$
		3	20 520.9029		$^6\Delta(II)$	$^4\Delta(II)$
		4	20 523.6290		$^6\Phi$	$^4\Phi$
		5	20 523.8999		$^6\Gamma$	$^4\Gamma$

Table 2.8: Chromium atom dissociation energy limits and list of respective electronic molecular states expected for CrH up to approximately 20 000 cm^{-1}.

In tables 2.7 and 2.8, configuration refers to the atomic electron configuration of the respective neutral atoms where the Aufbau principle is used to fill the electron orbitals. An explanation of the notation used is given in section 2.1. For the case of the Chromium atom, which has 24 electrons, the first 18 electrons fill the $1s$, $2s$, $2p$, $3s$ and $3p$ atomic orbitals forming an "Argon inner-shell" denoted by [Ar] which has configuration $1s^22s^22p^63s^23p^6$ in standard atomic notation. In table 2.8 the values of E_J can be averaged in a "weighted average" sum to obtain a value of E_0 by Eq. 2.22:

$$E_0 = \frac{\sum_J (2J+1)E_J}{\sum_J 2J+1}. \tag{2.22}$$

For the a^7S and a^5S term values the value of E_0 is simply 0.000 cm^{-1} and 7 593.1484 cm^{-1} respectively as there is only a single value of J. For the case of the a^5D the value of E_0 is 8090.1903 cm^{-1}.

For a set of two atomic dissociation terms, the molecular states which are expected to arise from them can be deduced by applicaiton of the Wigner-Witmer or correlations rules (Zare 2007). Hence, we have a list of electronic states of which the aim is to calculate *ab inito* potential energy curves, dipole moment curves and couplings for.

2.7.5 Specifying the Electronic Configuration for CrH

In the `MOLPRO` package, the electronic configuration of each of the desired electronic states needs to be specified. This is done by specifying the number of `closed` and occupied, `occ` orbitals which can simply be thought of as the "core" orbitals and the sum of the "core" and valence orbitals respectively. The syntax is `closed,sym1, sym2, sym3, sym4` where `sym1, sym2, sym3, sym4` denotes the number of orbitals within each of the four symmetries respectively. Similarly for occupied (`occ`) orbitals. The desired orbitals are deduced by considering the electron configuration within the C_{2v} framework.

Referring to table 2.8 the relevant electron configuration for the outer orbitals of the molecule CrH correspond to the Cr atom been in the configurations $3d^54s^1$ and $3d^44s^2$

and as discussed the single electron associated with the hydrogen nuclear having configuration $1s$. It is assumed that the inner electrons within the CrH molecule form a configuration of that of the argon atom namely $1s^2 2s^2 2p^6 3s^2 3p^6$.
Hence for the molecule CrH, the electron configuration ie closed and occupied orbitals for the molecular electronic states we are interested in is simply $5220 - 9331$ as demonstrated in table 2.9.

Configuration	Atomic Orbitals	C_{2v} Symmetry			
		1	2	3	4
Argon configuration	$1s^2$	1	0	0	0
	$2s^2$	1	0	0	0
	$2p^6$	1	1	1	0
	$3s^2$	1	0	0	0
	$3p^6$	1	1	1	0
TOTAL INNER ELECTRONS		5	2	2	0
Valence configuration	$4s^{1 \text{ or } 2}$	1	0	0	0
	$3d^{5 \text{ or } 1}$	2	1	1	1
	$1s$(from H nucleus)	1	0	0	0
TOTAL VALENCE ELECTRONS		4	1	1	1
TOTAL OCCUPIED ELECTRONS		9	3	3	1

Table 2.9: Deduction of closed and occupied orbitals for CrH

2.7.6 Specification of "wf" card for CrH

Owing to the C_{2v} symmetry framework employed by `MOLPRO`, electronic states are calculated by specifying a `wf` card. Put simply, a `wf` card is a description of the multipliicty and symmetry of a desired electronic state. The form of the `wf` card is as follows:

```
wf, number of electrons, symmetry, 2S
```

For the CrH molecule, the number of electrons is simply 25 where 24 electrons are associated with the Chromium nucleus and the 1 electron from the Hydrogen nucleus. The "symmetry" is either 1, 2, 3, 4 as defined in section 2.6. Referring to table 2.6, the ramification of using C_{2v} framework is that, as an example for a Π state, two `wf` cards need to be specified-one with symmetry 2 and the other with symmetry 3. Theoretically the values of properties such as energy, dipole moment produced by these two wf cards should be numerically the same within the convergence thresholds selected. Ditto for Δ states with the symmetries required been symmetry 1 and symmetry 4. Finally, within the `wf` card, $2S$ is simply the multiplicity minus 1. So for a state of multiplicity 6, $2S$ is 5, for multiplicity 4, $2S$ is 3 etc. To fully clarify table 2.10 shows the different "wf" cards required for the various types of molecular states calculated for CrH.

Molecular state	"wf" card(s) required
$^4\Sigma^+$	25, 1, 3
$^4\Pi$	25, 2, 3 and 25, 3, 3
$^4\Delta$	25, 1, 3 and 25, 4, 3
$^6\Sigma^+$	25, 1, 5
$^6\Pi$	25, 2, 5 and 25, 3, 5
$^6\Delta$	25, 1, 5 and 25, 4, 5
$^8\Sigma^+$	25, 1, 7

Table 2.10: Specification of "wf" cards required to calculate the various molecular states of interest for CrH.

For the case of multiple states requiring the same `wf` card the option `state, value` is inserted. As an example for the simultaneous calculation involving a single $^6\Sigma^+$ and single $^6\Delta$ state the relevant `wf` cards required are:

```
wf,25, 1, 5; state,2
wf,25, 4, 5; state,1
```

where the Δ state will have components in both symmetry 1 and symmetry 4 and the Σ^+ state is simply within symmetry 1.

For a $^6\Sigma^+$ state the only `wf` card required is simply `wf, 25, 1, 5`. As a further example for clarity for the calculation of three $^6\Sigma^+$ states and a single $^6\Delta$ state, the required `wf` cards are:

```
wf,25, 1, 5; state,4
wf,25, 4, 5; state,1.
```

In this case, one of the energy values produced by the `wf,25, 1, 5;state,4` card will theoretically be numerically the same as that produced by the `wf,25, 4, 5;state,1` card-this corresponds to the Δ state. The other states within the `wf,25,1,5;state,4` will simply be the Σ^+ states. It should be noted that the ordering of states, which is done by `MOLPRO` based on energy can change due to crossing particularly as the internuclear distance, R approaches zero and hence the potential energy of that particular state goes asymptotically to infinity.

To define some important notation for proceeding results, hereafter a "multiplicity-symmetry block" will simply refer to "wf" card which has multiple states eg the 'multiplicity-symmetry block" for a "`wf`" card of:

```
wf,25, 1, 5; state,2
```

is simply 6, symmetry 1 (remembering that in the `wf` notation 5 here refers to $2S$: the multiplicity of a state is given by $2S+1$ which for this case is 6 ie sextet state. In a plot of PECs (or any other curves) produced from using this `wf` card the curves will be labelled as:

6, symmetry 1, state 1 and

6, symmetry 1, state 2

respectively.

There is an option within `MOLPRO`, `lqaunt`, which can be used within the CASSCF calculation, but not CI calculation to specify the λ value desired which is 0,1 and 2 for Σ, Π and Δ states respectively. Based on previous experience, it was decided not to use this option but as further investigative work this option could be explored.

2.7.7 Deduction of Molecular states to be calculated for MnH

In a similar manner for CrH, the molecular states for MnH which are expected to dissociate to the various atomic dissociation limits below approximately 20 000 cm^{-1}(see section 2.7.3 for discussion) can be deduced by inspection of the atomic dissociation limits for the Mn atom and also the H atom. As discussed in section 2.7.3 for the electron associated with the hydrogen nuclei within a diatomic metal hydride it can be assumed that it will occupy a $1s$ atomic orbital. Table 2.11 shows the first four low-lying dissociation limits for the Manganese atom.

Configuration	Term	J	E_J (cm^{-1})	E_0 (cm^{-1})	Molecular States		
$3d^5 4s^2$	a^6S	2.5	0.000	0.000	$^5\Sigma^+$	$^7\Sigma^+$	
$3d^6(^5D)4s$	a^6D	4.5	17 052.29	17 301.21	$^5\Sigma^+(II)$	$^7\Sigma^+(II)$	
		3.5	17 282.00		$^5\Pi$	$^7\Pi$	
		2.5	17 451.52		$^5\Delta$	$^7\Delta$	
		1.5	17 568.48				
		0.5	17 637.15				
$3d^5(^6S)4s4p(^3P^o)$	z^8P^o	2.5	18 402.46	18 571.73		$^7\Sigma^+(III)$	$^9\Sigma^+$
		3.5	18 531.64			$^7\Pi(II)$	$^9\Pi$
		4.5	18 705.37				
$3d^6(^5D)4s$	a^4D	3.5	23 296.67	23 509.22	$^5\Sigma^+(III)$	$^7\Sigma^+(II)$	
		2.5	23 549.20		$^5\Pi(II)$	$^7\Pi(III)$	
		1.5	23 719.52		$^5\Delta(II)$	$^7\Delta(II)$	
		0.5	23 818.87				

Table 2.11: Manganese atom dissociation energy limits and list of molecular states for MnH which dissociate to these.

As for the case of the Chromium atom, a value of E_0 as given by Eq. 2.22 can be calculated for the each term value for the Manganese atom: these values are shown in table 2.11 along with the molecular states for MnH which are expected to dissociate to them. The decision was made to initially calculate the molecular states that dissociate to the first three atomic limits of the Manganese atom. However upon later discovery of experimental data for higher lying $^5\Sigma^+$ and $^5\Pi$ states dissociating to the a^4D term, calculations were done for these states as well as the $^5\Delta$ molecular state of MnH dissociating to this particular atomic dissociation limit.

2.7.8 Specifying the Electronic Configuration for MnH

As can be seen from table 2.11, the first two dissociation limits and the fourth (ordered in terms of increasing energy) for the Manganese atom have electrons in the $3d$ and $4s$ orbitals: the third dissociation limit has electrons occupying the $3d$, $4s$ and $4p$ atomic orbitals. Deduction of the closed and active space for these two different configurations within the C_{2v} framework imposed within `MOLPRO` is shown in table 2.12.

Orbitals		C_{2V} Symmetry			
		A_1	B_1	B_2	A_2
closed	$1s^2$	1	0	0	0
	$2s^2$	1	0	0	0
	$2p^6$	1	1	1	0
	$3s^6$	1	0	0	0
	$3p^6$	1	1	1	0
Total closed		5	2	2	0
Active	$4s^2$	1	0	0	0
	$3d^5$	2	1	1	1
	$1s^1$ (H)	1	0	0	0
Total active		4	1	1	1
Total occupied		9	3	3	1

(a)

Orbitals		C_{2V} Symmetry			
		A_1	B_1	B_2	A_2
closed	$1s^2$	1	0	0	0
	$2s^2$	1	0	0	0
	$2p^6$	1	1	1	0
	$3s^6$	1	0	0	0
	$3p^6$	1	1	1	0
Total closed		5	2	2	0
Active	$4s^1$	1	0	0	0
	$3d^5$	2	1	1	1
	$4p^1$	1	1	1	0
	$1s^1$(H)	1	0	0	0
Total active		5	2	2	1
Total occupied		10	4	4	1

(b)

Table 2.12: Electronic configurations for low-lying states of diatomic molecule MnH
(a) Closed and Occupied orbitals for the molecular states arising from the a^6S and a^6D atomic terms
(b) Closed and Occupied orbitals for the molecular states arising from the z^8P^0 atomic terms

Hence in summary the closed and active spaces for the two different cases are (5, 2, 2, 0)/(9, 3, 3, 1) and (5, 2, 2, 0)/(10, 4, 4, 1). It was later found that the subtle change in adding an extra atomic p orbital to the active space had a profound and physically significant effect upon the results of calculations.

For future reference these active spaces will be refereed to as "LOWER" and "UPPER" respectively

2.7.9 Specification of "wf" card for MnH

As a reminder the form of the "wf" card within `MOLPRO` (see section 2.7.6) is of the form: `wf, number of electrons, symmetry, 2S`
The number of electrons within the MnH atom is 26. Hence, referring to sections 2.7.6 and 2.7.2 the "wf" card required for the calculation of the various molecular states for MnH are shown in table 2.13 as examples.

Molecular state	"wf" card(s) required
$^5\Sigma^+$	26, 1, 4
$^5\Pi$	26, 2, 4 and 26, 3, 4
$^5\Delta$	26, 1, 4 and 26, 4, 4
$^7\Sigma^+$	26, 1, 6
$^7\Pi$	26, 2, 6 and 26, 3, 6
$^7\Delta$	26, 1, 6 and 26, 4, 6
$^9\Sigma^+$	26, 1, 8
$^9\Pi$	26, 2, 8 and 26, 3, 8

Table 2.13: Specification of "wf" cards required to calculate the various molecular states of interest for MnH.

Again, as is the case of CrH there are several "wf" cards which have multiple occurrences. For example by referring to table 2.11 there are three low-lying $^5\Sigma^+$

states and two low-lying $^5\Delta$ molecular states for the MnH molecule. To calculate all five simultaneously, bearing in mind that the $^5\Delta$ states have components in both symmetry 1 and symmetry 4, two "wf" cards need to be specified namely:

```
wf, 26, 1, 4; state 5; ! This is the symmetry 1 components
wf, 26, 4, 4; state 5; ! This is the symmetry 4 components
```

The order (in energy) of these quintet states is generally not known until calculations are done: in order to deduce which of the energy values calculated in symmetry 1 are the Δ states (as opposed to the Σ^+ states) a comparison needs to be done with the energies produced by the symmetry 4 calculation. For the Δ states the energy values produced in symmetry 1 and symmetry 4 should be numerically equal. Similarly to check the assignment of states within the symmetry 1 calculation a comparison of the expectation dipole moment calculations can be done: again this is a method to determine what order the various Σ^+ and Δ states lie in.

2.8 Description of MRCI calculations

In this project, MRCI calculations were performed to obtain potential energy curves, dipole moment curves, spin-orbit & angular momentum coupling curves. These calculations follow three distinct steps namely:

1. Complete Active Space Self-Consistent Field (CASSCF) calculation in which energies and dipole moments are calculated.

2. Configuration Interaction (CI) calculation, where the orbitals generated in the CASSCF calculations are used for CI calculations of energy and dipole moments.

3. CI calculations of couplings (dipole, angular momentum, spin-orbit) between states which use the CI orbitals generated in the CI part of the calculation.

Hence it is imperative that care is taken in generating the highest quality orbitals possible in the CASSCF in order to obtain convergence but also continuity in the CI calculations. It should be noted that continuity of curves, be it potential energy curves, dipole moment curves, spin-orbit coupling curves is not always guaranteed from obtaining convergence. Each input file for a `MOLPRO` calculation was divided into "procedures", labelled as "`PROCS`s". A loop was then run over the matrix of inter-nuclear distance values of R (see section 2.7.1) and each "`PROC`" calculated as necessary. It should be noted that a CASSCF (and indeed CI) calculation for each point is independent of calculations for all other points: thus the order in which calculations were run for different points has no consequences for the end result.

2.8.1 CASSSCF orbital testing calculations

The result of the initial CASSCF calculations are PECs and DMCs. For both CrH and MnH extensive testing of CASSCF orbitals was undertaken: these orbitals were varied by doing CASSCF calculations where different combinations of molecular states were requested. Practically, each different CASSCF orbital set to be tested was inputted into `MOLPRO` as a "`PROC`" within a single input file. The process of testing

was automated such that a run file was used in which the "PROC" to be tested was specified in the command line and thus calculations run over the matrix of inter-nuclear distances, R for this "PROC. "

An example of such a CASSCF orbital "PROC" is shown for CrH below: PROC MULTIRUN-A

```
{multi;maxiter,40;occ,9,3,3,1;closed,5,2,2,0;frozen,0,0,0,0;
wf,25,1,5;state 1;
wf,25,1,7;state 1;
wf,25,2,3;state 1;
wf,25,3,3;state 1;
orbital,2352.1}
enermulti1=energy(1)
enermulti2=energy(2)
enermulti3=energy(3)
enermulti4=energy(4)
dipz_multi1=dmz(1)
dipz_multi2=dmz(2)
dipz_multi3=dmz(3)
dipz_multi4=dmz(4)
XY = 'AAA'
table, XY,rpl,enermulti1, enermulti2,enermulti3,enermulti4,dipz_multi1,
dipz_multi2, dipz_multi3, dipz_multi4
DIGITS, 0, 4, 12, 12, 12, 12, 12, 12, 12, 12, 12, 12, 12, 12
ENDPROC
```

Here the

- "PROC" is called MULTIRUN-A,
- The occupied and closed orbitals within the C_{2v} symmetry framework as (9, 3, 3, 1) and (5, 2, 2, 0) respectively as discussed in section 2.7.5.
- A $^6\Sigma^+$, $^6\Sigma^+$ and a $^4\Pi$ state are calculated within this CASSCF calculation-see section 2.7.6 for explanation of "wf" cards.
- The orbital, 2352.1 refers to how MOLPRO saves this CASSCF orbital: this can then be called upon in proceeding CI calculations.
- The "enermulti" and "dipz_multi" are simply labels used and formatted in a table to assist with the extraction of data from the output files.

Once a CASSCF calculation has been done proceeding CI calculations can be done: for each value of the inter-nuclear distance R the starting orbital used is the orbital calculated in a proceeding CASSCF calculation.

2.8.2 Calculation of PECs and DMCs at MRCI level

Using the orbitals calculated in the "PROC MULTIRUN-A" in sectionn 2.8.1 as starting points, CI calculations can then be performed. An exmaple of a CI calculation for a $^4\Sigma^+$ state for CrH. PROC CIRUN-S1

```
!4 SIGMA + In FORTRAN notation upon which MOLPRO based, a "!" is a comment
```
to help the reader of the code.

```
ci;occ,9,3,3,1;core,5,2,2,0;wf,25,1,3;state 1;orbital,2352.1; save,3051.2;
thresh,energy=1.d-9,coeff=1.d-8,thrint=1.d-8,zero=1.d-8;maxiter,4000;maxit,4000;
enerci1_1 = energy(1);
dipzci1_1 = dmz(1);
XY = 'xxyyS1'
table, XY,rpl,enerci1_1,dipzci1_1
DIGITS, 0, 4, 12, 12
ENDPROC
```

Here the

- "PROC" is called "S1"
- The occupied and closed orbitals within the C_{2v} symmetry framework as (9, 3, 3, 1) and (5, 2, 2, 0) respectively as discussed in section 2.7.5.
- A quartet state within symmetry 1 is requested
- The orbital 2352.1 is used as a starting point: see proceeding section.
- The orbital calculated from this CI calculation is then saved as 3051.2
- Some convergence thresholds are given
- The `enerci1_1` and `dipzici1_1` labels are simply ways of assisting with the extraction of values of energy and expectation dipole moment respectively from the calculation

The calculation is done on the assumption that the first molecular state within the multiplicity-symmetry block of quartet-symmetry 1 is indeed a Σ^+ state and not a Δ state(which would require also the calculation of a quartet state with symmetry 4).
An example of a calculation for a $^6\Pi$ state for CrH.

```
PROC CIRUN-S8
!6 PI
ci;occ,9,3,3,1;core,5,2,2,0;wf,25,2,5;state 1; orbital,2352.1;save,3065.2;
thresh,energy=1.d-9,coeff=1.d-8,thrint=1.d-8,zero=1.d-8;maxiter,8000;maxit,8000;
enerci4_1 = energy(1);
dipzci4_1 = dmz(1);
ci;occ,9,3,3,1;core,5,2,2,0;wf,25,3,5;state 1; orbital,2352.1; save,3066.2;
thresh,energy=1.d-9,coeff=1.d-8,thrint=1.d-8,zero=1.d-8;maxiter,8000;maxit,8000;
enerci4_2 = energy(1);
dipzci4_2 = dmz(1);
XY = 'xxyyS6'
table, XY,rpl,enerci4_1,enerci4_2,dipzci4_1, dipzci4_2
DIGITS, 0, 4, 12, 12, 12, 12
ENDPROC
```

- "PROC" is called "S8"

- The occupied and closed orbitals within the C_{2v} symmetry framework as (9, 3, 3, 1) and (5, 2, 2, 0) respectively as discussed in section 2.7.5.
- A sextet state within symmetry 2 is requested
- The orbital 2352.1 is used as a starting point: see proceeding section.
- The orbital calculated from this CI calculation is then saved as 3056.2
- Some convergence thresholds are given
- A sextet state within symmetry 3 is requested
- The orbital 2352.1 is used as a starting point: see proceeding section.
- The orbital calculated from this CI calculation is then saved as 3057.2
- Some convergence thresholds are given
- The `enerci` and `dipzici` labels are simply ways of assisting with the extraction of values of energy and expectation dipole moment respectively from the calculation

In this calculation of energy and dipole moment, both the symmetry 2 and symmetry 3 components of a $^6\Pi$ state for CrH are calculated. For both components the starting orbitals used, saved as 2352.1 are those calculated from a proceeding CASSCF orbital calculation (as in the example shown in section 2.8.1) and the orbitals produced are saved as 3056.2 and 3057.2 respectively. These can then be used in proceeding calculations of coupling terms between the various components of various states.

As an example of CI calculation for multiple states within a multiplicity-symmetry block the `PROC` for the calculation of the three $^6\Sigma^+$ and one $^6\Delta$ state is shown below:

```
PROC CIRUN-S8
!3 6 SIGMA+ states, 6 DELTA
ci;occ,9,3,3,1;core,5,2,2,0;wf,25,1,5;state 4; orbital,2352.1; save,3063.2;thresh,energy=1.d
enerci8_1 = energy(1)
etc
dipzci8_1 = dmz(1);
etc
ci;occ,9,3,3,1;core,5,2,2,0;wf,25,4,5;state 1; orbital,2352.1;save,3064.2;
thresh,energy=1.d-9,coeff=1.d-8,thrint=1.d-8,zero=1.d-8;maxiter,8000;maxit,8000;
enerci8_5 = energy(1)
dipzci8_5 = dmz(1);
XY = 'xxyyS8'table, XY,rpl,enerci8_1,enerci8_2,enerci8_3,enerci8_4,enerci8_5,
dipzci8_1, dipzci8_2, dipzci8_3, dipzci8_4, dipzci8_5
DIGITS, 0, 4, 12, 12, 12, 12, 12, 12, 12, 12
ENDPROC
```

Table 2.14 gives a summary for CrH of the different CI `PROC`s tested out along with the relevant save cards upon which the orbitals were saved.

PROC	wf card(s)	save card	Molecular states corresponding to
S1	25, 1, 3; state 1	3051.2	$a^4\Sigma^+$
S2	25, 1, 3; state 2	3052.2	$a^4\Sigma^+$, $^4\Delta$(sym 1)
	25, 4, 3	3053.2	$^4\Delta$(sym 4)
S3	25, 1, 3; state 3	3054.2	$a^4\Sigma^+$, $^4\Delta$(sym 1), $^4\Sigma^+(II)$
	25, 4, 3	3055.2	$^4\Delta$(sym 4)
S4	25, 2, 3	3056.2	$^4\Pi$(sym 2)
	25, 3, 3	3057.2	$^4\Pi$(sym 3)
S5	25, 1, 5	3058.2	$X^6\Sigma^+$
S6	25, 1, 5; state 2	3059.2	$X^6\Sigma^+$, $A^6\Sigma^+(II)$
S7	25, 1, 5; state 3	3061.2	$X^6\Sigma^+$, $A^6\Sigma^+(II)$, $^6\Delta$(sym 1)
	25, 4, 5	3062.2	$^6\Delta$(sym 4)
S8	25, 1, 5; state 4	3063.2	$X^6\Sigma^+$, $A^6\Sigma^+(II)$, $^6\Delta$(sym 1), $^6\Sigma^+(III)$
	25, 4, 5	3064.2	$^6\Delta$(sym 4)
S9	25, 2, 5	3065.2	$^6\Pi$(sym 2)
	25, 3, 5	3066.2	$^6\Pi$(sym 3)
S10	25, 1, 7	3067.2	$^8\Sigma^+$

Table 2.14: Summary of CI PROCs tested for CrH

A similar table for MnH is shown below in table 2.15 where the "LOWER" and "UPPER" phrases refer to the two different active spaces deduced in section 2.7.8.

lower	PROC	wf card	States	card number
Lower	S1	wf,26,1,4;state,1;	$a^5\Sigma^+$	3051.2
	S2	wf,26,1,4;state,2;	$a^5\Sigma^+$, $^5\Delta$(sym 1)	3052.2
		wf,26,4,4;state,1;	$^5\Delta$(sym 4)	3053.2
	S3	wf,26,1,4;state,3;	$a^5\Sigma^+$, $^5\Sigma^+$, $^5\Delta$(sym 1)	3054.2
		wf,26,4,4;state,1;	$^5\Delta$(sym 4)	3055.2
	S4	wf,26,2,4;state,1;	$^5\Pi$(sym 2)	3056.2
		wf,26,3,4;state,1;	$^5\Pi$(sym 3)	3057.2
	S5	wf,26,1,6;state,1;	$X^7\Sigma^+$	3058.2
	S6	wf,26,1,6;state,2;	$X^7\Sigma^+$, $^7\Delta$(sym 1)	3059.2
		wf,26,4,6;state,1;	$^7\Delta$(sym 4)	3060.2
	S7	wf,26,1,6;state,3;	$X^7\Sigma^+$, $^7\Sigma^+(II)$, $^7\Delta$(sym 1)	3061.2
		wf,26,4,6;state,1;	$^7\Delta$(sym 4)	3062.2
	S8	wf,26,2,6;state,1;	$A^7\Pi$(sym 2)	3063.2
		wf,26,3,6;state,1;	$A^7\Pi$(sym 3)	3064.2
Upper	S9	wf,26,1,6;state,4;	$X^7\Sigma^+$, $^7\Sigma^+(II)$,$^7\Sigma^+(III)$, $^7\Delta$(sym 1)	3065.2
		wf,26,4,6;state,1;	$^7\Delta$(sym 4)	3066.2
	S10	wf,26,2,6;state,2;	$A^7\Pi$(sym 2), $E^7\Pi$(sym 2)	3067.2
		wf,26,3,6;state,2;	$A^7\Pi$(sym 3), $E^7\Pi$(sym 3)	3068.2
	S11	wf,26,1,8;state,1;	$^9\Sigma^+$	3069.2
	S12	wf,26,2,8;state,1;	$^9\Pi$(sym 2)	3070.2
		wf,26,4,8;state,1;	$^9\Pi$(sym 3)	3071.2

Table 2.15: Summary of CI PROCs tested for MnH

Table 2.15 summarises the initial states that were targeted for MnH: see the proceeding sections for how this then increased to include upper $^5\Sigma^+$, $^5\Pi$ and $^5\Delta$ states.

2.8.3 Calculation of Couplings at MRCI level

In this project three types of coupling between electronic molecular states were calculated namely transition dipole, angular moment and spin-orbit: these are described

in sections 2.8.3, 2.8.3 and 2.8.3 respectively. To calculate these couplings, coupling "PROCs" were used.

Transition Dipole Moment Calculations

The μ_z operator links states of the same multiplicity and Λ value e.g. the three low-lying $^6\Sigma^+$ molecular states for CrH and the two $^7\Pi$ states for MnH. These are calculated automatically by MOLPRO within the CI calculations for PECs and dipole moments.

As an example of the results of this calculation for the TDMs between the three low-lying $^6\Sigma^+$ molecular states for CrH, using the "S8" PROC described in table 2.14 there are 6 values at each inter-nuclear distance calculated. These are $\langle 2.1|DMZ|1.1\rangle$, $\langle 3.1|DMZ|1.1\rangle$, $\langle 4.1|DMZ|1.1\rangle$, $\langle 3.1|DMZ|2.1\rangle$, $\langle 4.1|DMZ|2.1\rangle$ and $\langle 4.1|DMZ|3.1\rangle$. In this notation which MOLPRO uses to output data, "4.1" signifies the fourth state calculated in symmetry 1. Unfortunately MOLPRO does not include the multiplicity-hence this created the need to run separate calculation for quartet and sextet states for the case of CrH and quintet, septuplet and nonuplet states for the case of MnH. As an example the term "<4.1|DMZ|1.1> signifies the μ_z operator acting between the 4th and 1st state within symmetry 1. Since the order of the electronic states frequently changes, upon "grepping out" (standard UNIX command) this data, the three transition dipole moments would then be constructed over the range of inter-nuclear distance R.

R(Å)	$\langle 2.1\vert DMZ\vert 1.1\rangle$	$\langle 3.1\vert DMZ\vert 1.1\rangle$	$\langle 4.1\vert DMZ\vert 1.1\rangle$	$\langle 3.1\vert DMZ\vert 2.1\rangle$	$\langle 4.1\vert DMZ\vert 2.1\rangle$	$\langle 4.1\vert DMZ\vert 3.1\rangle$
0.70		●	●			●
0.80		●	●			●
0.90		●	●			●
1.00	●		●		●	
1.10	●		●		●	
1.20-2.50	●		●		●	
2.55	●		●		●	
2.60	●		●		●	
2.65	●		●		●	
2.70	●	●		●		
2.75	●	●		●		
2.80	●	●		●		
2.85	●	●		●		
2.90-7.00	●	●		●		

Table 2.16: Overview of TDM deduction for $^6\Sigma^+$ states for CrH

Table 2.16 gives an overview of the raw data produced by a MOLPRO calculation for the TDMs between $^6\Sigma^+$ states which have been calculated by requesting 4 states within a sextet symmetry 1 calculation. Four states are required as there is also a $^6\Delta$ state which has a component in symmetry 1(as well as symmetry 4). In table 2.16, the *rgeom* values are shown down the vertical axis-these represent the internuclear distances. The horizontal axis is the list of TDMs calculated by MOLPRO. The coloured bullets i.e. ●, ● and ● indicate the values of *rgeom* for which MOLPRO produced a value for the given TDM such as "$\langle 3.1|\,DMZ\,|1.1\rangle$" in MOLPRO notation. Out of this table of values the goal is to determine the three transition dipole moments concerning the

$^6\Sigma^+$ states i.e. $\langle A^6\Sigma^+|\,\mu_z\,|X^6\Sigma^+\rangle$, $\langle {}^6\Sigma^+(III)|\,\mu_z\,|X^6\Sigma^+\rangle$ and $\langle {}^6\Sigma^+(III)|\,\mu_z\,|A^6\Sigma^+\rangle$ from the 6 different TDMs produced by `MOLPRO` e.g. $\langle 2.1|\,DMZ\,|1.1\rangle$, $\langle 3.1|\,DMZ\,|1.1\rangle$ etc. By inspection of the values, continuous curves can be formed which is indicated using the three different colours for the •s. The change in ordering of the electronic states(three $^6\Sigma^+$ states and the $^6\Delta$ state) is apparent but, looking at the limits when the internuclear distance is around 10 Å, we can see from 2.16 that the $^6\Delta$ state is highest in energy within this sextet, symmetry 1 calculation in the limit of atomic dissociation.

Calculation of μ_x and μ_y couplings

The selection rules for the μ_x, μ_y coupling are $\Delta\Lambda$=$\pm$1, $\Delta\Sigma$=0 and ΔS=0. Hence applying these to the ten electronic states of interest, the expected non-zero matrix elements are those between Σ^+ and Π states and also between Π and Δ states which have the same spin (multiplicity) e.g. between $^6\Pi$ and $^6\Delta$ for the case of CrH and $^5\Sigma^+$ and $^5\Pi$ for the case of MnH.

Again using the example of CrH and referring to table 2.14 to calculate the μ_x matrix elements acting between the symmetry 1 components of the $^6\Sigma^+$ and $^6\Delta$ states with the $^6\Pi$ state, the following command is needed:

```
{ci;trans,3063.2,3065.2,dm;}
```
(2.23)

Here the 3063.2 and 3065.2 are the `save` cards that are defined in table 2.14: the `MOLPRO` program records these CI orbitals when the PECs and DMCs are calculated at CI level (see section 2.8.2) and then here is using them to calculate the coupling requested. 3063.2 is the symmetry 1 orbitals of the sextet-symmetry 1 calculation (for 4 states) and 3065.2 is for the symmetry 2 component of the $^6\Pi$ state. This line of code will produce the following matrix elements in `MOLPRO` notation:

$$< 1.1|DMX|1.2 > \tag{2.24}$$

$$< 2.1|DMX|1.2 > \tag{2.25}$$

$$< 3.1|DMX|1.2 > \tag{2.26}$$

$$< 4.1|DMX|1.2 > \tag{2.27}$$

Here the "bra" vector refers to the symmetry 1 calculation(4 states) and the "ket" vector is the symmetry 2 component of the $^6\Pi$ state. In order to obtain the μ_y matrix element between these states, the symmetry 3 component of the $^6\Pi$ state would be requested i.e. use the command `{ci;trans,3063.2,3066.2,dm;}` where "3066.2" is the `save` card for the third symmetry component of the $^6\Pi$ state.

In practice only μ_x matrix elements were calculated as these were implemented into the Duo program: in practice the μ_x and μ_y components simply have the opposite sign.

To calulate the μ_x coupling between the symmetry 4 component of the $^6\Delta$ state and the $^6\Pi$ state, the following command was required:

```
{ci;trans,3064.2,3066.2,dm;}
```
(2.28)

Again referring to table 2.14, "3064.2" refers to the `save` card of the symmetry 4 component of the $^6\Delta$ state and "3066.2" refers to the symmetry three component of the $^6\Pi$ state. This command (Eq. 2.28 produces the following output:

```
<1.4|DMX|1.3>
```
(2.29)

In practice the value of output 2.29 will be numerically equal to one of the outputs 2.24, 2.25 and 2.26 (which will change for different values of the inter-nuclear distance). As is the case for the TDM calculations involving the $^6\Sigma^+$ states a certain element of "de-tangling" is required (see section 2.8.3). Once continuous curves have been formed from the raw `MOLPRO` output, these curves need to be assigned i.e. deduce which of the $^6\Sigma^+$ states they are associated with. This was usually reasonably obvious. Nevertheless, one technique to "assign" the correct curve was to inspect coupling calculations in which fewer states were requested in the of sextet multiplicity and symmetry 1.

Angular Momentum coupling Calculations

The selection rules for the electronic angular momentum operators, $\hat{L}_x$ and $\hat{L}_y$ are the same as those for the dipole moment operators μ_x and μ_y namely: $\Delta\Lambda$=$\pm$1, $\Delta\Sigma$=0, $\Delta S = 0$. Thus as was the case for the μ_x and μ_y operators, $\hat{L}_x$ and $\hat{L}_y$ connect Σ^+ with Π states and Π states with Δ states that are of the same multiplicity.

However, in terms of `MOLPRO` implementation to obtain the desired L_x couplings (to calculate the L_y couplings would be degenerate and unnecessary) the symmetries of the $^\Pi$ states is reversed in comparison to the μ_x couplings. As an example of calculating the L_x coupling between the three $^6\Sigma^+$ states and $^6\Delta$ state with the $^6\Pi$ state, the following commands were required:

```
{ci;trans,3063.2,3066.2,lop;}
```
(2.30)

```
{ci;trans,3064.2,3065.2,lop;}.
```
(2.31)

Here the values of "3063.2, 3064.2" etc refer to the `save` files in table 2.14. These two input thus produced the following outputs in `MOLPRO` notation:

$$< 1.1|LX|1.3 > \tag{2.32}$$

$$< 2.1|LX|1.3 > \tag{2.33}$$

$$< 3.1|LX|1.3 > \tag{2.34}$$

$$< 4.1|LX|1.3 > \tag{2.35}$$

$$< 1.4|LX|1.2 > \tag{2.36}$$

By comparing the values of 2.36 command with 2.32, 2.33, 2.34 and 2.35 the coupling between the $^6\Delta$ and $^6\Pi$ state could be deduced. Then, as was explained in sections

2.8.3 and 2.8.3, a "detangling" process was undertaken.

For $\hat{L}_z$ couplings the selection rules are the same as for μ_z coupling namely $\Delta\Lambda$=0, $\Delta\Sigma$=0 and ΔS=0 with the additional rule that $\Lambda \neq 0$. Hence $\hat{L}_z$ coupling occurs between the different symmetry components of Π and Δ states. The calculated values of these matrix elements were found to be imaginary and numerically constant with a magnitude of 1 for Π states and 2 for Δ states. To calculate the L_z coupling between the two components of the single $^4\Pi$ state in CrH, the following command was used:

```
{ci;trans,3056.2,3057.2,lop;}
```
(2.37)

In command 2.37, "3056.2" and "3057.2" refer to the *save* files (see table 2.14) used by `MOLPRO` to save the orbitals of the symmetry 2 and symmetry 3 components respectively.

To calculate the L_z coupling with the $^4\Delta$ state for the case where 3 states with quartet multiplicity and symmetry 1 (refer to table 2.14, `PROC S3`) the following command was inputted:

```
{ci;trans,3054.2,3055.2,lop;}.
```
(2.38)

This command produced the following output values:

$$< 1.1|LZ|1.4 > \tag{2.39}$$

$$< 2.1|LZ|1.4 > \tag{2.40}$$

$$< 3.1|LZ|1.4 > \tag{2.41}$$

Since there is no L_Z coupling "within" Σ^+ states, over the range of calculated inter-nuclear distances, the majority of the output values of 2.39, 2.40 and 2.41 will be zero. The non-zero values which are numerically equal to ± 2 represent the L_z coupling between the symmetry 1 and symmetry 4 components of the $^4\Delta$ state in question. In practice, calculating an L_z coupling was a useful way of deciphering if a state was a Σ^+ or Δ or Γ state for the different values of inter-nuclear distance as the order of states did change for the cases of allowed crossings.

Spin-Orbit calculations

Spin-orbit matrix elements formed between electronic states using the $\hat{SO}_x$, $\hat{SO}_y$ and $\hat{SO}_z$ operators were calculated using the Breit-Pauli method. For spin-orbit coupling, the expected couplings can be deduced by consideration of the symmetry of the operators $\hat{SO}_x$, $\hat{SO}_y$, $\hat{SO}_z$ as shown in table 2.17 and by the product table for C_{2v} symmetry shown in table 2.18.

OPERATOR	SYMMETRY
$\hat{SO}_x$	3
$\hat{SO}_y$	2
$\hat{SO}_z$	4

Table 2.17: Symmetry states of Spin-Orbit operators $\hat{SO}_x$, $\hat{SO}_y$, $\hat{SO}_z$

For there to be non-zero spin-orbit coupling, the overall product of the matrix element
$\langle$state 1 symmetry$|$ operator symmetry $|$state 2 symmetry$\rangle$
must be symmetry 1.

X	1	2	3	4
1	1	2	3	4
2	2	1	4	3
3	3	4	1	2
4	4	3	2	1

Table 2.18: C_{2v} symmetry operators multiplication table

Thus by by reference to tables 2.17 and 2.18, it can be shown that the matrix elements presented in the first column of table 2.19 will be non-zero for any system obeying C_{2v} symmetry. It is is irrelevant which state is the bra wave-function and which is the ket wave-function as the C_{2v} symmetry product table is commutative. Additionally, for a spin-orbit coupling to be non-zero, the following rules concerning spin, S and Λ apply: $\Delta S = 0, \pm 1$ and $\Delta\Lambda = 0, \pm 1$. Hence spin-orbit coupling between Σ^+ states (symmetry 1) and the symmetry 4 component of Δ states is forbidden. Hence by application of these rules, the non-zero spin-orbit matrix elements expected for CrH are tabulated in the second column of table 2.19. See table 2.8 for a summary of the electronic molecular states of interest in this project for CrH. As was the case for μ_z, μ_x, L_x and L_z coupling calculations, only the x and z coupling matrices were calculated for spin-orbit coupling (calculating the SO_y in addition to the SO_x coupling would be a degenerate operation).

Matrix Element	Application to CrH
$\langle\Sigma^+\vert\, \hat{SO}_x \,\vert\Pi(\text{sym } 3)\rangle$	$\langle X^6\Sigma^+\vert\, \hat{SO}_x \,\vert^6\Pi\rangle$
	$\langle A^6\Sigma^+\vert\, \hat{SO}_x \,\vert^6\Pi\rangle$
	$\langle {}^6\Sigma^+(III)\vert\, \hat{SO}_x \,\vert^6\Pi\rangle$
	$\langle X^6\Sigma^+\vert\, \hat{SO}_x \,\vert^4\Pi\rangle$
	$\langle A^6\Sigma^+\vert\, \hat{SO}_x \,\vert^4\Pi\rangle$
	$\langle {}^6\Sigma^+(III)\vert\, \hat{SO}_x \,\vert^4\Pi\rangle$
	$\langle a^4\Sigma^+\vert\, \hat{SO}_x \,\vert^4\Pi\rangle$
	$\langle {}^4\Sigma^+(II)\vert\, \hat{SO}_x \,\vert^4\Pi\rangle$
	$\langle a^4\Sigma^+\vert\, \hat{SO}_x \,\vert^6\Pi\rangle$
	$\langle {}^4\Sigma^+(II)\vert\, \hat{SO}_x \,\vert^6\Pi\rangle$
$\langle\Pi(\text{sym } 2)\vert\, \hat{SO}_x \,\vert\Delta(\text{sym } 4)\rangle$	$\langle {}^6\Pi\vert\, \hat{SO}_x \,\vert^6\Delta\rangle$
	$\langle {}^6\Pi\vert\, \hat{SO}_x \,\vert^4\Delta\rangle$
	$\langle {}^4\Pi\vert\, \hat{SO}_x \,\vert^6\Delta\rangle$
	$\langle {}^4\Pi\vert\, \hat{SO}_x \,\vert^4\Delta\rangle$
$\langle\Pi(\text{sym } 2)\vert\, \hat{SO}_z \,\vert\Pi(\text{sym } 3)\rangle$	$\langle {}^4\Pi\vert\, \hat{SO}_z \,\vert^4\Pi\rangle$
	$\langle {}^6\Pi\vert\, \hat{SO}_z \,\vert^6\Pi\rangle$
	$\langle {}^4\Pi\vert\, \hat{SO}_z \,\vert^6\Pi\rangle$
$\langle\Delta(\text{sym } 1)\vert\, \hat{SO}_z \,\vert\Delta(\text{sym } 4)\rangle$	$\langle {}^4\Delta\vert\, \hat{SO}_z \,\vert^4\Delta\rangle$
	$\langle {}^6\Delta\vert\, \hat{SO}_z \,\vert^6\Delta\rangle$
	$\langle {}^4\Delta\vert\, \hat{SO}_z \,\vert^6\Delta\rangle$

Table 2.19: List of non-zero matrix elements for spin-orbit coupling in C_{2v} symmetry for CrH

Table 2.19 shows all the spin-orbit couplings between the various molecular states of interest for CrH. Similarly, table 2.20 lists out the spin-orbit coupling curves for MnH acting between the different molecular states of interest.

Matrix Element	Application to MnH
$\langle \Sigma^+ \vert \hat{SO}_x \vert \Pi(\text{sym } 3) \rangle$	$\langle X^7\Sigma^+ \vert \hat{SO}_x \vert A^7\Pi(I) \rangle$
	$\langle {}^7\Sigma^+(II) \vert \hat{SO}_x \vert A^7\Pi(I) \rangle$
	$\langle {}^7\Sigma^+(III) \vert \hat{SO}_x \vert A^7\Pi(I) \rangle$
	$\langle X^7\Sigma^+ \vert \hat{SO}_x \vert E^7\Pi(II) \rangle$
	$\langle {}^7\Sigma^+(II) \vert \hat{SO}_x \vert E^7\Pi(II) \rangle$
	$\langle {}^7\Sigma^+(III) \vert \hat{SO}_x \vert E^7\Pi(II) \rangle$
	$\langle X^7\Sigma^+ \vert \hat{SO}_x \vert {}^5\Pi \rangle$
	$\langle {}^7\Sigma^+(II) \vert \hat{SO}_x \vert {}^5\Pi \rangle$
	$\langle {}^7\Sigma^+(III) \vert \hat{SO}_x \vert {}^5\Pi \rangle$
	$\langle X^7\Sigma^+ \vert \hat{SO}_x \vert {}^9\Pi \rangle$
	$\langle {}^7\Sigma^+(II) \vert \hat{SO}_x \vert {}^9\Pi \rangle$
	$\langle {}^7\Sigma^+(III) \vert \hat{SO}_x \vert {}^9\Pi \rangle$
	$\langle a^5\Sigma^+ \vert \hat{SO}_x \vert {}^5\Pi \rangle$
	$\langle {}^5\Sigma^+(II) \vert \hat{SO}_x \vert {}^5\Pi \rangle$
	$\langle a^5\Sigma^+ \vert \hat{SO}_x \vert A^7\Pi(I) \rangle$
	$\langle {}^5\Sigma^+(II) \vert \hat{SO}_x \vert A^7\Pi(I) \rangle$
	$\langle a^5\Sigma^+ \vert \hat{SO}_x \vert E^7\Pi(II) \rangle$
	$\langle {}^5\Sigma^+(II) \vert \hat{SO}_x \vert E^7\Pi(II) \rangle$
$\langle \Pi(\text{sym } 2) \vert \hat{SO}_x \vert \Delta(\text{sym } 4) \rangle$	$\langle {}^5\Pi \vert \hat{SO}_x \vert {}^5\Delta \rangle$
	$\langle {}^5\Pi \vert \hat{SO}_x \vert {}^7\Delta \rangle$
	$\langle A^7\Pi(I) \vert \hat{SO}_x \vert {}^5\Delta \rangle$
	$\langle E^7\Pi(II) \vert \hat{SO}_x \vert {}^5\Delta \rangle$
	$\langle A^7\Pi(I) \vert \hat{SO}_x \vert {}^7\Delta \rangle$
	$\langle E^7\Pi(II) \vert \hat{SO}_x \vert {}^7\Delta \rangle$
$\langle \Pi(\text{sym } 2) \vert \hat{SO}_z \vert \Pi(\text{sym } 3) \rangle$	$\langle {}^5\Pi \vert \hat{SO}_z \vert {}^5\Pi \rangle$
	$\langle {}^7\Pi(I) \vert \hat{SO}_z \vert A^7\Pi(I) \rangle$
	$\langle {}^7\Pi(II) \vert \hat{SO}_z \vert E^7\Pi(II) \rangle$
	$\langle {}^9\Pi \vert \hat{SO}_z \vert {}^9\Pi \rangle$
$\langle \Delta(\text{sym } 1) \vert \hat{SO}_z \vert \Delta(\text{sym } 4) \rangle$	$\langle {}^5\Delta \vert \hat{SO}_z \vert {}^5\Delta \rangle$
	$\langle {}^7\Delta \vert \hat{SO}_z \vert {}^7\Delta \rangle$
	$\langle {}^5\Delta \vert \hat{SO}_z \vert {}^7\Delta \rangle$

Table 2.20: List of non-zero matrix elements for spin-orbit coupling in C_{2v} symmetry for MnH.

Spin-Orbit calculations: Practical Implication

To calculate spin-orbit couplings using the `MOLPRO` package, the procedure is very similar to calculating the dipole moment and angular momenta couplings. As an example for CrH to calculate the SO_x coupling between the $^6\Sigma^+$ states and $^6\Delta$ with the $^4\Pi$ state, the commands used were as follows:

```
{mrci;hlsmat,ls,3063.2,3057.2;options,matel=1;print}        (2.42)
```

```
{mrci;hlsmat,ls,3064.2,3056.2;options,matel=1;print}        (2.43)
```

Refer to table 2.15. Statement 2.42 calculates the matrix element formed using the SO_x operator between states of sextet multiplicity and symmetry 1 and the symmetry

3 component of the $^4\Pi$ state. Statement 2.43 calculates the matrix element formed using the SO_x operator between the symmetry 4 component of the $^6\Delta$ state and the symmetry 2 component of the $^4\Pi$ state. Again, a process of "de-tangling" was required to ascertain which matrix values for different values of inter-nuclear distance corresponded to the desired couplings sought. As an example of calculating the spin-orbit coupling between the symmetry 2 and symmetry 3 components of a Π state, for the case of the $^6\Pi$ state of CrH the following command was used:

```
{mrci;hlsmat,ls,3065.2,3066.2;options,matel=1;print}.
```
(2.44)

And finally to calculate the spin-orbit coupling between the symmetry 1 and symmetry 4 component of, as an example the $^4\Delta$ state of CrH,

```
{mrci;hlsmat,ls,3054.2,355.2;options,matel=1;print}.
```
(2.45)

(Again refer to table 2.15-this is for the case of `PROC S3` where three states are requested of quartet multiplcity and symmetry 1). The result of command 2.45 were the following matrix values:

$$< 1.1|LZ|1.4 > \tag{2.46}$$

$$< 2.1|LZ|1.4 > \tag{2.47}$$

$$< 3.1|LZ|1.4 > \tag{2.48}$$

Again, as for the case of L_z couplings, from these matrix elements spanning the range of inter-nuclear distances, a single curve was constructed. For the case of L_z coupling this had constant numerical value of ± 2. For the case of spin-orbit coupling, since there is no spin-orbit coupling "within" Σ states, the majority of printed values would be zero. The remaining values (typically of order around 200 cm^{-1}) would thus form the SO_z coupling curve between the symmetry 1 and symmetry 4 components of the Δ state.

2.8.4 Behaviour of Spin-Orbit matrix elements at dissociation limits: CrH

The atomic dissociation limits can also be used to give an estimate of the atomic spin-orbit constant in the dissociation limit. We expect that in the limit of R tending to infinity (dissociation limit) spin-orbit coupling between molecular electronic states which converge to different asymptotes will tend to zero.

Since there is only one value of J for the a^7S and a^5S atomic terms we therefore expect in the limit of large R for the spin-orbit coupling to be zero between molecular states which converge to these respective limits. To elaborate, for the case of a^7S limit, to which the $X^6\Sigma^+$ and $^8\Sigma^+$ states converge, it is expected anyway from the selection rules that for all R the spin-orbit coupling will be zero between them which was indeed the case. Similarly there is only one value of J for the a^5S limit to which the $A^6\Sigma^+$ and $X^4\Sigma^+$ converge and again, as per selection rules at all R spin-orbit coupling is forbidden as was calculated.

For the molecular states which converge to the a^5D atomic dissociation limit which are namely $^6\Sigma^+(III)$, $^6\Pi$, $^6\Delta$, $a^4\Sigma^+$, $^4\Pi$, $^4\Delta$. We expect there to be non-zero spin-orbit coupling in the atomic dissociation limit as there are several J values associated with the a^5D dissociation limit(see table 2.8).

The energy levels, E_J corresponding to $J = 0, 1, 2, 3, 4$ are then theoretically linked to E_0 (given by Eq. 2.22) by:

$$E_J = E_0 + \xi \frac{[J(J+1) - L(L+1) - S(S+1)]}{2} \tag{2.49}$$

where ξ is the atomic spin-orbit parameter, L is the atomic orbital angular momentum and S is the atomic spin orbital angular momentum. In this case $L = 2$ (hence the D letter) and $S = 2$ where the "5" in the term value a^5D represents the multiplicity of the spin, $2S + 1$. Re-arranging Eq. 2.49, it can be shown that:

$$E_{J+1} - E_J = \xi(J+1) \tag{2.50}$$

using the fact that L and S are constant for an atomic dissociation limit. Thus, Eq. 2.50 can be used to ascertain value of ξ using different pair of E_J values.

In practice, the parameter ξ was fitted by applying the values of E_J with their respective J values as listed in table 2.8 to Eq. 2.49. For each E_J value the residual is defined as the difference between the known E_J value shown in table 2.8 and that calculated for a given trial ξ using Eq. 2.49. The sum of the squared residuals is simply the sum of the five squared residual values. Using this data, ξ was fitted and found to be 55.72 cm^{-1} as is shown in figure 2.4. The Wigner-Eckart theorem can then be used to calculate the scaling factor which should be applied to this atomic spin-orbit coupling parameter to obtain a theoretical value of the spin-orbit coupling between two states (which both converge to this atomic dissociation limit a^5D) in the dissociation limit.

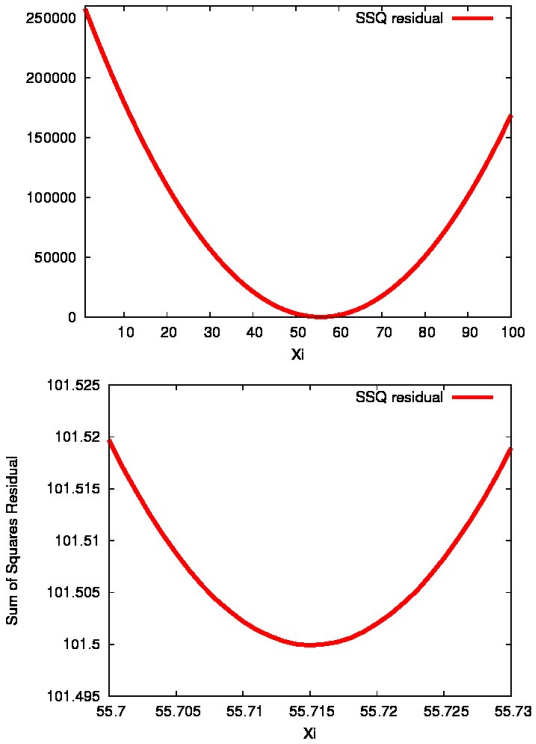

Figure 2.4: Sum of Squared residuals for varying ζ

2.8.5 Behaviour of Spin-Orbit matrix elements at dissociation limits: MnH

Again, as was the case for CrH, for MnH the atomic dissociation limits of the Manganese atom can be used to give an estimation of the spin-orbit coupling constant at dissociation. Refer back to table 2.11 and equations 2.22 and 2.49.

For the case of MnH, the first dissociation limit, the a^5S term has no dependence on J. The values of ξ are tabulated for the next three dissociation limits in table 2.21 with respective plots demonstrating the fitting of ξ shown in figure 2.5.

Dissociation Limit Term	Magnitude of ξ (cm^{-1})
a^6D	48.69
Z^8P^0	37.90
a^4D	69.67

Table 2.21: Summary of ξ values determined for the various atomic dissociation limits of the Manganese atom.

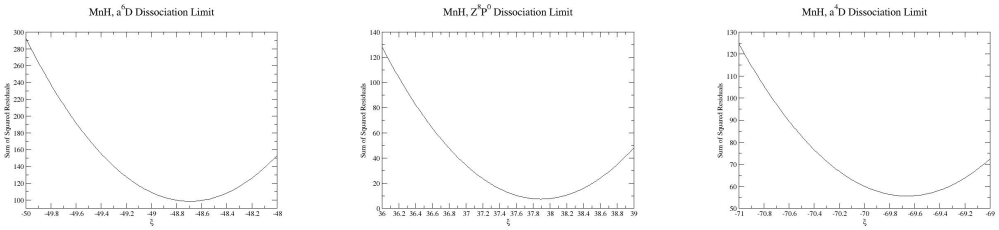

(a) (b) (c)

Figure 2.5: Sum of Squared residuals for varying ξ for the three atomic dissociation limits of relevance to this project on MnH.

2.9 Duo program

Once the *ab initio* calculations had been run and hence PECs, DMCs, TDMs and spin-orbit and angular momentum couplings obtained, the rovibronic Schrödinger equation (see section 2.4) was then solved using the in-house program Duo. Duo is a program that has been built by members of the ExoMol group along with Andrey Stolyarov from Moscow State University. Duo is now freely available to download via the website GitHub (https://github.com/Trovemaster/Duo) and can also be accessed through the CCCPForge website under the project Diatomics. The motivation for creating Duo was that there was not a known program available which could solve the rovibronic Schrödinger equation for open-shell diatomics with couplings. The accompanying paper describing the Duo program and Manual have both been published (Yurchenko, Lodi, Tennyson & Stolyarov 2016). To create a linelist using Duo from the *ab initio* data, two steps are required:

1. The PECs need to be refined to any available experimental data in order for the final linelist to be of an accuracy desired by the exoplanet and brown dwarf community for characterisation purposes. Also historically, detections of molecules in space have been made by using experimental measurements thus our linelists need to at least match this level of accuracy where experimental measurements of transition wavelengths are available.

2. Once these curves are then fitted, Duo can then be used to calculate a fitted linelist by solving the coupled rovibronic Schrödinger equation.

It is possible to calculate a purely *ab initio* linelist using Duo but it is always preferable to use available experimental data to constrain any theoretical inputs as best as possible. Calculating a purely *ab initio* linelist can however help give useful insight of which electronic transition bands could potentially be of greatest relative intensity: an important note to consider when there are potentially a myriad of electronic transitions, some of which are more important ultimately from an astronomy perspective than others.

2.9.1 Input structure of a Duo file

At the start of any Duo input file the masses of the two nuclei are defined, the number of electronic states to be taken into consideration and the reference range in J required. The number of electronic states to be taken into account is simply the number of bound states which will thus produce physically bound energy levels. The categorisation of states into "bound" and "unbound" states is not a simple "black and white" story: very shallow curves can still give rise to bound transitions. The grid of points in then defined which is simply the range in inter-nuclear distance and also the spacing between successive points on this grid. The vibronic contraction is then defined which is defined by the user specifying the maximum number of vibrational basis functions the program to use to construct rovibronic basis functions (see section 2.9.5). Finally the parameters for the input diagonaliser are then defined which are simply the number of roots which the user wishes to calculate (related to the accuracy of the resulting calculation) and the maximum energy cut-off.

The remaining structure of a Duo input file is as follows:

- Fitted PECs presented in an empirical form.
- Experimental data inputted in the"Duo format" along with corresponding instruction for Duo of what to fit during the process of fitting
- *Ab initio* curves which are labelled as state 1, 2, 3 etc
- An set of instructions for the intensity where the user specifies the energy ranges desired in the linelist calculation.

The fitting process is described in detail in section 2.9.3 and the calculation of linelist (list of energy levels and intensities) in section 2.9.5.

2.9.2 Using Duo interpolation to determine PEC properties

One functionality within Duo is that of interpolation. This functionality was used to determine properties of the *ab initio* curves calculated.

- Each *ab initio* PEC (up to 88 points) was put into a Duo file and a new inter-nuclear distance grid set from 0.700 to 10.000 Åin steps 0.001 Å. The interpolation functionality within Duo was used to "fill" this new grid using the *ab initio* points.
- For each PEC, the minima on the interpolated grid of points was determined. The range in each of the R_e values indicates what R values covered had this same minima to an accuracy of 1 cm^{-1}.
- The dissociation energy of each interpolated grid was then determined by simply subtracting the minimum value from the dissociation value.
- For each PEC, a Duo calculation has been run using a basis of 20 vibronic basis functions. The value of the first vibronic energy level has been recorded and compared to literature available. For future values these term values are denoted by $E(\nu = 1)$.

- The values in T_e presented show the difference in energy in minima between all the equilibrium points of the PECs under study.

2.9.3 Using Duo to refinement PECs

In any fitting process, the aim is to minimise the functional SSQ: the sum of the squared errors which quantifies deviations between the raw data points and any curve fitted to this data. Differentiation is the method typically used to minimise (or indeed maximise) any function as, on a fundamental level differentiation is about finding the gradient of any function with "stationary points" (minima, maxima or points of inflection) occurring when the gradient is zero. An example of using this process for the case of fitting a straight line through a set of points is described below for the purposes of demonstration. It should be noted that in Duo the process of fitting is actually a multi-D process where D is the number of parameters fitted.

Linear regression

The process of linear regression is where a straight line of the form $y = ax + b$ is "fitted" through a set of data points (X_i, Y_i) which, when plotted appear to be linked by a linear relation. The assumptions made in linear regression are that the data points and errors are independent with the errors following a Gaussian distribution. If Y_f is used to denote the fitted value of Y given a data point X_i from a set of N data points, the SSQ to be minimised, Q can be expressed as:

$$Q = \sum_{i}^{N} \left(Y_f - Y_i\right)^2 = \sum_{i}^{N} \left(a + bX_i - Y_i\right)^2 \tag{2.51}$$

To minimise the quantity Q, partial derivatives of Q with respect to the gradient, a and slope intercerpt, b of the fitted line can be taken:

$$\frac{\partial Q}{\partial a} = \sum_{i=1}^{N} \left(2(a + bX_i - Y_i\right)^1 = 0. \tag{2.52}$$

Take out the factor of 2 to hence obtain:

$$aN + b\sum_{i=1}^{N} X_i - \sum_{i=1}^{N} Y_i = 0. \tag{2.53}$$

Hence by re-arranging:

$$a = \frac{1}{N}\left(\sum_{i=1}^{N} Y_i - b\sum_{i=1}^{N} X_i\right) = \bar{Y_i} - b\bar{X_i} \tag{2.54}$$

where $\bar{Y_i}$ and $\bar{X_i}$ denotes the respective averages of the data points to which a linear curve is been fitted.

Now taking the partial derivative of Q with respect to b.

$$\frac{\partial Q}{\partial b} = \sum_{i=1}^{N} 2(a + bX_i - Y_i)X_i = 0. \tag{2.55}$$

Divding through by 2:

$$\sum_{i=1}^{N}(a + bX_i - Y_i)X_i = 0 \tag{2.56}$$

Substitute in the expression for a given by Eq. 2.54 into Eq. 2.56 to thus obtain:

$$\sum_{i=1}^{N}(\bar{Y}X_i - b\bar{X}X_i + bX_i^2 - Y_iX_i) = 0 \tag{2.57}$$

Hence separating out into two terms and re-arraning for b

$$\sum_{i=1}^{N}\left(\bar{Y}X_i - Y_iX_i\right) + b\sum_{i=1}^{N}\left(X_i^2 - X_i\bar{X}\right) = 0 \tag{2.58}$$

$$b = \frac{\sum_{i=1}^{N} X_iY_i - \bar{Y}X_i}{\sum_{i=1}^{N} X_i^2 - X_i\bar{X}} \tag{2.59}$$

we thus obtain that:

$$b = \frac{\sum_{i=1}^{N} X_iY_i - n\bar{X}\bar{Y}}{\sum_{i=1}^{N} x_i^2 - n\bar{X}^2} \tag{2.60}$$

Hence overall the process of minimising Q by taking partial derivatives of it with respect to a and b thus yields formulae for these desired quantites. Thus a straight line can be fitted through a set of data points (X_i, Y_i) of the form $Y = aX + b$ under the knowledge that a and b are formulated such that the squared sum of the deviations between the initial data points and fitted data points is minimised.

Morse Potential

A common function used to model the PEC of an electronic state is the Morse Potential which takes the form shown in Eq. 2.61.

$$V(r) = D_e\left(1 - e^{-\alpha(R-R_e)}\right)^2 \tag{2.61}$$

In Eq. 2.61, D_e is the dissociation limit, R_e is the equilibrium point and R is the internuclear distance. α is a quantity determined below. It can be seen from equatiion 2.61 that in the limit that $R \to \infty$, $V(R) \to D_e$ as expected. Equations 2.62 and 2.63 below show the deduction of the first and second derivatives of the Morse function.

$$\frac{\mathrm{d}V(R)}{\mathrm{d}R} = 2D_e\alpha[e^{-\alpha(R-R_e)}][1-e^{-\alpha(R-R_e)}]\frac{\mathrm{d}V(R)}{\mathrm{d}R}|_{R=R_e} = 2D_e\alpha(1)(1-0) = 0 \tag{2.62}$$

$$\frac{\mathrm{d}^2V(R)}{\mathrm{d}R^2} = 2D_e\alpha^2e^{-\alpha(R-R_e)}[-1 + 2e^{-\alpha(R-R_e)}]\frac{\mathrm{d}^2V(R)}{\mathrm{d}R^2}|_{R=R_e} = 2D_e\alpha^2 \tag{2.63}$$

As Eq. 2.62 shows, $\frac{\mathrm{d}V(R)}{\mathrm{d}R}|_{R=R_e} = 0$ for a Morse Potential as expected. If we model the vibration of a diatomic molecule (or for a polyatomic a single vibronic mode) as spring obeying Hooke's Law, Force $= -k_eR$ where k_e is the spring constant then, from standard formulae linking V to F we know that $\frac{\mathrm{d}^2V(R)}{\mathrm{d}R^2} = k_e$. Hence the "spring-constant" of a vibrating diatomic molecule can hence be approximated as $k_e = 2D_e\alpha^2$.

Thus re-arranging α can be expressed in terms of k_e by Eq. 2.64

$$\alpha = \sqrt{\frac{k_e}{2D_e}}. \tag{2.64}$$

By Hookes' Law, $F = -kr = m\frac{\mathrm{d}^2R}{\mathrm{d}t^2}$ when an Ansatz of $R = R_0 cos(\omega t + \phi)$ is used the solution for ω is that $\omega = \sqrt{\frac{k}{m}}$. Hence substituting this into Eq. 2.64 we thus obtain an expression for α given by Eq. 2.65

$$\alpha = \omega_e \sqrt{\frac{m}{2D_e}} \tag{2.65}$$

with ν_0 given by:

$$\nu_0 = \frac{\alpha}{2\pi}\sqrt{\frac{2D_e}{m}}. \tag{2.66}$$

The solutions of the Schrödinger equation with Morse potential are given by Eq. 2.67,

$$E(\nu) = h\nu_0(\nu + \frac{1}{2}) - \frac{[h\nu_0(\nu + \frac{1}{2})]^2}{4D_e} \tag{2.67}$$

where the spacing of Energy levels in Morse Potential is:

$$E(\nu + 1) \; - \; E(\nu) = h\nu_0 - \frac{(h\nu_0)^2}{2D_e}(\nu + 1) \tag{2.68}$$

i.e. anharmonic spacing.

2.9.4 Fitting Experimental Data in Duo

The experimental data which is useful for the fitting of PECs can be classified as following:

1. Experimental measurements of the dissociation energy of a molecule. This measurement can then be linked to the dissociation energy of the ground state by application of knowledge of the atomic dissociation limits.

2. Experimentally measured spectroscopic parameters such as ω_e (e.g. Argon matrix experiments)

3. Experimental measurements of wavenumbers.

Duo can be used to fit an empirical curve to describe the behaviour of a PEC using experimental data either in the form of transitional frequencies or energy levels ("term values") to theoretically calculated PECs. In practice, it is easier to "fit" to term values first before fitting to frequencies to increase the accuracy of the fit. In fitting an empirical curve, Duo tries to minimise the sum of squared energy differenced between the fitted curve and the experimental data as well as the *ab initio* data. The relative weight ("preference") given to the experimental data or *ab initio* PECs can be adjusted based on knowledge of the accuracy obtained by the experimentalists and the relative degree of "trust" of experimental versus theoretical work.

The form of the empirical PEC can be implemented in several forms: Dunham variables, Taylor polynomial expansion, Simons-Parr-Finlan expansion, Murrell-Sorbie

(MS), Chebyshev polynomial expansion, Perturbed Morse Oscillator, Extended Morse Oscillator (EMO), Morse Long-Range (MLR) function, Surkus-polynomial expansion and Surkus-polynomial expansion with a damping function. For full mathematical details see the Duo reference paper (Yurchenko et al. 2016). The form used in this project for the fitted PECs was the extended Morse Oscillator.

Spin-orbit, Spin-spin, spin-rotation and Born-Oppenheimer breakdown potentials can also be added to improve the accuracy of the fit.

Where no experimental frequencies or term values are available, the program PGOpher can be used to calculate a list of term values using experimental (or theoretical) molecular constants. PGopher is a program developed within Colin Western's laser group at Bristol University which is the amalgamation of several programs developed within this group to simulate and fit molecular experimental data. It can be used to model diatomic, linear, symmetric and antisymmetric top molecules. It is an open source program available to download onto mac, windows and Linux platforms. The simulation aspect of PGopher allows a user to input in molecular constants and obtain a list of rovibronic energy levels. The fitting functionality (the reverse of the simulation functionality) of PGopher can be used to fit constants to band contours, intensities or line positions.

For the case of only experimental frequencies been available, the program MARVEL (T. Furtenbacher, A. G. Csàszàr, and J. Tennyson 2007) can be used to calculate a set of self-consistent energy levels. This process of "building up a network" of energy levels can be done manually using a spreadsheet where quantum numbers of the lower and upper states are "matched" in a zig-zag ladder-like manner.

Any list of rovibronic energy values first needs to be converted into "Duo format" before any fitting can take place. This format is of the following form:
J, parity, "Running number", Energy, ν, Λ, Σ, Ω and "weight".
The quantum numbers of J, ν, Λ, Σ and Ω take on the standard definitions described in section 2.2. The parity of the state can either be described in terms of e/f parity or rotationless parity of +/-. The "Running number" is simply an internal label used by Duo-each rovibronic state has a unique label. Finally the "weight" is simply a measure of the emphasis the user wants Duo to put on the particular energy level in fitting i.e. use a lower weight for energy levels that have been obtained by a form of extrapolation in comparison to energy levels which are known with greater certainty. Now that the reference data is in Duo format, the user can then fit an empirical curve to this data and also the *ab initio* data.

In practice, the process of fitting, starting for low J and then increasing to higher J, can be described as an oscillation between the following steps:

- running a Duo calculation of energy values and correcting the assignment of quantum numbers to that which Duo is calculating.
- An iteration run in which parameters in the empirical PEC and associated empirical functions(such as spin-spin etc) are systematically varied in order to reduce the overall differences between experimental energies and those calculated by Duo using the empirical functions been fitted to ("obs-calc").

The choice of parameters to be varied is motivated by observing any systematic increases in the "obs-calc" values which depend on vibrational or rotational effects. For the case of vibrational dependence the most appropriate parameters to vary in the Extended Morse Oscillator potential are B0, B1 and B2. For rotational effects R_e and D_e should be adjusted in the first instance to obtain a reasonable quality of fit at lower J. At higher J the effects of Born-Oppenheimer breakdown may become significant. Initial parameters of any spin-spin and spin-rotation functions added can often be obtained by searching through experimental papers in which such effects have been considered. Once a fit has been obtained to energy values, experimental frequencies can then be used to constrain the fit. The input structure for inputting in experimental frequencies for fitting into Duo is similar to that for energies and takes the following form: J, parity, "Running number" of the lower state followed by
J, parity, "Running number" of the upper state followed by
the experimental frequency of the transition between the two states
(ν, Λ, Σ and Ω of the lower state) followed by (ν, Λ, Σ and Ω) of the upper state.

2.9.5 Solving the Rovibronic Schrödinger equation

To create a linelist, the non-relativistic Hamiltonian to be solved is of the following form:

$$\hat{H}_{\text{Total}} = \hat{H}_e \ + \ \hat{H}_\mu \ + \ \hat{H}_{vib} \ + \ \hat{H}_{rot} \tag{2.69}$$

In Eq. 2.69,

- $\hat{H}_e$ is the electronic Hamiltonian (i.e. the Hamiltonian describing the electronic structure of the molecule)
- $\hat{H}_\mu$ is the mass polarisation term which qualitatively is a result of treating the nuclei of having finite mass when a transformation of co-ordinate system is undertaken. It is given by $\hat{H}_\mu = \frac{\hbar^2}{2m_N}\sum_{i=1}^{N_e}\sum_{j=1}^{N_e}\delta_i.\delta_j$ where m_N is the total mass of the two nuclei, N_e is the total number of electrons and co-ordinates i and j describe their position.
- The vibronic kinetic energy operator is given by $\hat{H}_{vib} = -\frac{\hbar^2}{2\mu}\frac{\mathrm{d}^2}{\mathrm{d}r^2}$ where r is the inter-nuclear distance and μ is the reduced mass of the system.
- $\hat{H}_{rot}$ is the Hamiltonian describing the rotational motion of the molecule, given by
  $\hat{H}_{rot} = \frac{\hbar^2}{2\mu r^2}\hat{\mathbf{R}}^2$ where $\hat{\mathbf{R}} = \hat{\mathbf{J}} - \hat{\mathbf{L}} - \hat{\mathbf{S}}$. Here $\hat{\mathbf{J}}$ is the total angular momentum of the system and $\hat{\mathbf{L}}$ and $\hat{\mathbf{S}}$ represent the electronic orbital and spin momentum respectively.

Duo uses a body-fixed axis system (axis along the inter-nuclear axis of the diatomic molecule) to describe co-ordinates. The $\hat{H}_{rot}$ term can be re-written by use of the Ladder Operators:

$$\hat{J}_\pm = J_+ \pm iJ_y \tag{2.70}$$

$$\hat{L}_\pm = L_+ \pm iL_y \tag{2.71}$$

$$\hat{S}_\pm = S_+ \pm iS_y. \tag{2.72}$$

The use of ladder operators is a standard operation within undergraduate level quantum mechanics textbooks. Hence using these ladder operators, the rotational Hamiltonian, $\hat{H}_{rot}$ can hence be written as:

$$\hat{H}_r = [(\hat{J}^2-\hat{J}_z^2)+(\hat{L}^2-\hat{L}_z^2)+(\hat{S}^2-\hat{S}_z^2)+(\hat{J}_+\hat{S}_-+\hat{J}_-\hat{S}_+)-(\hat{J}_+\hat{L}_-+\hat{J}_-\hat{L}_+)+(\hat{S}_+\hat{L}_-+\hat{S}_-\hat{L}_+)] \tag{2.73}$$

Duo uses the expression in Eq. 2.73 to solve the rovibronic Schrödinger equation within the framework of Hund's case (a).

Thus Duo can be used to solve the rovibronic equation for a given set of PECs for a diatomic molecule. These PECs, indicated by $V_{\text{state}}(r)$ are assumed to obey the following:

$$\hat{H}_e \left|\text{state}, \Lambda, S, \Sigma\right\rangle = V_{\text{state}}(r) \left|\text{state}, \Lambda, S, \Sigma\right\rangle . \tag{2.74}$$

In Eq. 2.74, "state" is simply a number given to each PEC e.g. if 6 PECs were calculated for a diatomic these would be labelled 1, 2, 3, 4, 5, and 6 in Duo. Λ, S and Σ have the usual definitions in molecular spectroscopy (see section 2.2).

For reference, the 1-dimensional Schrödinger Eq. is given by:

$$-\frac{\hbar^2}{2\mu}\frac{\mathrm{d}^2}{\mathrm{d}r^2}\psi_{\nu J}(r) + V_{\text{state}}(r) \; + \; \frac{J(J+1)}{2\mu r^2}]\psi_{\nu J}(r) = E_{\nu J}\psi_{\nu J}(r) \tag{2.75}$$

The procedure that Duo uses to solve the rovibronic Schrödinger equation is as follows:

- For each PEC inputted, the 1-dimensional Schrödinger equation is solved (see Eq. 2.75) for the case of $J = 0$ to give, for each PEC a set of vibronic wavefunctions, $\langle \text{state}, \nu|$ with eigenvalues, E_ν. Here ν is the vibrational quantum number given by 0, 1, 2, etc. E_ν are ordered in terms of energy.
- A basis set of rovibronic wavefunctions is then formed by selecting a set of size N_ν of these vibronic wavefunctions. These rovibronic wavefunctions have the form:

$$\left|\text{state}, J, \Omega, \Lambda, S, \Sigma, \nu\right\rangle = \left|\text{state}, \Lambda, S, \Sigma\right\rangle \left|\text{state}, \nu\right\rangle \left\langle J, \Omega, M\right| \tag{2.76}$$

Eq. 2.76 clearly shows the Born-Oppenheimer approximation: i.e. the total basis functions been split into electronic basis functions, $|\text{state}, \Lambda, S, \Sigma\rangle$, vibronic basis functions, $|\text{state}, \nu\rangle$ and rotational basis functions $|J, \Omega, M\rangle$. In Eq. 2.76, $\Omega = \Lambda + \Sigma$ and M is the projection of the total angular momentum J on the inter-nuclear axis. The complete rovibonic Hamiltonian expressed by Eq. 2.69 is then solved using this defined rovibronic basis set composed of the vibronic basis functions for the individual PECs. Hund's case (a) is used. Within the framework of Hund's case (a), several identities are used to solve the total rovibronic Schrödinger equation. In the case of Hund's case (a), L and S both independently precess around the inter-nuclear axis, little z hence their indivual projections are constant so hence sum is constant. For the rigid rotor functions describing the rotational motion given by $|J, \Omega, M\rangle$ these are:

- $\left\langle J, \Omega, M\right| \hat{J}_z \left|J, \Omega, M\right\rangle = \Omega$
- $\left\langle J, \Omega, M\right| \hat{J}^2 \left|J, \Omega, M\right\rangle = J(J+1)$

- $\langle J, \Omega \mp 1, M | \, \hat{J}_{pm} \, | J, \Omega, M \rangle = \sqrt{J(J+1) - \Omega(\Omega \mp 1)}$.

For the electronic wavefunctions given by $|\text{state}, \Lambda, S, \Sigma\rangle$ the identities of practical use are:

- $\langle \text{state}, \Lambda, S, \Sigma | \, \hat{S}^2 \, | \text{state}, \Lambda, S, \Sigma \rangle = S(S+1)$
- $\langle \text{state}, \Lambda, S, \Sigma | \, \hat{S}_z \, | \text{state}, \Lambda, S, \Sigma \rangle = \Sigma$
- $\langle \text{state}, \Lambda, S, \Sigma \pm 1 | \, \hat{S}_{\pm} \, | \text{state}, \Lambda, S, \Sigma \rangle = \sqrt{S(S+1) - \Sigma(\Sigma \pm 1)}$

One of the unique features about Duo is that it takes into account the coupling between electronic states. For full technical details see the Duo reference paper (Yurchenko, Lodi, Tennyson & Stolyarov 2016).

The output of solving the rovibronic equation in Duo is a set of energies and wavefunctions. These can be used to produce a linelist. When Duo is used to create a linelist, the following files are the outputs:

1. A "`states`" file which gives a list of states with energy values and identifying quantum numbers. Each energy level is given a unique identifying number.
2. A "`trans`" file which gives a list of transitional wavenumbers with calculated Einstein A-coefficients. For each transition the two energy states that give rise to it are referenced by their unique identifying number.

The Einstein A-coefficient, A_{fi} gives the probability of spontaneous emission between state i and f. Together with the Einstein A coefficients and partition function, $Q(T)$ the associated line intensity between these two states can be calculated. Background information of what the Einstein A-coefficient and partition function physically represent are given in sections 2.9.6 and 2.10.1 respectively. The line intensity of a line emitted as a result of a transition between state i and f is given by:

$$I(f \leftarrow i) = \frac{g_{ns}(2J_f + 1)A_{fi}}{8\pi hc\tilde{\nu}^2} \frac{e^{-\frac{E_i}{k_B T}}(1 - \frac{-hc\tilde{\nu_{if}}}{k_B T})}{Q(T)} \tag{2.77}$$

In Eq. 2.77, $\tilde{\nu}$ is the vibrational frequency in units of s^{-1} and J_f is the total angular momentum quantum number for the final state. For full details of how Duo calculates the Einstein A-coefficient (measured in s^{-1}) for a given transition, refer to Yurchenko et al. (2016). Put very simply the Einstein A-coefficient is proportional to the expectation value of the transition dipole moment between two states acted upon by the two wavefunctions of the two states concerned.

2.9.6 Einstein A-coefficients

The Einstein A-coefficient can best be described by considering the emission and absorption processes(in the absence of broadening) that occur within a two state system e.g. a molecule which has two bound states with energies such that $E_2 > E_1$.

In an emission process, for the case of an atom, an electron in state 2 drops down to state 1 and in doing so, by the conservation of energy a photon of energy corresponding to $E_2 - E1$ is emitted. In the process of an absorption a photon of energy $E_2 - E_1$ is absorbed and thus excites an electron in state 1 to state 2. Continuum

radiation is emitted when the state E_2 is not bound and thus an electron in a lower energy level that is excited by a photon is thus ejected if the energy imparted onto it by the photon is sufficient. There are three processes which allow molecules to change whether they are in state 1 or 2 namely spontaneous emission, absorption and induced emission.

- A_{21} is the Einstein A coefficient for spontaneous emission from state 2 to state 1
- B_{12} is the Einstein absorption coefficient for a transition from the lower state of energy E_1 to the upper state of energy E_2.
- B_{21} is the Einstein coefficient for induced emission from the upper state 2 to the lower state, state 1.

Note that the units of the Einstein A coefficient are s^{-1} and the units of the Einstein B coefficients are $J^{-1}m^3s^{-1}$. The number densities n_2 and n_1 refer to how many molecules in a gas are in state 2 and in state 1 respectively. In thermodynamic equilibrium, the rates of emission and absorption can be determined using the Einstein A & B coefficients, n_1, n_2 and the spectral energy density given by $\rho(\nu)$. The result of spontaneous emission is that the number density of the upper state, 2 will decrease as the number density of the lower state 1, is increased by the process.

$$\left(\frac{\mathrm{d}n_2}{\mathrm{d}t}\right)_{\text{spontaneous emission}} = -A_{21}n_2 \tag{2.78}$$

$$\left(\frac{\mathrm{d}n_1}{\mathrm{d}t}\right)_{\text{spontaneous emission}} = +A_{21}n_2 \tag{2.79}$$

Stimulated emission occurs when an electron in state 2 decays down to state 1-this process is induced when an electromagnetic field which has a frequency at or near the frequency corresponding to the difference in the energy between the two states is present. This electromagnetic field which causes this process of simulated emission is assumed to be isotropic with a spectral energy density of frequency ν of $\rho(\nu)$.
Thus the occupations of molecules in state 1 and 2 will thus be changed by the process of stimulated emission according to:

$$\left(\frac{\mathrm{d}n_2}{\mathrm{d}t}\right)_{\text{stimulated emission}} = -B_{21}n_2\rho(\nu) \tag{2.80}$$

$$\left(\frac{\mathrm{d}n_1}{\mathrm{d}t}\right)_{\text{stimulated emission}} = B_{21}n_2\rho(\nu) \tag{2.81}$$

Another manner in which the matter(molecules) can interact with the radiation is by the process of absorption whereby an electron from the lower state 1 absorbs a photon from the electromagnetic radiation field and is thus excited to the upper state, state 2. Thus the populations are altered by

$$\left(\frac{\mathrm{d}n_2}{\mathrm{d}t}\right)_{\text{photon absorption}} = B_{12}n_1\rho(\nu) \tag{2.82}$$

$$\left(\frac{\mathrm{d}n_1}{\mathrm{d}t}\right)_{\text{photon absorption}} = -B_{12}n_1\rho(\nu) \tag{2.83}$$

where B_{12} is the Einstein B coefficient describing the probability of an electron in state 1 absorbing a photon of the correct energy to be excited to the upper state 2.

Hence putting these three processes together, the populations of molecules in state 1 and state 2 will change with time by interaction with a radiation field as well spontaneous emission by the following:

$$\left(\frac{\mathrm{d}n_2}{\mathrm{d}t}\right)_{\text{spontaneous emission}} = -A_{21}n_2 \; - \; B_{21}n_2\rho(\nu) \; + \; B_{12}n_1\rho(\nu) \tag{2.84}$$

$$\left(\frac{\mathrm{d}n_1}{\mathrm{d}t}\right)_{\text{spontaneous emission}} = A_{21}n_2 \; + \; B_{21}n_2\rho(\nu) \; - \; B_{12}n_1\rho(\nu) \tag{2.85}$$

The phrase "detailed balance" is used to describe when the rate of molecules changing from state 1 to state 2 balances the rate that molecules go from state 2 to state 1. i.e.

$$\left(\frac{\mathrm{d}n_2}{\mathrm{d}t}\right)_{\text{spontaneous emission}} = -A_{21}n_2 \; - \; B_{21}n_2\rho(\nu) \; + \; B_{12}n_1\rho(\nu) = 0 \tag{2.86}$$

Or equivalently,

$$\left(\frac{\mathrm{d}n_1}{\mathrm{d}t}\right)_{\text{spontaneous emission}} = A_{21}n_2 \; + \; B_{21}n_2\rho(\nu) \; - \; B_{12}n_1\rho(\nu) = 0 \tag{2.87}$$

From statistical mechanics we know that:

$$\frac{n_1}{n} = \frac{g_1 \exp\left(-\beta E_1\right)}{Z} \tag{2.88}$$

$$\frac{n_2}{n} = \frac{g_2 \exp\left(-\beta E_2\right)}{Z} \tag{2.89}$$

where n is the total number density of all the molecules, g_1 and g_2 are the degeneracies of states 1 and 2 respectively and Z is the partition function.
The spectral energy distribution of the electromagnetic radiation field can be described by:

$$\rho(\nu) = \frac{8\pi\nu^3}{c^3}\frac{1}{\exp\beta h\nu - 1} = C(\nu)\frac{1}{\exp\beta h\nu - 1} \tag{2.90}$$

where $C(\nu)$ is simply introduced for convenience. Hence by substituting Eq. 2.90 in to equations 2.86 and 2.87 we thus obtain:

$$A_{21}g_2\exp\left(-\beta E_2\right) \; + \; B_{21}g_2\exp\left(-\beta E_2\right)\rho(\nu) = B_{12}g_1\exp\left(-\beta E_1\right)\rho(\nu). \tag{2.91}$$

Eq. 2.91 can be re-arranged and by equating like-terms it can be shown that:

$$A_{21}g_2 = B_{12}g_1C(\nu) \tag{2.92}$$

Hence the Einstein B coefficient are related to each other by $B_{12}g_1 = B_{21}g_2$ and the Einstein A-coefficient can be expressed as:

$$A_{21} = B_{12}\frac{g_1}{g_2}C(\nu) = B_{21}C(\nu) = B_{21}\frac{8\pi\nu^3}{c^3} \tag{2.93}$$

using the definition of $C(\nu)$ defined in Eq. 2.90.

2.10 The ExoCross Program

The output linelist of energy levels, transitional energy wavelengths and Einstein A coefficients can then be used directly by astronomers for input into models. For a comprehensive summary describing the format of the ExoMol database please see the ExoMol database paper (Tennyson et al. 2016).

Within the ExoMol group, the linelists produced by Duo for open-shell diatomics can be used to simulate spectra for different temperatures using different line broadening profiles using the in-house program ExoCross. The following sections describe the underlining physics of the different processes which can contribute to line broadening and are hence are critical in any simulations of atmospheres of planetary and stellar objects.

The ExoCross program can also be used to calculate the partition function and cooling functions for different temperatures as a function of J.

2.10.1 Partition Function

The partition function, Z is a thermodynamic function which physically speaking is the sum of the Boltzmann factors of individual quantum mechanical states weighted by their degeneracy. The symbol Z is chosen for the partition function from the German word *Zustandsumme*. The partition function is given by:

$$Q(T) = g_{ns} \sum_i (2J_i + 1) e^{-\frac{E_i}{k_B T}} \tag{2.94}$$

where g_{ns} is the nuclear statistical weight factor which depends on the nuclear spin of each of the two nuclei, I_a and I_b and is given by: $g_{ns} = (2I_b + 1)(2I_a + 1)$. For the special case when $I_a = I_b$ one needs to consider if the nuclei are ferminons (odd I) or bosons (even I). The sum is over the rovibronic energy levels E_i with the factor of $(2J_i + 1)$ to take into account the rotational degeneracy of the states. Finally, k_B is the Boltzmann constant and T is the temperature in Kelvin. The Boltzmann factor, $\frac{e^{-\frac{E_i}{k_B T}}}{Q(T)}$ gives a measure of probability that a molecule will be in a particular state of energy E_i at temperature T. By definition of the Partition function these probabilities add to unity. Physically, as the temperature increases, more energy levels are accessible to a molecule as the higher temperature allows electrons to occupy higher orbitals and for the nuclei to vibrate and rotate faster. The partition function can be used to determine thermodynamic properties such as the total energy of a system and its variation by taking partial derivatives of the Eq. 2.94.

2.11 Broadening of Spectral Lines

Atomic and molecular spectral lines can be broadened by three main mechanisms thus making individual spectral lines not perfectly monochromatic. Spectral lines are broadened by various processes, the main processes been:

- Natural broadening as a ramification of the Heisenberg Uncertainty principle
- Doppler broadening due to the random thermal motion of molecules in a sample following a Maxwellian distribution
- Collisional broadening due to collisions between molecules

These three processes are described in detail in sections 2.11.1, 2.11.2 and 2.11.3 respectively. Spectral lines are broadened by various processes which can be divided into two categories-homogeneous (Natural & Collisional) and inhomogeneous (Doppler) broadening in which different molecules are affected in different ways. A Voigt profile is formed when a Lorentzian and Gaussian profile are convoluted together: a Voigt profile is necessary to accurately describe the broadening of molecular lines as often populations of molecules are subject to all three broadening mechanisms simultaneously.

2.11.1 Natural broadening

In quantum mechanics, the Heisenberg uncertainty principle places a constraint on the accuracy that the position and momentum of a particle can simultaneously be determined, $\Delta x \Delta p \geq \frac{\hbar}{2}$. This is a result of the quantum mechanical description of wave-particle duality. Similarly there is a constraint on the minimum that the product of uncertainty in energy and uncertainty in time can be for a simultaneous measurement:$\Delta E \Delta t \geq \frac{\hbar}{2}$. Natural, or so called "lifetime" broadening is a direct consequence of the Uncertainty principle. Replacing ΔE with $\hbar\Delta\omega$, we obtain: $\Delta\omega \sim \frac{1}{\Delta} \sim \frac{1}{\tau}$ where we assume that the uncertainty in the lifetime of the excited state, δt is the statistically weighted natural lifetime of this state. Hence a natural spread in frequencies of emitted radiation, $\Delta\omega$ is observed. If it is assumed that the population of the upper state decays exponentially, then the distribution of this spead in frequency is a Lorentzian profile of the following form:

$$I(\omega) \sim \frac{1}{(\omega - \omega_0)^2 + (1/\tau)^2}. \tag{2.95}$$

In equation 2.95, ω_0 is the true frequency, $\omega - \omega_0$ is the change in frequency due to natural broadening and τ is the time that the molecule survives in a particular state.

2.11.2 Doppler Broadening

Within a gas of emitting molecules, different molecules will be moving at different speed and in different direction with respect to the line of sight through the sample. As molecules move towards or away from an observer, the wavelengths they emit will be shifted in frequency. This is known as the Doppler effect. When an atom or molecules moves away from the line of sight, a frequency emitted by it will be observed as:

$$\nu = \nu_0(1 + \frac{v_r}{c}) \tag{2.96}$$

where ν_0 is the rest frequency of emission, ν is the observed frequency, v_r is the relative velocity of the emitting species with respect to the observer amd c is the

speed of light. Hence the change in frequency is given by:

$$\Delta\nu = \nu - \nu_0 = \nu_0 \frac{v_r}{c}. \tag{2.97}$$

Assuming that the atoms or molecules are in local thermodynamic equilibrium (LTE) with a Maxwellian distribution of speeds, it can be shown that:

$$\frac{\mathrm{d}n(v_r)}{n_{\text{total}}} = \sqrt{\frac{m}{2\pi k_b T}} \exp(-\frac{mv_r^2}{2k_b T})\mathrm{d}v_r \tag{2.98}$$

Using Eq. 2.97 to replace v_r in Eq. 2.98 as $v_r = \frac{c(\nu-\nu_0)}{\nu_0}$, it can be shown that:

$$\frac{\mathrm{d}n(v_r)}{n_{\text{total}}} = \frac{1}{\sqrt{\pi}\Delta\nu_D} \exp(-(\frac{\nu-\nu_0}{\nu_D})^2)\mathrm{d}\nu \tag{2.99}$$

where the Doppler width has been defined as

$$\Delta\nu_D = \frac{\nu_0}{c}\sqrt{\frac{2k_b T}{m}} \tag{2.100}$$

This Doppler distribution of observed frequencies is of the form of a Gaussian distribution. The above derivation is for the case of random thermal motion of atoms and molecules within a gas which is obeying LTE. For this distribution, the Full-width Half-Maximum (FWHM) can be shown to be:

$$\text{FWHM} = 2\Delta\nu_D\sqrt{\text{In}(2)} \tag{2.101}$$

2.11.3 Collisional broadening

When molecules collide with each other their inherent energy levels are distorted by the collision leading to a change in phase of their oscillation. The frequency at which collisions occur is given by:

$$\nu_{\text{collision}} = v_{\text{thermal}} n \sigma_{\text{collision}} \tag{2.102}$$

where $v_{\text{thermal}} = \sqrt{\frac{2kT}{m}}$, n is the number density of emitting molecules and $\sigma_{\text{collision}}$ is collisional cross-sectional which is a measure of the probability for collision. Collisional broadening results in a Lorentzian profile of linewidths.

Chapter 3

Introduction to Chromium Hydride

In this chapter the astronomical importance of CrH will be put into context (section 3.4) with a summary of the existing linelist available in the literature to date (section 3.3). Experimentally CrH has been studied in the past-however theses studies concentrate only on the $A^6\Sigma^+ - X^6\Sigma^+$ transition (section 3.2). Due to the manifold of low-lying interacting electronic states of high spin, in keeping with neighbouring transition metal diatomics, CrH has found itself to be of considerable theoretical interest both as an individual molecule in itself but also as part of larger studies examining trends in properties such as bonding in these molecules (section 3.1).

3.1 Review of previous theoretical studies

Diatomic transition metal hydrides are of theoretical interest due to the presence of several low-lying atomic configurations, $4s^2 3d^n$, $4s^1 3d^{n+1}$, $4s^1 4p^1 3d^n$ of the metal atom which can be utilised in bonding with the hydrogen atom and thus give rise to several low-lying molecular electronic states. Since diatomic transition metal hydrides are open-shell molecules, single-configuration methods such as Hartree-Fock are not applicable but instead multi-configuration methods are required.

For these molecules, *ab initio* calculations are of particular importance as they can be used to predict electronic states which are yet to be observed in the laboratory and facilitate understanding of perturbation states. For the case of CrH this is a pertinent point as the only available experimental data is for the $X^6\Sigma^+$ and $A^6\Sigma^+$ states though it was recognised as early as 1959 by Kleman & Uhler that the upper $A^6\Sigma^+$ state is perturbed by interactions with other electronic states. When a PEC is perturbed it simply means that an otherwise regularly spaced pattern of its associated rovibronic energy levels is disrupted. Theses interactions between electronic states can take the form of spin-spin, spin-rotation or spin-orbit coupling to name a few. Following further work by Ram et al. (1993) it has been substantiated that the perturbation originates from the presence of a low-lying $a^4\Sigma^+$ state near 11 186 cm^{-1}.

Previous *ab initio* calculations have been performed for the first row transition metals by several authors. Bagus & Schaefer (1973) followed by Scott & Richards

(1974, 1975) performed Hartree-Fock calculations. Henderson, Das & Wahl (1975) and Das (1981) carried out preliminary Multi Configuration Self-Consistent Field (MCSCF) calculations. Das (1981) did a preliminary study of the bonding in these metal hydrides using the Phillips-Kleinman pseudo-potential method. Gropen et al. (1982) investigated the suitability of pseudo-potential methods for studying diatomic oxides and hydrides of scandium, titanium, chromium, nickel and zinc, and concluded that for all the operators they tested smaller core potentials would potentially be required to obtain more reliable results. Anglada et al. (1990a, 1990b) performed calculations on the low-lying states of both CoH^+ and TiH. More recently, Barone & Adamo (1997) investigated the properties of both neutral and cationic hydrides of the first-row transition metals using a self-consistent hybrid Hartree Fock/density functional method. Generally speaking, transition metals and their ions are of interest due to their established as well as further possible applications in catalytic converters, an area of research which is of global concern in industrialised countries(Blomberg & Siegbahn 1982, Walch 1984).

The early theoretical calculations from the 1970s largely neglected the effects of atomic correlation which, for several cases such as for vanadium hydride, VH seemed to be acceptable but later work by Bauschlicher & Walch (1982) disproved this as they showed that for nickel hydride, NiH and scandium hydride, ScH all atomic configuration terms needed to be implemented into calculations in a balanced manner.

Walch & Bauschlicher (1983) performed CASSCF/CI calculations ie Complete Active Space Self-Consistent Field/Configuration Interaction and predicted the ground states of serveral species to be TiH ($^4\Phi$), VH ($^5\Delta$), CrH ($^6\Sigma^+$), MnH ($^7\Sigma^+$) by consideration of atomic coupling arguments. Their work allows for electron correlation by correlating the $3d$ electrons at CI level and includes a detailed discussion of bonding inherent within diatomic transition metal hydrides arising from the various atomic configuration terms. In summary, for the case of molecular states arising from bonding involving a transition metal with atomic configuration of [Ar]$4s^1 3d^{n+1}$ the bonding is simply of the form [Sc](4s)-H(1s) bond polarised towards hydrogen.

For chromium hydride this is the case as chromium atom contains twenty-four electrons so due to the stability of having five electrons occupying the $3d$ orbitals, hence the bonding within chromium hydride arises predominantly from [Ar]$4s^1 3d^5$ chromium atom configuration and similarly for MnH the bonding arises primarily from a $4s^2 3d^5$ Manganese atomic configuration with stability gained from half-filled $3d$ shell. However, for nickel hydride the $4s^2 3d^n$ and $4s^1 3d^{n+1}$ configurations are almost degenerate leading to a complex manifold of electronic molecular states. For the case of both CrH and MnH little mixing occurs between these two atomic configurations (Mn forms $4s^2 3d^5$ states). For reference the atomic configuration of Argon, [Ar] is $1s^2 2s^2 2p^6 3s^2 3p^6$ i. e. eighteen electrons. Walch & Bauschlicher (1983) have calculated the spectroscopic constants R_e, ω_e, D_e for their calculated ground potential energy curves-for the case of CrH they are found to be in reasonable agreement with the experimental work available at the time documented in Huber & Herzberg (1979) and with the theoretical MCSCF work of Das (1981).

Following on from Walch & Bauschlicher's work on transition metal bonding, Chong et al. (1986) calculated theoretical dipole moments with fitted parameters

D_e, r_e, μ for first row transition metal hydrides using modified coupled pair functional (MCPF) theory and "better than" DZP basis sets. Since the dipole moments are dependent on the bonding mechanism involved, Chong et al. (1986) demonstrated how the magnitude of the dipole moment of a molecular electronic state would be a sensitive test of the bonding involved. For the case of CrH, their calculated values of r_e, μ for the ground $^6\Sigma^+$ state were found to be in good agreement with the experimental literature available at the time but, their value of D_e differed significantly from that of Gaydon (1968).

The most comprehensive study of electronic states beyond the ground state for CrH, $X^6\Sigma^+$ has been done by Dai & Balasubramanian (1993) who calculated PECs & DMCs along with fitted spectroscopic parameters (R_e, ω_e, T_e, D_e (eV)) for twenty-one low lying states by using all-electron complete active space multiconfiguration self-consistent field (CASMCSCF) followed by first-order configuration interaction (FOCI) and full second-order CI (SOCI) and multireference CI including Rydberg state calculations. They have found that their spectroscopic constants for the $A^6\Sigma^+$ and $X^6\Sigma^+$ states was in close agreement with experimental work done by Ram et al. (1993) and supportive of their prediction that the $A^6\Sigma^+$ state is heavily perturbed by an $a^4\Sigma^+$ state-indeed it was the experimental work of Ram et al. (1993) which prompted Dai & Balasubramanian to carry out *ab initio* calculations.

However, as their work does not contain couplings or values of D_e for all states it is insufficient to create a linelist. Hence the need to do *ab initio* calculations.

Roos (2003) has performed *ab initio* multiconfiguration second-order perturbation theory in the multi-state formalism(MS-CASPT2) calculations using the Molcas-5 software for the $X^6\Sigma^+$, $A^6\Sigma^+$ and $^6\Delta$ states of CrH and presents in addition to spectroscopic constants radiative lifetimes for the $\nu = 0, 1, 2, 3$ levels of the $A^6\Sigma^+$ state.

Finally, Ghigo et al. (2004) performed a theoretical study of the $X^6\Sigma^+$, $A^6\Sigma^+$, $^6\Sigma^+(III)$, $^6\Pi$, $^6\Pi(II)$, $^6\Pi(III)$ and $^6\Delta$ states of CrH and have presented PECs, DMCs and radiative lifetimes for these states. Their work is in good agreement with the available experimental data for the $X^6\Sigma^+$ and $A^6\Sigma^+$ states which are the only states for CrH which have been characterised experimentally.

Bauschlicher at al. (2001) performed a joint experimental and theoretical study of the $A^6\Sigma^+ - X^6\Sigma^+$ transition of CrH. Experimentally, they used the Fourier Transform Spectrometer at the National Solar Observatory to re-investigate the $9000 - 15\,000$ cm^{-1} region and thus measured the $1-0$ and $1-1$ bands. Using these experimental measurements they then calculated improved spectroscopic constants and additionally predicted the $2-0$ band origin to be at 14 468.6 cm^{-1} using the band head of 14 510 cm^{-1} reported by Kleman & Uhler (1959) as guidance. Theoretically they performed multireference configuration interaction (MRCI) calculations with the inclusion of both scalar relativistic corrections and $3s3p$ correlation. They report *ab initio* Einstein A coefficients and radiative lifetimes for the $A^6\Sigma^+$ state and conclude that as these values do not vary substantially with the level of theory employed they must be of reasonable accuracy. Of particular interest is their calculation of the transition dipole moment (TDM) between the $A^6\Sigma^+$ and $X^6\Sigma^+$ states.

3.2 Review of previous experimental studies

The diatomic molecule Chromium Hydride, hereafter referred to as CrH has been studied using a range of various experimental set-ups and techniques such as with a King Furnace, Fourier Transform Spectrometry, Laser Magnetic resonance (LMR). Descriptions and explanations of these techniques can be found in Corney (1977), Bernath (2000) and Evenson & Saykally (1980) respectively.

CrH was first studied in 1937 by Gaydon & Pearse who observed a band in the UV region spanning approximately $3600 - 3700$ Å region using a flame of hydrogen placed between a high-tension arc and chromium electrodes. This study formed part of a larger study of diatomics which came about from the need to identify impurities which were commonly observed in the laboratory. Gaydon & Pearse then went on to publish listings of molecular band heads for diatomic molecules in the 10 000 Å to 2000 Å range as at the time these were not available: instead users of spectroscopy had to manually calculate band head positions from spectroscopic constants, a process that would rely on the user having considerable knowledge and experience. In their work, Gaydon & Pearse placed an emphasis on molecules containing elements which were known or suspected to be cosmically abundant and hence helped precipitate the field of astrophysical spectroscopy.

Following on from this first observation of a UV band, a handful of experimental studies have been performed on CrH.

Kleman & Liljeqvist (1955) observed this UV band using a high temperature furnace: in addition, they observed a weaker UV band near 3290 Å and an infrared band centred at 8611 Å in the range $689 - 1065$ nm for which they undertook a rotational analysis. Thereafter Kleman & Uhler (1959) extended this analysis of the IR system at 8611 Å and showed that it arose from a $^6\Sigma^+ - ^6\Sigma^+$ transition.

Thereafter, O'Connor (1967) photographed this infrared system in emission using a high current discharge tube and re-analysed the $1 - 0$ and $1 - 1$ vibrational bands of this $A^6\Sigma^+ - X^6\Sigma^+$ transition of CrH and also did a rotational analysis of the $0 - 0$ vibrational band of chromium deuteride, CrD. The vibrational quantum number is ν and in this notation $1 - 0$ signifies that the upper state has vibrational quantum of $\nu' = 1$ and the lower state has $\nu'' = 0$.

In 1973, Smith published a study on the absorption spectra of diatomic hydrides and deuterides of the second row transition metals between 290 nm and 700 nm using a shock tube experimental set-up with temperatures up to $\approx$ 3000 to 4000 K. Of particular interest was analysis of new bands which were found during the work undertaken on NiH and CoD. Using this experimental set-up, Smith observed the two ultraviolet systems noted by Gaydon & Pearse (1937), Kleman & Liljeqvist (1955) and O'Connor (1969).The advantages of using a shock tube set up is the high temperatures which can be reached in comparison with using King Furnaces. Smith found that for CrH & CrD, using gas inset gas mixtures of 50% hydrogen/deuterium to 50% Argon, the optimal reflected shock temperature is around 3000 K and powdered particle size between 5 and 30 μm.

Independent confirmation of the ground state of CrH to be $^6\Sigma^+$ was provided by Van Zee et al. (1985) who measured fine structure and hyperfine splittings by

trapping CrH and CrD in an argon matrix. It is interesting to note Jacox (1987)'s study which compares the results obtained of around 230 electronic transitions for diatomic molecules in the gas phase and inert solid matrices.

Ram et al. (1993) have studied the emission spectra of the ^{52}Cr isotopologue of CrH in the infra-red region spanning 10 000 − 17 500 cm^{-1} at the National Solar Observatory at Kitt Peak via use of a hollow cathode discharge lamp alongside the Fourier Transform spectrometer associated with the McMath Solar Telescope. CrH has four naturally occurring isotopologues, namely ^{50}CrH, ^{52}CrH, ^{53}CrH and ^{54}CrH with abundances of 4.8, 83.8, 9.5 and 2.4% respectively. Isotopologues are simply molecules consisting of atoms with the same number of protons but differing number of neutrons. The observed wavelengths published for the $0-0$ vibrational band of the $A^6\Sigma^+ - X^6\Sigma^+$ transition of CrH is in the range from approximately $N = 0$ to $N = 31$ in the structure of six P branches ($\Delta J = -1$) and six R branches ($\Delta\ J = +1$) which is consistent with the $A^6\Sigma^+$–$X^6\Sigma^+$ assignment for CrH. Using standard spectroscopic notation, N here refers to the total angular momentum of the molecule excluding contributions from the nuclear and electron spins and J refers to the total angular momentum of the molecule excluding nuclear spin. Their work is of great interest from a theoretical respect for their observation and analysis of the perturbation of the $A^6\Sigma^+$ state-an observation originally noted by Kleman & Uhler. Kleman & Uhler observed that all six spin components, F_1, F_2, F_3, F_4, F_5 and F_6 of the $A^6\Sigma^+$ state were perturbed between $N = 20$ and $N = 21$ and thus reasoned that the perturbing state was the dissociative $^8\Sigma^+$ state which converges at the same asymptote as the $X^6\Sigma^+$ state. Here F refers to the total angular momentum of the molecule. In contrast, Ram et al.'s observations showed that only the F_1, F_2 and F_3 spin components were perturbed between $N = 9$ and $N = 10$ with severe non-local perturbation to the F_2, F_3, F_4 and F_5 components between $N = 20$ and $N = 21$. Given that the perturbation was found to affect four different J values at constant N, via use of selection rules, Ram et al. thus concluded that a $a^4\Sigma^+$ state was responsible for the perturbations which will interact with the $^6\Sigma^+$ states via the spin-spin operator.This conclusion is supported by O'Connor's study of CrD which showed that the F_1, $F2$ and F_3 spin components of the $A^6\Sigma^+$ state were perturbed at $N = 18$. By fitting to a N^2 Hamiltonian provided by Brown & Milton (1978) and thus performing a rotational analysis of the $0-0$ band, Ram et al.(1993) thus obtained improved rotational constants for the $X^6\Sigma^+$,$A^6\Sigma^+$ and $a^4\Sigma^+$ states of CrH.

The first reported study undertaken on the pure rotational spectrum of CrH in its ground electronic state, $X^6\Sigma^+$ was done by Corkery et al. (1991) who used a far-infrared laser magnetic resonance technique (LMR). This work was undertaken as part of a larger study of first row transition metal hydrides by LMR technique (Beaton et al. 1988, Nelis et al. 1991). Corkery et al. (1991) assigned spectra for the first five rotational transitions for the predominant isotopomer, namely ^{52}CrH for the $\nu = 0$ label of the $X^6\Sigma^+$ state and thus fitted rotational, spin and hyperfine spectroscopic constants.

As a compliment to this work, Lipus et al. (1991) undertook a study of rovibrational spectrum for the $1-0$ and $2-1$ vibrational bands of the CrH molecule in its $X^6\Sigma^+$ ground state by use of Faraday laser Magnetic resonance (LMR) technique.

In addition, Brown et al. (1993) measured the frequencies of the lowest rotational transitions in ground electronic state by using an LMR technique. As elucidated in their paper in the early 1990s the field of far infra-red astronomy was burgeoning due to the development of spectrometer technology. Hence a study measuring the rotational lines of diatomic molecules to aid astrophysical detection was initiated.

More recently Halfen & Ziurys (2004) have measured the $N = 0$ to $N = 1$ (pure-rotational) transitions of the $A^6\Sigma^+$ and $X^6\Sigma^+$ states in CrH directly using sub-millimetre absorption spectroscopy. In addition,the $N = 1$ to $N = 2$ transition of CrD have been measured. In both cases, experimentally the relevant species was produced via reaction of vaporised Chromium metal with D_2 and H_2 respectively. By fitting to a Hund's case (b) Hamiltonian, Halfen & Ziurys have produced refined rotational, spin and hyperfine constants for the CrH molecule and also established for the first time spectroscopic constants for the CrD molecule.

The bond dissociation energy of CrH has been studied by Chen et al. (1993) using gas phase thermochemistry reactions of Cr^+ with mono-, di- and tri-methylamine. This study was motivated by the disagreement between previous experimental work (Sallans et al. 1985, Kant & Moon 1979, Gaydon 1968) and the available theoretical work (Walch & Bauschlicher 1983, Ziegler et al. 1987). Chen et al. (1993) obtained $D_0(\mathrm{Cr}^+ - \mathrm{H}^-) = 7.95 \pm 0.07$eV and the 0K value D_0(Cr-H) to be 1.93 ± 0.07 eV.

The photoelectric spectrum of the CrH^- ion has been measured by Miller et al.(1987) and has been shown to be in excellent agreement with the theoretical calculations performed by Lin & Ortiz (1990).

The dipole moment of both the $\mathrm{A}^6\Sigma^+(\nu = 0)$ and $\mathrm{X}^6\Sigma^+(\nu = 0)$ states has been measured via use of the Stark effect by Chen et al. (2007) who have compared and contrasted the μ_e and $\frac{\mu_e}{R_e}$ values obtained with previous theoretical and experimental work for first row transition metal hydrides. Here μ_e refers to the dipole moments of these states at the equilibrium bond length denoted R_e.

The radiative lifetime of the ν=0, 1 levels of the $\mathrm{A}^6\Sigma^+$ state for the lesser isotopologue ^{50}CrH has been studied by Shin et al. (2005) using a time-delayed resonant two photon ionisation method. Using this technique, Shin et al.(2005) found the measured lifetime to differ by $\approx 16 - 45\%$ than those published in the theoretical literature and that calculated by Burrows et al. (2002) for use in a study of L type dwarfs. The lifetimes they measured are $\nu = 0: \ 0.939 \pm 0.019$ μs and for $\nu = 1: \ 1.027 \pm 0.066$ μs. This observation has ramifications for opacity functions used by astronomers in determining the column density and abundance of CrH. Theoretically, both Ram et al.(1993) and also Bauschlicher et al. (2001) attributed the perturbation of the $\nu = 1$ level of the $\mathrm{A}^6\Sigma^+$ state due to a $\mathrm{a}^4\Sigma^+$ state. Thus it can be concluded that any perturbation of this $\nu = 1$ state of the upper $\mathrm{A}^6\Sigma^+$ state by this state is likely to increase its fluorescence lifetime so that it is greater than the $\nu = 0$ lifetime owing to varying levels of mixing by the $a^4\Sigma^+$ state with the $\mathrm{A}^6\Sigma^+$ state.

As a result of this perturbation it is thus non-trivial to extrapolate an opacity function from these lifetimes. Furthermore, Shin et al. (2005) have also found during their rotational analysis of the $\mathrm{A}^6\Sigma^+ - X^6\Sigma^+$ 0−0 vibrational band of CrH departures from Hund's case (b) allowed transitions ie forbidden lines implying that either or both of the $\mathrm{X}^6\Sigma^+$ and $\mathrm{A}^6\Sigma^+$ states do not fully obey Hund's case (b).

As noted by Shin et al.(2005), to date there are no published experimental measurements of the intensity of the $A^6\Sigma^+ - X^6\Sigma^+$ system and thus astronomers have to thus rely on theoretical estimates. Included in Shin's study are line positions for the $0-0$ band of the $A^6\Sigma^+ - X^6\Sigma^+$ system of the ^{50}CrH isotopomer which have been fitted to the standard matrix Hamiltonian via a least-squares fitting procedure.

In summary the $A^6\Sigma^+ - X^6\Sigma^+$ system of CrH has been extensively studied by several experimental groups since the 1930s. What is striking is that it appears that no other electronic systems are observable. This may be due to either constraints of experimental set-ups (i.e. if other electronic systems appeared in regions which are hard to be measure experimentally) or that the spectra of CrH is dominated purely by the $A^6\Sigma^+ - X^6\Sigma^+$ system. Our new linelist for CrH does shed light on this observation (see chapter 5). From our linelist is can be concluded that the $A^6\Sigma^+ - X^6\Sigma^+$ system is dominant in the spectra of CrH but there is the possibility that some bands of the $B^6\Pi - X^6\Sigma^+$ system could be observed. This demonstrates the interplay which should occur over time between experimental and theoretical studies.

3.3 Existing CrH linelist

Using the work of Bauschlicher et al. (2001), Burrows et al. (2002) then generated the only published linelist available at present for CrH. This linelist contains transition frequencies and ground state energies with associated quantum numbers of the 12 bands of the $A^6\Sigma^+ - X^6\Sigma^+$ electronic system of CrH for $\nu' = 0, 1, 2$ and $\nu'' = 0, 1, 2, 3$ up to $J = 39.5$. The twelve bands consist of 6 P ($\Delta J = -1$) branches and 6 R ($\Delta J = +1$) branches corresponding to $\Sigma = -5/2, -3/2, -1/2, 1/2, 3/2, 5/2$ where Σ represents the projection of the total electron spin S on the inter-nuclear axis.

This linelist was constructed by using the spectroscopic constants reported by Bauschlicher et al. (2001) to determine ground state term values with the upper state term values determined by these constants for the cases where there was no experimental transition wavenumbers available. Line strengths were evaluated by using the Einstein A coefficients reported by Bauschlicher at al. (2001) along with calculated Hönl-London factors calculated by M. Dulick of the National Solar Observatory (private communication).

As an application of their created linelist, Burrows et al. (2002) created three synthetic models of the atmosphere of the L5 dwarf 2MASS1507038-151648: by comparing these to observations of this L5 dwarf they concluded that the the abundance of CrH relative to H_2 was around $(2 - 4 \times 10^{-9})$ which is in broad agreement with what can be expected from chemical equilibrium models.

3.4 CrH in astrophysics

It has been speculated that CrH is present in several astrophysical settings and in particular, has found itself of considerable interest in the emerging field of brown dwarfs which are defined as sub-stellar objects which do not reach the required mass to ignite hydrogen but instead ignite deuterium.

It has been estimated by Grevesse & Sauval (1998) that the transition metal chromium is a cosmically abundant metal with Cr/H $\approx 2 \times 10^{-5}$. Table 3.1 shows the percentage abundances of the top twenty elements in the universe and in the sun which is the ramification of big bang and solar nuclear synthesis. This data is then represented pictorially in figure 3.1 which show the percentage abundance of elements in the Universe and Sun with the exception of Hydrogen and Helium.

Rank	Element	Percentage abundance(%)		Rank	Element	Percentage abundance(%)	
		Universe	Solar			Universe	Solar
1	Hydrogen	75.00	75.00	11	Argon	0.0200	0.0070
2	Helium	23.00	23.00	12	Calcium	0.0070	0.0070
3	Oxygen	1.00	0.90	13	Nickel	0.0060	0.0080
4	Carbon	0.50	0.30	14	Aluminium	0.0050	0.0060
5	Neon	0.13	0.10	15	Sodium	0.0020	0.0040
6	Iron	0.11	0.10	16	Chromium	0.0015	0.0020
7	Nitrogen	0.10	0.10	17	Manganese	0.0008	0.0010
8	Silicon	0.07	0.09				0.0008 (Chlorine)
9	Magnesium	0.06	0.07	18	Phosphorus	0.0007	0.0007
10	Sulphur	0.05	0.04	19	Potassium	0.0003	0.0004
				20	Titanium	0.0003	0.0004

Table 3.1: Percentage abundances of the top twenty elements in the universe and their abundances in the sun

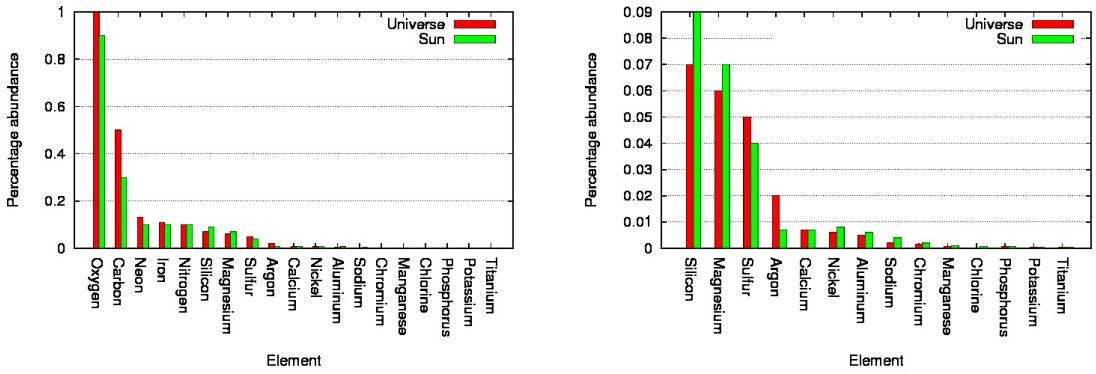

Figure 3.1: Percentage abundances of the top twenty elements in the universe and their abundances in the sun

In terms of first row transition metals, after Iron and Nickel, Chromium is the most abundant in the universe as shown by figure 3.2a which excludes Iron and Nickel which have abundances that dwarf those of the other metals. In the Sun, Chromium is the fifth most abundance first row transition metal after Iron, Titanium, Nickel and Vanadium as shown in figure 3.2b which excludes Iron and Titanium which are the predominant first-row transition metals in the sun.

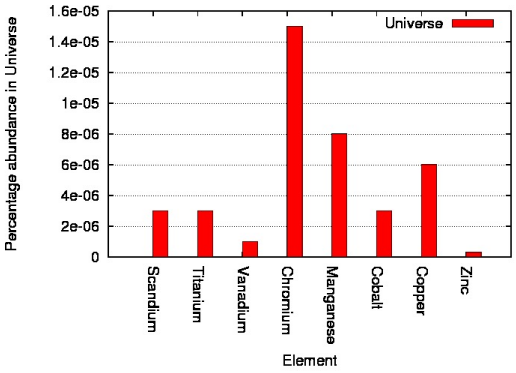

(a) Percentage abundance of selected first-row transition metals in the Universe

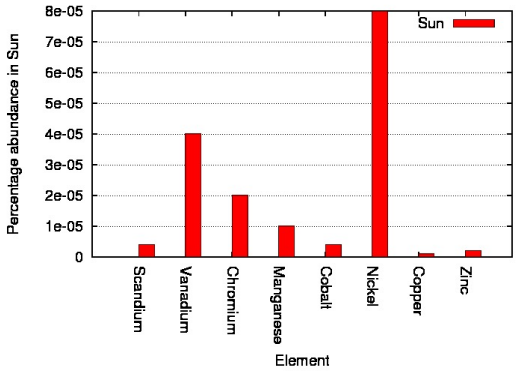

(b) Percentage abundance of selected first-row transition metals in the Sun

Figure 3.2: Percentage abundance of selected first-row transition metals

In 1980, Engvold et al. speculated that CrH was present in high resolution visible spectral observations of the large sunspot (diameter of around 27 arcsec) observed on March 31, 1976, Roma number 6751 using the results of the rotational transitions in the $A^6\Sigma^+ - X^6\Sigma^+$ $0-0$ spectrum, band head at 8611 Å recorded by Kleman & Uhler (1959). Using a statistical analysis designed to eliminate chance coincidences, 169 such transitions were identified. These observations of the sunspot were taken using the Fourier Transform Spectrometer housed in the McMath Solar Telescope at the Kitt Peak National Observatory. Data was taken during dry days to limit effects of terrestrial absorption lines and was predominantly recorded in the region 6 000 Å to 10 000 Å as this corresponds to where best quality data was available-the FTS was capable of resolution up to 0.005 cm^{-1}.

Also in 1980, Lindgren & Olofsson investigated the origin of first three of the so-called "Keenan Bands" named after Keenan (1950, 1957) who discovered 4 red-degraded strong bonds in S stars in the region of $8000 - 9000$Å namely at 8271 Å 8464 Å 8611 Å and 8820 Å. Previously, Dubois (1977) suggested that BaF, BaCl were responsible for the three bands-however this was put into doubt by Wyckoff and Clegg (1978) who analysed a medium-resolution spectrograph of the S star R Cyg. To clarify the situation, Lindgren & Olofsson measured in the lab absorption spectra of BaF and BaCl in the region 7000 to 8800 Å using a King Furnace and compared results of this experimental work to spectra of the S star R Cyg and two cool M stars, T Cep and M6 dwarf HD 1326 B in the red and infrared spectral region obtained using a Boller and Chivens spectrograph attached to the 1 m reflector at Stockholm University. Their conclusion was that BaF and BaCl were not responsible for the bands but instead the bandhead of the $A^6\Sigma^+ - X^6\Sigma^+$ transition of CrH with bandhead at 8611 Å was responsible for the Keenan band at 8611 Å. However they note that a higher resolution spectrograph would be required for line-by-line identification. For references, a single spectral line is formed by the wavelength of light emitted when a molecule changes from one state to another. When several spectral lines within an interval overlap, the overall intensity of the resulting spectra is simply the sum of the individual intensities. Rovibronic spectra from molecules typically takes on a regular pattern of “bands” in which the intensity rises as the wavelength increases due to this

superposition effect-when the intensity drops down again to begin the next band, a bandhead is formed.

Using data from the 2-Micron All-Sky Survey (2MASS) Kirkpatrick et al. (1999) identified twenty stellar objects with spectral types later than M9.5. At the time only 6 such objects had been found. By analysing spectroscopically these objects using the Low Resolution Imaging Spectrograph (LRIS) at the W. M. Keck Observatory, Kirkpatrick et al.(1999) defined a new spectral class "L" which is characterised by the disappearance of TiO and VO bands which dominate"M" objects and the appearance of metal hydrides CrH, FeH, CaH as well as neutral alkali metals. One of the objects of selection, GI-229B was classed as a methane-dominated object which Kirkpatrick proposed to be called a "T" dwarf. Since these objects were found to contain the lithium doublet at 6708 Å it was confirmed that they were sub-stellar. In order for Lithium to be burned the mass of the star needs to be greater than $> 75\ M_J$ (Pavlenko et al. 2008). Previously Kirkpatrick, Beichman & Skrutskie (1997) as well as Delfosse et al. (1997) had defined the M-dwarf classification scheme.

To define subclasses within this L classification scheme (e.g. L0, L1, L2 etc), Kirkpatrick et al.(1999) investigated suitability of spectral ratios which had been previously devised by Kirkpatrick, Henry & McCarthy(1991) and are defined as "a measure of the summed flux in a region containing a line or band of interest divided by the summed flux in a nearby region approximating the local pseudo-continuum". For CrH they investigated the suitability of two such ratios which they labelled CrH-a and CrH-b corresponding to the $0-0$ bandhead at 8611 Å and the $0-1$ bandhead at 9969 Å of the $A^6\Sigma^+ - X^6\Sigma^+$ electronic transition system. They found that the later was unsuitable as a spectral diagnostic due to poor sensitivity of CCD at this region. However, the CrH-a ratio was found to follow a well-defined trajectory whereby the ratio increased in strength from late M dwarfs to early L dwarfs with a peak at L5 V before decaying to later L dwarfs. This is shown in figure 3.3 which is taken from the paper.

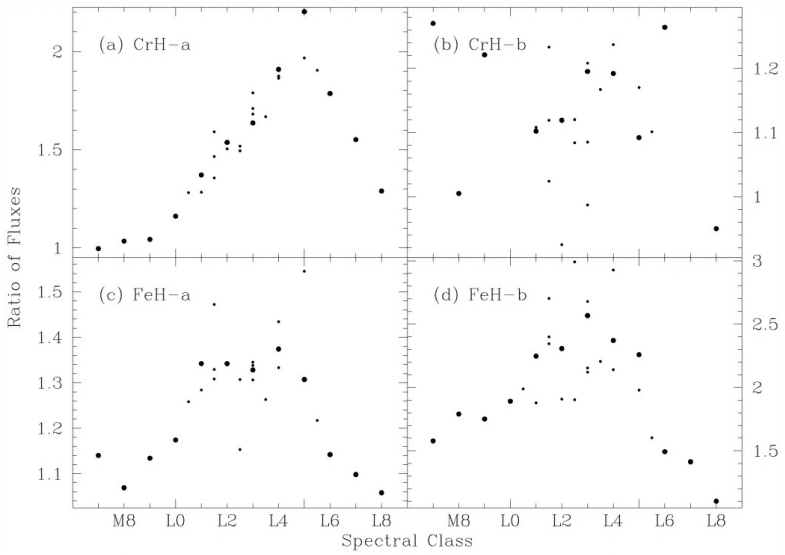

Figure 3.3: Selected spectral ratios investigated by Kirkpatrick et al. (1999). As can be seen from the top-left hand figure, the absorption feature, labelled CrH-a rises to a peak at L5 before decreasing.

Thus Kirkpatrick et al. (1999) defined a recipe for classifying L type dwarfs using the following criteria:

- metal hydride ratio
- Oxide ratio
- alkaline metal ratio
- redness (colour) ratio
- broadening of Potassium doublet lines

where the metal hydride ratio selected was CrH-a. Ratios involving FeH were dismissed. This CrH ratio is defined as the flux in the $8580.0 - 8600.0$ Å region divided by the flux in the $8621.0 - 8041.0$ region which thus gives a quantitative measure of the 8611 Å feature of CrH. Having defined spectral-diagnostics, Kirkpatrick et al. (1999) then classified the twenty-five objects using a least-squares minimisation technique described in Kirkpatrick, Henry & McCarthy (1991) within their new defined L classification scheme which has been widely accepted. Figure 3.4 is taken from Kirkpatrick et al.'s 1999 paper and shows enlarged spectra of M9, L3 and L8 classified objects (taken from the 2MASS catalogue) with prominent features marked such as the disappearance of oxides going from M9 to L3 along the with the subsequent increase in metal hydride bands and alkaline metal bands. Table 3.2 demonstrates quantitatively how the spectroscopic ratios devised were used to classify objects into "L" subclasses.

Object	Type	CrH-a	Rb-b/TiO-b	Cs-a/VO-b	Color-d
2MASSW J1214063 + 202702	M7 V	0.996	0.649	0.867	2.793
2MASSW J1434264 + 194050	M8 V	1.034	0.588	0.795	3.725
2MASSW J1239194 + 202952	M9 V	1.043	0.576	0.736	5.345
2MASP J0345432 + 254023	L0 V	1.161	0.662	0.781	6.654
2MASSW J1439284 + 192915	L1 V	1.371	0.812	0.856	7.333
Kelu-1	L2 V	1.537	1.048	1.029	6.7
2MASSW J1146345 + 223053	L3 V	1.636	1.155	1.125	7.21
2MASSW J1155009 + 230706	L4 V	1.909	1.323	1.258	9.713
DENIS-P J1228.2 − 1547	L5 V	2.203	1.658	1.488	14.406
2MASSS J0850359 + 105716	L6 V	1.786	1.703	1.561	15.549
DENIS-P J0205.4 − 1159	L7 V	1.551	2.189	1.604	22.027
2MASSW J1632291 + 190441	L8 V	1.289	2.564	1.626	30.015

Table 3.2: Values of Spectroscopic Ratios used by Kirkpatrick et al. (1999) to classify various objects into "L" subclasses. Table reproduced from Kirkpatrick et al. (1999)

As well as been used to classify "L-type" objects, CrH has been the subject of studies to determine if it could be used as a sensitive detector of magnetic fields in brown dwarfs.

The Zeeman-effect in atoms is commonly used to measure the magnetic field of stellar objects (Robinson Jr 1980; Saar 1988; Valenti & Johns-Krull 2001a). However, for temperatures less than approximately 3000 K, atomic lines become too weak to be observed hence with the discovery of brown-dwarfs and sub-stellar objects with lower temperatures, investigations into using molecules began as summarised by Bernath

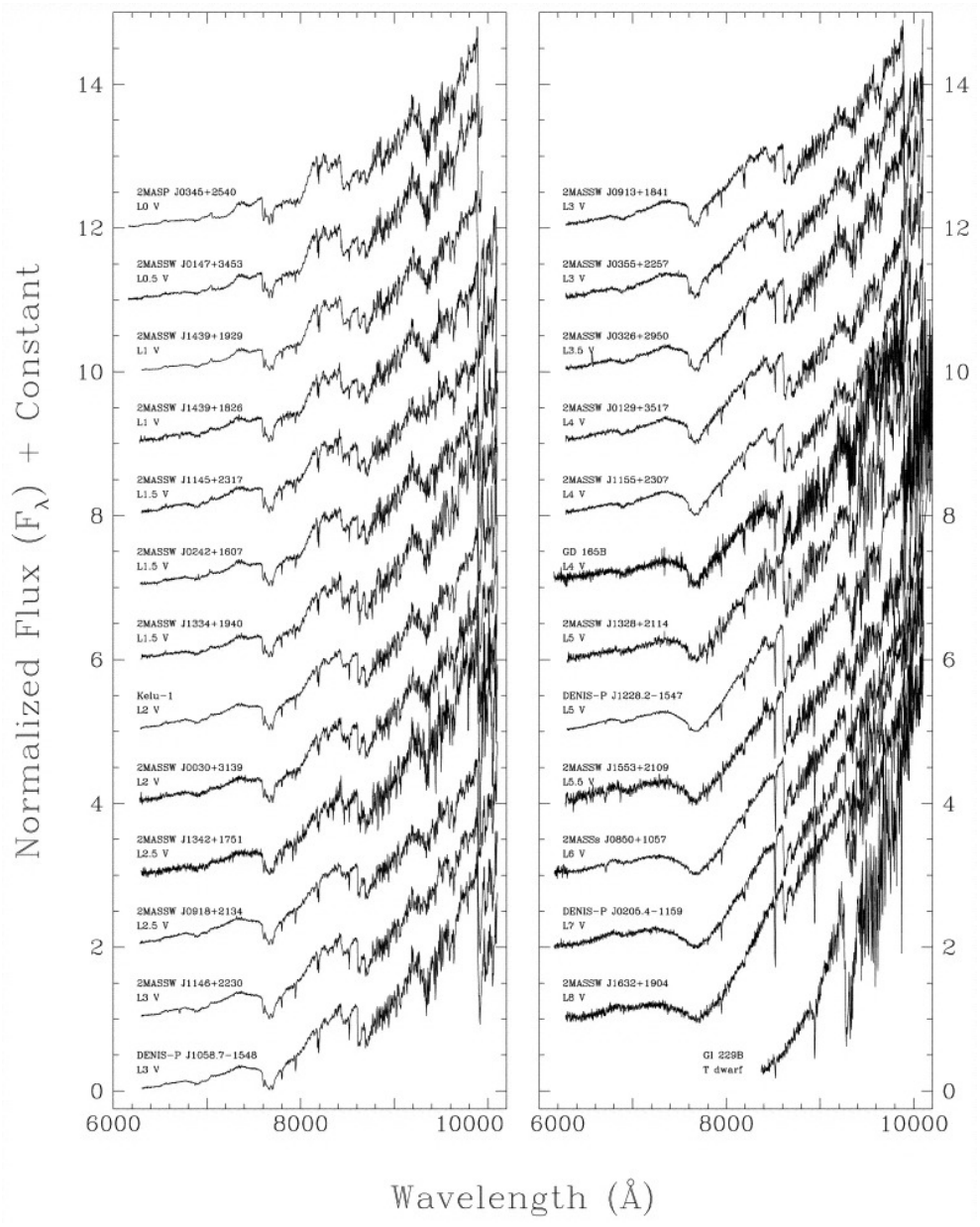

Figure 3.4: Spectral classification of L dwarfs according to Kirkpatrick et al. (1999).

(2009). Following on from the suggestions of Valenti et al. (2001b) and Berdyugina et al. (2001), Berdyugina & Solanki (2002) and Berdyugina et al. (2003) investigated the use of FeH as a magnetic field strength diagnostic in such objects as part of the HotMol project.

Kuzmychov & Berdyugina (2013a, 2013b) investigated if the Paschen-Back (case of strong magnetic field that breaks coupling between orbital and spin angular momenta of electrons) could be exploited in the $0-0$ band of the $A^6\Sigma^+ - X^6\Sigma^+$ electronic transition of CrH to measure magnetic fields. They performed quantum mechanical calculations to determine the vibrational-rotational energy structure with and without the presence of an external magnetic field and also the associated transition wavenumbers and Hönl-London factors. Using these results and by solving analytically under the Milne-Eddington approximation the transport equation for polarised

radiative transfer in a stellar atmosphere, the four Stokes parameters were calculated. The Stoke's parameters $(I/I_c, Q/I_c, U/I_c, V/I_c)$ are a formalism universally used in astrophysics for describing analytically the intensity and polarisation of electromagnetic radiation. Thus the effect of the strength & orientation of the magnetic field on the polarisation signal was calculated.

The key results are shown in figure 3.5 which shows the calculated fine-structure splitting induced by an external magnetic field for $N = 3$ and $N = 4$ in standard spectroscopic notation. Each of the six fine structure levels J splits into 2J + 1 magnetic levels M, which are perturbed by nearby levels with the same M number.

In summary, Kuzmychov & Berdyugina (2013a, 2013b) demonstrated theoretically that in Paschen-Back regime (strong-field limit) a net polarisation can be detected due to the asymmetry induced into the Stokes parameters for the CrH molecule.

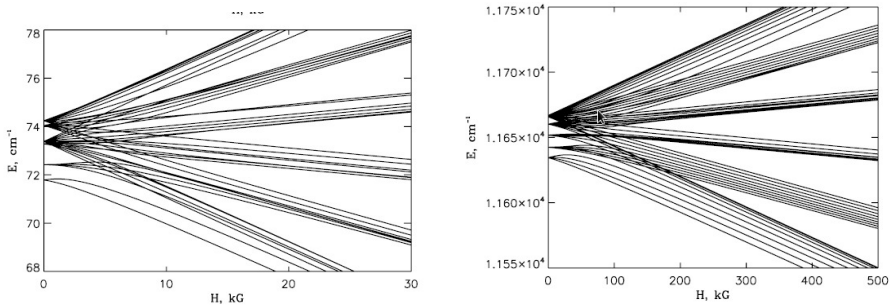

(a) $N = 3$ (b) $N = 4$

Figure 3.5: Fine structure splitting of the rotational levels due to the presence of an external magnetic field. Figure reproduced from Kuzmychov & Berdyugina(2013a)

These results were then utilised by Kuzmychov et al. (2013) who modelled the spectra of two observed radio pulsating brown dwarfs and predict that they have magnetic fields of order kG which is in agreement with previous determinations using simultaneous ratio, Hα and X-Ray observations of a similar dwarf by Hallinan et al.(2006, 2007).

Since the publication of the linelist for CrH of Burrows et al. (2002), several authors have used this to study astronomical objects of interest: however, it is apparent that the incompleteness of this linelist presents a limit to the progress of their work. The construction of the linelist is described in section 3.1.

For example, Pavlenko et al. (2006) have computed a spectral energy distribution for the M dwarf GJ406 in the spectral region $(0.35 - 5)\mu$m and by comparing with observational data have determined $T_{\rm eff} = (2800 \pm 100)$K and also $M_{\rm bol} = (12.13 \pm 0.10)$. These parameters indicate that GJ406 has an age of approximately 0.1 - 3.5 Gyr and is thus in a state of high evolutionary activity which is supported by the evolutionary models of Baraffe et al. (2003). However, Pavlenko et al. (2006) note that their work is limited by the incompleteness of molecular lines in particular those for both FeH and CrH.

The spectral energy distribution they generated for GJ406 was created by use of the NextGen Dusty and Cloud Model atmospheres(Hauschildt et al. 1999) assuming Voigt profiles with linelists taken from various sources for H_2O, TiO, FeH, CO, MgH

and CrH (Burrows et al. 2002) and the atomic VALD linelists for input. GJ406, which is referred to by many names is described as an "archetype dwarf of spectral type M6V"(Mohanty et al. 2004) and it has been determined by Henry et al. (2004) that GJ406 sits at a distance of 2.39 pc from our sun.

M type dwarfs have been found to form a significant fraction of observable stars: indeed it has been estimated that approximately 70% of the stars within 10 parsecs of our own sun are indeed M dwarfs: it is likely that this density is prevalent throughout our galaxy.

In a similar fashion to Pavlenko et al. (2006), Lyubchik et al. (2007) have computed synthetic spectra for comparison with observed high resolution spectra of five ultra cool dwarfs at the peak of their energy distribution, located in the J band from M6 to L0. Their calculations are done using the approximations of Local Thermodynamic Equilibrium(LTE), hydrostatic equilibrium, in the absence of sources and sinks of energy by use of the WITA6 programme (Pavlenko et al. 2000) alongside the NextGen model structures again with various sources of molecular linelists. One of their key findings is that several features predicted by the existing linelists for CrH and FeH predict features which are not apparent in the observed spectra. The authors have hence concluded that the incompleteness of these linelists are the "main limiting factor" in their study. For the wavelength region ($12800-13010$ Å, Lyubchik et al. (2007) have computed the effect of individual molecular and atomic species upon the calculated spectral energy distribution and found that the total opacity is dominated by contributions from FeH and CrH as $T_{\rm eff}$ drops below around 2500 K. Owing to the high multiplicity of both the A and X states, Lyubchik et al. (2007) have found fitting computed synthetic spectra containing CrH to observational data very problematic-indeed in all five cases, the fit improved by omitting the CrH linelist of Burrows et al. (2002) from their synthetic spectra generation calculation. Indeed, Lyubchik et al.(2007) have made persistent reference to the incompleteness of the existing CrH and FeH linelists (Dulick et al. 2003) as explanation for the poor fit they obtained between observed and synthetic spectra calculated.

Pavlenko et al. (2008) investigated the potential use of both MgH/MgD and CrH/CrD as diagnostics for the so-called "deuterium test". For objects with $M < 13M_J$ where M_J is mass of Jupiter, deuterium burning does not occur as the core does not reach a temperature of around 8×10^5 K which is required for deuterium to ignite and fuse to form ^{3}He. A brown dwarf is defined as an object than has sufficient mass to burn deuterium but insufficient mass to burn ^{1}H to ^{4}He. In larger stars, deuterium burning happens within the first several million years after formation hence by measuring the abundance of deuterium, the evolutionary history of a stellar object can be determined. Also, since the deuterium abundance of objects with $M < 13M_J$ is unchanged from when they formed, brown dwarfs can thus be distinguished from these objects. Previously, Chabrier et al. (2000) and Pavlenko (2002) had investigated if H_2O and HDO could be used as a probe of the abundance of deuterium. However despite the HDO vibrational bands are shifted sufficiently with respect to the H_2O bands they are hard to observe as their intensity is dwarfed by that of strong H_2O lines.

By using the Burrows et al. (2002) linelist of energies and extrapolating energy

states using spectroscopic constants determined by Bauschlicher et al. (2001) for the dominant isotopomer of CrH namely ^{52}CrH, Pavlenko et al.(2008) generated "Just Overlapping Line Approximation"(JOLA) synthetic band spectra for $A^6\Sigma^+ - X^6\Sigma^+$ electronic transition between 1200-1800 K using the COND grid of Allard et al. (2001) implemented into the WITA6 program (Pavlenko 2000). The WITA6 program models a one dimensional stellar atmosphere with no sources or sinks of energy under the assumptions of Local Thermodynamic Equilibrium (LTE) and hydrostatic equilibrium using solar metallicity determined by Anders & Grevesse 1989. The energy levels for CrD were calculated by adjusting those for CrH by multiplying the relevant rotational-vibrational spectroscopic parameters by orders of the reduced mass ratio of the two species as formulated by Craybeal 1988. Similarly JOLA band spectra was generated for the dominant species of MgH, ^{24}MgH for the electronic transition $A^2\Pi - X^2\Sigma^+$ and MgD by use of the spectroscopic parameters determined by Balfour & Cartwright (1976) and Lemoine et al. (1988). Frank-Condon factors were used to calculate vibrational frequencies. All models used log g = 5.0 as is commonly determined for brown dwarfs where g is the gravitational constant. The results are shown in figures 3.6 for CrH/CrD and MgH/MgD.

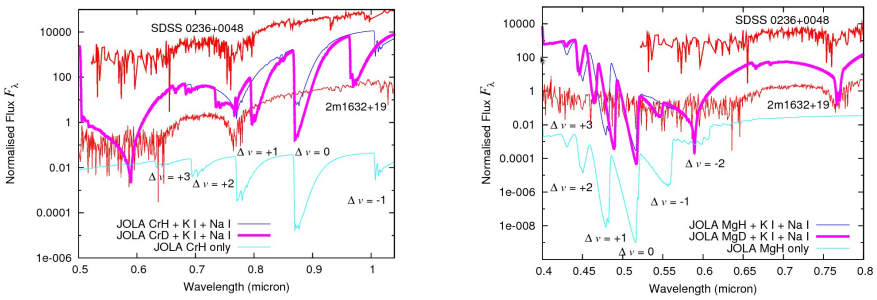

(a) Computed Molecular Bands of the $A^6\Sigma^+ - X^6\Sigma^+$ systems of CrH and CrD

(b) Computed Molecular Bands of the $A^2 - X^2\Sigma^+$ systems of MgH and MgD

Figure 3.6: Synthetic Spectra generated using COND model atmosphere at 1800K with D/H=1 for MgH/MgD and CrH/CrD. Both figures show observed spectra of two L dwarfs L dwarfs 2MASS1632+19 (Martìn et al. 1999) and SDSS 0236+0048 (Leggett et al. 2001) for comparison. In both figures the red lines indicate real observations with the purple and blue lines indicating synthetic spectra generated in the study.

Referring to figure 3.6 which are taken from Pavlenko et al. (2008), it can be seen that the MgH/MgD bands are almost coincident. However, the CrH and CrD bands are reasonably distinct for $\Delta\nu = +1$ at 0.795 μm and $\Delta\nu = -1$ at 0.968 μm with the $\Delta\nu = 0$ bands coincident.Pavlenko et al. (2008) note that the $\Delta\nu = -1$ band could potentially be especially useful for use in the "deuterium test" as the near infra-red band in this location is relatively devoid of strong absorption lines from other species with the exception of the $0 - 0$ Wing-Ford bands of FeH located at 0.99 μm and potentially certain water bands. Pavlenko et al. (2008) note that more accurate and detailed linelists required to investigate this possibility and explicitly mention that there are perturbations in spectra from electronic states which need to be quantified.

Combining all these previous astronomical studies, it is clear that there is a need for a new linelist of CrH which is more complete in wavelength coverage. CrH is

obviously an important molecule astronomically as even with the various problems in modelling its abundance, it has nonetheless been found to potentially be useful for several applications (i.e magnetic field studies, “Deuterium test”).

Chapter 4

Ab initio calculations for CrH

In this chapter *ab initio* results will be presented for CrH. As was mentioned in section 2.5, the calculation of excited states for transition metal diatomics is in the development stage with no standardised methods available as yet to obtain good quality *ab initio* curves. In published papers in which MRCI calculations have been performed, the states used in the proceeding CASSCF calculations are rarely mentioned. Hence for CrH, a full investigation of how combining different states in a CASSCF calculation produces a huge variation in quality of *ab initio* curves has been undertaken. These calculations are summarised in section 4.2 with Appendix B showing the results. Following on from these CASSCF test calculations, 7 different "CASSCF state-combinations" were selected. These were then tested out by performing MRCI calculations using the orbitals that they generated. At MRCI level of theory, the number of states of a particular symmetry and multiplicity calculated was also found to have an effect (e.g number of sextet states of symmetry 1). The notation which will be used to describe this is as follows: 2+1 indicates that two states of symmetry 1 and one state of symmetry 4 of a particular multiplicity (i.e either quartet or sextet) was calculated at MRCI level of theory. Referring back to table 2.3, Σ^+ states are calculated within symmetry 1 and Δ states have components in symmetry 1 and 4. The aim of all of this testing was to find the best feasible *ab initio* curves to input into creating a linelist. In section 4.4 the process for choosing these *ab initio* curves is presented for each curve with justification given. In summary this was a process of calculating MRCI calculations using each of the chosen seven CASSCF state-combinations and comparing which starting orbitals produced the best quality results.

4.1 Dai & Balasubramanian (1993) study

As was explained in section 2.4, the first step in calculating a linelist is to calculate *ab initio* curves for the molecular electronic states of interest. Previously, Dai & Balasubramanian (1993) had calculated the PECs and DMCs for the lowest lying 21 states of CrH using high level MRCI theory. However, their work is now dated as the atomic dissociation limit data for the Chromium atom has since been updated. In their study they had assumed the dissociation limit data shown in table 4.1. This

table lists out the molecular electronic states which are expected to converge for these respective atomic dissociation limits for which they presented results for 21 of the molecular states. Table 4.1 highlights the molecular electronic states for which Dai &

Atomic State Term Cr + H	Atomic Term	Molecular States			Energy			
					FOCI	SOCI	SOCI+Q	Exp(a)
$(3d^5 4s^1)a^7Sg +^2 Sg$	a^7S	$^8\Sigma^+$		$^6\Sigma^+$	0	0	0	0
$(3d^5 4s^1)a^5Sg +^2 Sg$	a^5S		$^4\Sigma^+$	$^6\Sigma^+$(II)	8416	7803	7344	7593
$(3d^4 4s^2)a^5Dg +^2 Sg$	a^5D		$^4\Sigma^+(II)$ $^4\Pi$ $^4\Delta$	$^6\Sigma^+$(III) $^6\Pi$ $^6\Delta$	8244	8275	7997	8090
$(3d^4 4s^2)b^5Dg +^2 Sg$	b^5D		$^4\Sigma^+$(III) $^4\Pi$(II) $^4\Delta$(II)*	$^6\Sigma^+(IV)$ $^6\Pi$(II) $^6\Delta(II)$	22 672	26 938	22 612	24 292
$(3d^4 4s^2)a^3Fg +^2 Sg$	a^3F	$^2\Sigma^-$ $^2\Pi$ $^2\Delta$ $^2\Phi$	$^4\Sigma^-$ $^4\Pi$(III) $^4\Delta$(III) $^4\Phi$		24 863	27 478	26 619	25 097
$(3d^4 4s^2)b^3Gg +^2 Sg$	b^3G	$^2\Sigma^+$ $^2\Pi$(II) $^2\Delta$(II) $^2\Phi$(II) $^2\Gamma$	$^4\Sigma^+$(IV) $^4\Pi$(IV) $^4\Delta$(IV) $^4\Phi$(II) $^4\Gamma$		26 215	28 217	27 468	27 722

Table 4.1: Summary of molecular states (highlighted in green, blue and magneta) calculated by Dai & Balasubramanian (1993). The atomic experimental dissociation limits data available at the time which these authors used in their study is indicated as well as the dissociation limits they obtained for the various molecular electronic states using various levels of theory. States marked * are shown in the plots of Dai & Balasubramanian (1993) to dissociate to another limit from that indicated.

Balasubramanian (1993) obtained PECs and DMCs. Table 4.2 is an extended version of table 2.8 which has the most up to date data from the NIST atomic database. As was done for table 2.8, the molecular states which are expected to dissociate to the various atomic limits have been deduced by use of the correlation rules and the values of E_0 calculated using equation 2.22. Hence comparing the atomic dissociation limits presented in tables 4.1 and 4.2 it can be seen that:

- the first three atomic limits of the Cr atom (i.e. a^7S, a^5S and a^5D terms) are unchanged from the older data set which Dai & Balasubramanian (1993) had used. Hence their results for molecular states dissociating to these limits are still very valid and hence act as a valuable source of comparison for new theoretical calculations. These states appear in green in table 4.2.

- However, with advances in experimentation, new knowledge of the low-lying atomic limits of the Chromium atom has been gained in the last 20 years. Thus a different set of low-lying molecular states are expected as shown in table 4.2. Hence this lays question about the validity of Dai & Balasubramanian (1993) work.

- In Dai & Balasubramanian's (1993) study, they calculated the PECs of a $^4\Pi$,$^4\Sigma^+$ and a $^6\Pi$ state dissociating to the same dissociation limit which they label at a^5D. In table 4.2 it is assumed that these states are those that actually dissociate

Cr atom configuration	Term	E_0 (cm^{-1})	Molecular States		
$3d^5(^6S)4s$	a^7S	0.0000	$^8\Sigma^+$		$X^6\Sigma^+$
$3d^5(^6S)4s$	a^5S	7 593.1484		$^4\Sigma^+$	$A^6\Sigma^+$
$3d^44s^2$	a^5D	8 090.1903		$^4\Sigma^+(II)$ $^4\Pi$ $^4\Delta$	$^6\Sigma^+(III)$ $^6\Pi$ $^6\Delta$
$3d^5(^4G)4s$	a^5G	20521.4036		$^4\Sigma^+(III)$ $^4\Pi(II)$ $^4\Delta(II)$ $^4\Phi$ $^4\Gamma$	$^6\Sigma^+(IV)$ $^6\Pi(II)$ $^6\Delta(II)$ $^6\Phi$ $^6\Gamma$
$3d^5(^4P)4s$	a^5P	21846.3752		$^4\Sigma^-$ $^4\Pi(III)$	$^6\Sigma^-$ $^6\Pi(III)$
$3d^44s^2$	a^3P	23796.08145	$^2\Sigma^-$ $^2\Pi$	$^4\Sigma^-(II)$ $^4\Pi(IV)$	
$3d^5(^6S)4p$	Z^7P^0	23415.1784	$^8\Sigma^+$ $^8\Pi$		$^6\Sigma^+(V)$ $^6\Pi(IV)$
$3d^44s^2$	a^3H	24079.5068	$^2\Sigma^-(II)$ $^2\Pi(II)$ $^2\Delta$ $^2\Phi$ $^2\Gamma$ ^2H	$^4\Sigma^-(III)$ $^4\Pi(V)$ $^4\Delta(III)$ $^4\Phi(II)$ $^4\Gamma(II)$ ^4H	

Table 4.2: List of atomic dissocation limits for the Cr atom up to 24 000 cm^{-1} with the corresponding molecular states of CrH which are expected to dissociate to these various limits.

to the a^5G state. These states are highlighted in blue in table 4.2.

- In figure 2 of their study, Dai & Balasubramanian (1993) show nine PECs of doublet and quartet states dissociating to two limits which are separated by around 0.1 Hartree i.e. about 2.19×10^4 cm^{-1} apart. These nine states are highlighted in magneta in table 4.2 with the assumption that the $^2\Delta(II)$ and $^4\Delta(II)$ states are actually $^2\Sigma^-$ and $^4\Sigma^-$ states. This figure is reproduced in figure 4.1 below. Without a colour copy of this plot available it is visually challenging to "untangle" the states and thus determine which PECs dissociate to the two limits shown.

- By inspection of table 4.2, it can be seen that it appears that Dai & Balasubramanian have been able to calculate $^4\Sigma^-$ and $^4\Delta$ states (which appear in symmetry 4 under C_{2v} construct which they used) without calculating lower lying states which dissociate to a lower atomic dissociation limit. This should not be possible. For example they appear to have been able to calculate a PEC for the $^4\Sigma^-(II)$ state without calculating the $^4\Delta(II)$ & $^4\Gamma$ states which theoretically dissociate to the lower lying a^5G atomic term and also the $^4\Sigma^-$ term which theoretically dissociates to the lower lying a^5P atomic term.

- Dai & & Balasubramanian (1993) were using high-level MRCI theory to obtain their results. Thus it is a cause for concern that molecular states can be calculated which may not physically exist, or may appear to dissociate along with other electronic states to a particular atomic dissociation limit.

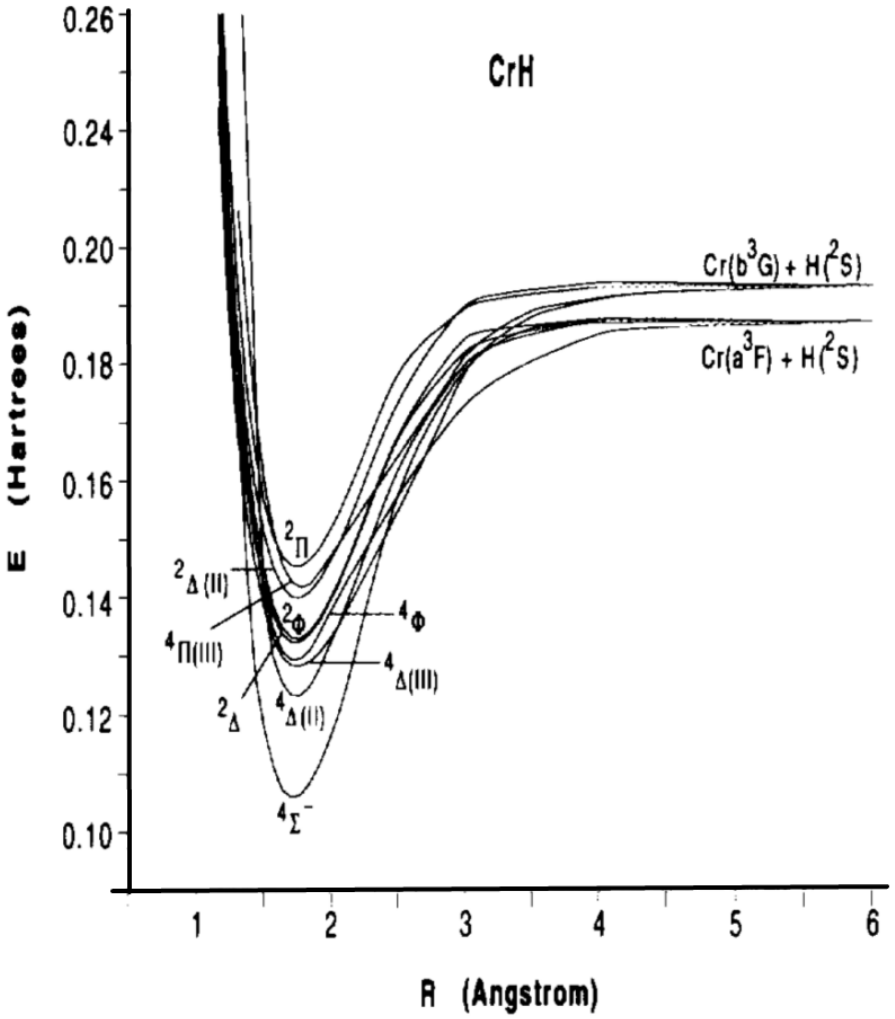

Figure 4.1: Figure 2 from the study of Dai & Balasubramanian (1993) showing the PECs of nine quartet and double states they calculated in their theoretical study of low-lying states of CrH.

With this knowledge, it was decided to proceed with caution in the calculation of new *ab initio* curves for CrH. For the creation of a linelist, transition dipole moment curves are required as well as spin-orbit and angular momenta coupling curves. Unfortunately in Dai & Balasubramanian's study they did not calculate these couplings: for transition metal bearing molecules spin-orbit couplings are expected to be large and indeed were found to be of order several hundred wavenumbers.

Also, the states used in the initial CASSCF calculations which proceed any CI calculations are rarely, if ever stated. An obvious exception is the FeH linelist paper of Dulick et al. (2003) where the authors explicitly say how many $^4\Delta$ states they used in these initial calculations.

Previous small-scale preliminary work done within the ExoMol group by Dr Lodi indicated that obtaining convergence and continuity of curves for CrH would be challenging: thus it was decided to undertake a study in which different combinations of states were varied within a CASSCF calculation to test which combination produced subsequent CI curves which showed physical behaviour.

4.2 Testing at CASSCF level of theory

In order to obtain high-quality CI results, extensive CASSCF calculations were undertaken in order to generate the best quality molecular orbitals which are then used as a starting approximation in proceeding CI calculations. The ten molecular electronic states of interest as shown in table 2.8 in section 2.7.4 were implemented into MOLPRO: the result of this implementation was 10 `wf` "blocks" which is a consequence of how multiple states with the same multiplicity and belonging to the same symmetry are calculated. These 10 `wf` blocks are as shown in table 4.3.

Molecular States	wf cards	Label
$X^6\Sigma^+$	`wf,25,1,5;state,1;`	A
$^8\Sigma^+$	`wf,25,1,7;state,1;`	B
$a^4\Sigma^+$	`wf,25,1,3;state,1;`	C
$X^6\Sigma^+$, $A^6\Sigma^+(II)$	`wf,25,1,5;state,2`	D
$a^4\Sigma^+$, $^4\Sigma^+(II)$	`wf,25,1,3;state,2`	E
$^4\Pi$	`wf,25,2,3;state,1;` `wf,25,3,3;state,1;`	F
4Δ	`wf,25,1,3;state,1;` `wf,25,4,2;state,1;`	G
$X^6\Sigma^+$, $A^6\Sigma^+(II)$, $^6\Sigma^+(III)$	`wf,25,1,5;state,3;`	H
$^6\Pi$	`wf,25,2,5;state,1;` `wf,25,3,5;state,1;`	I
$^6\Delta$	`wf,25,1,5;state,1` `wf,25,4,5;state,1;`	J

Table 4.3: List of "`wf`" blocks tested at CASSCF level of theory. It should be noted that this notation of using letters to denote single or combinations of `wf` cards is not standard-it was simply devised for the purposes of this project. It should not be confused with the standard spectroscopic notation for electronic states used for molecules where "X" denotes the ground state and electronic states of the same multiplicity to the ground state labelled "A", "B", "C", "D", "E" etc in order of increasing energy: those states with a different multiplicity to the ground state are simply labelled "a", "b", "c" etc.

All possible combinations of these `wf` blocks (letters A, B, C...J) were then tested out in MOLPRO in a CASSCF calculation where energy and expectation dipole values were calculated. These combinations of "wf" blocks will subsequently be referred by the phrase "state-combinations" which gives a more physical meaning to the process. Naively, the total number of combinations is

$$\text{Total number of possible combinations} = \sum_{i=2}^{i=10} {}^{10}C_i \tag{4.1}$$

where ${}^{10}C_i$ is the number of combinations of making groups of size i from 10 objects which is given by

$${}^{10}C_i = \frac{10!}{(10-i)!i!} \tag{4.2}$$

where "!" is the standard mathematics notation for factorial e.g. $4! = 4 \times 3 \times 2 \times 1$.

Thus explicitly carrying out this sum shown in equation ,

$$= {}^{10}C_2 + {}^{10}C_3 + {}^{10}C_4 + {}^{10}C_5 + {}^{10}C_6 + {}^{10}C_7 + {}^{10}C_8 + {}^{10}C_9 + {}^{10}C_{10} \tag{4.3}$$

$$= 45 + 120 + 210 + 252 + 210 + 120 + 45 + 10 + 1 = 1013. \quad (4.4)$$

Hence, naively the total sample space to test is 813 ie 813 possible calculations. However, on closer inspection of table 4.3, it can be seen that the following combinations would be nonsensical: A with D, A with H, D with H and C with E. Appendix A demonstrate how these simple rules eliminate the vast majority of combinations with those forbidden highlighted in red. Figure 4.2 demonstrates visually how the number of combinations to investigate is reduced drastically from the naive guess with the values summarised in the adjoining table.

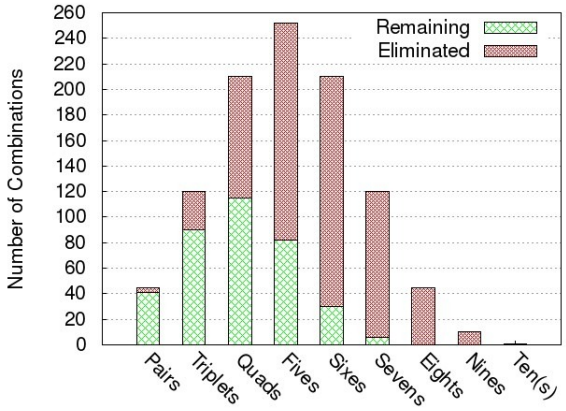

	Naive guess	Eliminated	Remaining
Pairs	45	4	41
Triplets	120	30	90
Quads	210	95	115
Fives	252	170	82
Sixes	210	180	30
Sevens	120	114	6
Eights	45	45	0
Nines	10	10	0
Ten(s)	1	1	0
Total	1013	649	364

Figure 4.2: Figure and table demonstrating how significant majority of CASSCF "wf" blocks can be eliminated using the four rules above

Thus, the total number of state-combinations to test out was thus reduced from 1013 to 364. The testing procedure for each of these 364 state-combinations was as follows:

1. A CASSCF calculation was performed for several different inter-nuclear distances ("points") around equilibrium, which for states in the CrH atom is typically between $1.6 - 1.8$ Å. The result of a CASSCF calculation is energy and dipole for each state at that point.

2. If these points did not converge, based on previous experience it was unlikely there would be convergence elsewhere. Hence no further CASSCF calculations done for this particular combination of states.

3. If however these points did converge, then more CASSCF calculations were performed for different points outside this range, and if again, convergence was

reached, more points were calculated out from equilibrium and thus produce PECs and DMCs in the range from approximately $0.7 - 10.0$ Å were produced if convergence was systematically reached. The method used to calculate DMCs was by calculating the expectation value of the dipole operator with the electronic wavefunctions.

It should be noted that:

1. A CASSCF (and indeed CI) calculation for each point is independent of calculations for all other points: thus the order in which calculations were run for different points has no consequences for the end result.

2. As noted previously, convergence does not guarantee that curves will be continuous.

These plots of PECs and DMCs are shown in appendix B.

4.3 Results of CASSCF testing

Having undertaken the CASSCF testing for the state-combinations described in section 4.2, all plots of Potential Energy Curves and Dipole Moment curves from combinations that produced convergence were visually inspected-those combinations which showed the best continuity where then used as starting point for trial CI calculations.

If CASSCF calculation of PECs and DMCs has an obvious visible discontinuity then all PECs and DMCs calculated at CI level will have discontunity in that same region. To demonstrate this refer to figures

Referring to figures 4.3 and 4.4 it can be seen that the discontinuities visible from the PECs and DMCs calculated from the CASSCF calculations propagate into the subsequent respective CI calculations. From experience it was realised that increasing the size of the basis set(e.g. to cc-pVQZ) or augmenting it would not alleviate these issues. Also at CI level of calculation adding more states would not alleviate the fundamental discontinuities. Hence Hence for the purposes of testing which CASSCF calculations produced the best quality orbitals for use in final CI calculations used cc-pVDZ basis sets to maximise the efficiency of computer time used.

With this knowledge the plots of PECs and DMCs shown in appendix 4.3 were inspected and from these 7 state-combinations were then selected. These state-combinations are listed in table 4.4 which outlines for clarity the "wf" cards that they are composed of for a more physical understanding. Table 4.4 also outlines the consistent colour scheme which is used in the following graphs and text.

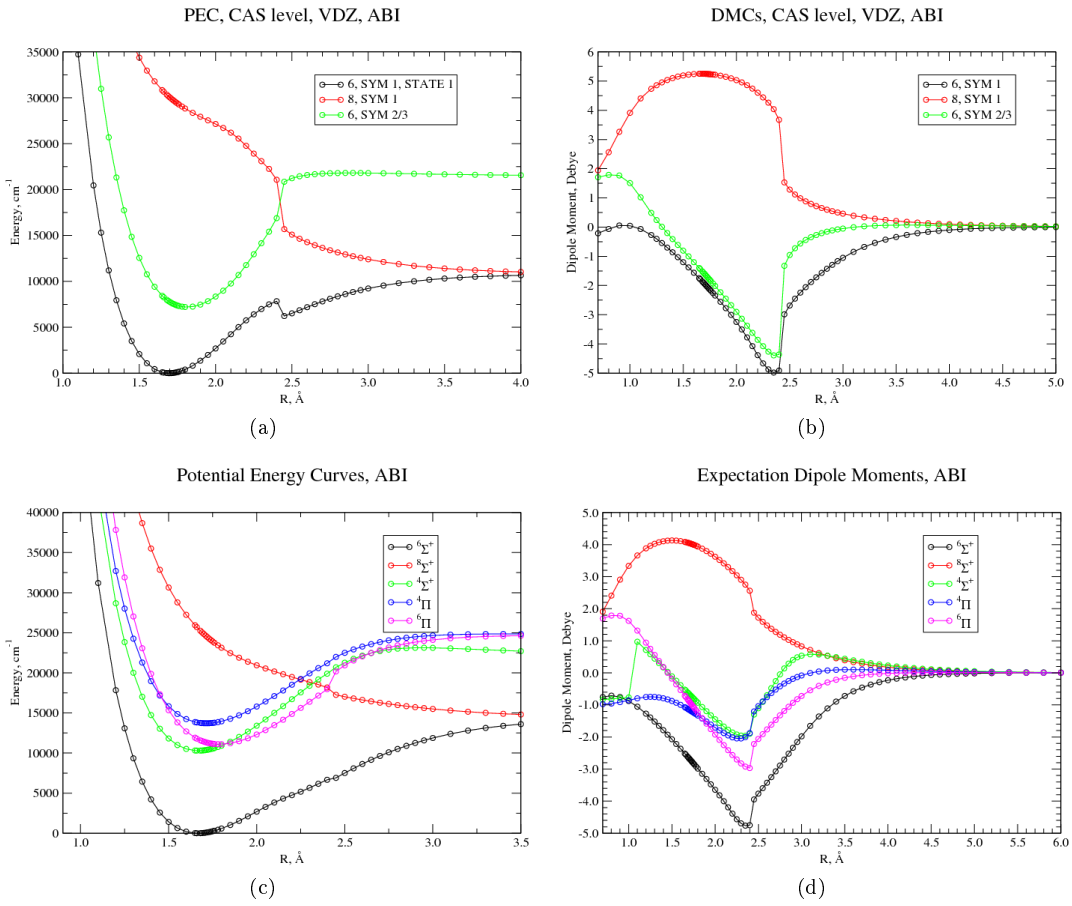

Figure 4.3: Calculation of PECs and DMCs using a cc-pVDZ basis set at CASSCF level then CI level for the case where the states used in the CASSCF calculation are those labelled by "ABI" as defined in table 4.3.

State-combination	*wf* cards used	Physical interpretation
AB	25, 1, 5	6, SYM 1
	25, 1, 7	8, SYM 1
AF	25, 1, 5	6, SYM 1
	25, 2, 3	4, SYM 2
	25, 3, 3	4, SYM 3
ABF	25, 1, 5	6, SYM 1
	25, 1, 7	8, SYM 1
	25, 2, 3	4, SYM 2
	25, 3, 3	4, SYM 3
BF	25, 1, 7	8, SYM 1
	25, 2, 3	4, SYM 2
	25, 3, 3	4, SYM 3
BFH	25, 1, 7	8, SYM 1
	25, 2, 3	4, SYM 2
	25, 3, 3	4, SYM 3
	25, 1, 5, STATE 3	3 states of 6, SYM 1
BJ	25, 1, 7	8, SYM 1
	25, 1, 5	6, SYM 1
	25, 4, 5	6, SYM 4
BFJ	25, 1, 7	8, SYM 1
	25, 2, 3	6, SYM 2
	25, 3, 3	6, SYM 3
	25, 1, 5, STATE 3	3 states of 6, SYM 1

Table 4.4: Summary of state-combinations which produced promising results within CASSCF calculations which were then used for subsequent CI calculations.

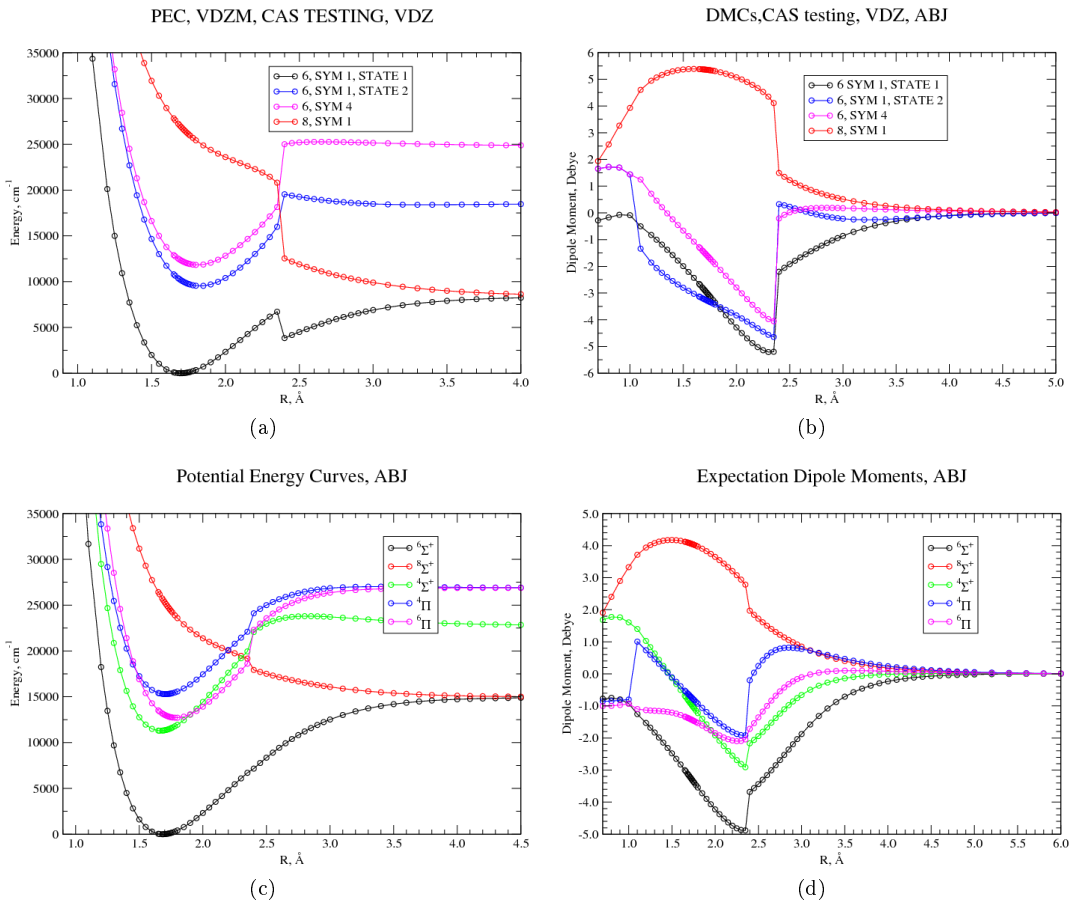

Figure 4.4: Calculation of PECs and DMCs using a cc-pVDZ basis set at CASSCF level then CI level for the case where the states used in the CASSCF calculation are those labelled by "ABJ" as defined in table 4.3.

4.4 MRCI calculations

In the following section MRCI calculations of PECs, DMCs, TDMS, off-diagonal TDMs, angular momentum and spin-orbit couplings will be presented for the low-lying states of CrH. For these calculations a basis set of cc-pVQZ was used throughout-the justification for using a quadruple basis set is outlined in section 4.4.1. For each of these curves, MRCI calculations were performed for each of the 7 CASSCF state-combinations chosen in table 4.4 and the results compared. It should be noted that since the $^8\Sigma^+$ was found to be anti-bonding in nature, for the purposes of the linelist it was not included as at present, Duo is only designed for bound states. However, for completeness an analysis of MRCI calculations of this state has been undertaken (see section 4.15).

4.4.1 Basis Set Investigation

An investigation of the effects of basis set for the various PECs, DMCs and dissociation values of spin-orbits couplings calculated at MRCI level for CrH was carried out. To allow a fair comparison and for consistency, the state-combination used in the proceeding CASSCF calculations was that of "ABF" (see table 4.3). The basis sets

tested out were from the Dunning family and were as follows: cc-pVDZ, cc-pVTZ, cc-pVQZ along with the corresponding augmented basis sets of aug-cc-pVDZ, aug-cc-pVTZ, aug-cc-pVQZ. Additionally, as part of this investigation the effect of "freezing" core orbitals in the CASSCF calculation was investigated: by this we mean that the core orbitals of 5, 2, 2, 0 (see section 2.7.5) were doubly occupied in all configurations and not optimized i.e. only the valence orbitals of 4, 1, 1, 0 were allowed to vary. These calculations are referred to in the following sections as "frozen". A comparison of the CPU time and disk space required for a sample MRCI calculation is shown in table 4.5. For the case of the "frozen" calculations, the relative scaling between calculations involving a progression in basis set was similar: the absolute values were around a factor of 2 greater.

Basis set	CPU times (s)	Disk used (Mb)
cc-pVDZ	16.88	36.35
cc-pVTZ	95.89	138.92
cc-pVQZ	355.4	792.43
aug-cc-pVDZ	80.71	65.25
aug-cc-pVTZ	167.99	453.79
aug-cc-pVQZ	1301.46	2870

Table 4.5: Comparison of CPU times and Disk memory used for various basis sets for an MRCI calculation at $R = 1.35$ Å for the PECs and DMCs of $X^6\Sigma^+$, $A^6\Sigma^+(II)$, $^6\Delta$, $^6\Sigma^+(III)$ and $^6\Pi$ and the spin-orbit coupling between these states. The basis sets tested are Dunning types. For a fair and consistent comparison, the state-combination used in the CASSCF calculations which these MRCI calculations built upon was "ABF" (see table 4.3).

Referring to table 4.5, it can be seen that both the memory and CPU time required increases non-linearly for both the augmented and non-augmented basis sets. Going from a double to triple basis set the memory required increases by a factor of approximately 6 and 2 respectively for the non-augmented and augmented basis sets and, going from triple to quadruple the factors are around 4 and 8. CPU increases as well by factors of approximately 4 and 7 going from double to triple and by around 6 going from triple to quadruple. Theoretically, as the size of a basis set increases, the complete basis limit is approached. An obvious question to ponder, is why was five-zeta, six-zeta etc not investigated? Pragmatically, the computing power required increases in terms of both CPU and memory. As will be shown in proceeding sections, generally speaking the greatest difference in properties of PECs was found when changing from a "double" basis set to a "triple" basis set. Hence it was decided that performing 5-zeta calculations would be irrelevant when all factors affecting the accuracy of *ab initio* calculations are considered. Test calculations for all inter-nuclear distances defined in the regom matrix (see section 2.7.1) at CASSCF level for the state combination of "ABF" was performed using a cc-pV5Z basis set and the CPU and disk space required compared to the same calculations performed using a cc-pVQZ basis set. In summary the CPU time increased by a factor between 3.12 and 6.88 and the disk space required by a factor between 3.87 and 5.11.

Also, it was found that as the size of the basis set increased, the number of points which converged decreased. More pertinently, the regions of non-convergence tended to be around equilibrium which is crucial in determining the rovibronic structure of

linelists subsequently calculated. Table 4.6 compares the number of points (out of a possible 88) which converged for MRCI calculations of PECs and DMCs of the various states of CrH.

Basis set	States calculated in single CI calculation					
	$^4\Pi$	$^6\Pi$	$^8\Sigma^+$	$a^4\Sigma^+$, $^4\Delta$	$a^4\Sigma^+$, $^4\Delta$, $^4\Sigma^+(III)$	$X^6\Sigma^+$, $A^6\Sigma^+$, $^6\Delta$, $^6\Sigma^+(III)$
cc-pVDZ	88	88	88	81	59	72
cc-pVTZ	88	88	88	82	60	64
cc-pVQZ	87	88	88	79	62	55
aug-cc-pVDZ	88	88	88	83	64	72
aug-cc-pVTZ	88	88	88	82	67	62
aug-cc-pVQZ	88	88	88	82	67	60
cc-pVDZ(f)	88	88	88	79	66	54
cc-pVTZ(f)	88	88	88	84	77	57
cc-pVQZ(f)	88	88	88	85	73	51
aug-cc-pVDZ(f)	88	88	88	79	66	55
aug-cc-pVTZ(f)	88	88	88	85	74	51
aug-cc-pVQZ(f)	88	88	88	85	71	50

Table 4.6: Comparison of number of points converged using the various basis sets tested for MRCI calculations of PECs and DMCs of electronic states of CrH. The basis sets tested are Dunning types. "Basis set(f)" indicates that the core orbitals of (5, 2, 2, 0) of the C_{2v} framework in the CASSCF calculation were frozen. For a fair and consistent comparison, the state-combination used in the CASSCF calculations which these MRCI calculations built upon was "ABF" (see table 4.3).

As can be seen from table 4.6 for single MRCI calculations of PECs and DMCs of the $^4\Pi$, $^6\Pi$ and $^8\Sigma^+$ states, all calculations for the 88 inter-nuclear distances tested converged. (The one exception is for the cc-pVQZ basis set R=2.85 Å did not converge for the $^4\Pi$ state). Hence for these states, it seems that regardless of basis set these states are "well behaved".

Comparing columns 5 and 6 which show two different CI calculations for quartet states, it can be seen that adding an extra state into symmetry 1 in the MRCI calculation results in significantly fewer points converging across all basis sets. Generally speaking for these two different MRCI calculations there is no clear trend across all basis set families of either fewer or more points converging as the size of the basis set is increased. The final column of table 4.6 shows the results for a MRCI calculation of the four sextet Σ^+ and Δ states. As can be seen, for each basis set family, the number of points converging decreases as the size of the basis set is increased. This is a troublesome result as theoretically a larger basis set should produce more accurate results as the basis set limit is approached. This finding can be explained very simply in terms of how adding more basis set functions allows the variational calculations more room for variation and hence a greater a chance of no convergence been obtained within the parameter set by the program.

The number of points converged is a crude, but valuable metric for determining the quality of an *ab initio* calculation. To gain more physical insight of where non-convergence occured, "maps" of convergence were created for these latter MRCI calculations. These are shown in tables 4.7, 4.8 and 4.9 respectively.

Table 4.7 shows how for all 6 calculations performed there was no convergence between 5.60 and 5.80 Å with convergence occurring for all for $R > 8.50$ Å. For the case

Basis set family	cc-pVnZ			aug-cc-pVnZ			cc-pVnZ(f)			aug-cc-pVnZ(f)		
R(Å)/Basis set size	D	T	Q	D	T	Q	D	T	Q	D	T	Q
0.70	●	●	●	●	●	●	●	●	●	●	●	●
0.80-1.55	●	●	●	●	●	●	●	●	●	●	●	●
1.60	●	●	●	●	●	●	●	●	●	●	●	●
1.65-4.60	●	●	●	●	●	●	●	●	●	●	●	●
4.70	●	●	●	●	●	●	●	●	●	●	●	●
4.80	●	●	●	●	●	●	●	●	●	●	●	●
4.90	●	●	●	●	●	●	●	●	●	●	●	●
5.00	●	●		●	●	●	●	●	●	●	●	●
5.20	●	●		●	●	●	●	●	●	●	●	●
5.40	●	●		●	●	●	●	●	●	●	●	●
5.60	●	●		●	●	●	●	●	●	●	●	●
5.80	●	●		●	●	●	●	●	●	●	●	●
6.00	●	●		●	●	●	●	●	●	●	●	●
6.20	●	●	●	●	●	●	●	●	●	●	●	●
6.50-7.50	●	●	●	●	●	●	●	●	●	●	●	●
7.70	●	●	●	●	●	●	●	●	●	●	●	●
8.00	●	●	●	●	●	●	●	●	●	●	●	●
8.50	●	●	●	●	●	●	●	●	●	●	●	●
9.00	●	●	●	●	●	●	●	●	●	●	●	●
10.00	●	●	●	●	●	●	●	●	●	●	●	●

Table 4.7: "Map of convergence" across various basis sets tested for an MRCI calculation of the $a^4\Sigma^+$ and $^4\Delta$ states. A ● indicates that convergence was obtained for this calculation at the respective inter-nuclear distance(s) and basis set. A ● indicates that convergence was not obtained. In this table four "families" of basis sets are presented(Dunning type Basis sets). The size of the basis set(n) for each family is indicated by the letters "D", "T" and "Q" which denote "double", "triple" and "quadruple'. Here "(f)" indicates that the core orbitals of (5, 2, 2, 0) of the C_{2v} framework in the CASSCF calculation were frozen. For a fair and consistent comparison, the state-combination used in the CASSCF calculations which these MRCI calculations built upon was "ABF"(see table 4.3).

of the "frozen" calculations, the regions of non-convergence decrease when going up the basis set. Table 4.8 clearly shows the large regions of non-convergence. Compare this to table 4.7 in which one less quartet state of symmetry 1 has been calculated. For all basis sets tested and for non-frozen and frozen all MRCI calculations of the $a^4\Sigma^+$, $^4\Delta$ $^4\Sigma^+(II)$ (table 4.8) did however converge between 2.75 Å and 3.40 Å fit. Table 4.9 shows the "map of convergence" for MRCI calculations using cc-pVQZ basis set of $X^6\Sigma^+$, , $A^6\Sigma^+$, $^6\Delta$ and $^6\Sigma^+(III)$ for the case of a proceeding CASSCF calculation using the state-combination of ABF. This table shows two important features: the "frozen" calculations result in less points converging in the crucial region around equilibrium (around 1.70 Å) and, the regions of non-convergence increase with increasing basis set. This is a very unfortunate result as the reverse would normally be expected: i.e. the number of points converging to increase with the size of the basis set.

Tables 4.10, 4.11, 4.12 and 4.13 show the properties of the PECs obtained from these calculations described in this section. For all tables the MRCI calculations of the $a^4\Sigma^+$ and $^4\Delta$ states only are shown. The process for determining these properties is described in section 2.9.2.

Table 4.10 shows that the effect of increasing the size of a basis set is to reduce the value of R_e by up to 0.1 Å. Augmenting a basis set or applying the "frozen" option generally have the same effect of increasing R_e by 0.10 Å when compared to the respective cc-pVnZ calculation. The highest values of R_e are obtained where an augmented basis set has been used and the core orbitals frozen.

Basis set family	cc-pVnZ			aug-cc-pVnZ			cc-pVnZ(f)			aug-cc-pVnZ(f)		
R(Å)/Basis set size	D	T	Q	D	T	Q	D	T	Q	D	T	Q
0.70-1.70	●	●	●	●	●	●	●	●	●	●	●	●
1.71	●	●	●	●	●	●	●	●	●	●	●	●
1.72-2.20	●	●	●	●	●	●	●	●	●	●	●	●
2.25	●	●	●	●	●	●	●	●	●	●	●	●
2.30	●	●	●	●	●	●	●	●	●	●	●	●
2.35	●	●	●	●	●	●	●	●	●	●	●	●
2.40	●	●	●	●	●	●	●	●	●	●	●	●
2.45	●	●	●	●	●	●	●	●	●	●	●	●
2.50	●	●	●	●	●	●	●	●	●	●	●	●
2.55	●	●	●	●	●	●	●	●	●	●	●	●
2.60	●	●	●	●	●	●	●	●	●	●	●	●
2.65	●	●	●	●	●	●	●	●	●	●	●	●
2.70	●	●	●	●	●	●	●	●	●	●	●	●
2.75-3.40	●	●	●	●	●	●	●	●	●	●	●	●
3.50	●	●	●	●	●	●	●	●	●	●	●	●
3.60	●	●	●	●	●	●	●	●	●	●	●	●
3.70	●	●	●	●	●	●	●	●	●	●	●	●
3.80	●	●	●	●	●	●	●	●	●	●	●	●
3.90	●	●	●	●	●	●	●	●	●	●	●	●
4.00	●	●	●	●	●	●	●	●	●	●	●	●
4.10	●	●	●	●	●	●	●	●	●	●	●	●
4.20	●	●	●	●	●	●	●	●	●	●	●	●
4.30	●	●	●	●	●	●	●	●	●	●	●	●
4.40	●	●	●	●	●	●	●	●	●	●	●	●
4.50	●	●	●	●	●	●	●	●	●	●	●	●
4.60	●	●	●	●	●	●	●	●	●	●	●	●
4.70	●	●	●	●	●	●	●	●	●	●	●	●
4.80	●	●	●	●	●	●	●	●	●	●	●	●
4.90	●	●	●	●	●	●	●	●	●	●	●	●
5.00	●	●	●	●	●	●	●	●	●	●	●	●
5.20	●	●	●	●	●	●	●	●	●	●	●	●
5.40	●	●	●	●	●	●	●	●	●	●	●	●
5.60	●	●	●	●	●	●	●	●	●	●	●	●
5.80	●	●	●	●	●	●	●	●	●	●	●	●
6.00	●	●	●	●	●	●	●	●	●	●	●	●
6.20	●	●	●	●	●	●	●	●	●	●	●	●
6.50	●	●	●	●	●	●	●	●	●	●	●	●
6.70	●	●	●	●	●	●	●	●	●	●	●	●
7.00	●	●	●	●	●	●	●	●	●	●	●	●
7.20	●	●	●	●	●	●	●	●	●	●	●	●
7.40-10.00	●	●	●	●	●	●	●	●	●	●	●	●

Table 4.8: "Map of convergence" across various basis sets tested for an MRCI calculation of the $a^4\Sigma^+$, $^4\Delta$ and $^4\Sigma^+(II)$ states(compare with table 4.7 which is for two quartet states only). A ● indicates that convergence was obtained for this calculation at the respective inter-nuclear distance(s) and basis set. A ● indicates that convergence was not obtained. In this table four "families" of basis sets are presented(Dunning type Basis sets). The size of the basis set(n) for each family is indicated by the letters "D", "T" and "Q" which denote "double", "triple" and "quadruple'. Here "(f)" indicates that the core orbitals of (5, 2, 2, 0) of the C_{2v} framework in the CASSCF calculation were frozen. For a fair and consistent comparison, the state-combination used in the CASSCF calculations which these MRCI calculations built upon was "ABF" (see table 4.3).

Table 4.11 shows the shocking variation is dissociation energy for the various electronic states as a function of basis set. As the size of the basis set increases, the size of the dissociation energy increases. For each state, the lowest dissociation energy was obtained when using a cc-pVDZ basis set and the highest when the core orbitals were frozen and a cc-pVQZ basis set used. The difference between these two values varies between 3928 cm^{-1} for the $A^6\Sigma^+$ state and 1387 for the $^4\Pi$ state. The variation in D_e (cm^{-1}) for the other electronic states is as follows: $^6\Pi$ (1501), $a^4\Sigma^+$ (3758), $^4\Delta$ (1404), $X^6\Sigma^+$ (1918), $^6\Delta$ (3600).

Basis set family	cc-pVnZ			aug-cc-pVnZ			cc-pVnZ(f)			aug-cc-pVnZ(f)		
R(Å)/Basis set size	D	T	Q	D	T	Q	D	T	Q	D	T	Q
0.70-1.30	●	●	●	●	●	●	●	●	●	●	●	●
1.35	●	●	●	●	●	●	●	●	●	●	●	●
1.40	●	●	●	●	●	●	●	●	●	●	●	●
1.45	●	●	●	●	●	●	●	●	●	●	●	●
1.50	●	●	●	●	●	●	●	●	●	●	●	●
1.55	●	●	●	●	●	●	●	●	●	●	●	●
1.60	●	●	●	●	●	●	●	●	●	●	●	●
1.65	●	●	●	●	●	●	●	●	●	●	●	●
1.66	●	●	●	●	●	●	●	●	●	●	●	●
1.68	●	●	●	●	●	●	●	●	●	●	●	●
1.69	●	●	●	●	●	●	●	●	●	●	●	●
1.70	●	●	●	●	●	●	●	●	●	●	●	●
1.71	●	●	●	●	●	●	●	●	●	●	●	●
1.72	●	●	●	●	●	●	●	●	●	●	●	●
1.73	●	●	●	●	●	●	●	●	●	●	●	●
1.74	●	●	●	●	●	●	●	●	●	●	●	●
1.75	●	●	●	●	●	●	●	●	●	●	●	●
1.76	●	●	●	●	●	●	●	●	●	●	●	●
1.78	●	●	●	●	●	●	●	●	●	●	●	●
1.80	●	●	●	●	●	●	●	●	●	●	●	●
1.85	●	●	●	●	●	●	●	●	●	●	●	●
1.90	●	●	●	●	●	●	●	●	●	●	●	●
1.95	●	●	●	●	●	●	●	●	●	●	●	●
2.00	●	●	●	●	●	●	●	●	●	●	●	●
2.05	●	●	●	●	●	●	●	●	●	●	●	●
2.10	●	●	●	●	●	●	●	●	●	●	●	●
2.15	●	●	●	●	●	●	●	●	●	●	●	●
2.20	●	●	●	●	●	●	●	●	●	●	●	●
2.25	●	●	●	●	●	●	●	●	●	●	●	●
2.30-2.75	●	●	●	●	●	●	●	●	●	●	●	●
2.80	●	●	●	●	●	●	●	●	●	●	●	●
2.85-4.70	●	●	●	●	●	●	●	●	●	●	●	●
4.80	●	●	●	●	●	●	●	●	●	●	●	●
4.90	●	●	●	●	●	●	●	●	●	●	●	●
5.00	●	●	●	●	●	●	●	●	●	●	●	●
5.20	●	●	●	●	●	●	●	●	●	●	●	●
5.40	●	●	●	●	●	●	●	●	●	●	●	●
5.60	●	●	●	●	●	●	●	●	●	●	●	●
5.80	●	●	●	●	●	●	●	●	●	●	●	●
6.00	●	●	●	●	●	●	●	●	●	●	●	●
6.20	●	●	●	●	●	●	●	●	●	●	●	●
6.50	●	●	●	●	●	●	●	●	●	●	●	●
6.70	●	●	●	●	●	●	●	●	●	●	●	●
7.00	●	●	●	●	●	●	●	●	●	●	●	●
7.20	●	●	●	●	●	●	●	●	●	●	●	●
7.40	●	●	●	●	●	●	●	●	●	●	●	●
7.50	●	●	●	●	●	●	●	●	●	●	●	●
7.70	●	●	●	●	●	●	●	●	●	●	●	●
8.00	●	●	●	●	●	●	●	●	●	●	●	●
8.50	●	●	●	●	●	●	●	●	●	●	●	●
9.00	●	●	●	●	●	●	●	●	●	●	●	●
10.00	●	●	●	●	●	●	●	●	●	●	●	●

Table 4.9: "Map of convergence" across various basis sets tested for an MRCI calculation of the $X^6\Sigma^+$, $A^6\Sigma^+$, $^6\Delta$ and $^6\Sigma^+(II)$ states. A ● indicates that convergence was obtained for this calculation at the respective inter-nuclear distance(s) and basis set. A ● indicates that convergence was not obtained. In this table four "families" of basis sets are presented(Dunning type Basis sets). The size of the basis set(n) for each family is indicated by the letters "D", "T" and "Q" which denote "double", "triple" and "quadruple'. Here "(f)" indicates that the core orbitals of (5, 2, 2, 0) of the C_{2v} framework in the CASSCF calculation were frozen. For a fair and consistent comparison, the state-combination used in the CASSCF calculations which these MRCI calculations built upon was "ABF" (see table 4.3).

Table 4.12 shows the variation in the calculated value of the $\nu = 1$ energy state for each electronic state as a function of basis set. Thankfully the variation is much less

Basis set	Electronic state						
	$X^6\Sigma^+$	$A^6\Sigma^+$	$^6\Pi$	$^6\Delta$	$a^4\Sigma^+$	$^4\Pi$	$^4\Delta$
cc-pVDZ	1.680(4)	1.780(2)	1.786(2)	1.777(4)	1.664(3)	1.705(5)	1.672(4)
cc-pVTZ	1.672(3)	1.780(4)	1.784(3)	1.774(3)	1.663(4)	1.703(3)	1.668(1)
cc-pVQZ	1.672(4)	1.783(1)	1.784(4)	1.779(2)	1.661(3)	1.702(2)	1.667(4)
aug-cc-pVDZ	1.687(4)	1.786(4)	1.793(4)	1.784(1)	1.670(2)	1.712(3)	1.679(2)
aug-cc-pVTZ	1.676(2)	1.784(2)	1.788(4)	1.778(3)	1.665(4)	1.707(4)	1.672(5)
aug-cc-pVQZ	1.673(5)	1.783(2)	1.787(4)	1.777(1)	1.663(2)	1.703(3)	1.669(2)
cc-pVDZ(f)	1.690(4)	1.921(3)	1.791(5)	1.932(3)	1.669(5)	1.711(3)	1.677(1)
cc-pVTZ(f)	1.584(3)	1.789(1)	1.790(5)	1.786(2)	1.671(5)	1.709(4)	1.671(5)
cc-pVQZ(f)	1.580(2)	1.789(2)	1.790(5)	1.787(1)	1.670(2)	1.708(2)	1.671(4)
aug-cc-pVDZ(f)	1.697(5)	1.908(1)	1.798(4)	1.914(3)	1.676(4)	1.719(5)	1.684(3)
aug-cc-pVTZ(f)	1.585(3)	1.789(2)	1.795(2)	1.788(2)	1.674(2)	1.712(5)	1.676(2)
aug-cc-pVQZ(f)	1.667(2)	1.788(2)	1.792(3)	1.783(2)	1.671(3)	1.710(2)	1.672(4)
Ref.	1.690	1.772	1.803	1.824	1.693	1.714	1.717

Table 4.10: R_e values obtained for the various PECs calculated at MRCI level of theory using an initial CASSCF calculation with the state-combination of ABF for various basis sets. Here the number in the brackets indicates the error on the minima obtained by using the interpolation functionality of Duo, see section 2.9.2. In this table the R_e values calculated by Dai & Balasubramanian (1993) have been shown for reference.

than for the D_e values hence indicating that the range in D_e values will only affect the number of higher-order vibronic states obtained for each PEC as opposed to the actual energy of these individual vibronic states. By examination of table 4.12 there is no clear trends as for some electronic states the highest value is for the case of a cc-pVDZ basis set and for others the highest value is for a cc-pVQZ basis set where the core orbitals have been frozen.

Finally, table 4.13 how the absolute position on the energy scale of PECs of each electronic state varies as a function of basis set. As can be seen a PEC of any particular state can appear up to 13 000 cm^{-1} higher or lower in energy depending on the basis set used. For all states, it can be seen that the lowest PECs obtained are for the cases of quadruple basis sets used: this is consistent with the Variational Theorem and the idea of the Basis Set Limit. In practice, all PECs were moved up/down the energy scale according to where they should lie as determined by the atomic dissociation limits of the Chromium atom for the calculation of the final linelist. In our study, relativistic basis sets and those for core-correlation were not investigated as it was know from previous work that their effects tend to cancel, see Lodi et al. (2008).

4.5 Effect of CASSCF state-combination upon MRCI calculations

Using the seven chosen state-combinations for CASSCF calculations shown in table 4.4, CI calculations were perfomed. The results produced by these CI calculations which each used one of these state-combinations in the proceeding CASSCF calculations were then compared. To reiterate for the construction of a linelist several *ab initio* curves are necessary:

- PECs: the parameters of these PECs for each of the molecular states determine

Basis set	Electronic state						
	$X^6\Sigma^+$	$A^6\Sigma^+$	$^6\Pi$	$^6\Delta$	$a^4\Sigma^+$	$^4\Pi$	$^4\Delta$
cc-pVDZ	15700	12129	13104	11621	12130	11210	10744
cc-pVTZ	16734	13320	14278	12826	13623	12471	12003
cc-pVQZ	16988	13258	14520	13073	13758	12866	12405
aug-cc-pVDZ	16242	12433	13817	12334	12433	11928	11451
aug-cc-pVTZ	16924	13180	14452	13023	13596	12760	12296
aug-cc-pVQZ	17069	13216	14575	13144	13747	12966	12508
cc-pVDZ(f)	16286	12451	13136	10862	13130	10949	10460
cc-pVTZ(f)	16043	21565	14320	20535	15336	12120	11660
cc-pVQZ(f)	16245	21545	14561	20639	15769	12499	12046
aug-cc-pVDZ(f)	16801	12867	13857	11697	13417	11660	11139
aug-cc-pVTZ(f)	16163	21323	14490	20555	15667	12400	11949
aug-cc-pVQZ(f)	17618	16057	14614	15221	15888	12597	12148

Table 4.11: D_e values obtained for the various PECs calculated at MRCI level of theory using an initial CASSCF calculation with the state-combination of ABF for various basis sets. For a bound PEC, a D_e value is simply the difference in energy between the minima of the of PEC and the value at dissociaiton.

Basis set	Electronic state						
	$X^6\Sigma^+$	$A^6\Sigma^+$	$^6\Pi$	$^6\Delta$	$a^4\Sigma^+$	$^4\Pi$	$^4\Delta$
cc-pVDZ	1483	1714	1757	1722.082366	1685	1573	1522
cc-pVTZ	1509	1715	1757	1718.655687	1687	1576	1532
cc-pVQZ	1511	1711	1756	1717.432249	1686	1574	1533
aug-cc-pVDZ	1465	1699	1748	1713.447707	1669	1566	1516
aug-cc-pVTZ	1497	1710	1755	1717.661735	1678	1569	1526
aug-cc-pVQZ	1501	1712	1754	1716.275966	1682	1570	1529
cc-pVDZ(f)	1642	1378	1673	1322.517761	1655	1529	1479
cc-pVTZ(f)	1339	3041	1617	3192.160096	1645	1523	1490
cc-pVQZ(f)	1337	3038	1618	3164.201293	1646	1524	1492
aug-cc-pVDZ(f)	1637	1426	1658	1393.747181	1637	1520	1471
aug-cc-pVTZ(f)	1291	3019	1614	3162.938876	1637	1516	1482
aug-cc-pVQZ(f)	1499	1974	1615	2151.46828	1642	1520	1487

Table 4.12: Energy levels of the $\nu = 1$ vibronic states of the various PECs calculated at MRCI level of theory using an initial CASSCF calculation with the state-combination of ABF for various basis sets.

the energy levels

- DMCs and TDMs: these curves determine the relative intensities of transitions between rovirbonic energy levels
- Angular-momentum coupling (i.e. L_x, L_z operators) which acts as a perturbation on the PECs
- Spin-orbit coupling (i.e. SO_x, SO_z operators) which acts as a perturbation on the PECs.

Hence, to a "first order" it is important to strive to obtain the "best quality" PECs, DMCs and TDMs as possible. The "quality" of the curves was selected in terms of the following criteria:

- Convergence of the curves-are the regions where convergence has not occurred (i.e. no numbers produced hence gaps) of physical importance? Generally

Basis set	Electronic state						
	$X^6\Sigma^+$	$A^6\Sigma^+$	$^6\Pi$	$^6\Delta$	$a^4\Sigma^+$	$^4\Pi$	$^4\Delta$
cc-pVDZ	5890	11390	6158	13677	6398	6443	6404
cc-pVTZ	2011	7436	1882	9401	2144	2080	2074
cc-pVQZ	240	5766	212	7742	277	257	260
aug-cc-pVDZ	4735	10261	4951	12480	5271	5231	5214
aug-cc-pVTZ	1282	6756	1248	8749	1352	1331	1326
aug-cc-pVQZ	0	5520	0	7514	0	0	0
cc-pVDZ(f)	6528	12342	6052	14098	6682	6630	6350
cc-pVTZ(f)	5010	1637	1926	1495	2881	2517	2220
cc-pVQZ(f)	3318	0	288	0	1054	741	443
aug-cc-pVDZ(f)	5389	11094	4829	12768	5566	5417	5176
aug-cc-pVTZ(f)	4303	1046	1268	993	2065	1749	1449
aug-cc-pVQZ(f)	1768	5176	68	5252	768	476	175

Table 4.13: Relative T_e values for each electronic state where the minima (0) for each is taken from the basis-set which produces the lowest-lying PEC for the particular state. Note this table is not showing where the various states lies with respect to each other: it is showing how for each state the effect of basis-set is to move the calculated PEC of this state up/down the energy scale. These differences in energy were taken at the equilibrium point for each of the different states. The PECs were calculated at MRCI level of theory using an initial CASSCF calculation with the state-combination of ABF for various basis sets.

speaking, the "well' of a PEC is more crucial than any "missing" asymptotic points provided there are plenty others to act as reference.

- Continuity of the curves. This was checked by visual inspection of the various plots but also by taking the gradient of the curves as a means to determine discontinuities. An explanation of this process is given below.

- Another check of "quality" was considering the behaviour of these various curves when different numbers of states of the same symmetry and multiplicity were calcualted at CI level. As an example comparing the case of 1+0, 2+1 and 3+1 calculations for $^4\Sigma^+$ and $^4\Delta$.

- For the case of $X^6\Sigma^+$ and $A^6\Sigma^+$, comparisons were made to experimental data. For the other electronic states it is interested to compare to previous theoretical work however in these cases it can be hard to ascertain either way which study is more accurate without experimentally derived reference values.

To help determine how continuous the various *ab initio* curves where, gradients of the curves were calculated and plotted. This was done using a "finite difference method" to produce PEC-G and DMC-G plots. To generate a PEC-G plot, the set of inter-nuclear points $R_1^*, ...R_N^*$ for the respective PEC was firstly used to construct a new set of inter-nuclear distances, size $N-1$ denoted R^* where N is the number of inter-nuclear points in the respective PEC using the formula, $R_a^* = \frac{1}{2}(R_a + R_{a+1})$ where a goes from 1 to $N-1$. The corresponding gradient of energy, denoted $E^{'}$ for each of these new R^* valus was calculated by $E_a^{'} = \frac{E_{a+1}-E_a}{R_{a+1}-R_a}$ where a runs from 1 to $N-1$. Hence the PEC-G curve contained $N-1$ data points where N is the number of inter-nuclear points, R for the original PEC. For clarity, table 4.14 demonstrates the use of these formula in constructing PEC-G curves.

PEC	Gradient of PEC
R_1, E_1	
	$R_1^* = \frac{1}{2}(R_1 + R_2), E_1^{'} = \frac{E_2 - E_1}{R_2 - R_1}$
R_2, E_2	
	$R_2^* = \frac{1}{2}(R_2 + R_3), E_2^{'} = \frac{E_3 - E_2}{R_2 - R_1}$
R_3, E_3	
	$R_3^* = \frac{1}{2}(R_3 + R_4), E_3^{'} = \frac{E_4 - E_3}{R_4 - R_3}$
R_4, E_4	
R_{N-2}, E_{N-2}	
	$R_{N-2} + R_{N-1}), E_{N-2}^{'} = \frac{E_{N-1} - E_{N-2}}{R_{N-1} - R_{N-2}}$
R_{N-1}, E_{N-1}	
	$R_{N-1}^* = \frac{1}{2}(R_{N-1} + R_N), E_{N-1}^{'} = \frac{E_N - E_{N-1}}{R_N - R_{N-1}}$
R_N, E_N	

Table 4.14: Schematic showing how PEC-Gs were constructed using a "finite difference method". Here the original PEC has N points withe inter-nuclear values of R_1, R_2,...RN with corresponding energy values E_1, E_2,..., E_N. The constructed PEC-G graph has $N-1$ data points. DMC-Gs were constructed in a similar manner by taking the difference of dipole moment values instead of energies.

In a similar fashion, DMC-G curves were calculated using this "finite difference" method.

In the following sections, the PECs, DMCs & TDMS calculated at CI level of theory using the seven different CASSCF state-combinations in table 4.4 are compared and discussion presented for each decision made. For the angular momentum and spin-orbit couplings calculated at CI level it was found that these are generally speaking independent to within several percent of the state-combinations used in the proceeding CASSCF calculation. A summary of the *ab initio* curves hence used in the final linelist for CrH is given in section 5.1.

4.6 Choice of Method for calculation of DMCs

With respect to the DMCs, there are two methods (Tennyson 2014) in which to calculate the dipole moment namely the expectation method and the finite field method where the former calculates the matrix element formed by acting the dipole moment operators $\hat{\mu}_x$, $\hat{\mu}_y$, $\hat{\mu}_z$ on the electronic wave-functions and the latter makes use of the Stark Effect. In this work all DMCs were calculated using the expectation method. In order to obtain accurate intensity values, it is paramount that we obtain accurate DMCs.

In sections 4.11 4.8 and 4.10 the DMCs presented are those that have been calculated using expectation method. Figure 4.5 shows DMCs calculated using the finite-difference method for the $^8\Sigma^+$, $^6\Pi$ and $^4\Pi$ states. Each plot shows DMCs calculates using a different family of basis. For each calculation the state-combination used in

the proceeding CASSCF calculation was "ABF".

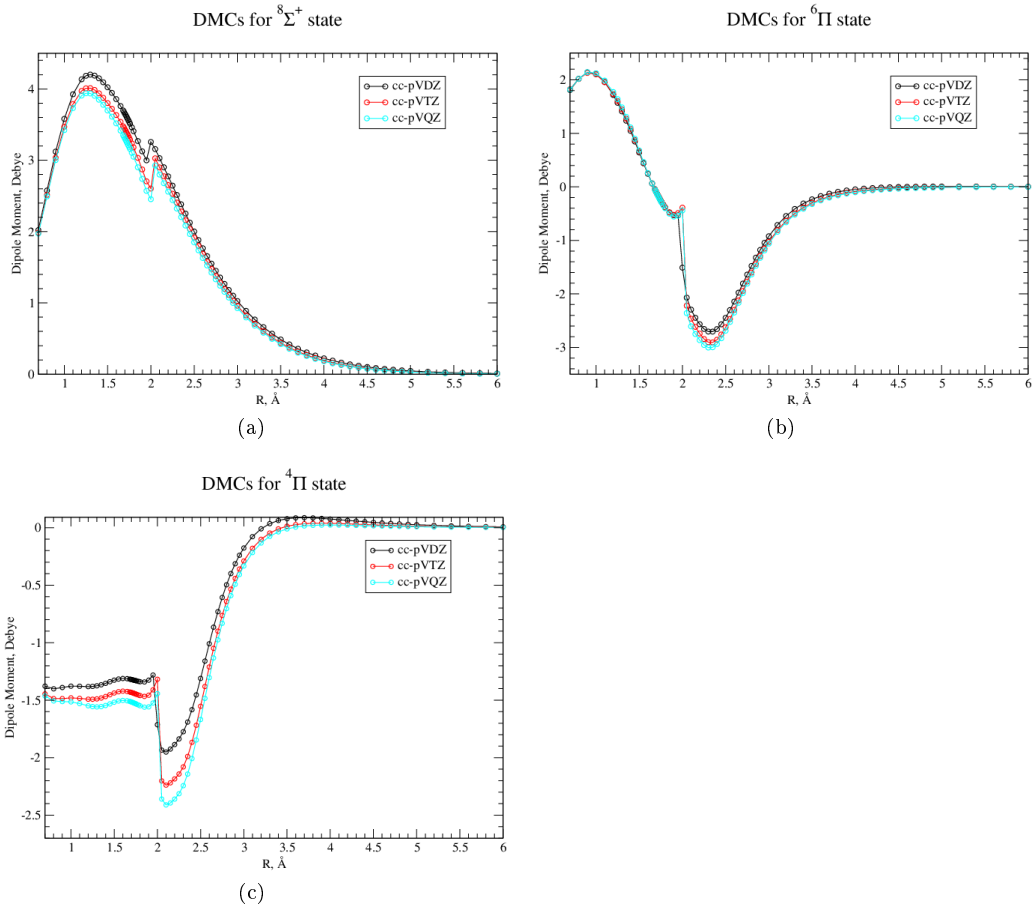

Figure 4.5: Calculation of DMCs at MRCI level of theory for various electronic states using the finite-field method. Each plot shows a comparison of curves calculated using increasingngly larger basis sets within a Dunning basis set family. In all of these MRCI calculations the CASSCF state-combination used was "ABF" to allow for a fair comparison.

Figure 4.5 demonstrates that increasing the size of the basis set generally does not alleviate discontinuities. For all plots, clear discontinuities can be seen and appear more significant than those for the "ABF" curves presented in sections 4.11, 4.8 and 4.10 where the expectation value method was used. Hence on this comparison it was decided to continue to use the expectation method to calculate the full DMCs of electronic states. For the case of the $X^6\Sigma^+$ and $A^6\Sigma^+$ states a comparison between the two methods has been made: see section 4.7.2.

4.7 PECs, DMCs and diagonal TDMs for the $^6\Sigma^+$ and $^6\Delta$ states

As a reminder, Δ states have components in both symmetry 1 and 4 within the c_{2v} framework, hence $^6\Sigma^+$ and $^6\Delta$ states need to be calculated together. It was established from the CASSCF testing that the relative order of these states in terms of potential energy is $X^6\Sigma^+$, $A^6\Sigma^+(II)$, $^6\Delta$ and $^6\Sigma^+(III)$. Thus when calculating curves at CI

level it makes sense to perform calculations which reflect this. Thus for each different CASSCF state-combination, 4 CI calculations of PEC, DMC and TDMs were carried out as summarised in table 4.15. This testing was done to investigate how CI results for a particular proceeding CASSCF state-calculation are affected by the number of states requested at CI levels in the various symmetries. As a reminder, the notation 4+1 indicates a CI calculation in which four sextet states within symmetry 1 and one state of symmetry 4 are calculated. Table 4.15 also shows the number of inter-nuclear distance points, R out of a total of 88 tested (see section 2.7.1 which defines the grid used) which converged. It should be noted that as well as the raw number of points that converge, the regions where non-convergence takes place is also important i.e. if there is "gaps" deep in the "well" of potentials compared to at dissociation.

CI *PROC*	Meaning	AB	AF	ABF	BF	BFH	BJ	BFJ
S5	1+0	88	88	88	88	88	88	88
S6	2+0	57	62	81	61	88	71	68
S7	3+1	53	72	81	73	62	69	84
S8	4+1	42	25	55	48	40	68	31

Table 4.15: Summary of MRCI calculations carried out for the $^6\Sigma^+$ and $^6\Delta$ states. In the results the notation for the CI *PROC*s defined here will be used throughout. The notation 3+1 signifies that three sextet states of symmetry 1 and one sextet state of symmetry 4 were calculated in an MRCI calculation. This table indicates the number of points(out of a possible 88) which converged for the various MRCI calculations which were performed for the various proceeding CASSCF state-combination calculations (as indicated by AB, AF etc).

As can be seen from table 4.15, for *PROC S5*, all 88 PECs and DMCs converged for the seven CASSCF state-combinations tested. As was mentioned previously, having a series of calculations converge does not guarantee that all these points will form a continuous curve. Figure 4.6 shows plots of PECs, PEC-Gs and DMCs calculated at CI level produced by *PROC S5* for the seven CASSCF state-combinations under test.

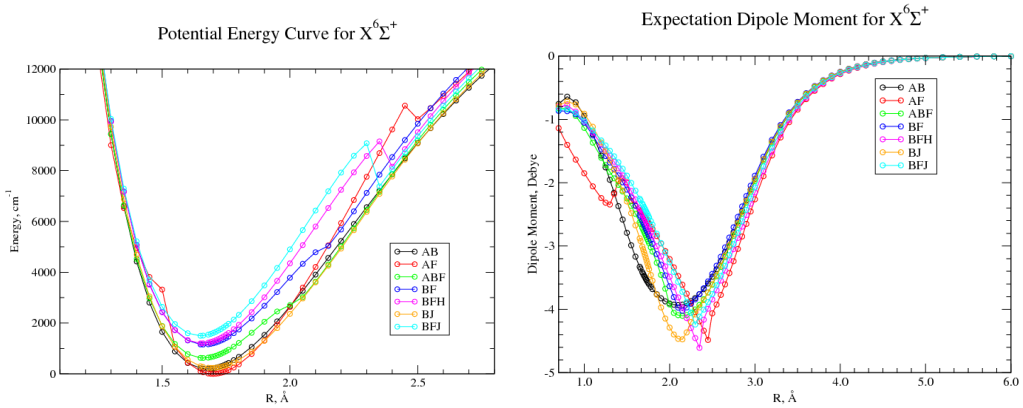

(a) (b)

Figure 4.6: Comparison of PECs and DMCs calculated at MRCI level of theory using a cc-pVQZ basis set for various CASSCF state-combinations for the $X^6\Sigma^+$ state of CrH.

Figure 4.6 shows the PECs calculated of the $X^6\Sigma^+$ state: as can be seen the AF, BF and BFH curves all "jump" at between 2.3 and 2.5 ÅḞigure 4.6 shows the DMCs:

it is clear that the AB curve is the only continuous curve. A plot of the PEC and DMC calculated at CI level for the $X^6\Sigma^+$ state using the *PROC S5* (i.e. a 1+0 calculation) is shown in figure 4.7.

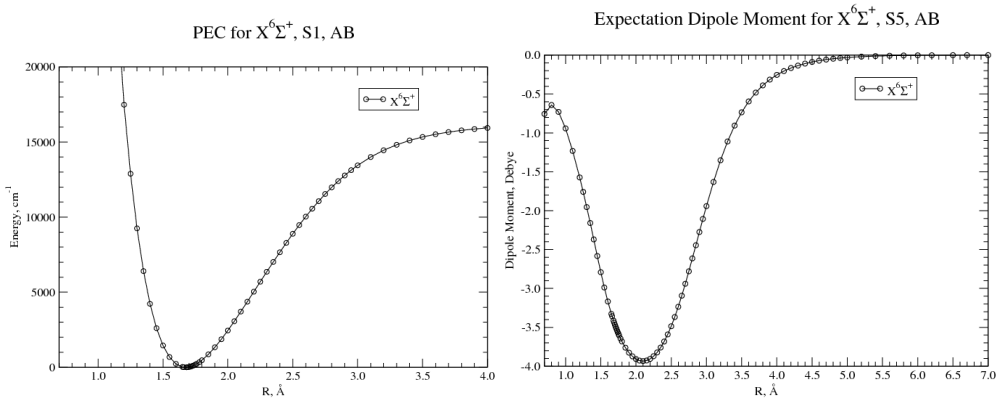

Figure 4.7: PECs and DMCs calculated at MRCI level of theory using a cc-pVQZ basis set and CASSCF state-combination of AB for the $X^6\Sigma^+$ state of CrH.

Figure 4.7 show that the PEC and DMC produced by a 1+0 CI calculation using the CASSCF state-combination of AB are both appear to be continuous. Unfortunately, refering to table 4.15 for CI calculations using *PROC*s *S6*, *S7* and *S8* for AB drops. But what is not revealed by this table that the region of non-convergence is a crucial region: it is between approximately 1.90 and 3.60 Åfor *PROC*s *S2*, *S3* and *S4* which is the region in which the shape of the PECs is paramount to the calculation of accurate vibronic energy levels.

Throughout the following analysis of these CI *PROC*s the colouring scheme shown in table 4.16 is used in plots which show PECs and DMCs for the $^6\Sigma^+$ and $^6\Delta$ states calculated using the *PROC*S *S5*, *S6*, *S7* and *S8* as defined in table 4.15.

Colour	State
Black	$X^6\Sigma^+$
Red	$A^6\Sigma^+$
Green	$^6\Delta$(sym 1)
Magneta	$^6\Sigma^+(III)$
Blue	$^6\Delta$(sym 4)

Table 4.16: Summary of colour scheme used throughout figures 4.8 to 4.14.

Figure 4.8 shows this colour scheme in action for the case of a CASSCF state-combination of AB been used in a CI calculation of four sextet states in symmetry 1 and one sextet state in symmetry 4(i.e. 4+1 calculation, *PROC S4*).

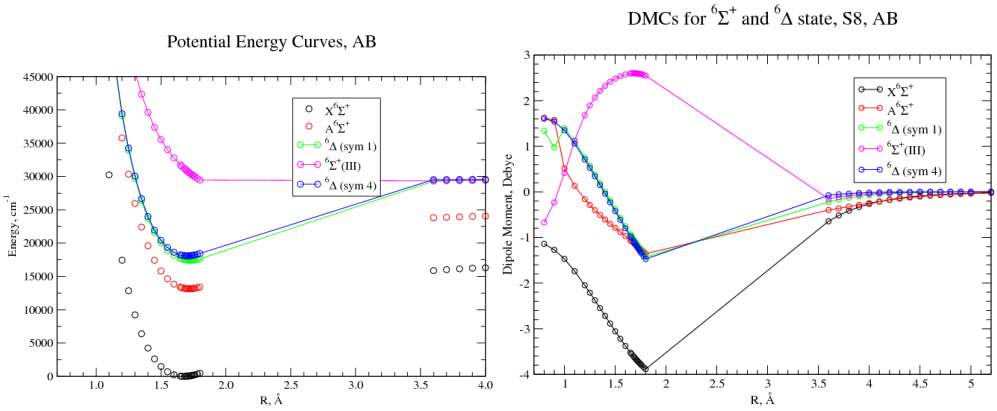

Figure 4.8: AB: PECs and DMCs calculated at MRCI level of theory using a cc-pVQZ basis set and CASSCF state-combination of AB for the $X^6\Sigma^+$, $A^6\Sigma^+$, $^6\Delta$ and $^6\Sigma^+(III)$ electronic states of CrH.

As figure 4.8 shows, CASSCF state-combination of AB produces PECs and DMCs at CI level which have gaps in the crucial region.

In the following pages, the colour scheme described in table 4.16 is employed to show the results of CI calculations of *PROC*s *S5*, *S6*, *S7* and *S8* defined in table 4.15 of PECs and DMCs produced using the six remaining CASSCF state-combinations as respective proceeding calculations. Table 4.17 provides a summary of the key distinguishing features of Figures 4.9 to 4.14. In summary, all CASSCF state-combinations produce their best CI results when the *S7 PROC* is used.

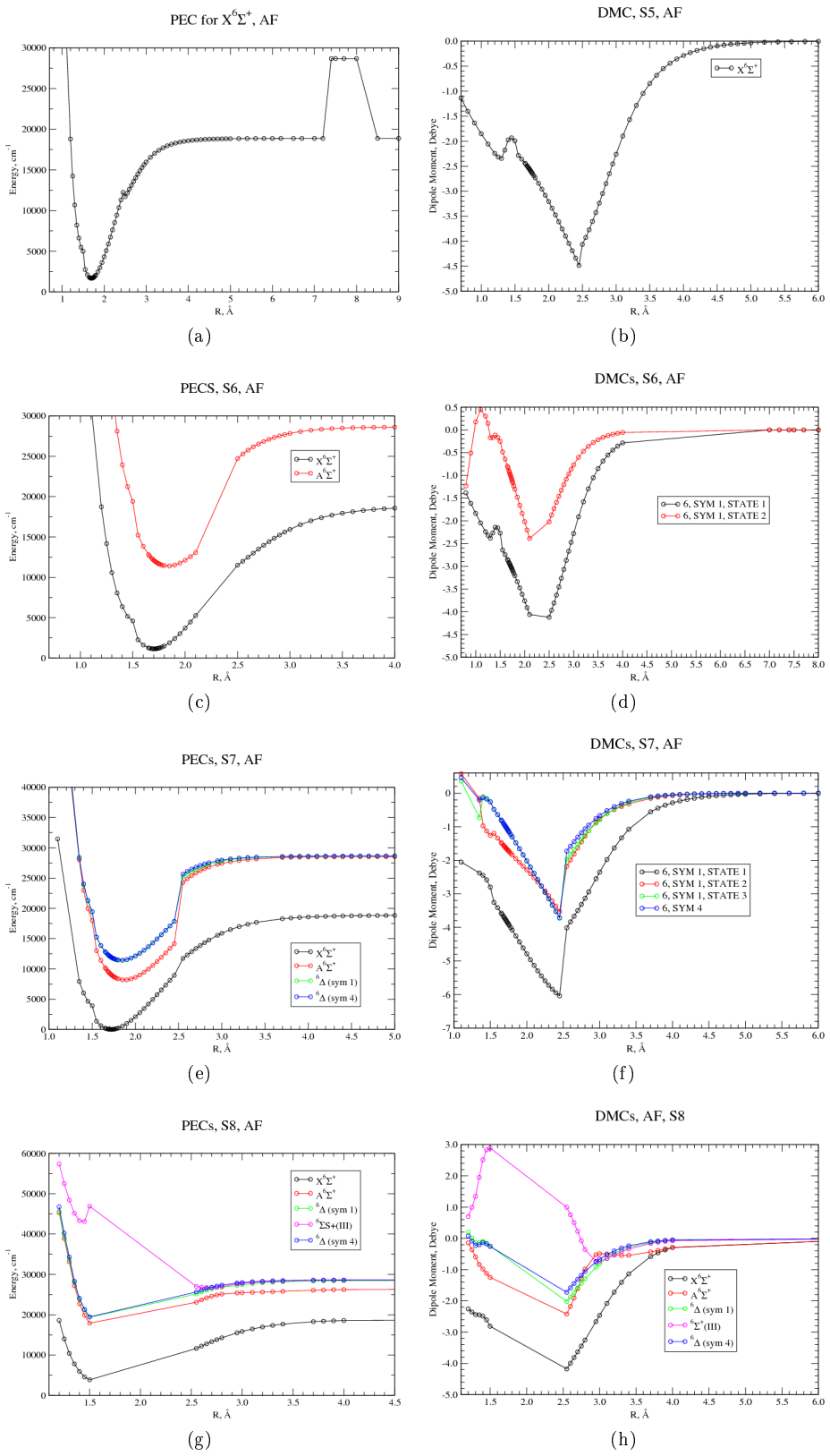

Figure 4.9: MRCI calculations of PECs and DMCs of the $X^6\Sigma^+$, $A^6\Sigma^+$, $^6\Delta$ and $^6\Sigma^+(III)$ electronic states of CrH using a cc-pVQZ basis set which are built upon the CASSCF state-combination of AF.

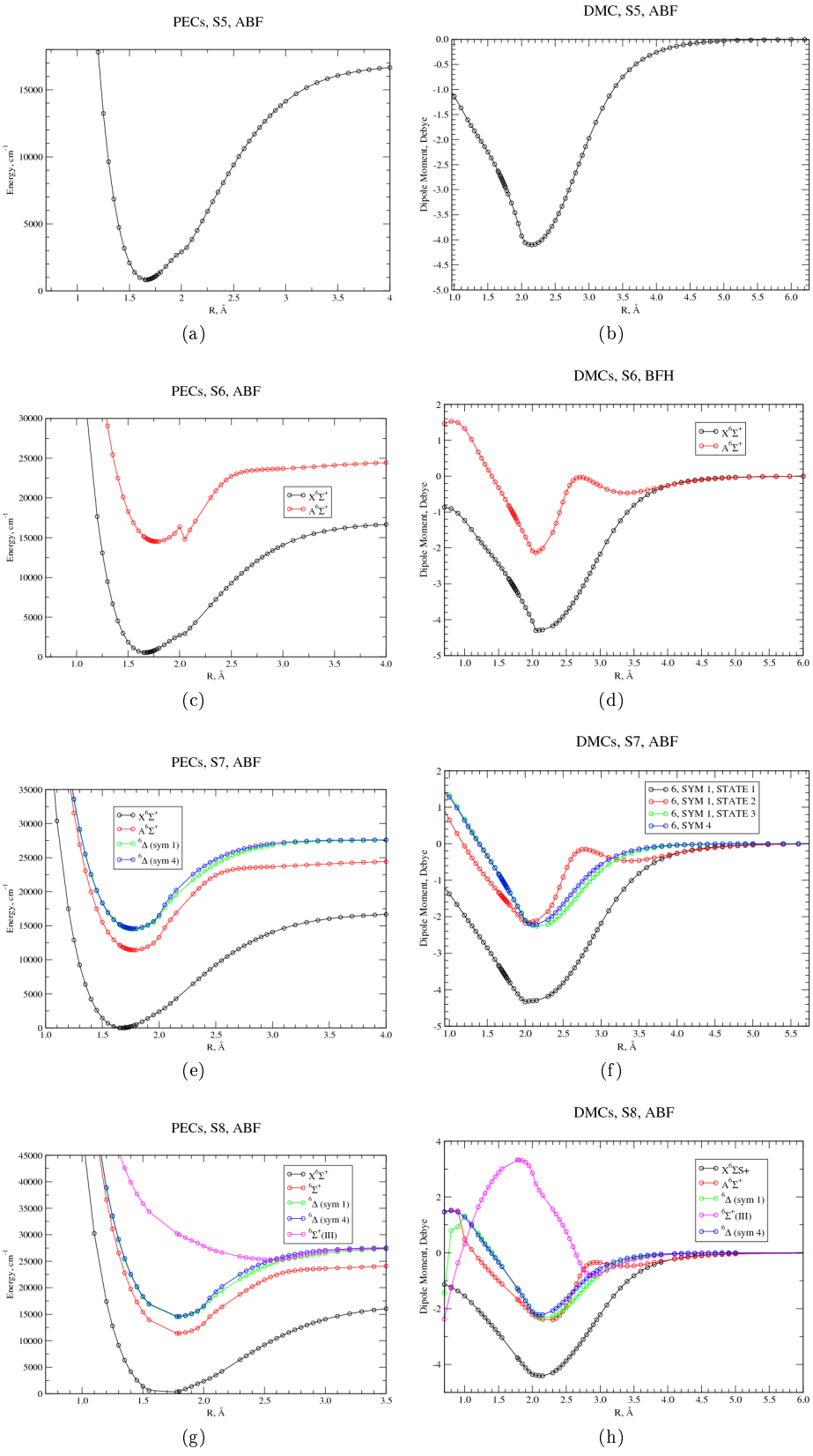

Figure 4.10: MRCI calculations of PECs and DMCs of the $X^6\Sigma^+$, $A^6\Sigma^+$, $^6\Delta$ and $^6\Sigma^+(III)$ electronic states of CrH using a cc-pVQZ basis set which are built upon the CASSCF state-combination of ABF.

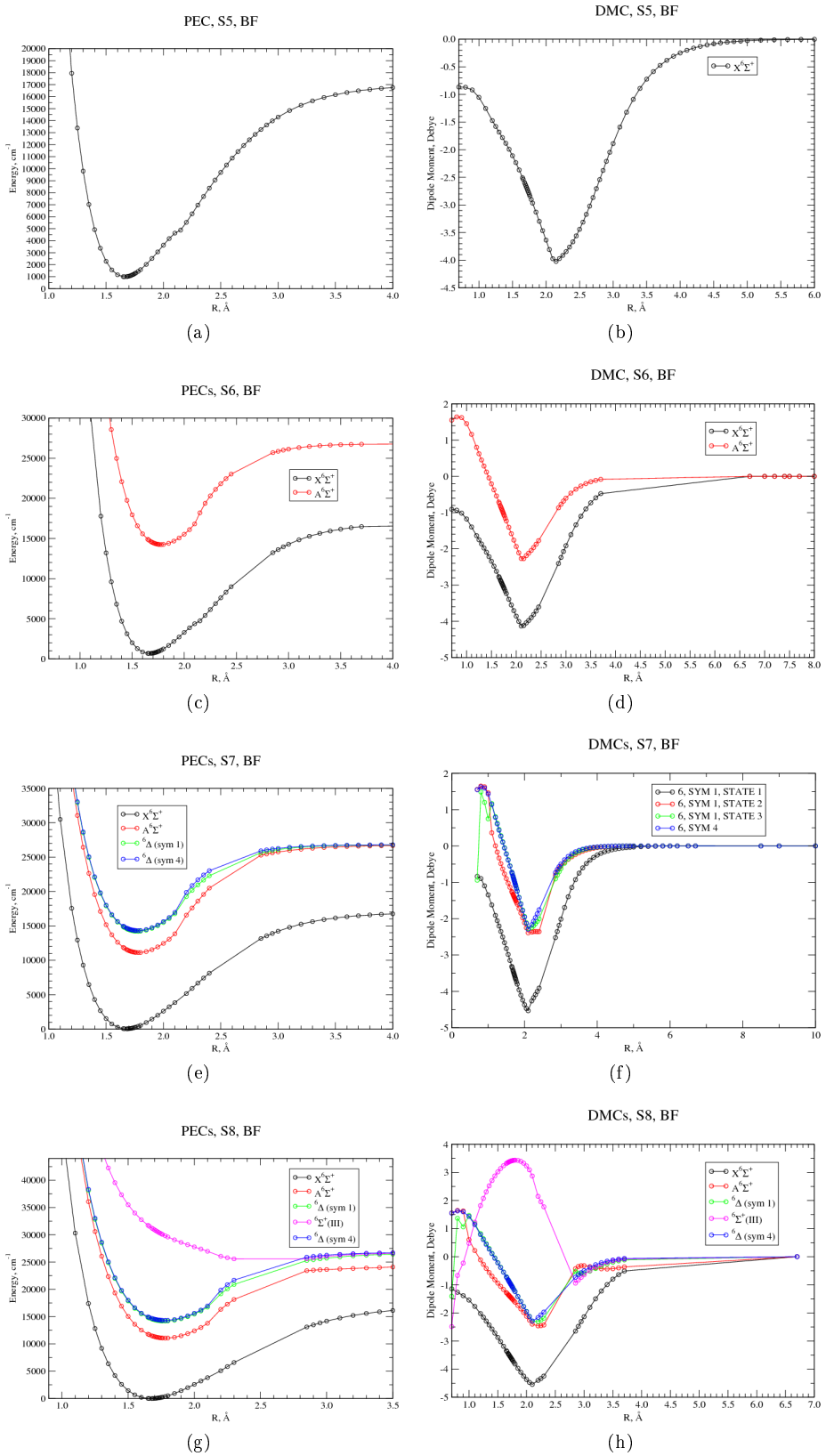

Figure 4.11: MRCI calculations of PECs and DMCs of the $X^6\Sigma^+$, $A^6\Sigma^+$, $^6\Delta$ and $^6\Sigma^+(III)$ electronic states of CrH using a cc-pVQZ basis set which are built upon the CASSCF state-combination of BF.

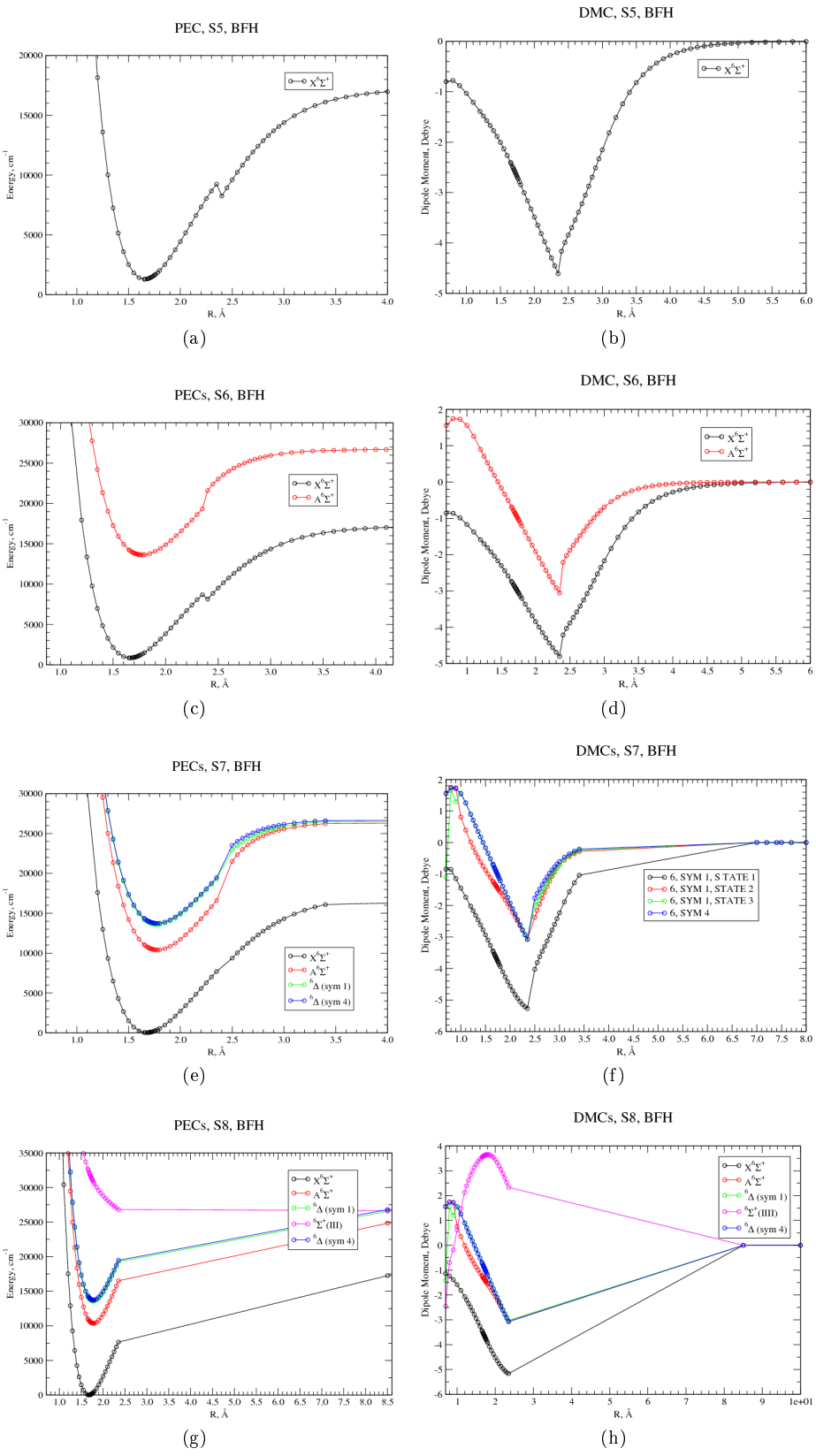

Figure 4.12: MRCI calculations of PECs and DMCs of the $X^6\Sigma^+$, $A^6\Sigma^+$, $^6\Delta$ and $^6\Sigma^+(III)$ electronic states of CrH using a cc-pVQZ basis set which are built upon the CASSCF state-combination of BFH.

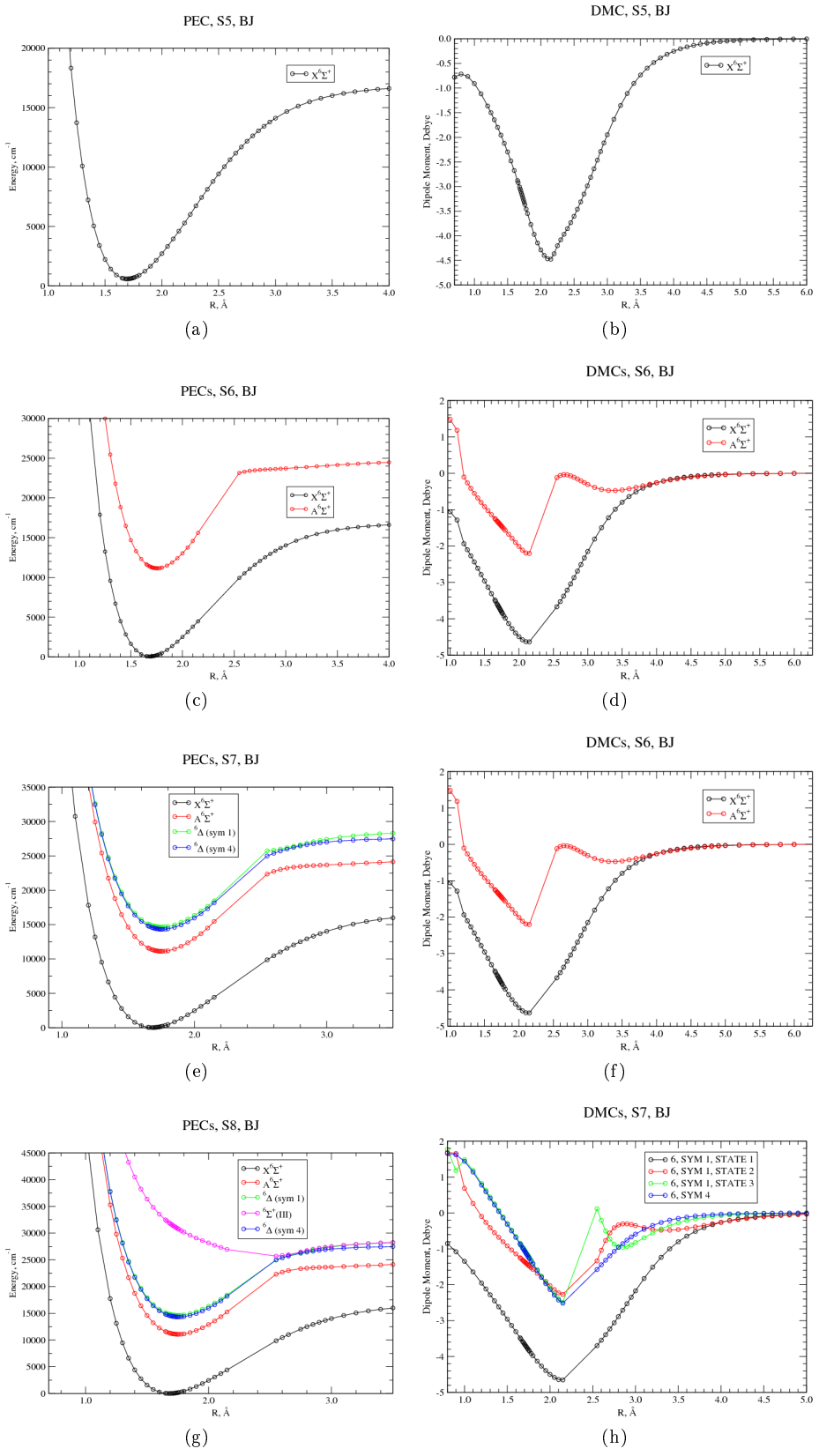

Figure 4.13: MRCI calculations of PECs and DMCs of the $X^6\Sigma^+$, $A^6\Sigma^+$, $^6\Delta$ and $^6\Sigma^+(III)$ electronic states of CrH using a cc-pVQZ basis set which are built upon the CASSCF state-combination of BJ.

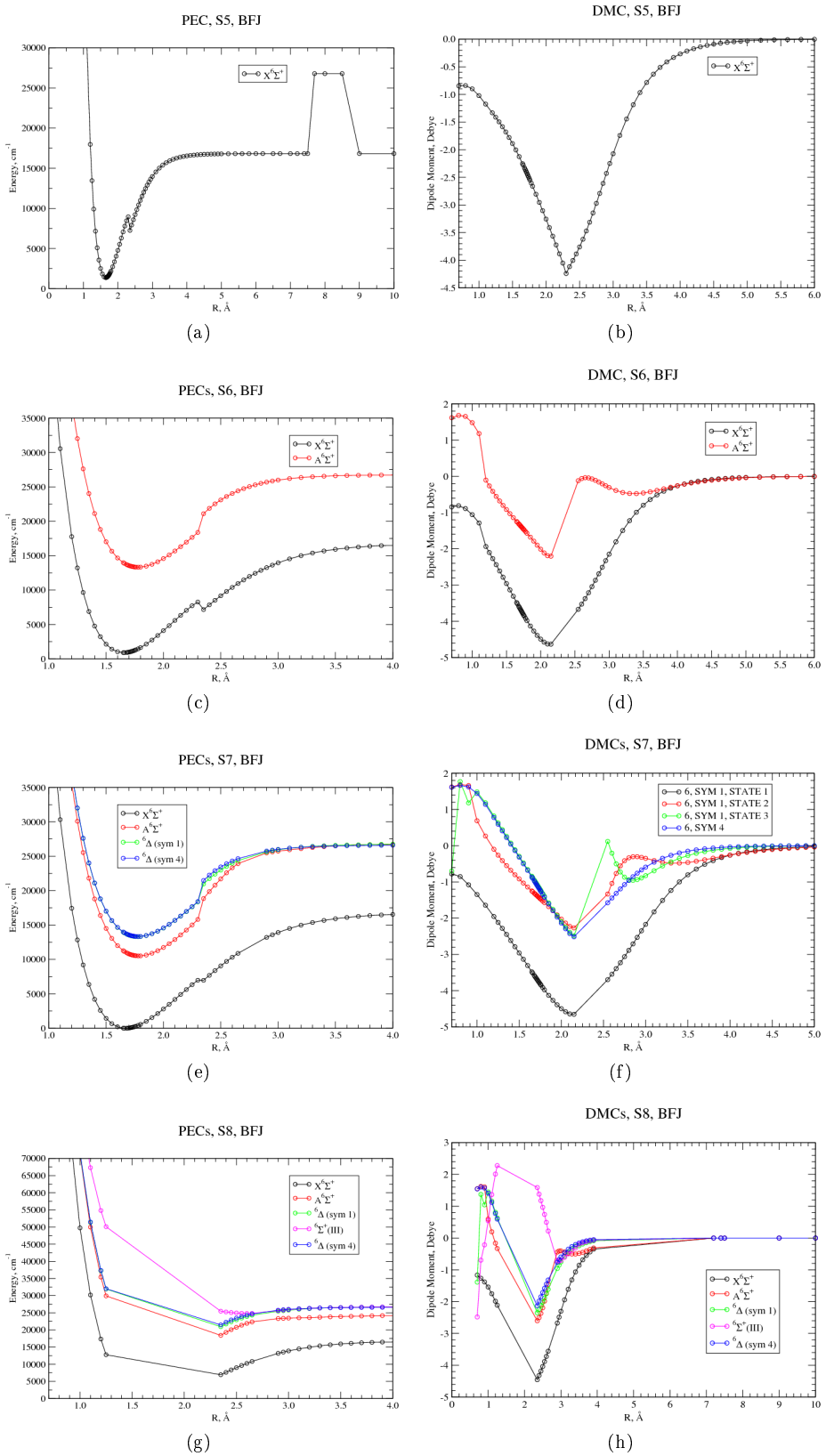

Figure 4.14: MRCI calculations of PECs and DMCs of the $X^6\Sigma^+$, $A^6\Sigma^+$, $^6\Delta$ and $^6\Sigma^+(III)$ electronic states of CrH using a cc-pVQZ basis set which are built upon the CASSCF state-combination of BFJ.

CASSF	*PROC*	Notes	
AF	*S5*	PEC: Minor discontinuity at 2.2 Å and between 7.00 and 8.00 Å "jump" up to another asymptote	Three "stray" points between 1.30 and 1.50 Å and a "sharp" change in behaviour at 2.5 Å.
	S6	Discontinuity at 1.5 Å in both PECs: gaps between 2.1 and 2.5 Å	
	S7	Very obvious discontinuity at 2.5 Å	
	S8	Gap in convergence between 1.5 and 2.5 Å	
ABF	*S5*	PEC: Small "hump" around 2.10 Å	DMC(s) appears of good quality
	S6	PEC: Discontinuity of $A^6\Sigma^+$ state around 2.10 Å.	
	S7	All curves continuous and of good quality	
	S8	Gap in convergence between 1.55 Å and 1.80 Å(affects PECs more than DMCs)	
BF	*S5*	Continuous curves: PEC does have a "bump" around 2.2 Å comparable in size to the S5 calculation of ABF	
	S6	Gap in convergence between 2.50 Å and 3.00 Å and also between 3.60 Å and 6.7 Å: the former is not as significant as there are sufficient points either side in which to reconstruct curve.	
	S7	PEC: Jump between 2.30 and 2.40 Åfor the upper states and a	DMC: Sharp cusp around 2.1 Å for all DMC
	S8	gap in convergence between 2.40 Å and 2.80 Å.	DMC & PEC: gap in convergence between 2.4 Å and 2.8 Å
BFH	*S5*	PECs: Discontinuity at 2.30 Å.	DMCs: sharp change in behaviour at 2.4 Å.
	S6		
	S7	PECs: gap and an apparent "jump" between 2.40 Å and 2.60 Å for the upper states	
	S8	No convergence in the crucial region between 2.40 Å and 8.40 Å.	
BJ	*S5*	PEC: continuous and well-behaved	DMC: shows a slightly steep change in character at 2.1 Å but nevertheless of good quality.
	S6	Gap in convergence between 2.10 and 2.60 Å but appear of good quality.	DMC of several upper states appears to have an abrupt change-exception is $^6\Delta$ state
	S7		
	S8		
BFJ	*S5*	PEC: Discontinuity at 2.40 Å.	DMC: Sharp change in behaviour at 2.4 Å.
	S6		DMC of ground state more smooth than S5 but $A^6\Sigma^+$ state has a change in behaviour in this region.
	S7		DMC of third sextet state of symmetry 1 abruplty changes between 2.10 Å and 2.50 Å.
	S8	No convergence in the crucial region between 1.2 and 2.3 Å.	

Table 4.17: Summary of distinguishing features of the various MRCI calculations performed of the $X^6\Sigma^+$, $A^6\Sigma^+$, $^6\Delta$ and $^6\Sigma^+(III)$ electronic states of CrH for different CASSCF state-combinations tested. All calculations were performed with a cc-pVQZ basis set. The relevant figures which this table refers to are figure 4.9 to 4.14.

4.7.1 PECs for the $X^6\Sigma^+$ and $A^6\Sigma^+$ states

Gathering together all the "good quality" PECs and DMCs for the $X^6\Sigma^+$ state, R_e, D_e and ω_e were calculated. These values are shown in table 4.18.

CASSCF state-combination	CI *PROC*	R_e(Å)	Dissociation energy (cm^{-1})	$\nu = 1$ energy (cm^{-1})	T_e relative (cm^{-1})
ABF	*S5*	1.675(2)	16229	1507.05	553
ABF	*S5*	1.660(1)	16120	1434.18	979
ABF	*S7*	1.673(2)	16949	1508.81	150
BFH	*S7*	1.673(3)	17235	1565.19	285
BF	*S5*	1.662(4)	16042.00	1527.36	1508
	S6	1.666(3)	16363	1530.32	1187
	S7	1.675(4)	16995	1535.95	555
	S8	1.673(3)	17053	1537.55	509
BJ	*S5*	1.694(2)	16305.00	1452.89	589
	S6	1.682(4)	16837	1522.70	57
	S7	1.682(4)	16870	1522.32	27
	S8	1.682(4)	16897	1520.43	0

Table 4.18: Summary of properties determined for various PECs of the $X^6\Sigma^+$ which were judged to be of good quality.

The PEC properties shown in table 4.18 were determined by using the procedure described in section 2.9.2. As table 4.18 shows, the values of R_e for these chosen PECs vary between 1.660 and 1.694. Within the BF calculations the trend is an increase in R_e as more states are added at CI level up to 3+1. For the BJ calculations, the value of R_e is constant for the *S6*, *S7* and *S8* values. These values of R_e can be compared to the theoretical values calculated by Dai & Balasubramanian(1993) which are shown in table 4.19. Additionally, table 4.20 shows previous theoretical determination of R_e obtained in other studies.

Method	Basis	R_e (Å)	ω_e (cm^{-1})	D_0 (cm^{-1})
MCSCF	ANO	1.721	1525	11211.40
IC-MRCI	ANO	1.684	1581	16615.45
IC-MRCI+Q	ANO	1.685	1577	17422.02
IC-MRCI	ANO+	1.681	1586	16857.42
IC-MRCI+Q	ANO+	1.682	1584	17583.34
IC-MRCI+dd'	ANO	1.679	1593	16776.76
IC-MRCI+Q+dd'	ANO	1.679	1596	17180.05
IC-MRCI+pp	ANO	1.683	1586	16615.45
IC-MRCI+Q+pp	ANO	1.683	1582	17422.02
IC-MRCI	GEN	1.683	1581	16454.13
IC-MRCI+Q	GEN	1.684	1577	17422.02
IC-MRCI+3s3p	GEN	1.673	1595	15970.19
IC-MRCI+Q+3s3p	GEN	1.670	1601	17422.02
MRCI	GEN	1.681	1585	16696.11
MRCI+Q	GEN	1.682	1581	17502.68
DK-MRCI	GEN	1.669	1631	17341.37
DK-MRCI+Q	GEN	1.669	1628	17502.68
Experiment work(within paper)		1.655	1656	15566.90(564.60)

Table 4.19: Summary of PEC properties of the $X^6\Sigma^+$ state of CrH obtained by Bauschlicher et al. (2001).

By comparing table 4.18 to tables 4.19 and 4.20 it can be seen that the range of R_e for the $X^6\Sigma^+$ state of CrH calculated within this study is consistent with previous theoretical work.

The estimates for $\nu = 1$ vibronic state can be compared against the joint experimental

Study	Method	R_e (Å)
Barone & Adamo (1997)	CISDa	1.691
	CPFa	1.694
	MCPFa	1.694
	BLYP/DZP	1.652
	B3LYP/DZP	1.654
	Experiment	1.662
Roos(2003)	CASPT2	1.642
	MSPT2	1.641
	Experiment	1.655
Koseki Matsushita & Gordon (2006)	ECP	1.676

Table 4.20: Summary of R_e values of the $X^6\Sigma^+$ state of CrH determined in previous theoretical studies with the experimental comparison available at the time.

and theoretical study of Bauschlicher et al. (2001) who obtained an experimental value of 1595.068 70(14) cm^{-1}. As can be seen all estimates presented in table 4.18 are too low. As table 4.18, there is a variation between 1434.18 and 1527.36 cm^{-1} for the values determined. However, this variation in both $\nu = 1$ energy level and indeed also the dissociation energy is a result in itself. It is hence reasonable to suppose that there will be a variation in ω_e. Bauschlicher et al. (2001) obtained an experimental value of ω_e of 1656.05115(54) cm^{-1} which they commented was "remarkably similar" to their theoretical prediction of 1653.6 cm^{-1}.The values calculated are around 150 cm^{-1} lower than the experimental value. Finally the relative energy spacing of the minima of these PECs is given in table 4.18: this demonstrates how the energy scale for different CASSCF calculations leading into CI calculations can vary by potentially 1000 s of wavenumbers. Table 4.19 is taken from the study of Bauschlicher et al. (2001) and shows the PEC properties they calculated using various basis sets and also methods. This table indicates how sensitive calculated PECs are to both basis set and method. In this study of CrH both of these have been validated.

Moving onto the $A^6\Sigma^+$, a similar analysis as was carried out for the $X^6\Sigma^+$ state has been carried out for the good quality PECs identified in table 4.17. Referring to table 4.15, an unusual feature of AF, BF and BFJ is that more points converge for *PROC S7* then they do *PROC S6*. This defies the trend of fewer points converging as more states are added at CI level. Table 4.21 quantifies the gap at dissociation between the various sextet states for the different calculations. For ABF and BJ the gap between the $A^6\Sigma^+$ state and $X^6\Sigma^+$ state stays constant at around 7700 cm^{-1} and around 11 000 cm^{-1} irrespective of the CI *PROC* used. However, for *PROC S6* for AF, BF, BFH and BFJ the $A^6\Sigma^+$ state is clearly dissociating to the wrong dissociation limit: referring back to table 2.8, the $A^6\Sigma^+(II)$ state should dissociate to a lower asymptote than the $^6\Delta$ and $^6\Sigma^+(III)$ states. Hence this is evidence that these CASSCF state-combinations give inaccurate results when a proceeding CI calculation with 2+0(i.e. *S6*) states is used.

Gap at dissociation between (cm^{-1})	CI *PROC*	AF	ABF	BF	BFH	BJ	BFJ
$A^6\Sigma^+(II)$ and $X^6\Sigma^+$	*S6*	9815	7717	9815	9469	7814	9965
$A^6\Sigma^+(II)$ and $X^6\Sigma^+$	*S7*	9688	7706	9688	9335	7803	9939
$^6\Delta$ and $X^6\Sigma^+$		9782	10667	9782	9439	11671	10022
$A^6\Sigma^+(II)$ and $X^6\Sigma^+$	*S8*	7607	7694	7607	7574	7792	7625
$^6\Delta$ and $X^6\Sigma^+$		9652	10603	9652	9301	11470	9901
$^6\Sigma^+(III)$ and $X^6\Sigma^+$		9752	10721	9752	9408	11650	9984

Table 4.21: Summary of gaps in energy between various electronic states of CrH at dissociation calculated at MRCI level of theory for various CASSCF state-combinations.

Table 4.22 gives a summary of the parameters obtained for the $A^6\Sigma^+$ PECs of interest: these were calculated in the same manner as they were for the $X^6\Sigma^+$ state.

CASSCF state-combination	CI *PROC*	R_e(Å)	Dissociation energy (cm^{-1})	Vibronic (cm^{-1})	T_e relative (cm^{-1})
ABF	*S7*	1.782(3)	13224	1737	506
ABF	*S8*	1.781(4)	13261	1714	458
BF	*S7*	1.785(4)	15604	1556	559
BF	*S8*	1.783(3)	13584	1547	505
BJ	*S7*	1.756(2)	13582	1624	43
BJ	*S8*	1.757(3)	13614	1611	0

Table 4.22: Summary of properties of PECs calculated for the $A^6\Sigma^+$ state of CrH.

As can be seen from table 4.22, R_e varies between 1.757 Å and 1.782 ÅṪhis can be compared to the theoretical value obtained by Dai & Balasubramanian (1993) of 1.772 Å which lies just about middle of the values presented in table 4.22. Again, as was the case for the $X^6\Sigma^+$ state, these can be compared to those obtained by Bauschlicher et al. (2001) whose results are shown in table 4.23.

Method	Basis	R_e	ω_e (cm^{-1})
MCSCF	ANO	1.876	1337
IC-MRCI	ANO	1.782	1516
IC-MRCI+Q	ANO	1.774	1537
IC-MRCI	ANO+	1.779	1521
IC-MRCI+Q	ANO+	1.771	1542
IC-MRCI+dd'	ANO	1.776	1525
IC-MRCI+Q+dd'	ANO	1.774	1531
IC-MRCI+pp	ANO	1.781	1520
IC-MRCI1Q1pp	ANO	1.773	1538
IC-MRCI+ppdd'	ANO		
IC-MRCI	GEN	1.78	1519
IC-MRCI+Q	GEN	1.772	1539
IC-MRCI+3s3p	GEN	1.778	1506
IC-MRCI+Q+3s3p	GEN	1.764	1514
MRCI	GEN	1.779	1515
MRCI+Q	GEN	1.771	1535
DK-MRCI	GEN	1.783	1494
DK-MRCI+Q	GEN	1.775	1517
Experiment work(within paper)		1.786	1525

Table 4.23: Summary of R_e and ω_e values determined for the $A^6\Sigma^+$ state of CrH by Bauschlicher et al. (2001) for various methods and basis sets.

As table 4.23 shows, Bauschlicher et al. (2001) obtained a spread in R_e values between 1.764 Å and 1.876 Å. With the exception of the BJ values this present study is consistent with the calculations of Bauschlicher et al. (2001). A very obvious outlier in dissociation energy is that of the BF, *S7* calculation producing a result of 15 604 cm^{-1}: the other five values determined vary between 13224 cm^{-1} and 13614 cm^{-1}. The estimates of ω_e obtained show huge variation with the lowest estimate of 1547 and the highest of 1737. Bauschlicher et al. (2001) obtained an experimental value of 1524.80(5) cm^{-1} and a theoretical value of 1525.2 cm^{-1}.

Table 4.23 also shows the variation in ω_e which Bauschlicher et al. (2001) obtained: the range is from 1337 to 1535 with the experimental value measured been 1525. This is consistent with the variation of the $\nu = 1$ energy level presented in table 4.22.

In summary for both the $X^6\Sigma^+$ and $A^6\Sigma^+$ states of CrH, there is significant variation in the PEC properties calculated as both a function of the CASSCF state-combination used and number of sextet states of symmetry 1 calculated at MRCI level. Pragmatically for the linelist experimental data was obtained of these two states and two empirical PECs fitted to this data. Hence *ab initio* PECs for these two states were simply used as a guide in starting off the process of fitting to experimental data. Hence, for the final linelist the final PEC chosen for each of these states is largely irrelevant.

4.7.2 Equilibrium Dipole Moments for the $X^6\Sigma^+$ and $A^6\Sigma^+$ states

To test out the stability of the equilibrium dipole moments obtained for both the $X^6\Sigma^+$ and $A^6\Sigma^+$ states, calculations at MRCI level theory were performed using different state-combinations in the initial CASSCF calculation. These values were calculated for a single point, namely for the case of an inter-nuclear distance of 1.672 Åfor the $X^6\Sigma^+$ state and 1.781 Åfor the $A^6\Sigma^+$ state respectively. Additionally, the effect of the number of states calculated at MRCI level was tested. For each CASSCF state-combination, four MRCI calculations were performed each with a different number of sextet states calculated within symmetry 1. Each of these MRCI calculations was performed using a finite-field method(FFD) and expectation method(EXP) For all calculations, a cc-pVQZ basis set was used. Tables 4.24 and 4.25 show these results.

	EXP	FFD	EXP	FFD	EXP	FFD	EXP	FFD
No. values	56	55	55	54	54	54	21	16
Mean	2.581	3.723	2.958	3.840	3.670	3.936	3.473	3.696
Median	2.465	3.692	2.836	3.729	3.528	3.732	3.441	3.674
Minimum	2.031	2.259	2.489	2.341	3.318	2.364	3.308	3.506
Maximum	4.082	4.599	3.877	4.879	4.717	5.093	3.721	3.884

Table 4.26: Summary statistics for the dipole moments calculated for the $A^6\Sigma^+$ state at $R = 1.672$ Å. See table 4.24 for details of these calculations. Here "EXP" and "FFD" refer to the two methods which can be used to calculate dipole moments namely, expecation value method and finite-field method.

Method	EXP	FFD	EXP	FFD	EXP	FFD	EXP	FFD
CASSCF	Number of states in CI calculation							
	1		2		3		4	
A	3.900							
B	3.882	3.900	2.835	3.934				
AB	3.391	4.022	3.476	4.009	3.502	3.967	3.584	3.930
ABF	2.172	3.648	2.557	3.711	3.329	3.734		
ABF-IJ	2.059	3.375	2.489	3.514	3.318	3.667	3.308	3.649
ABFI	2.172	3.648	2.557	3.711	3.329	3.734		
ABFJ	2.180	3.633	2.575	3.708	3.352	3.748		
ABI	2.426	3.862	2.744	3.845	3.425	3.724	3.422	
ABIJ	2.160	3.425	2.571	3.539	3.385	3.647	3.373	3.632
ABJ	3.011	3.908	3.677	3.719	3.663	3.716		
AF	2.479	4.108	2.898	4.334	3.644	4.611		
AFI	2.411	3.631	2.914	3.967	3.844	4.485		
AFJ	2.734	3.799	3.309	4.156	4.102	4.547		
AI	2.520	3.455	3.016	3.806	3.993	4.409		
AJ	2.896	3.792	3.484	4.178	4.340	4.640		
BD	3.371	3.858	3.712	3.762	3.719	3.755	3.721	3.744
BDF	2.310	3.901	2.661	3.907	3.365	3.823		
BDF-IJ	2.173	3.507	2.595	3.605	3.434	3.672		
BDFI	2.099	3.480	2.514	3.591	3.321	3.693	3.313	3.674
BDFJ	2.327	3.736	2.708	3.772	3.486	3.725	3.475	
BDI	2.247	3.588	2.628	3.654	3.399	3.675	3.389	3.661
BDJ	2.693	3.850	2.981	4.473	3.611	3.688	3.597	3.680
BF	2.571	4.191	2.834	4.116	3.388	3.907	3.417	3.884
BFGI	2.099	3.480	2.512	3.589	3.322	3.693	3.314	3.674
BFH	2.465	3.905	2.803	3.891	3.511	3.761	3.502	3.749
BFH-IJ	2.331	3.651	2.698	3.699	3.450	3.688		
BFHI	2.233	3.611	2.636	3.679	3.447	3.689	3.436	
BFHJ	2.521	3.866	2.836	3.857	3.501	3.748	3.498	
BFI	2.119	3.553	2.528	3.638	3.343	3.696		
BFIJ	2.099	3.480	2.512	3.589	3.322	3.693	3.314	3.674
BFJ	2.310	3.901	2.658	3.905	3.368	3.823		
BH	3.011	3.908	3.677	3.719	3.656	3.714		
BHI	2.465	3.710	2.809	3.727	3.538	3.657	3.524	3.647
BHIJ	2.495	3.706	2.822	3.723	3.517	3.662		
BHJ	2.714	3.974	2.991	4.514	3.597	3.735		
BI	2.383	3.673	2.715	3.685	3.436	3.618	3.441	3.602
BIJ	2.247	3.588	2.625	3.652	3.401	3.676	3.392	3.661
BJ	2.973	4.089	3.559		3.555	3.779	3.557	3.768
D	3.100	3.927	3.822	3.662	3.795	3.659		
DF	2.464	4.127	2.945	3.731	3.813	3.729		
DFIJ	3.009	4.429	3.663	4.779	4.492	5.093		
DFI	2.443	3.600	2.965	3.955	3.929	4.509		
DFJ	3.095	4.599	3.719	4.879	4.501	5.071		
DI	2.554	3.466	3.078	3.840	4.091	4.472		
DIJ	3.220	4.417	3.877	4.756	4.717	5.030		
DJ	2.508	2.259	2.928	2.341	3.709	2.364	3.694	
F	2.031	4.085	2.840	4.330	3.587	4.596		
FHIJ	2.205	3.451	2.609	3.556	3.402	3.646		
FHJ	2.345	3.666	2.714	3.715	3.456	3.705		
FI	2.367	3.573	2.916	3.948	3.894	4.514		
HI	2.879	3.069	3.441	3.660	4.362	3.514		
HIJ	2.332	3.497	2.711	3.156	3.478	3.358		
H	2.219	3.692	3.043	3.576	3.686	3.622	3.663	3.506
I	2.493	3.289	3.063	3.725	4.173	4.467		
IJ	2.554	3.466	3.074	3.837	4.091	4.473		
J	4.082	3.738	3.158	4.042	4.073	4.549		

Table 4.24: Calculation of equilibrium dipole moment for the $X^6\Sigma^+$ state(in Debye) at $R = 1.672$ Å using a cc-pVQZ basis set. The values shown here are the magnitudes. This table shows the values obtained when varying the state-combinations used in the CASSCF calculation(horizontal) and the number of sextet states calculated in symmetry 1 for the proceeding MRCI calculations which built upon the orbitals generated in the preliminary CASSCF calculations. Finally, "EXP" and "FFD" refer to the method used at MRCI level to calculate the dipole moment namely the expectation method(EXP) and finite-field method(FFD).

Method	EXP	FFD	EXP	FFD	EXP	Method	EXP	FFD	EXP	FFD	EXP
CASSCF	Number of states in CI calculation					CASSCF	Number of states in CI calculation				
	2		3		4		2		3		4
B	0.803	1.693	0.997	1.319		ABF	1.724	1.372	1.716		
BD	1.310	1.312	1.219	1.315	1.210	ABF-IJ	1.762	1.493	1.486		
BDF	1.697	1.257				ABFI	1.724	1.372	1.716		
BDF-IJ	1.641	1.421				ABFJ	1.725	1.396	1.715		
BDFI	1.747	1.449	1.738	1.443		ABI	1.666	1.306	1.659		
BDFJ	1.579	1.343	1.565			ABIJ	1.745	1.483	1.733	1.477	
BDI	1.718	1.428	1.707	1.423		ABJ	1.435	1.437	1.247		
BDJ	1.516	1.307	1.500			AF	1.795	1.796			
B	0.788	1.748				AFI	1.877	2.105			
BF	1.556	0.925	1.574	0.916		AFJ	1.573	1.696			
BFGI	1.747	1.449	1.737	1.443		AI	2.100	2.230			
BFH	1.533	1.275	1.521	1.271		AJ	1.752	1.837			
BFH-IJ	1.629	1.352				D	1.266	1.266	1.180		
BFHI	1.612	1.384	1.598			DF	1.794	1.309			
BFHJ	1.558	1.253	1.550			DFIJ	1.483	2.043			
BFI	1.666	1.380				DFI	1.855	2.110			
BFIJ	1.747	1.449	1.737	1.443		DFJ	1.430	1.809			
BFJ	1.697	1.257				DI	2.014	2.177			
BH	1.435	1.438	1.246			DIJ	1.570	1.884			
BHI	1.570	1.360	1.555	1.355		DJ	1.547	1.290			
BHIJ	1.586	1.336				HI	1.553	1.112			
BHJ	1.978	1.556	1.280			HIJ	1.674	1.781			
BI	1.594	1.320	1.588	1.316		H	1.492	1.421	1.480	1.101	
BIJ	1.717	1.428	1.706	1.423		I	1.938	2.151			
BJ	1.527	1.530	1.541	0.986		IJ	2.014	2.177			
F	1.499	1.597				J	2.058				
FHIJ	1.714	1.432									
FHJ	1.648	1.340									
FI	1.750	2.077									

Table 4.25: Calculation of equilibrium dipole moment for the $A^6\Sigma^+$ state (in Debye) at 1.781 Å using a cc-pVQZ basis set. The values shown here are the magnitudes. This table shows the values obtained when varying the state-combinations used in the CASSCF calculation (horizontal) and the number of sextet states calculated in symmetry 1 for the proceeding MRCI calculations which built upon the orbitals generated in the preliminary CASSCF calculations. Finally, "EXP" and "FFD" refer to the method used at MRCI level to calculate the dipole moment namely the expectation method (EXP) and finite-field method (FFD).

Method	EXP	FFD	EXP	FFD	EXP
no.values	55	54	27	14	1
Mean	1.639	1.540	1.529	1.302	1.210
Median	1.666	1.430	1.565	1.337	1.210
Minimum	0.788	0.925	0.997	0.916	1.210
Maximum	2.100	2.230	1.738	1.477	1.210

Table 4.27: Summary statistics for the dipole moments calculated for the $X^6\Sigma^+$ state at $R = 1.781$ Å. See table 4.25 for details of these calculations. Here "EXP" and "FFD" refer to the two methods which can be used to calculate dipole moments namely, expecation value method and finite-field method.

For comparison, the minima shown by the calculation of Ghigo et al. (2004) is around (2.38 Å, -5.210 Debye). Using this plot it can be shown that at approximately 1.672 Å, the value calculated by Ghigo et al. (2004) has a magnitude of around 3.6 Debye.

For the $A^6\Sigma^+$ state of CrH, Chen, Steimle & Merer (2007) experimentally determined an equilibrium dipole moment of 1.15(3) D.

Study	Method	μ_e (D)
Chong et al. (1986)	SDCI	4.250
	CPF	3.779
	MCPF	3.807
Dai & Balasubramanian (1993)	SOCI	3.864
Koseki, Matsushita & Gordon (2006)	ECP-FOCI	4.190
Chen, Steimle & Merer (2007)	Experimental	3.510(33) (CrD)

Table 4.28: Summary of equilibrium dipole moment of the $X^6\Sigma^+$ state obtained in previous studies.

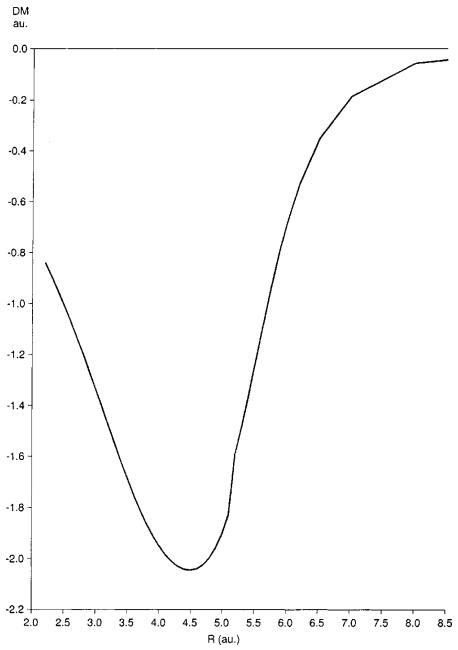

Figure 4.15: DMC of the $X^6\Sigma^+$ state calculated by Ghigo et al. (2004). Here the units of the axis are atomic units.

4.7.3 PECs and DMCs for the $^6\Delta$ state

For CrH, unfortunately experimental data is only available on the $X^6\Sigma^+$ and $A^6\Sigma^+$ states. Hence for the higher-lying electronic states, the only constraining factor is knowing the relative energy (with respect to the $X^6\Sigma^+$ state) which they should dissociate to. As was shown in tables 4.17 and 4.22, PECs for a single state can move up and down the energy scale depending on what state-combinations are used in the inital CASSCF calculation and then also how many states are calculated within a particular symmetry for a given multiplicity at CI level. Figure 4.16 demonstrates the latter effect for the case of using the state-combination of ABF at CASSCF level and then calculating different number of states at CI level.

For the $^6\Delta$ state it was decided to use the PEC calculated using the CASSCF state-combination of ABF for the case where the proceeding CI calculation of *S7* (i.e. 3+1). Table 4.15 shows that for the *S7* calculation, ABF had the greatest number of points converged. For all CASSCF state-combinations the number of points which converge dramatically drops off when going from an *S7* calculation to an S8 calcula-

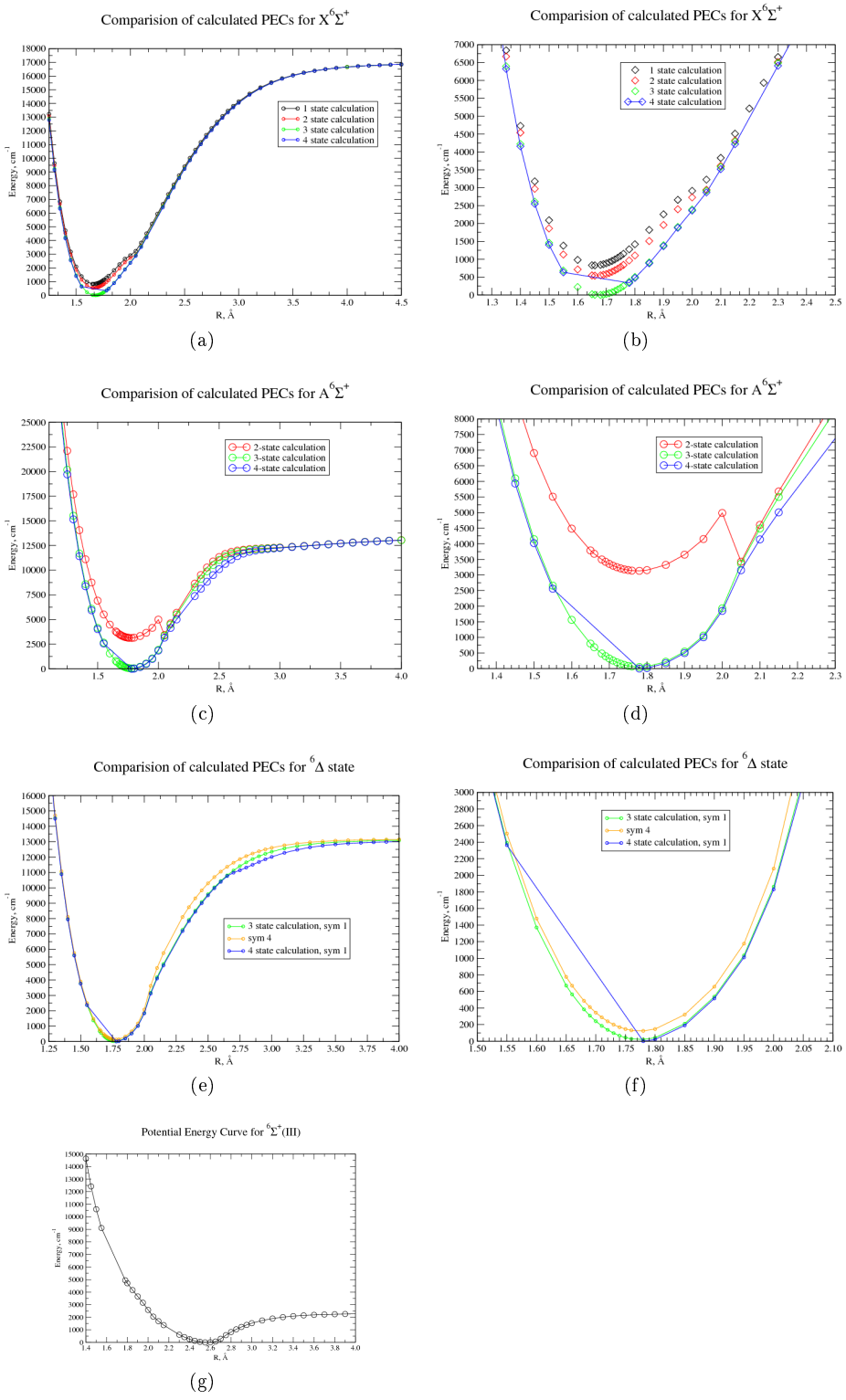

Figure 4.16: Comparison of PECs obtained at MRCI level of theory for sextet states when the number of sextet states in symmetry 1 calculated is varied. Each of these MRCI calculations builds on a CASSCF state-combination of ABF and have been calculated using a cc-pVQZ basis set.

tion with the exception of BJ for which an almost identical number of points converge. Inspection of figure 4.9e, 4.12e and 4.14e show obvious discontinuities around 2.5 Å.

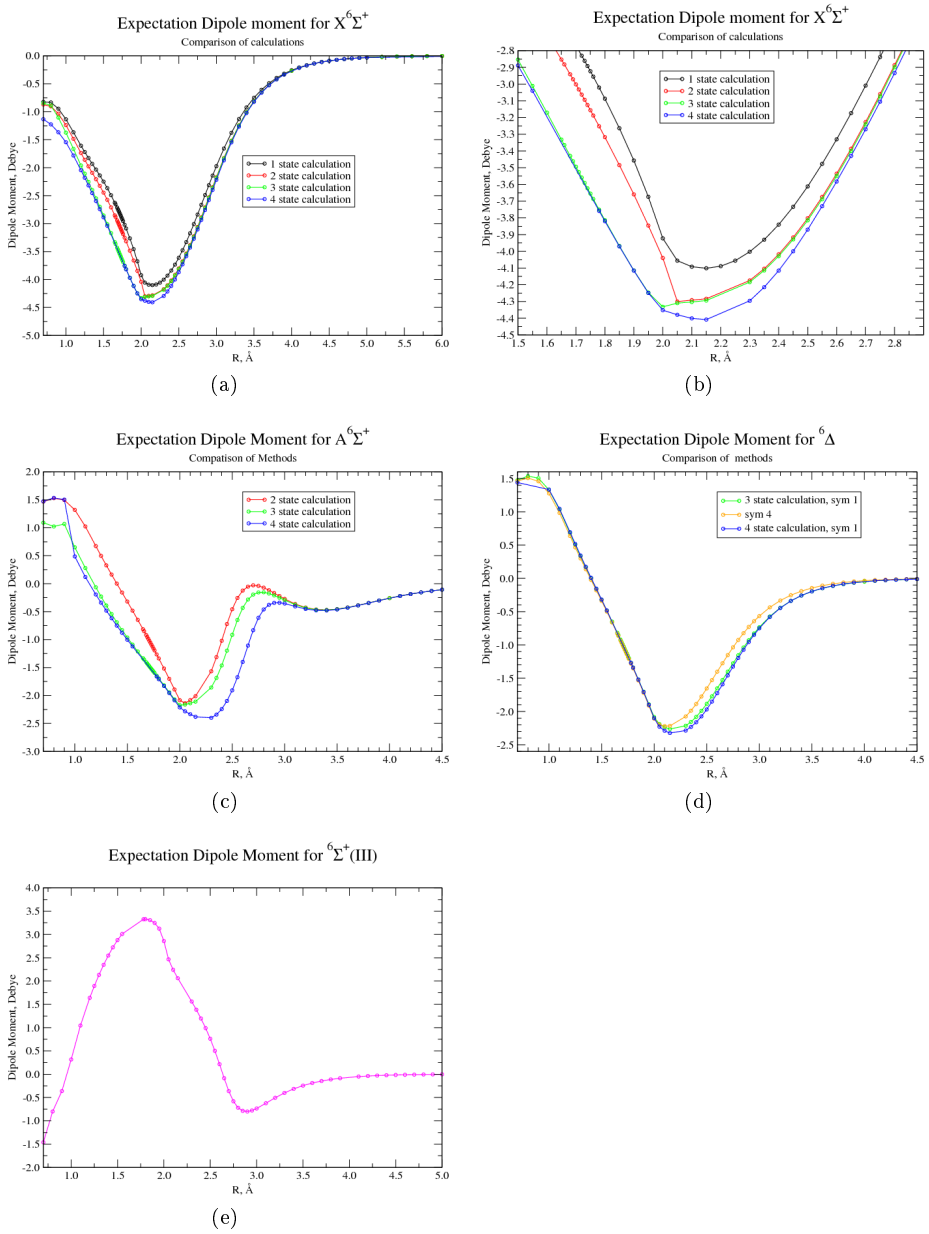

Figure 4.17: Comparison of DMCs obtained at MRCI level of theory for sextet states when the number of sextet states in symmetry 1 calculated is varied. Each of these MRCI calculations builds on a CASSCF state-combination of ABF and have been calculated using a cc-pVQZ basis set.

Hence the AF, BFH and BFJ are not suitable for the $^6\Delta$ state. Comparing figures 4.10e, 4.11e and 4.13e for the *S7* calculations of ABF, BF and BJ respectively it can be seen that all three are of good quality. On the basis of number of points converged it was decided to use the PEC calculated using the CASSCF state-combination of ABF as this had the greatest number of inter-nuclear points converged(see table 4.15).

The *S7* MRCI calculation using the CASSCF state combination of "ABF" was used for the $^6\Delta$ state in the final linelist.

4.7.4 PECs and DMCs for the $^6\Sigma^+(III)$ state

Figure 4.7.4 shows all the PECs calculated at CI level using the *S8 PROC* for each of the seven different proceeding CASSCF state-combinations. Figure 4.18a clearly

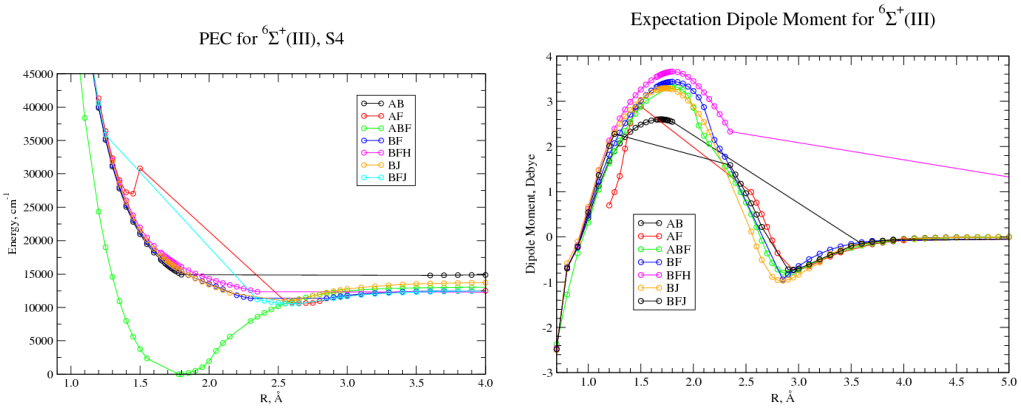

(a) (b)

Figure 4.18: Calculation of PEC and DMCs for the $^6\Sigma^+(III)$ state of CrH at MRCI level of theory.

shows that the $^6\Sigma^+(III)$ state, appears to be anti-bonding. However the ABF calculation produces a bound state. The Variational Theorem states that, the energy obtained from a quantum-mechanical calculation will be greater than or equal to the true value. Hence with this in mind, ABF seems the best choice. This figure is clearly highlighting the how using different state-combinations in CASSCF calculations can have a significant effect on any subsequent CI calculations which use these CASSCF generated orbitals. Figure 4.18a also shows how the AF calculation appears to "jump" to a higher state between 1.60 Å and 2.60 Å.

The S8 MRCI calculation using the CASSCF state combination of "ABF" was used for the $^6\Sigma^+(III)$ state in the final linelist.

4.7.5 TDMs between the three $^6\Sigma^+$ states

The transition dipole moments between the three $^6\Sigma^+$ states were calculated at CI level for each of the seven CASSCF state-combinations listed in table 4.4. These plots are shown in figure 4.19. The legend of each plot is summarised as follows:

- Black for the TDM of the $\langle A^6\Sigma^+(II)|\,\mu_z\,|X^6\Sigma^+\rangle$ transition.
- Red for the TDM of the $\langle {}^6\Sigma^+(III)|\,\mu_z\,|X^6\Sigma^+\rangle$ transition
- Green for the TDM of the $\langle {}^6\Sigma^+(III)|\,\mu_z\,|A^6\Sigma^+\rangle$ transition
- "square" signifying a two-state calculation, i.e. two sextet states of symmetry 1 calculated.
- "circle" signifying a three-state calculation.
- "+" sign signifying a four-state calculation.

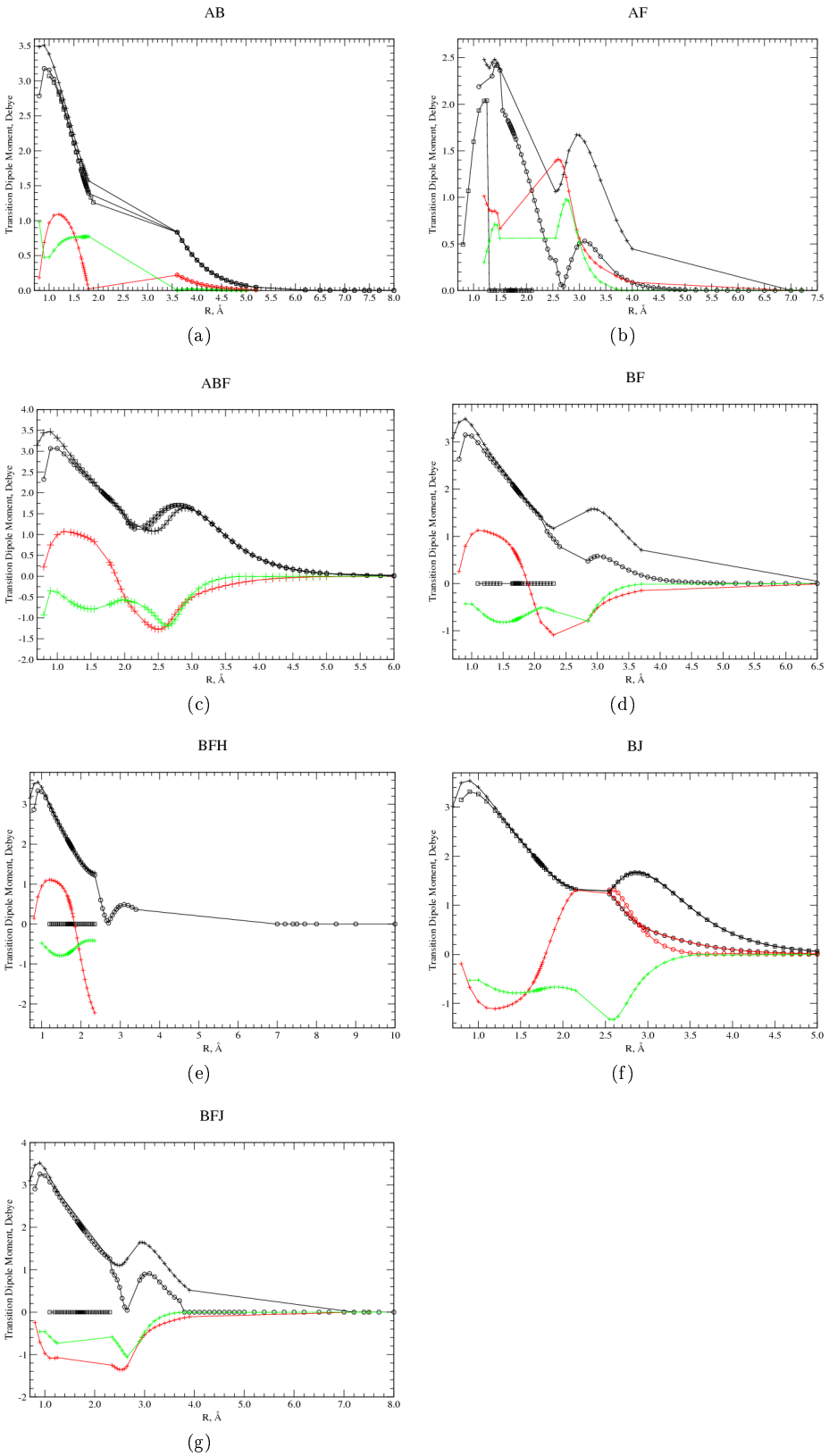

Figure 4.19: Calculation of TDMs between the three $^6\Sigma^+$ states at MRCI level of theory using a cc-pVQZ basis set. The CASSCF state-combination is indicated by the title of each plot.

As can be seen from figure 4.19 the various CASSCF state-combinations produce TDMs with various degrees of discontinuity and also "gaps" in convergence. By inspection, it can be seen that the ABF calculation produces the most complete and continuous TDMs at MRCI level of theory. One noticeable feature however is the variation between the four-state calculation and the two- and three-state calculations for the $\langle A^6\Sigma^+(II)|\,\mu_z\,|X^6\Sigma^+\rangle$ transition: this is shown more clearly in figure 4.20a. For all CASSCF state-combinations, in order to obtain the $^6\Sigma^+(III)$ state, and hence any TDM involving it, a four-state calculation is required. This is because within the sextet states which are calculated within symmetry 1 the ordering is as follows: $X^6\Sigma^+$, $A^6\Sigma^+$, $^6\Delta$ and $^6\Sigma^+(III)$.

The TDMs shown in figure 4.19 for the $\langle A^6\Sigma^+(II)|\,\mu_z\,|X^6\Sigma^+\rangle$ transition can be compared to the coupling curve calculated by Bauschlicher et al. (2001) as shown in figure 4.20. Figure 4.20 shows a comparison between the TDM for the $A^6\Sigma^+ - X^6\Sigma^+$

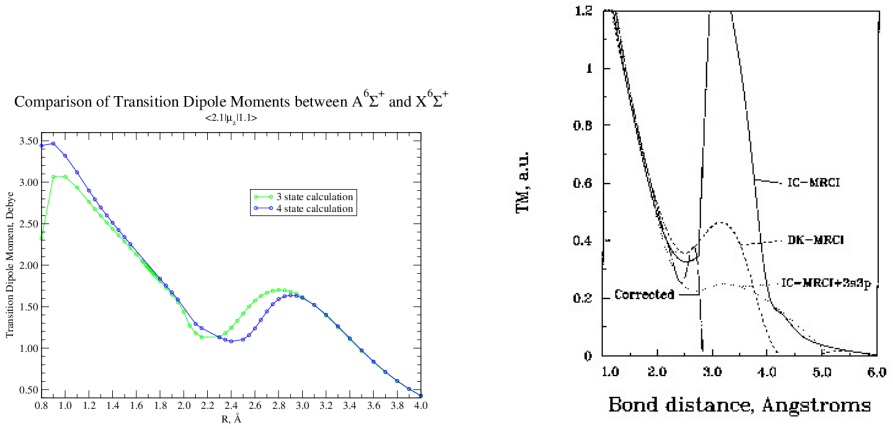

(a) (b)

Figure 4.20: Comparison of Transition dipole moment calculated for the $\langle A^6\Sigma^+(II)|\,\mu_z\,|X^6\Sigma^+\rangle$ transition in this study of CrH and by Bauschlicher et al. 2001

calculated in this study and that calculated by Bauschlicher et al. (2001). Figure 4.20a shows the variation in the TDM produced when three or four sextet states of symmetry 1 are calculated at MRCI level using a cc-pVQZ basis set built upon a CASSCF calculation using the state-combination of ABF. Figure 4.20b shows the various curves obtained by Bauschlicher et al. (2001) in their joint theoretical and experimental study using various basis sets and levels of theory. On a very crude visual inspection, the curves appear to have similar shape. Table 4.29 shows a more analytical comparison of the curves where the curves presented by Bauschlicher et al. (2001) have been converted into units of Å and Debye. As table 4.29 shows, the absolute values of the local minima and maxima obtained by Bauschlicher et al. (2001) in their theoretical calculations is lower by around 0.14 Debye and 0.54 Debye respectively. Also the local maxima is shifted more than the minima. Without experimental constraints of intensity, the exact shape of this TDM is open to question. As a closing note, Ghigo et al. (2004) calculated this TDM using various levels of theory: these are shown in figure 4.21. These curves highlight the difficulties which

Stationary Point	Present study		Bauschlicher et al. (2001)
	3-state calculation	4-state calculation	DK-MRCI curve
Minima	(2.15-2.20, 1.13)	(2.40-2.45, 1.08)	(2.50 0.99)
Maxima	(2.80-2.85, 1.70)	(2.90, 1.64)	(3.25, 1.16)

Table 4.29: Analytical comparison of the stationary points of the $\langle A^6\Sigma^+(II)|\,\mu_z\,|X^6\Sigma^+\rangle$ coupling curves obtained in this study and by Bauschlicher et al. (2001).Here the units are Å for the inter-nuclear distance and Debye for the TDM.

in producing continuous curves and also open up the possibility that the TDM has an entirely different shape.

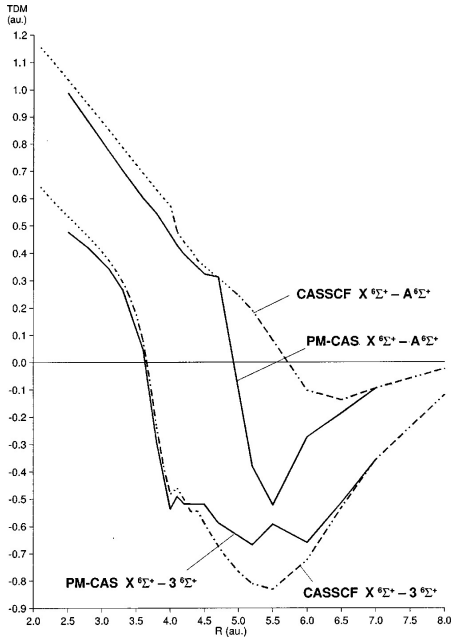

Figure 4.21: TDMs calculated between the three low-lying $^6\Sigma^+$ states of CrH by Ghigo et al. (2004).

4.8 PEC and DMC for the $^6\Pi$ state

For the case of the electronic state of $^6\Pi$, there are no nearby Π (or Φ etc) states of sextet multiplicity nearby in energy to this low-lying state for CrH. Hence as was the case for $^8\Sigma^+$ the choice of PECs and DMCs to use was hence relatively straightforward. Figure 4.22 shows plots of PECs, PEC-Gs, DMCs, DMC-Gs calculate for this $^6\Pi$ state at CI level using the seven proceeding CASSCF state-combinations detailed in table 4.4. Figure 4.22a shows the PECs: this figure clearly shows that all curves with the exceptions of of AB, ABF and BJ have clear discontinuities in the region 2.3 - 2.5 Å. This is further shown by figure 4.22c which shows the gradients of these PECs: this plot also indicates that both ABF and BJ have discontinuities. Hence on the basis of these two figures, AB seems like the best choice. This decision can also be reached by inspection of figures 4.22b and 4.22d which show the DMCs and DMC-Gs respectively of these CI curves: as can be seen AB is the only CASSCF state-combination from the choice of seven summarised in table 4.4 which does not

appear to produce discontinuities in CI calculations of the PEC and DMC for the $^6\Pi$ state when used as a starting point. The minima values of these various PECs

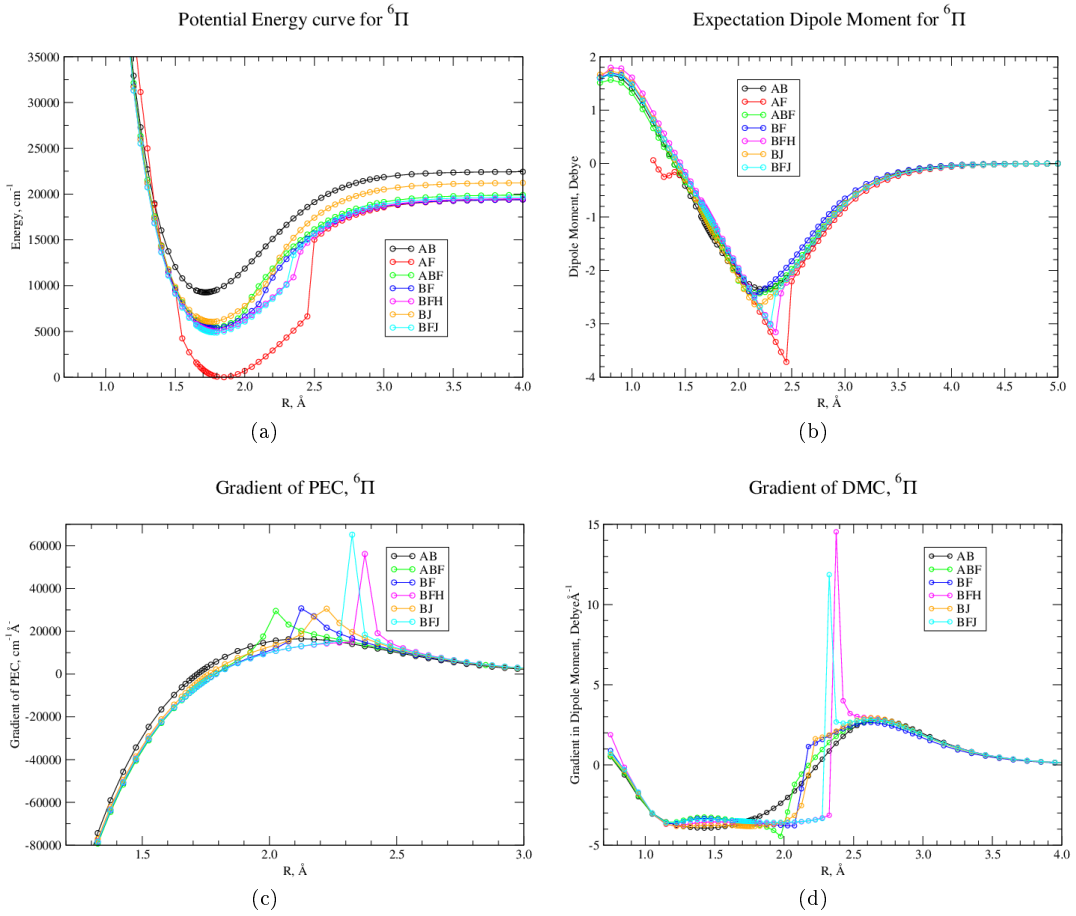

Figure 4.22: PECs and DMCs for the $^6\Pi$ state of CrH calculated at MRCI level of theory.

calculated for the $^6\Pi$ state can be compared to the theoretical study of Roos(2003) and also Dai & Balasabaranium(1993). Table 4.30 shows this comparison. As can be

CASSCF state combination	R_e (Å)
AB	1.72
AF	1.85
ABF	1.78
BF	1.78
BFH	1.78
BJ	1.76
BFJ	1.80

(a)

Study	Method	R_e (Å)
Roos(2003)	CASPT2	1.749
	MSPT2	
Dai & Balasabaranium(1993)	MRCI	1.803

(b)

Table 4.30: Comparison of minima values obtained in this study (table 4.30a) and the previous theoretical studies of Roos(2003) and Dai & Balasabaranium(1993), table 4.30b.

seen from table 4.30 the minima of the *ab initio* curves calculated in this study at MRCI level of theory compare favourably to the two previous theoretical studies: the values obtained here lie between the previously predicted values of 1.749 Åand 1.803

Åwith the exception of the AB and AF calculations which still nevertheless lie close by.

For both PEC & DMC of $^6\Pi$ choice is AB

4.9 PECs and DMCs for the $a^4\Sigma^+$ and $^4\Delta$ states

In a similar fashion for the $^6\Sigma^+$ and $^6\Delta$ states, the PECs, DMCs and TDMs concerning the $^4\Sigma^+$ and $^4\Delta$ states were calculated at CI level using various *PROC*s for the seven different CASSCF state-combinations listed in table 4.4. A summary of these *PROC*s is given in table 4.31 which also shows how many points for each of these *PROC*s converged when the various CASSCF state-combinations were used. As table

CI *PROC*	Symbol	Meaning	AB	AF	ABF	BF	BFH	BJ	BFJ
S1	Square	1+0	88	88	87	88	88	88	88
S2	Circle	2+1	88	80	82	81	88	86	78
S3	+	3+1	85	74	63	74	83	87	71

Table 4.31: Summary of points converged (out of a possible 88) for the various MRCI calculations performed for quartet states of symmetry 1 and 4 which built upon the various CASSCF state-combinations. In this table the notation "3+1" indicates that three quartet states of symmetry 1 and one quartet state of symmetry 4 were calculated at MRCI level of theory. All calculations used a cc-pVQZ basis set. The symbols indicated are then used througout the following plots.

4.31 shows, generally speaking all of the CASSCF state-combinations resulted in CI calculations using *PROC S1* and *S2* which converged for over 80 of the 88 inter-nuclear distance points. For *PROC S3* there was a wider variation. As has been mentioned previously, obtaining convergence over a series of points does not always guarantee that all those points will form a continuous curve. This is demonstrated by figures 4.23 and 4.24. These figures show plots of the PECs and DMCs obtained for the CI calculations run: each plot shows either a PEC or DMC in which different CI calculations(i.e. *PROC*s *S1*, *S2*, *S3*) have been performed for one of the CASSCF state-combinations. The legend colour scheme for each of these plots is set out in table 4.32: table 4.31 also indicates the symbols used to distinguish the different MRCI calculations summarised in table 4.31.

Colour	State
Black	$a^4\Sigma^+$
Red	$^4\Delta$(sym 1)
Green	$^4\Delta$(sym 4)
Blue	3rd quartet state of symmetry 1

Table 4.32: Overview of legend colour scheme used to distinguish the various quartet electronic states calcualated at MRCI level of theory.

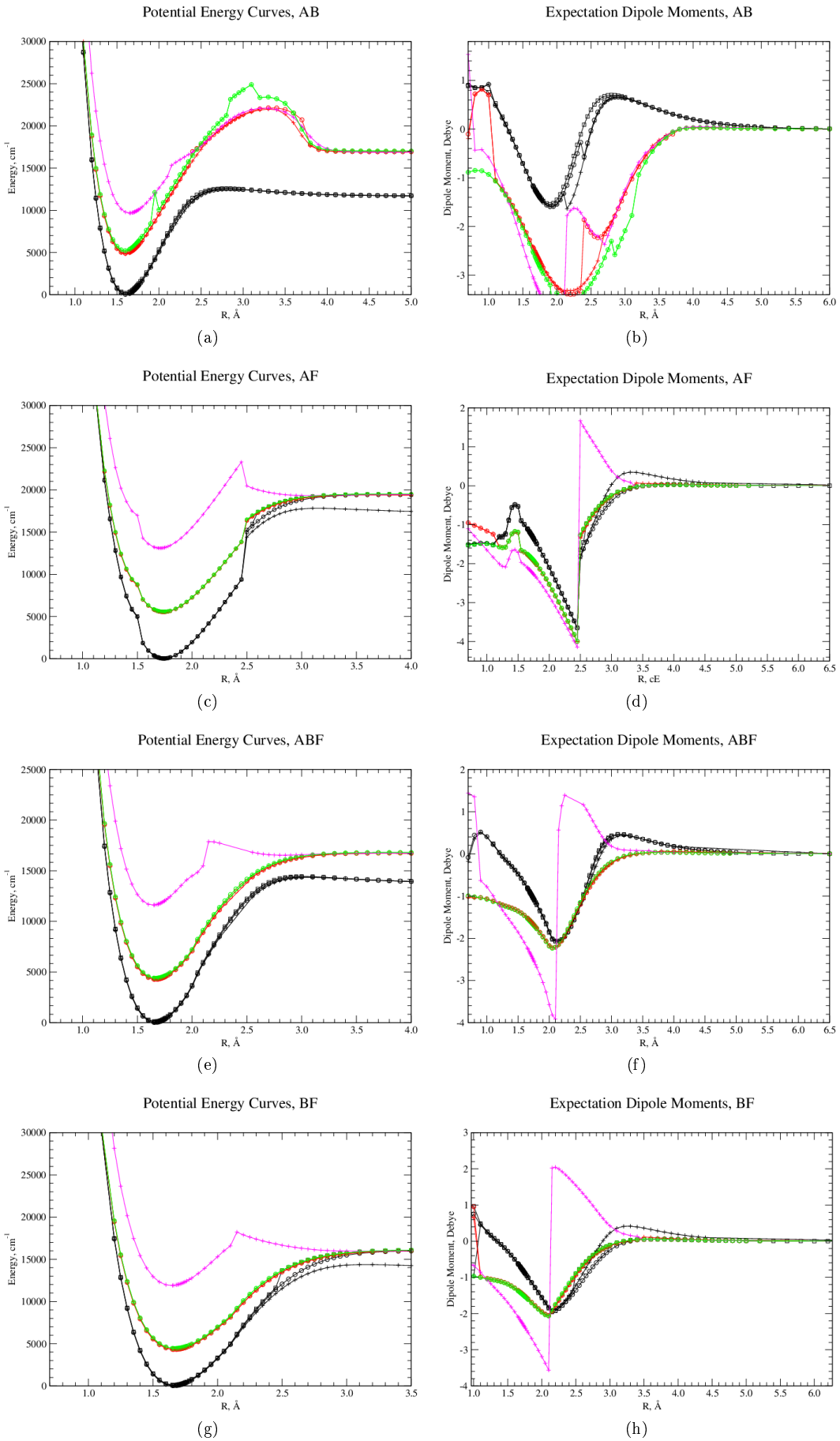

Figure 4.23: Analysis of PECs and DMCs calculated at CI level of theory using VQZ basis set for quartet Σ^+ and Δ states using various CASSCF state combinations as defined in table 4.3.

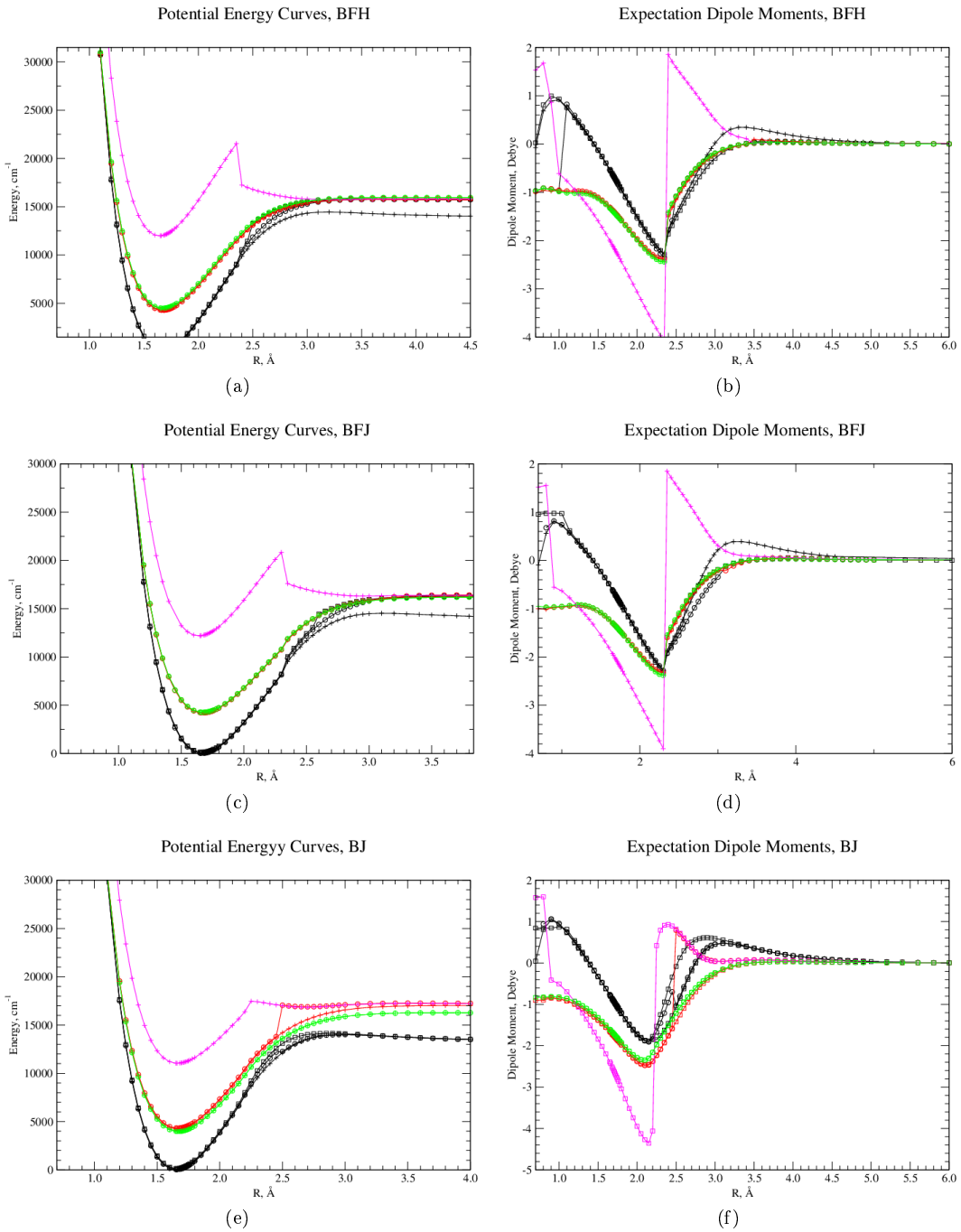

Figure 4.24: Analysis of PECs and DMCs calculated at CI level of theory using VQZ basis set for quartet Σ^+ and Δ states using various CASSCF state combinations as defined in table 4.3.

Referring to figure 4.23a, as was the case for the $^4\Pi$ state, the AB calculation shows an unphysical "hump" in the PEC of the upper states (see figure 4.23c). The DMCs of the $a^4\Sigma^+$ state calculated for AF also show variation between that calculated using *S1*, *S2* and *S3* (see figure 4.23d). As was discussed in section 4.10 this particular state-combination at CASSCF level is totally unsuitable for the calculation of quartet states as "AB" refers to the combination of a $^6\Sigma^+$ state and a $^8\Sigma^+$ state.

Referring to figures 4.23c and 4.23d, all PECs and DMCs have acute changes at around 2.4 Å which is indicative of an allowed crossing. This section hence concen-

trates on the $a^4\Sigma^+$ and $^4\Delta$ states.

In figures 4.24 and 4.24, generally speaking all of the plots show, at first sight good quality PECs for the $a^4\Sigma^+$ state with the exception of this AF calculation. However upon closer inspection, figures 4.23g, 4.24a and 4.24c for BF, BFH and BJ show that the dissociation limit of this $a^4\Sigma^+$ state changes depending on how many quartet states of symmetry 1 are calculated at CI level(i.e. *PROC*s *S1*, *S2*, *S3*). From table 2.8, we know that the $a^4\Sigma^+$ state must converge to a lower asymptote than the $^4\Delta$ and $^4\Sigma^+(II)$ states. Given that these CASSCF state-combinations are capable of producing CI results in which the ground state converges to the wrong asymptote, it would be unwise to use them. Both figures 4.23e and 4.24e for ABF and BJ respectively show slight variations in the shape of the $a^4\Sigma^+$ curve does vary depending on how many states at CI level are calculated but crucially all of the curves have converged to the correct dissociation limits. Thus this hence leaves ABF and also BJ as possible choices.

ABF was chosen over BJ for the calculation of quartet states for several reasons. Firstly, on closer inspection of the PECs calculated using *PROC S2*, BJ it can be seen that the PEC of the $^4\Delta$ state has a discontinuity around 2.50 Å where the PEC "jumps" from (2.45 Å, 13796.83 cm^{-1}) to (2.50 Å, 17052.50 cm^{-1}). This is clearly shown in figure 4.25. Figure 4.25 compares the MRCI calculations of the

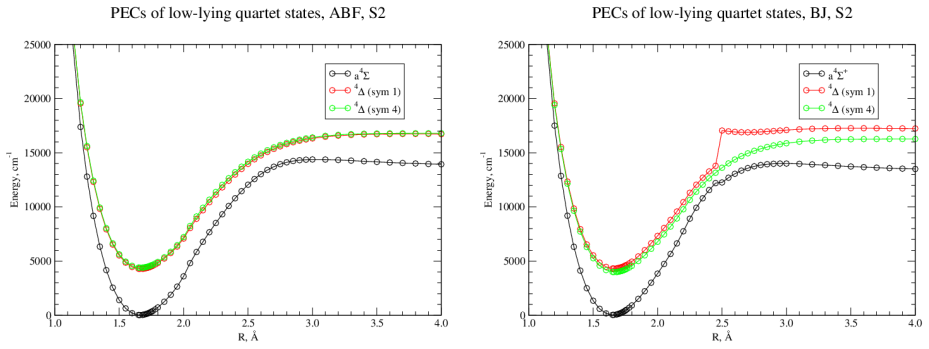

(a) (b)

Figure 4.25: Comparison of calculation of PECs for $a^4\Sigma^+$ and $^4\Delta$ states at MRCI level of theory (*PROC* S2) using a cc-pVQZ basis set using the CASSCF state combinations of ABF and BJ.

PECs of $a^4\Sigma^+$ and $^4\Delta$ states performed using the CASSCF state-combinations of ABF and BJ. The energy difference between the PEC calculated using the *S2* and *S1* "*PROCS*" for ABF and BJ is shown in figure 4.26a. The energy difference between the symmetry 1 and symmetry 4 components of the $^4\Delta$ state calculated using *PROC S2* for ABF and B is shown in figure 4.26b. As is clearly shown in figure 4.26, the CASSCF state-combination of ABF produces less variation in magnitude subsequent CI calculations of the PECs of the $a^4\Sigma^+$ and $^4\Delta$ states. Also figure 4.26b again indicates the discontinuity in the BJ, S2 calculation. Finally, to put forward another case for choosing ABF over BJ for quartet states, figure 4.27 shows the variation in the DMC of the $a^4\Sigma^+$ obtained at MRCI level of theory for the CASSCF state-combinations of ABF and BJ. As is shown in figure 4.27 the BJ CASSCF state-combination results in MRCI calculations which are less consistent with each other

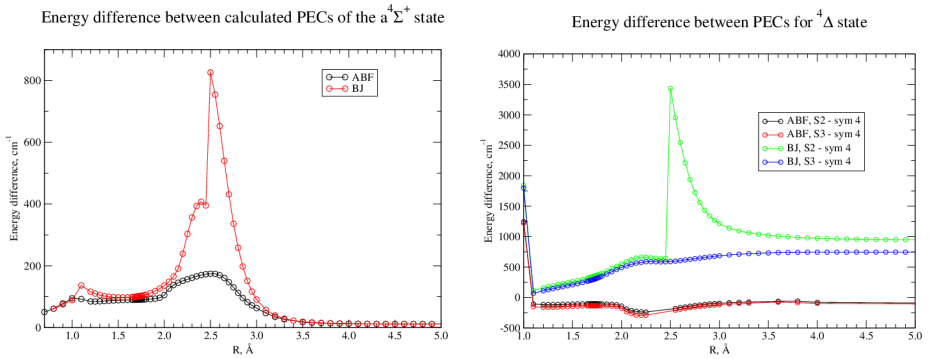

(a) (b)

Figure 4.26: Difference in energy between calculated PECs at MRCI level of theory for the CASSCF state-combinations of ABF and BJ. In figure 4.26a the difference in energy shown is that between an MRCI calculation in which 2 quartet states of symmetry 1 are calculated ("*PROC S2*") and one in which only one quartet state of symmetry 1 is calculated ("*PROC S1*"). In figure 4.26a the differences in energy shown are those between the symmetry 4 and symmetry 1 components for the case where two quartet symmetry 1 state were calculated ("*PROC S2*") and for the case of three quartet symmetry 1 states were calculated ("*PROC S3*").

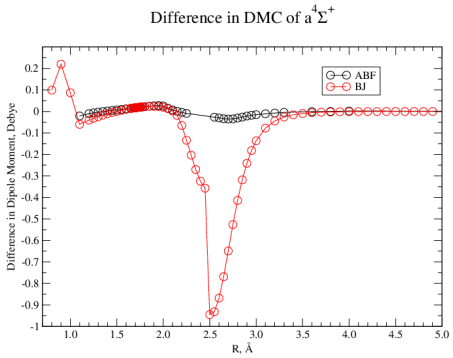

Figure 4.27: Difference in DMC calculated at MRCI level of theory for the $a^4\Sigma^+$ state. Here the difference is between the DMC calculated when two quartet states of symmetry 1 are calculates and when only one quartet state of symmetry 1 is calculated at MRCI level of theory. The labels ABF and BJ refer to which CASSCF state-combination the calculations were based on.

compared with those based on a CASSCF state-combination of ABF.

Hence to summarise: for quartet states of symmetry 1 and 4, there is a clear avoided crossing between two states at around 2.4 ÅṪhis behaviour is shown for all MRCI calculations based on the seven different CASSCF state-combinations under test. Examining the behaviour of the lower-lying $a^4\Sigma^+$ and $^4\Delta$ states it can be argued that the CASSCF state-combination of ABF produces the most reliable results in terms of consistency between MRCI calculations with varying number of quartet states of symmetry 1.

4.9.1 Higher-lying Quartet states

As was mentioned previously, there is clearly a crossing occuring between quartet states lying about the $a^4\Sigma^+$ and $^4\Delta$ states. Further calculations were performed in

an effort to decipher the identity of the states involved. Figure 4.28 shows such a calculation for the PEC and DMCs. As can be seen from figure 4.28 the order of

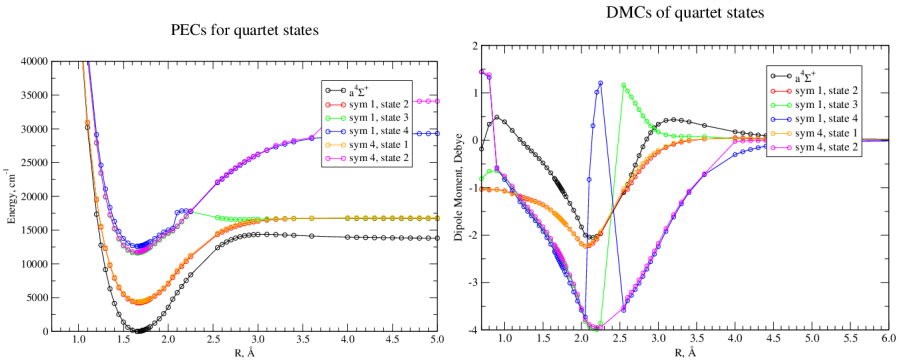

Figure 4.28: Calculation of PECs and DMCs for quartet states at MRCI level of theory using a cc-pVQZ basis set and a CASSCF state-combination of ABF. The MRCI calculations were for four quartet states of symmetry 1 and two quartet states of symmetry 4.

quartet states with symmetry 1 and 4 components is as follows: $a^4\Sigma^+$ followed by a $^4\Delta$ and then a crossing between two states: one which has a component only in symmetry 1 and another which goes to a higher asymptote that has a component in symmetry 1 and symmetry 4. By consideration of $\hat{L}_z$ coupling terms the idendity of these two later states was identified as the $^4\Sigma^+(II)$ state and a $^4\Gamma$ state. The *ab inito* data for the PEC of the $^4\Sigma^+(II)$ state can be extrapolated to produce a continuous curve with its dipole remaining as shown in figure 4.28 which shows the classic crossing picture. The DMC for the $^4\Gamma$ state is simply assumed to be that shown in figure 4.28 (sym 1, state 4 and sym 4, state 2 curves) with the exception of the few "stray" points in the region between 2.00 Å and 2.50 Å. By considering data from the NIST atomic database, we know that this $^4\Gamma$ state must dissociate to an Cr term value of a^5G which lies $\approx$ 12 500 cm^{-1} above the a^5D atomic term to which the $^4\Pi$, $^4\Delta$ and $^4\Sigma^+(II)$ terms dissociate to. This interpretation is consistent with the PECs shown in figure 4.28. For the purposes of the linelist, these PECs and DMCs of these two crossing states were not included.

4.10 PEC and DMC for the $^4\Pi$ state

Repeating the process of analysing PECs, PEC-Gs, DMCs and DMC-Gs for CI calculation of the $^4\Pi$ state, some interesting and quite shocking results are observed as shown in figure 4.29. Figure 4.29a shows the PECs calculated at CI level for the $^4\Pi$ state: as can be seen the AB curve has a "hump" not seen in the other PECs with one "stray" point around 2.90 Å. Otherwise the PEC appears continuous. Examining figure 4.29b which shows the DMC this "stray" point is again observed. It should be noted that, referring back to table 4.3, AB corresponds to combining a $^6\Sigma^+$ state and $^8\Sigma^+$ state in a CASSCF calculation to produce orbitals to use for the following CI calculation. Since neither of these are of quartet multiplicity or of symmetry 2 or 3(required to calculate a $^4\Pi$ state, it raises the question of why can this seemingly unsuitable state-combination CASSCF calculation thus help produce even any

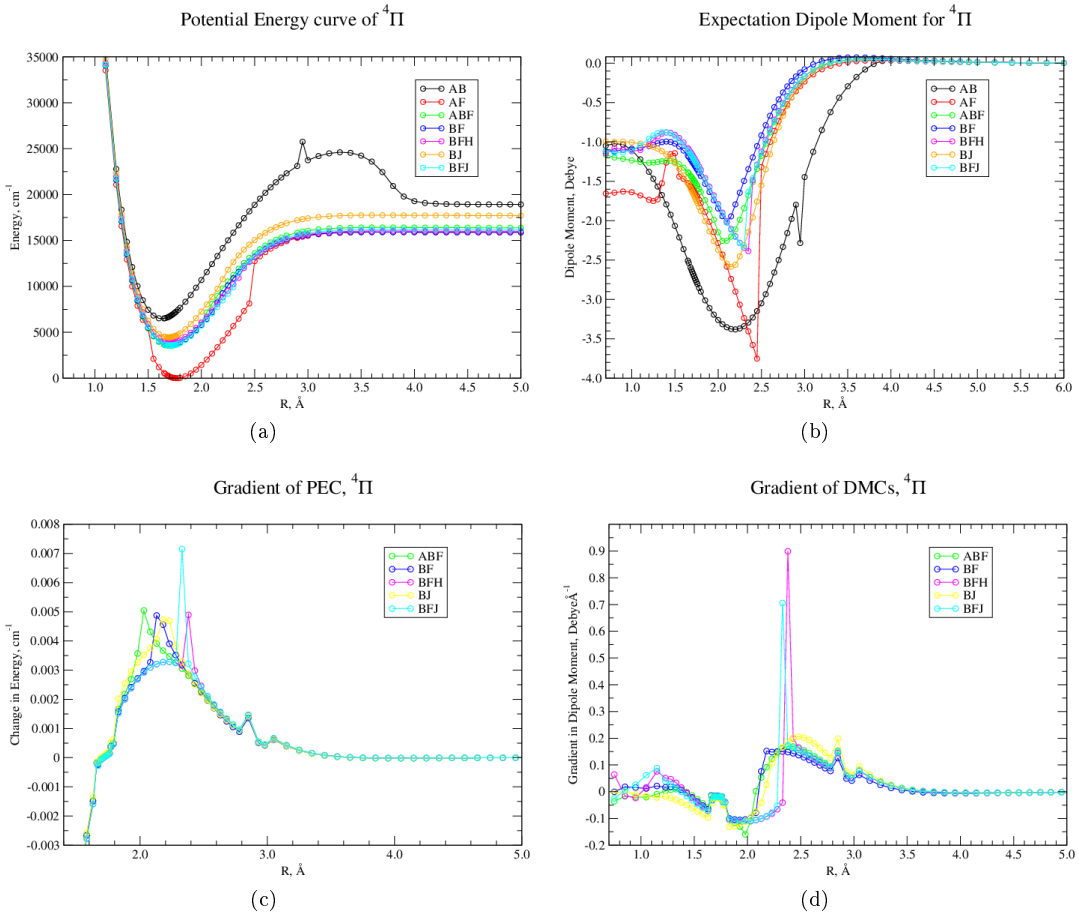

Figure 4.29: Calculation at MRCI level of theory of PECs and DMCs for the $^4\Pi$ state using a VQZ basis set and various CASSCF state-combinations.

convergence at CI level? With this in mind it was decided to discard this AB. Also from figures 4.29a and 4.29b it can be seen that AF has a clear discontinuity around 2.5 Å. Hence both AB and AF were discarded. The R_e values for each PEC can be compared to that calculated of Dai & Balasubramanian (1993) who calculated a value of 1.714 ÅThe R_e values are as follows: AB (1.65), AF (1.76), ABF (1.70), BF (1.70), BFH (1.71), BJ (1.69) and BFJ(1.71). Hence generally speaking with the exception of AB and AF the values obtained match those of Dai & Balasubramanian (1993) within 0.2 Å. Figures 4.29c and 4.29d show the PEC-Gs and DMC-Gs of the five remaining choices respectively. As can be seen from both of these figures, all five remaining choices of state-combinations at CASSCF produce CI curves which are discontinuous. In practice, all kind of arguments could be put forward but for the sake of consistency with the quartet Σ^+ and Δ states, the ABF option was chosen.

For both PEC & DMC of $^4\Pi$ choice is ABF.

4.11 $^8\Sigma^+$ state

For the anti-bonding $^8\Sigma^+$ state, figure 4.30 shows the PECs, PEC-Gs, DMCs and DMC-Gs calculated at CI level for the different CASSCF state-combinations presented

in table 4.4. Obtaining good quality, unambiguous results for the $^8\Sigma^+$ state was relatively straightforward as there are no other octuplet states of CrH in the energy region which are more pertinently have a symmetry 1 component(i.e. Σ^+ states, Σ^- or Δ states). Figure 4.30a shows a clear anomaly for the AF calculation in which

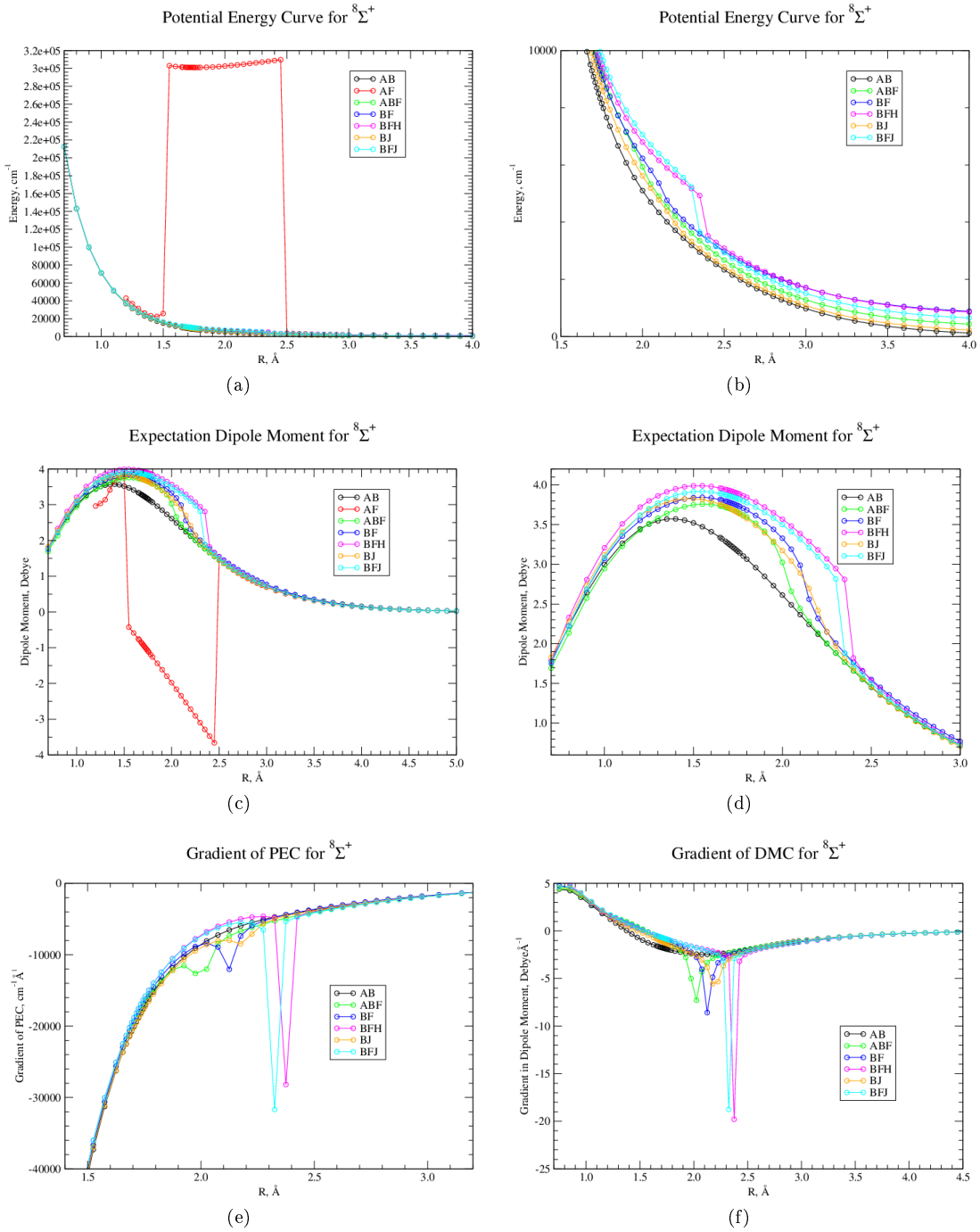

Figure 4.30: Calculation at MRCI level of theory of PECs and DMCs for the $^8\Sigma^+$ state using a VQZ basis set and various CASSCF state-combinations.

the calculated PEC "jumps" to a higher PEC at around 1.5 Åbefore returning to the lower PEC of interest at 2.5 Å. Figure 4.30b is thus a zoomed in graph of the PECs with the exception of the AF PEC. As can be seen from this plot, BFH and BFJ have clear visible discontinuities at 2.4 Å. Figure 4.30d shows the calculated DMCs:

again as for the PECs, the AF calculation clearly "alternates" between two states. Similarly to figure 4.30b, figure 4.30d shows the calculated DMCs for the other 6 CI calculations: It can be seen that with the exception of the AB calculation, all of the curves have a "jump' around 2.5 Å. Thus it would seem that the AB state-combination produces the most continuous orbitals for calculation of the $^8\Sigma^+$ state at CI level. To further corroborate this argument, figures 4.30e and 4.30f show the calculated gradients of the PECs and DMCs (with the exception of AF for clarity) constructed using the procedure summarised in table 4.14. These figures both show that, all curves with the exception of AB have visible discontinuities. A conclusion from this work is that the $^8\Sigma^+$ state is almost certainly anti-bonding in nature, which is in line with the previous theoretical study of Dai & Balasubramanian (1993). Hence it was not included in our final linelist for CrH.

4.12 Off-diagonal Transition Dipoles

The off-diagonal transition dipoles formed by acting the μ_x operator on states of the same multiplicity were calculated at MRCI level of theory using a cc-pVQZ basis set with the CASSCF state-combination of ABF used. Figure 4.32 shows these coupling curves for the quartet states and Figure 4.31 for the sextet states.

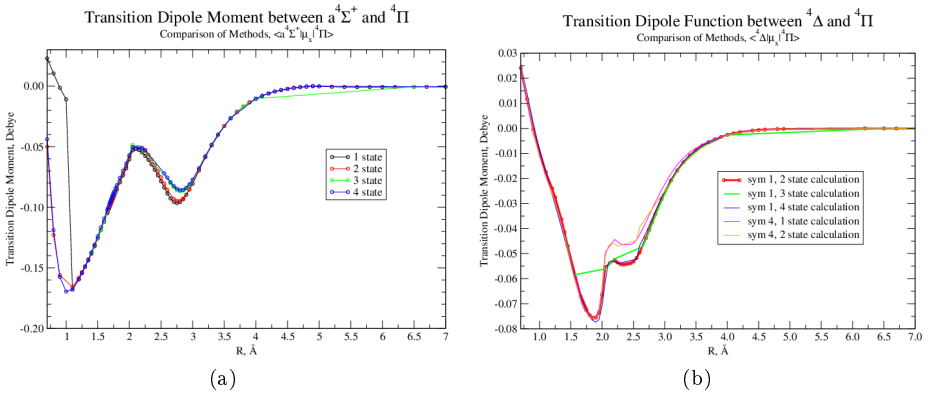

(a) (b)

Figure 4.31: Off-diagonal transition dipole moment coupling curves between the quartet states calculated at MRCI level of theory using a cc-pVQZ basis set and the CASSCF state-combination of ABF.

Figures 4.31a and 4.31b show the transition dipole coupling between the $^4\Pi$ state and the $a^4\Sigma^+$ and $^4\Delta$ states respectively. Both figures show the variation obtained in the coupling curves when different numbers of quartet states of symmetry 1 are calculated. For the case of the Δ state the variation between the symmetry 1 and symmetry 4 calculations is shown as well. In summary the transition dipole moment of both is under 0.20 Debye which is significantly smaller than the transition dipole moments calculated between the three $^6\Sigma^+$ states.

Similarly, figure 4.32 shows the off-diagonal transition dipole couplings between the sextet states as a function of the number of sextet states of symmetry 1 calculated for the relevant Σ^+ and Δ states. It is worth noting that the relative scale of the plots: figure 4.32c which involves the $^6\Delta$ state is significantly smaller than the couplings

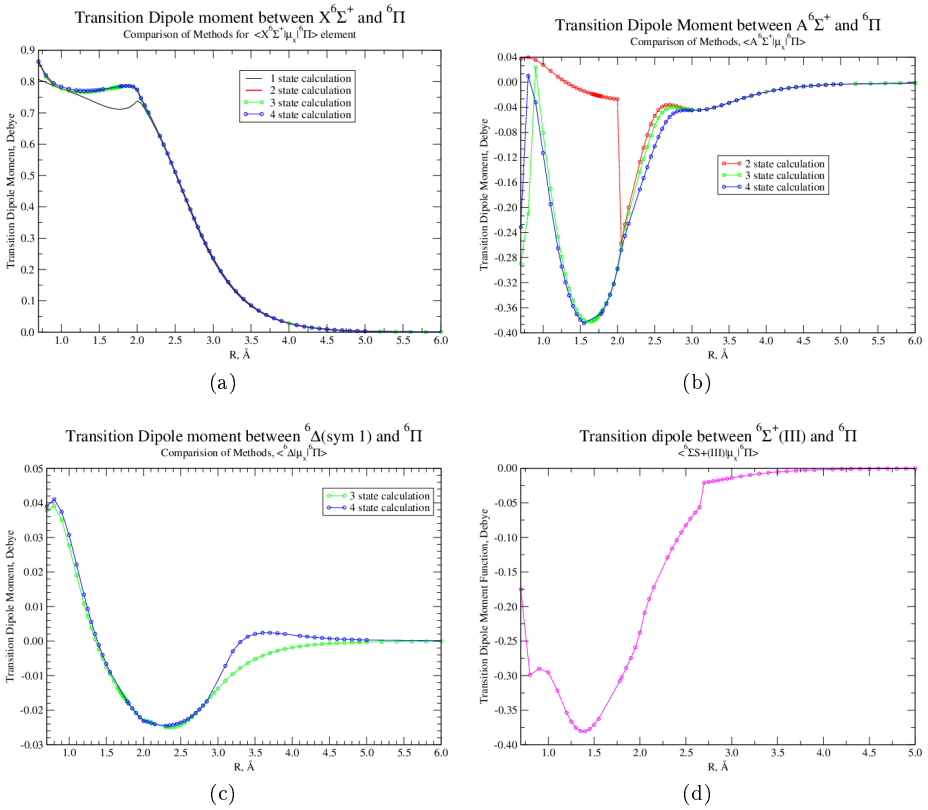

Figure 4.32: Off-diagonal transition dipole moment coupling curves between the sextet states calculated at MRCI level of theory using a cc-pVQZ basis set and the CASSCF state-combination of ABF.

involving the $^6\Sigma^+$ states with the $^6\Pi$ state.

4.13 Angular-Momenta coupling

As was explained in section 2.8.3, the angular momenta operator of $\hat{L}_x$ couples Σ^+ and Δ states to Π states of the same multiplicity. Figure 4.33 shows the calculated angular momenta coupling curves created using the $\hat{L}_x$ operator for low-lying electronic states of CrH. Figure 4.33 shows the calculated angular-momenta couplings between Σ^+ and Π states calculated using MRCI level of theory with a cc-pVQZ basis set. For all figures the CASSCF state-combination used was ABF. Figures 4.33a and 4.33b show the L_x coupling between the $^6\Pi$ state and the $X^6\Sigma^+$ and $A^6\Sigma^+$ states respectively. In both figures the effect of changing the number of sextet states of symmetry 1 used to calculate the respective $^6\Sigma^+$ state is shown. For the $X^6\Sigma^+$ state the size of the "hump" decreases by 0.2 going from a one-state to a four-state calculation. For the $A^6\Sigma^+$ state, it can be seem that the two-state calculation produces a stark change in behaviour of the coupling obtained at around 2.00 Å. It can be seen that the four-state calculation produces a more continuous coupling curve than the three-state calculation which has a sharp peak around 2.00 Å. Figure 4.33c shows the coupling between the $^6\Sigma^+(III)$ state and the $^6\Pi$ state as starting from zero and increasing in an approximately linear fashion up to $\sqrt{3}$ at 2.6 Å. Finally, figure 4.33d shows the

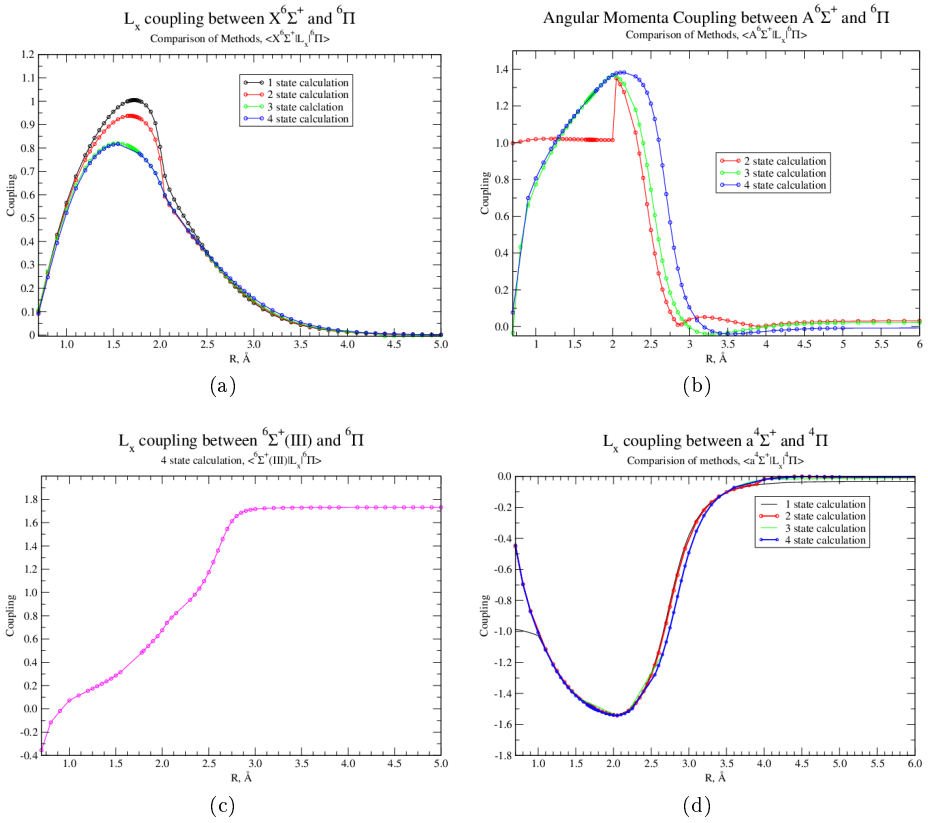

Figure 4.33: Angular momenta coupling curves calculated at MRCI level of theory using a cc-pVQZ basis set. The CASSCF state-combination used was ABF.

coupling between the $a^4\Sigma^+$ and $^4\Pi$ state as a function of the number of quartet states of symmetry 1 calculated at MRCI level of theory. As can be seen from this figure, the variation between the four-state calculation and the other three has a maximum of 0.05. The coupling between the Δ and Π states for both quartet and sextet multiplicity was found to be -1 with a variation of around 0.02.

The angular momentum operator of $\hat{L}_z$ operates within individual Π and Δ states and produces a constant value. These values were found to be +1i for the $^4\Pi$ and $^6\Pi$ states and +2i and -2i for the $^4\Delta$ and $^6\Delta$ states respectively.

4.14 Spin-Orbit coupling

The spin-orbit couplings between the various low-lying electronic states of CrH were calculates using MRCI level of theory. Plots of these couplings are shown in this section which demonstrate the variation obtained for a single coupling curve by varying both the CASSCF state combination and also the number of states calculated at MRCI level of theory of a particular multiplicity and symmetry, e.g. sextet states of symmetry 1. For spin-orbit coupling there are two methods, namely the mean-field and Breit-Pauli. The asymptotic values obtained of spin-orbit couplings between various states using these two methods are shown in table 4.33 which also shows the effect of basis set. As can be seen from table 4.33 the variation difference between

Basis Set/Method	$\langle^4\Pi\vert \hat{SO}_z \vert^4\Pi\rangle$		$\langle^6\Pi\vert \hat{SO}_z \vert^6\Pi\rangle$		$\langle^4\Pi\vert \hat{SO}_z \vert^6\Pi\rangle$	
	BP	MF	BP	MF	BP	MF
cc-pVTZ	102.41	108.51	113.79	120.57	-22.76	-5.06
cc-pVQZ	102.48	108.59	113.86	120.65	-22.77	-5.02
aug-cc-pVDZ	102.30	108.40	113.66	120.44	-22.73	-5.10
aug-cc-pVTZ	102.26	108.36	113.62	120.40	-22.72	-5.02
aug-cc-pVQZ	102.43	108.54	113.81	120.60	-22.76	-5.00

(a)

Basis Set/Method	$\langle^4\Delta\vert SO_z \vert^4\Delta\rangle$		$\langle^6\Delta\vert \hat{SO}_z \vert^6\Delta\rangle$		$\langle^4\Delta\vert \hat{SO}_z \vert^6\Delta\rangle$	
	BP	MF	BP	MF	BP	MF
cc-pVTZ	-207.42	-220.11	-230.51	-245.07	46.16	7.99
cc-pVQZ	-207.68	-220.38	-230.79	-245.38	46.22	7.90
aug-cc-pVDZ	-207.32	-220.00	-230.39	-244.95	46.13	7.92
aug-cc-pVTZ	-207.15	-219.85	-230.21	-244.79	46.10	7.90
aug-cc-pVQZ	-207.60	-220.31	-230.70	-245.29	46.20	7.86

(b)

Table 4.33: Comparison of asymptotic spin-orbit coupling values obtained using the Breit-Pauli ("BP") and mean-field ("MF") methods for various basis sets.

the Breit-Pauli and Mean-field for spin-orbit coupling within an indivual state is between 6 cm^{-1} and 15 cm^{-1} with the mean-field always having a greater magnitude. For the cases of spin-orbit coupling between the two Π and Δ states, the difference is more significant. Indeed, plots of these couplings show the mean-field to produce non-continuous couplings. For this reason, it was decided to use the Breit-Pauli method which is shown for all proceeding figures. Table 4.33 also shows that the variation due to basis set alone is of order < 0.3 cm^{-1}.

The spin-orbit coupling within the individual $^4\Pi$ and $^6\Pi$ states is shown in figure 4.34 which shows analysis of these two curves. Figure 4.34a shows the spin-orbit coupling within the $^4\Pi$ state calculated at MRCI level of theory using a cc-pVQZ basis set for the various CASSCF state-combinations tested out. As can be seen from this plot, the AB calculation is significantly different in character and magnitude from the other six. This is consistent with what was found for calculations of the PEC and DMC of this $^4\Pi$ state. As was discussed in section 4.10 this is an inappropriate CASSCF state-combination to use for the calculation of any properties of the $^4\Pi$ state. Figure 4.34b is simply a repeat of figure 4.34a with the AB calculation taken out so that the differences between the other calculations can be more clearly seen. As this figure shows, the BJ calculation is approximately up to 10 cm^{-1} different in magnitude for certain inter-nuclear distances.

Figure 4.34c shows the spin-orbit coupling within the $^6\Pi$ state calculated at MRCI level of theory using a cc-pVQZ basis set for the various CASSCF state-combinations tested out. This figure shows the variation in the calculated values depending on the CASSCF state-combination used previously. As can be seen, the AF calculation produces a non-continuous coupling curve. Figure 4.34d then shows the difference between the AB calculation and the remaining five calculations. As this plot shows, the variation is typically up to 3 cm^{-1}.

In summary, the variation between coupling curves calculated using different

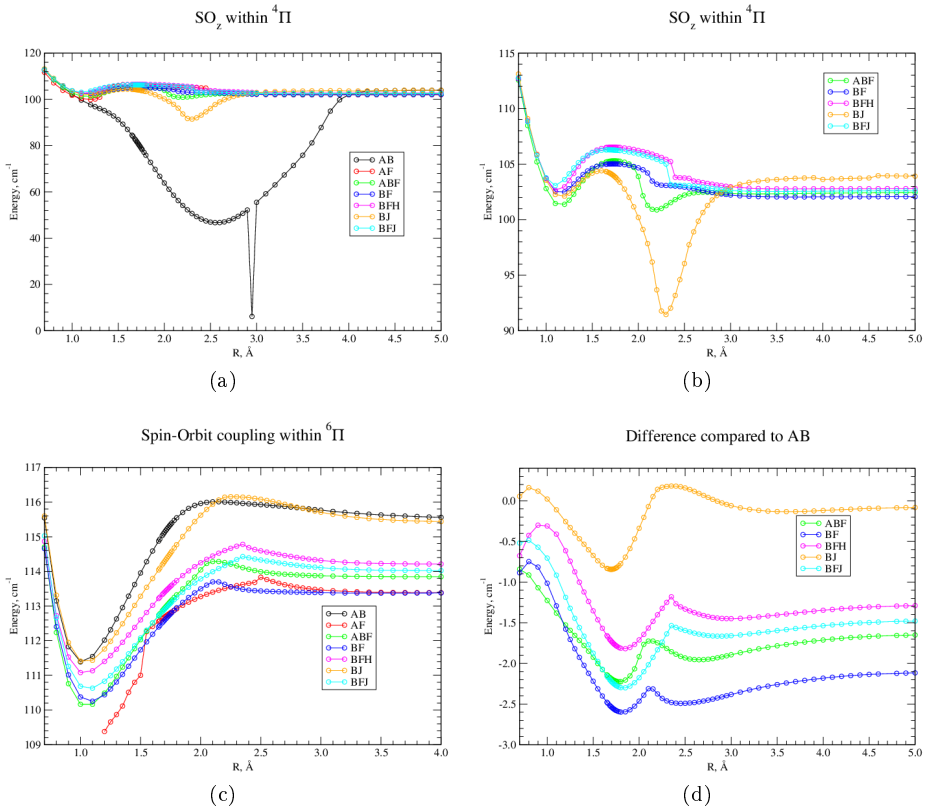

Figure 4.34: Spin-Orbit coupling within the individual $^4\Pi$ and $^6\Pi$ states calculated at MRCI level of theory using a cc-pVQZ basis set. The different CASSCF state-combinations tested are indicated in the legends of the plots.

CASSCF state-combinations was found to vary up to around 10 cm^{-1}. This may seem significant: however, compared to the variation in the D_e and T_e values found for the PECs this is reasonably insignificant. With this in mind, it was decided to calculate the remaining spin-orbit couplings using the CASSCF state-combination of ABF for consistency.

Figure 4.35 shows the calculated spin-orbit coupling involving the $^4\Delta$ and $^6\Delta$ states and also the spin-orbit coupling between these states and the two Π states. Refer to figure 4.35. In all cases the CASSCF state-combination used is ABF. Figure 4.35a shows the spin-orbit coupling calculated within the $^4\Delta$ state at MRCI level of theory. The three calculations shown are those where two, three and four quartet states of symmetry 1 have been calculated respectively. This figure shows the variation between these different MRCI calculations of been of order 1 cm^{-1}. Similarly, figure 4.35b shows the calculated spin-orbit coupling within the $^6\Delta$ state for the cases where three and four sextet states of symmetry 1 have been calculated. For the sextet states the third state of symmetry 1 is the $^6\Delta$ state hence a two-state calculation would not produce the desired coupling curve. Again this figure shows the variation between different MRCI calculations of spin-orbit coupling to be of order 1 cm^{-1}. Figure 4.35c shows the spin-orbit coupling between the $^4\Delta$ and $^6\Delta$ states. In this figure a four-state calculation has been used for the $^6\Delta$ state: the legend refers to the number of states used to calculate the $^4\Delta$ state. Finally, figure 4.35d shows the spin-orbit

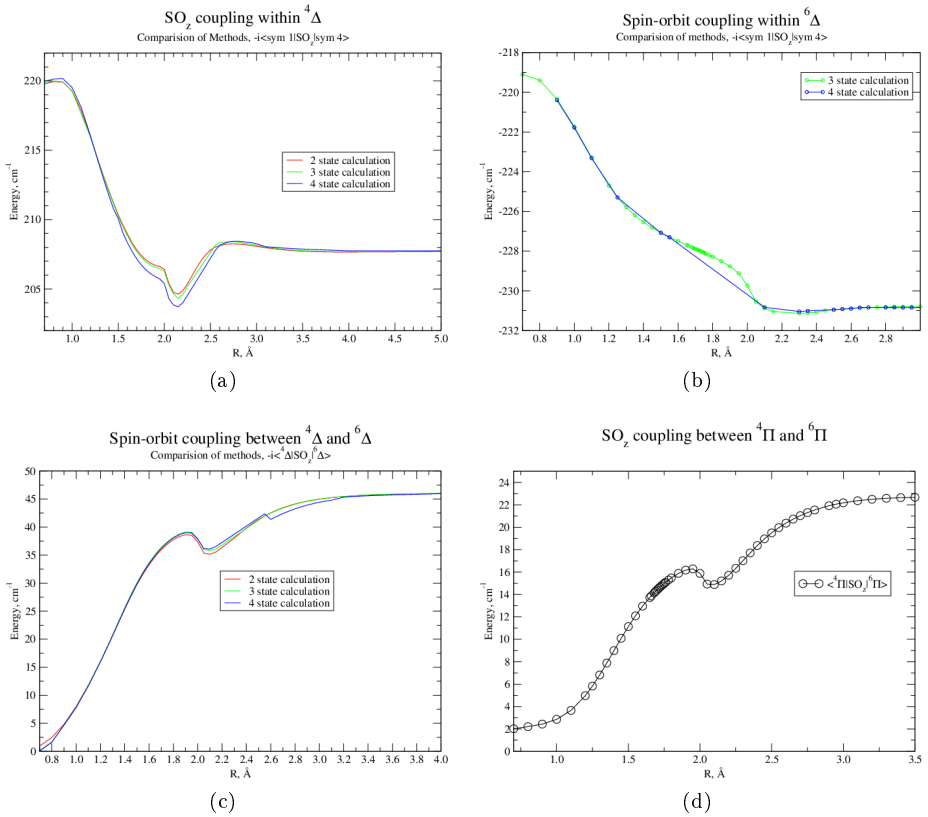

Figure 4.35: Spin-Orbit coupling of various calculated at MRCI level of theory using a cc-pVQZ basis set. The CASSCF state-combination used is ABF.

coupling between the $^4\Pi$ and $^6\Pi$ states calculated at MRCI level of theory using a cc-pVQZ basis set.

As well as these been spin-orbit coupling acting between and within states which involves the z-component of the spin-orbit operator, SO_z, there is also spin-orbit coupling involving the SO_x operator. Refer to section 2.8.3 which presents the relevant theory. In summary the SO_x operator links Σ^+ and Δ states to Π states.

Figure 4.36 shows the calculated spin-orbit coupling between the three $^6\Sigma^+$ states and the $^4\Pi$ and $^6\Pi$ states.

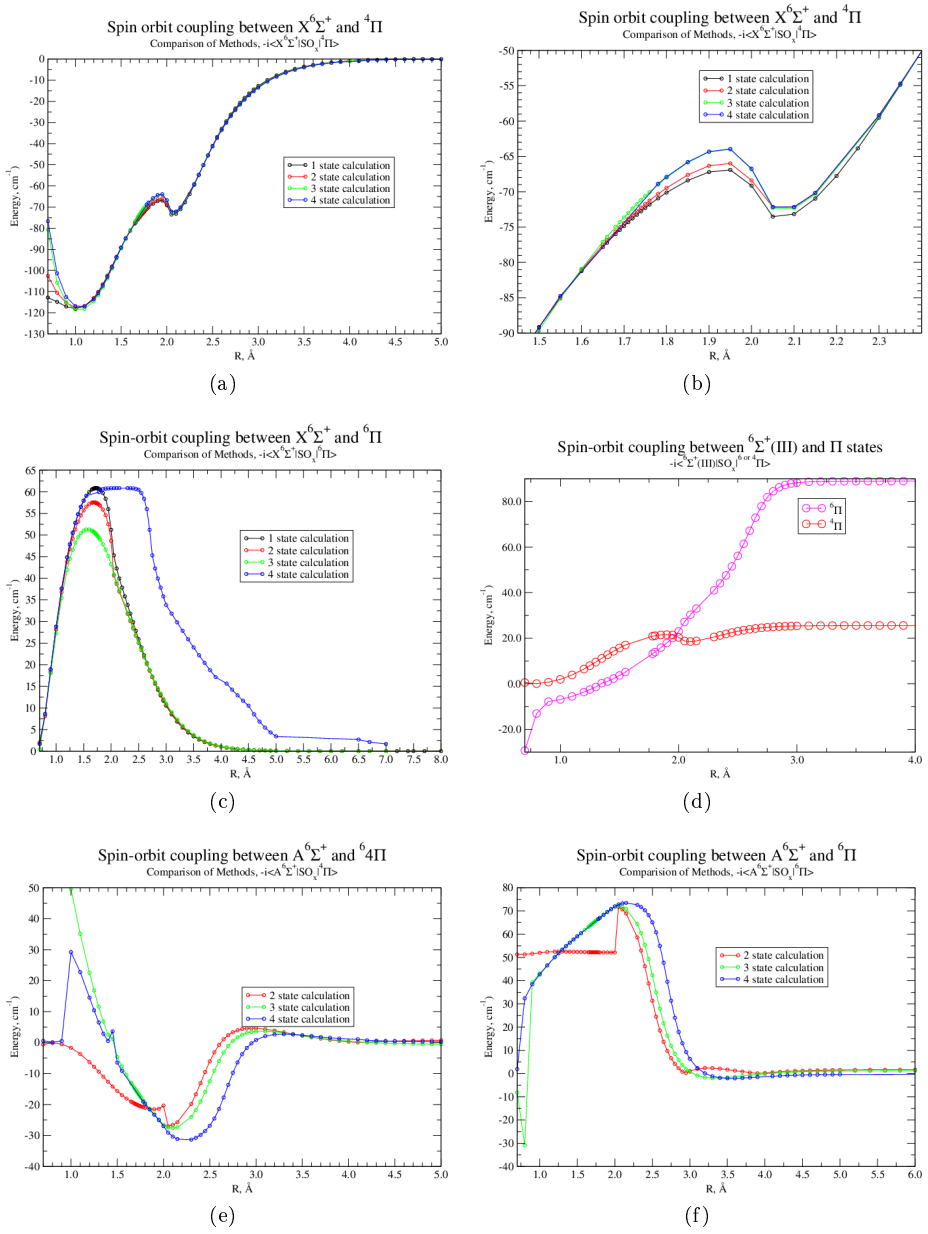

Figure 4.36: Spin-orbit coupling calculated between the three $^6\Sigma^+$ states and the $^4\Pi$ and $^6\Pi$ states using MRCI level of theory and a cc-pVQZ basis set. The CASSCF state-combination used is ABF. These figures show the variation in coupling calculated when different number of sextet states of symmetry 1 are calculated.

Refer to figure 4.36. Figures 4.36a and 4.36b show the spin-orbit coupling between the $X^6\Sigma^+$ and $^4\Pi$ state with the latter plot been a blown-up version of the former. These plots show the variation to be up to approximately 3 cm^{-1}. Figure 4.36c shows the spin-orbit coupling between the $X^6\Sigma^+$ state and $^6\Pi$ state. As can be seen the size of the "hump" for the one-, two- and three-state calculations varies by around 10 cm^{-1}. The four-state calculation shows a significant departure in behaviour from the previous three calculations: the "hump" is wider (around 1 Å) and for $R > 2$ Å the calculated spin-orbit coupling is up to around 30 cm^{-1} higher in value. Figure 4.36e and 4.36e shows the spin-orbit coupling between the $A^6\Sigma^+$ state and the $^4\Pi$ and $^6\Pi$

states respectively. Each figure shows the variation between two-, three- and four-state calculations of been of order of several cm^{-1}. Again, the four-state calculation results in coupling curves that are visibly different in behaviour from the two- and three-state calculations. The coupling between the $^6\Delta$ and Π states is not shown simply as it is approximately a constant of 25 cm^{-1} and 51 cm^{-1} for the $^6\Pi$ and $^4\Pi$ states respectively. Finally, figure 4.36d shows the spin-orbit coupling between the $^6\Sigma^+(III)$ state the two Π states. As $^6\Sigma^+(III)$ is the fourth sextet state of symmetry 1, only a four-state calculation will produce the desired coupling. (Higher order calculations would but this would be outside the realm of study).

Finally, figure 4.37 shows the spin-orbit couplings calculated between the $a^4\Sigma^+$ state and $^4\Pi$ and $^6\Pi$ states. Refer to figure 4.37. Figures 4.37a and 4.37b show the

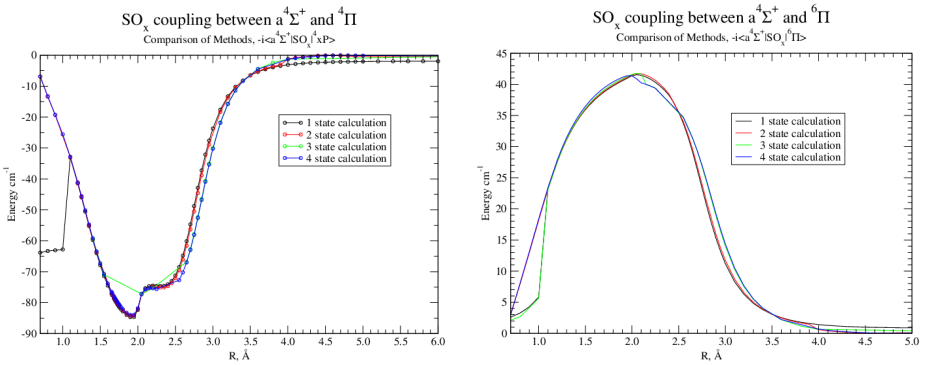

(a) (b)

Figure 4.37: Spin-orbit coupling calculated involving the $a^4\Sigma^+$ with the $^4\Pi$ and $^6\Pi$ states calculated at MRCI level of theory using a cc-pVQZ basis set. The CASSCF state-combination used was ABF.

spin-orbit coupling between the $a^4\Sigma^+$ state the $^4\Pi$ and $^6\Pi$ states respectively. For each figure, the variation in the coupling calculated when a one-, two- three- and four-state calculation has been used for the $a^4\Sigma^+$ state is shown. Here this terminology refers to quartet states of symmetry 1. The spin-orbit coupling between the $^4\Delta$ state and the $^4\Pi$ and $^6\Pi$ state was approximately 59 cm^{-1} and 25 cm^{-1} respectively.

For completeness of this *ab initio* study, the spin orbit matrix elements at MRCI level between the repulsive $^8\Sigma^+$ state and the $^6\Pi$ state was calculated using the seven different state-combinations for the preliminary CASSCF calculations. Figure 4.38 shows this spin-orbit coupling between these two states and the variation found between the MRCI calculations that were built upon different state-combinations at CASSCF level. Refer to figure 4.38. Figure 4.38a shows the spin-orbit coupling between $^8\Sigma^+$ and $^6\Pi$ calculated at MRCI level of theory using a cc-pVQZ basis set for different CASSCF state-combinations. By inspection of this plot it appears that, with the exception of the AF calculation, the remaining six calculations produce a continuous curve representing this coupling. Figure 4.38b shows the gradient of these remaining six coupling curves. The gradient has been calculated for each curve as per the procedure defined in section 4.5. This figure shows that BFH and BFJ have a discontinuity around 2.3 Å and BF and BJ around 2.1 Å. Figures 4.38c and 4.38d quantify the difference in value between the AF and ABF calculations respectively

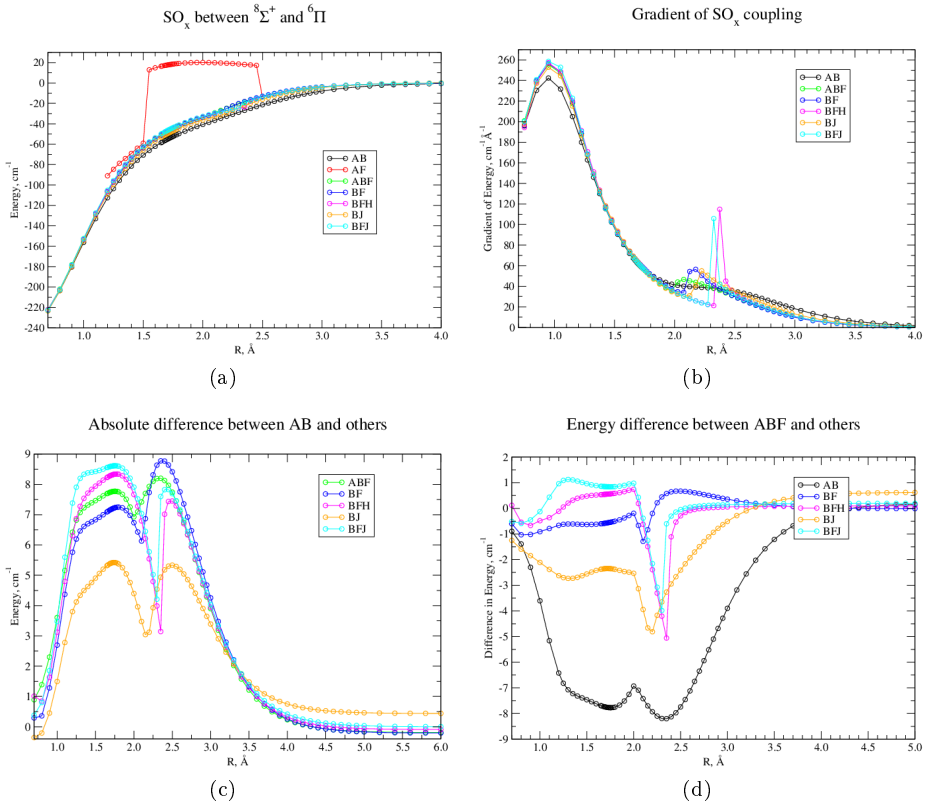

Figure 4.38: Spin-orbit coupling between the $^8\Sigma^+$ state and the $^6\Pi$ state calculated at MRCI level of theory using a cc-pVQZ basis set. The different CASSCF state-combinations tested are indicated in the legends of the plots.

and the five other calculations. As these figures show, the difference in magnitude between the different calculations of the the spin-orbit coupling varies between 1 and 10 cm^{-1}.

Hence, in summary the figures shown in this section for the calculates spin-orbit couplings between the various low-lying states of CrH demonstrate the effect of changing both the CASSCF state-combination used and also the number of states of a particular multiplicity and symmetry at MRCI level.

Finally, tables 4.33 and 4.34 show the non-zero asymptotic values of spin-orbit coupling obtained using the SO_z and SO_x operators respectively. As was calculated in section 2.8.4, the atomic spin-orbit parameter ξ for CrH is 55.72 cm^{-1} based on measured atomic dissociation values of the Chromium atom. In tables 4.33 and 4.34, the "factor" refers to the scaling factor applied to this value for the relevant spin-orbit coupling. This factor can be computed by using the Wigner-Eckart theorem. As these tables show the calculated asymptotic values are up to 10 cm^{-1} different from the theoretical values.

4.15 Concluding Remarks

In this chapter, a systematic study of how changing the states used in a CASSCF calculation affects the quality of the PECs and DMCs calculated has been presented. This type of study has never been done for CrH. By inspection of these results (shown

Coupling	Value	Theory	Factor
$\langle {}^6\Delta \vert \hat{SO}_x \vert {}^6\Pi \rangle$	25.63	27.86	0.5
$\langle {}^6\Delta \vert \hat{SO}_x \vert {}^4\Pi \rangle$	51.19	55.72	1.0
$\langle {}^6\Sigma^+(III) \vert \hat{SO}_x \vert {}^6\Pi \rangle$	89.02	78.80	$\sqrt{2}$
$\langle {}^6\Sigma^+(III) \vert \hat{SO}_x \vert {}^4\Pi \rangle$	44.51	48.25	$\frac{\sqrt{3}}{2}$
$\langle {}^4\Delta \vert \hat{SO}_x \vert {}^6\Pi \rangle$	44.50	48.25	$\frac{\sqrt{3}}{2}$
$\langle {}^4\Delta \vert \hat{SO}_x \vert {}^4\Pi \rangle$	103.43	111.44	2.0
$\langle {}^4\Sigma^+(II) \vert \hat{SO}_x \vert {}^6\Pi \rangle$	25.62	27.86	0.5
$\langle {}^4\Sigma^+(II) \vert \hat{SO}_x \vert {}^4\Pi \rangle$	59.45	55.72	1.0

Table 4.34: Summary of non-zero asymptotic spin-orbit coupling values obtained using the Breit-Pauli ("BP") method at MRCI level of theory for the various couplings involving the SO_x operator

in Appendix B), 7 CASSCF state-combinations were chosen. It was found that even if a calculation converges it does not always follow that the resulting curves will be continuous. These 7 CASSCF state-combinations were then used to tested out by calculating MRCI calculations which used these CASSCF calculations as their starting orbitals for 11 low-lying electronic states of CrH. Previously, Dai & Balasubramanian (1993) had calculated PECs and DMCs for 21 low-lying electronic states. It was shown in section 4.1 that their results for the higher-lying 11 electronic states raised questions about the state-of the art methods they had used. The only other theoretical study in which electronic states beyond the $X^6\Sigma^+$ and $A^6\Sigma^+$ states had been calculated is that of Roos (2003), see section 3.1.

This *ab initio* study presented in this chapter was done with the goal of selecting the best quality *ab initio* curves which could be calculated for input into our final CrH linelist. The size of the basis set used for these calculations was justified in section 4.4.1 in which it was shown that increasing the size of the basis set can actually decrease the number of inter-nuclear distances for which a calculation will converge (see table 4.15).

For each PEC and DMC, MRCI calculations which used the 7 different CASSCF state-combinations were inspected and analysed. *Ab initio* curves were selected by the following criteria: the number of points converging, judgement of if regions of non-convergence were important, inspection of plots of these curves (and their gradients, see section 4.5 for obvious discontinuities, comparison of MRCI results in which the number of states of a particular symmetry and multiplicity had been varied and finally also by using a knowledge of which electronic states should converge to which atomic dissociation limits. Thus a set of criteria for selection of *ab initio* curves has been developed within this study. Previously there has not been a study in which different MRCI calculations produced using different CASSCF state-combinations have been compared.

For the DMCs, a choice was made to use the expectation value method rather than the finite-field method (see section 4.6). For the $X^6\Sigma^+$ and $A^6\Sigma^+$ states calculations were run to test the stability of these DMCs around equilibrium. For these tests performed at MRCI level of theory, the CASSCF state-combination was varied as well as the number of sextet states of symmetry 1 varied in each MRCI calculation. The difference between using the expectation value method and the finite-field method

at equilibrium was also investigated, see tables 4.24 and 4.25. Again, this type of study has never been undertaken and it demonstrates clearly that both the CASSCF state-combination used and the number of states calculated at MRCI level of theory are two factors which should always be specified when quoting any MRCI results. These results were compared to previous theoretical and experimental studies and found to be in broad agreement. The TMDs acting between the three $^6\Sigma^+$ states has been calculated at MRCI level of theory. The TDM between the $A^6\Sigma^+ - X^6\Sigma^+$ has been compared to that calculated by Bauschlicher et al. (2001). At present, without experimental measurements of intensity for this system it is difficult to ascertain which result is more correct. However, it is encouraging that we have calculated a TDM with a similar functional form of Bauschlicher et al. (2001). We have also shown that the exact shape does depend significantly on whether 3 sextet states of symmetry 1 or 4 sextet states of symmetry 1 are used in the calculation. The TDMs for the $D^6\Sigma^+(III) - X^6\Sigma^+$ and $D^6\Sigma^+(III) - A^6\Sigma^+$ transitions have been calculated and have been found to be around a factor of 4 smaller around equilibrium compared to the $A^6\Sigma^+ - X^6\Sigma^+$ transition (see figure 4.19c). The consequences for the linelist is that these two electronic systems are then expected to give rise to transitions which are at least an order of magnitude smaller than those arising from the $A^6\Sigma^+ - X^6\Sigma^+$ system.

Moving onto the quartet states, the calculations presented in this chapter indicate that the $c^4\Sigma^+(II)$ state undergoes a crossing with a higher-lying quartet state: by consideration of L_z coupling calculations this state was identified as been a $^4\Gamma$ state.

Finally, for the first time for CrH, electronic angular momenta and spin-orbit couplings have been calculated. For the electronic angular momenta couplings calculated it was found that the number of states used in the MRCI calculation had a bearing on the shape of the coupling curve produced, e.g. see figures 4.33a and 4.33b. The spin-orbit calculations were found to vary by up to, at most 10 cm^{-1} depending on the CASSCF state-combination used for the MRCI calculation. Typically these spin-orbit couplings between 25.63 and 103.42 cm^{-1} at dissociation (see table 4.34). In the context of producing an accurate linelist this is important as it demonstrates that for transition-metal bearing compounds, spin-orbit coupling should not be ignored.

In summary, from this "forest" of data presented in this chapter, PECs, DMCs, TDMs, electronic angular momenta and spin-orbit coupling curves were selected to the form the basis of our linelist for CrH. During this journey through testing out CASSCF state-combinations and varying the number of states in a given MRCI calculation, significant variations were found which demonstrate the need for published MRCI calculations to specify these parameters which at present is not commonly done.

Chapter 5

Chromium Hydride Linelist

In this chapter a summary of the *ab initio* curves used in the construction of the final linelist for CrH will be summarised in section 5.1. The refining of the *ab initio* PECs for the $X^6\Sigma^+$ and $A^6\Sigma^+$ electronic states using available experimental data is discussed in section 5.2. In this section the calculation using these refined potentials is summarised. Finally section 5.3 presents the linelist computed for the various isotopologues of CrH.

5.1 *Ab initio* curves input into linelist

In section 4.4, PECs and DMCs of 11 low-lying electronic states of CrH were presented. In our final linelist we included 8 of them, namely $X^6\Sigma^+$, $A^6\Sigma^+$, $B^6\Pi$, $C^6\Delta$, $D^6\Sigma^+(III)$, $a^4\Sigma^+$, $b^4\Pi$ and $c^4\Delta$. These *ab initio* PECs are shown in figure 5.1. Table 5.1 summarises all PEC and DMC *ab initio* curves, calculated at MRCI level of theory, inputted into the final linelist for CrH with table 5.2 summarising the couplings. In table 5.1 the "CASSCF" refers to the combination of states used in the proceeding CASSCF calculation. In both tables 5.1 and 5.2, the notation "2+1" indicates that two states of symmetry 1 and one state of symmetry 4 have been used for a particular multiplicity (i.e. either quartet or sextet) within the MRCI calculation. The term "N/A" simply means non-applicable which is for the cases of the $B^6\Pi$ and $b^4\Pi$ states as there no other states which have components in symmetry 2 and 3 to consider e.g. Π, Φ states (see table 2.6).

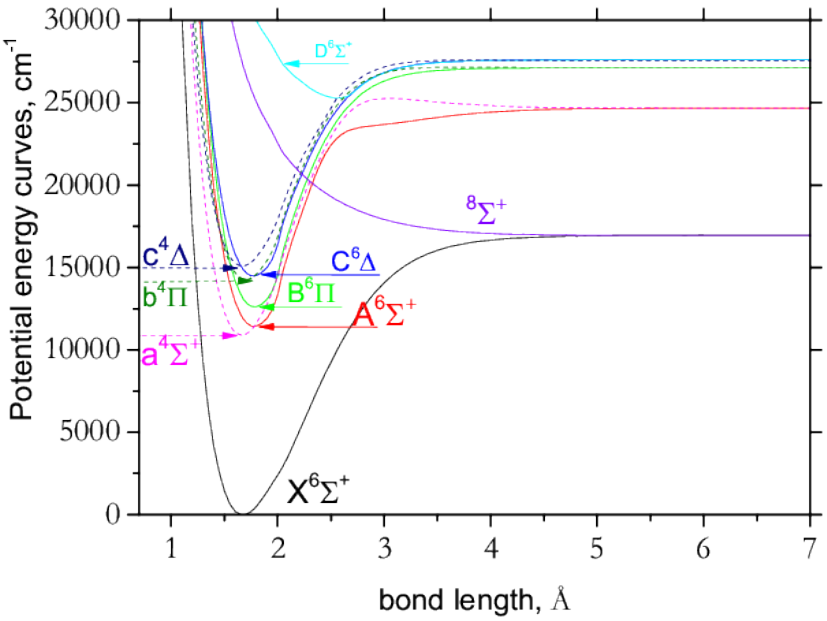

Figure 5.1: PECs for 9 low-lying electronic states of CrH calculated using MRCI level of theory and a cc-pVQZ basis set. In our final linelist all of these states were included with the exception of the anti-bonding $^8\Sigma^+$ state.

State	CASSCF	PEC		DMC	
		MRCI	Figure	MRCI	Figure
$X^6\Sigma^+$	ABF	3+1	4.16b	4+1	4.17b
$A^6\Sigma^+$	ABF	3+1	4.16d	4+1	4.17c
$B^6\Pi$	AB	N/A	4.22	N/A	4.22
$C^6\Delta$	ABF	3+1	4.16f	4+1	4.17d
$D^6\Sigma^+(III)$	ABF	4+1	4.18a	4+1	4.18b
$a^4\Sigma^+$	ABF	2+1	4.25a	2+1	4.23f
$b^4\Pi$	ABF	N/A	4.29	N/A	4.29
$c^4\Delta$	ABF	4+1	4.28	2+1	4.23f

Table 5.1: Summary of *ab initio* PECs and DMCs used in the calculation of the final linelists with references to the relevant figures. In this table the notation 2+1 means two states calculated in symmetry 1 and one state calculated in symmetry 4 for the given multiplicity (i.e. either sextet or quartet) at MRCI level of theory.

5.2 Fitting to experiment

As was mentioned in section 3.2, experimental data was used to refine the *ab initio* potentials of the $X^6\Sigma^+$ and $A^6\Sigma^+$ states of CrH. Unfortunately for CrH there is only experimental data available for these two electronic states. Table 5.3 gives a summary of this data which is available.

Coupling		MRCI	Figure
	$\langle A^6\Sigma^+ \vert \mu_z \vert X^6\Sigma^+\rangle$	4+1	4.19c
	$\langle D^6\Sigma^+(III) \vert \mu_z \vert X^6\Sigma^+\rangle$	4+1	4.19c
	$\langle D^6\Sigma^+(III) \vert \mu_z \vert A^6\Sigma^+\rangle$	4+1	4.19c
TDM	$\langle X^6\Sigma^+ \vert \mu_x \vert B^6\Pi\rangle$	3+1	4.32a
	$\langle A^6\Sigma^+ \vert \mu_x \vert B^6\Pi\rangle$	3+1	4.32b
	$\langle D^6\Delta \vert \mu_x \vert B^6\Pi\rangle$	4+1	4.32c
	$\langle D^6\Sigma^+(III) \vert \mu_x \vert B^6\Pi\rangle$	4+1	4.32d
	$\langle a^4\Sigma^+ \vert \mu_x \vert b^4\Pi\rangle$	3+1	4.31a
	$\langle c^4\Delta \vert \mu_x \vert b^4\Pi\rangle$	2+1	4.31b
$\hat{L}_x$	$\langle X^6\Sigma^+ \vert \hat{L}_x \vert B^6\Pi\rangle$	3+1	4.33a
	$\langle A^6\Sigma^+ \vert \hat{L}_x \vert B^6\Pi\rangle$	4+1	4.33b
	$\langle C^6\Delta \vert \hat{L}_x \vert B^6\Pi\rangle$	4+1	4.33b
	$\langle D^6\Sigma^+(III) \vert \hat{L}_x \vert B^6\Pi\rangle$	4+1	4.33c
	$\langle a^4\Sigma^+ \vert \hat{L}_x \vert b^4\Pi\rangle$	3+1	4.33d
	$\langle c^4\Delta \vert \hat{L}_x \vert b^4\Pi\rangle$	3+1	4.33d
$S\hat{O}_x$	$\langle X^6\Sigma^+ \vert S\hat{O}_x \vert B^6\Pi\rangle$	3+1	4.36c
	$\langle A^6\Sigma^+ \vert S\hat{O}_x \vert B^6\Pi\rangle$	4+1	4.36f
	$\langle C^6\Delta \vert S\hat{O}_x \vert B^6\Pi\rangle$	3+1	4.36f
	$\langle D^6\Sigma^+(III) \vert S\hat{O}_x \vert B^6\Pi\rangle$	4+1	4.36d
	$\langle X^6\Sigma^+ \vert S\hat{O}_x \vert b^4\Pi\rangle$	4+1	4.36b
	$\langle A^6\Sigma^+ \vert S\hat{O}_x \vert b^4\Pi\rangle$	3+1	4.36e
	$\langle C^6\Delta \vert S\hat{O}_x \vert b^4\Pi\rangle$	3+1	4.36e
	$\langle D^6\Sigma^+(III) \vert S\hat{O}_x \vert b^4\Pi\rangle$	4+1	4.36d
	$\langle a^4\Sigma^+ \vert S\hat{O}_x \vert b^4\Pi\rangle$	4+1	4.37a
	$\langle c^4\Delta \vert S\hat{O}_x \vert b^4\Pi\rangle$	2+1	4.37a
	$\langle a^4\Sigma^+ \vert S\hat{O}_x \vert {}^6\Pi\rangle$	2+1	4.37b
	$\langle c^4\Delta \vert S\hat{O}_x \vert B^6\Pi\rangle$	2+1	4.37b
$S\hat{O}_z$	$\langle B^6\Pi \vert S\hat{O}_z \vert B^6\Pi\rangle$	N/A	4.34d
	$\langle b^4\Pi \vert S\hat{O}_z \vert b^4\Pi\rangle$	N/A	4.34b
	$\langle b^4\Pi \vert S\hat{O}_z \vert B^6\Pi\rangle$	N/A	4.35d
	$\langle C^6\Delta \vert S\hat{O}_z \vert C^6\Delta\rangle$	3+1	4.35b
	$\langle c^4\Delta \vert S\hat{O}_z \vert c^4\Delta\rangle$	4+1	4.35a
	$\langle c^4\Delta \vert S\hat{O}_z \vert C^6\Delta\rangle$	3+1 (q), 4+1) (s)	4.35c

Table 5.2: Summary of *ab initio* coupling curves used in the calculation of the final linelists. All of these curves were calculated at MRCI level of theory using a cc-pVQZ basis set and a CASSCF state-combination calculation of ABF (see table 4.3). In this table the notation 2+1 means two states calculated in symmetry 1 and one state calculated in symmetry 4 for the given multiplicity (i.e. either sextet or quartet) at MRCI level of theory. In this table for the SO_z couplings, "(q)" indicates the MRCI calculation for the quartet states and "(s)" indicates the MRCI calculation for the sextet states.

Study	Isotopologue	Band	Branches	Range in N
O'Connor(1967)	CrH	(1, 1)	R_1, R_2, R_3, R_4, R_5, R_6, P_1, P_2, P_3, P_4, P_5, P_6	0-24
	CrH	(1, 0)		0-27
	CrD	(0, 0)		0-31
Ram et al. (1993)	CrH	(0, 0)		0-30
Ram et al. (1995)	CrD	(0, 0)		0-48
		(0, 1)		0-25
		(1, 0)		0-35
		(1, 2)		0-24
Bauschlicher et al. (2001)	CrH	(1, 0)		1-27
		(1, 1)		2-24
Shin et al. (2005)	^{50}CrH	(0, 0)	R_1, R_2, R_3, R_4, R_5 Q_{21}, Q_{32}, Q_{43}, Q_{54}, Q_{65} P_{42}, P_{53}, P_{64}	0-7

Table 5.3: Summary of experimental frequencies available for the $A^6\Sigma^+ - X^6\Sigma^+$ transition of CrH. In this table N is the rotational number for a system been modelled as a Hund's case (b). For details see section 2.2.

As well as these pure measured experimental frequencies summarised in table 5.3, there is also the existing linelist of Burrows et al. (2001). This data is in the form of energies and intensities for 12 vibrational bands ((0, 0), (0, 1), (0, 2), (0, 3), (1, 0), (1, 1), (1, 2), (1, 3), (2, 0), (2, 1), (2, 2) and (2, 3)). All of this data was processed into "Duo" format. Experimental frequencies were typically labelled with the quantum numbers of N, ν', ν'' and a transition label of P_{1-6}, Q_{1-6} or R_{1-6}. As a reminder of the information presented in section 2.2, ν' is the vibrational number of the upper state and ν'' is the vibrational number of the lower state. A "P" transition corresponds to $\Delta N = -1$ (or ΔJ), a "Q" transition is for $\Delta N = 0$ and a "R" transition for $\Delta N = +1$ where $\Delta N = N' - N''$. The subscripts 1 to 6 (e.g P_1, P_2, P_3, P_4, P_5 and P_6) are the spin-components numbers which are used to describe the frequencies in increasing order for each P branch, Q or R branch. It was assumed that the N presented corresponded to the lower state (as is convention) so hence from knowing if the transition was "P", "Q" or "R" the N value of the upper state was easily deduced. To link N to J the rules shown in table 5.4a where deducted from the data of Shin et al. (2005) whom had listed both J and N for the transitions.

Spin-component	Rule
1	$J = N + 2.5$
2	$J = N + 1.5$
3	$J = N + 0.5$
4	$J = N - 0.5$
5	$J = N - 1.5$
6	$J = N - 2.5$

(a)

$J - 0.5$	Branch nunber	Parity
Even	Even	-
Even	Odd	+
Odd	Even	+
Odd	Odd	-

(b)

Table 5.4: Mapping between J and N as a function of the spin-component number (1-6) and also assignment of parity depending on J and the spin-component number. N is the rotational number in Hund's case (b) and J is the rotational number in Hund's case (a).

The relations shown in table 5.4a were also independently verified by doing a cross-check between the Burrows et al. (2001) linelist and the experimental frequencies of Ram et al. (1993). The e/f parities presented in the linelist of Burrows et al. (2002) were converted into rotationless parity by using the Kurucz parity conversion (Brown & Carrington 2003):
e: Parity= $(-1)^{J-0.5}$
f: Parity= $(-1)^{J+0.5}$.
Hence the relation between parity, J and spin-component number was obtained as shown in table 5.4b was deduced and then applied to the experimental frequency data. For the upper state the parity is simply opposite in sign to the lower state. Hence the quantum numbers of the upper and lower states were converted into Duo format which were then used to refine the *ab initio* potentials.

For the refinement process and indeed the calculation of the final linelist, the program Duo was used (see section 2.9). The generic process of the line list production employed within the ExoMol project is explained in detail by Tennyson & Yurchenko (2012) and involves a solution of a nuclear motion problem using PECs within the Born-Oppenheimer framework which are coupled by spin-orbit and elec-

tronic angular momenta (Yurchenko, Lodi,Tennyson & Stolyarov 2016). For CrH (or indeed any transition metal hydride) a more sophisticated method for solving the nuclear Schrödinger equation is required than the commonly used nuclear programme LEVEL (Le Roy 2007), due to the high spin (multiplicity 6) of the ground state $^6\Sigma^+$ and also due to the nature of electronic structure (manifolds of low-lying coupled electronic states).

Duo has previously been used within the group for building accurate, empirical line lists for diatomic molecules including AlO (Patrascu et el. 2014 & 2015), ScH (Lodi, Yurchenko & Tennyson 2015) and CaO (Yurchenko et al. 2016).

In order to facilitate the refinement procedure, which was done for the $X^6\Sigma^+$ and $A^6\Sigma^+$ states only, we excluded all other states from the Duo calculations. This was also the method of choice of Burrows et al. (2002). The CrH PECs of the $X^6\Sigma^+$ and $A^6\Sigma^+$ states were represented as analytical functions using the Morse Oscillator (MO):

$$V(r) = T_{\rm e} + (A_{\rm e} - T_{\rm e})\,(1 \; - \; \exp\{-a(R - R_{\rm e})\})^2\,, \tag{5.1}$$

where $A_{\rm e}$ is the corresponding asymptotic limit relative to the minimum of the $X^6\Sigma^+$ state. Due to the lack of the vibrational coverage in the experimental data ($v' \leq 1$ and $v'' \leq 2$), $T_{\rm e}$, $D_{\rm e}$, $R_{\rm e}$, and a were the only parameters we could vary, and only for the two states $X^6\Sigma^+$ and $A^6\Sigma^+$. In order to improve the fit, we have also introduced the following two empirical Hamiltonian terms: spin-spin and spin-rotation couplings, which were represented using a Šurkus-polynomial expansion (Šurkus et al. 1984):

$$F(r) = (1 - y_p) \sum_{i \geq 0} a_i y_p^i + y_p a_{\rm inf}, \tag{5.2}$$

where

$$y_p = \frac{R^p - R_{\rm e}^p}{R^p + R_{\rm e}^p}$$

with $p = 2$. During the refining process, initially the linelist of Burrows was used before switching to use experimental frequencies for the final fit. In this final fit the various experimental sources were weighted accordingly to their accuracy and the vibrational energies within the linelist of Burrows et al. (2002) which had been generated by extrapolation put to a lower weighting.

Table 5.5 gives a representative summary of the accuracy of refinement obtained. As can be seen from table 5.5, for the (0, 0) band we typically achieved an accuracy of between 0.04 $\rm cm^{-1}$ and 1.52 $\rm cm^{-1}$. For the (1,0) band the accuracy of our fit was less satisfying. However in this wavelength region, an accuracy of 2.0 $\rm cm^{-1}$ corresponds to a required resolution of 6467.

For the calculation of this final refined linelist, we used a grid of 501 points in conjunction with the a grid-based Sinc method with R ranging from 0.72 to 8.0 Å to solve the un-coupled vibrational eigenvalue problems for each state separately. The lowest 40 vibrational eigenfunctions were then used as the vibrational basis functions for the ro-vibronic, fully coupled problem in a Hund's case (a) representation, which was then solved variationally for each total angular momentum quantum number, J, and parity by explicit diagonalisation of the coupled-states Hamiltonian matrix.

The chromium atom has 4 stable isotopes namely ^{50}Cr, ^{52}Cr, ^{53}Cr, ^{54}Cr with ^{52}Cr

J'	P'	J"	P"	Obs	Calc	Obs-Calc	state	ν'	σ'	state"	ν''	σ''
1.5	+	2.5	+	36.094	36.2251	-0.1311	1	0	1.5	1	0	0.5
2.5	+	2.5	+	121.592	121.7525	-0.1605	1	0	1.5	1	0	0.5
2.5	-	3.5	+	11530.215	11530.3074	-0.0924	2	0	-2.5	1	0	2.5
3.5	+	4.5	-	11468.068	11468.1719	-0.1039	2	0	2.5	1	0	-2.5
4.5	-	3.5	+	11584.601	11584.6938	-0.0928	2	0	-1.5	1	0	2.5
5.5	-	6.5	+	11455.821	11455.8596	-0.0386	2	0	-2.5	1	0	2.5
6.5	+	7.5	-	11361.653	11361.7392	-0.0862	2	0	1.5	1	0	-1.5
7.5	+	6.5	-	11580.873	11580.9465	-0.0735	2	0	2.5	1	0	-2.5
8.5	+	9.5	-	11446.171	11446.2453	-0.0743	2	0	0.5	1	0	-0.5
9.5	+	10.5	-	11395.508	11395.4364	0.0716	2	0	1.5	1	0	-1.5
10.5	-	11.5	+	11286.612	11286.5576	0.0544	2	0	-2.5	1	0	2.5
12.5	+	11.5	-	11607.067	11607.5784	-0.5114	2	0	0.5	1	0	-0.5
14.5	+	15.5	-	11297.066	11297.3514	-0.2854	2	0	0.5	1	0	-0.5
16.5	-	15.5	+	11399.62	11399.5023	0.1177	2	0	-0.5	1	0	0.5
18.5	+	19.5	-	11055.639	11054.1227	1.5163	2	0	2.5	1	0	-2.5
20.5	-	21.5	+	11037.646	11036.1805	1.4655	2	0	-1.5	1	0	1.5
23.5	+	24.5	-	10609.034	10608.8773	0.1567	2	0	0.5	1	0	-0.5
26.5	+	27.5	-	10537.798	10537.9552	-0.1572	2	0	1.5	1	0	-1.5
29.5	+	28.5	-	11271.729	11271.1692	0.5598	2	0	1.5	1	0	-1.5
1.5	+	2.5	+	13052.85	13054.3744	-1.5244	2	1	1.5	1	0	0.5
4.5	+	5.5	-	12957.323	12953.911	3.412	2	1	2.5	1	0	-2.5
5.5	-	6.5	+	12934.593	12932.5252	2.0678	2	1	-2.5	1	0	2.5
6.5	-	5.5	+	11482.081	11481.9318	0.1492	2	1	-1.5	1	1	2.5
8.5	+	9.5	-	12766.919	12769.8779	-2.9589	2	1	1.5	1	0	-1.5
10.5	+	9.5	-	13081.765	13081.2057	0.5593	2	1	0.5	1	0	-0.5
12.5	-	13.5	+	12778.776	12778.4819	0.2941	2	1	-1.5	1	0	1.5
14.5	+	13.5	-	13059.986	13059.5309	0.4551	2	1	0.5	1	0	-0.5
16.5	+	15.5	-	13037.58	13037.1626	0.4174	2	1	0.5	1	0	-0.5
18.5	+	19.5	-	11075.42	11075.128	0.292	2	1	0.5	1	1	-0.5

Table 5.5: Representative sample of refinement accuracy obtained for the $A^6\Sigma^+ - X^6\Sigma^+$ system of CrH. In this table "obs" is an experimentally measured frequency, "calc" is the frequency calculated using our refined model and "Obs-Calc" is simply the difference of the two. State 2 refers to the $A^6\Sigma^+$ state and state 1 refers to the $X6\Sigma^+$ state. The quantum numbers shown take on their usual meanings as explained in section 2.2. For simplicities sake, given that the two states of interest are both Σ^+ states, the Λ' and Λ'' columns have been omitted as they are simply both zero and also the Ω' and Ω'' columns as they are simply the same value as Σ' and Σ'' respectively.

been naturally the most abundant (84%). Hence 8 linelists have been computed for ^{50}CrH, ^{52}CrH, ^{53}CrH, ^{54}CrH and their deuterated counterparts. In total the linelist for ^{52}CrH has 89, 121 states and 11, 595, 704 transitions with a coverage from $J = 0.5$ to $J = 82.5$.

5.3 Spectra simulated from CrH linelist

Using the refined linelist created for CrH, spectra have been simulated using the ExoCross program (see section 2.10). In the following figures, "HWHF" is an abbreviation for "Half-width-half-maximum". Figure 5.2 shows the absorption spectra simulated using the ^{52}CrH linelist for a Gaussian line profile.

Figure 5.2 shows that the $X^6\Sigma^+ - X^6\Sigma^+$ and $A^6\Sigma^+(II) - X^6\Sigma^+$ electronic transitions dominate the spectra. The contribution from the other electronic transition systems is labelled as "minus A-X". This model in which the $X - X$ and $A - X$ transi-

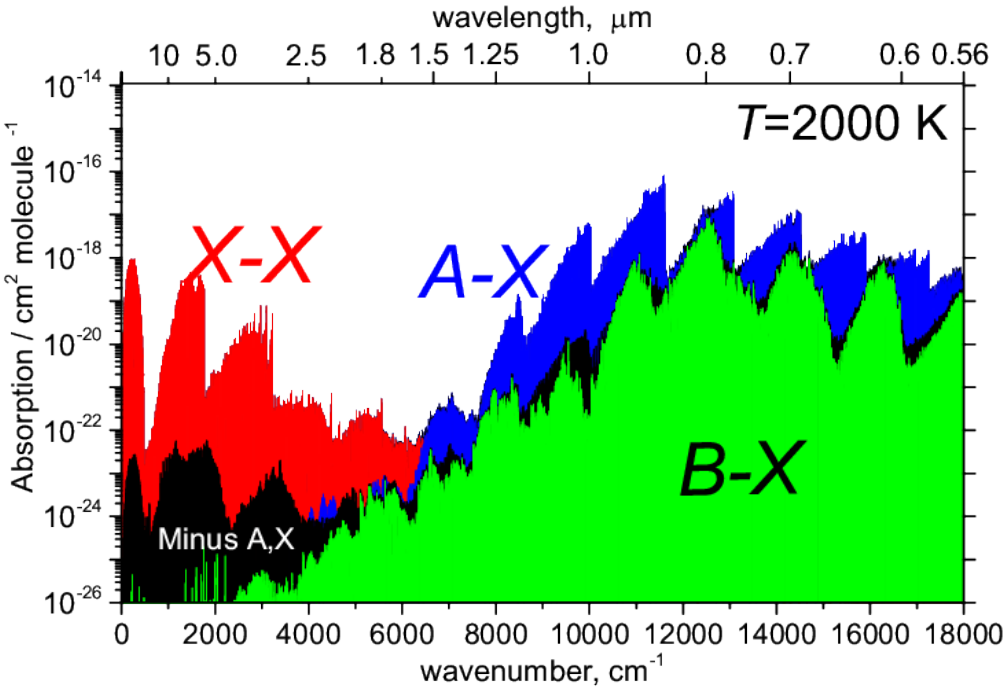

Figure 5.2: Simulated absorption spectra for the ^{52}CrH linelist calculated using a Gaussian line profile with a half width at half maximum (HWHM) is 1 cm^{-1}) at a temperature of 2000 K.

tions dominate the spectra is consistent with previous experimental studies in which to date here are no experimentally recorded transitions which have been positively identified as belonging to the $B^6\Pi - X^6\Sigma^+$ system (see section 3.2). As can be seen from figure 5.2 there is a possibility that with a favourable shift in T_e, bands from the $B - X$ system could be observed. With the uncertainties in T_e values of higher excited states for transition-metal diatomics, the question of whether the $B - X$ system can actually be observed is now an experimental one. Indeed Professor Dennis Tokaryk from the University of New Brunswick in Canada has expressed an interest searching experimentally for the $B - X$ system of CrH. Figure 5.3 shows a comparison of simulated spectra for a purely *ab initio* linelist (no refinement of PECs) and the final fitted linelist.

As can be seen from figure 5.3 the effect of refinement is to make the band heads more pronounced and the spectra more structured. Thus this figure demonstrates that for open-shell diatomics it is imperative to fit *ab initio* curves to any experimental data which is available. As can be seen from the top panel of figure 5.3 the positions of our refined linelist agree extremely well to those of the existing linelist of Burrows et al. (2002). This is not surprising given that we fitted our *ab initio* linelist to the experimental data set used by Burrows et al. (2002) as well as earlier experimental data sets. Figure 5.4 shows a zoomed in comparison of our refined linelist to the experimental measurements made by Bauschlicher et al. (2001) for the (1, 0) band of the $A^6\Sigma^+ - X^6\Sigma^+$ system. Figure 5.5 shows a comparison with the (1, 0) band

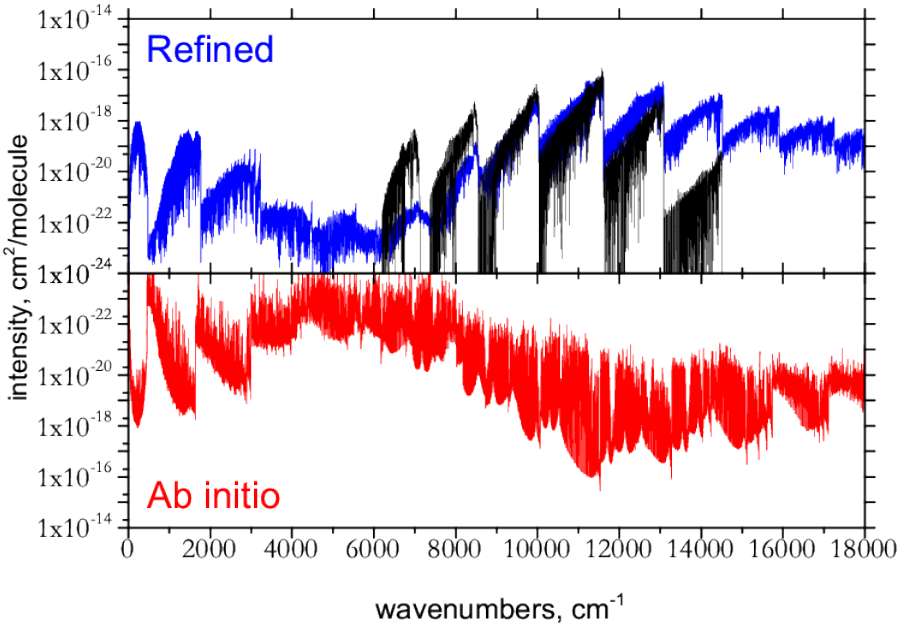

Figure 5.3: Comparison of spectra simulated using purely *ab initio* data, the refined linelist to that of the linelist of Burrows et al. (2002) as indicated by the black spectra.

measured by Chowdhury et al. (2006).

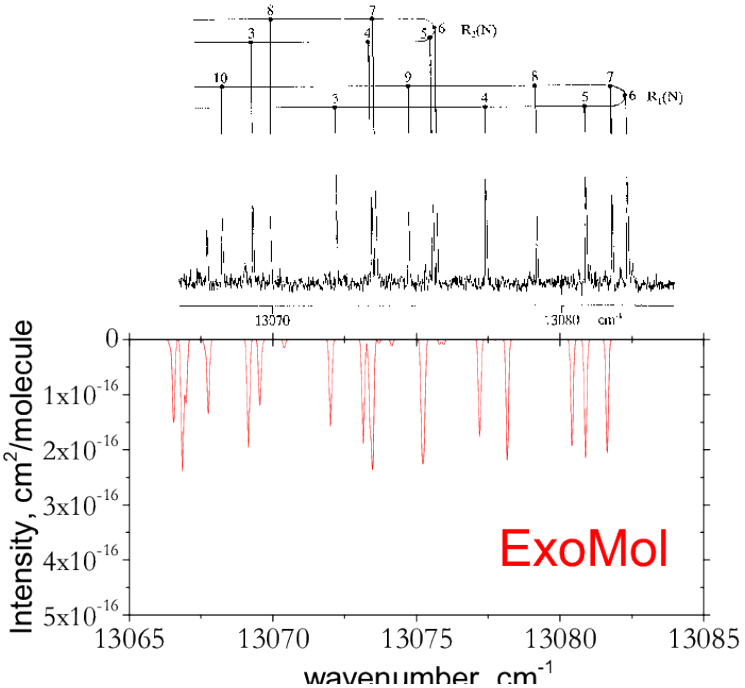

Figure 5.4: Comparison of our refined linelist to the experimental spectrum measured by Bauschlicher et al. (2001) for the (1, 0) band of the $A^6\Sigma^+ - X^6\Sigma^+$ system.

As can be seen from figure 5.4 our line positions agree well with those of experiment and also demonstrates that our linelist is more complete than what can be feasibly measured by experiment.

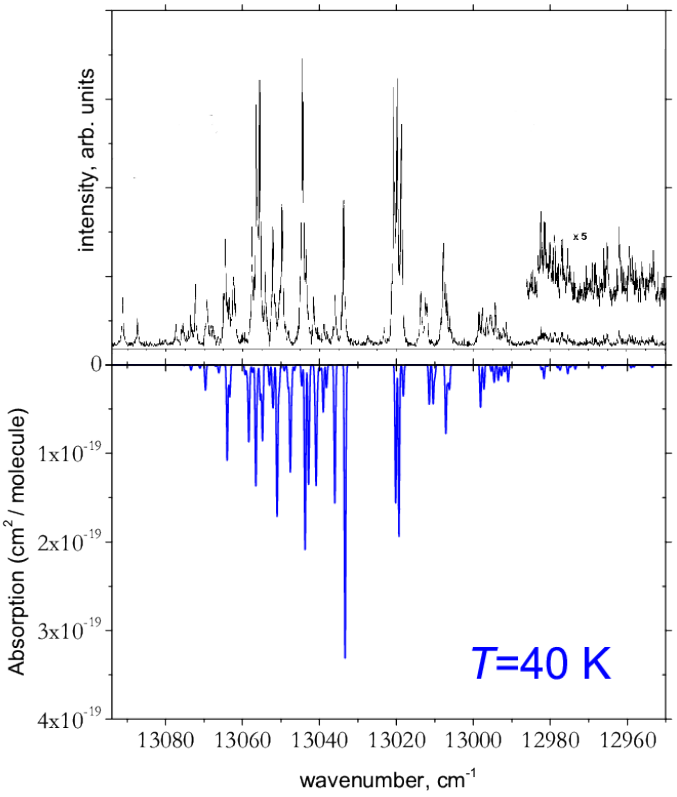

Figure 5.5: Comparison to experimental absorption cross-sections (Chowdhury et al. 2006) at 40 K using a Gaussian profile with a HWHM of 2 cm^{-1} for the (1, 0) band of the $A^6\Sigma^+ - X^6\Sigma^+$ system. The top panel is the measured experimental spectra and the bottom panel the simulated spectra using the linelist.

In terms of astronomical applications, any significant temperature effect in simulated spectra can potentially be used as a temperature diagnostic. Figure 5.6 shows absorption spectra calculated using the linelist for different temperatures using a Gaussian profile with a HWHM of 5 cm^{-1}.

As can be seen from figure 5.6 between 1000 K and 2000 K the intensity of the spectra can differ by up to two orders of magnitude for each band. Pavlenko et al. (2008) have suggested that the shift in line positions seen between CrH and CrD bands could be used in the so-called "deuterium test" (see section 3.4). Figure 5.7 shows the comparison of bands for the $A^6\Sigma^+ - X^6\Sigma^+$ system for two most abundant isotopologues of CrH, ^{52}CrH and ^{52}CrD. Figure 5.7 shows that the bandhead of (0, 1) band is shifted by 0.04 μm. In order to observe this shift a resolution of 25 would be required.

Figure 5.8 shows the spectra of 2 L dwarfs observed by Rayner et al. (2009). In the bottom panel of figure 5.8 the CrH linelist presented in this thesis and the linelist for FeH of Dulick et al. (2004) have been used to generate absorption cross-sections at $T = 2200$ K. As can be seen from this figure there is a good agreement with observations with CrH dominating around 0.86 μm before the FeH spectra dominates at 1 μm.

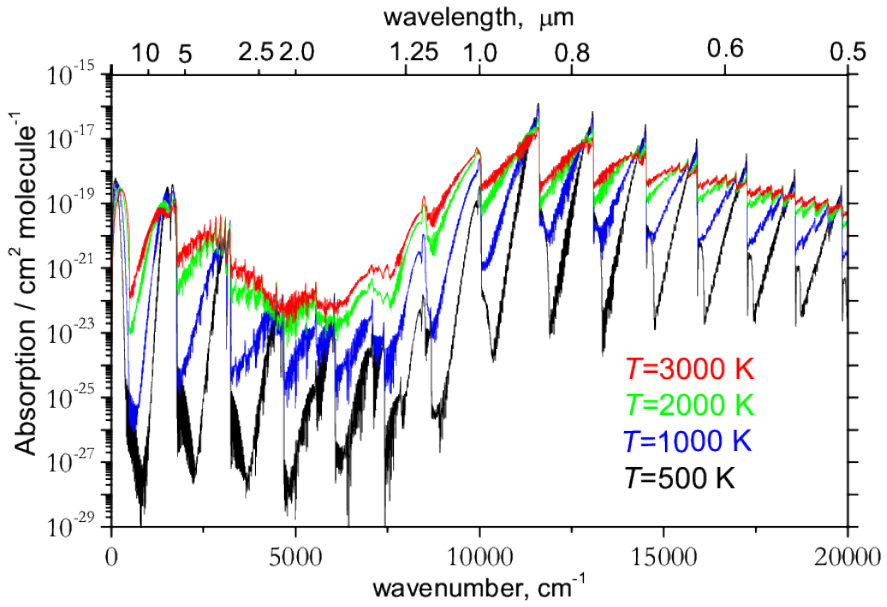

Figure 5.6: Temperature dependence of the absorption spectra of CrH (Gaussian profile, HWHM=5 cm^{-1}).

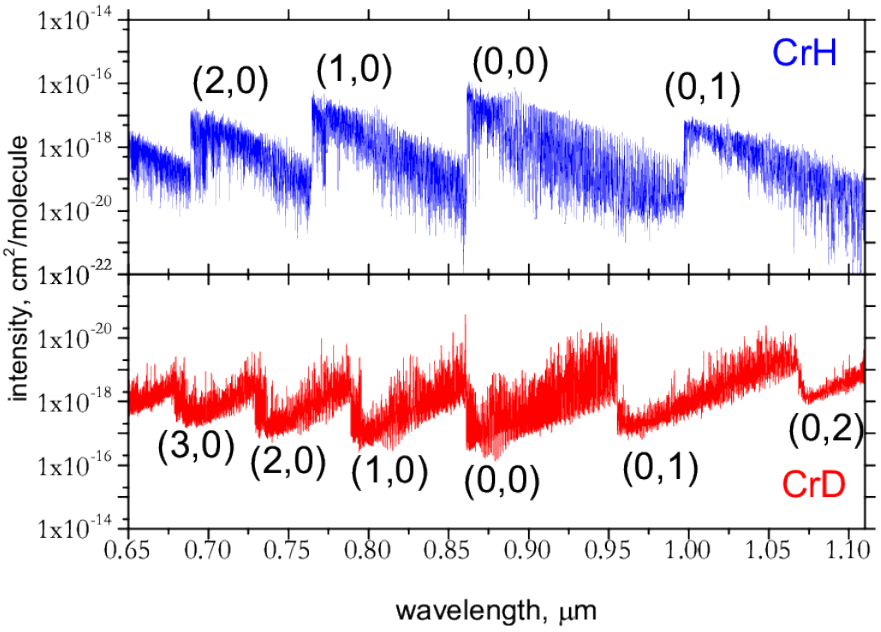

Figure 5.7: Comparison of spectra for the $A^6\Sigma^+ - X^6\Sigma^+$ system of ^{52}CrH and ^{52}CrD

The partition function, Q, is a measure of the completeness of a linelist. Sauval & Tatum (1984) have calculated for CrH polynomial coefficients for the partition function using the spectroscopic constants presented in Huber & Herzberg (1979) for the temperature range $1000 - 9000$ K. These constants are presented in table 5.6. This was done as part of a larger study of around 300 molecules by these authors.

The equation used to calculate the partition function, Q as a function of temper-

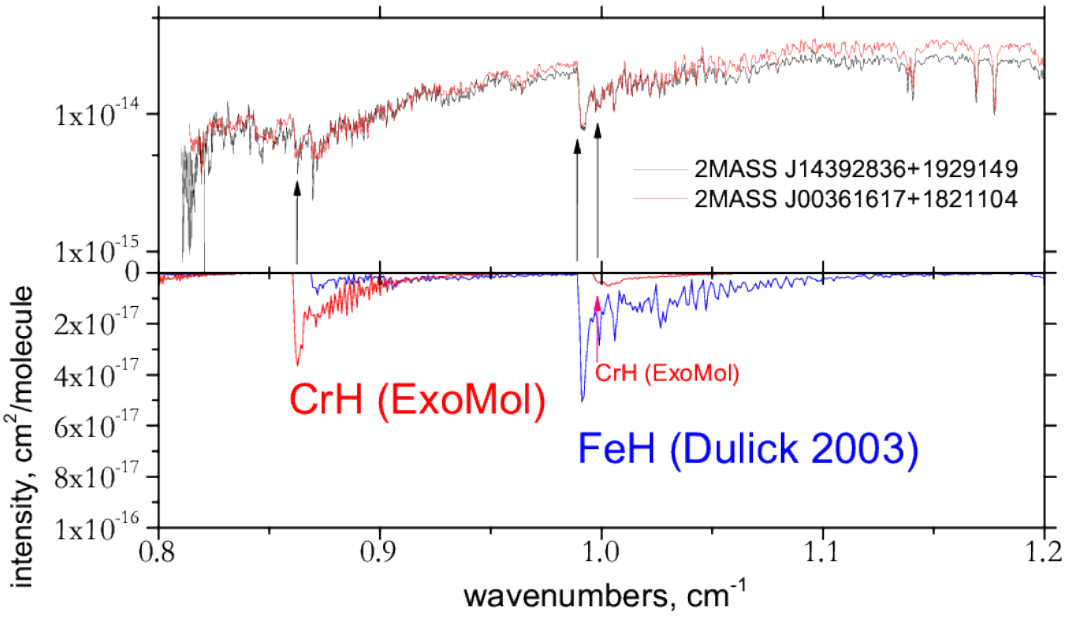

Figure 5.8: Comparison of spectra from 2 L dwarfs and simulated spectra using the CrH ExoMol linelist and the linelist for FeH of Dulick (2003).

Coefficient	Value
a_0	4.0929
a_1	-22491
a_2	0.8923
a_3	-0.1787

Table 5.6: Partition Function Coefficients calculated by Sauval & Tatum 1984

ature T using these coefficients is

$$\log Q = \sum_{n=0}^{n=3} a_n (\log \theta)^n \tag{5.3}$$

where $\theta = 5040/T$ is a dimensionless parameter with T given in Kelvin, valid for the range $1000 - 9000$ K. Using these coefficients presented by Sauval & Tatum the resultant theoretical partition function was calculated which is valid for the $A^6\Sigma^+$ and $X^6\Sigma^+$ states only. Figure 5.9 gives a comparison between our calculated partition function and that of Sauval & Tatum (1984).

Figure 5.9 shows that our work is in agreement with that of Sauval & Tatum (1984) up to temperatures of 3000 K after which we are predicting a greater partition function which could indicate our model is more complete. CrH is of interest in L dwarfs which have temperatures up to 2200 K.

In summary a new linelist for CrH has been created for the 8 major isotopologues. The existing linelist of Burrows et al. (2002), see section 3.3 only covers the $A^6\Sigma^+ - X^6\Sigma^+$ system up to $\nu = 3$. Our model includes not only this system but the contribution from 6 other electronic states with vibrational coverage up to $\nu = 40$ and J coverage up to 82.5. These contributions could this prove to be important in cor-

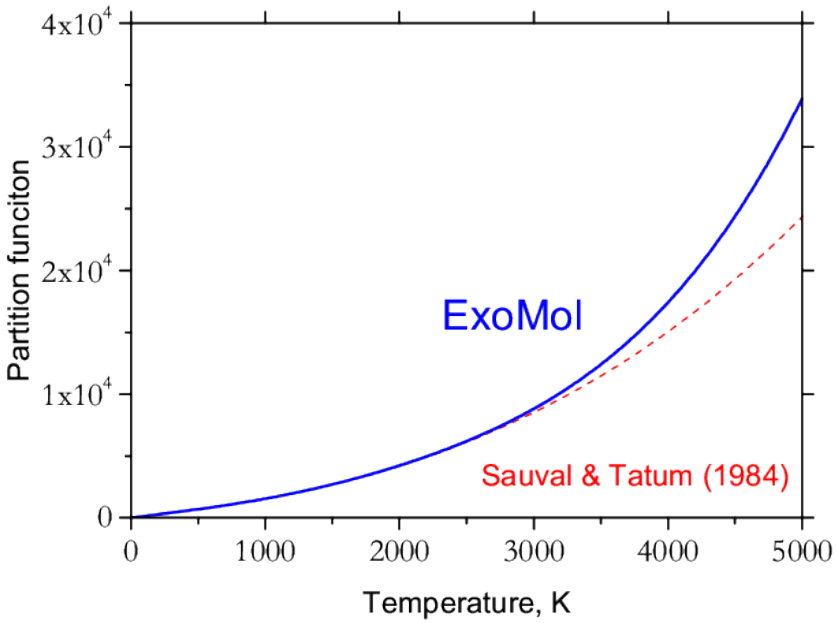

Figure 5.9: Comparison of calculated partition functions of CrH as a function of temperature to that of Sauval & Tatum (1984).

rectly modelling the opacity of L type dwarfs which to date has proved troublesome (see section 3.2).

Chapter 6

Introduction to Manganese Hydride

Following on from the the work done on Chromium Hydride (CrH), the diatomic metal hydride Manganese Hydride (MnH) was studied. As is is the case for CrH, the MnH molecule has a complex manifold of low-lying electronic states with high multiplicity which makes it another interesting molecule to investigate theoretically. Additionally the Manganese nucleus has a high nuclear spin ($I = 5/2$) which gives rise to complex hyperfine structure which has been studied extensively by experimentalists. Previous theoretical studies and experimental are outlined in sections 6.1 and 6.2 respectively.

At present there are no astrophysical detections of Manganese hydride to date. However, as is pointed out by Halfen & Ziurys (2008, 2006), the cosmic Manganese abundance is of similar order of magnitude to Chromium (see table 3.1). The diatomic molecule Chromium Hydride (CrH) has been found to be important in various astrophysical settings (see section 4.15). Furthermore the abundance of both chlorine & fluorine is less than that of Manganese yet HCl and HF have been detected in molecular clouds. Given that diatomic hydrides such as CH and OH are widely observed in the inter-stellar medium it seems possible that MnH could yet to be observed in space. The joint experimental observational work undertaken by the Ziruys group is reviewed in section 6.3.

At present there is no existing linelist of MnH available in the literature. In this study I have a calculated a linelist for the 10 low-lying electronic states of MnH where the $X^7\Sigma^+$ and $A^7\Pi$) states have been refined to experimental data. In a similar fashion to CrH, this linelist was constructed by first calculating the potential energy curves (PECs), dipole moments, angular momenta couplings and spin-orbit couplings for the various electronic states and then implementing these into the in-house programme Duo (Yurchenko et al. 2015). Chapter 7 outlines the *ab initio* calculations undertaken on MnH and chapter 8 presents the linelist calculated.

6.1 Previous theoretical studies of MnH

The diatomic molecule MnH has previously been studied theoretically by several authors as a single molecule but also as part of larger studies of diatomic transition

metal hydrides such as those by Das (1981), Walch & Bauschlicher (1983) and Chong et al. (1986). Balabanova and Peterson (2005) have generated, for each of the first row transition metals, two families of basis sets that converge systematically: these families are non-relativistic and Douglas-Kroll-Hess.

Langhoff, Bauschlicher & Rendell (1989) used a state-averaged CASSCF/MRCI method to calculate low-lying quintet and septuplet states up to 30 000 cm^{-1} of MnH with a particular focus on the $A^7\Pi - X^7\Sigma^+$, $b^5\Pi - a^5\Sigma^+$ and $c^5\Sigma^+ - a^5\Sigma^+$ systems. In their study, SA-CASSCF curves were presented for the lowest-lying $^7\Sigma^+$ and $^7\Pi$ states as shown in figure 6.1.

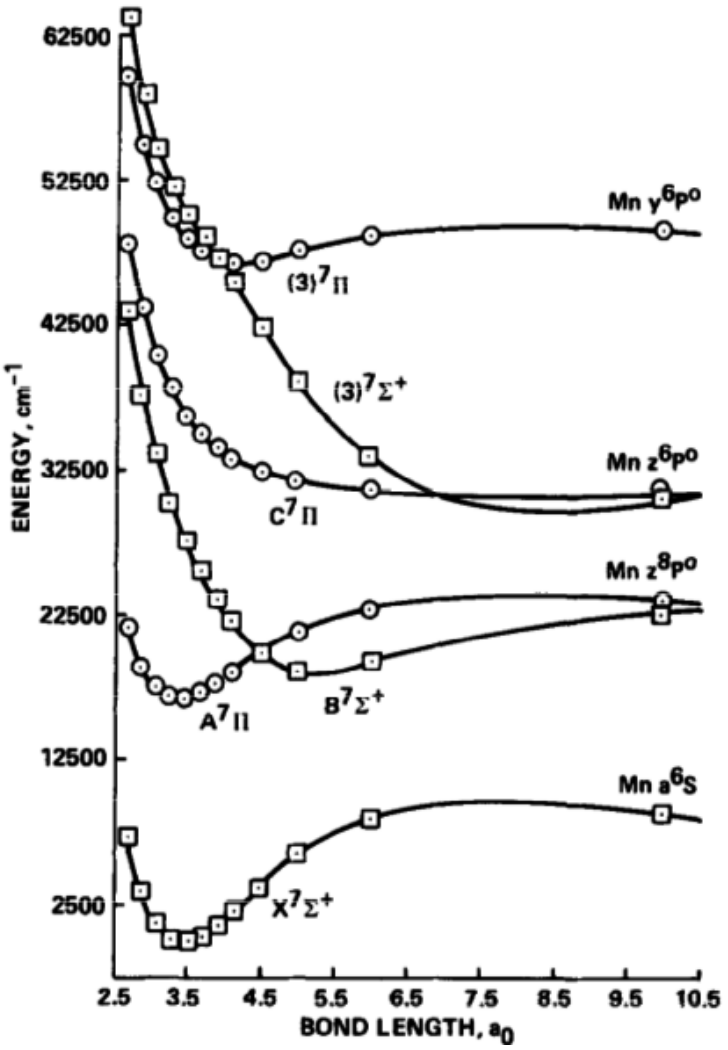

Figure 6.1: SA-CASSCF potential curves for the lowest three $^7\Sigma^+$ and $^7\Pi$ states of MnH.

At MRCI level, the authors calculated PECs and DMCs for the $X^7\Sigma^+$, $A^7\Pi$, $a^5\Sigma^+$, $b^5\Pi$ and $c^5\Sigma^+$ states and also the TMDs for the $A^7\Pi - X^7\Sigma^+$, $b^5\Pi - a^5\Sigma^+$ and $c^5\Sigma^+ - a^5\Sigma^+$ transitions. Radiative lifetimes of the $A^7\Pi$, $b^5\Pi$ and $c^5\Sigma^+$ for $\nu' = 0$ were calculated as 96.6 ns, 3.2 μs and 0.39 μs.

More recently, Wang & Andrews (2003) have undertaken a joint experimental and theoretical study of Manganese and Rhenium Hydrides. Experimentally, they

reacted laser-ablated Mn atoms with H_2 gas and thus made measurements of the MnH formed in neon and argon matrices. On the theoretical side they used DFT (density functional theorem) to calculate R_e and ω_e for the $X^7\Sigma^+$ and $a^5\Sigma^+$ state using various DFT methods and basis sets.

Tomonari, Nagashima & Hirano (2009) then re-calculated the *ab inito* curves of the $X^7\Sigma^+$, $A^7\Pi$ and low-lying quintet states using Slater-type basis sets in a $C_{\inf v}$ construction using multireference single and double excitation configuration interaction (MR-SDCI) with Davidson's correction (+Q).

6.2 Previous experimental studies of MnH

The first observation of the $A^7\Pi - X^7\Sigma^+$ band system of MnH was made by Heimer in 1936 using optical spectroscopy. Soon after Pearse & Gaydon in 1937 and 1938 observed and tentaviely assigned 4 bands within this system using a discharge tube source in a high temperature ark. These 4 bands with the tentative assignments proposed by Pearse & Gaydon in 1937 are shown in table 6.1.

Colour	Band head(s) (Å)	Tentative Assignment
green	5172 5205	(0, 0)
Yellow/green degraded to violet	5678 (strong) 5722 (weaker)	(1, 0)
red	6204	(0, 1)
blue degraded to red	around 4500	no assignment made

Table 6.1: Band heads of $A^7\Pi - X^7\Sigma^+$ system of MnH observed and tentatively assigned by Pearse & Gaydon in 1937.

Pearse & Gaydon concluded at the time that, due to the complexity of the vibrational bands they observed, the electronic transition concerned was most likely a $\Pi - \Sigma$ transition. They believed this had multiplicity of 5 (i.e. "quintet" states) as, by following the rule of Heitler and London only the $^5\Sigma^+$ state going to the first atomic dissociation of Manganese atom, namely ^6S would be stable. We now know that the ground state of MnH is actually $X^7\Sigma^+$ and is a bound stable state. Both the $a^5\Sigma^+$ and $X^7\Sigma^+$ states of Manganese hydride go to the first dissociation limit of the Manganese atom in the atomic dissociation limit.

Heimer had at the time already recorded the first three bands and concluded the same vibrtional band assignment. Heimer had recorded a band structure in the region $4\,700 - 4\,850$ Å which Pearse & Gaydon had also observed upon closer observation of their plates. However the band structure recorded by Heimer was different to the band structure observed by Pearse & Gaydon at 4500 Å. The bands were however observed to overlap suggesting that they could arise from two different, but related electronic or vibrational transitions. In 1938, Pearse & Gaydon re-measured the first three bands using a new design for the discharge tube which allowed tham to photograph spectrum under higger dispersion as shown in table 6.2. They note that as the rotational structure is complex, the band heads are tricky to locate exactly hence the updated band head locations assigned for the yellow-green and red bands.

Band	λ (Å)	ν (cm^{-1})
Blue-green	5172	19 330
Yellow-green	5677	17 610
Red	6237	16 030

Table 6.2: New measurements of band heads recorded by Pearse & Gaydon in 1938.

From these band-head values Pearse & Gaydon calculated the $\omega_0^{'}$ and $\omega_0^{"}$, for the initial and final electronic states as 1720 and 1580 cm^{-1}. Table 6.3 shows the comparison they made with other diatomic metal hydrides using their own measurements.

Species	$\omega_0^{'}$	$\omega_0^{"}$
CaH	1333	1299
MnH	1720	1580
NiH	1493	(1900)
CuH	1611	1866
ZnH	1824	1552
ZnH^+	1337	1832

Table 6.3: Vibrational frequencies for a selection of diatomic metal hydrides as recorded experimentally and hence calculated by Pearse & Gaydon.

Pearse & Gaydon also comment further on the blue band which they observed to degrade to red with band heads at 4741 Å and 4794 Å. They concluded that due to the rotational structure it must be the $(0, 0)$ band of a different system from the 3 other bands. Since they observed 5 branches of type P structure they concluded that this blue band must be transitions involving quintet states namely a $^5\Pi - ^5\Sigma^+$. Previously they had postulated that the first three bands arised from quintet states-in their 1938 paper, with this new deduction, they simply state that "It is fairly certain that the blue and blue-violet bands show a multiplicity of five, and the multiplicity of the yellow-green band also appears to be very high; we are thus led to expect many branches of unusual form in addition to the strong P, Q, and R branches."

Following on from this early work on MnH, the group led by Nevin and co-workers published six papers on MnH and MnD between 1942 and 1957 in which they measured rovibronic transitions in emission using a 21 foot grating spectrometer. Nevin (1942 and 1945) measured the rovibronic transition of the (0, 0) and (0, 1) bands of the $A^7\Pi - X^7\Sigma^+$ system of MnH which lie around 568 nm and 624 nm respectively. Hence with this data the authors undertook a rotational analysis and hence determined molecular parameters (ω_e, $\omega_e\chi_e$, B_e, α_e, D_e, β_e, H_e, γ_e, γD_e, ϵ) as well as spin-rotation and spin-spin for the $X^7\Sigma^+$ electronic state of MnH. To obtain these parameters, the authors assumed that the ground state followed a case (b) Hamiltonian. Nevin & Doyle (1948) then measured the (1, 0) band.

The (0, 0) and (0, 1) transitions of MnD were then photographed by Nevin, Conway & Cranley (1952): here the band heads lie at 5703.7 Å and 6073.3 Å respectively. By their rotational analysis the authors deduced that the spectra has considerable fine structure due to coupling between rotation and spin: crucially they also found that the $^7\Pi$ state appears to be perturbed with showing Hund's case (a) behaviour at low J before transitioning to Hund's case(b) for higher J. Neven & Stephens (1953) then calculated Dunham coefficients for the $X^7\Sigma^+$ state of MnD which hence allowed

them to compare MnH and MnD. Improved constants for the $X^7\Sigma^+$ state of both MnH and MnD were obtained by Hayes, McCarvill & Nevin 1957 who measured the (0, 2) vibrational band of the $A^7\Pi - X^7\Sigma^+$ transition of MnH and MnD. The early work on MnH by Nevin and co-workers, which is regarded as been pioneering for the time based on the complexity of the spectra, established that the ground state was $X^7\Sigma^+$.

Pacher (1974) and Kovacs & Pacher (1975) then re-derived from a theoretical perspective the molecular constants for the $\nu = 0$ and $\nu = 1$ states for the $X^7\Sigma^+$ state by taking into account the interaction with the $A^7\Pi$ state and thus synthesising a new fine structure interpretation. Their work on MnH was part of a larger more general study of $^7\Sigma^+$ and $^7\Pi$ electronic states of diatomic molecules.

Van Zee et al. (1978) performed ESR (electron spin-resonance) experiments in the visible and infra-red on the $X^7\Sigma^+$ state of MnH and MnD in matrix trapping experiments using both Argon and Neon at a temperature of 4 K. These matrix-trapping experiments helped to confirm experimentally that the ground state of MnH is indeed $X^7\Sigma^+$. As a side-note, these experimentalists also studied MnH_2 and MnD_2 molecules which until then was unknown and also observed evidence for MnH_3 molecules. The results of their studies on MnH and MnD are magnetic parameters such as the Hyperfine (A) tensor parameters and also a published series of experimentally measured hyperfine line positions.

Van Zee et al. (1986) then followed up this preliminary work by carrying out ENDOR (Electron nuclear double resonance) experiments on MnH in solid argon. At the time the technique of ENDOR had recently been applied to triatomic and tetratomic molecules. The motivation for their new study was to use the technique of ENDOR for studying the high-spin state of MnH. The results of this new analysis was the determination of the hyperfine constant and also the nuclear quadrupole coupling constant. Hence the authors then made predictions of the Zeeman energy levels for the $X^7\Sigma^+$ state of MnH for the case of $M_S = 0$.

The ground $X^7\Sigma^+$ state of ^{55}MnH was then further studied by Urban & Jones (1989) using diode laser spectroscopy in the infrared region. At the time of publication Urban & Jones's lab had recorded spectra on other diatomic molecules including NaH, RbH, CsH , SrH, BaH, GaH, InH, TiH, ZnH, AgH, CdH. A summary of the branches they recorded for MnH, with an accuracy of around 0.001 cm^{-1} is shown in table 6.4.

Vibrational band	Branches
$\nu = 1 \leftarrow 0$	P(2), P(3), P(4), P(5), P(6), P(7), P(8), P(9), P(10), P(11), P(17)
$\nu = 2 \leftarrow 1$	P(7), P(14), P(15), R(2), R(11), R(14)
$\nu = 3 \leftarrow 2$	P(7), P(8), P(10), P(11), R(4), R(5), R(18)(S= 0 only)

Table 6.4: Summary of branches recorded of $X^7\Sigma^+$ of MnH by Urban & Jones in 1989.

Using their recorded transitions Urban & Jones then produced ground state parameters by fitting to a Hund's case (b) Hamiltonian-briefly this means that the energy of a state is given by:

$E = E_{VR} + E_{SR} + E_{SS}$

where E_{VR} is rovibronic energy, E_{SR} is spin-rotation contribution and E_{SS} is spin-

spin contribution. In this coupling scheme, for each value of N, the quantum number J takes one of seven values namely $N-3$, $N-2$, $N-1$, N, $N+1$, $N+2$, $N+3$ as $S=3$ for the $X^7\Sigma^+$ state.

Following on from their work on MnH, in 1991 Urban & Jones recorded infrared transitions in the $X^7\Sigma^+$ state of MnD. The motivation behind this study was to determine mass-independent parameters and also Watson's mass-scaling coefficients by comparing their new results with their work on MnH. This was part of a larger study exploring diatomic metal hydrides and their corresponding diatomic deuterides. Table 6.5 summarises the branches for MnD recorded by Urban & Jones in 1991.

Vibrational band	Branches
$\nu = 1 \leftarrow 0$	P(4), P(5), P(7), P(8), P(9), P(10), P(12), P(13), P(16), R(2), R(3), R(4), R(5), R(8), R(10), R(12), R(13), R(14), R(16), R(17), R(19), R(20)
$\nu = 2 \leftarrow 1$	P(6), P(7), P(9), P(10), R(5), R(8), R(9), R(11), R(13), R(14), R(15), R(16), R(17), R(20)
$\nu = 3 \leftarrow 2$	P(3), P(5), P(6), P(7), R(6), R(7), R(8), R(9), R(10), R(14), R(15), R(17), R(18)

Table 6.5: Branches of the $X^7\Sigma^+$ state for MnD recorded by Urban & Jones in 1991.

Urban & Jones then combined their two studies on MnH and MnD to generate mass-independent Dunham coefficients and mass-scaling factors.

The nuclear hyperfine interaction within MnH was then studied by Varberg (1990, 1991 1992) for his PhD: his measurements were obtained by laser fluorescence excitation spectroscopy with sub-Doppler resolution using a discharge tube to generate MnH. Varberg built on the work on Nevin et al. by measuring the missing spin components in the low J values and corrected any misassignments as necessary for the (0, 0) band of the $A^7\Pi - X^7\Sigma^+$ electronic transition. Varberg speculated the misassignments he found in Nevin's work were due to rapid spin-uncoupling of the $A^7\Pi$ state. From his rotational analysis of the $A^7\Pi - X^7\Sigma^+$ system of MnH he was able to obtain improved rotational and fine structure constants for the $X^7\Sigma^+$ state and also for the $A^7\Pi$ state. Varberg found that certain transitions at low J obeyed the rule $\Delta J = \pm 2$ which is normally forbidden: he speculated that these transitions were due to hyperfine interactions of the Manganese nucleus mixing the electron spin components in the ground state. Using a least-squares fitting procedure, $A^7\Pi - X^7\Sigma^+$ hyperfine splitting were fitted to a hyperfine Hamiltonian and hence 14 hyperfine parameters were determined. Varberg (1990) found that the Fermi-contact interaction, b_F was 11 % lower when measured in the gas phase compared to when measured in an Argon matrix and hence put forward an explanation in terms of bonding and polarization effect of the argon matrix.

More recently, Gordon et al. (2005) have extended the work of Urban & Jones by using a Fourier Transform emission method to measure a much more extensive list of branches for several vibronic transitions for the $X^7\Sigma^+$ state of MnH & MnD and have thus produced improved spectroscopic constants for this state. A summary of the transitions they recorded is shown in table 6.6.

Species	Vibrational transition	Branches
MnH	$\nu = 1 \rightarrow 0$	P(1), P(2), P(3),....P(26), P(27) Q(0), Q(1), Q(2), Q(3) R(1), R(2), R(3),.....R(24), R(25)
	$\nu = 1 \rightarrow 0$	P(2), P(3), P(4),.....P(23), P(24) R(1), R(2), R(3),.....R(23), R(24)
	$\nu = 3 \rightarrow 2$	P(4), P(5), P(6),.....P(17), P(18) R(3), R(4), R(5),.....R(20), R(21)
MnD	$\nu = 1 \rightarrow 0$	P(0), P(1), P(2),.....P(24), P(25) Q(0), Q(2) R(0), R(1), R(2),.....R(36), R(37)
	$\nu = 2 \rightarrow 1$	P(1), P(2), P(3),.....P(21), P(22) R(1), R(2), R(3),.....R(35), R(36)
	$\nu = 3 \rightarrow 2$	P(4), P(5), P(6),.....P(16), P(17) R(4), R(5), R(6),.....R(32), R(33)
	$\nu = 4 \rightarrow 3$	R(10), R(11), R(12),...R(28), R(29)

Table 6.6: Branches recorded by Gordon et al. 2005 using a Fourier-Transform emission experimental set-up for the $X^7\Sigma^+$ state of MnH.

Comparisons of the ground state equilibrium parameters obtained for the $X^7\Sigma^+$ state obtained by Nevin, Urban & Jones and Gordon et al. (2005) for MnH and for MnD are shown in tables 6.7 and 6.8 respectively.

Parameter	Gordon 2005	Urban & Jones 1989	Nevin(1945)	
$Y_{1,0}$	1546.84518(65)	1546.8536(15)	ω_e	1548.0^b
$Y_{2,0}$	-27.59744(39)	-27.6028(91)	$\omega_e\chi_e$	28.8^b
$Y_{3,0}$	-0.309037(67)	-0.30822(15)		
$Y_{0,1}$	5.6856789(103)	5.685795(37)	B_e	5.68548
$Y_{1,1}$	-0.1602038(70)	-0.160488(22)	$\alpha_2 \times 10$	1.6079
$10^4Y_{2,1}$	-1.2(40)	0.405(91)		
$10^4Y_{3,1}$	-3.0252(72)	-3.255(13)		
$10^4Y_{0,2}$	-3.05384(58)	-3.063(30)	$D_e \times 10^4$	3.0315
$10^6Y_{1,2}$	1.397(22)	2.983(68)	$\beta_e \times 10^6$	1.46
$10^7Y_{2,2}$	-2.823(83)	-12.01(16)		
$10^7Y_{3,2}$	-1.225(16)			
$10^9Y_{0,3}$	9.467(128)	8.68(60)	$E_e \times 10^9$	9.10
$10^9Y_{1,3}$	-1.551(48)			
$10^{12}Y_{0,4}$	1.36(89)			
$10^{13}Y_{1,4}$	9.16(39)			
$10^2\gamma_{0,1}$	3.1749(35)	3.2055(83)	γ_e	3.13
$10^4\gamma_{1,1}$	-7.698(54)	-8.32(13)		
$10^5\gamma_{2,1}$	-4.1(101)	-3.4(33)		
$10^6\gamma_{0,2}$	-6.763(53)	-7.54(21)	$\gamma D_e \times 10^6$	$-65(4)^c$
$10^7\gamma_{1,2}$	-2.554(98)			
$10^3\lambda_{0,0}$	-3.758(92)	$-3.35(12)^a$	$\epsilon \times 10^3$	-4.0
$10^4\lambda_{1,0}$	-2.623(117)			
$10^6\lambda_{0,1}$	-5.39(43)	$-0.0195(27)^a$		

Table 6.7: Comparison of equilibrium parameters for the $X^7\Sigma^+$ state of MnH obtained by various experimentalists. In this table, ^{a} indicates a value calculated using $\epsilon_{01} \times 10^3 = -2.234(22)$ and $\epsilon_{02} \times 10^4 = 1.3(18)$ given by Urban & Jones (1989), ^{b} indicates a value taken from Hayes, McCarvill & Nevin 1957 and ^{c} indicates a value taken from Pacher 1974. Numbers in parentheses represent one standard deviation in units of the last digit.

Parameter	Gordon 2005	Urban & Jones 1991	Nevin, Conway & Cranley (1952)
$Y_{1,0}$	1104.65312(51)	1104.65225(93)	1102.0
$Y_{2,0}$	-14.22657(31)	-14.22656(54)	-13.9
$Y_{3,0}$	-0.085848(52)	-0.085813(90)	
$Y_{0,1}$	2.8987214(57)	2.898685(12)	2.89725
$Y_{1,1}$	-0.0581028(33)	-0.0580972(79)	-0.05532
$10^4 Y_{2,1}$	-1.065(20)	-0.943(31)	-0.2698
$10^4 Y_{3,1}$	-0.45(35)	-0.4784(44)	
$10^4 Y_{0,2}$	-0.796939(190)	-0.79584(54)	-0.795
$10^6 Y_{1,2}$	0.2543(41)	0.201(21)	
$10^7 Y_{2,2}$	-0.521(22)	-0.897(40)	
$10^7 Y_{3,2}$	-0.087(38)		
$10^9 Y_{0,3}$	1.5713(197)	1.58(12)	1.03
$10^9 Y_{1,3}$	-0.0957(30)		
$10^2 \gamma_{0,1}$	1.6234(30)	1.6388(67)	
$10^4 \gamma_{1,1}$	-3.026(37)	-2.954(76)	
$10^5 \gamma_{2,1}$	-0.831(99)	-1.03(18)	
$10^6 \gamma_{0,2}$	-1.968(39)	-2.19(13)	
$10^3 \lambda_{0,0}$	-1.823(55)	-1.44(21)^a	
$10^4 \lambda_{1,0}$	-1.17(11)	-1.33(19)^a	
$\alpha_{01} \times 10^4$		-9.6(14)	
$\alpha_{11} \times 10^5$		-8.9(13)	

Table 6.8: Comparison of equilibrium parameters for the $X^7\Sigma^+$ state of MnD obtained by various experimentalists. In this table, [a] indicates that the value in question was calculated from the values of $\alpha_{0,1}$ and $\alpha_{1,1}$ listed by Urban & Jones 1991. Numbers in parentheses represent one standard deviation in units of the last digit.

Additionally, Gordon et al.(2005) estimated the Born-Oppenheimer breakdown constants, $\delta^H_{l,m}$ using the Le Roy formalism. Using their recorded transitions, Gordon et al. (2005) obtained equilibrium parameters for MnH and MnD using a Dunham-type fit using the program SPFIT for MnH and MnD. For MnD they did not include the data for the $\nu = 4 \rightarrow 3$ transitions as most of these were heavily blended and thus distorted the fit.

The most recent experimental study of the $A^7\Pi - X^7\Sigma^+$ system is that of Gengler et al. (2007) who have measured and rotationally analysed the (0, 0) band using a laser-induced fluorescence (LIR) technique to an accuracy of ± 0.003 cm^{-1}.

As well as the $A^7\Pi - X^7\Sigma^+$ transition of MnH lying around 568 nm been of interest, there is also quintet manifolds which have been studied by Balfour and co-workers (1988, 1990, 1992) using the technique of Fourier-Transform Spectroscopy. Balfour (1988) studied both MnH and MnD in emission from a King furnace at 1850 K in the region of 11 250 $-$ 12 250 cm^{-1} with an estimated Doppler linewidth of 0.04 cm^{-1}. Their spectra showed 10 distinct P and R branches which they deduced to be from a $^5\Sigma^+ - ^5\Sigma^+$ transition and hence for $\nu = 0$ they determined B, D and r_e constants for these two electronic states. Balfour et al. (1990) then analysed the systems around 846 nm and 1060 nm in both MnH and MnD: they concluded that both of these systems have a common lower ground state. They assigned these two systems as corresponding to $c^5\Sigma^+ - a^5\Sigma^+$ and $b^5\Pi - a^5\Sigma^+$ respectively. Finally Balfour et al. (1992) undertook a study of the 450 nm ($e^5\Sigma^+ - a^5\Sigma^+$) and 480 nm ($d^5\Pi - a^5\Sigma^+$) of MnH and and also the 480 nm system of MnD. Table 8.7 summarises the quintet bands studied by Balfour and co-workers.

Theoretically, in the absence of coupling, transitions between quintet and septuplet states are spin-forbidden transitions. However, experimental work has been undertaken to determine the energy gap between the $X^7\Sigma^+$ and $a^5\Sigma^+$ electronic states. Stevens et al. (1983) undertook a laser photoelectric spectroscopy study of both MnH^-, MnD^-, FeH^- and FeD^- as part of a larger experimental study of electronic structure of metal hydrides. Their motivation for studying MnH^- and MnD^- was as a "stepping stone" to shedding light on the electronic structure of FeH which they describe as been a "formidable challenge". The key result of their work is their determination that the $a^5\Sigma^+$ state lies 1725 ± 50 cm^{-1} above the $X^7\Sigma^+$ state.

6.3 Experimental and Observational work undertaken by Ziury's Group

Lucy Ziurys leads a group of experimentalists at the University of Arizona. Over the years from the mid-ninties this group has studied experimentally the rotational structure of many diatomic molecules and ions and thus provided data in the millimeter and submillimeter regions which can be used for detection. These diatomic molecules include hydrides, halides, nitrides, oxides and sulphides. Table 6.9 shows a sample of molecules and ions studied by the Ziury's group.

Group	Species	Electronic state
Metal Hydrides	AlH	$X^1\Sigma^+$
	CrH	$X^6\Sigma^+$
	MnH	$X^7\Sigma^+$
	MgH	$X^2\Sigma^+$
	CaH	$X^2\Sigma^+$
	KH	$X^1\Sigma^+$
Metal ions	VCl^+	$X^4\Sigma^-$
	$TiCl^+$	$X^3\Phi_r$
	TiF^+	$X^4\Phi_r$
	$FeCO^+$	$X^4\Sigma^-$
	SH^+	$X^3\Sigma^-$
Metal halides	MnCl	$X^7\Sigma^+$
	ZnF	$X^2\Sigma^+$
	ZnCl	$X^2\Sigma^+$
	$TiCl^+$	$X\Phi_r$)
	VCl^+	$X^4\Sigma^-$
Cyanides	$^{52}Cr^{12}C^{14}N$	
	$^{53}Cr^{12}C^{14}N$	$X^6\Sigma^+$
	$^{52}Cr^{13}C^{14}N$	
	HZnCN	$X^1\Sigma^+$
	ZnCN	$X^2\Sigma^+$
	AlNC	$X^1\Sigma^+$
	CoCN	$X^3\Phi_i$

Table 6.9: Summary of metal Hydrides, ions, halides and cyanides which have been studied experimentally by the Ziurys group for the purposes of astronomical detections.

As well as provide data for astronomers, the group has also actively made searches for molecules using the IRAM 30 m telescope based at the Arizona Radio Observatory.

Halfen et al. (2005) note that in the Inter-stellar medium (ISM) both neutral and ionic forms of diatomic hydrides are basic building blocks of the interstellar chemistry and comment that refractory elements in dense gas may be "carried" by ionic forms of diatomic hydrides. Before 2005 there was scant high resolution data available for metal hydride species hence their motivation to study them. The authors note that this data is essential for the long-term success of missions such as SOFIA and HERSCHEL. SOFIA, which is a collaboration between NASA and the German Aerospce Centre (DLR) is a specially modified Boeing 747-SP aeroplane which has on board a 2.5 m diameter reflecting telescope. SOFIA is at present studying many astrophysical settings including regions of star birth & death, nebulae, dust in galaxies, planets, comets and is been used to identify complex molecules in space. SOFIA operates in the near, mid and far infrared. The Herschel spacecraft (2009-2013) studied the sub-millimetre and far infra-red regions: regions in which diatomic hydride molecules tend to produce spectra.

As a side note, well as diatomic molecules, the Ziurys group has also searched for organic molecules including Glycolaldehyde ($HOCH_2$-CH=0) which, along with Formeldehyde (CH_2O) is an important molecule in the formation of life on earth. Their search for Glycolaldehyde was conducted using the ARO 12m telescope operating 2/3 mm aimed at the molecular cloud Sgr B2(N) positioned in the galactic centre of the Milky Way (Halfen, Apponi & Ziurys 2005). The conclusion of their work was that Formaldehyde may be a precursor to Glycolaledhyde.

6.3.1 Manganese bearing diatomics studied by the Ziurys' Group

The Ziurys group has extensively studied Manganese-bearing diatomics. Sheridan & Ziurys (2003) have studied the diatomic molecule of Manganese Fluoride (MnF) using millimeter/sub-miliitmeter absorption methods they measured the pure rotational spectrum of its' $X^7\Sigma^+$ ground state and thus determined rotational, spin-rotational, spin-spin and hyperfine parameters. They comment that "some of the most complicated spectra of molecules containing 3d transition metals are those with Manganese" and go on to explain how the nuclear spin of $I_1 = 5/2$ for ^{55}Mn requires that a hyperfine analysis is usually required to resolve and assign any spectra of molecules containing Manganese. The nuclear spin of ^{19}F is $I_2 = 1/2$ hence, to a first approximation, every rotational transition in MnF ($X^7\Sigma^+$) is split into $(2S+1)(2I_1+1)(2I_2+1) = 7(6)(2) = 84$ separate fine/hyperfine components. They found that as the spin-interactions are small the spacing between them becomes insignificant so hence the resultant spectrum is almost continuous and hard to resolve. Similarly for MnO, MnS and MnCl a full hyperfine analysis was needed to resolve transitions when their rotational spectra were measured by Namiki & Saito (1997), Thompsen, Brewster & Ziurys (2002) and Launila (1992) respectively. This is consistent with the finding of Varberg (1992) who found the hyperfine interactions to be substantial in MnH. By examining the Fermi contact term, b_F and the dipole c constant for various Manganese-bearing compounds as shown in table 6.10, Sheridan & Ziurys have tentatively concluded that there is a decrease in ionic character going down a column in the periodic table (i.e. Mn0/MnS, MnF/MnCl). From the diatomic

compounds presented in table 6.10, it can be seen that MnH and MnS are the most covalent in character and MnO the most ionic in character.

Molecule	Ground State	b_F (MHz)	c (MHz)	Reference
MnH	$X^7\Sigma^+$	279(1)	36.0(2.4)	Varberg, Field & Merer (1991)
MnF		431.615(30)	35.584(3)	Sheridan & Ziurys (2003)
MnCl		376(11)	-102(30)	Baumann, Van Zee & Weltner (1982)
MnO	$X^6\Sigma^+$	479.861(100)	-48.199(178)	Namiki & Saito (1997)
MnS		206.51(79)	-27.8(1.6)	Thompsen, Brewster & Ziurys (2002)

Table 6.10: Hyperfine parametes for Manganese-bearing diatomic molecules

To date, no *ab initio* calculations have been done on MnF. However, experimentally, $A^7\Pi - X^7\Sigma^+$, $b^5\Delta - a^5\Sigma^+$, $c^5\Sigma^+ - a^5\Sigma^+$ and $d^5\Pi - a^5\Sigma^+$ have been recorded by Launila, Simard and collaborators.
In 2008, Halfen & Ziurys measured the sub-millimeter spectrum of both MnH and MnD for the ground $X^7\Sigma^+$ state. They created the respective species for study by reacting Manganese vapour with H_2 and D_2 using a DC discharge. The authors measured the $N = 0 \rightarrow 1$ transition of MnH near 339 GHz and the $N = 2 \rightarrow 3$ transition of MnD near 517 GHz with a precision of $\pm$100 kHz. Experimentally, up to 70 scans needed to be averaged for the authors to obtain a signal-to-noise ratio which they deemed to be adequate. From their analysis they produced refined hyperfine structure and rotational constants.

Hence in summary, Manganese bearing diatomics have been extensively studied by the Ziury's group in anticipation that they are indeed to be discovered in space and could inform important constituents of ISM chemistry.

6.4 Concluding Remarks

Theoretically, MnH has been studied by several authors who have calculated PECs, DMCs and TDMs for low-lying electronic states. As for CrH, it acts as a "playground" in which to test out different theoretical approaches. From an experimental perspective, MnH is clearly a molecule of fascination due to its inherent and complicated fine, rotational and hyperfine structures which have been found to perturb each other. The $A^7\Pi - X^7\Sigma^+$ system has been studied by several experimental groups since the 1930s and molecular parameters for these states progressively refined for both MnH and MnD. Balfour and co-workers have recorded measured transition frequencies for the $e^5\Sigma^+(II) - a^5\Sigma^+$, $d^5\Pi - a^5\Sigma^+$, $c^5\Sigma^+(I) - a^5\Sigma^+$ and $b^5\Pi - a^5\Sigma^+$ systems of MnH and MnD. As will be explained in chapter 8 these experimental measurements were used in our linelist for MnH along with *ab initio* calculations which are presented in chapter 7. As validation for making the effort to produce a linelist for MnH (at present there is not a linelist available in the literature), it should be noted that Manganese bearing diatomics have been studied by the Ziurys experiemental group with the aim of detecting these species in space. Also, the universal abundance of Manganese is approximately half that of Chromium, (see table 3.1). The universal abundance of Iron is around 75 times that of Chromium. Given these pieces of information, it seems plausible that Manganese bearing compounds could, and should indeed be detected

in space. If MnH was to be detected in space, there are possibilities for work to be done in finding applications such as measuring the stellar magnetic fields or to play a role in the "deuterium test" for which CrH has been shown to potentially of use (see section 3.4).

Chapter 7

Ab initio Calculations for MnH

In this chapter the *ab initio* calculations performed for MnH will be presented. Section 7.1 gives an overview of the CASSCF state-combination testing which was undertaken. In these CASSCF calculations different combinations of states were taken; a CASSCF calculation was performed for the corresponding PECs and DMCs. The results of these calculations are shown in appendix C. In contrast to the case for CrH, it was found that increasing the number of states in a CASSCF calculation improved the quality of the PECs and DMCs obtained. Hence it was decided for the proceeding MRCI calculations to use a CASSCF state-combination which combined the 8 lowest-electronic states of MnH: this is referred to throughout the chapter as "ABC-DEF" where the components A, B, C, D, E and F are described in table 7.1. In section 7.2 the *ab initio* calculations performed using this proceeding CASSCF state-combination are presented. For reference MRCI calculations which built upon different CASSCF state-combinations are presented to demonstrate again that the details of CASSCF calculations (which feed into MRCI calculations) cannot be "swept under the carpet". For MnH, the active space used was found to be crucial in determining the properties of PECs: two active spaces are defined, "LOWER" and "UPPER" (see section 2.7.8). Indeed the behaviour of the $A^7\Pi$ state changed dramatically when using the "UPPER" active space. Additionally, as was the case for CrH, the number of states calculated with a particular multiplicity and symmetry at MRCI level of theory had an effect on the behaviour of *ab initio* curves.

7.1 CASSCF testing

As was stated in section 4.3, before running any calculations at MRCI level, it is imperative to obtain good quality CASSCF orbitals to use as input for proceeding CI calculations. As was the case for CrH, extensive testing at CASSCF level of theory was undertaken.

Refer back to table 2.11 in section 2.7.7 which lists out the molecular states of interest for MnH. It was decided to run CASSCF test calculations which included the lowest lying $^7\Sigma^+$ and $^5\Sigma^+$ states as it was known from the experimental literature that both the quintet and septuplet manifolds of MnH are of sufficient intensity for observation. The variations in CASSCF orbitals were then obtained by taking combi-

nations of the 6 states which dissociate to the a^6D dissociation limit, $E_0 = 17\,301.21$ cm^{-1}, i.e. $^5\Sigma^+$, $^5\Pi$, $^5\Delta$, $^7\Sigma^+$, $^7\Pi$ and $^7\Delta$. Table 7.1 lists out these states and summarises the colour scheme and letter assigned to each one which is used in the results section in appendix C. Referring back to section 2.7.8, the active space hence used for these CASSCF calculations was 9331/5220 i.e. an "occupied space" of 9331 and a closed space of 5220 as defined within the C_{2v} symmetry framework. All of these CASSCF orbital testing calculations were carried out using a cc-pVQZ basis.

State	Colour in plots	"Letter" used in CASSCF calculations	"wf card"
$X^7\Sigma^+$	RED	Included in all CASSCF test calculations	26, 1, 6
$a^5\Sigma^+$	BLACK		26, 1, 4
$^5\Sigma^+$	GREEN	A	26, 1, 4
$^5\Pi$	BLUE	B	26, 2, 4 26, 3, 4
$^5\Delta$	CYAN	C	26, 1, 4
	DARK GREEN		26, 4, 4
$^7\Sigma^+$	MAGNETA	D	26, 1, 6
$^7\Pi$	ORANGE	E	26, 2, 6 26, 3, 6
$^7\Delta$	INDIGO	F	26, 1, 6
	MAROON		26, 4, 6

Table 7.1: Table summarising the list of states used in combination to test out CASSCF orbitals for MnH.

It should be noted that the relevant "wf" cards are additive as was explained in section 2.7.6.

It should be noted that before any CASSCF orbital testing calculations were carried out, it was unknown what order the various Σ and Δ states for a given multiplicity (i.e. for MnH these are quintet, septuplet and nonuplet) lay in. All possible combinations of the letters A, B, C, D, E and F were tested out. A summary of these combinations with references to relevant plots is given in table 7.3 with the number of converged points (out of the possible 88 as defined in the inter-nuclear distance grid, see section 2.7.1) given. A brief comment about quality of the orbitals as indicated by the continuity of the PECs and DMCs calculated at CASSCF level of theory is given in table 7.2 for cases where the ground $a^5\Sigma^+$ and $X^7\Sigma^+$ states were combined with a single component defined in table 7.1.

Combination	Ref	P.C (/88)	Notes
GROUND	C.1a, C.1b	84	Gap in DMCs at 2.5 Å of 3.5 Debye for the $X^7\Sigma^+$ state and 3.0 Debye for the $a^5\Sigma^+$ state.
A	C.3a, C.3b	80	There is an obvious gap in convergence between 2.3 and 2.4 Å, spurious points at 2.5 and 2.7 Å and between 2.5 and 2.6 Å there is also a "jump".
B	C.3c C.3d	87	In the PEC at 2.5 Å there is a jump of around 1000 cm^{-1} for the $X^7\Sigma^+$ state. In the DMC there is a jump at 2.5 Å for the $a^5\Sigma^+$ of around 4.0 Debye, 2.75 Debye for the $X^7\Sigma^+$ state and 1 Debye for the $^5\Pi$ state.
C	C.3e C.3f	85	In the PEC at 2.4 Å there is an obvious jump of around 1000 cm^{-1}. In the DMC there is a jump at 2.5 Å for the $a^5\Sigma^+$ of around 3.5 Debye and 1.5 Debye for the $X^7\Sigma^+$ state.
D	C.6a, C.6b	88	For the PEC of the second septuplet state of symmetry 1 there is jump of around 1000 cm^{-1} at 3.5 Å. For the DMC of the second septuplet state of symmetry 1 there is jump between -12 Debye and 0 Debye at 3.5 Å.
E	C.6c, C.6d	89	Both PEC and DMC are continuous.
F	C.6e, C.6f	88	For the PEC between 3.1 Å and 3.2 Å there is an obvious jump in all PECs. For the DMC of the second septuplet state of symmetry 1 there is jump between -12 Debye and 0 Debye at 3.2 Å.

Table 7.2: Summary of results for CASSCF orbital testing for MnH for the case of adding a single component defined in table 7.1 with the ground $a^5\Sigma^+$ and $X^7\Sigma^+$ states. For the graphs showing these PECs and DMCs, and for all other combinations of states tested at CASSCF level, see appendix C.

In summary, as can be seen from table 7.2, combining a single component as defined in table 7.1 with the $a^5\Sigma^+$ and $X^7\Sigma^+$ states produces poor quality discontinuous PECs and DMCs at CASSCF level of theory. Looking through the results in section C it can be seen that there is a general trend in improvement of the continuity of the PECs and DMCs as more states are added: hence this indicates that the CASSCF orbitals are of higher quality and thus more likely to produce continuous CI curves.

AB	C.7a, C.7b	82	ABC	C.12a, C.12b	86	ABCD	C.21a, C.21b	88
AC	C.7c, C.7d	84	ABD	C.14a, C.14b	87	ABCE	C.21c, C.21d	88
AD	C.7e, C.7f	86	ABE	C.14c, C.14d	88	ABCF	C.21e, C.21f	88
AE	C.5a, C.5b	88	ABF	C.14e, C.14f	80	ABDE	C.22a, C.22b	88
AF	C.5c, C.5d	86	ACD	C.15a, C.15b	84	ABDF	C.22c, C.22d	88
			ACE	C.15c, C.15d	88	ABEF	C.22e, C.22d	87
			ACF	C.15e, C.15f	87	ACDE	C.23a, C.22f	88
			ADE	C.16a, C.16b	88	ACDF	C.23c, C.23d	87
			ADF	C.16c, C.16d	88	ACEF	C.23e, C.23f	88
			AEF	C.16e, C.16f	84	ADEF	C.25a, C.25b	88
BC	C.4a, C.4b	80	BCD	C.17a, C.17b	88	BCDE	C.24a, C.24b	88
BD	C.8a, C.8b	88	BCE	C.17c, C.17d	87	BCDF	C.24c, C.24d	88
BE	C.8c, C.8d	88	BCF	C.17e, C.17f	87	BCEF	C.24e, C.24f	88
BF	C.8e, C.8f	88	BDE	C.13a, C.13b	88	BDEF	C.25c, C.25d	88
			BDF	C.13c, C.13d	88	CDEF	C.25e, C.25f	87
			BEF	C.18a, C.18b	86	ABC-DE	C.26a, C.26b	88
CD	C.9a, C.9b	73	CDE	C.20a, C.20b	88	ABC-DF	C.26c, C.26d	88
CE	C.9c, C.9d	88	CDF	C.19c, C.19d	88	ABC-EF	C.26e, C.26f	88
CF	C.9e, C.9f	88	CEF	C.18c, C.18d	88	ABD-EF	C.27a, C.27b	88
DE	C.10a, C.10b	88	DEF	C.18e, C.18f	88	ACD-EF	C.27c, C.27d	88
DF	C.10c, C.10d	88				BCD-EF	C.27e, C.27f	88
EF	C.11a, C.11b	88				ABC-DEF	C.2a, C.2b	88

Table 7.3: Summary of the CASSCF orbitals tested formed by combinations of the components (i.e. states) defined in table 7.1.

In summary, it was decided to use CASSCF orbitals that combined all the lower 8 electronic states (see table 2.11 in section 2.7.7): this corresponds to using all 6 components defined in table 7.1. Generally speaking, the quality of a CASSCF calculation should improve as more states are added which was indeed what was found for MnH. Physically, it makes sense to include all the electronic states which are desired within any CASSCF calculations which are used to generate orbitals for proceeding MRCI calculations. In summary the "wf" cards used during the CASSCF part of the calculations for MnH (refer back to section 2.8 which explains how there are two parts to a CI calculation: CASSCF part following by the CI part) are as shown in table 7.4.

"wf" card	Electonic States
26, 1, 6; state 3 26, 2, 6 26, 3, 6	$X^7\Sigma^+$, $^7\Sigma^+(II)$, $^7\Delta$ (symmetry 1) $^7\Pi$
26, 4, 6	Symmetry 4 component of $^7\Delta$ state
26, 1, 4; state 3 26, 2, 4 26, 3, 4	$a^5\Sigma^+$, $^5\Sigma^+(II)$, $^5\Delta$ (symmetry 1) $^5\Pi$
26, 4, 4	Symmetry 4 component of $^5\Delta$ state

Table 7.4: Summary of "wf" cards with corresponding states used for proceeding CI calculations for MnH.

As can be seen from Appendix C, there are several other state-combinations which produce continuous curves. For reference these have been used in the proceeding section which discusses the CI results for the purposes of comparison of how different state-combinations within CASSCF calculations affects the results of proceeding CI

calculations.

7.2 MRCI results of MnH

As for the case of CrH, CI calculations were performed using the orbitals generating in proceeding CASSCF calculations. Before discussing results, it is important to reiterate and define some notation which will be used throughout the proceeding section:

- The CASSCF orbitals used will be referred to as the components defined in table 7.1, i.e. "AB", ABC" etc.
- Refering back to section 7.1, the occupied and closed orbitals for the CASSCF calculations used was 9331/5220.
- For the CI calculations there was a choice in which closed and occupied orbitals to use: referring back to section 2.7.8 the two choices were 9331/5220 (hereafter denoted as "LOWER active space") and 10441/5220 (hereafter denoted "UPPER active space".
- For the calculation of Σ^+ and Δ states within a given multiplicity (e.g. quintet, septuplet), a "3+1" calculation signifies that three states were calculated within symmetry 1 and one state calculated within symmetry 4. The curves are then labelled accordingly on the graph legends as, for example for septuplet states: "7, symmetry 1, state 1"; "7, symmetry 1, state 2"; "7, symmetry 1, state 3" and "7 symmetry 4".

For the final linelist it was decided to use MRCI calculations which were built upon CASSCF state-combination calculation of "ABC-DEF" (i.e. the first 8 low-lying electronic states). The figures presented in the remainder of this chapter show these figures. Comparison has however been made with MRCI calculations built upon other CASSCF state-combinations to demonstrate and emphasize that the CASSCF state-combination used is of significant importance: it cannot be ignored as is commonly done in published MRCI calculations.

7.2.1 Potential Energy Curves

Initially, PECs and DMCs were calculated for both available active spaces in order to determine the relative order of the states within each multiplicity. As was the case for CrH, all potential energies have been converted from Hartrees to cm^{-1} with the PECs normalised to the lowest lying electronic state to allow relative comparison of the energies. Initially the "LOWER active space" was used for CI calculations of the 8 lowest electronic states (i.e. the electronic states that dissociate to the a^6S and a^6D atomic dissociation limits of manganese as defined in table 2.11 in section 2.7.7). However, it was realised that this active space produced an anti-bonding (i.e. dissociative) curve for the $^7\Pi(I)$ state: since there have been experimental studies in which bound transitions have been measured for the $^7\Pi - X^7\Sigma^+$ transition, it was concluded that this "LOWER active space" was not sufficient for calculating the

correct behaviour of the various electronic states. Using the "UPPER active space" this problem was remedied and this also allowed calculation of electronic states higher up in energy (i.e. the nonuplet states, see table 2.11). Figure 7.1 shows the PECs calculated using the "LOWER active space" for the lowest lying eight electronic states of MnH.

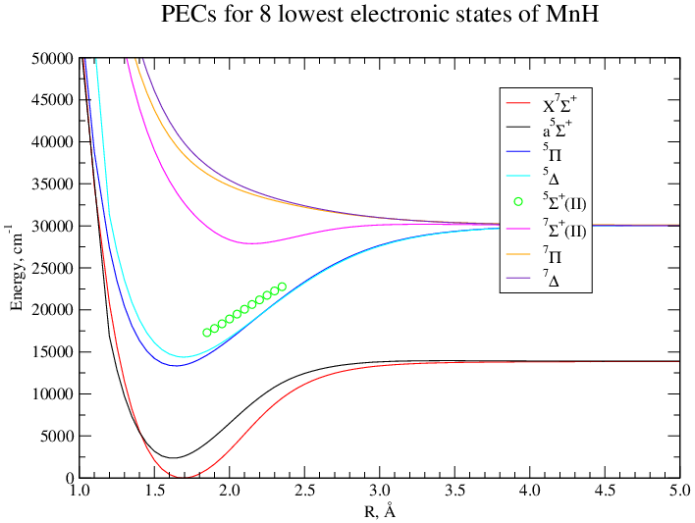

Figure 7.1: PECs curves for the lowest-lying 8 states of MnH calculated using a cc-pVQZ basis set at CI level using the "LOWER active space" for the CI calculations as defined in section 2.7.8. These CI calculations are based on orbitals generated by combining states ABC-DEF as defined in tabel 7.1.

PECs for quintet states

For the calculation of quintet Σ^+ and Δ states, a 3+1 calculation was performed at CI level, i.e. 3 states were calculated in symmetry 1 and one state in symmetry 4. As can be seen, the relative order of the quintet states appears to be $a^5\Sigma$, $^5\Pi$, $^5\Delta$ followed by $^5\Sigma^+(II)$ state. The identity of the $^5\Delta$ state was deduced by comparing the energies calculated in symmetry 1 with that calculated in symmetry 4; the energy corresponding to the second state of symmetry 1 was numerically similar to that calculated in symmetry 4. As can be seen, fewer points converged for the $^5\Sigma^+(II)$ state. For clarity, figure 7.1 shows the results of a 2+1 calculation for the $a^5\Sigma$, $^5\Pi$ and $^5\Delta$ states and the results of the 3+1 calculation for $^5\Sigma^+(II)$. The variation between the results of the 2+1 and 3+1 calculations for these low-lying states is minimal and does not affect the relative energy order. The lower-lying quintet states were assigned in figure 7.1 as $a^5\Sigma^+$, $b^5\Pi$, $c'^5\Delta$ and $c^5\Sigma^+$ (to keep in line with previously discovered experimentally-named electronic states). It should be noted that this relative ordering of quintet states did not change when using the "UPPER" active space: what did change was that the number of points converging for the $c^5\Sigma^+$ state did increase. This is shown in figure 7.2.

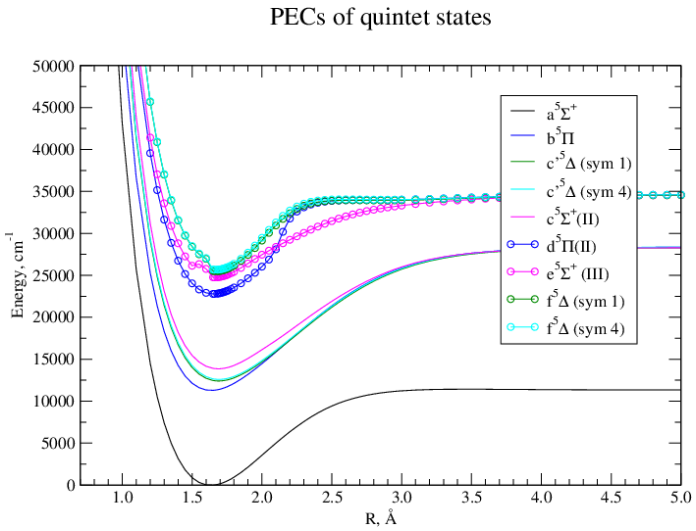

Figure 7.2: Calculation of PECs of quintet states at MRCI level of theory using a cc-pVQZ basis set, the "UPPER active space" and a CASSCF state-combination of ABC-DEF . The PECs shown here for the $a^5\Sigma^+$, $c'^5\Delta$ and $c^5\Sigma^+(II)$ states were calculated using a 3+1 calculation at MRCI level of theory. The PECs for the $e^5\Sigma^+(III)$ and $f^5\Delta$ states were calculated using a 5+2 calculation. Finally the PECs for the $b^5\Pi$ and $d^5\Pi(II)$ states were calculated using one-state and two-state calculations respectively.

Refer back to table 2.11. Since there is experimental data available for the $d^5\Pi$ and $e^5\Sigma^+$ states, it was decided to calculate the PECs, DMCs of these states and the relevant TDMs linking them to the lower quintet states. These curves were also calculated for the $f^5\Delta$ state which dissociates to the same atomic limit as the $d^5\Pi$ and $e^5\Sigma^+$ states. Figure 7.2 shows the calculation of the PECs of these upper quintet states. Table 7.5 gives a summary of PEC properties determined for the various quintet states when the basis set, the CASSCF state-combination and number of states at MRCI level of theory is varied.

State	MRCI	8	7	8	7	8	7	8	7	8	7	8	7
		cc-pVQZ		aug-cc-pVQZ		cc-pVQZ		aug-cc-pVQZ		cc-pVQZ		aug-cc-pVQZ	
		R_e (Å)				D_e (cm^{-1})				E ($\nu = 1$) (cm^{-1})			
$a^5\Sigma^+$	1+0	1.624(4)	1.624(5)	1.624(4)	1.624(2)	11103	10776	11619	11286	1693	1661	1717	1689
$a^5\Sigma^+$	2+1	1.624(3)	1.625(3)	1.625	1.624(2)	11121	10801	11653	11327	1691	1660	1711	1684
$a^5\Sigma^+$	3+1	1.633(3)	1.635(5)	1.633	1.634(1)	11371	11111	11893	11620	1641	1622	1662	1644
$a^5\Sigma^+$	4+0	1.648(2)	1.630(1)	1.633	1.633(3)	11383	11162	11915	11646	1627	1613	1640	1619
$a^5\Sigma^+$	5+2	1.639(2)	1.631(4)	1.620(2)	1.664(2)	11454	11210	12030	11664	1629	1618	1663	1626
$c'^5\Delta$(sym 4)	2+1	1.692(4)	1.687(4)	1.694	1.688(5)	15788	15817	15828	15842	1484	1481	1493	1488
$c'^5\Delta$(sym 4)	5+2	1.683(1)	1.681(2)	1.684(1)	1.680(5)	15989	16009	16086	16070	1514	1507	1528	1523
$c'^5\Delta$(sym 1)	2+1	1.690(3)	1.685(2)	1.692	1.687(3)	15889	15876	15926	15902	1486	1483	1494	1491
$c'^5\Delta$(sym 1)	3+1	1.690(5)	1.685(4)	1.692	1.686(4)	15910	15899	15954	15932	1485	1483	1492	1490
$c'^5\Delta$(sym 1)	4+0	1.673(1)	1.658(1)	1.684(5)	1.680(5)	16083	16011	16110	16091	1499	1486	1534	1526
$c'^5\Delta$(sym 1)	5+2	1.682(5)	1.680(5)	1.676(3)	1.678(7)	16058	16038	16165	16095	1494	1486	1490	1489
$c^5\Sigma^+(II)$	3+1	1.688(5)	1.689(5)	1.691(1)	1.692(5)	14459	14208	13941	13583	1486	1461	1517	1484
$c^5\Sigma^+(II)$	4+0	1.694(1)	1.683(1)	1.688(5)	1.753(1)	14685	14424	14019	13716	1516	1501	1512	1487
$c^5\Sigma^+(II)$	5+2	1.674(5)	1.676(2)	1.620(1)	1.682(1)	14721	14461	14340	13919	1513	1500	1565	1518
$e^5\Sigma^+(III)$	4+0	1.694(1)	1.683(1)	1.785(1)	1.754(1)	9855	9443	8960	8769	1746	1700	1672	1592
$e^5\Sigma^+(III)$	5+2	1.656(2)	1.665(2)	1.615(1)	1.682(1)	9820	9437	9894	8969	1600	1606	1680	1602
$f^5\Delta$ (sym 1)	5+2	1.678(1)	1.672(3)	1.615(1)	1.682(1)	9088	8808	10218	8496	1982	1932	1875	1862
$f^5\Delta$ (sym 4)	5+2	1.677(3)	1.677(3)	1.669(2)	1.662(2)	8953	8579	8721	8287	1988	1972	2027	2066
$b^5\Pi$	1 SC	1.637(3)	1.631(4)	1.639(4)	1.633(3)	17096	17094	17123	17118	1559	1563	1556	1560
$b^5\Pi$	2 SC	1.635(4)	1.630(3)	1.637	1.648(1)	17300	17292	17230	17209	1565	1568	1522	1534
$d^5\Pi(II)$	2 SC	1.653(2)	1.657(5)	1.754(1)	1.714(1)	11841	11628	8712	8399	1644	1646	1669	1850

Table 7.5: Summary of properties determined for PECs of quintet states calculated using various number of states at MRCI level of theory using a choice of two basis sets and two CASSCF state-combinations. The two basis sets tested were "cc-pVQZ" and "aug-cc-pVQZ". In this table, "8" refers to the CASSCF state-combination of ABC-DEF and "7" refers to the CASSCF state-combination of "BC-DEF". These PEC properties have been determined using the procedure described in section 2.9.2.

For the case of the $a^5\Sigma^+$ state, table 7.5 can be compared to table 7.6 which gives a summary of previously determined spectroscopic properties for this state from both experimental and theoretical studies. For the R_e value of the $a^5\Sigma^+$ state the

Study	Method	R_e (Å)	ω_e (cm^{-1})
Stevens et al. (1983)	Experiment	1.605(20)	1720 ± 55
Balfour 1988		1.638(r_0)	
Balfour et al. (1990)		1.624 631(51)	
Huber & Herzberg (1979)		1.628	1623
Varberg et al. (1992)		1.6383(r_0)	
Gengler et al. (2007)		1.8381(r_0)	
Langhoff et al. (1989)	MR-SDCI+Q		1549.9
Wang & Andrews (2003)	BPW91/6-311++G (d,p)	1.590	1739.1 (20)
	BPW91/6-311++G (3df,3pd)	1.588	1727.5 (17)
	B3LYP/6-311++G (d,p)	1.590	1612.4 (195)
	B3LYP/6-311++G (3df,3pd)	1.644	1604.5 (189)
Tomonari, Nagashima & Hirano(2009)	13-ref CI+Q	1.6527	1559
	15-ref CI+Q	1.6505	1560
	17-ref CI+Q	1.6501	1559

Table 7.6: Summary of spectroscopic properties determined in previous experimental and theoretical studies for the $a^5\Sigma^+$ state.

experimental studies cumulatively predicted it to be in the range 1.605 and 1.628 Å. The past theoretical predictions varying in the range from 1.588 and 1.6527 Å: By inspection of table 7.5 it can be seen that the R_e values obtained in this study generally lie in this upper range. It can also be seen that for the 1+0, 2+1 and 3+1 calculations, the variation between the two basis sets and CASSCF state-combinations is of order 0.02 Å: going to higher-order MRCI calculations produces more erratic predictions. There are no published D_e values to compare against (bear in the mind the ground state of MnH is $X^7\Sigma^+$) for this $a^5\Sigma^+$ state. Table 7.6 shows that the PECs in this study had D_e values in the range from 10776 to 12030 cm^{-1}. Theoretically, the $a^5\Sigma^+$ and the $X^7\Sigma^+$ states dissociate to the same dissociation limit. Taking the value of the gap between the $a^5\Sigma^+$ state and the $X^7\Sigma^+$ state determined by Stevens et al. (1983) of 1725 ± 50 cm^{-1} and adding this to the D_e values of the $a^5\Sigma^+$ state determined gives a prediction of D_e of the $X^7\Sigma^+$ state of been between 12 451 and 13 805 cm^{-1}. Referring to table 7.10 this value can be compared to previous theoretical predictions of 8669, 13470, 13550, 13792, 13873 and 15325 cm^{-1}. This is obviously a huge range in D_e but it seems that we are consistent with several of the studies. From table 7.9 it can be seen that our predications for D_e of the $X^7\Sigma^+$ state lie in the range 13267 to 14613 cm^{-1}. Given Steven's value the lower half of this range is consistent with the range predicted for D_e of the $a^5\Sigma^+$ state. Table 7.6 presents previously predicted ω_e values for the $a^5\Sigma^+$ state which have a range of 170 cm^{-1}. This is consistent with the variability found in the energy values of the $\nu = 1$ state as shown in table 7.5 which range between 1626 and 1717 cm^{-1}.

For the other quintet states, an examination of table 7.5 reveals the following features:

- For the $b^5\Pi$ and $c'^5\Delta$ states the R_e values obtained using the CASSCF state

combination of BC-DEF is generally lower than when using the ABC-DEF state-combination: the effect of augmentation of the basis set is to increase the predicted R_e.

- The D_e values for the individual states are in ranges shown in table 7.7:

State	Range in D_e (cm^{-1})	Variability (cm^{-1})
$a^5\Sigma^+$	10776 - 12030	1254
$b^5\Pi$	17096 - 17300	204
$c^5\Sigma^+(II)$	13583 - 14721	1138
$c'^5\Delta$	15788 - 16165	377
$d^5\Pi(II)$	8399 - 11841	3442
$e^5\Sigma^+(III)$	8769 - 9894	1125
$f^5\Delta$	8287 - 10218	1931

Table 7.7: Range in D_e values calculated for individual quintet states.

It is striking that the $b^5\Pi$ and $c'^5\Delta$ states seem the most tightly constrained compared to the $^5\Sigma^+$ states which have a large variation depending on how many of them are calculated at MRCI level of theory.

- The corresponding ranges in the $\nu = 1$ energy vibronic energy levels for each electronic state are shown in table 7.8.

State	Range in $E(\nu = 1)$ (cm^{-1})	Variability (cm^{-1})
$a^5\Sigma^+$	1613 - 1717	104
$b^5\Pi$	1522 - 1568	46
$c^5\Sigma^+(II)$	1461 - 1518	57
$c'^5\Delta$	1481 - 1534	53
$d^5\Pi(II)$	1644 - 1850	206
$e^5\Sigma^+(III)$	1592 - 1700	108
$f^5\Delta$	1862 - 2066	204

Table 7.8: Range in $E(\nu = 1)$ energy levels for individual quintet states calculated.

As was the case for the D_e values, the range for the $\nu = 1$ vibronic energy level is largest for the excited states: additionally the $a^5\Sigma^+$ state is very dependent on how many states are calculated at MRCI level of theory.

In summary, in order to constrain the properties shown in table 7.6, experimental studies of these quintet states is required as it appears that MRCI theoretical predications are very sensitive to both the basis set and the CASSCF state-combination used.

PECs for Septuplet states

As can be seen from figure 7.1, it appears that the order of the septuplet states is as follows: $X^7\Sigma^+$, $A^7\Sigma^+(II)$, $B^7\Pi$, $C^7\Delta$. These septuplet states are the result of a 3+1 calculation. Now refer to figure 7.3 which compares the order of the septuplet states when the "LOWER" and "UPPER" active spaces are used. Both plots show the result of performing a 3+1 calculation for the $^7\Sigma^+$ and $^7\Delta$ states with only the $X^7\Sigma^+$ and $^7\Sigma^+(II)$ states shown simply for clarity of the plots.

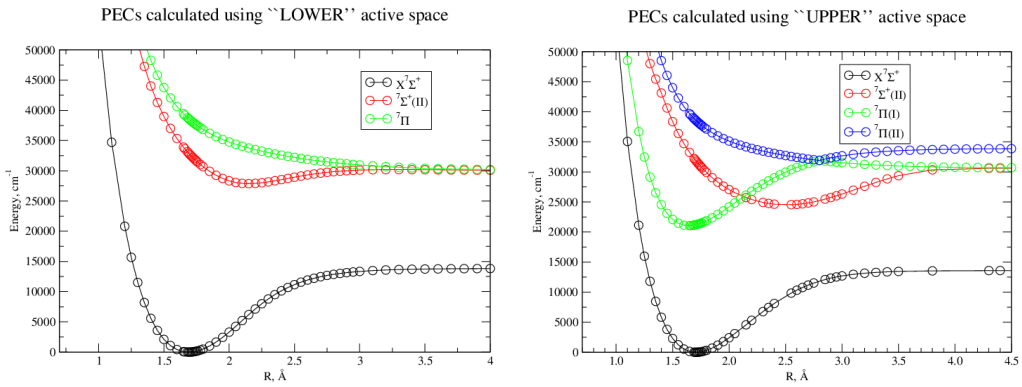

Figure 7.3: Comparison of PECs calculated at CI level for low-lying septuplet states using the two different active spaces as defined in section 2.7.8 using cc-pVQZ basis set. Figure 7.3a shows the case where a single $^7\Pi$ state is calculated and figure 7.3b shows where two $^7\Pi$ states are calculted: the need for calculating two such states for the case of using the "UPPER" active space is demonstrated in figure 7.4. For both cases the CI calculations are based on orbitals generated by combining states ABC-DEF as defined in tabel 7.1.

For figure 7.3a a single $^7\Pi$ state has been calculated and for figure 7.3b, two $^7\Pi$ states have been calculated. See figure 7.4 which shows how the PECs of $^7\Pi$ states changes using the "UPPER" active space for the case when a single $^7\Pi$ state is requested at CI level and for the case when two $^7\Pi$ states are requested at CI level.

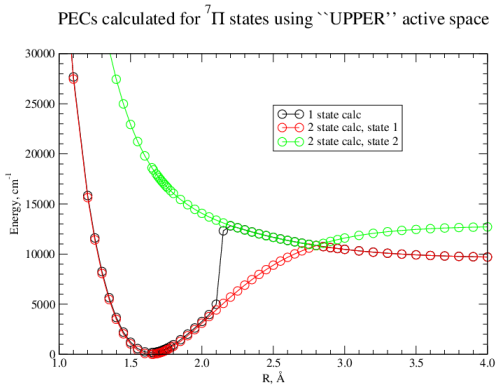

Figure 7.4: Comparison of PECs calculated at CI level, using a cc-pVQZ basis set, for $^7\Pi$ states using the "UPPER" active space (see section 2.7.8) for the cases when 1 $^7\Pi$ state is requested and when two $^7\Pi$ states are requested. These CI calculations are based on orbitals generated by combining states ABC-DEF as defined in tabel 7.1.

This "idenitity crises" of the two $^7\Pi$ states is discussed more in detail in section 7.2.3. Thus by comparison of figures 7.1, 7.3 and 7.4 it can be seen that the shape (and hence properties) of the lowest $^7\Pi$ state is dependent on both the active space and the number of $^7\Pi$ states calculated at CI level. It can also be concluded from figure 7.3b, which is for the case of the extended active space, that the first $^7\Pi$ state lies below the $^7\Sigma^+(II)$ state: this is consistent with the experimental literature which refers to this first $^7\Pi$ state as $A^7\Pi$.

As was stated previously, using this extended "UPPER" active space allows the

calculation of electronic states that dissociate to the z^8P^o atomic dissociation limit of Mn: referring back to table 2.11 these states are $^7\Sigma^+(III)$, $^7\Pi(II)$, $^9\Sigma^+$ and $^9\Pi$. Remembering that there are lower-lying $X^7\Sigma^+$, $^7\Delta$ and $^7\Sigma^+(II)$ states, to calculate this $^7\Sigma^+(III)$ state, it is thus necessary to perform a 4+1 calculation. Figures 7.5a and 7.5b show the PECs obtained when a 3+1 and 4+1 calculation is performed at CI level. From both figures it can be concluded that the first two states in symmetry 1 are $^7\Sigma^+$ states.

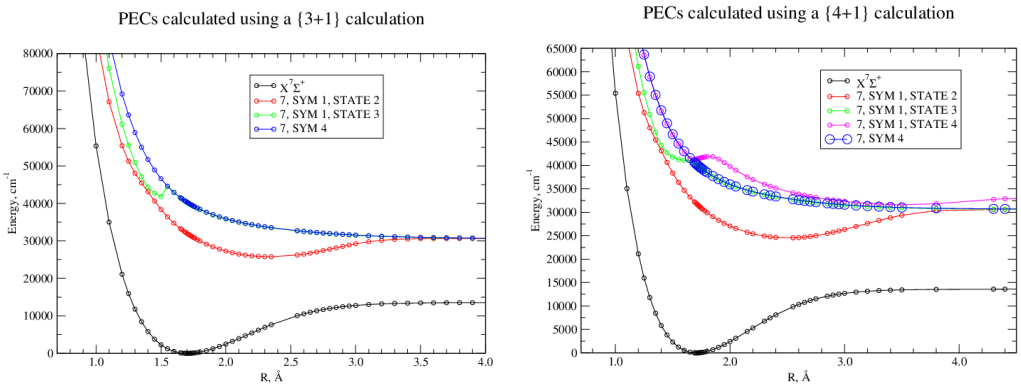

(a) (b)

Figure 7.5: Comparison of PECs calculated at CI level, using the "UPPER" active space (see section 2.7.8 and a cc-pVQZ basis set, for low-lying $^7\Sigma^+$ and $^7\Delta$ states. Figure 7.5a shows the case when three states of septuplet multiplicity are calculated in symmetry 1 and figure 7.5b shows the case when four such states are calculated. In both cases a single state of septuplet multiplicity is calculated in symmetry 4. These CI calculations are based on orbitals generated by combining states ABC-DEF as defined in tabel 7.1.

Referring to figure 7.5a at around 1.6 Å, the third state within symmetry 1 "switches" from been a distinctive PEC to becoming numerically the same as the PEC calculated in symmetry 4. Thus it would seem that until 1.5 Å this PEC is a $^7\Sigma^+$ state and then "switches" to been a $^7\Delta$ state. Figure 7.5b resolves this ambiguity. Using the rule that Σ^+ and Δ states are allowed to cross each other, it can thus be deduced that it is possible to construct the $^7\Sigma^+(III)$ state from stitching together the part of the third state of symmetry 1 from R=0.7 to 1.5 Å with that of the fourth state of symmetry 1 from 1.5Å onwards. The PEC of $^7\Delta$ state is simply the PEC calculated in symmetry 4. Thus, in order to calculate the $X^7\Sigma^+$, $^7\Sigma^+(II)$, $^7\Sigma^+(III)$ and $^7\Delta$ states, a 4+1 calculation is required at CI level using the "UPPER active space" with the necessary "stitching" together of energies done by examining plots of the raw energies produced by the MOLPRO calculations.

Thus putting together all the PECs of septuplet states onto one figure, the order of the relative upper states can be determined. Figure 7.6 shows PECs calculated using the "UPPER active space" with two $^7\Pi$ states calculated and a 4+1 calculation done for the $^7\Sigma^+$ and $^7\Delta$ states.

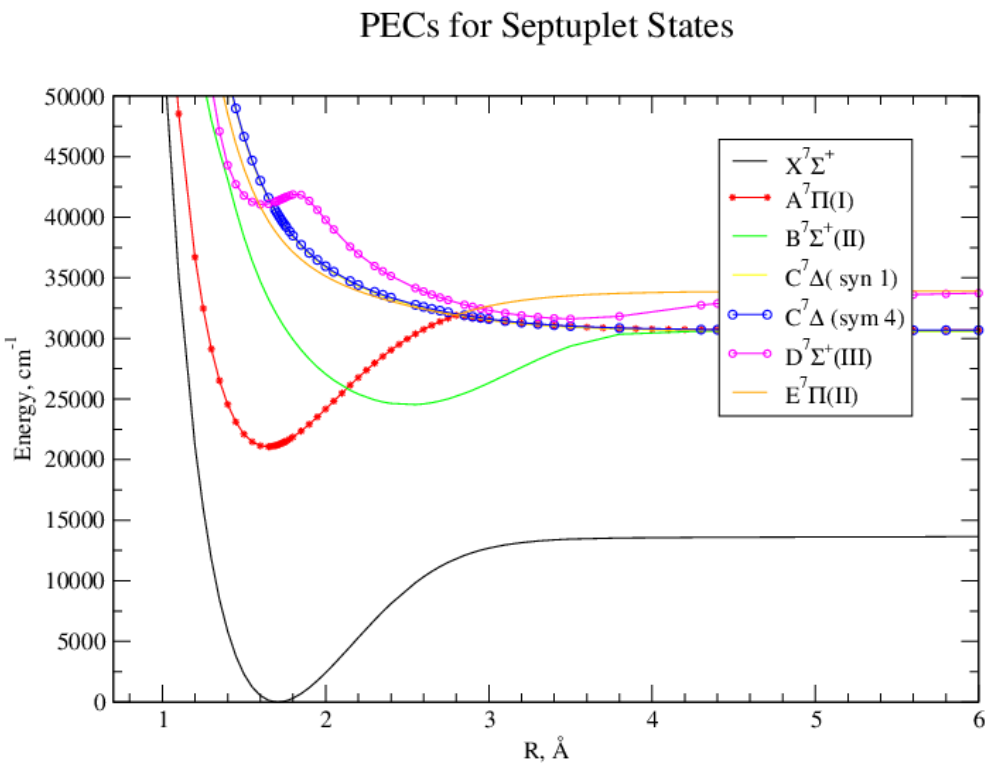

Figure 7.6: Compilation of PECs for low-lying septuplet states calculated at CI level, using the "UPPER" active space (see section 2.7.8 and a cc-pVQZ basis set. The allowed crossing between the $^7\Sigma^+(III)$ state and $^7\Delta$ can be seen where the $^7\Sigma^+(III)$ has been constructed by "stitching" together energy values produced in MOLPRO calculations for different states of symmetry 1 and septuplet multiplicity. The $^7\Sigma^+$ and $^7\Delta$ states shown here where calculated using a 4+1 calculation at CI level and the two $^7\Pi$ states were calculated by requesting two states of symmetries 2 and 3, septuplet multiplicity. These CI calculations are based on orbitals generated by combining states ABC-DEF as defined in table 7.1.

In figure 7.6, the $^7\Sigma^+(III)$ state has been constructed as described previously with the allowed crossing over the $^7\Delta$ state clearly shown. Moving onto the analysis of these calculated PECs, table 7.9 shows the variation between MRCI calculations for a fixed CASSCF state-combination of ABC-DEF.

State	MRCI	8	7	8	7	8	7	8	7	8	7	8	7
		cc-pVQZ		aug-cc-pVQZ		cc-pVQZ		aug-cc-pVQZ		cc-pVQZ		aug-cc-pVQZ	
		R_e (Å)				D_e (cm^{-1})				E($\nu = 1$) (cm^{-1})			
$X^7\Sigma^+$	1+0	1.703(3)	1.708(2)	1.699(2)	1.703(3)	13499	13102	13888	13436	1656	1620	1697	1660
$X^7\Sigma^+$	2+0	1.704(4)	1.710(2)	1.701(3)	1.706(4)	13605	13234	14006	13578	1630	1594	1671	1634
$X^7\Sigma^+$	3+1	1.706(1)	1.711(2)	1.702(4)	1.707(4)	13618	13257	14035	13621	1623	1589	1660	1623
$X^7\Sigma^+$	4+1	1.707(3)	1.713(2)	1.703(4)	1.708(4)	13659	13307	14047	13634	1608	1573	1649	1611
$B^7\Sigma^+(II)$	2+0	2.342(3)	2.371(8)	2.372(10)		4611	4664	3689		1733	1763	1598	
$B^7\Sigma^+(II)$	3+1	2.339(4)	2.368(8)	2.302(8)	2.334(7)	4788	4851	3892	3968	868	864	838	764
$B^7\Sigma^+(II)$	4+1	2.511(8)	2.522(5)	2.29(4)	2.413(7)	6093	6158	4318	4742	764	780	799	845
$C^7\Delta$(sym 1)	3+1	5.412(134)	5.398(107)		5.516(95)	5	5	7	2	32	31	32	31
$C^7\Delta$(sym 1)	4+1	5.428(17)	5.309(57)	5.413(28)	5.517(380)	12	18	7	8	33	34	30	31
$C^7\Delta$(sym 4)	3+1	5.734(314)	5.757(425)	5.684(175)		4	4	9		33	32	32	
$D^7\Sigma^+(III)$	4+1	3.537(10)	3.573(5)	2.970(8)	2.995(7)	2307	2232	5475	5394	423	415	907	759
$A^7\Pi$(I)	2SC	1.643(4)	1.647(5)	1.654(4)	1.657(2)	9616	9428	2589	2419	1588	1579	1548	1545
$E^7\Pi$(II)	2SC	2.793(1)	2.795(3)	2.222(2)	2.211(3)	1990	1960	6168	6104	710	705	1376	1372

Table 7.9: Summary of properties determined for PECs of septuplet states calculated using various number of states at MRCI level of theory using a choice of two basis sets and two CASSCF state-combinations. The two basis sets tested were "cc-pVQZ" and "aug-cc-pVQZ". In this table, "8" refers to the CASSCF state-combination of ABC-DEF and "7" refers to the CASSCF state-combination of "BC-DEF". These PEC properties have been determined using the procedure described in section 2.9.2.

By examination of table 7.9 it can be seen that the predicted values of R_e for the $X^7\Sigma^+$ state generally decrease when augmented values basis functions are used and increases when the CASSCF state-combination is decreased from that of "ABC-DEF" to "BC-DEF". Both the $X^7\Sigma^+$ and $A^7\Pi$ states have been studied previously theoretically and experimentally so hence there are studies to compare with. Hence table 7.9 is providing new theoretical predictions of the properties of the PECs for the $B^7\Sigma^+(II)$, $C^7\Delta$, $D^7\Sigma^+(III)$ and $E^7\Pi$(II) states. Starting with the $X^7\Sigma^+$ state, table 7.10 gives a summary of previous experimental and theoretical predictions for this state. Table 7.11 shows the variation in spectroscopic parameters determined for the $X^7\Sigma^+$ state at MRCI level of theory as a function of the CASSCF state-combination used.

Study	Method	R_e (Å)	ω_e (cm^{-1})	D_e (cm^{-1})
Huber & Herzberg (1979)	Experiment	1.7311	1548	
Nevin (1945)		1.73089		
Urban & Jones (1989)		1.730842(5)	1547	
Varberg et al. (1992)		1.7432		
Gordon et al. (2005)		1.7432(r_0)	1547	
Gengler et al. (2007)		1.7398601(47)		
Halfen & Ziurys (2008)		1.7310		
Das (1981)	MCSCF		1432	15325
Walch & Bauschlicher (1983)	CAS/CISD		1639	13792
Chong et al. (1986)	CISD		1553	13873
	CPF		1530	13550
	MCPF		1530	13470
Langhoff et al. (1989)	MR-SDCI+Q		1517.6	
Barone & Adamo (1997)	B3LYP		1586	8669
Wang & Andrews (2003)	W91/6-311++G(d,p)	1.710	1548.3(540)	
	BPW91/6-311++G(3df,3pd)	1.711	1522.0(528)	
	B3LYP/6-311++G(3df,3pd)	1.735	1507.0(496)	
Tomonari, Nagashima & Hirano (2009)	9-ref CI+Q	1.7372	1542	
	13-ref CI+Q	1.7359	1540	
	14-ref CI+Q	1.7356	1544	
	15-ref CI+Q	1.7343	1542	
	16-ref CI+Q	1.7344	1542	

Table 7.10: Summary of spectroscopic properties determined in previous experimental and theoretical studies for the $X^7\Sigma^+$ state.

CASSCF	R_e (Å)			D_e (cm^{-1})			T_e (cm^{-1})			E $\nu = 1$ (cm^{-1})		
	X	B	D	X	B	D	X	B	D	X	B	D
ABE	1.701(2)	2.520(4)	3.704(17)	13764	1444	1814	679	984	293	1613	771	371
AEF	1.726(2)	2.511(4)	3.525(8)	13516	2255	2069	927	490	0	1522	807	422
AE	1.721(2)	2.516(5)	4.001(9)	13719	1539	1411	223	346	215	1605	801	309
BCE	1.697(5)	2.527(5)	3.656(10)	13592	1379	1938	1019	1247	311	1619	765	386
BDE	1.726(4)	2.466(12)	3.645(19)	14043	1664	1954	400	541	167	1596	773	385
BDF	1.735(1)	2.468(12)	3.652(11)	14236	1654	1968	207	522	121	1609	767	382
BEF	1.720(4)						998			1131	4277	
BE	1.715(4)	2.514(2)	3.771(22)	13835	1511	1661	402	690	301	1663	784	341
CDE	1.718(3)	2.477(8)	3.653(14)	13986	1627	1948	457	567	122	1564	768	388
CDF	1.722(5)	2.390(10)	3.684(17)	13906	1684	1903	537	537	191	1578	787	373
CEF	1.720(4)	2.509(6)	3.682(17)	13499	2233	1912	1114	740	304	1520	789	372
CE	1.706(4)	2.517(8)	3.778(17)	13692	1481	1646	539	702	236	1584	783	338
DEF	1.730(2)	2.546(2)	3.652(9)	13215	2180	1989	1227	485	98	1544	807	
EF	1.733(4)	2.507(10)	3.696(8)	13433	1627	1829	798	198	53	1530	818	364
E	1.734(2)	2.531(4)		13408	2273		142	0		1570	847	
ABC-EF	1.702(2)	2.506(4)	3.548(10)	13890	6081	2268	1053	1269	251	1626	75	426
ABD-EF	1.715(2)	2.521(4)	3.583(17)	13344	6347	2191	1506	1019	258	1575	791	410
ABDF	1.719(2)	2.492(9)	3.627(15)	14184	6473	2038	424	839	189	16528	748	396
ACD-EF	1.714(4)	2.513(3)	3.566(13)	13625	6339	2242	1227	992	202	1600	786	416
ACDF	1.727(4)	2.479(4)	3.611(17)	14613	6488	2084	0	829	156	1748	749	399
ADEF	1.724(4)	2.532(8)	3.626(5)	13267	6636	2064	1341	675	164	1555	808	393
BCDF	1.705(3)	2.504(10)	3.610(17)	13993	6212	2108	747	1105	249	1632	743	403
BCEF	1.711(4)	2.516(6)		13493	6181		1360	1153		1579	767	
BDEF	1.718(3)	2.524(8)	3.594(16)	13364	6588	2155	1379	844	212	1574	802	404
CDEF	1.720(4)	2.524(4)	3.608(10)	13274	6436	2117	1470	862	223	1560	801	400

Table 7.11: Effect of changing the CASSCF state-combination upon the PECs calcualted at MRCI level of theory for the $^7\Sigma^+$ states of MnH using a cc-pVQZ basis set. These PEC properties have been determined using the procedure described in section 2.9.2. In this table "X" refers to the $X^7\Sigma^+$ state, "B" refers to the $B^7\Sigma^+(II)$ state and "D" refers to the $^7\Sigma^+(III)$ state.

Refer to tables 7.9 7.11 and 7.10. Experimentally, previous studies for the $X^7\Sigma^+$ state predict R_e to be in the range from 1.730842 and 1.7432 Å with previous theoretical studies predicting R_e to be between 1.710 and 1.7372 Å. In this study it has been shown that MRCI calculations can predict R_e to be in the range from 1.697 to 1.734 Å depending on which CASSCF state-combination is used. The upper part of this range overlaps with the experimental range. The D_e values were discussed in conjunction with the $a^5\Sigma^+$ state in section 7.2.1. For ω_e, previous theoretical studies predict values between 1432 and 1586 cm^{-1} and experimental studies a value of 1548 ± 1 cm^{-1}. From table 7.11 it can be seen that MRCI calculations predict a range in the $\nu = 1$ vibronic energy state to vary between 1521 and 1632 cm^{-1} (there is a clear outlier at 1131 cm^{-1}). Table 7.11 also shows how the position of PECs calculated for the $X^7\Sigma^+$ state can vary up and down the absolute energy scale (values of T_e). Moving onto the $A^7\Pi$ state, table 7.12 shows the variation in spectroscopic parameters determined for the $X^7\Sigma^+$ state at MRCI level of theory as a function of the CASSCF state-combination used. Table 7.13 gives a summary of previous experimental and theoretical predictions for this state.

CASSCF	R_e (Å)	D_e (cm^{-1})	T_e (cm^{-1})	E($\nu = 1$) (cm^{-1}
ABE	1.645(1)	10193	621	1619
AE	1.654(2)	10672	404	1595
AEF	1.656(3)	10102	881	1551
BCE	1.625(3)	10018	836	1591
BDE	1.658(4)	10671	180	1614
BDF	1.664(3)	10845	119	1603
BE	1.650(2)	10413	468	1630
BEF	1.653(4)	9996	857	1592
CDE	1.654(1)	10781	234	1613
CDF	1.653(3)	10862	385	1616
CE	1.646(2)	11265	586	1601
CEF	1.652(3)	10036	989	1556
DEF	1.660(3)	10353	1395	1544
E	1.659(5)	10846	407	1557
EF	1.662(2)	10175	838	1547
ABC-DE	1.637(4)	10010	893	1625
ABD-EF	1.649(2)	9478	1399	1579
ABDF	1.657(4)	10726	253	1664
ACD-EF	1.648(4)	9707	1287	1578
ACDF	1.663(3)	11214	0	1724
ACEF	1.645(2)	10185	810	1614
ADEF	1.656(4)	9558	1409	1556
BCDF	1.644(3)	10542	454	1671
BCEF	1.644(1)	9823	1082	1597
BDEF	1.652(5)	9509	1343	1577
CDEF	1.653(3)	9542	1454	1562

Table 7.12: Effect of changing the CASSCF state-combination upon the PECs calculated at MRCI level of theory for the $A^7\Pi$ and $E^7\Pi(II)$ states of MnH ("2-state calculation) using a cc-pVQZ basis set. These PEC properties have been determined using the procedure described in section 2.9.2.

Study	Method	R_e(Å)	ω_e(cm^{-1})
Langhoff et al. (1989)	MR-SDCI+Q		1639
Tomonari, Nagashima & Hirano (2009)	3-ref CI+Q	1.6415	1653
	6-ref CI+Q	1.6407	1659
	7-ref CI+Q	1.6403	1659

Table 7.13: Summary of spectroscopic properties determined in previous experimental and theoretical studies for the $A^7\Pi$ state.

Refer to tables 7.12 and 7.13. In the previous theoretical study of the $A^7\Pi$ state, Tomonari, Nagashima & Hirano (2009) have predicted R_e to be 1.64 Å. Table 7.12 shows our predictions to lie in the range from 1.625 and 1.664 Å depending on which CASSCF state-combinations are used.

PECs for nonuplet states

Figure 7.7 shows the calculation of the two nonuplet states, $^9\Sigma^+$ and $^9\Pi$.

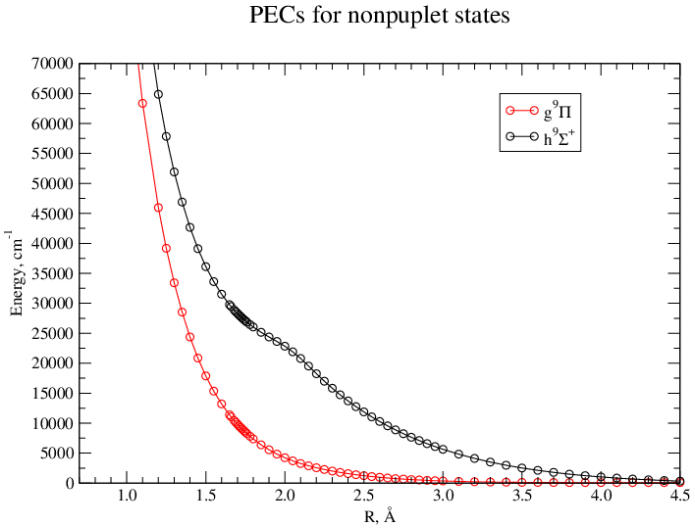

Figure 7.7: Compilation of PECs for the $^9\Sigma^+$ and $^9\Pi$ states at CI level, using the "UPPER" active space(see section 2.7.8 and a cc-pVQZ basis set. These PECs shown were calculated using a 3+1 calculation. These CI calculations are based on orbitals generated by combining states ABC-DEF as defined in tabel 7.1.

Figure 7.7 shows that both nonuplet states appear to be anti-bonding in nature with the $^9\Pi$ state lying below the $^9\Sigma^+$ state. These have been labelled "g" and "h" using the convention of lower-case letters for electronic states that are of different multiplicity from the ground state. Analysis of these curves does however reveal the that they are both very shallow potentials with the properties shown in table 7.14.

State	R_e (Å)	D_e (cm^{-1})	E($\nu = 1$) (cm^{-1})
$g^9\Pi$	4.057(126)	32	24
$h^9\Sigma^+$	5.461(47)	124	81

Table 7.14: PEC properties of the nonuplet states calculated at MRCI level of theory using a cc-pVQZ basis set and a CASSCF state-combination of ABC-DEF.

PECs of 15 low-lying electronic states of MnH

Finally, putting together all quintet, septuplet and nonuplet PECs into one plot, figure 7.8 shows a plot all 15 of the PECs calculated using the "UPPER" active space.

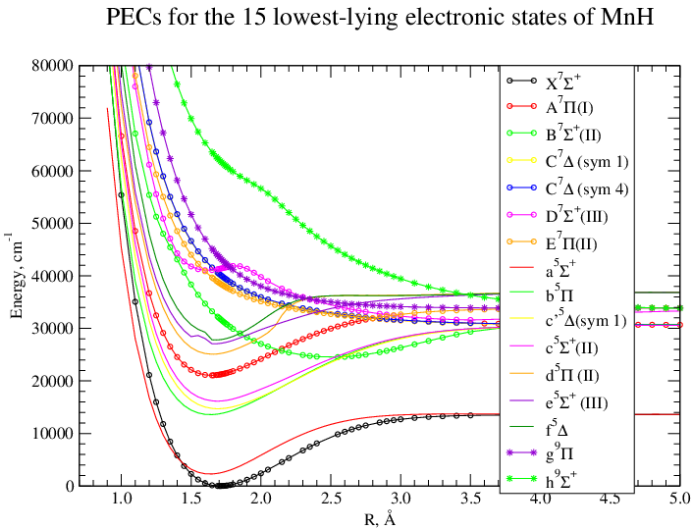

Figure 7.8: PECs for 15 low-lying electronic states of MnH calculated at MRCI level of theory using a cc-pVQZ basis set and a CASSCF state-combination of ABC-DEF.

In figure 7.8, continuous lines have been used to show the quintet and nonuplet states with circles used to indicate the septuplet states.

7.2.2 Dipole Moment Curves

In the calculation of dipole moments at CI level, the expectation dipole moment was calculated in all cases. The results of using the "LOWER" active space were used as a method in order to identify the DMCs produced using the "UPPER" active space.

7.2.3 DMCs for the quintet states

Starting with the quintet states, figure 7.10 shows DMCs calculated at MRCI level for the $a^5\Sigma^+$ state.

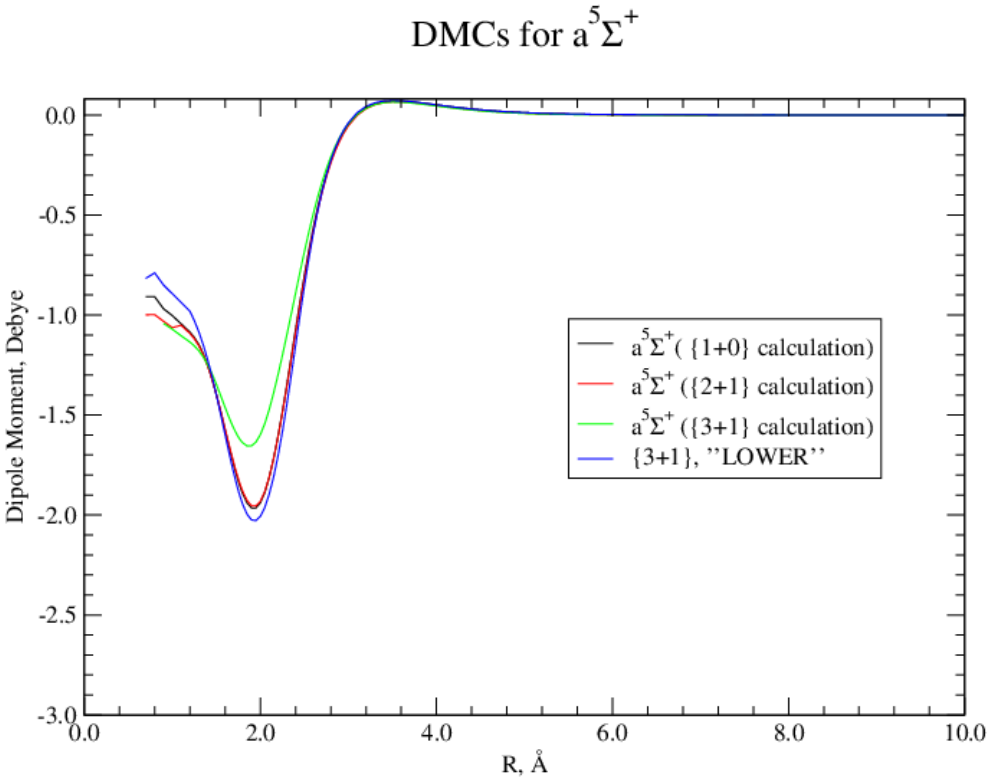

Figure 7.9: Comparison of DMCs calculated at CI level, using a cc-pVQZ basis set, for the $a^5\Sigma^+$ state. The "LOWER" and "UPPER" active spaces are defined in section 2.7.8. All of these CI calculations are based on orbitals generated by combining states ABC-DEF as defined in tabel 7.1.

As figure 7.10 shows, the shape (and hence minima) of the DMC calculated for the $a^5\Sigma^+$ vary as shown in table 7.15.

MRCI calculation	Position of minima (Å)	Value (Debye)
1+0	1.95	-1.964
2+1	1.95	-1.955
3+1	1.85	-1.655

Table 7.15: Positions and values of minima for calculated DMCs of the $a^5\Sigma^+$ state at MRCI level of theory using a cc-pVQZ basis set. These values presented are from the purely *ab initio* curves.

Table 7.16 shows a comparison of calculated DMC quintets with the study of Langhoff et al. (1989). The DMCs calculated for the $b^5\Pi$, $c'^5\Delta$, and $c^5\Sigma^+(II)$ states is shown in figure 7.10.

Langhoff et al. (1989)				Present Study							
R(Å)	$a^5\Sigma^+$	$b^5\Pi$	$c^5\Sigma^+$	R(Å)	$a^5\Sigma^+$				$b^5\Pi$	$c^5\Sigma^+(II)c$	
					1+0	2+1	3+1	5+2		3+1	5+2
1.32	1.21	2.74	0.94	1.30	1.15	1.15	1.18	1.18	1.95	0.86	1.27
				1.35	1.19	1.20	1.21	1.21	2.12	1.10	1.48
1.43	1.19		1.38	1.40	1.25	1.25	1.25	1.24	2.30	1.32	1.68
				1.45	1.32	1.32	1.29	1.28	2.48	1.53	1.87
1.53	1.20	3.27	1.76	1.50	1.40	1.40	1.35	1.33	.66	1.73	2.04
				1.55	1.48	1.48	1.40	1.40	2.84	1.92	1.95
1.59	1.23	3.37	1.93	1.60	1.58	1.57	1.46	1.46	3.01	2.09	2.13
1.64	1.26	3.47	2.09	1.65	1.67	1.66	1.52	1.50	3.17	2.26	2.46
1.69	1.31	3.57	2.24	1.69	1.74	1.73	1.56	1.55	3.29	2.38	2.55
1.75	1.36	3.65	2.39	1.75	1.83	1.82	1.61	1.61	3.44	2.54	2.66
1.85	1.48	3.81	2.65	1.85	1.94	1.93	1.65	1.70	3.63	2.74	2.81
1.96	1.60	3.93	2.87	1.95	1.96	1.96	1.64	1.73	3.76	2.86	2.92
2.06	1.70	4.02	3.06	2.05	1.89	1.88	1.54	1.69	3.82	2.93	2.98
2.17	1.77	4.08	3.21	2.15	1.72	1.72	1.39	1.56	3.80	2.95	3.01
				2.20	1.61	1.61	1.30	1.47	3.76	2.96	3.02
2.28	1.80	4.09	3.30	2.30	1.35	1.36	1.10	1.26	3.64	2.95	3.04

Table 7.16: Comparison of DMCs obtained for low-lying quintet states of MnH in this present with that of the theoretical study undertaken by Langhoff et al. (1989). In this study the DMCs have been calculated using a cc-pVQZ basis set at MRCI level of theory.

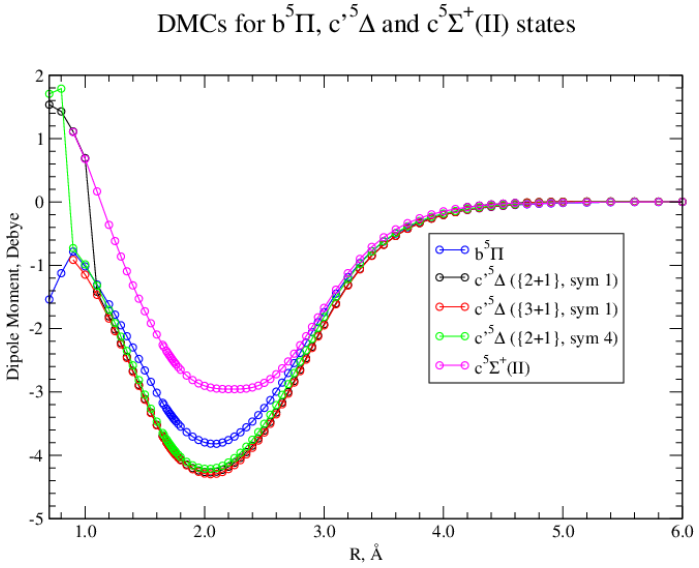

Figure 7.10: Calculation of DMCs at CI level, using a cc-pVQZ basis set, for quintet states using the "UPPER" active space(see section 2.7.8). These CI calculations are based on orbitals generated by combining states ABC-DEF as defined in tabel 7.1.

As can be seen from table 7.16 for the $a^5\Sigma^+$ state there is a change in character for the DMC dependent on the MRCI calculation used. These calculations differ to those of Langhoff et al. (1989) by up to 0.4 Debye for this $a^5\Sigma^+$ state and by up to 0.2 Debye for the $b^5\Pi$ and $c^5\Sigma^+$ state calculations. Without experimental data it is an unknown question what the true values are for these DMCs.

To complete this section on the DMCs of the quintet states, figure 7.11 shows the calculated DMCs of the $d^5\Pi(II)$, $e^5\Sigma^+$ and $f^5\Delta$ states.

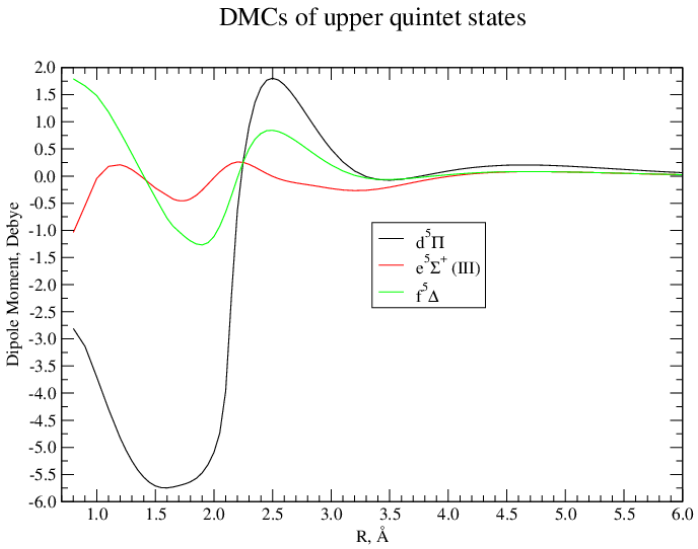

Figure 7.11: DMCs calculated at MRCI level of theory for higher-lying quintet electronic states. These DMCs have been calculated using the "UPPER" active space as is necessary, a cc-pVQZ basis set and a CASSCF state-combination of ABC-DEF.

DMCs for the $^7\Sigma^+$ and $^7\Delta$ states

Moving onto the septuplets, again variation was found between calculations which used either the "LOWER" or "UPPER" active space and also the number of septuplet states of a given symmetry calculated at CI level. Figure 7.12 shows a comparison of the DMCs produced at CI level using the "UPPER" active space for the various $^7\Sigma^+$ and $^7\Delta$ states. Figure 7.12a shows the case when a 3+1 calculation is done and figure 7.12b shows the case of a 4+1 calculation.

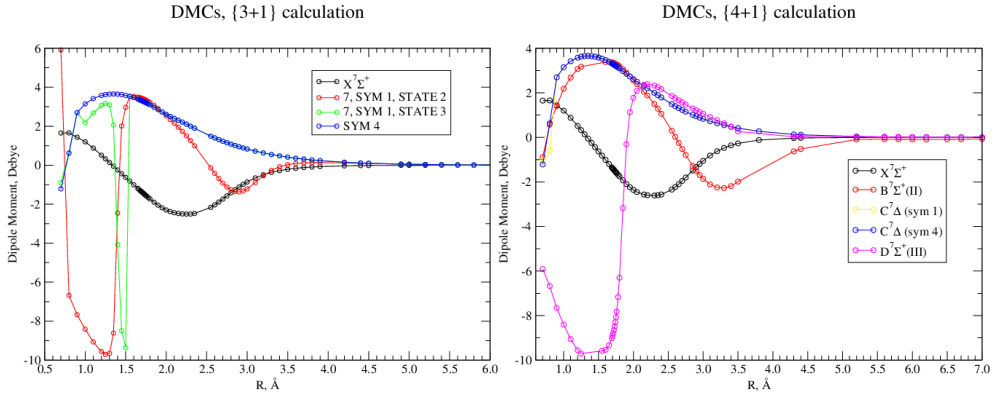

(a) (b)

Figure 7.12: Calculation of DMCs at CI level, using a cc-pVQZ basis set, for $^7\Sigma^+$ and $^7\Delta$ states using the "UPPER" active space(see section 2.7.8). These CI calculations are based on orbitals generated by combining states ABC-DEF as defined in tabel 7.1.

As was the case of the PECs, the identity of the third state of symmetry 1 is remedied when changing from a 3+1 calculation to a 4+1 calculation. The third state of symmetry 1 is initially $^7\Sigma^+(III)$ for low inter-nuclear distances before changing to $^7\Delta$.

DMCs for the $A^7\Pi$ and $E^7\Pi$ states

When calculations were undertaken at MRCI level of theory for the DMCs and associated TDMs, angular momenta couplings and spin-orbit couplings for the $A^7\Pi$ and $E^7\Pi(II)$ states, it was found that there was an "identity crises" involving these two states. Figure 7.13 shows the DMCs obtained for these states for the case of one $^7\Pi$ state been calculated at MRCI level of theory and for the case of two states been calculated at MRCI level of theory. Figure 7.13 shows the expectation dipole moments

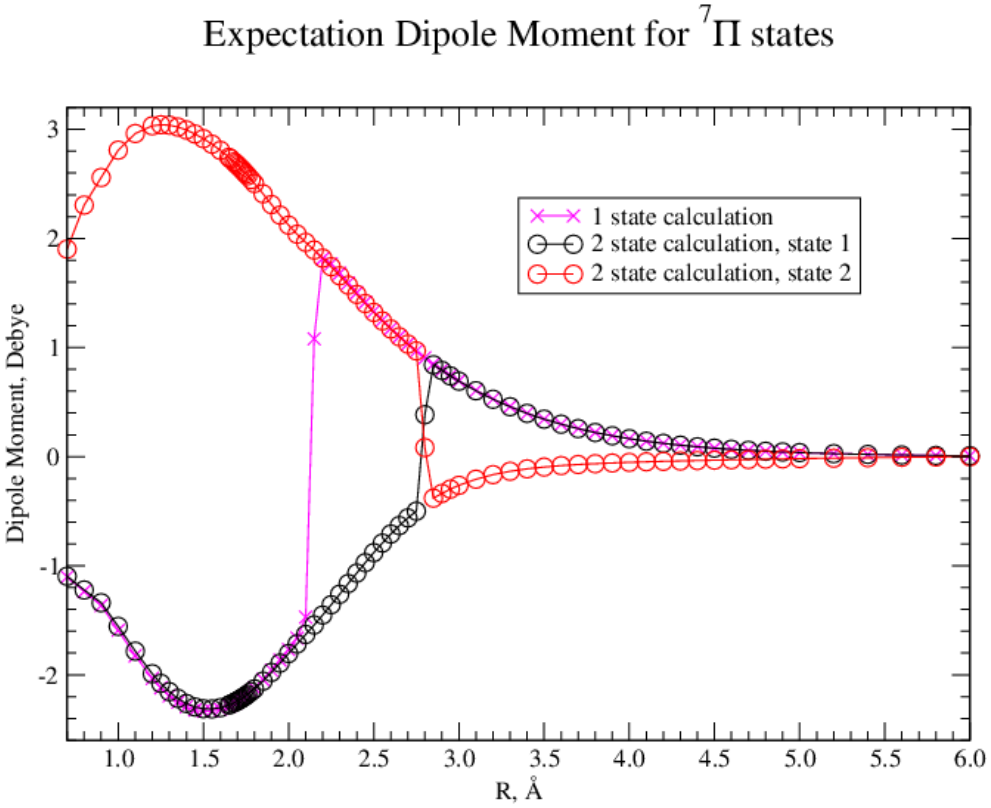

Figure 7.13: Calculation of Expectation Dipole Moments for $^7\Pi$ states

obtained for $^7\Pi$ states using a cc-pVQZ basis set and "ABC-DEF" CASSCF space. As the plot shows, for the 1 state calculation, the dipole moment calculated "flips" from -0.58 Debye at R=2.10 Å to 0.43 Debye at R=2.15. The result of a 2 state calculation shows the possibility of two distinct continuous curves-one with positive values and one with negative values. As can be seen from the figure 7.13, the identity of the states (i.e. which one is state 1 and which is state 2) "flips" between 2.80 Å and 2.90 Å. It is not clear which curve belongs to which state. Figure 7.16 shows these two DMCs untangled for the 2 state calculation in CI: one has a maximum magnitude of around 3 Å and the other a maximum magnitude of around 2 Å. Thus the question is, when the states are "untangled", which curve belongs to the first $^7\Pi$ state and which one belongs to the second $^7\Pi$ state?. To solve this puzzle, various calculations were inspected.

A similar story with couplings involving these two $^7\Pi$ states was found. Figures 7.14 and 7.15 show this story for a sample of angular momenta and spin-orbit couplings respectively. For these couplings we know that since the $A^7\Pi$ state dissociates to the

same dissociation limit as the $B^7\Sigma^+(II)$ and $c'^5\Delta$ states any couplings between it and these states must be non-zero in the dissociation limit. Also, and more crucially that any couplings involving the $E^7\Pi(II)$ state and the $B^7\Sigma^+(II)$ and $c'^5\Delta$ states must tend to zero in the dissociation limit as the $E^7\Pi(II)$ state dissociates to a higher dissociation limit. Hence with this knowledge, figures 7.14a and 7.15a have been de-tangled and the identity of the coupling $^7\Pi$ state revealed as indicated by figures 7.14b and 7.15a respectively.

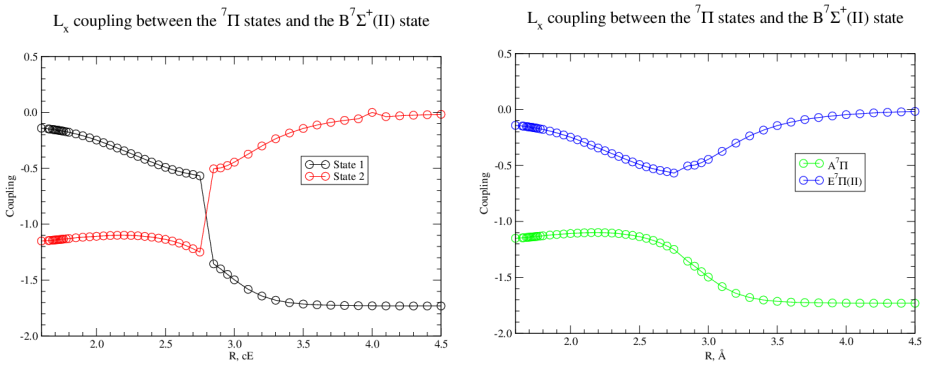

(a) (b)

Figure 7.14: L_x coupling between the $^7\Pi$ states and the $B^7\Sigma^+(II)$ state calculated at MRCI level of theory using a cc-pVQZ basis set, "UPPER" active space and a CASSCF state-combination of ABC-DEF. The MRCI calculation for the $B^7\Sigma^+(II)$ was simply a 2+0 calculation for simplicity. Figure 7.14a shows the "raw" MOLPRO output obtained: figure 7.14b shows the resolved couplings where the coupling between the $A^7\Pi$ and $B^7\Sigma^+(II)$ state goes to a non-zero value in the dissociation limit and the coupling between the $E^7\Pi(II)$ and $B^7\Sigma^+(II)$ state tends to zero.

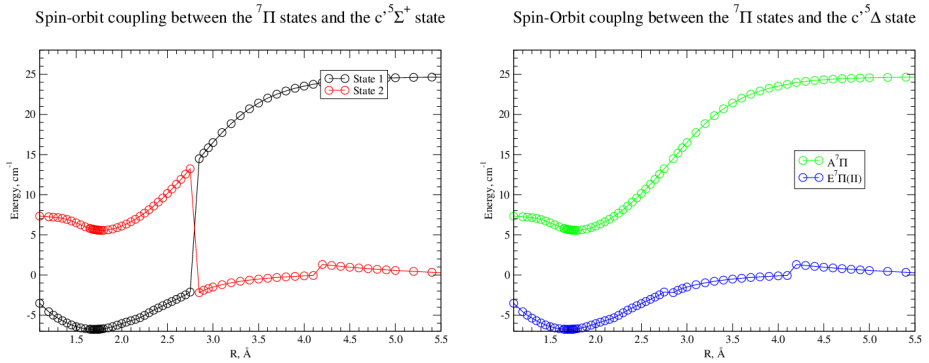

(a) (b)

Figure 7.15: Spin-orbit couplings between the two $^7\Pi$ states and the $c'^5\Sigma^+$ state calculated at MRCI level of theory using a cc-pVQZ basis set, "UPPER" active space and a CASSCF state-combination of ABC-DEF. The MRCI calculation for the $c'^5\Delta$ was simply a 2+1 calculation for simplicity. Figure 7.15a shows the "raw" MOLPRO output obtained: figure 7.15b shows the resolved couplings where the coupling between the $A^7\Pi$ and $c'^5\Delta$ state goes to a non-zero value in the dissociation limit and the coupling between the $E^7\Pi(II)$ and $c'^5\Delta$ state tends to zero.

By examination of figures 7.14 and 7.15, it can be seen that the mapping between the raw MOLPRO output (i.e. state 1, state 2) and the actual physical states is as shown in table 7.17.

R (Å)	State 1	State 2
0.70 - 2.80	$E^7\Pi(II)$	$A^7\Pi$
> 2.80	$A^7\Pi$	$E^7\Pi(II)$

Table 7.17: Mapping between "raw" `MOLPRO` output and the true identity of DMCs and couplings for the $A^7\Pi$ and $E^7\Pi(II)$ states.

Hence, applying this mapping to figure 7.13 we can thus resolve the identity of the DMCs for the two $^7\Pi$ states. This mapping was found to be consistent for all couplings involving the $^7\Pi$ states using the arguments presented above for knowing which couplings should tend to zero in the atomic dissociation limit.

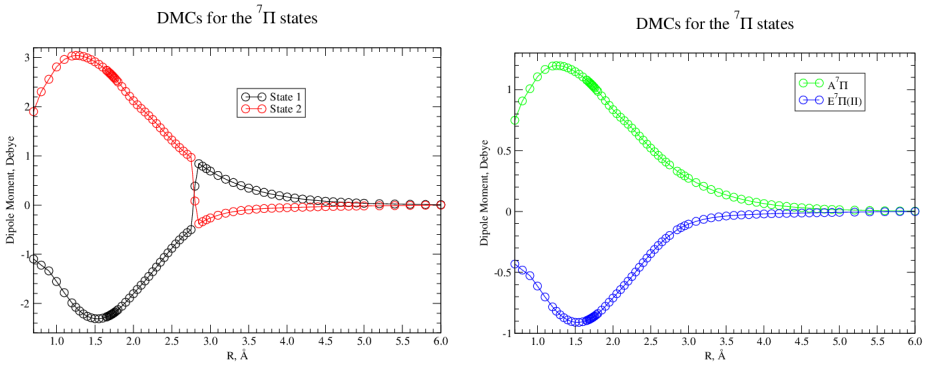

(a) (b)

Figure 7.16: Calculation of DMCs for the $^7\Pi$ states at MRCI level of theory using a cc-pVQZ basis set, the "UPPER" active space and a CASSCF state-combination of ABC-DEF. Figure 7.16a shows the "raw" `MOLPRO` output and figure 7.16b shows the resolved DMCs in which the mapping detailed in table 7.17 has been applied.

To demonstrate the variability in the peak of the DMCs for these two $^7\Pi$ states, several calculations can be inspected. Firstly, the peak values of pure CASSCF calculations in which only one $^7\Pi$ state is calculated. Referring back to table 7.1, these are the CASSCF state-combinations which include the component "E". Table 7.18 shows these peaks. Figure 7.17 shows the CASSCF calculation of a DMC in which a single $^7\Pi$ state is calculated for the state-combinations of "ABC-DEF", "BC-DEF" and the basis sets of cc-pVQZ and aug-cc-pVQZ.

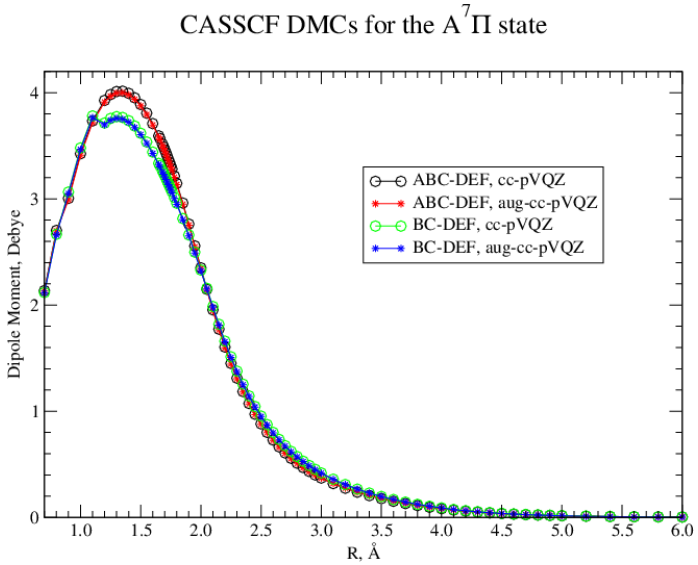

Figure 7.17: Calculation of DMC for the $A^7\Pi$ state at CASSCF level of theory. In this figure the CASSCF state-combination and basis set for each of the four calculations is indicated in the legend.

CASSCF	R_{max} (Å)	D_{max} (Debye)
ABC-DEF	1.35	4.015
ABC-DEF (aug-cc-pVQZ)	1.35	4.000
BC-DEF	1.10	3.781
BC-DEF (aug-cc-pVQZ)	1.10	3.766
ABE	1.50	4.552
AE	1.50	4.689
AEF	1.30	4.203
BDE	1.35	3.846
BEF	1.30	3.856
BE	1.50	4.286
CDE	1.30	4.235
EF	1.30	3.967
E	1.50	4.534

Table 7.18: Position and value of peaks of DMCs calculated at CASSCF level of theory for a single $^7\Pi$ state. Unless otherwise stated, the basis set used was cc-pVQZ. See table 7.1 for a guide to the various CASSCF state-combinations presented.

Moving onto MRCI results, the variation in the "peak" of the DMCs can be compared for MRCI calculations which use the "LOWER" active space (calculation of one state) and for those which use the "UPPER" active space (calculation of either one or two states) and build upon different CASSCF state-combinations. Table 7.19 shows these values. The picture shown in figure 7.16a whereby a 2 state calculation has the identity of states 1 & 2 flipping around 2.80 Å was found to be common for all CASSCF variations tested at CI level.

CASSCF	$A^7\Pi(I)$		$E^7\Pi(II)$	
	R_{max} (Å)	D_{max} (Debye)	R_{min} (Å)	D_{min} (Debye)
1 state calculations, "LOWER" active space				
ABC-DEF	1.35	3.247		
ABC-DEF (aug-cc-pVQZ)	1.30	3.190		
BC-DEF	1.30	3.165		
BC-DEF (aug-cc-pVQZ)	1.30	3.107		
1 state calculations, "UPPER" active space				
ABC-DEF			1.50	-2.334
ABC-DEF (aug-cc-pVQZ)			1.35	-2.446
BC-DEF			1.50	-2.314
BC-DEF (aug-cc-pVQZ)			1.40	-2.446
2 state calculations-"UPPER" active space				
ABC-DEF	1.25	3.042	1.55	-2.313
ABC-DEF(aug-cc-pVQZ)	1.30	3.097	1.40	-2.378
BC-DEF	1.10	2.983	1.55	-2.295
BC-DEF(aug-cc-pVQZ)	1.30	3.018	1.40	-2.376
E	1.25	3.143	1.55	-2.509
AE	1.20	3.181	1.55	-2.483
BE	1.30	3.034	1.55	-2.352
CE	1.25	3.162	1.55	-2.427
EF	1.20	3.044	1.55	-2.476
ABE	1.25	3.106	1.55	-2.373
AEF	1.20	3.099	1.55	-2.474
BCE	1.30	3.082	1.50	-2.316
BDE	1.20	2.921	1.55	-2.361
BDF	1.20	2.926	1.55	-2.388
BEF	1.25	2.979	1.55	-2.369
CDE	1.20	3.046	1.55	-2.424
CDF	1.20	3.021	1.55	-2.366
CEF	1.20	3.085	1.55	-2.417
DEF	1.25	3.079	1.50	-2.481
ABDF	1.20	3.005	1.55	-2.333
ACDF	1.20	3.014	1.60	-2.392
ACEF	1.25	3.072	1.55	-2.368
ADEF	1.25	3.126	1.50	-2.421
BCDF	1.25	2.984	1.55	-2.283
BCEF	1.25	3.034	1.55	-2.273
BDEF	1.25	3.016	1.55	-2.383
CDEF	1.25	3.111	1.55	-2.368
ABC-EF	1.25	3.019	1.55	-2.299
ABD-EF	1.25	3.075	1.55	-2.336
ACD-EF	1.25	3.094	1.55	-2.379

Table 7.19: Comparison of DMC peak values obtained for different MRCI calculations. For the two-state calculations the mapping outlined in table 7.17 has been applied to assign the "untangled" DMC to the correct $^7\Pi$ state. Unless otherwise indicated the basis set used was cc-pVQZ.

Refer to table 7.19. For the one state-calculations (1SC) performed at MRCI level of theory using the "LOWER" active space the output shape of the DMC calculation was that of figure 7.17 but with a lower peak value. For the one state-calculations performed using the "UPPER" active space, the shape of the curve for each CASSCF state-combination was that indicated in figure 7.13 i.e. the DMC of the $E^7\Pi(II)$ state up to 2.80 Å is calculated before the calculation "switches" to calculating the DMC of the $A^7\Pi$ state. As can be seen for a 2-state calculation (2SC) using the "UPPER"

active space, the peak of the DMC for the $A^7\Pi$ state calculated using MRCI level of theory varies between 2.921 and 3.181 Debye with a position between 1.20 and 1.30 Å depending on the CASSCF state-combination used. For these calculations, the minima of the DMC for the $E^7\Pi$ state is located between 1.40 Å and 1.60 Å and varies between -2.295 and -2.505 Debye depending on which CASSCF state-combination is used.

DMCs for the nonuplet states

Finally, the DMCs of the $e^9\Pi$ and $f^9\Sigma^+$ state were calculated at CI level as shown in figure 7.18: for these states it is only possible to use the "UPPER" active space.

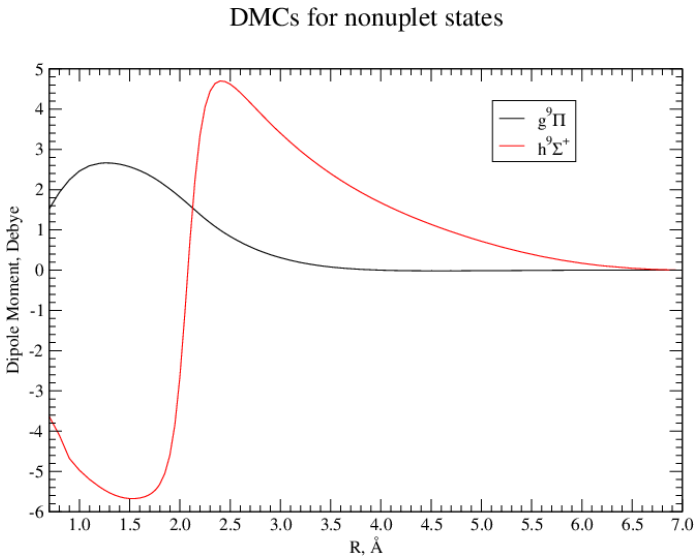

Figure 7.18: Calculations of DMCs at CI level, using a cc-pVQZ basis set, for the $e^9\Pi$ and $f^9\Sigma^+$ states using the "UPPER" active space(see section 2.7.8). These CI calculations are based on orbitals generated by combining states ABC-DEF as defined in table 7.1.

Even though the DMC of the $f^9\Sigma^+$ state is comparitively large, it should be remember that this state(as well as the $e^9\Pi$ state) is an antibonding curve as shown in figure 7.7. Comparing figures 7.10, 7.11, 7.16, 7.12 and 7.18 it can be seen that, in terms of magntidue around equilibrium (1.7 Å), $D^7\Sigma^+(III)$ is the largest by about a factor of two compared to other DMCs.

7.2.4 Transition Dipole Moments (TDMs)

The TDMS between electronic states were calculated and are shown in the following figures: TDMs couple states of the sane multiplicity. Starting with the quintet states, the TDMs between the various $^5\Sigma^+$ and $^5\Delta$ states are shown in figure 7.19 and the TDMs to the $b^5\Pi$ state is shown in figure 7.20.

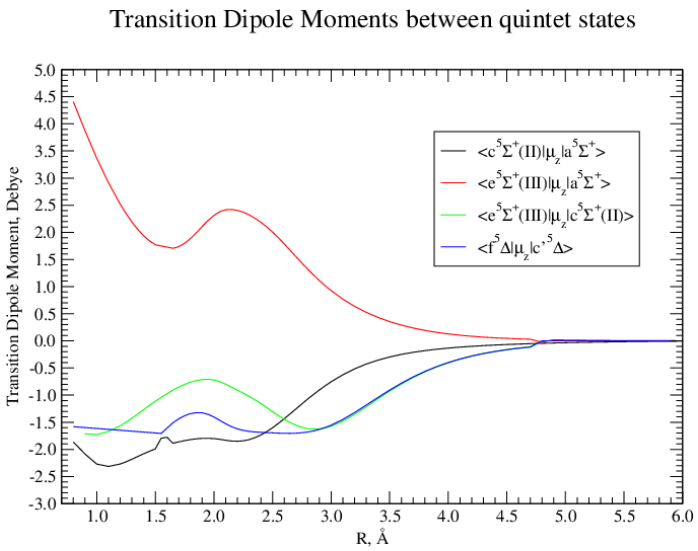

Figure 7.19: TDMs between the three quintet states and two delta states calculated at MRCI level of theory using a cc-pVQZ basis set and a CASSCF combination of ABC-DEF. The $\langle c^5\Sigma^+(II)|\,\mu_z\,|a^5\Sigma^+\rangle$ TDM shown is using a 3+1 MRCI calculation: all other couplings shown are for a 5+2 MRCI calculation: i.e. five quintet states of symmetry 1 and two quintet states of symmetry 4 calculated.

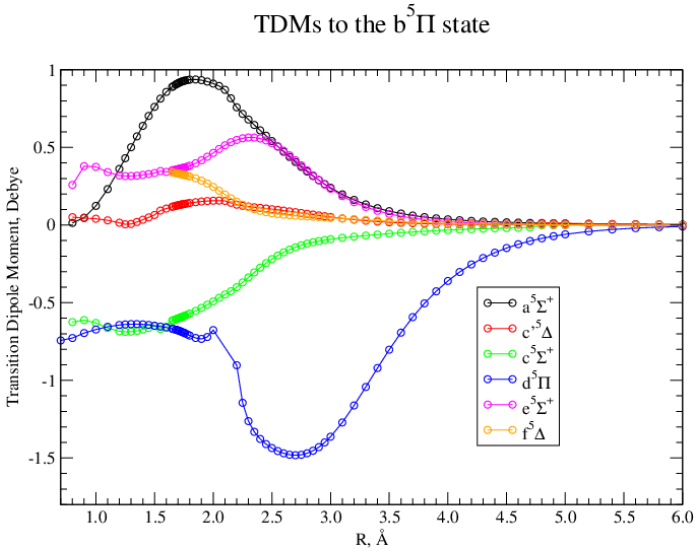

Figure 7.20: TDMs to the $b^5\Pi$ state calculated at MRCI level of theory using a cc-pVQZ basis set and a CASSCF state-combination of ABC-DEF and the "UPPER" active space. For this figure, as an example, the curve listed as "$a^5\Sigma^+$" is the $\langle a^5\Sigma^+|\,\mu_z\,|b^5\Pi\rangle$. For the $a^5\Sigma^+$, $c'^5\Delta$, $c^5\Sigma^+(II)$ and $e^5\Sigma^+(III)$ states the MRCI calculation performed was of the form "5+2", i.e. five quintet states of symmetry 1 and two quintet states of symmetry 4 calculated. For all calculations shown in this figure, two $^5\Pi$ states were calculated within a single MRCI calculation.

These TDMs calculated can for these quintet states can be compared to those calculated by Langhoff et al. (1989) whose calculations are shown in figure 7.21. As can be seen from figure 7.21, Langhoff et al. (1989) have unfortunately mislabelled one of their coupling curves (one of them should be for the $c^5\Sigma^+ - b^5\Pi$ transition). However, the authors did provide a table of values which are shown in table 7.20 in

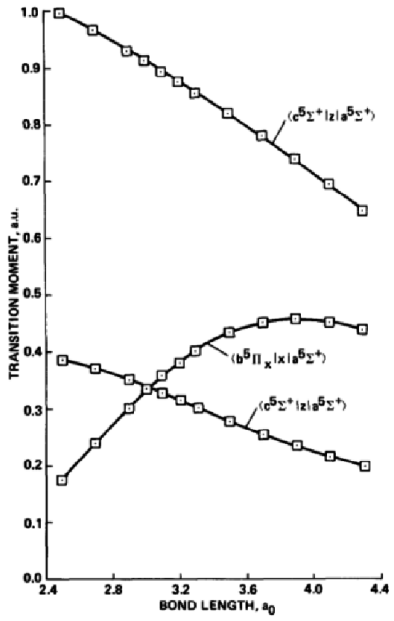

Figure 7.21: MRCI transition moment functions(a.u) for the $c^5\Sigma^+ - a^5\Sigma^+$, $b^5\Sigma^+ - a^5\Sigma^+$ and $c^5\Sigma^+ - b^5\Pi$ band systems of MnH calculated by Langhoff et al. (1989).

which a comparison is done with the results obtained in this study.

Langhoff et al. (1989)			Present Study		
R (Å)	$c^5\Sigma^+(II) - a^5\Sigma^+$	$b^5\Pi - a^5\Sigma^+$	R (Å)	$c^5\Sigma^+(II) - a^5\Sigma^+$	$b^5\Pi - a^5\Sigma^+$
1.32	2.53	0.45	1.30	2.18	0.50
			1.35	2.13	0.57
1.43	2.46	0.61	1.40	2.08	0.64
			1.45	2.03	0.70
1.53	2.37	0.77	1.50	1.99	0.76
			1.55	1.79	0.81
1.59	2.32	0.84	1.60	1.78	0.86
1.64	2.27	0.91	1.65	1.89	0.89
1.69	2.22	0.97	1.69	1.87	0.91
1.75	2.18	1.02	1.75	1.84	0.93
1.85	2.08	1.10	1.85	1.81	0.94
1.96	1.98	1.14	1.95	1.80	0.92
2.06	1.87	1.16	2.05	1.81	0.90
2.17	1.76	1.15	2.15	1.85	0.82
			2.20	1.85	0.76
2.28	1.64	1.12	2.25	1.84	0.72
			2.30	1.82	0.68

Table 7.20: Comparison of TDMs calculated for the $c^5\Sigma^+(II) - a^5\Sigma^+$ and $b^5\Pi - a^5\Sigma^+$ transitions with that of Langhoff et al. (1989). The units of the TDMs are in Debye. The TDMs calculated in this study were calculated at MRCI level of theory using a cc-pVQZ basis set, the "UPPER" active space, a CASSCF state-combination of "ABC-DEF. At MRCI level of theory there were three states of symmetry 1 and one state of symmetry 4 calculated.

As can be seen from table 7.20 for the $b^5\Pi - a^5\Sigma^+$ we do compare favourably but for the $c^5\Sigma^+(II) - a^5\Sigma^+$ TDM our values differ from those of Langhoff et al. (1989)

by around 0.4 Debye.

Figure 7.22 shows the variation in the TDM between the $B^7\Sigma^+(II)$ and $X^7\Sigma^+$ states obtained for various calculations. As can be seen from figure 7.22 the variation

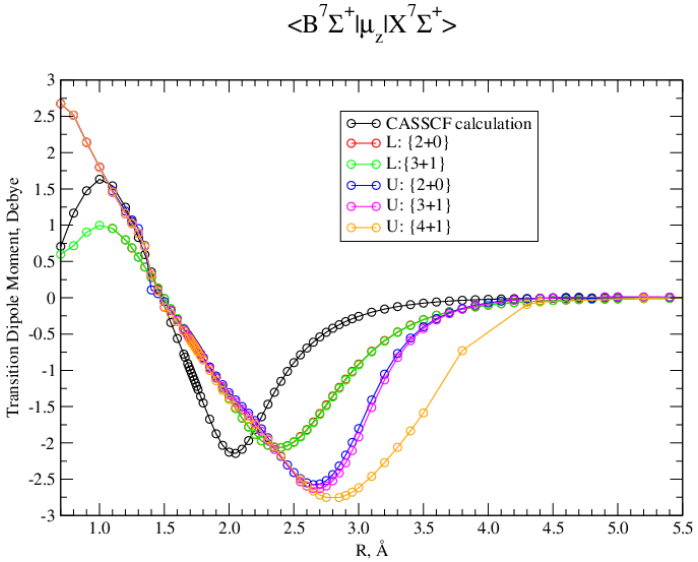

Figure 7.22: Calculation of the $\langle B^7\Sigma^+(II)|\,\mu_z\,|X^7\Sigma^+\rangle$ coupling using a cc-pVQZ basis set. The first curve is for a CASSCF calculation and the others are for MRCI calculations which built upon this CASSCF calculation which has a state-combination of ABC-DEF. In this figure "L" and "U" refer to calculations using the "LOWER" and "UPPER" active spaces respectively. The notation "3+1" indicates that an MRCI calculation of three septuplet states of symmetry 1 and one septuplet state of symmetry 4 was used.

in the position of the minimum of the calculation is of order 0.8 Å. There is a difference in behaviour between using the "LOWER" and 'UPPER" active space. Both active spaces produce self-consistent results for 2+0 and 3+1 calculations with the "UPPER" active space showing a change in behaviour when a "4+1" calculation is used. Figure 7.23 shows the TMDs coupling the $D^7\Sigma^+(III)$ state (fourth septuplet state of symmetry 1) to the $X^7\Sigma^+$ and $B^7\Sigma^+(II)$ states.

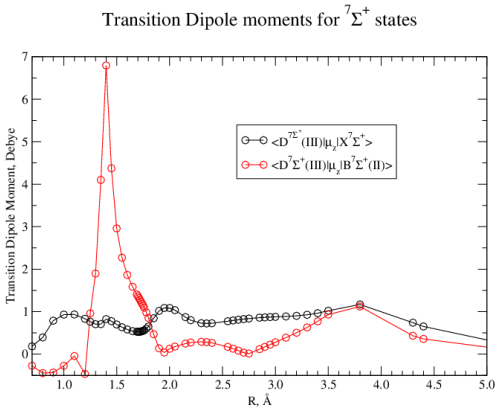

Figure 7.23: TDMs coupling the $D^7\Sigma^+(III)$ to the $X^7\Sigma^+$ and $B^7\Sigma^+(II)$ states calculated at MRCI level of theory using a cc-pVQZ basis set and a CASSCF state-combination of ABC-DEF. The MRCI calculation is for four septuplet states of symmetry 1 and one septuplet state of symmetry 4 i.e. 4+1 calculation.

As can be seen from figure 7.23, more work is clearly required to produce continuous coupling curves involving the $D^7\Sigma^+(II)$ states. Given that there are at least eight electronic states lying below the $D^7\Sigma^+(III)$ state, the $D^7\Sigma^+(III) - B^7\Sigma^+(II)$ is of overall lower priority given that to date there is no published linelist for MnH. Hence producing a linelist for MnH involving even just the eight low-lying electronic states is a contribution to knowledge in itself. Figure 7.24 shows the transition dipole moments coupling the $A^7\Pi$ and $E^7\Pi(II)$ states to the $X^7\Sigma^+$, $B^7\Sigma^+(II)$ and $C^7\Delta$ states.

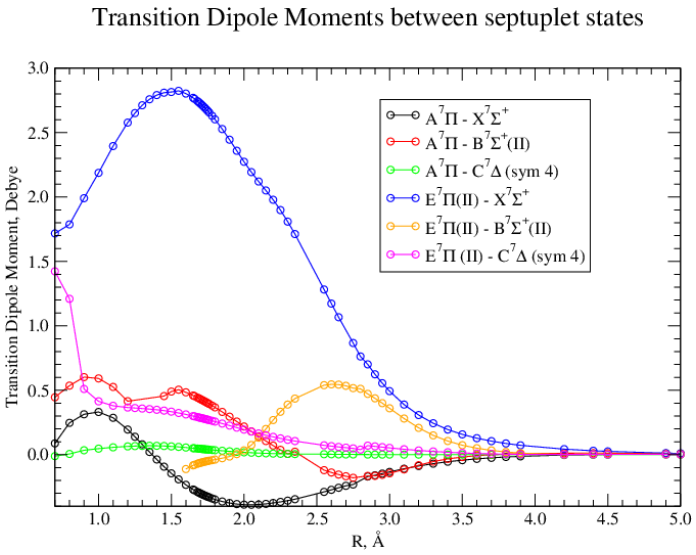

Figure 7.24: TDMs coupling the $A^7\Pi$ and $E^7\Pi(II)$ and $X^7\Sigma^+$, $B^7\Sigma^+(II)$ and $C^7\Delta$ states calculated at MRCI level of theory using a cc-pVQZ basis set, the "UPPER" active space and a CASSCF state-combinaiton of "ABC-DEF". At MRCI level of theory the $X^7\Sigma^+$, $B^7\Sigma^+(II)$ and $C^7\Delta$ states have been calculated by calculating three septuplet states of symmetry 1 and one septuplet state of symmetry 4.

In figure 7.24 it can be seen that the strongest transition dipole moment is that between the $E^7\Pi(II)$ and $X^7\Sigma^+$ state. This may seem a surprising result. However the magnitude of the TDM between the $A^7\Pi$ and $X^7\Sigma^+$ state was verified by comparing against CASSCF calculations of this coupling and also MRCI calculations in which there are fewer septuplet states of symmetry 1 calculated.

Figure 7.25 shows the TDM between the two $^7\Pi$ states.

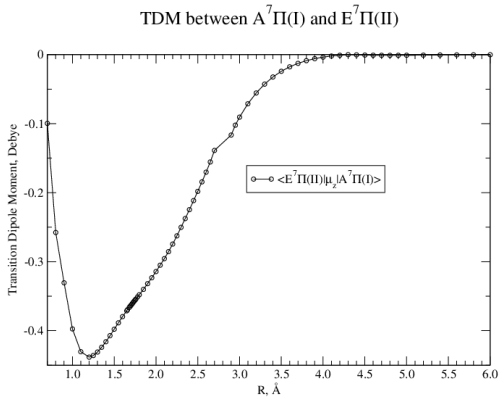

Figure 7.25: TDM between the $E^7\Pi(II)$ and $A^7\Pi(I)$ states calculated at MRCI level of theory using a cc-pVQZ basis set and a CASSCF state-combination of ABC-DEF. This calculation shown uses the "UPPER" active space as is necessary for the calculation of the $E^7\Pi(II)$ state but also for obtaining the correct bonding behaviour of the $A^7\Pi(I)$ state.

As can be seen from figure 7.25 the transition dipole coupling between the two $^7\Pi$ states is comparable to that between the $A^7\Pi$ and $X^7\Sigma^+$ state.

Finally, moving onto the nonuplet states, figure 7.26 shows the TDM calculated between the $h^9\Sigma^+$ and $g^9\Pi$ states.

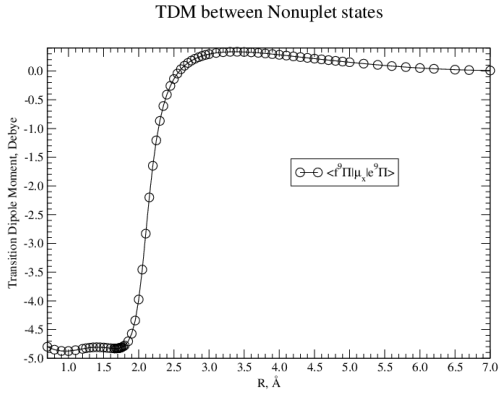

Figure 7.26: TDM coupling the $h^9\Sigma^+$ and $g^9\Pi$ states calculated at MRCI level of theory using a cc-pVQZ basis set and a CASSCF state-combination of ABC-DEF. As is necessary for the calculation of these states the "UPPER" active space was used.

7.2.5 Angular Momenta coupling

The angular momenta coupling linking Σ^+ and Δ states to Π states of the same multiplicity was calculated. Figures 7.27, 7.28 and 7.29 show this coupling for the low-lying quintet, septuplet and nonuplet states respectively. Figure 7.27 shows the variation between the $\langle a^5\Sigma^+|\,\hat{L}_x\,|b^5\Pi\rangle$ couplings calculated when the number of quintet states of symmetry 1 calculated is varied. As can be seen having three states instead of one or two of symmetry 1 within the MRCI calculation makes a difference of the order 0.2 (angular momenta coupling is a dimensionless quantity). The asymptotic value of the $\langle c^5\Sigma^+(II)|\,\hat{L}_x\,|b^5\Pi\rangle$ coupling is $\sqrt{3}$. As expected the $\langle a^5\Sigma^+|\,\hat{L}_x\,|b^5\Pi\rangle$ coupling tends to zero in the atomic dissociation limit as the $a^5\Sigma^+$ and $b^5\Pi$ states dissociate to different Mn atom terms. As can be seen in figure 7.28, the $\langle B^7\Sigma^+(II)|\,L_x\,|A^7\Pi(II)\rangle$

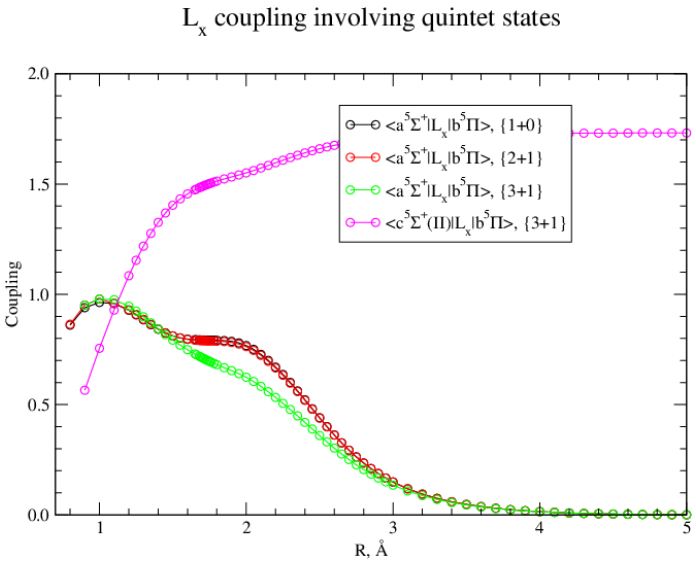

Figure 7.27: L_x coupling between low-lying $^5 5\Sigma^+$ and the $b^5\Pi$ state calculated at MRCI level of theory using a cc-pVQZ basis set and a CASSCF state-combination of ABC-DEF. In this figure the notation "2+1" indicates that two quintet states of symmetry 1 and one quintet state of symmetry 4 were calculated. All curves show the couplings using the "UPPER" active space.

coupling tend to a non-zero value of $\sqrt{3}$ in the dissociation limit: this is expected as these two states involved dissociate to the same atomic dissociation limit. As expected, the other couplings tend to zero as they couple molecular electronic states which dissociate to different atomic dissociation limits. The $\langle C^7\Delta|\, L_x\, |A^7\Pi\rangle$ coupling has a constant of value of 0.99 ± 0.02 and the $\langle C^7\Delta|\, L_x\, |E^7\Pi(II)\rangle$ coupling is numerically zero as expected. Figure 7.29 shows the L_x coupling between the $h^9\Sigma^+$ and $g^9\Pi$ states which tends to a constant value of $+1$ in the dissociation limit. The angular momentum coupling within individual Π and Δ states was calculated and can be summarised as follows: for the $b^5\Pi$, $d^5\Pi$, $A^7\Pi$, $E^7\Pi(II)$ and $g^9\Pi$ this had a magnitude of $+1$, for the $C^7\Delta$ a value of $+2$ and for both the $c'^5\Delta$ and $f^5\Delta$ states a value of -2.

7.2.6 Spin-Orbit coupling

The diagonal spin-orbit coupling elements were calculated within individual Π states and individual Δ states. Figure 7.30 shows these couplings. Figure 7.30a shows the results for when one $^7\Pi$ state is calculated using the "LOWER" active space and two states were calculated using the "UPPER" active space. In figure 7.30b the quintet state calculations were calculated using a "3+1" calculation: i.e. three quintet states of symmetry 1 and one quintet state of symmetry 4. For the septuplet states, it was found that results gained using "3+1" and "4+1" calculations showed the same behaviour with a variation between them of a few cm^{-1}. The curves shown in figure 7.30b are for the 3+1 calculations. As can be seen from figure 7.30 the variation between curves calculated using the "LOWER" and "UPPER" active spaces is of order < 1 cm^{-1}. Figure 7.31 shows the calculated spin-orbit couplings between Π and Δ states. In figure 7.31a the $\langle c'^5\Delta|\, SO_z\, |C^7\Delta\rangle$ coupling has been calculated using a 3+1

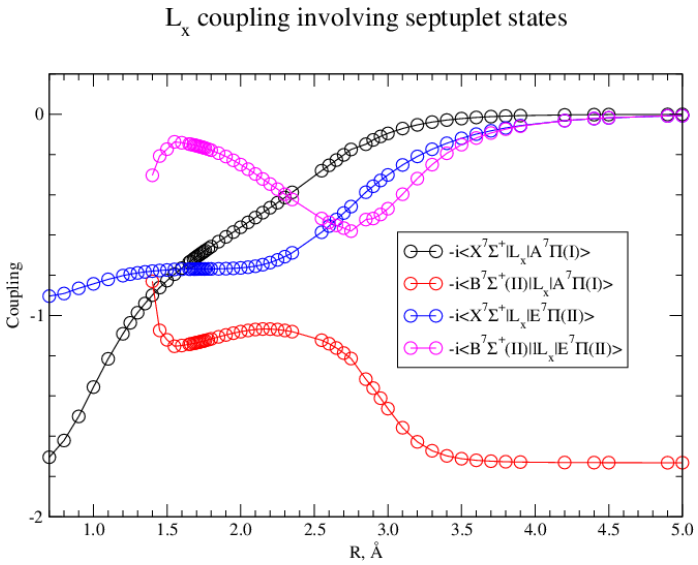

Figure 7.28: L_x between low-lying $^7\Sigma^+$ and $^7\Delta$ states and the two $^7\Pi$ states calculated at MRCI level of theory using a cc-pVQZ basis set and a CASSCF state-combination of ABC-DEF. This figure shows couplings in which three septuplet states of symmetry 1 and one septuplet state of symmetry 4 have been calculated and coupled with the two $^7\Pi$ states. All curves show the couplings using the "UPPER" active space.

calculation for both the quintet and septuplet states. In figures 7.31b and 7.31c for the calculations using the "UPPER" active space, two $^7\Pi$ states were calculated and for the "LOWER" active space, one $^7\Pi$ state was calculated.

Moving onto the off-diagonal spin-orbit couplings, the $\hat{SO}_x$ operator couples Σ^+ and Δ states to Π states provided they have the same multiplicity or it differs by two. Figure 7.32 shows such couplings for quintet and septuplet states. Figure 7.32a shows the couplings between low-lying quintet states in the case where one $^5\Pi$ state has been calculated. In this figure the notation "2+1" indicates that two quintet states of symmetry 1 and one quintet state of symmetry 4 have been calculated at MRCI level of theory. As can be seen from figure 7.32a the variation between the $\langle a^5\Sigma^+|\, SO_z\, |b^5\Pi\rangle$ coupling curves calculated is of the order several cm^{-1} when the number of quintet states of symmetry 1 is varied. Figure 7.32b shows the spin-orbit coupling between the $a^5\Sigma^+$, $c'^5\Delta$, $c^5\Sigma^+(II)$ states with the $A^7\Pi$ and $E^7\Pi$ states. In these calculations the $^5\Sigma^+$ and $^5\Delta$ states have been calculated at MRCI level of theory using a "3+1" calculation, i.e. three quintet states of symmetry 1 and one state of symmetry 4. For all curves shown the $^7\Pi$ states were calculated using a "two-state" calculation. Finally, figure 7.33 shows the spin-orbit coupling between the $g^9\Pi$ and $h^9\Sigma^+$ states. As is the case for CrH, to date in the literature there are no recorded spin-orbit couplings. Table 7.21 lists out the non-zero dissociation values of the spin-orbit couplings obtained in this study.

7.3 Concluding Remarks

In this chapter, *ab initio* calculations have been performed for MnH. A systematic study of CASSCF state-combinations has been carried out with results shown in

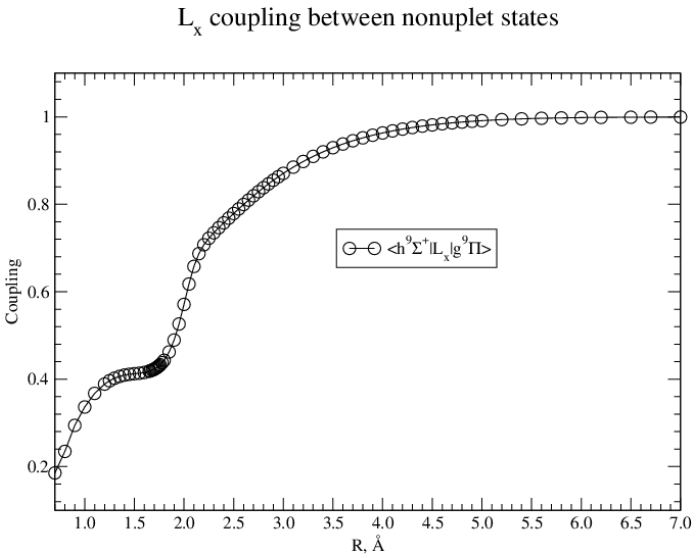

Figure 7.29: L_x coupling between the nonuplet states calculated at MRCI level of theory using a cc-pVQZ basis set and a CASSCF state-combination of ABC-DEF.

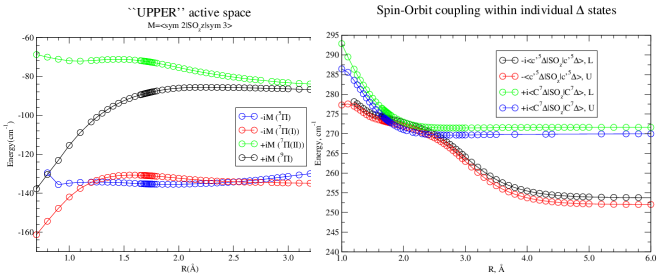

(a) (b)

Figure 7.30: Spin-orbit matrix elements within individual Π and Δ states. These curves were calculated using MRCI level of theory with a cc-pVQZ basis set and a CASSCF state combination of ABC-DEF. In these figures "L" and "U" refer to calculations were the "LOWER" and "UPPER" active spaces have been used respectively.

appendix C. To our knowledge, this type of study has never been undertaken for MnH. By examining the PECs and DMCs computed for these CASSCF calculations, a CASSCF state-combination of "ABC-DEF" (see table 7.1) was then used to generate starting orbitals for MRCI calculations. This CASSCF state-combination combines all the 8 lowest electronic states of MnH (see table 2.11). In contrast to the case of CrH, it was found that generally speaking the quality of the CASSCF PECs and DMCs obtained improved as more states were added to the CASSCF calculation.

For the MRCI calculations, PECs and DMCs were calculated for 15 low-lying electronic states of MnH including, for the first time the nonuplet states of $g^9\Pi$ and $h^9\Sigma^+$. Were applicable, these PECs and DMCs calculated were compared to the previous theoretical study of Langhoff et al. (1989) in which PECs had been calculated for 8 low-lying electronic states. Some differences were found. However, in our new study for each PEC, several calculations were performed. Again, as was the case for CrH, it was found that varying both the CASSCF state-combination used and the basis set had an affect on the properties of the PECs and also the DMCs.

The effect of changing the CASSCF state-combination in MRCI calculations of

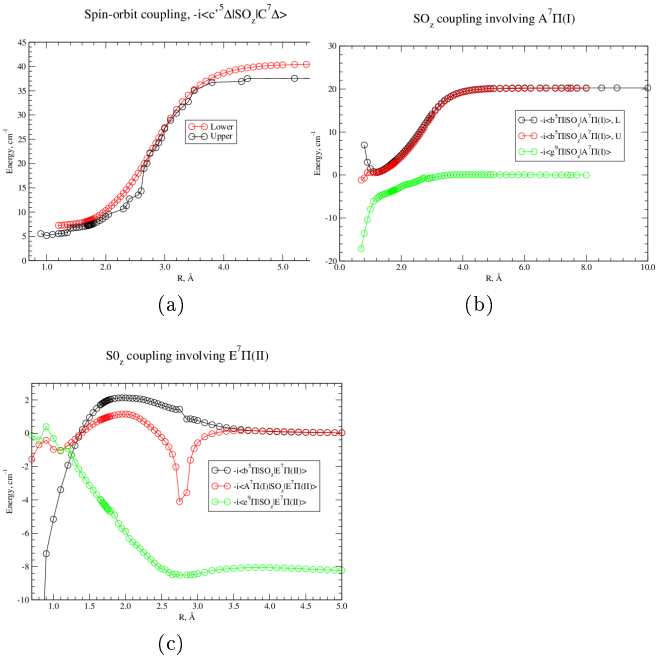

Figure 7.31: Spin-orbit matrix elements between Π and Δ states. These curves were calculated using MRCI level of theory with a cc-pVQZ basis set and a CASSCF state combination of ABC-DEF. In these figures "L" and "U" refer to calculations were the "LOWER" and "UPPER" active spaces have been used respectively.

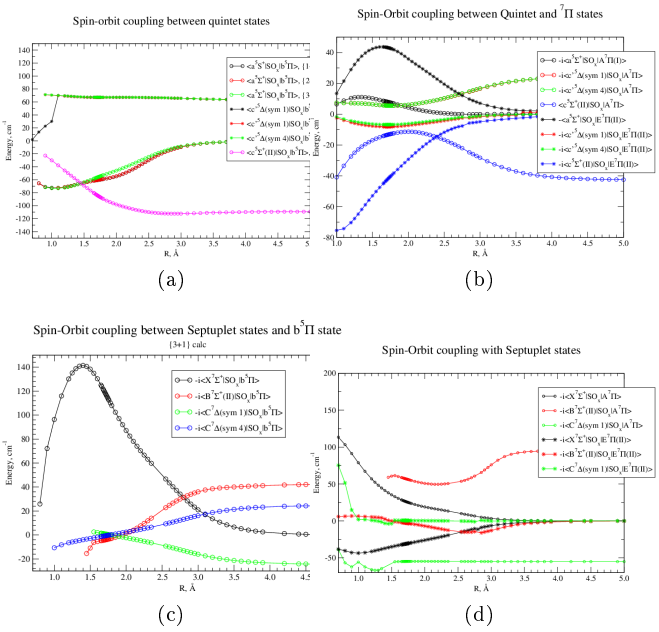

Figure 7.32: Off-diagonal spin-orbit coupling curves. These curves were calculated using a cc-pVQZ basis set at MRCI level of theory using a CASSCF state-combination of ABC-DEF. In all these figure the "UPPER" active space was used.

PECs was investigated for the $X^7\Sigma^+$, $B^7\Sigma^+(II)$, $D^7\Sigma^+(III)$, $A^7\Pi$ and $E^7\Pi(II)$ states and found to be significant in varying parameters such as r_e, D_e, T_e and $E(\nu = 1)$. Again this is a new and significant result as published MRCI results seldom mention the states used in the CASSCF calculation proceeding any MRCI

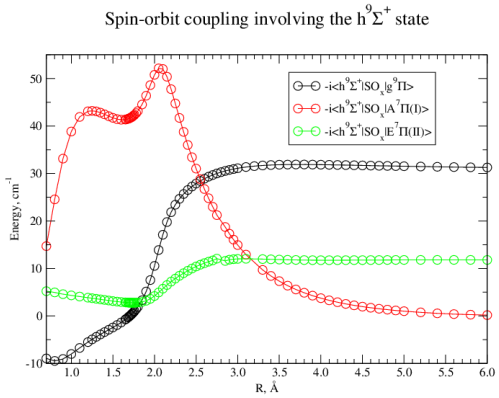

Figure 7.33: Spin-orbit coupling between the nonuplet states calculated at MRCI level of theory using a cc-pVQZ basis set. In this calculation the CASSCF state-combination used was ABC-DEF.

Mn Atom dissociation term	Coupling	Magnitude (cm^{-1})
a^6D	$\langle B^7\Sigma^+(II)\vert\, SO_x \,\vert A^7\Pi\rangle$	95.46
	$\langle C^7\Delta\vert\, SO_x \,\vert A^7\Pi\rangle$	55.19
	$\langle B^7\Sigma^+(II)\vert\, SO_x \,\vert b^5\Pi\rangle$	42.72
	$\langle C^7\Delta\vert\, SO_x \,\vert b^5\Pi\rangle$	24.68
	$\langle c^5\Sigma^+(II)\vert\, SO_x \,\vert b^5\Pi\rangle$	109.65
	$\langle c'^5\Delta\vert\, SO_x \,\vert b^5\Pi\rangle$	62.09
	$\langle c^5\Sigma^+(II)\vert\, SO_x \,\vert A^7\Pi\rangle$	42.68
	$\langle c'^5\Delta\vert\, SO_x \,\vert A^7\Pi\rangle$	24.67
	$\langle b^5\Pi\vert\, SO_z \,\vert b^5\Pi\rangle$	126.16
	$\langle A^7\Pi\vert\, SO_z \,\vert A^7\Pi\rangle$	135.21
	$\langle b^5\Pi\vert\, SO_z \,\vert A^7\Pi\rangle$	20.15
Z^8P^0	$\langle h^9\Sigma^+\vert\, SO_x \,\vert g^9\Pi\rangle$	31.16
	$\langle h^9\Sigma^+\vert\, SO_x \,\vert E^7\Pi(II)\rangle$	11.77
	$\langle g^9\Pi\vert\, SO_z \,\vert g^9\Pi\rangle$	88.15
	$\langle E^7\Pi(II)\vert\, SO_z \,\vert E^7\Pi(II)\rangle$	84.96
	$\langle E^7\Pi(II)\vert\, SO_z \,\vert g^9\Pi\rangle$	8.33

Table 7.21: Non-zero dissociation spin-orbit coupling values obtained for MnH at MRCI level of theory using a cc-pVQZ basis set and a CASSCF state-combination of ABC-DEF.

calculations. The r_e values of both the $a^5\Sigma^+$ and $X^7\Sigma^+$ have been found to be consistent with previous experimental studies. The TDMs acting between these 15 low-lying electronic states have been calculated. Previously Langhoff et al. (1989) has calculated the TDMs between the TDMs for the $c^5\Sigma^+ - a^5\Sigma^+$, $c^5\Sigma^+ - b^5\Pi$ and $b^5\Pi - a^5\Sigma^+$ transitions.

For the $^7\Pi$ states, it was found that for the $A^7\Pi$ state, the PEC underwent a dramatic change in character from been anti-bonding to bonding in nature when an increased active space was used. This is very important as naively, one could undertake MRCI calculations using a lower active space for one $^7\Pi$ state and obtain a PEC which seems continuous and reasonable in character. Also the DMCs and couplings of the $A^7\Pi$ and $E^7\Pi(II)$ states needed to be "de-tangled".

Finally, for the first time, electronic angular momenta and spin-orbit couplings have been calculated for MnH for couplings acting between the 15 low-lying electronic states acting. The spin-orbit couplings within individual Π states and Δ states were

found to be between 85-135 cm^{-1} and 255-275 cm^{-1} respectively: the spin-orbit couplings connecting different electronic states were found to be up to 40 cm^{-1}. These spin-orbit couplings have been plotted and non-zero dissociation values tabulated. These results are important in the context of creating accurate linelists and go to show that couplings between electronic states for transition metal diatomics should not be ignored when aiming for spectroscopic accuracy.

Chapter 8

Manganese Hydride Linelist

In this chapter the linelist calculated for MnH will be presented. Section 8.1 briefly summarises the *ab initio* calculations used in the construction of the linelist. In order to improve this *ab initio* model, experimental data was gathered and processed into Duo format (see section 8.2) and used to produce refined potentials for the $X^7\Sigma^+$ and $A^7\Pi$ states. This processing for the $A^7\Pi - X^7\Sigma^+$ system is described in section 8.2.1 and that for the quintet systems described in section 8.2.2. Section 8.3 presents spectra generated using ExoCross for this linelist with a discussion of possible astronomical applications. The spectra simulated ties in with previous experimental observations and helps shed light on why certain electronic transitions have been observed previously but not others.

8.1 *Ab initio* calculations used in the linelist

Using the *ab initio* results presented in chapter 7.2, a 10 state linelist for MnH was calculated. Since the $D^7\Sigma^+(III)$, $E^7\Pi(II)$, $g^9\Pi$ and $h^9\Sigma^+$ states are anti-bonding in nature (see section 7.2.1), these were not included in the final linelist. Figure 8.1 shows the *ab initio* PECs of the 10 electronic states included in the final linelist. In this linelist the $A^7\Pi$ and $X^7\Sigma^+$ were fitted to the available experimental data as described in section 8.2.1. For the quintet states, the experimental data available was used to replace rovibronic states calculated hence making the linelist of experimental accuracy. The electronic states included were the $X^7\Sigma^+$, $A^7\Pi$, $B^7\Sigma^+(II)$, $a^5\Sigma^+$, $b^5\Pi$, $c'^5\Delta$, $c^5\Sigma^+(II)$, $d^5\Pi$, $e^5\Sigma^+(III)$ and $f^5\Delta$ states with all TDMs included coupling the $X^7\Sigma^+$, $a^5\Sigma^+$ and $b^5\Pi$ electronic states to the upper electronic states.

8.2 Processing Experimental data for MnH

This section describes how experimental data for both the septuplet (section 8.2.1) and quintet states (section 8.2.2) which is available in literature was processed into Duo format. Once the data was in Duo format it was then used to refine the respective PECs of the electronic states it was for. The process of fitting experimental data is described in section 2.9.3. For a Duo input file, the required format is as shown in table 8.1.

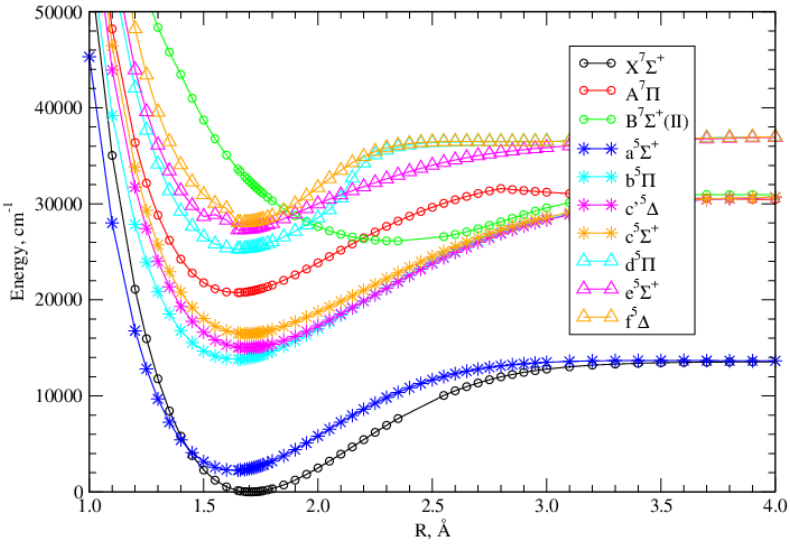

Figure 8.1: *Ab initio* PECs used in the construction of the linelist for MnH. These PECs have been calculated using a cc-pVQZ basis set at MRCI level of theory. See chapter 7 for details of these calculations.

J	Parity	Running #	Energy	E-state	ν	Λ	Σ	Ω

Table 8.1: Input format of reference experimental energies for a Duo input file.

8.2.1 Processing experimental data for the $A^7\Pi - X^7\Sigma^+$ system of MnH

As was summarised in section 6.2, there has been several studies of the $A^7\Pi - X^7\Sigma^+$ system and $X^7\Sigma^+$ state of MnH.

Starting with the $X^7\Sigma^+$ ground state only, the programme PGopher (Western, 2010 & 2015) was used to generate a list of "experimental" energies to fit to. For an overview of the PGopher program see section 2.9.4. Using the experimental constants presented by Gordon et al. (2005) for the $X^7\Sigma^+$ state, $\nu = 0, 1, 2$, PGopher was used to generate the list of experimental energies. These constants are shown in table 8.2. The molecular constants presented by Gordon et al. (2005) were used instead of those presented by Varberg (1992), Gengler et al. (2007) and Halfen & Ziurys as these later three studies only focussed on $\nu = 0$ for low values of J.

Constant	$\nu = 0$	$\nu = 1$	$\nu = 2$	$\nu = 3$
T_ν		1490.644889	2923.31542(34)	4296.15620(55)
B_ν	5.6055050(96)	5.4441092(96)	5.2797006(106)	5.1104876(160)
$10^4 D_\nu$	3.04743(57)	3.04512(62)	3.05665(76)	3.08943(128)
$10^9 H_\nu$	8.639(131)	7.532(152)	5.926(196)	3.38(39)
$10^{12} L_\nu$	1.861(96)	2.473(122)	3.324(174)	5.12(39)
γ_ν	0.031349(36)	0.030497(37)	0.029559(38)	0.028548(38)
$10^6 \gamma_{D_\nu}$	-6.902(58)	-7.159(64)	-7.399(71)	-7.681(80)
λ_ν	-0.004020(92)	-0.004230(92)	-0.004462(95)	-0.004778(103)
$10^6 \lambda_{D_\nu}$	-5.20(46)	-5.22(49)	-5.40(55)	-5.32(60)

Table 8.2: pectroscopic constants (in cm^{-1}) for the $X^7\Sigma^+$ ground state of MnH presented by Gordon et al. (2005). These constants were used to generate a list of experimental energies for this $X^7\Sigma^+$ state to fit the *ab initio* curves to.

Gordon et al. (2005) derived these spectroscopic constants by doing a Dunham-type fit to their measured experimental data for transitions within this ground state, $X^7\Sigma^+$ for $N' = 0$ to 26 and $N'' = 0$ to 27. The accuracy of this list of energies, each denoted E(PG) generated using PGopher was checked using the vibrational frequencies recorded by Gordon. Using the quantum numbers given in this list of energies generated and the frequencies given by Gordon et al. 2005 an upper energy, E' was constructed as follows:

E'(check)=E"(PG) + ν(Gordon)

This energy, E'(check) was then compared to $E'(PG)$ and the average absolute value of the difference between these two energies were found to be 0.0027 cm^{-1} thus suggested that the list of energies constructed using PGopher was consistent with observed experimental frequencies.

In a similar fashion for the $X^7\Sigma^+$ state, PGopher was used to construct a list of energies for the $A^7\Pi$ state. For this state, the spectroscopic parameters produced by Gengler et al. (2007) for the $\nu = 0$ state were used (constants for higher ν are not at present available for this electronic state). These constants are shown in table 8.3.

Study	Gengler et al. (2007)		Varberg(1991, 1992)
Constant	N^2 fit	R^2 fit	R^2 fit
A	40.52859(45)	40.51621(25)	40.51878(93)
A_D	0.00512(16)	0.00471(25)	0.00223(71)
η	9.75(33) $\times$ 10^{-4}	0.001011(50)	0.00166(27)
B	6.34829(11)	6.34784(17)	6.346098(91)
D	4.025(24) $\times$ 10^{-4}	4.099(36) $\times$ 10^{-4}	3.7204(82) $\times$ 10^{-4}
γ	−0.01703(38)	−0.01801(58)	−0.0231(16)
λ	0.30164(30)	0.30239(45)	0.3050(12)
λ_D	−2.66(62) $\times$ 10^{-5}	−2.20(86) $\times$ 10^{-5}	−5.70(54) $\times$ 10^{-5}
$o+p+q$	−0.065425(66)	−0.065405(96)	−0.06566(39)
$p+2q$	0.062687(79)	0.06257(12)	0.06218(23)
q	0.005826(39)	0.005753(59)	0.005430(63)
$(o+p+q)_D$	1.72(39) $\times$ 10^{-5}	1.71(58) $\times$ 10^{-5}	1.53(78) $\times$ 10^{-5}
$(p+2q)_D$	−2.12(37) $\times$ 10^{-5}	−1.56(55) $\times$ 10^{-5}	−1.93(28) $\times$ 10^{-5}
$T_{00}(A-X)$	17660.4723(49)	17666.8067(75)	17666.791(19)
Standard dev	0.0021	0.0021	

Table 8.3: Spectroscopic parameters determined for the $A^7\Pi$, $\nu = 0$ state of MnH by Gengler et al. (2007) using an N^2 fit and an R^2 fit and by Varberg et al. (1991, 1992) using an R^2 fit.

Table 8.3 compares the parameters derived for this state with those obtained by Varberg et al. (1991, 1992). As a reminder both the studies of Gordon et al. (2005) and Halfen & Ziurys (2008) were on the $X^7\Sigma^+$ state only. It was decided to use the parameters for the N^2 fit performed by Gengler et al. (2007) as these are more recent and from a study which covered a larger range in the N quantum number.

Hence for both the $X^7\Sigma^+$ and $A^7\Pi$ states we thus had a list of energies generated from PGopher using molecular parameters fitted by experimentalists to their measured results. By default this energy list produced by PGopher gave all the quantum numbers required by Duo: hence the process of putting these lists of energies into Duo format (see table 8.1) was relatively straightforward.

Finally using these two lists of experimental energies for the $X^7\Pi$ and $A^7\Pi$ states,

spectroscopic parameters were fitted and hence used in the construction of the linelist. So this process was similar to that for CrH (see section 5.2). Tables 8.4, 8.5 and 8.6 show illustratrive examples of the accuracy of refinement to these experimental energies obtained for the $X^7\Sigma^+$ and $A^7\Pi$ states.

J	Parity	Obs	Calc	Obs-Calc	State	ν	Λ	Σ	Ω
0	-	66.8797	66.9877	-0.1080	1	0	0	0	0
1	+	33.3994	33.4809	-0.0815	1	0	0	1	1
2	-	66.9511	67.0122	-0.0611	1	0	0	-2	-2
3	+	33.5154	33.5128	0.0026	1	0	0	3	3
4	-	312.2376	312.3879	-0.1503	1	0	0	-1	-1
5	+	33.8215	33.8088	0.0127	1	0	0	1	1
6	+	112.1331	112.0941	0.0390	1	0	0	2	2
7	-	168.0995	168.0541	0.0454	1	0	0	-2	-2
8	+	235.1653	235.113	0.0523	1	0	0	2	2
9	-	733.8222	733.9458	-0.1236	1	0	0	-2	-2
10	+	402.414	402.347	0.0670	1	0	0	2	2
12	+	866.8764	866.8825	-0.0061	1	0	0	3	3
14	-	1327.2584	1327.3236	-0.0652	1	0	0	-2	-2
16	+	1164.543	1164.4364	0.1066	1	0	0	2	2
18	+	1503.1853	1503.0729	0.1124	1	0	0	2	2
20	+	1882.7619	1882.6524	0.1095	1	0	0	2	2
23	-	3002.8158	3002.8584	-0.0426	1	0	0	-3	-3
26	-	3518.0413	3518.0569	-0.0156	1	0	0	-3	-3
29	-	4069.2593	4069.2419	0.0174	1	0	0	-2	-2
1	+	1598.981	1599.0098	-0.0288	1	1	0	0	0
3	+	1490.6449	1490.5736	0.0713	1	1	0	3	3
5	-	1794	1794.0472	-0.0472	1	1	0	-1	-1
7	+	1718.7731	1718.7079	0.0652	1	1	0	3	3
10	-	2203.4679	2203.524	-0.0561	1	1	0	-2	-2
13	+	2619.9621	2620.0601	-0.0980	1	1	0	2	2
16	+	2948.8854	2948.9646	-0.0792	1	1	0	3	3
20	-	4402.6303	4402.9978	-0.3675	1	1	0	-1	-1
23	+	3725.7691	3725.7865	-0.0174	1	1	0	1	1
27	-	4904.3798	4904.624	-0.2442	1	1	0	-2	-2
30	+	6298.0233	6298.0619	-0.0386	1	1	0	3	3

Table 8.4: Representative example of refinement accuracy obtained for the $\nu = 0$ and $\nu = 1$ bands of the $X^7\Pi$ state of MnH. In this table and in table 8.5 and 8.6, the quantum numbers shown take on their usual meanings as explained in section 2.2. "State" refers to the electronic state: state 1 refers to the $X^7\Sigma^+$ electronic states and state 2 refers to the $A^7\Pi$ state. "Obs" is an experimentally derived energy level and "Calc" is one calculated using the refined parameters. Hence "Obs-Calc" gives an indication of the accuracy of refinement obtained.

As can be seen from tables 8.4, 8.5 and 8.6 we typically obtained a refinement accuracy of under 0.5 cm^{-1}.

8.2.2 Processing experimental data for the quintet states of MnH

As was mentioned in section 6.1, Balfour and co-workers performed FTS experiments on the quintet states of MnH and MnD. From their measured experimental frequencies they derived term values (i.e. energy levels) for the various quintet states. A summary of the experimental work undertaken by Balfour and co-workers is shown in table 8.7.

J	Parity	Obs	Calc	Obs-Calc	State	ν	Λ	Σ	Ω
3	-	3081.0069	3081.1046	-0.0977	1	2	0	-1	-1
5	-	3081.2417	3081.2896	-0.0479	1	2	0	-3	-3
7	+	3301.4585	3301.5275	-0.0690	1	2	0	2	2
10	+	3738.7177	3738.8151	-0.0974	1	2	0	2	2
14	+	3740.1251	3740.043	0.0821	1	2	0	2	2
17	+	4337.1991	4337.1531	0.0460	1	2	0	3	3
21	+	4694.9924	4694.8533	0.1391	1	2	0	1	1
24	+	6480.5057	6480.5468	-0.0411	1	2	0	2	2
27	+	7012.688	7012.5697	0.1183	1	2	0	3	3
30	+	7014.7554	7014.6558	0.0996	1	2	0	2	2
2	-	4448.7161	4448.8642	-0.1481	1	3	0	0	0
4	+	4326.8159	4326.9048	-0.0889	1	3	0	3	3
6	-	4357.7098	4357.7677	-0.0579	1	3	0	-1	-1
8	+	4510.496	4510.5215	-0.0255	1	3	0	2	2
11	+	4663.2048	4663.1543	0.0505	1	3	0	1	1
14	+	5662.4751	5662.5341	-0.0590	1	3	0	2	2
17	-	6192.7258	6192.8293	-0.1035	1	3	0	-2	-2
20	-	6194.1575	6194.1675	-0.0100	1	3	0	-3	-3
22	+	7251.3592	7251.633	-0.2738	1	3	0	2	2
25	+	7253.0508	7253.3067	-0.2559	1	3	0	3	3
28	-	7986.7165	7987.0446	-0.3281	1	3	0	-3	-3
30	+	7576.1468	7575.6855	0.4613	1	3	0	3	3

Table 8.5: Representative example of refinement accuracy obtained for the $\nu = 2$ and $\nu = 3$ bands of the $X^7\Pi$ state of MnH. In this table the units of the calculated rovibronic states are in cm^{-1}. Refer to table 8.4 for details of the notation.

J	Parity	Obs	Calc	Obs-Calc	State	ν	Λ	Σ	Ω
0	-	17694.055	17694.0611	-0.0061	2	0	-1	1	0
1	+	17765.62	17765.5195	0.1005	2	0	1	0	1
2	+	17712.536	17712.4007	0.1353	2	0	1	0	1
3	-	17850.081	17849.8203	0.2607	2	0	-1	-2	-3
4	+	17695.333	17695.1433	0.1897	2	0	1	-1	0
5	+	17734.252	17734.047	0.2050	2	0	1	-3	-2
7	-	17934.733	17934.4701	0.2629	2	0	-1	-2	-3
9	+	18119.272	18119.3278	-0.0558	2	0	1	-3	-2
10	+	18232.7	18232.8153	-0.1153	2	0	1	-3	-2
13	-	18342.884	18343.1803	-0.2963	2	0	-1	1	0
14	+	18481.458	18481.8011	-0.3431	2	0	1	-1	0
15	+	18629.549	18629.2057	0.3433	2	0	1	-1	0

Table 8.6: Representative example of refinement accuracy obtained for the $A^7\Pi$ state of MnH. In this table the units of the calculated rovibronic states are in cm^{-1}. Refer to table 8.4 for details of the notation.

Referring to table 8.7, term values for the $a^5\Sigma^+$, $b^5\Pi$ and $c^5\Sigma^+$ states were obtained from the 1990 study and term values for the $a^5\Sigma^+$, $d^5\Pi$ and $e^5\Sigma^+$ states obtained from the 1992 study. A check was done to compare the two sets of term values for the $a^5\Sigma^+$ state from the 1990 and 1992 studies: they were found to be self-consistent within experimental error. Hence the term values for the $a^5\Sigma^+$ state from the 1992 study were used as these contained energy levels for $\nu = 2$ which the 1990 study did not.

For each of the $^5\Sigma^+$ states, the term values presented by Balfour and co-workers were labelled by quantum numbers J and ν and label F_i where $i = 1, 2, 3, 4, 5$ i.e. 5

Study	Region(cm^{-1})	System (nm)	Electronic Transition	Bands	
				MnH	MnD
1990	9 000 – 10 380	1060	$b^5\Pi - a^5\Sigma^+$	(0, 0)	(0, 0)
1990	11 200 – 12 500	846	$c^5\Sigma^+ - a^5\Sigma^+$	(0, 0), (1, 1)	(0, 0)
1992	20 200 – 21 200	480	$d^5\Pi - a^5\Sigma^+$	(0, 0), (1, 1), (2, 2)	(0, 0)
1992	21 400 – 22 400	450	$e^5\Sigma^+ - a^5\Sigma^+$	(0, 0), (1, 1)	

Table 8.7: Summary of FTS experimental measurements on the quintet states of MnH and MnD undertaken by Balfour and co-workers.

spin-state components. For each value of J and ν there were five of them: these spin-components were simply labelled in order of increasing energy, F_1, F_2, F_3, F_4, F_5. Refer to table 8.1 which gives the required Duo input format for reference experimental data. For these $^5\Sigma^+$ states, J, ν were taken as given and, by definition of a Σ^+ state, $\Lambda = 0$. To deduce the parity, Σ and Ω, a single Duo input file containing an *ab initio* PEC of the $a^5\Sigma^+$ state was created: this Duo file was then compiled hence producing a calculation of rovibronic energies and transitions for this unrefined PEC. The output energy file of this calculation was then examined. For each value of J and ν there were five energies calculated (i.e. the 5 spin components). By examining various "blocks" of output data of constant J and ν, the deductions about the ordering of Parity and the quantum numbers of Σ and Ω for the spin-components as shown in table 8.8 were made. This process was repeated for sample *ab initio* calculations of $c^5\Sigma^+$ and $e^5\Sigma^+$ states and the same deductions made. For the $b^5\Pi$ and $d^5\Pi$ states,

J	Spin-Component	Parity	Σ	Ω
EVEN	F_1	+	1	1
	F_2	-	-2	-2
	F_3	+	2	2
	F_4	-	-1	-1
	F_5	+	1	1

(a)

J	Spin-Component	Parity	Σ	Ω
ODD	F_1	-	-2	-2
	F_2	+	2	2
	F_3	-	-2	-2
	F_4	+	1	1
	F_5	-	-1	-1

(b)

Table 8.8: Summary of deductions concerning the assignment of Parity, Σ and Ω for constant J and ν for $^5\Sigma^+$ states using the $c^5\Sigma^+(I)$ and $a^5\Sigma^+$ term values presented in Balfour (1990) and also the term values presented for the $e^5\Sigma^+(II)$ and $a^5\Sigma^+$ electronic states presented in Balfour (1992). For each values of J there are 5 components labelled F_1, F_2, F_3, F_4 and F_5 which are presented in increasing order of energy.

a similar process of running a Duo calculation of rovibronic transitions and energies and examining the energy file to assign quantum numbers was performed to process the term values presented for these states into Duo format. For these $^5\Pi$ states, the term values presented were again labelled by J and ν: for each value of J and ν there were 10 components: contrast this to the case of the $^5\Sigma^+$ states which had 5 such components for each J and ν. These 10 components were labelled with parity as either "e" or "f" and an integer number from the selection 3, 2, 1, 0, -1: for each J, ν and parity these components were presented in increasing order of energy. This e/f parity which is commonly used was converted into the "rotationless" parity used by Duo using the rules:
e: Parity $= (-1)^J$
f: Parity $= (-1)^{J+1}$.

Hence running seperate Duo input files with *ab initio* PECs of the $b^5\Pi$ state and $d^5\Pi$ state respectively, the deductions concerning Λ, Σ and Ω shown in table 8.9 for these $^5\Pi$ states were made. Hence with the deductions made by running these sample Duo

J	Parity	Component	Λ	Σ	Ω
ODD	-	3e	-1	-1	-2
		2e	-1	-2	-3
		1e	-1	-1	-2
		0e	-1	2	1
		-1e	-1	1	0

(a)

J	Parity	Component	Λ	Σ	Ω
ODD	+	3f	1	2	3
		2f	1	2	3
		1f	1	1	2
		0f	1	2	3
		-1f	1	-1	0

(b)

J	Parity	Component	Λ	Σ	Ω
EVEN	-	3f	-1	-2	-3
		2f	-1	0	-1
		1f	-1	1	0
		0f	-1	2	1
		-1f	-1	1	0

(c)

J	Parity	Component	Λ	Σ	Ω
EVEN	+	3e	1	2	3
		2e	1	0	1
		1e	1	-1	0
		0e	1	-2	-1
		-1e	1	-1	0

(d)

Table 8.9: Summary of deductions concerning the assignment of Parity, Λ, Σ and Ω for constant J and ν for $^5\Pi$ states. These deductions were made by reference to the term values for the $b^5\Pi$ state presented in Balfour (1990) and the term values for the $d^5\Pi(II)$ state presented in Balfour (1992). For each J and parity pair, there are 5 components labelled in order of increasing energy as indicated in this table. This is in contrast to the $^5\Sigma^+$ states in which there are 5 components for each value of J as compared to 10 for these Π states.

input files, it was then possible to put the term values generated by Balfour for both the $^5\Sigma^+$ states (see table 8.8) and the $^5\Pi$ state (see table 8.9) into the required Duo input format presented in table 8.1. In table 8.1, the "E-state" label is simply a label which references each electronic state (1 for the $a^5\Sigma^+$, 2 for $b^5\Pi$, 3 for $c^5\Sigma^+$, 4 for $d^5\Pi$ and 5 for $e^5\Sigma^+$). The "Running #" is simply an internal Duo integer referencing label: all of the term values for all 5 states were put in increasing order and hence the terms labelled 1, 2, 3 etc. This list of experimentally derived term values was used in the final linelist.

8.3 Linelist Spectra

The Manganese atom has 1 stable isotope of atomic mass 55: additionally, there are over 25 radioisotopes with half-lives varying between 105 ns (^{44}Mn) and 3.7 $\times$ 10^6 years (^{53}Mn). In terms of astronomical importance, the ^{55}Mn isotope is of interest in supernova explosions (Iwamoto et al. 2009). Lugmair & Shukolyukov (1998) have investigated if the ^{53}Mn and ^{53}Cr isotopes can be used to determine timescales for solar system objects such as chondrites and meteorites. Also, since the possibility of using CrH and CrD spectra to infer the age of brown dwarfs has been postulated (see section 3.4) it was hence decided to generate linelists for the ^{55}MnH, ^{55}MnD, ^{53}MnH and ^{53}MnH isotopologues.

The number of rovibronic states in this linelist is 47 573 and the number of transitions is 5 408 337. All transitions up to $J = 50$ are included with the vibrational range

for each electronic state as follows: $X^7\Sigma^+$ ($\nu = 12$), $A^7\Pi$ (10), $B^7\Sigma^+(II)$ (14), $a^5\Sigma^+$ (9), $b^5\Pi$ (23), $c'^5\Delta$ (23), $c^5\Sigma^+(II)$ (22), $d^5\Pi(II)$ (10), $e^5\Sigma^+(III)$ (10) and $f^5\Delta(II)$ (10).

As was done for the calculated linelist of CrH, the program ExoCross (see section 2.10) was used to simulate spectra using the calculated linelist of MnH as input. Figure 8.2 shows the calculated absorption spectra at 1500 K for the ^{55}MnH isotopologue for the electronic transitions to the $X^7\Sigma^+$ and $a^5\Sigma^+$ electronic states. Figure 8.2

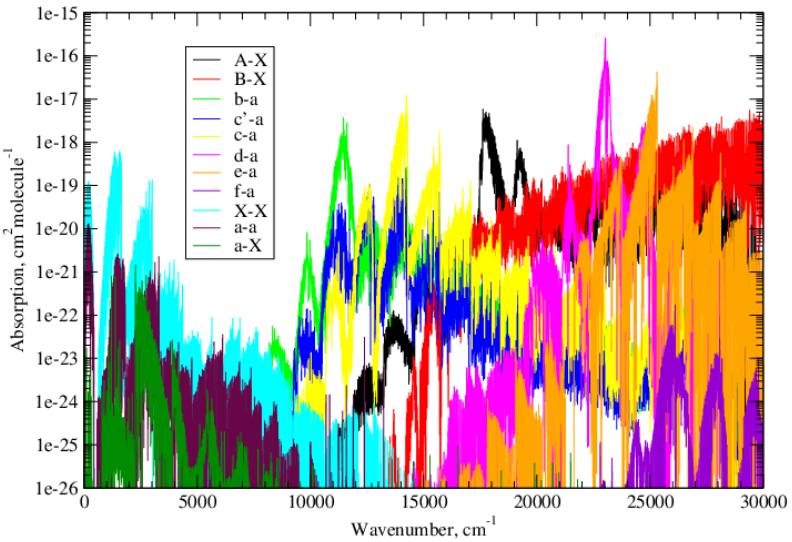

Figure 8.2: Cross-sectional absorption bands for the ^{55}MnH isotopomer calculated using a Gaussian profile with a half-width half-maximum of 1.0 at a temperature of 1500 K.

shows clear band structure for the various electronic transitions. As can be seen the various bands spans the the mid infrared to the near UV regions. As can be seen from figure 8.2 the $X - X$ rovibronic transitions dwarf those of the $a - a$ and also the spin-forbidden transitions of $X - a$. Thus this could explain why pure rovibronic spectra within the $a^5\Sigma^+$ has not been observed by experimentalists which seems surprising given that Balfour and co-workers have been able to measure the $b - a$, $c - a$, $d - a$ and $e - a$ transitions. Figure 8.2 clearly shows why they were able to measure these transitions as the band heads are clearly visible and each isolated. Also it can be seen that the $c' - a$ transitions are dwarfed by those of the $b - a$ transitions and similarly the $f - a$ transitions are dwarfed by the $e - a$ transitions. This is expected as both the and c' and f states are Δ states so hence not normally expected to couple to Σ^+ states. A band head of the $A - X$ transition is also clearly shown. Finally figure 8.2 raises the possibility that the $B - X$ transition could potentially be measured at wavelengths greater than approximately 27 000 cm^{-1} given a sufficiently sensitive experimental set-up given that there does not appear to be any other electronic bands obscuring it in this region.

Figure 8.3 shows the effect of temperature on the simulated spectra for all of the bands shown in figure 8.2. As can be seen from figure 8.3 between 500 K and 1500 K the difference in intensity generated is around 4 orders of magnitude. This temperature range is applicable to exoplanets and also T dwarfs. For L dwarfs in which diatomic hydrides such as FeH, CrH and CaH have been discovered the temperature

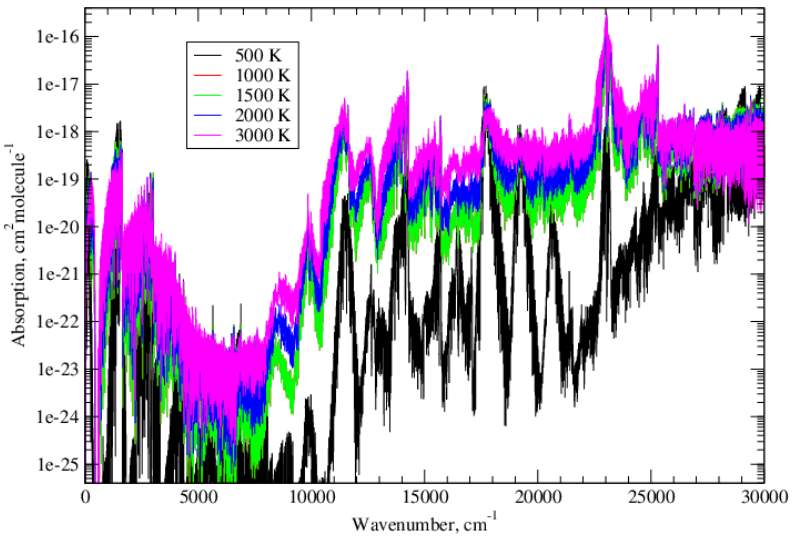

Figure 8.3: Effect of temperature on the absorption cross section for the $A^7\Pi - X^7\Sigma^+$ band of the ^{55}MnH isotopomer calculated using a Gaussian profile with a half-width half-maximum of 1.0

range is typically between 1500 and 2200 K. As figure 8.3 shows the difference in intensity between 1500 and 2000 K is around half an order of magnitude.

Moving onto the effects of isotopic substitution, figure 8.4 shows stick spectrum generated for the ^{55}MnH and ^{55}MnD linelists. As can be seen from figure 8.4 the

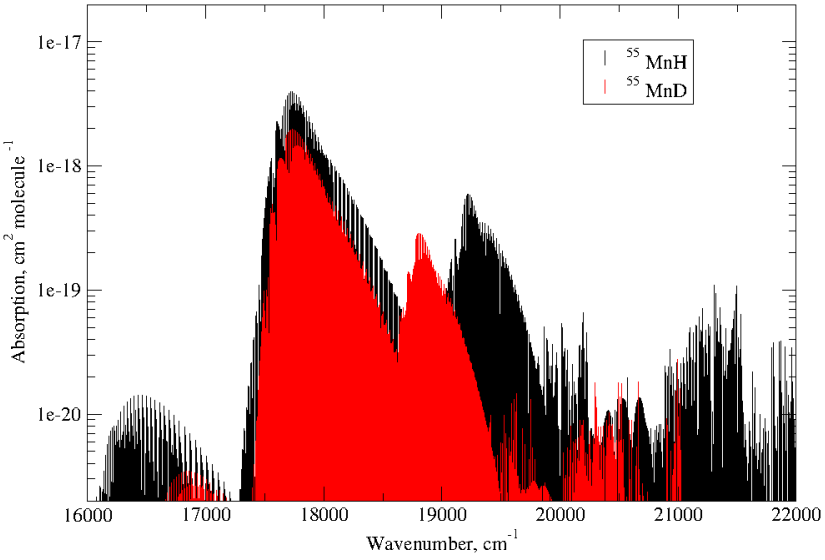

Figure 8.4: Comparison of the absorption band for the $A^7\Pi - X^7\Sigma^+$ band for ^{55}MnH and ^{55}MnD calculated using a Stick profile at a temperature of 1500 K.

^{55}MnH spectra dominates over the ^{55}MnD spectra at 17 700 cm^{-1}. However with the next peak there is a clear shift with the ^{55}MnH spectra peaking at 19 225 cm^{-1} and the ^{55}MnD peaking at 18 805 cm^{-1}. These peaks correspond to 0.5201 μm and 0.5317 μm respectively. Hence to observe this shift would require a resolution of $\approx$44

in the visible region.

Moving onto the partition function, figure 8.5 shows a comparison between the partition function calculated for the linelist and that of Sauval & Tatum (1984). The coefficients for the partition function which Sauval & Tatum (1984) derived using experimental data were $a_0 = 4.1860$, $a_1 = -2.1839$, $a_2 = 0.8747$, $a_3 = -0.2513$ which were inserted into equation 5.3 to generate the partition function shown in figure 8.5. As can be seen from figure 8.5 our partition function is larger which suggests hence

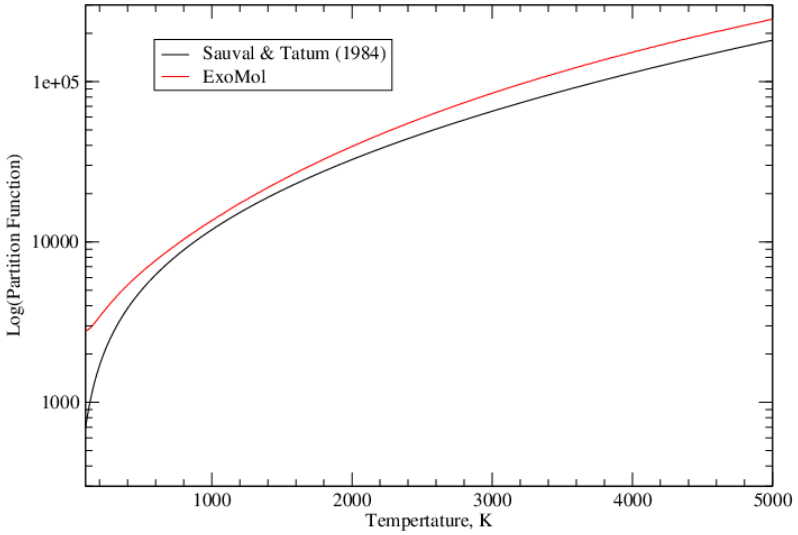

Figure 8.5: Comparison of total partition function calculated as a function of Temperature for the ^{55}MnH linelist with that predicted by Sauval & Tatum (1984). The partition function of Sauval and Tatum (1984) has been multiplied by a factor of 12 to account for the effects of nuclear spin statistics which they did not account for in their study.

our model of MnH more complete. Figure 8.6 shows the total partition function as a function of the quantum number J for different temperatures. Our linelist goes up to $J = 50$ as it was determined from initial Duo calculations that this would be sufficient. Figure 8.5 demonstrates this as it can be seen that for temperatures up to 3000 K the partition function is converging well before $J = 50$. To gain an idea of the completeness of the total partition function Q, a partition function $Q(E)$ can be calculated in which only states up to the first dissociation limit are populated. A comparison can be made between these two partition functions by plotting the percentage difference between them calculated as $100 \times (Q - Q(E))/Q$. This is shown in figure 8.7 as a function of temperature.

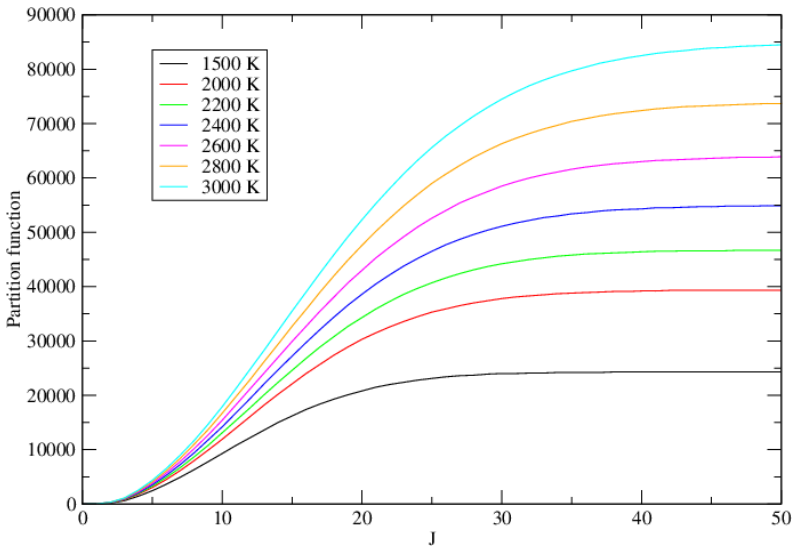

Figure 8.6: Partition function as a function of J for different temperatures which are applicable to the study of L and M dwarfs.

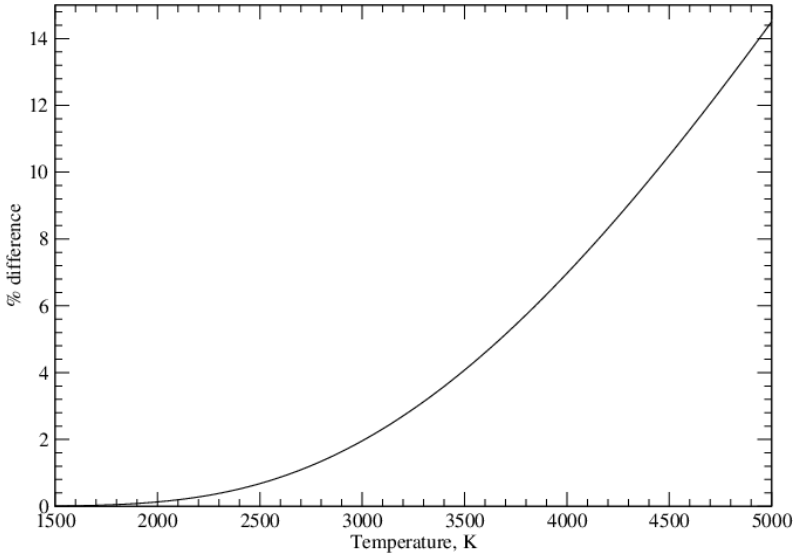

Figure 8.7: Percentage difference between the total partition function Q and the partition function $Q(E)$ in which only states up to the first dissociation limit of 12785 cm^{-1} are populated.

Since both the Partition function and intensity both have the same Boltzmann factor, an error in the partition function (i.e error in completeness) can be related to an error in intensities and hence opacities. As can be seen from figure 8.7 if an accuracy of 10% is judged to be acceptable then up to temperatures of 4500 K a linelist in which only states up to the first dissociation limit are populated is sufficiently complete.

In summary a linelist for MnH has been created by calculating *ab initio* curves and fitting to the available experimental data sets. At present there is no linelist in the literature for this molecule. Hence this creates the opportunity for a potential detection of this molecule in space. Given that the cosmic abundance of Chromium and Manganese are relatively similar (see table 3.1) it does beg the question of why it has not been observed to date. Given the problems astronomers have experienced

using the existing linelists for CrH and FeH to successfully model observed L dwarf spectra (see section 3.4) the possibility that MnH is accountable for at least some of the discrepancies in opacity can now be investigated.

Chapter 9

Further Research Directions and Conclusions

The calculation of linelists for CrH and MnH has opened up many possible future directions for research from theoretical, experimental and astronomical viewpoints. Also, having studied the molecules of CrH and MnH there is potential for linelists to be created for other diatomic metal hydrides.

9.1 Experimental work

The construction of the linelist for CrH highlighted how imperative it is to refine *ab initio* PECs to experimental data. As was shown in table 5.3 for CrH there is only experimental data available for the $A^6\Sigma^+ - X^6\Sigma^+$ system and only for a handful of vibrational bands. In order to better constrain the PECs of the $X^6\Sigma^+$ and $A^6\Sigma^+$ states experimental data of vibrational bands with $\nu > 2$ would be of significant assistance. The experimental group led by Amanda Ross in Universite Lyon 1 is planing to measure the intensities of CrH spectra: this would provide valuable assistance in constraining the transition dipole coupling the $A^6\Sigma^+$ and $X^6\Sigma^+$ electronic states.

For MnH, luckily there was experimental data available for 5 electronic transition systems ($X-A$, $b-a$, $c-a$, $d-a$ and $e-a$) but again this was limited to $\nu = 0, 1, 2$. Any new measurements going beyond $\nu > 2$ would be particularly useful in the context of brown dwarfs as the temperatures reached mean that these higher vibrational states are likely to be occupied.

Longer term, as has been the case for the water molecule, for the open-shell diatomics a productive and instructive way forward would be a bouncing back and forth pattern between theoretical calculations making predictions which are then tested by experimentalists whose data is then used by theorists to generate new models which are tested by experimentalists and so on and so forth.

9.2 Theoretical Work

There are several possible avenues in terms of basis set optimisation which could be explored. Throughout this study, relativistic and core-correlation effects have not been incorporated due to the demands they place on computing power: however it was known from previous studies within the group that for similar diatomic molecules that these tend to cancel each other out. A computational project could be to design algorithms to decrease the RAM required for such calculations.

When deciding what basis sets to use it is desirable to choose a basis set which best describes the behaviour of the valence electrons. Dr Laura K. McKemmish, a Research Associate within the ExoMol group worked on replacing the primitive core basis-functions within basis sets with a single RAMP function for her PhD. Using the analogy of a model of the Earth made out of Lego, if you are only interested in the surface (i.e. valence electrons) then you don't care what Lego blocks are used in the centre i.e. you are only interested in Lego blocks on and near to the surface. Hence in this case (which is the standard within quantum chemistry) it is allowable to use bigger Lego bricks to model the centre of the earth and then for the surface layers (i. e the valence electrons), use smaller bricks for the desired accuracy.
Taking the example of a carbon atom, the number of Gaussians used in a basis set typically is:

- 6 primitive functions to describe the 1s atomic orbitals
- 3 functions to describe the for 2s atomic orbitals
- 1 function to describe the 2p atomic orbitals
- 1 Gaussian function to describe harmonic behaviour.

The idea behind "RAMPS" basis functions is to replace the 6 primitive Gaussians with 1 Gaussian & 1 ramp to describe the core region. Since the functions describing the valence electrons are left the same, the behaviour of these electrons (which ultimately determine the chemistry of the species under consideration) remains unchanged. The advantage of replacing the core with this simplified pair of functions is that the speed of computational calculations can be significantly improved.

Taking the case of CrH and MnH both molecules have "core electrons" which form a core "Argon" electron configuration around the respective transition metal nucleus: the remaining electrons, 7 for the case of CrH and 8 for the case of MnH, act as valence electrons. A possible area of future research is thus to replace the core basis functions with a hybrid function of a primitive Gaussian and a "RAMP" into the basis sets used in order to increase the speed of calculations. This would hence allow more focus to be directed to improving the accuracy of results obtained. Since the valence electrons are dominant (as they determine the molecular orbitals) it would be wise for future research to investigate the effects of adding more primitive Gaussian functions to the basis sets used to hence more accurately describe the behaviour of these electrons.

9.3 Astronomical work

An educational school student project could be to undertake a search of literature for diatomic hydrides, chlorides, iodides, fluorides and oxides going through the periodic table up to the 2nd row of transition metals. For reference this section of the periodic table is shown in table 9.1. The aim of this search would be to ascertain if there are any such molecules not already covered by the ExoMol project which are of astronomical interest not just for stars and planets but also in settings such as the ISM. An understanding of the chemistry of the ISM is an active research area. For any such molecules identified, a search could be undertaken to ascertain the scope and accuracy of experimental and theoretical data available for detection and characterisation.

H 1																	He 2
Li 3	Be 4											B 5	C 6	N 7	O 8	F 9	Ne 10
Na 11	Mg 12											Al 13	Si 14	P 15	S 16	Cl 17	Ar 18
K 19	Ca 20	Sc 21	Ti 22	V 23	Cr 24	Mn 25	Fe 26	Co 27	Ni 28	Cu 29	Zn 30	Ga 31	Ge 32	As 33	Se 34	Br 35	Kr 36
Rb 37	Sr 38	Y 39	Zr 40	Nb 41	Mo 42	Tc 43	Ru 44	Rh 45	Pd 46	Ag 47	Cd 48	In 49	Sn 50	Sb 51	Te 52	I 53	Xe 54

Table 9.1: Periodic table for the first 36 elements with the alkaline earth metals of Be, Ca & Mg highlighted as well as the transition metals Mn & Cr

A potentially exciting project to undertake is a search for MnH in the sunspot spectra of Wallace et al. (2006) and also in spectra of brown dwarfs published such as those on the DwarfArchives webpage. The former could be a coding based project in which computer code is written which systematically searches for matches within an accuracy level which can be adjusted and then, for any "matches" found a statistical study undertaken to ascertain the probability of each "match" been a coincidence.

In terms of stellar astronomy, HotMol is an ERC funded project based in Freiberg led by Professor Svetlana Berdyugina (see section 3.4). One of the aims of Svetlana's work is to investigate if the Paschen-Back effect in molecules can be exploited as a method to determine the magnetic field strength of different classes of stars and brown dwarfs. Different molecules, and indeed different electronic states within molecules will be sensitive to various magnetic field strengths-the hope is that a set of molecules can be determined which can be used to determine the magnetic field strengths of various astrophysical objects which can cover a huge range of magnitudes. Oleksii Kuzmychov investigated CrH as a probe of magnetic field strengths for his PhD. If MnH was to be found within stellar objects, a similar quantum mechanical study for MnH could be undertaken now that PECs have been calculated within this PhD.

9.4 Creation of a new linelist for FeH

A diatomic hydride molecule which is an obvious candidate for further work is diatomic Iron Hydride, FeH. The atomic element Iron sits along the first row of the

transition metals in the periodic table after Chromium and Manganese. The molecule FeH has 27 electrons in total. FeH is of interest from an astronomical perspective as summarised in section 9.4.1. The existing linelist of the $F^4\Delta_i - X^4\Delta_i$ transition available to astronomers for characterisation is summarised in section 9.4.2. Section 9.4.3 then discusses a possible collaboration and source of funding which could be used to begin the process of constructing a new and more extensive linelist of FeH. Section 9.4.4 then gives a summary of the experimental work that has been done on FeH and could thus be used in fitting any calculated PECs. In summary there are a range of small student projects in working with the experimental data which would greatly assist with the refinement of any calculated *ab initio* curves. The theoretical work which has previously been undertaken on FeH is summarised in section 9.4.5. Finally, section 9.4.6 then discusses the theoretical difficulties that would be involved in calculating new *ab initio* data for use in the construction of a new linelist.

9.4.1 Astrophysical importance of FeH

Iron Hydride (FeH) is a molecule of significant interest in astronomy: the element Iron has one of the most stable nuclei in existence in the universe. In terms of transition metals, the abundance of iron dwarfs those of other metals (see section 3.4). The interest in FeH in space started back in 1972 when Carroll & McCormack first identified FeH in the solar spectrum. Wing, Cohen & Brault (1977) then confirmed this detection of the two bands at 9896 Å and 8691 Å. Mould & Wyckoff (1978) also modelled the FeH column densities of late-type stellar atmospheres and noted how sensitive the FeH Wing-Ford bands are to surface gravity. Additionally, Nordt, Lindgren & Wing (1977) made a tentative identification of a band of FeH near 9900 Å in M dwarfs and S stars using experimental data from Klymming & Lindgren. This identification in S stars was then confirmed by Clegg & Lambert in 1978: additionally Hirai & Chinami (1992) detected FeH in M, S and C stars. Since these early studies, numerous studies of FeH in the solar spectrum, cool stars and brown dwarfs have been undertaken including:

- The Wing-Ford band (9900 Å) detected and modelled in M dwarfs by several authors: Schiavon, Barbuy & Singh (1997); Reiners (2007); Wende, Reiners & Ludwig (2009); Wende, Reiners, Seifahrt & Bernath (2010); Shulyak et al. (2010);

- FeH is an important molecule in brown dwarfs in particular L type dwarfs. The presence and variability of FeH in dwarfs spanning different ages has been studied by numerous authors including Cushing et al. (2003), Knapp et al. (2004), McLean et al. (2007), Bailer-Jones (2008), Goldman et al. (2008), Burgo et al. (2009), Martìn et al. (2010), Hargreaves et al. (2010).

- Mulchaey (1989) measured the sunspot spectra and searched for the 7 different bands of FeH as measured by Phillips et al. (1987) and identified 3 of them. He then calculated an average effective rotational temperature of 1740 $\pm$ 100 K. This temperature he noted is significantly lower than previous rotational temperatures obtained using other molecules such as TiO.

- Fawzy, Youssef & Engvold (1998) have identified FeH in the sunspot using the (2, 0) and (2, 1) bands of the $^4\Delta - ^4\Delta$ system using the FTS spectrometer at the Kitt Peak Observatory.

- Wallace & Hinkle (2001) have identified the $E^4\Pi - A^4\Pi$ system of FeH near 1.6 μm in sunspot and cool star spectra.

- Ramos, Bueno and Collados (2004) have identified both linear and circular polarisation induced from the Zeeman effect from the $E^4\Pi - A^4\Pi$ system of FeH in sunspot spectra around 1.6 μm.

- Fawzy (2009) has used equivalent widths for the (0-0), (1-0), (2-0), and (2-1) band of the $^4\Delta - ^4\Delta$ system of FeH to derive a rotational temperature of the large sunspot "San Fernando 535" of $T_{\rm rot} = 2900 \pm 300$ K which Fawzy notes is in agreement with rotational temperatures for this sunspot derived using other molecules.

- Reiners, Schmitt & Liefke (2007) have undertaken a study of the magnetic flux variability of Wing-Ford band near 1 μm in the nearby flare star of CN Leonis.

- Bar-Nun, Pasternack & Barrett (1980) have proposed the existence of FeH and FeH_2 in interstellar clouds on the basis of previous Argon matrix trapping experiments

In summary, FeH is a molecule of significant interest to the solar, cool star and brown dwarf communities: the electronic system of $E^4\Pi - A^4\Pi$ has been identified as well as the $^4\Delta - ^4\Delta$ for which the current linelist for FeH contains.

9.4.2 Existing linelist of FeH of Dulick et al. (2003)

The existing linelist of FeH commonly in use is that of Dulick et al. (2003). This linelist is a list of the rovibronic wavelengths associated with the $F^4\Delta_i - X^4\Delta_i$ transition for 25 vibrational bands up to $J = 50.5$. The authors used existing term values for the $\nu = 0$, $\nu = 1$ and $\nu = 2$ levels of of the $X^4\Delta$ electronic state and then extrapolated to $\nu = 3$ and $\nu = 4$. For this linelist, the transition dipole moment function was calculated using *ab initio* theory and then used to calculate Einstin A-coefficients. The level of theory used was a SA-CASSCF calculations followed by MRCI with an active space of (6, 1, 1, 1) within the framework of C_{2v} symmetry. The SA-CASSCF orbitals were constructed using the three lowest $^4\Delta$ states and in the proceeding MRCI calculation, 4 states in symmetry 4 were requested which thus yielded the three lowest lying $^4\Delta$ states and one $^4\Sigma^-$ state. Using this data the authors calculated spectroscopic constants. The authors did not however, shift their theoretical potentials to be in line with their experimental potentials.

9.4.3 Potential collaboration with Uppsala University

Sara Lindgren is a fellow PhD student based at Uppsala University in Sweden who studies the metalicity of M type dwarfs. By constraining the metallicity of host stars,

the metallicity of the orbiting exoplanets can thus be deduced under the approximation that they were formed from the protoplanetary disc of their host star. To determine metalicity of a population of M type stars she is using the CRIRES spectrograph onboard on the VLT. Sara has made observations in the J band(1100-1400 nm) of around 30-40 M dwarfs and analysed the data using the SME (Spectroscopy Made Easy) programme. She has used the following inputs:

- MARCS model atmospheres
- Atomic linelists for Potassium and Sodium from the VALD database, with some additional atomic data from Melendez & Barbuy (1999)
- Linelist for CrH calculated by Burrow et al. (2002)
- Linelist of H_2O calculated by Barber et al. (2006)
- Line data calculated for FeH by Bertrand Plez, (unpublished)

In particular she has looked at FeH lines and constructed contour plots to investigate if there are degeneracy's between effective temperatures and metallicity. By comparing of accepted values of metalicities, she has concluded that metallicities can be determined accurately using the above technique. The lines of FeH from Bernard Plez are unpublished.

The Royal Society of Chemistry have a Researcher Mobility Grant scheme which is open to Masters, PhD students and early career researchers to apply to spend up to three months as an institution to carry out work which would benefit both their home and visiting institution. This is a possible source of funding which could be used to do preliminary work on the calculation of a new linelist of FeH: a new linelist for FeH would be of benefit for the ExoMol project based at UCL and also for Sara's work.

9.4.4 Experimental studies of FeH

FeH has been extensively studied experimentally: thus there is a large volume of data available on this radical. Of most pragmatic interest are measurements of experimental frequencies of transitions which can be used to fit *ab initio* data.

The spectrum of FeH has been measured by as far back as the experiments of Kleman & Kerland who used a King-like Furnace to observe a red degraded band at 9896 Å. This work was unpublished: however, Klynning & Lindgren (1973) did then later measure and publish the wavelengths witin this band.

FeH & FeD were then studied in the region of 2360 - 8900 Å by Carroll, McCormack, O'Connor (1976) who found two regions of complex structure in the:

- Blue: 4920 Å (2 regions of absorption)
- Green: 5320 Å (3 regions of absorption)

For the green they found no significant isotope shift for FeD so speculated that could be due to a (0, 0) band: similarly for one of the regions in the blue with the other could possibly be a (1, 0) band. They also measured another band with a band head

in the near infrared peaked at 8690.82 Å which degraded at longer wavelengths and made the tentative vibronic assignment to this system as shown in table 9.2.

Band	Band Head measurement (Å)
(0, 0)	9896.22
(1, 0)	8690.82
(2, 0)	7818.54

Table 9.2: Tentative vibronic assignment made by Carroll, McCormack, O'Connor (1976) of the near infra-red band they observed.

Carroll, McCormack, O'Connor(1976) also calculated vibronic constants for this band. Their work is of paramount important from an astrophysical perspective as they concluded that FeH could be in sunspots by comparing their measured experimental frequencies with the sunspot spectra of Moore, Monnaert, Houtgast 1966.
McCormack & O'Connor then went on in 1976 to measure these blue and green regions in detail and publish around 1700 rovibronic lines to aid the detection of FeH in space: they decided that, at the time the rotational analysis was too complex.

Dendramis, Van Zee & Weltner (1979) performed experiments in which both FeH & FeD were trapped in solid argon at 4 K and values of ω_e and $\omega_e\chi_e$ determined using a vibrational analysis. They observed 5 weak electronic transitions in visible region: a summary of the vibrational absorption bands observed is shown in table 9.3.

Band Designation	FeH			FeD		
	λ (Å)	ν (cm^{-1})	$\Delta\nu$ (cm^{-1})	λ (Å)	ν (cm^{-1})	$\Delta\nu$ (cm^{-1})
E	3996(10)	25 018(70)		4007(10)	24 949(70)	
			1130			929
D	4185(5)	23 888(30)		4162(5)	24 020(30)	
			1301			1101
C	4426(20)	22 587(100)		4362(20)	22 919(100)	
			1143			1383
B	4662(20)	21 444(100)		4642(20)	21 536(100)	
			1401			1518
A	4988(30)	20 043(120)		4994(30)	20 018(120)	

Table 9.3: Summary of vibrational absorption bands measured using an Argon-matrix trapping experiment for FeH & FeD by Dendramis, Van Zee & Weltner(1979).

Table 9.3 gives a summary of the vibrational bands measured by Dendramis, Van Zee & Weltner (1979) for FeH and FeD and also the vibronic constants determined by their rotational analysis. Their uncertainty is indicated for each value by the numbers in brackets. These values could be used as comparison to any theoretical *ab initio* curves.

Following on from this work, Phillips, Davis, Lindgren & Balfour (1987) used the FTS onboard the McMath telescope bases at Kitt Peak (National Solar Observatory) to undertake a rotational analysis of the $^4\Delta - ^4\Delta$ system of FeH. A summary of their vibronic band assignments with respective band heads and origins is shown in table 9.4. Table 9.5 shows a more in-depth summary of the range of J and ω values measured for the bands shown in table 9.4: the sub-band heads are also shown in table 9.6. The authors also calculated the wavelengths for the bands shown in table 9.7.

Band	Band head(Å)	Band Origin (Å)
(2, 0)	7786	12 769.46
(1, 0)	8692	11 419.44
(2, 1)	9020	11 006.53
(0, 0)	9896	9995.14
(1, 1)	10 253	9656.68
(0, 1)	11 939	8232.20
(1, 2)	12 389	7957.48

Table 9.4: Vibronic band assignments made by Phillips, Davis, Lindgren, Balfour, 1987 for the $^4\Delta - ^4\Delta$ system of FeH.

Band	Ω'	Ω''	J'' range
(1, 1)	7/2	7/2	5.5 to 19.5
	5/2	5/2	5.5 to 19.5
	3/2	3/2	4.5 to 18.5
	1/2	1/2	2.5 to 13.5
(1, 0)	7/2	7/2	3.5 to 28.5
	5/2	5/2	2.5 to 22.5
	3/2	3/2	2.5 to 22.5
	1/2	1/2	1.5 to 19.5
	7/2	5/2	5.5 to 24.5
	3/2	1/2	8.5 to 18.5
	5/2	7/2	5.5 to 18.5
	3/2	5/2	5.5 to 20.5
(2, 1)	7/2	7/2	4.5 to 21.5
	5/2	5/2	5.5 to 17.5
	3/2	3/2	4.5 to 19.5
	1/2	1/2	5.5 to 17.5
(2, 0)	7/2	7/2	3.5 to 22.5
	5/2	5/2	4.5 to 19.5
	3/2	3/2	4.5 to 18.5
	1/2	1/2	3.5 to 17.5
(0, 1)	7/2	7/2	3.5 to 21.5
	5/2	5/2	4.5 to 19.5
	3/2	3/2	4.5 to 19.5
	1/2	1/2	2.5 to 21.5
(1, 2)	7/2	7/2	5.5 to 15.5
	5/2	5/2	5.5 to 19.5
	3/2	3/2	5.5 to 18.5
	1/2	1/2	6.5 to 17.5

Table 9.5: Summary of range of experimental wavenumbers measures by Phillips, Davis, Lindgren & Balfour (1987) for the $^4\Delta - ^4\Delta$ system of FeH.

Sub-band	7/2-7/2	5/2-5/2	3/2-3/2	1/2-1/2
(0, 0)	9 928.71	10 026.03	10 038.75	9 983.78
(1, 0)	11 352.87	11 455.81	11 453.69	11 410.09
(2, 0)	12 697.22	12 806.58	12 795.52	12 754.81
(0, 1)	8 171.06	8 624.25	8 277.01	8 223.66
(1, 1)	9 595.44	9 694.00	9 691.94	9 649.86
(2, 1)	10 989.81	11 044.87	11 033.55	10 995.45
(1, 2)	7 895.74	8 000.46	8 005.95	7 936.05

Table 9.6: Sub band origins for the $^4\Delta - ^4\Delta$ system of FeH measured by Phillips, Davis, Lindgren & Balfour(1987).

Band	Band head(Å)
(2, 2)	10 639
(0, 2)	14 927

Table 9.7: Bands of the $^4\Delta - ^4\Delta$ system of FeH for which Phillips, Davis, Lindgren & Balfour (1987) calculated wavenumbers up to $J = 17.5$ for during their rotational analysis.

Phillips, Davis, Lindgren & Balfour (1987) used their experimental data summarised in tables 9.4, 9.5, 9.6 and 9.7 to calculate molecular constants (B, D, H for $\nu = 0, 1, 2$ and ω_e & $\omega_e\chi_e$ for both electronic states), term values, spin-splitting and λ doubling values. Later on, it was shown by Balfour & Klynning (1994) that the 700 nm region observed by Phillips, Davis, Lindgren, Balfour (1987) is actually due to CaH and CaD. They explain that the CaH data from Berg & Klynning for the $A^2\Pi - X^2\Sigma^+$ transition of CaH can be matched in the data recorded by Phillips. Previously Phillips & Davies 1993 had speculated that this anomalous band could be due to the presence of triatomic molecule, HFeH: in their paper they put forward arguments for and against this assignment. They conclude that the assignment of HFeH to the 700 nm region observed as unconfirmed.

The most recent sets of experimental frequencies which could be used for fitting *ab initio* curves comes from the group led by the late Professor John Brown at Oxford University who have undertaken many measurements of electronic transitions involving the $X^4\Delta$, $A^4\Pi$, $E^4\Pi$, $a^6\Delta$, $b^6\Pi$, $c^6\Sigma^+$ and $e^6\Pi$, states using dispersed & undispersed laser-induced fluorescence. A summary of the experimental frequencies measured within this group is shown in table 9.8. Table 9.8 gives a summary of the experimental frequencies measured by the John Brown group which would be available for refining *ab initio* curves. The table shows the electronic transitions measured with the associated range measured in terms of the quantum numbers ω and J. As can be seen from table 9.8 there are several electronic bands which have repeatedly measured. Of particular note are the measurements of the inter-combination system of $g^6\Phi - X^4\Delta$ which could be used to help constrain the energy shift between the quartet and sextet state systems. Additionally, the John Brown group has also calculated term values for each of the electronic transitions measured. Another project could be is to use the experimental frequencies with the program MARVEL (Furtenbacher, Császár & Tennyson 2007) to produce term values and compare with those presented in the respective papers. A summary of the experimentally derived term values are shown in table 9.9.

Table 9.9 summarises the range of term values calculated by the John Brown group using the respective experimental frequencies that they measured. In terms of fitting *ab initio* in practice it would be easier to first initially fit to the term values presented to get a "first guess" at molecular state curve parameters and then use the actual measured experimental frequencies to refine further aiming for higher accuracy. Other experimental work done by this group which would assist in the construction of a new linelist is the measurement of lifetimes of states of the $g^6\Phi$ electronic state by Carter & Brown (1994). This would assist in checking the intensities calculated using theoretical dipoles. For astronomers, the intensity of transitions is very important

Electronic transition	Band	Ω'	Ω''	J'' range	Source
$E^4\Pi - X^4\Delta$	(0, 0)	5/2	7/2	3.5 to 34.5	Balfour, Brown & Wallace (2004)
		3/2	5/2	3.5 to 29.5	
		1/2	3/2	3.5 to 24.5	
		5/2	5/2	1.5 to 23.5	
		3/2	3/2	1.5 to 26.5	
		1/2	1/2	1.5 to 22.5	
$E^4\Pi - A^4\Pi$	(0, 0)	5/2	5/2	2.5 to 21.5	
		3/2	3/2	2.5 to 19.5	
		1/2	1/2	3.5 to 19.5	
$e^6\Pi - X^4\Delta$	(0, 2)	7/2	7/2	4.5 to 10.5	Hullah, Barrow & Brown (1999)
$g^6\Phi - X^4\Delta$	(0, 0)	9/2	7/2	2.5 to 11.5	Carter, Steimle & Brown (1993)
		7/2	5/2	2.5 to 7.5	
$g^6\Phi - X^4\Delta$	(0, 0)	11/2	7/2	4.5 to 9.5	Carter & Brown (1994b)
		11/2	7/2	4.5 to 9.5	
$e^6\Pi - a^6\Delta$	(0, 0)	7/2	9/2	4.5 to 10.5	Goodridge, Carter & Brown (1997)
		5/2	7/2	3.5 to 8.5	
		3/2	5/2	2.5 to 5.5	
	(0, 1)	7/2	9/2	4.5 to 9.5	
		5/2	7/2	3.5 to 6.5	
		3/2	5/2	2.5 to 4.5	
	(0, 0)	1/2	3/2	1.5 to 4.5	Hullah, Wilson, Barrow & Brown (1998)
		7/2	9/2	9.5 to 12.5	
	(1, 1)	7/2	9/2	4.5 to 9.5	Wilson & Brown (1999)
		5/2	7/2	3.5 to 7.5	
		3/2	5/2	2.5 to 6.5	
		1/2	3/2	1.5 to 3.5	
	(0, 0)	7/2	7/2	3.5 to 13.5	Wilson, Cook & Brown (2001)
		5/2	5/2	2.5 to 10.5	
		3/2	3/2	1.5 to 7.5	
		1/2	1/2	0.5 to 4.5	
		-1/2	-1/2	0.5 to 4.5	
	(0, 0)	7/2	9/2	11.5 to 12.5	
		5/2	7/2	7.5 to 10.5	
		3/2	5/2	4.5 to 7.5	
		-1/2	1/2	0.5 to 5.5	
$g^6\Phi - a^6\Delta$	(0, 1)	11/2	9/2	4.5 to 10.5	Wilson & Brown (1999)
		9/2	7/2	3.5 to 10.5	
		7/2	5/2	2.5 to 7.5	
		5/2	3/2	1.5 to 7.5	
		1/2	3/2	1.5 to 4.5	
	(0, 0)	11/2	9/2	4.5 to 10.5	Carter & Brown (1994a)
		9/2	7/2	3.5 to 9.5	
		7/2	5/2	2.5 to 6.5	
$e^6\Pi - b^6\Pi$	(0, 0)	7/2	7/2	3.5 to 11.5	Hullah, Barrow & Brown (1999)
		5/2	7/2	3.5 to 6.5	
		7/2	5/2	2.5 to 6.5	
		5/2	5/2	2.5 to 6.5	
		3/2	5/2	2.5 to 5.5	
	(0, 0)	7/2	5/2	2.5 to 8.5	Goodridge, Hullah & Brown (1997)
		5/2	3/2	1.5 to 5.5	
		3/2	1/2	0.5 to 4.5	
$e^6\Pi - c^6\Sigma^+$	(0, 0)	1/2	-1/2	0.5 to 4.5	Hullah, Wilson, Barrow & Brown (1998)

Table 9.8: Summary of experimental frequencies values measured within the John Brown group.

Electronic transition	ν	Ω	J	Source
$X^4\Delta$	2	7/2	4.5 to 10.5	Hullah, Barrow & Brown (1999)
$A^4\Pi$	0	5/2	2.5 to 21.5	Balfour, Brown & Wallace (2004)
		3/2	3.5 to 20.5	
		1/2	3.5 to 19.5	
$E^4\Pi$	0	5/2	2.5 to 29.5	Balfour, Brown & Wallace (2004)
		3/2	2.5 to 29.5	
		1/2	1.5 to 21.5	
$a^6\Delta$	0	9/2	4.5 to 10.5	Carter & Brown (1994a)
		7/2	3.5 to 9.5	
		5/2	2.5 to 6.5	
		9/2	4.5 to 9.5	Goodridge, Carter & Brown (1997)
		7/2	4.5 to 6.5	
		5/2	2.5 to 4.5	
		3/2	1.5 to 4.5	Hullah, Wilson, Barrow & Brown (1998)
		9/2	11.5 to 12.5	
		9/2	12.5	Wilson, Cook & Brown (2001)
		7/2	10.5 to 13.5	
		5/2	7.5 to 10.5	
		3/2	5.5 to 7.5	
		1/2	0.5 to 4.5	
		-1/2	0.5 to 4.5	
	1	9/2	4.5 to 9.5	Goodridge, Carter & Brown, 1997
		9/2	3.5 to 6.5	
		9/2	2.5 to 4.5	
		9/2	4.5 to 10.5	Wilson & Brown (1999)
		7/2	3.5 to 10.5	
		5/2	2.5 to 7.5	
		3/2	1.5 to 7.5	
$b^6\Pi$	0	3/2	1.5 to 7.5	Hullah, Barrow & Brown (1999)
		5/2	2.5 to 6.5	
		7/2	3.5 to 11.5	
$c^6\Sigma^+$	0	5/2	2.5 to 8.5	Goodridge, Hullah & Brown (1997)
		3/2	1.5 to 5.5	
		1/2	0.5 to 4.5	
$e^6\Pi$	0	7/2	12.5	Wilson, Cook & Brown (2001)
		5/2	8.5 to 9.5	
		3/2	5.5	
		1/2	6.5	
		-1/2	0.5 to 4.5	
		7/2	3.5 to 9.5	Goodridge, Carter & Brown (1997)
		5/2	2.5 to 7.5	
		3/2	1.5 to 4.5	
		1/2	0.5 to 3.5	Hullah, Wilson, Barrow & Brown (1998)
		7/2	10.5 to 12.5	
	1	7/2	3.5 to 8.5	Wilson & Brown (1999)
		5/2	2.5 to 6.5	
		3/2	1.5 to 5.5	
$g^6\Phi$	0	9/2	4.5 to 10.5	Carter, Steimle & Brown (1993)
$g^6\Phi$	0	7/2	3.5 to 7.5	
$g^6\Phi$	0	5/2	2.5 to 7.5	Wilson & Brown (1999)

Table 9.9: Summary of term values derived by the John Brown group.

in determining the opacity produced by different molecules. Additionally, Brown, Körsgen, Beaton, Evenson (2006) have used LMR (laser magnetic resonance) in the far infra-red to measure $\nu = 0$ rotational states of the ground $X^4\Delta$ of the FeH

molecule. Similarly, Jackson, Zink, Towle, Riley & Brown (2009) have performed a similar experiment for the FeD molecule.

In summary, there is a large amount of experimental frequency data available for multiple electronic systems of FeH and also molecular constants determined using experimental data which could be used to assist in the construction of a new linelist for FeH.

9.4.5 Review of previous theoretical studies of FeH

Theoretically, FeH has an extremely complex electronic structure of low-lying electronic states which dissociate to closely-spaced dissociation limits which have different electronic configurations. It is noteable that Sauval & Tatum (1984) have not calculated empirical coefficients for a partition function for this molecule. In their extensive paper, in terms of the periodic table using the standardised defined rows & columns for groups 1, 2, 13, 14, 15, 16, 17, rows 2 to 5 have all the diatomic hydrides listed. For the first row of transition metals (row 4) have CrH, MnH, CoH, NiH, CuH, ZnH listed and for the second row of transition metals (row 5) have PdH, AgH & CdH listed and row for 6 have PtH, AuH, HgH listed (groups 10, 11, 12). Also from LaH, YbH & LuH which are hydrides formed from elements of the first row of the lanthanides.

Theoretically, the low-lying electronic states of FeH have been studied by:

- Scott & Richards (1974) who performed calculations of the low-lying $^6\Delta$, $^6\Sigma^+$, $^6\Pi$, $^4\Delta$ and $^4\Pi$ states using a matrix Hartree-Fock approximation.
- Langhoff & Bauschlicher (1990) have used the SA-CASSCF/MRCI method to calculate the PECs of 10 sextet and 9 quartet low-lying states below 25 000 cm^{-1}.
- Sodupe, Lluch & Oliva (1990) have performed Hartree-Fock and CI calculations using nonempirical pseudopotentials for the low-lying $^4\Sigma^+$, $^4\Pi$, $^4\Delta$ and $^6\Sigma^+$, $^6\Pi$, Δ states.
- Tanaka & Sekiya (2001) have used the Multireference coupled pair approximation [MRCPA4] technique for the $X^4\Delta$, $A^4\Pi$, $C^4\Phi$, $F^4\Delta$ and $a^6\Delta$, $b^6\Pi$, $c^6\Sigma^+$, $e^6\Pi$ states.

9.4.6 Calculating *ab initio* curves for FeH

Shown in table 9.10 are the first 10 atomic dissociation limits of the Iron atom which the FeH molecule will dissociate to (along with the H atom) in the range of large internuclear distance R. As table 9.10 shows there are many atomic dissociation limits up to around 20 000 cm^{-1}. Even more pertinently these limits have competing atomic configurations namely $3d^64s^2$, $3d^74s^1$ and $3d^64s4p$ which are highlighted in colour for clarity.

The a^5F limit at 7459.752 cm^{-1} is close enough to the a^5D term that there could be interaction between the molecular states dissociating to these limits which have different atomic configuration. The next limit up from the a^5D term which also has

a $3d^6 4s^2$ atomic configuration is a^3P^2 at approximately 18 000 cm^{-1}. This limit is close to the z^7D^0 which is the lowest (first) appearance of the entirely different configuration namely $3d^6 4s4p$.

Thus for any *ab initio* calculations to be done it would be prudent to start with only the states that dissociate to the lowest atomic term namely a^5D with atomic configuration $3d^6 4s^2$. To calculate any molecular states higher would consequently mean calculating molecular states that dissociate to a different atomic configuration namely $3d^7(^4F)4s^1$ to which corresponds to the a^5F, a^3F, a^3F terms. However the upper molecular states of these are likely also influenced by states dissociating to the a^3P^2 term (atomic configuration $3d^6 4s^2$) which in turn will be perturbed by states dissociating to the z^7D^0 term with atomic configuration of $3d^6(^5D)4s4p(^3P^0)$.

Confirguation	Term	J	Level (cm^{-1})	E_J (cm^{-1})	Molecular states	
$3d^6 4s^2$	a^5D	4	0.000	402.961	$^4\Sigma^+$	$^6\Sigma^+$
		3	415.933		$^4\Pi$	$^6\Pi$
		2	704.007		$^4\Delta$	$^6\Delta$
		1	888.132			
		0	978.074			
$3d^7(^4F)4s^1$	a^5F	5	6 928.268	7459.752	$^4\Sigma^+$	$^6\Sigma^+$
		4	7 376.764		$^4\Pi$	$^6\Pi$
		3	7 728.060		$^4\Delta$	$^6\Delta$
		2	7 985.785		$^4\Phi$	$^6\Phi$
		1	8 154.714			
$3d^7(^4F)4s^1$	a^3F	4	11 976.239	12407.403	$^4\Sigma^+$	$^2\Sigma^+$
		3	12 560.934		$^4\Pi$	$^2\Pi$
		2	12 968.554		$^4\Delta$	$^2\Delta$
					$^4\Phi$	$^2\Phi$
$3d^7(^4P)4s^1$	a^5P	3	17 550.181	17 684.5570	$^4\Sigma^+$	$^4\Sigma^+$
		2	17 726.988		$^4\Pi$	$^6\Pi$
		1	17 927.382			
$3d^6 4s^2$	a^3P^2	2	18 378.186	18 954.0200	$^4\Sigma^+$	$^2\Sigma^+$
		1	19 552.478		$^4\Pi$	$^2\Pi$
		0	20 037.816			
$3d^6(^5D)4s4p(^3P^0)$	z^7D^0	5	19 350.891	19 624.0671	$^8\Sigma^+$	$^6\Sigma^+$
		4	19 562.439		$^8\Pi$	$^6\Pi$
		3	19 757.032		$^8\Delta$	$^6\Delta$
		2	19 912.495		$^8\Phi$	$^6\Phi$
		1	20 019.635			
$3d^6 4s^2$	a^3H	6	19 390.168	19 575.6821	$^4\Sigma^-$	$^2\Sigma^-$
					$^4\Pi$	$^2\Pi$
		5	19 621.006		$^4\Delta$	$^2\Delta$
					$^4\Phi$	$^2\Phi$
		4	19 788.251		$^4\Gamma$	$^2\Gamma$
					^4H	^2H
$3d^6 4s^2$	b^3F^2	4	20 641.110	20813.6333	$^4\Sigma^-$	$^2\Sigma^-$
		3	20 874.482		$^4\Pi$	$^2\Pi$
		2	21 038.987		$^4\Delta$	$^2\Delta$
					$^4\Phi$	$^2\Phi$

Table 9.10: The first 8 atomic dissociation limits of the element iron, Fe and the various molecular electronic states of FeH expecting to dissociate to them.

Table 9.10 shows the molecular states expected to dissociate to the first 8 atomic terms of the Iron atom. In this table the E_0 values are are obtained by applying

equation (9.1):

$$E_0 = \frac{\sum_J (2J+1) E_J}{\sum_J (2J+1)} \tag{9.1}$$

where the values of J and E_J ("Levels") are presented in table 9.10.

Moving onto deducing what the closed and active space required would be, for all three atomic configurations namely $3d^6 4s^2$, $3d^7 4s^1$, $3d^6 4s^1 4p^1$, they all have the same closed space, namely that of an argon inner shell with 18 electrons. In the framework of C_{2v} symmetry this is represented in table 9.11.

Orbitals		C_{2V} Symmetry			
		A1	B1	B2	A2
closed	$1s^2$	1	0	0	0
	$2s^2$	1	0	0	0
	$2p^6$	1	1	1	0
	$3s^2$	1	0	0	0
	$3p^6$	1	1	1	0
Total closed		5	2	2	0

Table 9.11: Deduction of closed space for FeH within the C_{2v} framework.

Tables 9.12a 9.12b and 9.12c show the active space required for the $3d^6 4s^2$, $3d^7 4s^1$, $3d^6 4s^1 4p^1$ configurations respectively.

Orbitals		C_{2V} Symmetry			
		A1	B1	B2	A2
Active	$3d^6$	2	1	1	1
	$4s^2$	1	0	0	0
	$1s^1$(H)	1	0	0	0
Total active		4	1	1	1
Total occupied		9	3	3	1

(a)

Orbitals		C_{2V} Symmetry			
		A1	B1	B2	A2
Active	$3d^7$	2	1	1	1
	$4s^1$	1	0	0	0
	$1s^1$(H)	1	0	0	0
Total active		4	1	1	1
Total occupied		9	3	3	1

(b)

Orbitals		C_{2V} Symmetry			
		A1	B1	B2	A2
Active	$3d^6$	2	1	1	1
	$4s^1$	1	0	0	0
	$4p^1$	1	1	1	0
	$1s^1$(H)	1	0	0	0
Total active		5	2	2	1
Total occupied		10	4	4	1

(c)

Table 9.12: Deduction of the closed and occupied orbitals within the C_{2v} framework required for the various low-lying atomic dissociation limits for which various molecular states of FeH would dissociate to.

As can be seen from tables 9.12a and 9.12b, the configurations of $3d^6 4s^2$, $3d^7 4s^1$ require identical active space. Thus, as is a similar case with CrH, two of the low-lying dissociation limits require the same active space which arise from different atomic configurations.

For the case of MnH (even number of electrons), there is an energy gap of around 17 000 cm^{-1} between the first two lowest-lying dissociation limits (see table 2.11).

For CrH (odd number of electrons) this gap is around 7 000 cm^{-1}. Hence, for the case of FeH (odd number of electrons), it is likely that the CASSCF orbitals which would be of highest quality would be those involving fewer states.

Ideally, preliminary *ab initio* work would concentrate on calculating the 6 PECs that converge to the a^5D dissociation term. However, astronomers are now also interested in transitions involving the $E^4\Pi$ state (see section 9.4.1) so in practice it would be more useful, and also probably necessary from an MRCI prospective to consider the 8 molecular states dissociating to the a^5F term as shown in table 9.10. Indeed, there is also ample experimental data available on these states (most notably the $e^6\Pi$ and $g^6\Phi$) as summarised in section 9.4.4.

9.4.7 Concluding Remarks

Hence in summary:

- There is a significant astronomical interest in FeH.
- The existing linelist of Dulick et al. (2003) has been shown to be incomplete and lead to inaccurate modelling of stellar objects such as brown dwarfs.
- Ample experimental measurements have been made of several electronic transitions for FeH which could be used in refining calculated *ab initio* curves.
- Previous theoretical studies of the electronic structure of FeH have been undertaken and demonstrated that it has a complex structure.
- The calculation of new *ab initio* curves would be challenging: however the experience of doing so for CrH & MnH would assist in formulating a strategy.

9.5 Creation of new linelists for the Group II diatomic hydrides

Within the ExoMol group, the diatomic metal hydrides of group II of BeH, MgH and CaH were the first molecules for which linelists were calculated using the ExoMol methodology of calculating *ab initio* curves and then refining to experiment. This work was undertaken by a group of summer students in the summer of 2011. There results are published in the paper "The rovibrational spectrum of BeH, MgH and CaH at high temperatures in the $X^2\Sigma^+$ state: a theoretical summary". In summary, the students created rovibronic linelists for the ground state ($X^2\Sigma^+$) of each of these molecules which are applicable up to 2000 K using the programs of LEVEL and DPotFit. The isotopologues were: ^{9}BeH, ^{24}MgH, ^{25}MgH, ^{26}MgH and ^{40}CaH. In this study for both BeH and MgH, PECs were taken from the literature: a new PEC was calculated for CaH using MRCI level of theory and aug-cc-pwCV5Z basis set. For all three molecules, new *ab initio* DMCs were calculated using the finite field method. For BeH the level of theory used was MRCI and for MgH and CaH RCCSD(T): all were calculated using a aug-cc-pwCV5Z basis set. The dipole moments selected for the final linelists were those which agreed best with experimentally determined values at equilibrium. In terms of refinement, for BeH no refinement was made to

the spectroscopic parameters produced previously by Le Roy for an extended Morse Oscillator. The accuracy obtained of fitting the MgH and CaH curves to the available experimental data was less than 0.01 cm^{-1}. Thus, high-accurate rovibronic linelists covering the ground state were obtained. The number of rovibronic transitions in each of the linelists were 16 400, 10 354 and 15 278 for BeH, MgH and CaH respectively.

An obvious way to extend these linelists would be to include electronic transitions from excited electronic curves. Indeed, in astronomy, for all three molecules electronic transitions involving the $A^2\Pi - X^2\Sigma^+$ have been observed. This is further work which has the potential to create several small undergraduate projects and also, an activity for A-Level students to learn about Spectra. An outline of a Royal Society Partnership Grant application which I submitted is given in section 9.5.4. Within my PhD I have made a start on analysing the electronic structure of these molecules and for each of them undertaken a test of CASSCF orbitals involving the lowest 5 electronic states as was done in a similar manner for the lowest-lying states of CrH & MnH. This work is summarised in section 9.5.5. The astronomical interest in these molecules is reviewed in section 9.5.1 and summaries of previous theoretical and experimental work undertaken given in sections 9.5.2 and 9.5.3 respectively.

For the case of MgH, a linelist involving the $A^2\Pi - X^2\Sigma^+$ and $B'^2\Sigma^+ - X^2\Sigma^+$ transitions has been calculated by Nezhad, Shayesteh and Bernath (2013) who have used high accuracy *ab initio* dipole moment curves and along with am analytic potential curve for $X^2\Sigma^+$ and Rydberg-Klein-Rees curves for the $A^2\Pi$ and $B'^2\Sigma^+$ states. Previously published term values which were obtained from experimentally measured frequencies were used to constrain the rovibronic transitions. The authors used the program LEVEL to calculate the Einstein A-coefficients and Hönl-London factors for around 30, 000 rovibronic transitions. The range in ν is $\nu = 0 - 11$ for the $X^2\Sigma^+$ state, $\nu = 0, 1, 2$ and 3 for the $A^2\Pi$ state and $\nu = 0 - 9$ for the $B'^2\Sigma^+$. The authors did note the effect of perturbations: a possible project could be to quantify the effects of implementing spin-orbit and angular momenta coupling within a Duo calculation. Also, the program LEVEL can only account for singlet states: the authors did actually purposely "cheat" by introducing the X, A and B' states as singlet states to obtain rovibonic intensities. There is also a linelist for MgH computed previously by Kurucz (1992).

For the case of CaH a new linelist has been calculated by Li et al. (2012) for the $E^2\Pi - X^2\Sigma^+$ up to $J = 50.5$ using a similar methodology to that of Nezhad, Shayesteh and Bernath (2013) for MgH. The Frank-Condon factors of the $E^2\Pi - X^2\Sigma^+$ transition of CaH have also been calculated by Ureña. (2000).

9.5.1 Astrophysical importance of Group II diatomic Hydrides

The astronomical interest of the three diatomic molecules of BeH, MgH and CaH molecules is outlined in the following sections. In summary all three are of interest to the solar community in the study of sunspots: hence the potential for small-scale student projects in identifying these molecules within more recent sunspots than the original detections.

Astronomical Interest in BeH

BeH is of interest to astronomers for its confirmed presence in sunspots as far back as 1971 (Wohl). More recently,an over-abundance of Be has been detected in Hg-Mn stars.

Wöhl (1971) made a study of molecules in sunspots in the region $4000 - 8000$ cm^{-1} and re-identified several thousand molecules. He searched for 80 lines of the $A^2\Pi - X^2\Sigma^+$ (0, 0) band of BeH in the region 4825-5100 Å and found 45 lines which he classified as coincidences.

Shanmugavel et al. (2008) then did a higher resolution study searching for BeH, BeD and BeT in sunspot data of Wallace et al. (2010) in the region 15 000 to 20 500 cm^{-1} using various experimental sources shown in table 9.14.

Isotopologue	Vibronic bands	Rotational Temperature estimated (K)	Experimental Source
BeH	(0, 0) (1, 1) (2, 2)	 4228 4057	Olsson(1932)
BeD	(0, 0) (1, 1) (2, 2) (3, 3)	3941	Fosca et al. (1998)
BeT	(0, 0) (1, 1) (2, 2)	 3243	DeGreef and Colin (1974)

Table 9.13: Experimental sources used by Shanmugavel et al. (2008) to search for BeH, BeD and BeT in the sunspot data of Wallace et al. (2000) for the $A^2\Pi - X^2\Sigma^+$ transtion.

Shanmugavel et al. (2008) found that all the bands they searched for as shown in table 9.14 were present in the sunspot data with the addition of the (4, 4) band of BeD. Using these identifications, the authors then calculated effective rotational temperatures for various bands as shown in table 9.14.

Previously, calculations of Franck-Condon (FC) factors had been performed by Shanmugavel, Bagare & Rajamanickam (2006) for the systems of isotopologues of BeH presented in table 9.14.

Isotopologue	Electronic Transition studied
BeH	$C^2\Sigma^+ - X^2\Sigma^+$
BeD	$A^2\Pi - X^2\Sigma^+$
	$C^2\Sigma^+ - X^2\Sigma^+$
BeT	$A^2\Pi - X^2\Sigma^+$

Table 9.14: Summary of systems for which Shanmugavel, Bagare & Rajamanickam (2006) calculated Franck-Condon factors.

The motivation behind the study of Shanmugavel, Bagare & Rajamanickam (2006) was that the element beryllium has been observed to have an enhanced abundance in Hg-Mn stars of approximately 200 compared to the solar abundance of beryllium.

In summary, BeH is of established astronomical interest: a study of beryllium compounds in Hg-Mn stars is another potential field of research.

Astronomical Interest in MgH

The diatomic molecule MgH has been used by astronomers in a range of astrophysical settings for many novel applications. These can be summarised as follows:

- Visscher, Lodders & Fegley (2010) have undertaken a thermochemical study of how Fe, Mg and Si gases behave in the atmospheres of a range of astronomical objects including giant planets and brown dwarfs.

- Bell, Edvardsson & Gustafsson have used MgH features to determine a surface gravity of Arcturus star (brightest star in northern celestial hemisphere) of log g= 1.8 by first determining the abundance of Magnesium using Mg I lines. Additionally, Bonnell & Bell (1993) have used MgH features to constrain surface gravity of 5 cool giant stars.

- MgH has been tested as potential indicator of surface gravity for red giants (Berdyugina & Savanov 1992).

- Rao & Rangarajan (1999) have observed linear polarisation of the MgH molecule in sunspot spectra which they propose is due to coherent scattering processes

- Berdyugina et al. (2000) have calculated Zeeman Stokes' profiles of the $A^2\Pi - X^2\Sigma^+$ system: they found that there simulations did not completely reproduce observations. Ramos & Bueno (2005) have observed depolariztion in the rotational levels of MgH which they believe is due to collisional effects: this has consequences for understanding the spatial distribution of the sun's magnetic field. This has been analysed further by Bommier, DeglâĂŹInnocenti, Feautrier & Molodi (2006).

- Tomkin & Lambert (1980) observed lines of the $A^2\Pi - X^2\Sigma^+(0,0)$ band of MgH in 5 different 5 G & K dwarfs for the different isotopologues of ^{24}MgH, ^{25}MgH and ^{26}MgH. For four of these dwarfs they found that the relative abundance of the isotopes of MgH to be the same as on earth(within error bars) of ^{24}MgH:^{25}MgH:^{26}MgH=79.88: 10.00: 11.01 (de Bièvre & Barnes 1985). One dwarf, Gmb 1830 was found to have a different abundance profile which potentially has consequences for modelling of galaxy evolution. This result was then corroborated by Lambert & McWilliam(1986) who found a similar profile for another metal-rich subgiant of ν Indi.

- Gay & Lambert (2000) have also used this transition to constrain the isotopic abundances in 20 dwarf stars and found that the abundance of ^{25}MgH and ^{26}MgH to decrease with metallicity which is in agreement with galaxy evolution studies. Additionally, Yound, Lambert & Ivans (2003) have determined the abundance of 61 cool dwarfs and giants.

- Wallace, Hinkle, Li & Bernath(1999) have proposed that the $B^2\Sigma^+ - X^2\Sigma^+$ transition could also be used for isotope abundance elements with the principle advantage been that lines from this system are much less blended than those from the more intense $A^2\Pi - X^2\Sigma^+$ system. In their study they identified lines in the vibrational bands of (0, 3), (0, 4), (0, 5), (0, 6), (1, 3), (1, 7) and (1, 8)

of ^{24}MgH and also the (0, 7) bands of the ^{25}MgH and ^{26}MgH isotopologues and hence constrained the relative abundance of the isotopes.

- MgH lines of the $A^2\Pi - X^2\Sigma^+(0,0)$ band have been observed in the sun's photosphere by Moore, Minnaert & Houtgast(1966) and Lambert, Mallia, Pertford (1971). Kulaczcewski, Degenhardt & Kneer (1989) proposed that a spectral line of MgH near 5175 Å could be used as indicator of solar pressure and temperature in the photospheric region between $z = 0$ and $z = 30$ km.

Astronomical Interest in CaH

The first detection of CaH in outerspace was made by Fowler in 1907 who detected CaH in the spectra of M dwarfs. The next year in 1908 Olmsted established the presence of CaH in sunspot spectra. Later on, Öhman (1934) proposed that it could be used to classify M stars. Barbury et al. (2003) have modelled CaH lines in the photosphere and cool dwarfs to establish if CaH lines can be used as indicators of temperature and/or gravity. In T Tauri stars, CaH lines are used as indicators of surface gravity. McGovern et al. (2004) found that, as part of the Brown Dwarf Spectroscopic Survey Gravity Project, CaH lines are sensitive to surface gravity as well as lines of K I, Na I, Cs I, Rb I, TiO, VO, FeH and CaH. Burgasser, Kirkpatrick, Liebert & and Burrows (2003) have identified weak CaH lines in the spectra of T dwarfs in the red optical (6750 - 7150 Å) region. These lines identified are from the $A^2\Pi - X^2\Sigma^+$ (0, 0) band of CaH measured by Berg & Klynning 1974. The authors note that the precense of these lines could potentially indicate non-equilibrium chemistry as it would be expected that the element Calcium would be locked up in in minerals. Along with CrH and FeH, CaH is an imprtant species in the optical spectra of L dwarfs (Reiners et al. 2007). The possibility of using CaH as a probe of magnetic field strengths for astrophysical objects has been investigated by the HotMol group (see sections 9.3 and 3.4). Sakamoto et al. (1998) undertook a seach for absorption lines of both MgH and CaH in nearby molecular clouds for the $N = 0 \rightarrow 1$ transition: they found no trace. However, their study is important for the purposes of understanding grain formation. In 1993, Barclay, Anderson & Ziurys, measured the submilimeter spectrum of CaH & CaD using direct absorption spectroscopy and resolved the 6 hyperfine components of the $N = 0 \rightarrow 1$ transiton of CaH near 254 GHz and the main hyperfine components for CaD in the $N = 0 \rightarrow 1$, $N = 1 \rightarrow 2$, $N = 2 \rightarrow 3$ rotational transitions. A summary of the work the Ziury's group has done with particular regard to Manganese bearing species is presented in section 6.3.

9.5.2 Summary of previous theoretical studies

There have been several studies done on how propeties such as transition dipole moments vary within the group II diatomic hydrides. There has also been development work undertaken on electronic structure methodology for these molecules. A summary of studies of such studies is shown in table 9.15.

There are numerous theoretical studies of the individual molecules of BeH, MgH and CaH in the literature. From this vast literature, the studies which are most applicable and would act as reference checks during the construction of new *ab initio* curves

Category of Work done	Year	Authors
Electronic Structure		
Hartree-Fock-Heitler-London Method applied to first and second row diatomic hydrides	2006	Corongiu
Restricted Hartree-Fock calculations on open shell diatomics	1988	Laaksonen, Müller-Plathe &, Diercksen
MP2 method	1997	Kokayashi, Sasagane & Yamaguchi
Pseudopotential approaches	1991	Kaupp, Schleyer, Stoll & Preuss
Systematic DFT approach	2010	Kulika & Marzari
Application of DFT methods to open shell molecules	2000	Guan, Casida & Salahub
Coupled cluster approach	1995	Li & Paldus
Born-Oppenheimer Breakdown	1998	Uehara
Study of electron correlation effects in group I and II Hydrides	1975	Meyer & Rosmus
Basis set optimization for hyrides	2006	Klein & Zottola
Bonding and Dipole Moments		
Ground state propeties	1987	Fuentealba, Reyes, Stoll & Preuss
Hydride Affinities for group I and group II hydrides	2000	Wenthold
Ionic Bonding	1979	Klynning & Martin
Covalent Bonding	2003	Magnusson & Petrie
Transition dipole moments for the A-X transition	1999	Hefferlin & Kuznetsova
Variation of dipole moment for XH^+ ions	2010	Abe, Kajita, Hada & Moriwaki
Electronic Transition Probability ($A^2\Pi - X^2\Sigma^+$) for BeH & MgH	1971	Popkie
Fundamental Physics		
m_e/m_p variation	2008	Kajita
Hyperfine Structure Calculations		
Hyperfine splitting constants for the $X^2\Sigma^+$ state of BeH and MgH	1987	Richman, Shi and McCullough
Hyperfine coupling constants (hfcc), electron-spin g-factors, excitation energies (DE) and oscillator strengths (f-values) for the $X^2\Sigma^+$ states of BeH, MgH, CaH as well as other radicals	2003	Bruna & and Friedrich Grein

Table 9.15: Summary of Theoretical work studies undertaken developing methodology and examining trends in Group II metal hydrides.

are summarised in tables 9.16, 9.17 and 9.18 for BeH, MgH and CaH respectively.

9.5.3 Summary of experimental studies

9.5.4 Royal Astronomical Partnership Grant Proposal

In July 2015, me and Edward Simmons, Deputy Headteacher for STEM subjects from Graveney School in Tooting, made an application for a Royal Society Partnership Grant. These grants are available up to the value of 3000 pounds: the aim of the scheme is to help facilitate schools in helping their pupils carry out science investigations and thus gain experience of scientific research. Our proposed project was called 'Sixth form introduction To Astronomical Research (STAR)' which would be delivered to a select group of around twelve 6th former's. The project idea was as follows:

- I would teach GCSE astronomy for two hours a week: the students would then be given homework and encouraged to undertake significant independent

study thus helping with transition from school-based teaching to university style teaching. Additionally I would help train the teachers at the school so that in future years they would be able to teach this course thus making the project sustainable.

- Students would be introduced to Citizen Science projects such as "Galaxy Zoo". Galaxy Zoo was set up by was set up by Professor Kevin Schawinski & Professor Chris Lintott (host of BBC Sky at night) who realised that they could (and needed to) use the shared brain power of many users to help classify galaxy images obtained from over 900,000 images from the Sloan Digital Sky Survey (SDSS). Computer algorithms to distinguish elliptical and spiral galaxies often fail hence images need to be visually inspected by humans. The project is set up so that each image is "classified" by 10 users who are given guidance on how to clasify: if 8 or more classify it as an elliptical object then it is recorded as elliptical: otherwise further users are requested to inspect it. The team can track the contributions of individual users. These classifications are then used by researchers working on understanding the formation of galaxies and the early universe. In 2007 a Dutch school teacher called Hanny van Arkel observed an object in an image which has now been renamed as "Hanny's Voorwerp". The object has since been identified as a quasar ionization echo.

- Have a session using the free online resource of "Observing with NASA". This resource, based at the Harvard-Smithsonian Center for Astrophysics, allows users to pick a target from a list and request that the robotic telescope takes an image within 24 hours using a field of view, exposure time and filter chosen by

Category of Work done	Year	Authors
Investigation of a possible potential barrier in the ground state	1984	Larsson
Ab initio study of the ground state using Multi-Reference averaged couple-pair approach(MR-ACPF)	2011	Koput
Ab initio studies of the low-lying states of BeH	1968	Chan & Davidson
	1972	Bagus, Moser, Goethals & Verhaegen
	1979	Tino, Kilmo, Claxton & Burton
	1982	Claxton, Tinot & Burton
	1983	Coopers
	1984	Coopers
	1984	Henriet & Vekhaegen
	1984	Bird & Claxton
	1992	Petsalakis, Theodorakopoulos & Nicolaides
	2000	Szalay & Gauss
	2001	Martinazzo, Famulari & Raimondi
	2008	Pitarch-Ruiz, SÅąnchez-Marin, Velasco & Martin
Dirac-Hartree-Fock Calculations of BeH	2004	Quiney, Gluchkov & Wilson
Basis set optimisation	2004	Glushkov & Wilson

Table 9.16: Summary of Theoretical work done on calculating the electronic structure of the BeH molecule

Category of Work done	Year	Authors
Ab initio studies of the low-lying states of MgH	1976	Sink, Bandrauk, Henneker, Lefebvre-Brion & Raseev
	1978 & 1983	Saxon, Kirby & Liu
	1985	Jen & Brandt
	2009	Abdallah, Najar, Jaidane, Lakhdar, Feautrier, Spielfiedel & Lique
	2009	Mestdagh, Pujo, Soep, Spiegelman
	2010	Guitou, Spielfiedel, Feautrier
Study of MgH^+ ion	2009	Aymar, Gùerout, Sahlaoui & Dulieu
Spin-Splitting effects	1982	Cooper
	2008	Gui-Xia, Tao & Yun-Guang
Partion function & Dissociation constants	1979	Tripathi & Gaur

Table 9.17: Summary of Theoretical work done on calculating the electronic structure of the MgH molecule

the user (with guidance from the programme). Objects which can be observed (depending on the time of year) include Jupiter's Moons, our moon,Venus, Crab Nebula, Messier 15, the Andromeda Galaxy and the Whirlpool Galaxy. The images obtained are then emailed to the user whom can then download them and use the online software and/or their own to analyse the images obtained: these images can be stacked from multiple observations.

- A virtual science proposals bidding contest. In this session the students would be allocated in teams one of the proposed M4 Missions currently being considered by the Europen Space Agency: their task would be to create a poster and give a presentation outlining why the mission should be chosen. This would thus allow the students opportunity to carry out individual research within a group setting and help develop their organisational and communication skills. The three shortlisted M4 missions are: Atmospheric Remote-Sensing Infrared

Category of Work done	Year	Authors
Ab initio studies of the low-lying states of CaH	1980	Honjou, Noro, Takagi, Ohno, Makita
	1981	Honjou, Noro, Takagi, Ohno, Makita
	1981	Klynning & Martin
	1983	Jeung, Daudey & Malrieu
	1983	Rao
	1987	Shida, Tanaka & Ohno
	1988	Martin
	1989	Chambaud & Levy
	1992	Boutalib & Daudey
	1995	Leininger & Jeunga
	2007	Kerkines & Mavridis
Theoretical dipole moment studies	2006	Holka & Urban
Core vallence correlation effects	1983	Pettersson & Siegbahn
Spin-doublng effects	1980	Cooper & Richards 1980

Table 9.18: Summary of Theoretical work done on calculating the electronic structure of the CaH molecule

Electronic transition	Vibrational band	range in J/N	Source
$A^2\Pi - X^2\Sigma^+$	(0, 0) (0, 1) (1, 1) (1, 2) (2, 2) (2, 3) (3, 3) (3, 4) (4, 4) (4, 5) (5, 5) (5, 6) (6, 6) (6, 7)	2.5 to 50.5 4.5 to 30. 5 1.5 to 44.5 4.5 to 28.5 1.5 to 37.5 4.5 to 25.5 4.5 to 29.5 8.5 to 22.5 1.5 to 30.5 4.5 to 27.5 1.5 to 27.5 5.5 to 17.5 5.5 to 25.5 1.5 to 19.5	Focsa, Firth, Bernath, Colin (1998)
$X^2\Sigma^+ - X^2\Sigma^+$	(0, 0) (1, 1) (2, 2) (3, 3) (4, 4) (5, 5) (6, 6) (7, 7) (8, 7) (8, 8) (9, 7) (9, 8) (9, 9) (10, 9) (10, 10)	1.5 to 49. 5 1.5 to 45.5 1.5 to 37.5 1.5 to 36.5 1.5 to 33.5 2.5 to 24.5 5.5 to 25.5 2.5 to 26.5 3.5 to 24.5 1.5 to 22.5 3.5 to 19.5 2.5 to 19.5 2.5 to 15.5 3.5 to 11.5 1.5 to 9.5	Focsa, Firth, Bernath, Colin (1998)
$A^2\Pi - X^2\Sigma^+$	(0, 0) (1, 1) (2, 2)	0 - 41 0 - 42 0 - 27	De Greef & Colin (1974)
$A^2\Pi - X^2\Sigma^+$	(4, 4) (5, 5)	6 - 24 7 - 21	Colin, Dreeze & Steinhauer (1983)
$C^2\Sigma^+ - X^2\Sigma^+$	(0, 6) (0, 7) (0, 8) (0, 9) (1, 9) (2, 9) (1, 10)	21 -32 2 - 28 1 - 24 2 - 19 2 - 17 1 - 12 1 - 11	Colin, Dreeze & Steinhauer (1983)

Table 9.19: Summary of experimentally measured rovibronic transitions measured for BeH which could be used in constraining *ab initio* curves.

$A^2\Pi - X^2\Sigma^+$	(0, 0) (1, 1) (2, 2) (3, 3)	0 - 41 0 - 42 0 - 34 0 - 27	De Greef & Colin (1974)

Table 9.20: Summary of experimentally measured rovibronic transitions measured for BeT which could be used in constraining *ab initio* curves.

Exoplanet Large-survey (Ariel), the Turbulence Heating ObserveR (Thor) and the X-ray Imaging Polarimetry Explorer (Xipe). The PI of AERIAL is Professor

Electronic transition	Vibrational band	range in N	Source
$C^2\Sigma^+ - X^2\Sigma^+$	(0, 8) (0, 9) (0, 10) (0, 11) (0, 12)	19 - 42 20 - 41 5 - 37 7 - 28 5 - 19	Colin, Dreeze & Steinhauer (1983)
$A^2\Pi - X^2\Sigma^+$	(0, 0)	0 - 56	Focsa, Bernath, Mitzer, Colin (1998)
	(1, 1) (2, 2) (3, 3) (4, 4) (5, 5) (6, 6)	0 - 53 3 - 43 4 - 41 5 - 39 6 - 35 6 - 25	
	(0, 1) (1, 2) (2, 3) (3, 4) (4, 5) (5, 6)	9 - 30 4 - 32 5 - 31 7 - 38 8 - 29 4 - 28	

Table 9.21: Summary of experimentally measured rovibronic transitions measured for BeD which could be used in constraining *ab initio* curves.

Electronic Transition	Band	Range in N/J	Term Values	Source
$X^2\Sigma^+ - X^2\Sigma^+$ (^{24}MgD)	(0, 0) (1, 0) (2, 1) (3, 2) (4, 3) (5, 4)	0 - 4 0 - 26 0 - 21 0 - 15 3 - 24 9 - 20	Yes	Shayesteh, Appadoo, Gordon, Le Roy, Bernath (2004)
$X^2\Sigma^+ - X^2\Sigma^+$ (^{25}MgD)	(1, 0) (2, 1) (3, 2) (4, 3)	0 - 29 2 - 28 3 - 28 14,18,21		
$X^2\Sigma^+ - X^2\Sigma^+$ (^{26}MgD)	(1, 0) (2, 1) (3, 2) (4, 3)	0 - 19 2 - 28 3 - 21 13 - 21		
$A^2\Pi - X^2\Sigma^+$	(0, 0)	1 - 41	No	Balfour (1970b)
$^2\Pi - X^2\Sigma^+$(232.9 nm system)		5 - 26	No	Balfour (1980)
$C^2\Pi - X^2\Sigma^+$	(0, 0) (1, 0) (1, 1)	1- 28 4 -22 6 -25	No	Balfour (1970b)

Table 9.22: Summary of experimentally measured rovibronic transitions measured for MgD which could be used in constraining *ab initio* curves.

Giovanna Tinetti who is also PI of the TWINKLE mission.

- A practical session in using scale analysis and dimensional analysis to help solve physics problems and also a brief talk about the Mars Climate Observer.
- Visit to the Dark Skies festival in Hay on Wye in the Breacon Beacons in Wales. The festival is due to be held on the weekend of 1 to 3 April 2016 and will

encompass public lectures, activities, planetarium experiences.

- Visit to the Mill Hill Observatory in North London where Dr Steve Fossey and Dr Francisco Diego are based. Dr Steve Fossey was awarded the UCL Communication & Culture Award in 2014 after he, along with third year undergraduate students famously discovered the SN 2014J Supernova in the so called "Cigar Galaxy" (Messier 82) on January 21st 2014. I previously had demonstrated on this very same course. Dr Francisco Diego has appeared in several TV programmes and is the founding organiser of "Your Universe" which is an annual festival of astronomy put on for schools and the public featuring exhibitions and invited lectures. The observatory regularly hosts public tours and also school visits: the observatory has two classrooms fo teaching, and is home to the The Radcliffe 18/24-inch Double Refractor, The Allen 24-inch Reflector, The Fry 8-inch Refractor and Two Celestron C14 14-inch Reflectors which can be remotely controlled and are now connected to a system where users can request images to be taken from them which are prioritised and scheduled by the system.
- The students would undertake a project (outlined below) which would allow them to gain experience of working in teams, running calculations on cluster machines, plotting & analysing spectra, reading scientific papers and presenting their work both individually as a group.

Adopt Isotopologues, create & analyse spectra, test for applications

I am a PhD student working in the ExoMol project at UCL. My task is to create linelists (list of transitional energies between energy states with associated intensities in molecules) for diatomic metal hydrides-I do this by solving the Schrödinger equation using quantum chemistry packages to create 'ab initio' data (step 1). With this data I then run a programme called DUO to create a linelist (step 2) and then finally analyse the spectra simulated using these linelists (step 3).

For the diatomic molecules of Beryylium Hydride (BeH), Magnesium Hydride (MgH) & Calcium Hydride (CaH) I have completed step 1-the students can now do steps 2 & 3 thus helping me with my research.

The students would firstly be asked to research which stable isotopes of the atoms Hydrogen (H), Berrylium (Be), Magnesium (Mg) and Calcium(Ca) exist quoting all references. In total there are 20 possible stable isotopologues for BeH, MgH & CaH-the students will adopt 2 or 3 each.

Using my data from step 1, the students will adapt a DUO input file by changing the nuclear masses for each of their isotopologues respectively. They will then set off running these input files on the UCL clusters via internet connection on my laptop thus creating linelists (step 2 complete).

Using their calculated linelists (several days to calculate), for each isotopologues they will then simulate and plot spectra (step 3) for various input parameters which

they can change.

The students will then share their spectra and thus investigate if different isotopologues have spectra which can be distinguished (e.g. BeH, BeD). This is an important result as by tracking tracking different isotopes of elements astronomers can place constraints on formation of exoplanets and stars.

Finally, the students will then write reports with the help of relevant astronomical papers I will provide.

9.5.5 Preliminary calculations

Preliminary *ab initio* MRCI results have been obtained for the five lowest-lying electronic states which are $X^2\Sigma^+$, $^2\Sigma^+(II)$, $^2\Pi$, $^4\Sigma^+$ and $^4\Pi$ states for BeH, MgH and CaH. Also a CASSCF state-combination study has been undertaken for these molecules. These calculations are shown in appendix D. This work could act as a basis for further study examining the trends in these hydrides and also shedding light on convergence issues encountered during CI calculations.

9.5.6 Concluding remarks

There is a comprehensive range of experimental data available for these molecules which can be a source of student projects which would teach basic skills in ExCel. There is certainly a well-established interest in these molecules from an astrophysical perspective, in particular for MgH. The experimental data available on higher electronic states which create UV transitions could hence be used to create even more extensive linelists than those already available in the literature. Hence preliminary *ab initio* calculations have been done for this purpose.

9.6 Conclusions for PhD

In summary this PhD has generated work which is of interest to both quantum chemistry and astronomical communities.

For CrH, a set of 11 PECs, DMCs and all TDMs, angular momenta and spin-orbit couplings curves have been calculated at MRCI level of theory using a cc-pVQZ basis set. The effect of changing the size of the basis set was investigated by studying how many inter-nuclear distances certain calculations converged for and also considering the regions in R space in which they did not. It was demonstrated for CrH, that the expectation value method generally produces more continuous DMCs than the finite-dipole method. Nonetheless, these two methods were compared at equilibrium for the $X^6\Sigma^+$ and $A^6\Sigma^+$ states.

For CrH, a comprehensive analysis was undertaken for MRCI calculations of each PEC and DMC in order to obtain the best quality *ab initio* curves for input into our linelist. At present, there are no well-established methodologies for the calculation of higher-excited states for transition-metal bearing compounds or procedures for which to select high quality curves devoid of discontinuities. It was shown that the quality

of the PECs and DMCs for excited states of CrH varied considerably as the CASSCF state-combination used was varied.

Using the experience gained by analysing *ab initio* calculations for CrH, MnH was studied. For MnH, the PECs and DMCs for 7 low-lying quintet states, 6 low-lying septuplet states and two nonuplet states with all TDMs calculated connecting the $X^7\Sigma^+$ and $a^5\Sigma^+$ states to the upper electronic states were calculated. For this molecule it was found that the effect of increasing the active space had a significant effect on the behaviour of the $A^7\Pi$ state. This is significant as naively it is not obvious that the increased active space would be necessary.

The effect on PECs, DMCs and TDMs of changing the states used in CASSCF calculations has been systematically investigated for both CrH and MnH in MRCI calculations. Also the consequences of changing the number of states with a given multiplicity and symmetry within the MRCI calculation has been investigated. Additionally for MnH the effect of changing the active space used was found to be significant in determining the behaviour (i.e. bonding or anti-bonding) of PECs. This PhD shows that these variables should always be specified in any publication detailing MRCI calculations.

For both CrH and MnH, spin-orbit couplings and angular momenta couplings have been calculated for the first time. For both molecules the size of the spin-orbit couplings have been found to be of magnitude up to 240 cm^{-1}. This is important for the calculation of accurate linelists for these molecules.

Moving onto the astronomy side of this PhD, a comprehensive literature review of the astronomical importance of CrH has been undertaken. Also, reviews have been produced for the previous theoretical and experimental studies of this molecule. The available experimental data for the $A^6\Sigma^+ - X^6\Sigma^+$ system of CrH has been gathered from various resources and processed into Duo format. This processed data was then used to refine the *ab initio* PECs for the the $X^6\Sigma^+$ and $A^6\Sigma^+$ electronic states.

A new linelist for CrH has been created for the 8 main isotopologues of ^{50}CrH, ^{52}CrH, ^{53}CrH and ^{54}CrH and their deuterated counterparts. This linelist contains the contributions from 8 low-lying electronic states of CrH with all electronic angular momenta and spin-orbit couplings included. In this linelist the PECs for the $X^6\Sigma^+$ and $A^6\Sigma^+$ states have been refined to the available experimentally measured frequencies to an accuracy of between 0.04^{-1} and 1.52 cm^{-1} for the (0, 0) band and 2 cm^{-1} for the (1, 0) band. Our calculated linelist raises the question of whether any bands of the $B^6\Pi - X^6\Sigma^+$ system could be observed with a favourable shift in the T_e value of the $B^6\Pi$ state. Our linelist however shows that broadly speaking the spectra of CrH is dominated by the $X^6\Sigma^+ - X^6\Sigma^+$ and $A^6\Sigma^+ - X^6\Sigma^+$ systems. We have shown that our linelist predicts a partition function which is in agreement with Sauval & Tatum (1984) up to 3000 K before been greater which indicates our model is more complete. Our linelist has a wavelength covered from zero to $\approx$ 18 000 cm^{-1} which corresponds in astronomical units to 0.56 μm to $\approx$ 10 μm, i.e the infra-red region. Our vibrational and J coverage supersedes that of the linelist of Burrows et al. (2001) which is for only the $A^6\Sigma^+ - X^6\Sigma^+$ system. Hence this more complete linelist can now be used by astronomers to search for CrH in astrophysical objects and also assist with modelling of CrH in atmospheres of brown dwarfs for which it is an important

constituent. A creation of a new linelist for CrH was clearly required by the brown dwarf community due to the problems with correctly modelling the opacity of these objects (see section 3.4).

At present there is no linelist available in the literature for MnH. However, given that it has been speculated that MnH could exist in the ISM and the favourable abundance of manganese (see chapter 6), a linelist was thus created. Hence this opens up the possibility of a detection of MnH. This linelist created for MnH consists of 10 low-lying electronic states and the couplings acting between them. Using the available experimental data for the $A^7\Pi - X^7\Sigma^+$ system, the PECs of the $X^7\Sigma^+$ and $A^7\Pi$ states were refined to an accuracy of around 0.5 cm^{-1}. For the quintet states, the experimentally derived term values presented by Balfour (1990, 1992) for the $a^5\Sigma^+$, $b^5\Pi$, $c^5\Sigma^+(II)$, $d^5\Pi(II)$ and $e^5\Sigma^+$ states were processed into Duo format and used in the final linelist. Spectra simulated using our linelist is in line with the electronic systems which have been observed for MnH namely the $A^7\Pi - X^7\Sigma^+$, $b^5\Pi - a^5\Sigma^+$, $c^5\Sigma^+(II) - a^5\Sigma^+$, $d^5\Pi(II) - a^5\Sigma^+$ and $e^5\Sigma^+(III) - a^5\Sigma^+$ systems. Our linelist has a coverage in J up to 50 which we showed to be more than adequate for temperatures up to 3000 K and a wavelength range up to 32 000 cm^{-1} i.e. from 0.31 μm (visible region) onwards into the infra-red region.

Finally, preliminary work for the group II metal hydrides of BeH, MgH and CaH has been undertaken for the purposes of creating undergraduate and school student based projects. All of these molecules, in particular MgH are important astronomically. A literature search for experimental studies and previous theoretical studies for Iron Hydride, FeH has been undertaken with a view to creating a new linelist for this molecule in future. FeH is of considerable interest to astronomers: indeed in L dwarfs the spectra it produced tends to be intertwinned with that of CrH. At present there is a linelist for the $F^4\Delta_i - X^4\Delta_i$ (Dulick et al. 2003). However, as has been shown by the literature search undertaken there is vast sets of experimental data available for the sextet states of FeH. Also, as is the case of CrH, modelling of FeH in brown dwarf spectra has proved to be challenging with most authors pointing to the incompleteness of the existing linelist for FeH.

In summary this PhD has created a new linelist for CrH which was sought after and a linelist for MnH for which at present there is no linelist available for. During the process of calculating these linelists, the MRCI method has been investigated with a focus on the effects of changing the states in the preliminary CASSCF calculation. This is, to our knowledge, a new line of research in itself.

Electronic Transition	Band	Range in N/J	Term Values	Source
$X^2\Sigma^+ - X^2\Sigma^+$ (^{24}MgH)	(0, 0) (1, 0) (2, 1) (3, 2) (4, 3)	0 - 5 0 - 28 0 - 23 0 - 23 0 - 17	Yes	Shayesteh, Appadoo, Gordon, Le Roy, Bernath (2004)
$X^2\Sigma^+ - X^2\Sigma^+$ (^{25}MgH)	(1, 0) (2, 1) (3, 2)	0 - 24 1 - 21 4 - 16		
$X^2\Sigma^+ - X^2\Sigma^+$ (^{26}MgH)	(1, 0) (2, 1) (3, 2)	0 - 24 0 - 21 2 - 16		
$A^2\Pi - X^2\Sigma^+$ (^{24}MgH)	(0, 0) (0, 1)	0 - 49 2 - 36	No	Balfour (1970a)
$A^2\Pi - X^2\Sigma^+$ (^{25}MgH)	(0, 0) (0, 1)	15 - 42 4 - 27		
$A^2\Pi - X^2\Sigma^+$ (^{26}MgH)	(0, 0) (0, 1)	14 - 42 2 - 22		
$A^2\Pi - X^2\Sigma^+$	(0, 0)	3 - 14	No	Balfour(1970b)
$^2\Pi - X^2\Sigma^+$ (234.8 nm system)	(0, 0) (1, 1)	Q (1-21) Q (1-21)	No	Balfour (1980)
$A^2\Pi - X^2\Sigma^+$	(0, 0) (0, 1) (0, 2) (1, 0) (1, 1) (1, 2) (1, 3) (2, 1) (2, 2) (2, 3) (2, 4) (3, 2) (3, 5)	0 - 45 0 - 38 0 - 33 0 - 38 0 - 39 0 - 33 0 - 39 2 - 29 3 - 29 4 - 27 2 - 29 3 - 16 5 - 15	Yes	Balfour & Cartwright (1976b)
$A^2\Pi - X^2\Sigma^+$ (^{24}MgH)	(0, 0) (0, 1) (0, 2) (0, 3) (1, 0) (1, 1) (1, 2) (1, 3) (1, 4)	0 - 43 0 - 41 0 - 33 0 - 28 0 - 35 0 - 36 0 - 36 0 - 33 0 - 30	Yes	Shayesteh & Bernath (2011)
$A^2\Pi - X^2\Sigma^+$ (^{24}MgH)	(2, 1) (3, 2) (2, 3) (2, 4) (2, 5) (3, 2) (3, 3) (3, 4) (3, 5) (3, 6) (3, 7) (3, 8) (3, 9)	0 - 30 0 - 31 0 - 31 0 - 30 0 - 26 0 - 24 0 - 24 0 - 24 0 - 24 0 - 20 0 - 4 0 - 4 0 - 5	Yes	Shayesteh & Bernath (2011)

Table 9.23: Summary of experimentally measured rovibronic transitions measured for MgH which could be used in constraining *ab initio* curves.

Electronic Transition	Band	Range in N/J	Term Values	Source
$B'^2\Sigma^+ - X^2\Sigma^+$ (^{24}MgH)	(0, 2) (0, 3) (0, 4) (0, 5) (0, 6) (0, 7) (0, 8) (0, 9)	0 - 49 0 - 45 0 - 41 0 - 36 0 - 32 0 - 26 0 - 20 7 - 15	Yes	Shayesteh & Bernath (2011)
$B'^2\Sigma^+ - X^2\Sigma^+$ (^{25}MgH)	(1, 2) (1, 3) (1, 4) (1, 5) (1, 6) (1, 7) (1, 8) (1, 9) (1, 10)	0 - 48 0 - 44 0 - 39 0 - 29 0 - 32 0 - 27 0 - 21 0 - 13 0 - 8	Yes	Shayesteh & Bernath (2011)
$B'^2\Sigma^+ - X^2\Sigma^+$ (^{24}MgH)	(2, 1) (2, 2) (2, 3) (2, 4) (2, 5) (2, 6) (2, 7) (2, 8) (2, 9) (2, 10)	8 - 36 0 - 39 0 - 41 0 - 36 21 - 35 0 - 30 0 - 26 0 - 21 0 - 15 0 - 9	Yes	Shayesteh & Bernath (2011)

Summary of experimentally measured rovibronic transitions measured for MgH which could be used in constraining *ab initio* curves (continued).

Electronic Transition	Band	Range in N/J	Term Values	Source
$B'^2\Sigma^+ - X^2\Sigma^+$ (^{24}MgH)	(3, 1) (3, 2) (3, 3) (3, 4) (3, 5) (3, 6) (3, 7) (3, 8) (3, 9) (3, 10) (3, 11)	16 - 33 0 - 33 0 - 33 0 - 19 1 - 34 0 - 27 3 - 25 0 - 21 0 - 15 0 - 9 0 - 4	Yes	Shayesteh & Bernath (2011)
$B'^2\Sigma^+ - X^2\Sigma^+$ (^{24}MgH)	(4, 2) (4, 10) (4, 11)	4 - 21 0 -9 0 -4	Yes	Shayesteh & Bernath (2011)
$C^2\Pi - X^2\Sigma^+$	(0, 0) (1, 1)	1- 34 3 -20	No	Balfour (1970b)

Summary of experimentally measured rovibronic transitions measured for MgH which could be used in constraining *ab initio* curves (continued).

Electronic Transition	Band	Range in N/J	Term Values	Source
$X^2\Sigma^+ - X^2\Sigma^+$	(0, 1) (1, 2) (2, 3) (3, 4)	5 - 30 1 - 25 1 - 23 10,15,19	No	Petitprez, Lemoine, Demuynck, Destombes & Macke (1989)
	(1, 0) (2, 1)	1 - 20 8 - 19	No	Frum & Pickett (1993)
$X^2\Sigma^+ - X^2\Sigma^+$ (^{40}CaH)	(1, 0) (2, 1) (3, 2) (4, 3)	0 - 32 7 - 29 0 - 25 3 - 20	No	Shayesteh, Walker, Gordon, Appadoo & Bernath (2004)
$A^2\Pi - X^2\Sigma^+$	(0, 0) (0, 1) (0, 2)	0.5 - 42.5 3.5 - 40. 5 0.5 - 28.5	Yes	Berg & Klynning (1974)
	(1, 1) (1, 0) (2, 2) (2, 1) (3, 3) (3, 2)	2.5 - 30.5 1.5 - 27.5 3.5 - 36.5 2.5 - 26.5 7.5 - 26.5 2.5 - 27.5	No	Martin 1984
	(0, 0) (1, 0)	0 - 7 0 - 7	No	Pereira, Skowronek, Urena,Pardo, Poyato & Pardo (2002)
$B^2\Pi - X^2\Sigma^+$	(0, 1) (0, 2)	0.5 - 42.5 0.5 - 41.5	Yes	Berg & Klynning (1974)
$B^2\Sigma^+ - X^2\Sigma^+$	(1, 0) (2, 1)	0.5 - 26.5 0.5 - 18.5	No	Berg, Klynning & Martin (1976)
$C^2\Sigma^+ - X^2\Sigma^+$	(1, 0) (1, 1) (2, 1)	5 - 20 6 - 20 3 - 10	Yes	Kaving & Lindgren (1981)
$D^2\Sigma^+ - X^2\Sigma^+$	(4, 0) (5, 0) (6, 0) (7, 0) (8, 0) (9, 0) (10, 0) (11, 0) (12, 0) (12, 1)	0 - 10 0 - 15 0 - 20 0 - 16 0 - 21 0 - 14 0 - 19 8 - 20 2 - 17 3 - 9	Yes	Bell, Herman, Johns & Peck (1979)
$D^2\Sigma^+ - X^2\Sigma^+$	(13, 0)	2 -11	Yes	Kaving & Lindgren (1981)
$E^2\Pi - X^2\Sigma^+$	(0, 0)	0.5 - 28.5	No	Ram, Tereszchuk, Gordon, Walker, Bernath (2011)
$G^2\Sigma^+ - X^2\Sigma^+$	(0, 0)	0.5 - 18.5	Yes	Kavin & Lindgren (1974)
$J^2\Pi - X^2\Sigma^+$	(0, 0) (0, 1)	0.5 - 22.5 1.5 - 19.5		
$K^2\Sigma^+ - X^2\Sigma^+$	(0, 0) (0, 1)	1.5 - 32.5 1.5 - 18.5		
$L^2\Pi - X^2\Sigma^+$	(0, 0) (1, 0) (0, 1) (1, 1)	1.5 - 35.5 2.5 - 23.5 2.5 - 20.5 0.5 - 23.5		
$M^2\Delta - X^2\Sigma^+$	(0, 0)	2.5 - 7.5		

Table 9.24: Summary of experimentally measured rovibronic transitions measured for CaH which could be used in constraining *ab initio* curves.

Electronic Transition	Band	Range in N/J	Term Values	Source
$D^2\Sigma^+ - X^2\Sigma^+$	(0, 1-5) (1, 6) (2, 1-3 and 6) (3, 1 and 2) (4, 1-2 and 7 (5, 0 and 1 (6, 0 and 1) (7, 0) (8, 0) (9, 0) (10, 0) (11, 0) (12, 0) (13, 0 and 1) (14, 0 and 1) (15, 0 and 1) (16, 0 and 1) (17, 0 and 1)	$J = 0.5$ to 25.5	Yes	Gustavsson, Klynning & Lindgren (1985)

Summary of experimentally measured rovibronic transitions measured for CaH which could be used in constraining *ab initio* curves.

Electronic Transition	Band	Range in N/J	Term Values	Source
$X^2\Sigma^+ - X^2\Sigma^+$	(0, 1) (1, 2) (2, 3) (3, 4)	1 - 43 4 - 16 4 - 17 5 - 15	No	Petitprez, Lemoine, Demuynck, Destombes & Macke (1989)
$X^2\Sigma^+ - X^2\Sigma^+$ (^{40}CaD)	(1, 0) (2, 1) (3, 2) (4, 3)	1 - 26 3 - 16 4 - 17 5 - 15	Yes	Shayesteh, Walker, Gordon, Appadoo & Bernath (2004)
$G^2\Sigma^+ - X^2\Sigma^+$	(0, 0)	7.5-29.5	Yes	Kaving & Lindgren (1976)
$J^2\Pi - X^2\Sigma^+$	(0, 0)	0.5-33.5		
$K^2\Sigma^+ - X^2\Sigma^+$	(0, 0) (0, 1)	1.5-11.5 4.5-10.5		
$L^2\Pi - X^2\Sigma^+$	(0, 0) (0, 1) (1, 0) (1, 1) (2, 1) (2, 0)	1.5 - 49.5 4.5 - 33.5 1.5 - 23.5 3.5 - 41.5 5.5 - 29.5 5.5 - 29.5		

Table 9.25: Summary of experimentally measured rovibronic transitions measured for CaD which could be used in constraining *ab initio* curves.

Appendix A

CASSCF testing for CrH: elimination of possibilities

Red signifies that the combination is nonsensical as outlined in section 4.2.

AB								
AC	BC							
AD	BD	CD						
AE	BE	CE	DE					
AF	BF	CF	DF	EF				
AG	BG	CG	DG	EG	FG			
AH	BH	CH	DH	EH	FH	GH		
AI	BI	CI	DI	EI	FI	GI	HI	
AJ	BJ	CJ	DJ	EJ	FJ	GJ	HJ	IJ

Table A.1: Table showing various state-combinations in which there are two components combined as defined in table 4.3. However, as is explained in section 4.2 not all of these state-combinations are physically sensible due to how the "wf blocks" were defined. Such state-combinations are highlighted in red to thus give the visual impression of how many are eliminated by this realisation.

BFGIJ-AC	BFGIJ-AE
BFGIJ-DC	BFGIJ-DE
BFGIJ-HC	BFGIJ-HE

Table A.2: Table showing various state-combinations in which there are seven components combined as defined in table 4.3. However, as is explained in section 4.2 not all of these state-combinations are physically sensible due to how the "wf blocks" were defined. Such state-combinations are highlighted in red to thus give the visual impression of how many are eliminated by this realisation. The only way in which seven "wf blocks" can be combined is by using BFGIJ and one of A, D, H and one of C and E. All these combinations possible are shown in this table. Hence it is non sensical to combine more than seven of the "wf blocks" together to make a state combination.

ABC							
ABD							
ABE							
ABF							
ABG							
ABH							
ABI							
ABJ							
ACD	BCD						
ACE	BCE						
ACF	BCF						
ACG	BCG						
ACH	BCH						
ACI	BCI						
ACJ	BCJ						
ADE	BDE	CDE					
ADF	BDF	CDF					
ADG	BDG	CDG					
ADH	BDH	CDH					
ADI	BDI	CDI					
ADJ	BDJ	CDJ					
AEF	BEF	CEF	DEF				
AEG	BEG	CEG	DEG				
AEH	BEH	CEH	DEH				
AEI	BEI	CEI	DEI				
AEJ	BEJ	CEJ	DEJ				
AFG	BFG	CFG	DFG	EFG			
AFH	BFH	CFH	DFH	EFH			
AFI	BFI	CFI	DFI	EFI			
AFJ	BFJ	CFJ	DFJ	EFJ			
AGH	BGH	CGH	DGH	EGH	FGH		
AGI	BGI	CGI	DGI	EGI	FGI		
AGJ	BGJ	CGJ	DGJ	EGJ	FGJ		
AHI	BHI	CHI	DHI	EHI	FHI	GHI	
AHJ	BHJ	CHJ	DHJ	EHJ	FHJ	GHJ	
AIJ	BIJ	CIJ	DIJ	EIJ	FIJ	GIJ	HIJ

Table A.3: Table showing various state-combinations in which there are three components combined as defined in table 4.3. However, as is explained in section 4.2 not all of these state-combinations are physically sensible due to how the "wf blocks" were defined. Such state-combinations are highlighted in red to thus give the visual impression of how many are eliminated by this realisation.

ABCD
ABCE
ABCF
ABCG
ABCH
ABCI
ABCJ
ABDE
ABDF
ABDG
ABDH
ABDI
ABDJ
ABEF
ABEG
ABEH
ABEI
ABEJ
ABFG
ABFH
ABFI
ABFJ
ABGH
ABGI
ABGJ
ABHI
ABHJ
ABIJ

a

ACDE	BCDE
ACDF	BCDF
ACDG	BCDG
ACDH	BCDH
ACDI	BCDI
ACDJ	BCDJ
ACEF	BCEF
ACEG	BCEG
ACEH	BCEH
ACEI	BCEI
ACEJ	BCEJ
ACFG	BCFG
ACFH	BCFH
ACFI	BCFI
ACFJ	BCFJ
ACGH	BCGH
ACGI	BCGI
ACGJ	BCGJ
ACHI	BCHI
ACHJ	BCHJ
ACIJ	BCIJ

b

ADEF	BDEF	CDEF
ADEG	BDEG	CDEG
ADEH	BDEH	CDEH
ADEI	BDEI	CDEI
ADEJ	BDEJ	CDEJ
ADFG	BDFG	CDFG
ADFH	BDFH	CDFH
ADFI	BDFI	CDFI
ADFJ	BDFJ	CDFJ
ADGH	BDGH	CDGH
ADGI	BDGI	CDGI
ADGJ	BDGJ	CDGJ
ADHI	BDHI	CDHI
ADHJ	BDHJ	CDHJ
ADIJ	BDIJ	CDIJ

c

AEFG	BEFG	CEFG	DEFG
AEFH	BEFH	CEFH	DEFH
AEFI	BEFI	CEFI	DEFI
AEFJ	BEFJ	CEFJ	DEFJ
AEGH	BEGH	CEGH	DEGH
AEGI	BEGI	CEGI	DEGI
AEGJ	BEGJ	CEGJ	DEGJ
AEHI	BEHI	CEHI	DEHI
AEHJ	BEHJ	CEHJ	DEHJ
AEIJ	BEIJ	CEIJ	DEIJ

d

AFGH	BFGH	CFGH	DFGH	EFGH
AFGI	BFGI	CFGI	DFGI	EFGI
AFGJ	BFGJ	CFGJ	DFGJ	EFGJ
AFHI	BFHI	CFHI	DFHI	EFHI
AFHJ	BFHJ	CFHJ	DFHJ	EFHJ
AFIJ	BFIJ	CFIJ	DFIJ	EFIJ

e

AGHI	BGHI	CGHI	DGHI	EGHI	FGHI
AGHJ	BGHJ	CGHJ	DGHJ	EGHJ	FGHJ
AGIJ	BGIJ	CGIJ	DGIJ	EGIJ	FGIJ

f

AHIJ	BHIJ	CHIJ	DHIJ	EHIJ	FHIJ	GHIJ

g

Table A.4: Table showing various state-combinations in which there are four components combined as defined in table 4.3. However, as is explained in section 4.2 not all of these state-combinations are physically sensible due to how the "wf blocks" were defined. Such state-combinations are highlighted in red to thus give the visual impression of how many are eliminated by this realisation.

ABC-DE					
ABC-DF					
ABC-DG					
ABC-DH					
ABC-DI					
ABC-DJ					
ABC-EF	ABD-EF				
ABC-EG	ABD-EG				
ABC-EH	ABD-EH				
ABC-EI	ABD-EI				
ABC-EJ	ABD-EJ				
ABC-FG	ABD-FG	ABE-FG			
ABC-FH	ABD-FH	ABE-FH			
ABC-FI	ABD-FI	ABE-FI			
ABC-FJ	ABD-FJ	ABE-FJ			
ABC-GH	ABD-GH	ABE-GH	ABF-GH		
ABC-GI	ABD-GI	ABE-GI	ABF-GI		
ABC-GJ	ABD-GJ	ABE-GJ	ABF-GJ		
ABC-HI	ABD-HI	ABE-HI	ABF-HI	ABG-HI	
ABC-HJ	ABD-HJ	ABE-HJ	ABF-HJ	ABG-HJ	
ABC-IJ	ABD-IJ	ABE-IJ	ABF-IJ	ABG-IJ	ABH-IJ

a

ACD-EF		
ACD-EG		
ACD-EH		
ACD-EI		
ACD-EJ		
ACD-FG	ACE-FG	
ACD-FH	ACE-FH	
ACD-FI	ACE-FI	
ACD-FJ	ACE-FJ	
ACD-GH	ACE-GH	ACF-GH
ACD-GI	ACE-GI	ACF-GI
ACD-GJ	ACE-GJ	ACF-GJ
ACD-HI	ACE-HI	ACF-HI
ACD-HJ	ACE-HJ	ACF-HJ
ACD-IJ	ACE-IJ	ACF-IJ
		ACG-HI
		ACG-HJ
		ACG-IJ
		ACH-IJ

b

BCD-EF		
BCD-EG		
BCD-EH		
BCD-EI		
BCD-EJ		
BCD-FG	BCE-FG	
BCD-FH	BCE-FH	
BCD-FI	BCE-FI	
BCD-FJ	BCE-FJ	
BCD-GH	BCE-GH	BCF-GH
BCD-GI	BCE-GI	BCF-GI
BCD-GJ	BCE-GJ	BCF-GJ
BCD-HI	BCE-HI	BCF-HI
BCD-IJ	BCE-HJ	BCF-HJ
BCD-HJ	BCE-IJ	BCF-IJ
		BCG-HI
		BCG-HJ
		BCG-IJ
		BCH-IJ

c

Table A.5: Table showing various state-combinations in which there are five components combined as defined in table 4.3. However, as is explained in section 4.2 not all of these state-combinations are physically sensible due to how the "wf blocks" were defined. Such state-combinations are highlighted in red to thus give the visual impression of how many are eliminated by this realisation.

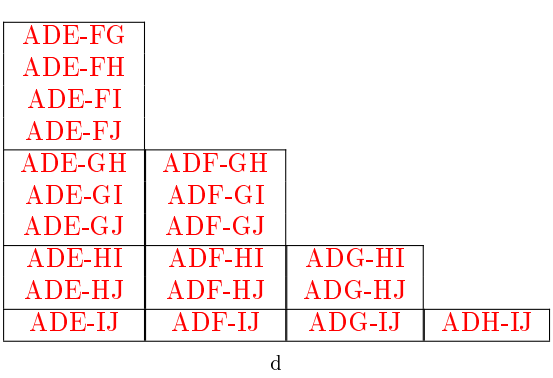

d

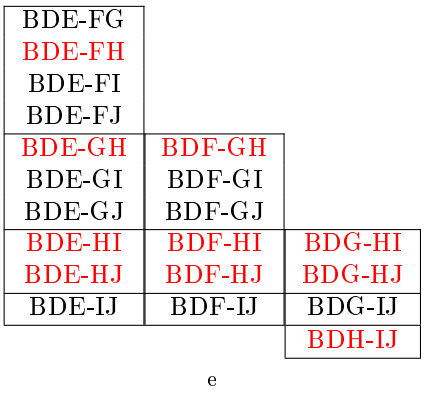

e

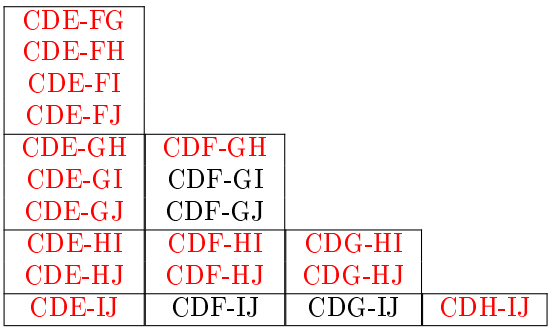

f

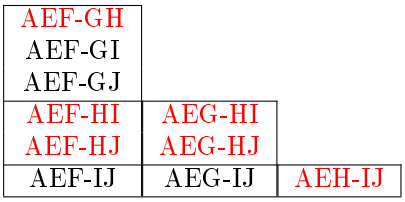

g

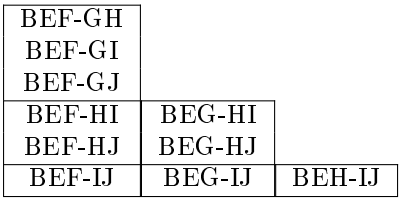

h

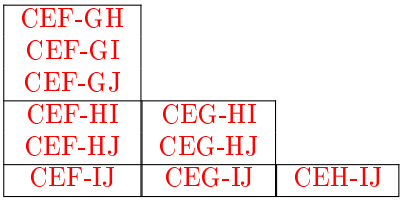

i

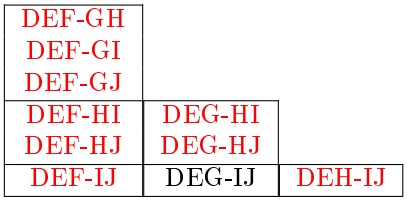

j

k

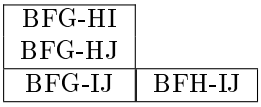

l

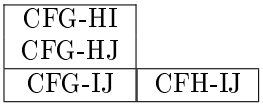

m

n

o

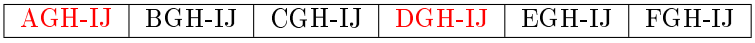

p

Table A.5 continued: This table shows various state-combinations in which there are five components combined as defined in table 4.3. However, as is explained in section 4.2 not all of these state-combinations are physically sensible due to how the "wf blocks" were defined. Such state-combinations are highlighted in red to thus give the visual impression of how many are eliminated by this realisation.

ABC-DEF				
ABC-DEG				
ABC-DEH				
ABC-DEI				
ABC-DEJ				
ABC-DFG				
ABC-DFH				
ABC-DFI				
ABC-DFJ				
ABC-DGH				
ABC-DGI				
ABC-DGJ				
ABC-DHI				
ABC-DHJ				
ABC-DIJ				
ABC-EFG	ABD-EFG			
ABC-EFH	ABD-EFH			
ABC-EFI	ABD-EFI			
ABC-EFJ	ABD-EFJ			
ABC-EGH	ABD-EGH			
ABC-EGI	ABD-EGI			
ABC-EGJ	ABD-EGJ			
ABC-EHI	ABD-EHI			
ABC-EHJ	ABD-EHJ			
ABC-EIJ	ABD-EIJ			
ABC-FGH	ABD-FGH	ABE-FGH		
ABC-FGI	ABD-FGI	ABE-FGI		
ABC-FGJ	ABD-FGJ	ABE-FGJ		
ABC-FHI	ABD-FHI	ABE-FHI		
ABC-FHJ	ABD-FHJ	ABE-FHJ		
ABC-FIJ	ABD-FIJ	ABE-FIJ		
ABC-GHI	ABD-GHI	ABE-GHI	ABF-GHI	
ABC-GHJ	ABD-GHJ	ABE-GHJ	ABF-GHJ	
ABC-GIJ	ABD-GIJ	ABE-GIJ	ABF-GIJ	
ABC-HIJ	ABD-HIJ	ABE-HIJ	ABF-HIJ	ABG-HIJ

a

AEF-GHI	
AEF-GHJ	
AEF-GIJ	
AEF-HIJ	AEG-HIJ

b

BEF-GHI	
BEF-GHJ	
BEF-GIJ	
BEF-HIJ	BEG-HIJ

c

CEF-GHI	
CEF-GHJ	
CEF-GIJ	
CEF-HIJ	CEG-HIJ

d

DEF-GHI	
DEF-GHJ	
DEF-GIJ	
DEF-HIJ	DEG-HIJ

e

AFG-HIJ	DFG-HIJ
BFG-HIJ	EFG-HIJ
CFG-HIJ	

f

Table A.6: Table showing various state-combinations in which there are six components combined as defined in table 4.3. However, as is explained in section 4.2 not all of these state-combinations are physically sensible due to how the "wf blocks" were defined. Such state-combinations are highlighted in red to thus give the visual impression of how many are eliminated by this realisation.

ACD-EFG		
ACD-EFH		
ACD-EFI		
ACD-EFJ		
ACD-EGH		
ACD-EGI		
ACD-EGJ		
ACD-EHI		
ACD-EHJ		
ACD-EIJ		
ACD-FGH	ACE-FGH	
ACD-FGI	ACE-FGI	
ACD-FGJ	ACE-FGJ	
ACD-FHI	ACE-FHI	
ACD-FHJ	ACE-FHJ	
ACD-FIJ	ACE-FIJ	
ACD-GHI	ACE-GHI	ACF-GHI
ACD-GHJ	ACE-GHJ	ACF-GHJ
ACD-GIJ	ACE-GIJ	ACF-GIJ
ACD-HIJ	ACE-HIJ	ACF-HIJ
		ACG-HIJ

g

BCD-EFG		
BCD-EFH		
BCD-EFI		
BCD-EFJ		
BCD-EGH		
BCD-EGI		
BCD-EGJ		
BCD-EHI		
BCD-EHJ		
BCD-EIJ		
BCD-FGH	BCE-FGH	
BCD-FGI	BCE-FGI	
BCD-FGJ	BCE-FGJ	
BCD-FHI	BCE-FHI	
BCD-FHJ	BCE-FHJ	
BCD-FIJ	BCE-FIJ	
BCD-GHI	BCE-GHI	BCF-GHI
BCD-GHJ	BCE-GHJ	BCF-GHJ
BCD-GIJ	BCE-GIJ	BCF-GIJ
BCD-HIJ	BCE-HIJ	BCF-HIJ
		BCG-HIJ

h

ADE-FGH		
ADE-FGI		
ADE-FGJ		
ADE-FHI		
ADE-FHJ		
ADE-FIJ		
ADE-GHI	ADF-GHI	
ADE-GHJ	ADF-GHJ	
ADE-GIJ	ADF-GIJ	
ADE-HIJ	ADF-HIJ	ADG-HIJ

i

BDE-FGH		
BDE-FGI		
BDE-FGJ		
BDE-FHI		
BDE-FHJ		
BDE-FIJ		
BDE-GHI	BDF-GHI	
BDE-GHJ	BDF-GHJ	
BDE-GIJ	BDF-GIJ	
BDE-HIJ	BDF-HIJ	BDG-HIJ

j

CDE-FGH		
CDE-FGI		
CDE-FGJ		
CDE-FHI		
CDE-FHJ		
CDE-FIJ		
CDE-GHI	CDF-GHI	
CDE-GHJ	CDF-GHJ	
CDE-GIJ	CDF-GIJ	
CDE-HIJ	CDF-HIJ	CDG-HIJ

k

Table A.6 continued: This table shows various state-combinations in which there are six components combined as defined in table 4.3. However, as is explained in section 4.2 not all of these state-combinations are physically sensible due to how the "wf blocks" were defined. Such state-combinations are highlighted in red to thus give the visual impression of how many are eliminated by this realisation.

Appendix B

CrH CASSCF Calculations: Results

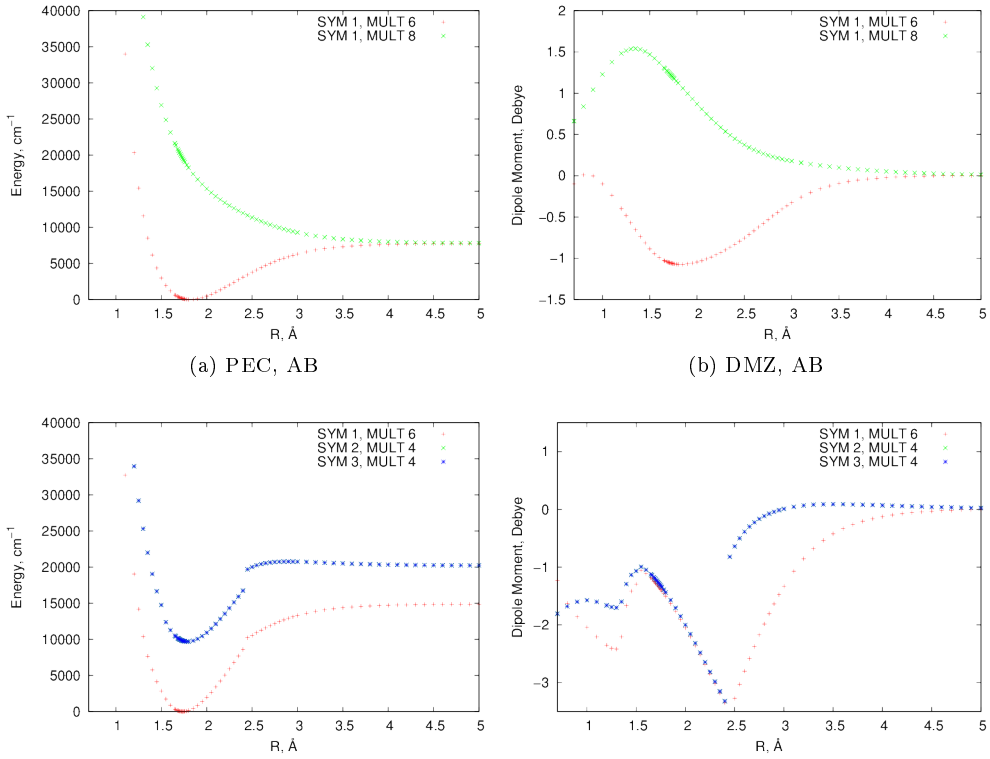

(a) PEC, AB

(b) DMZ, AB

(c) PEC, AF

(d) DMZ, AF

Figure B.1: CASSCF calculations using a cc-pVDZ basis set that combine a single $^6\Sigma^+$ state (A) with a single other component as defined in table 4.3

CASSCF results (continued)

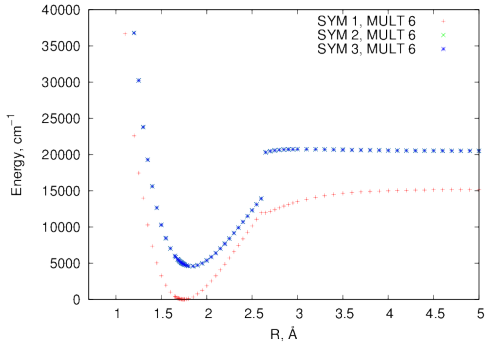

(a) PEC, AI

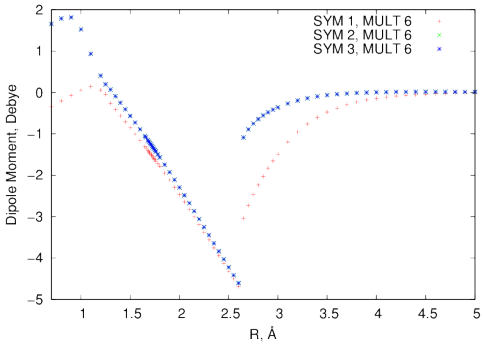

(b) DMZ, AI

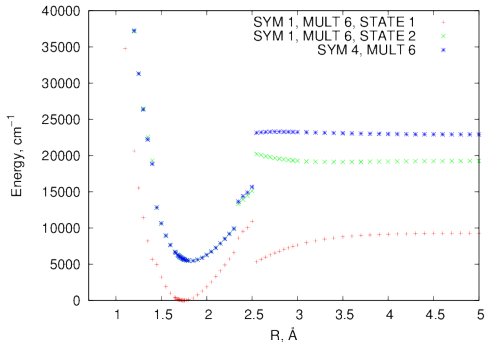

(c) PEC, AJ

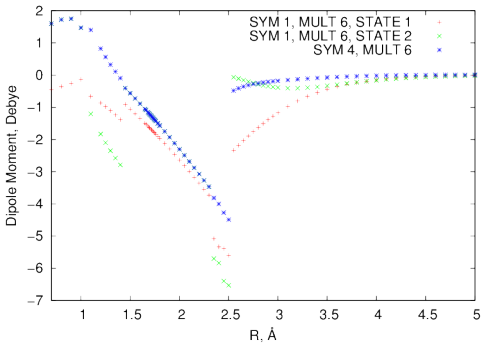

(d) DMZ, AJ

Figure B.2: CASSCF calculations using a cc-pVDZ basis set that combine a single $^6\Sigma^+$ state (A) with a single other component as defined in table 4.3

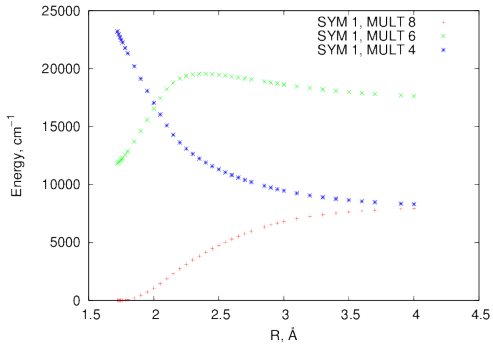

(a) PEC, ABC

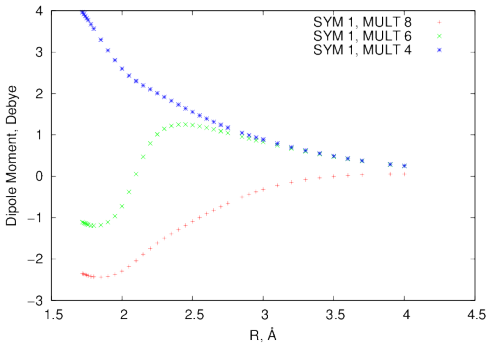

(b) DMZ, ABC

Figure B.3: CASSCF calculations using a cc-pVDZ basis set that combine a single $^6\Sigma^+$ state (A), a single $^8\Sigma^+$ state (B) and a $^4\Sigma^+$ state

CASSCF results (continued)

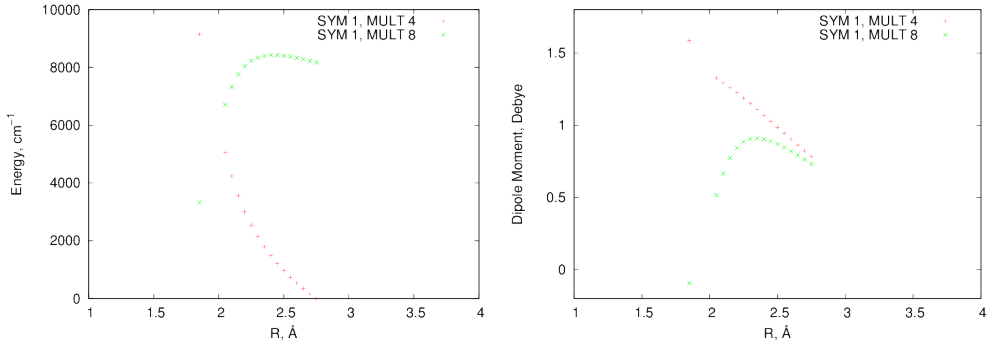

(a) PEC, BC

(b) DMZ, BC

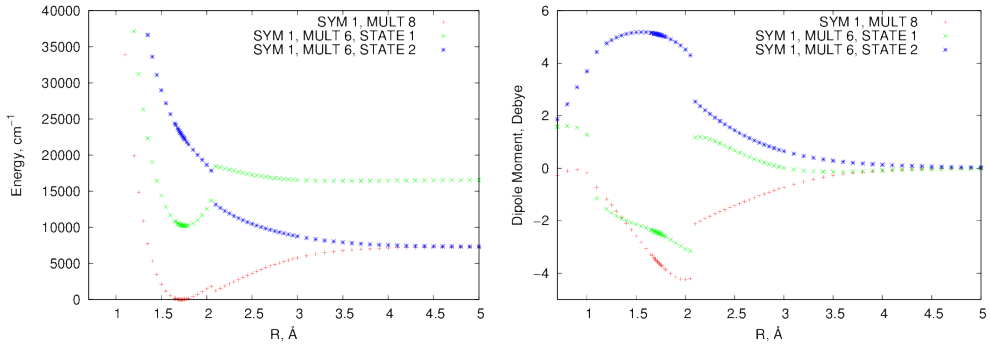

(c) PEC, BD

(d) DMZ, BD

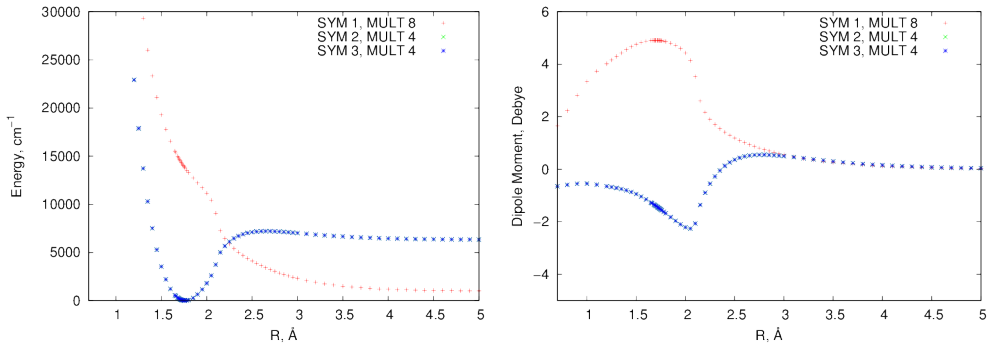

(e) PEC, BF

(f) DMZ, BF

Figure B.4: CASSCF calculations using a cc-pVDZ basis set that combine a single $^8\Sigma^+$ state (B) with a single other component as defined in table 4.3.

CASSCF results (continued)

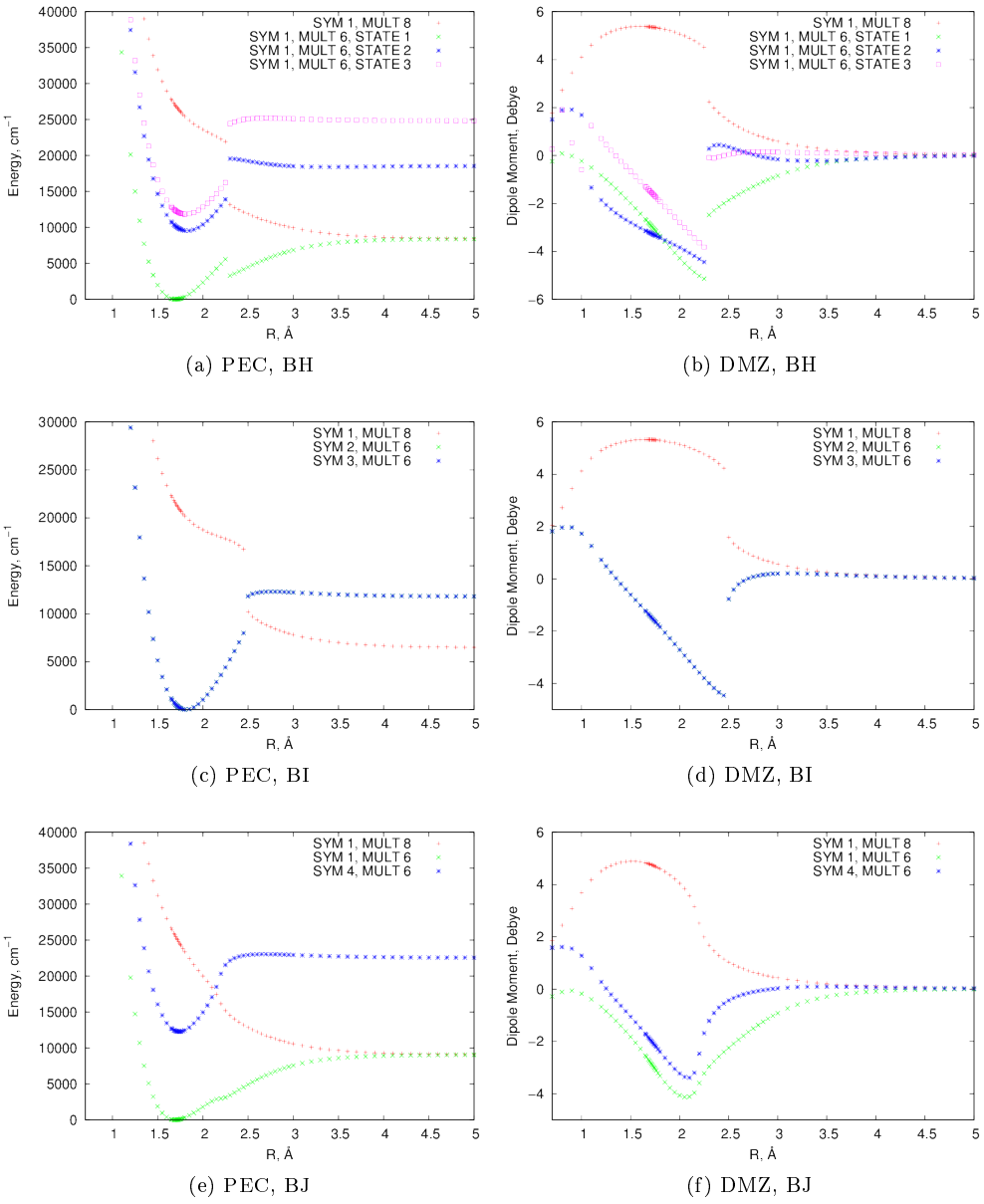

(a) PEC, BH (b) DMZ, BH

(c) PEC, BI (d) DMZ, BI

(e) PEC, BJ (f) DMZ, BJ

Figure B.5: CASSCF calculations using a cc-pVDZ basis set that combine a single $^8\Sigma^+$ state (B) with a single other component as defined in table 4.3. Continued from previous page

CASSCF results (continued)

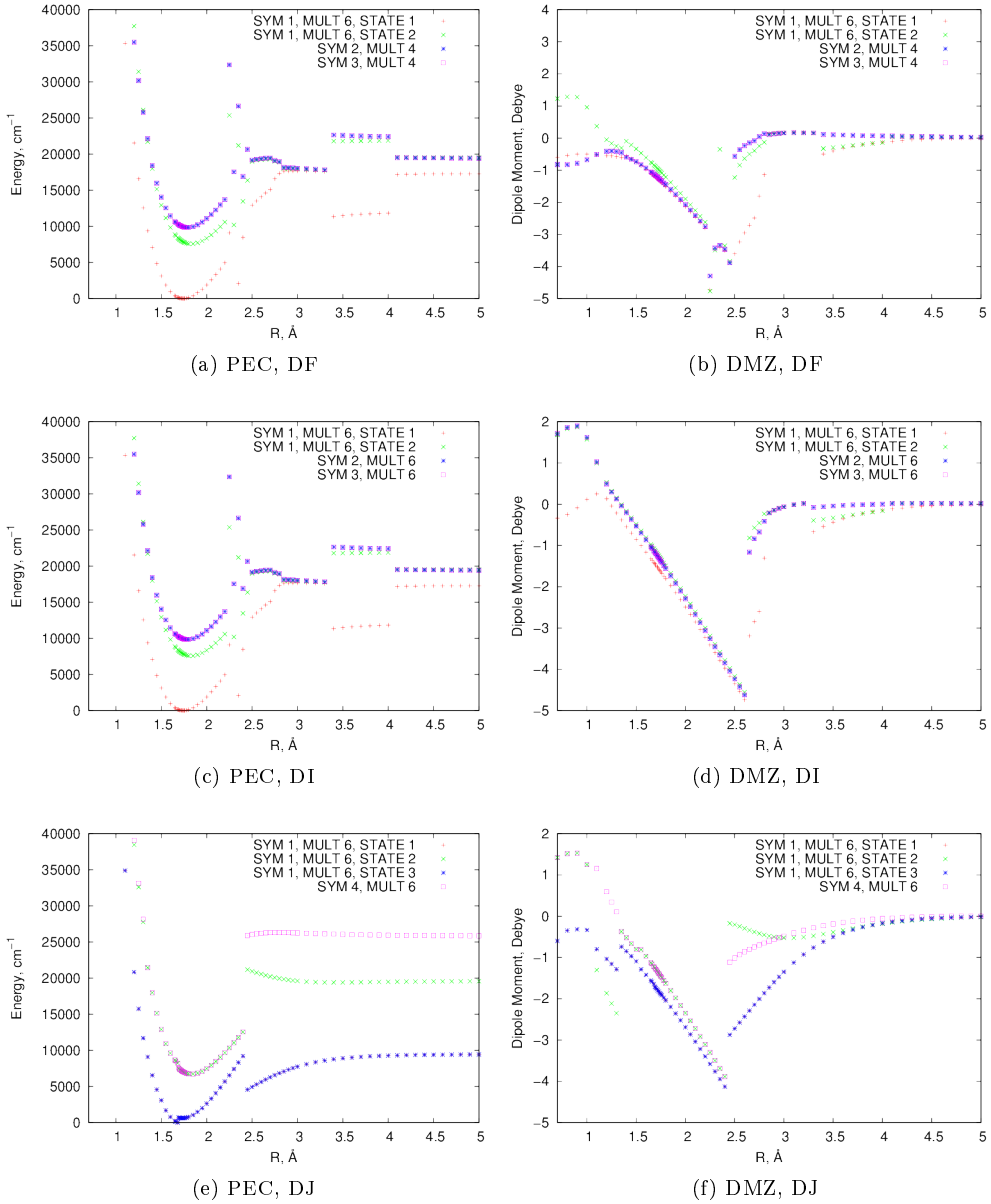

(a) PEC, DF (b) DMZ, DF

(c) PEC, DI (d) DMZ, DI

(e) PEC, DJ (f) DMZ, DJ

Figure B.6: CASSCF calculations using a cc-pVDZ basis set that combine two $^6\Sigma^+$ states (D) with a single other component as defined in table 4.3.

CASSCF results (continued)

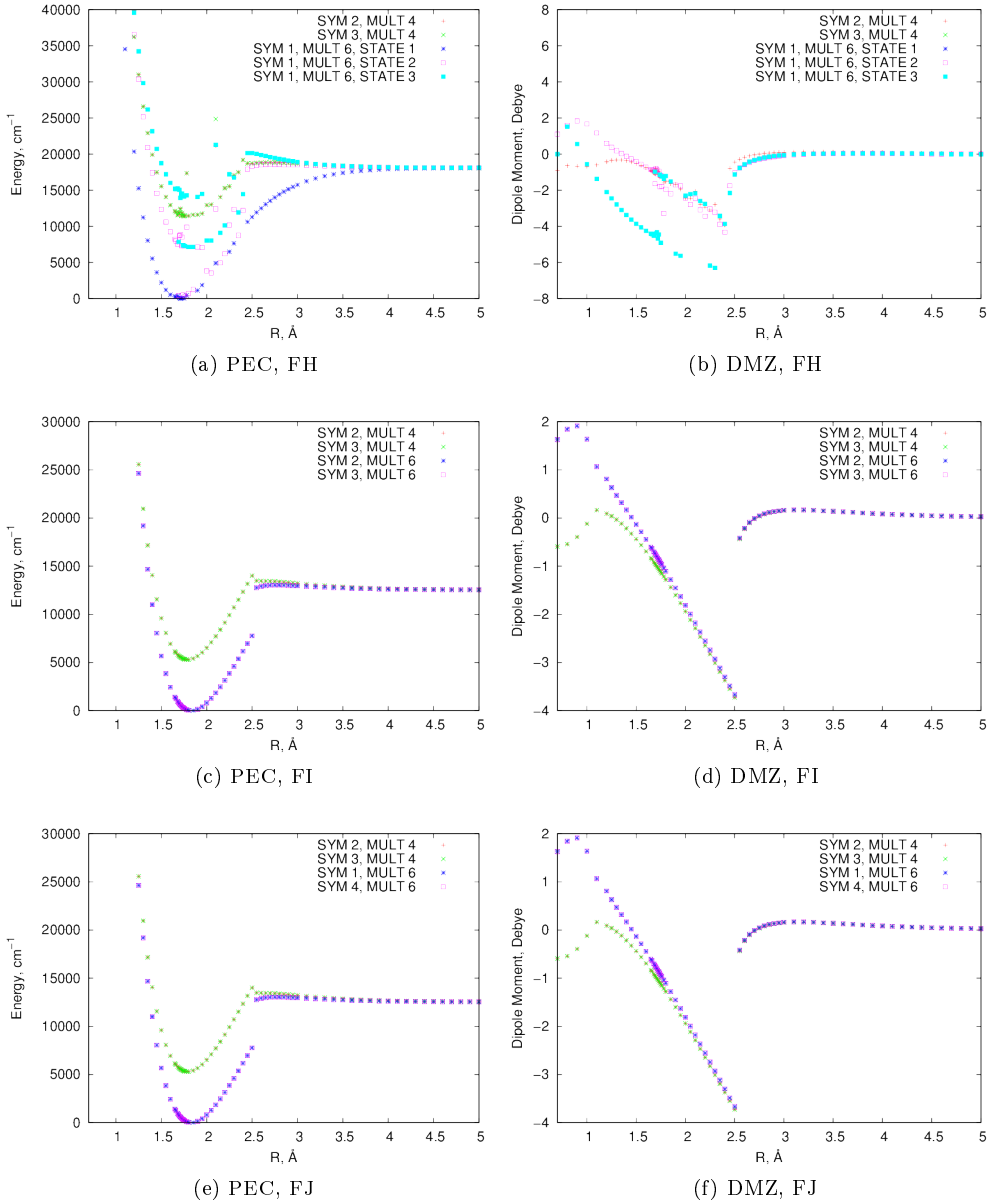

(a) PEC, FH

(b) DMZ, FH

(c) PEC, FI

(d) DMZ, FI

(e) PEC, FJ

(f) DMZ, FJ

Figure B.7: CASSCF calculations using a cc-pVDZ basis set that combine a single $^4\Pi$ state (F) with a single other component as defined in table 4.3.

CASSCF results (continued)

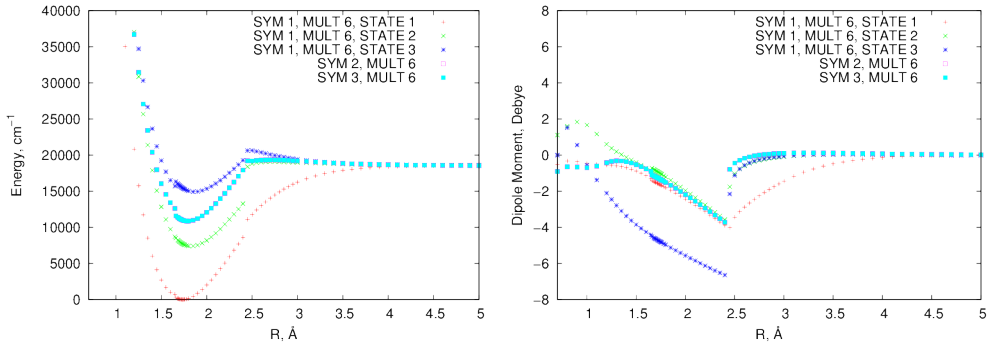

(a) PEC, HI

(b) DMZ, HI

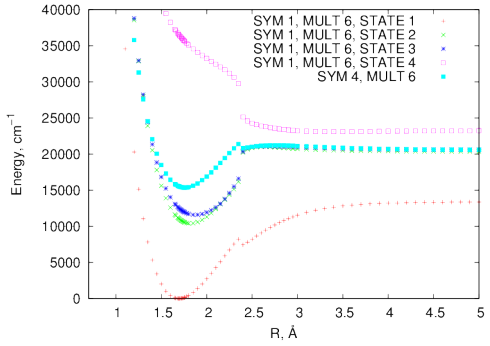

(c) PEC, HJ

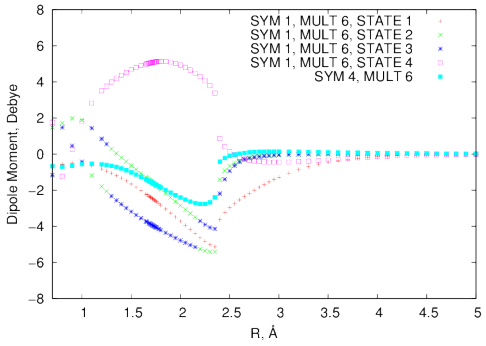

(d) DMZ, HJ

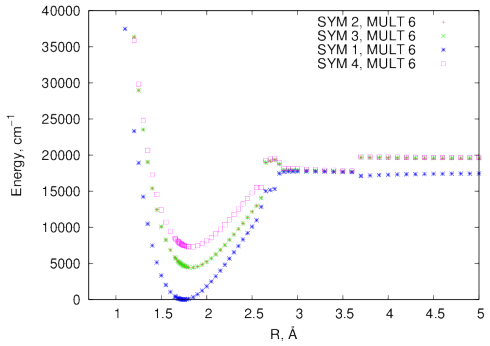

(e) PEC, IJ

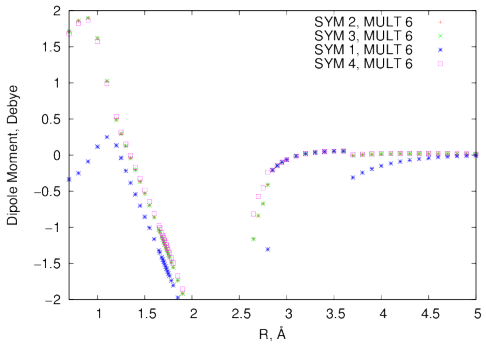

(f) DMZ, IJ

Figure B.8: Figures B.8a, B.8b, B.8c, B.8d show CASSCF calculations using a cc-pVDZ basis set that combine three $^6\Sigma^+$ states (H) with a single other component as defined in table 4.3 Figures B.8e andB.8f show results from a CASSCF calculations using a cc-pVDZ basis set that combine a single $^6\Pi$ (I) state with a single $^6\Delta$ (J) state as defined in table 4.3.

CASSCF results (continued)

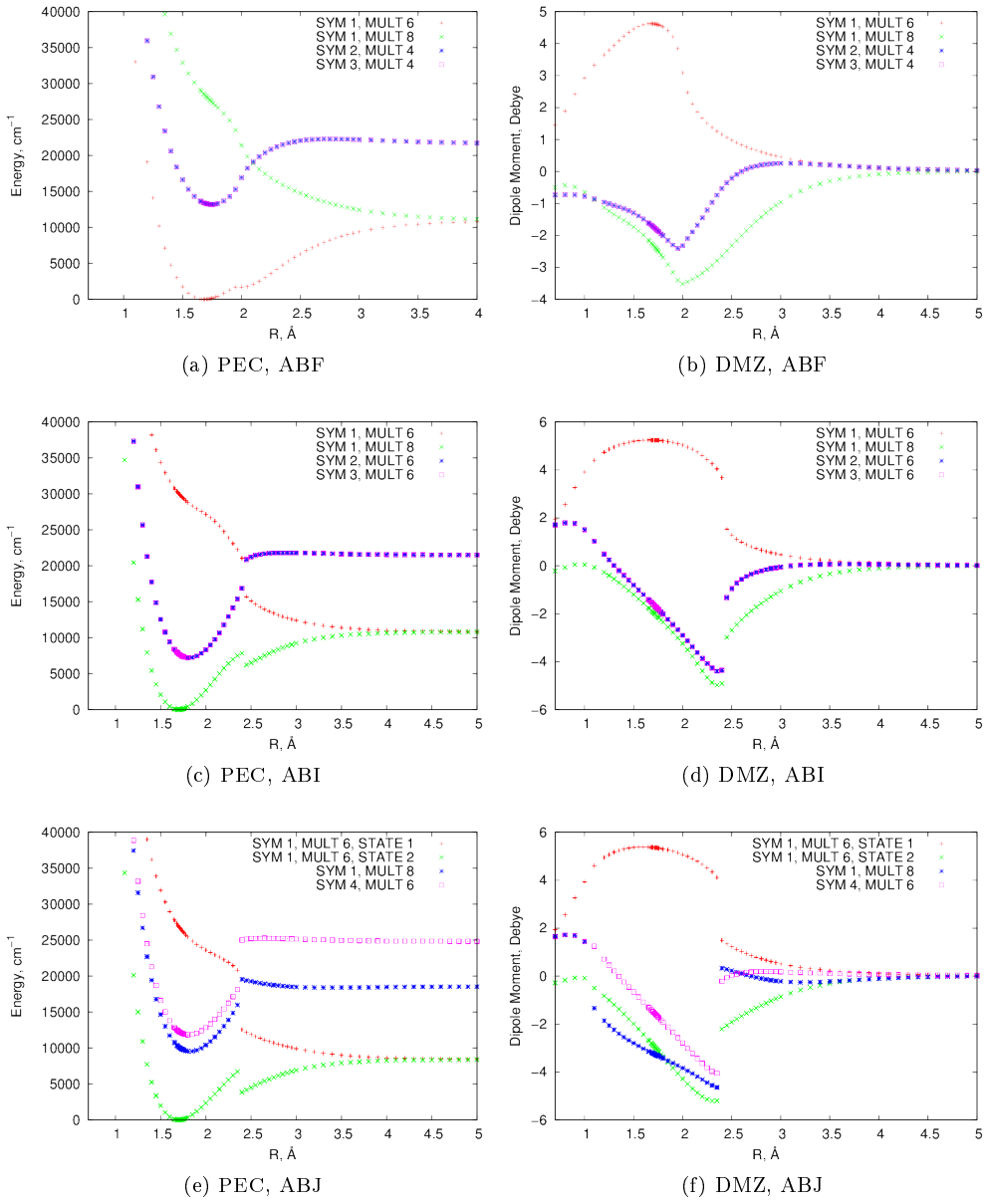

(a) PEC, ABF

(b) DMZ, ABF

(c) PEC, ABI

(d) DMZ, ABI

(e) PEC, ABJ

(f) DMZ, ABJ

Figure B.9: CASSCF calculations using a cc-pVDZ basis set that combine a single $^6\Sigma^+$ (A) state and a single $^8\Sigma^+$ (B) state with one other component as defined in table 4.3.

CASSCF results (continued)

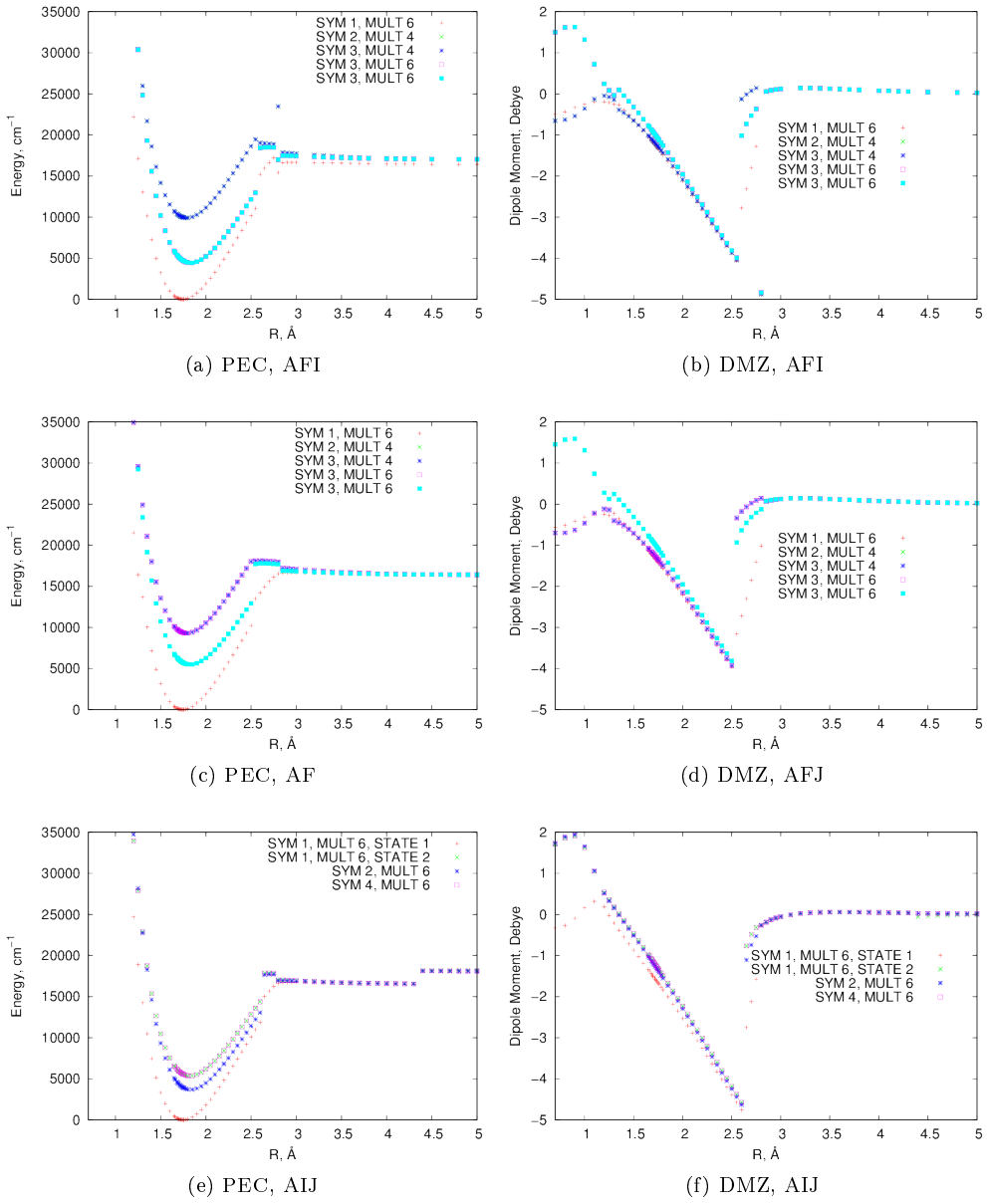

(a) PEC, AFI

(b) DMZ, AFI

(c) PEC, AF

(d) DMZ, AFJ

(e) PEC, AIJ

(f) DMZ, AIJ

Figure B.10: CASSCF calculations using a cc-pVDZ basis set that combine a single $^6\Sigma^+$ state (A) and eihter a single $^4\Pi$ state (F) or a single $^6\Pi$ state (I) along with one other component as defined in table 4.3.

CASSCF results (continued)

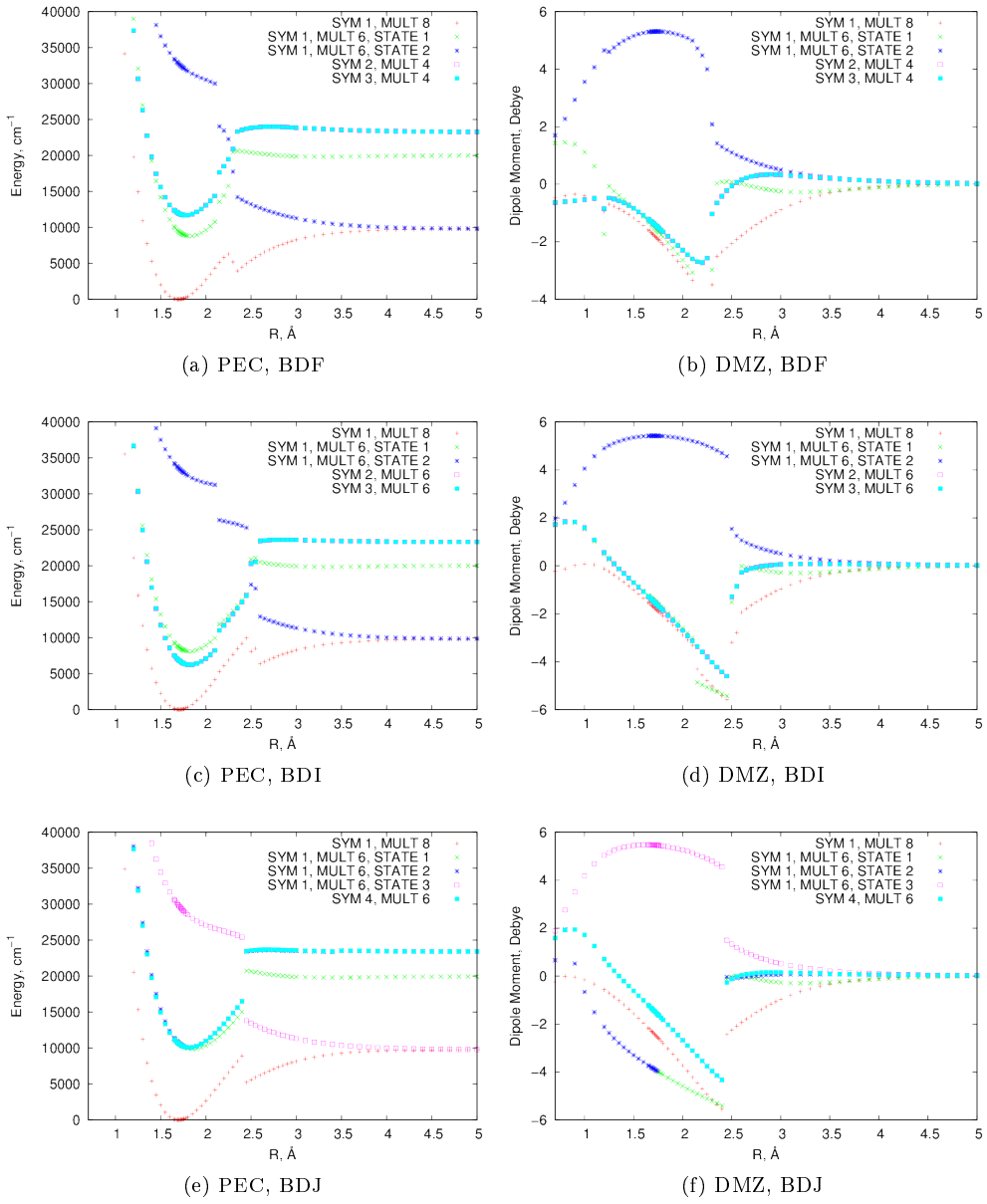

(a) PEC, BDF

(b) DMZ, BDF

(c) PEC, BDI

(d) DMZ, BDI

(e) PEC, BDJ

(f) DMZ, BDJ

Figure B.11: CASSCF calculations using a cc-pVDZ basis set that combine a single $^8\Sigma^+$ state (B) and two $^6\Sigma^+$ states (D) with one other component as defined in table 4.3.

CASSCF results (continued)

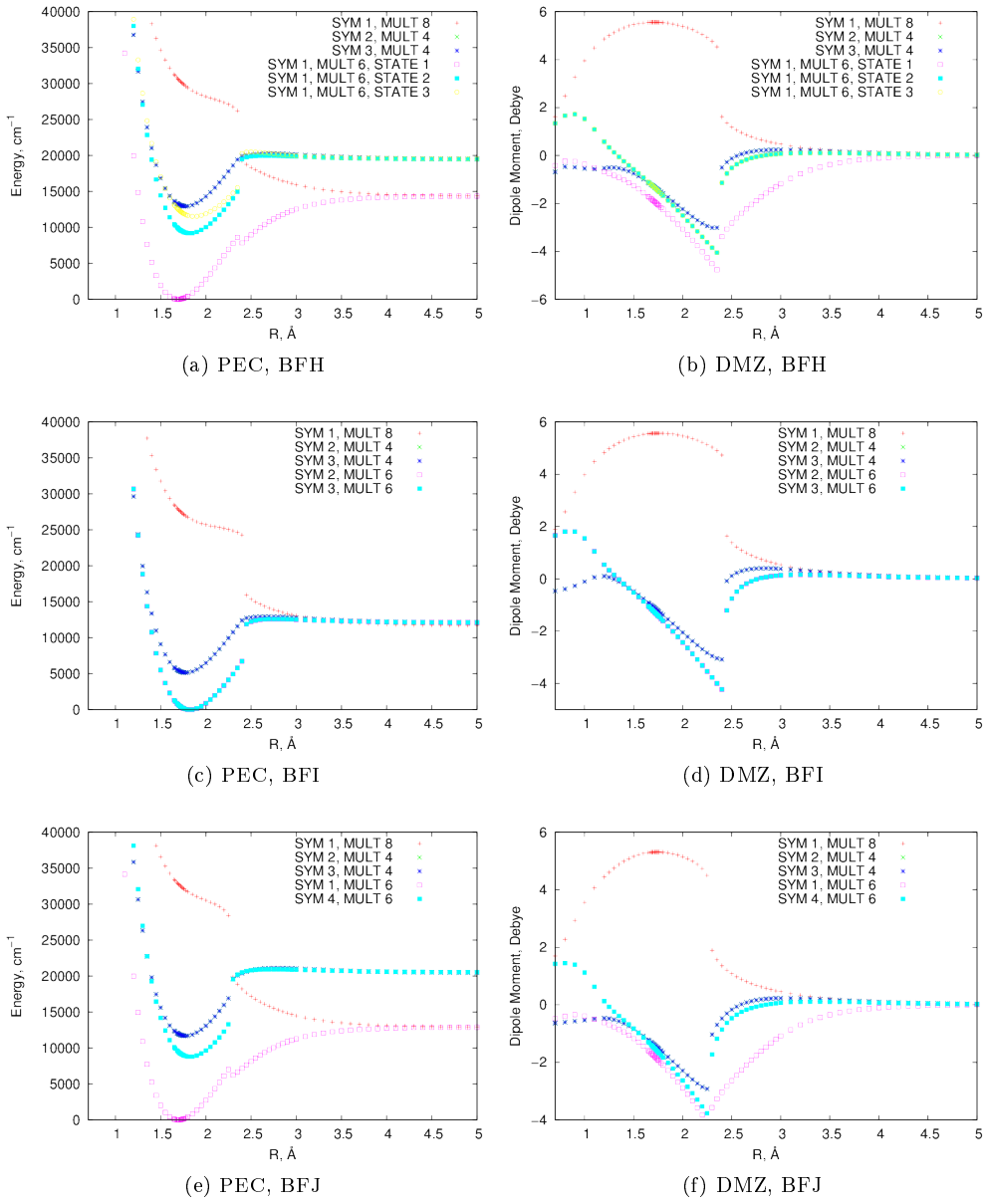

(a) PEC, BFH

(b) DMZ, BFH

(c) PEC, BFI

(d) DMZ, BFI

(e) PEC, BFJ

(f) DMZ, BFJ

Figure B.12: CASSCF calculations using a cc-pVDZ basis set that combine a single $^8\Sigma^+$ state (B) and two $^6\Sigma^+$ states (D) with one other component as defined in table 4.3.

CASSCF results (continued)

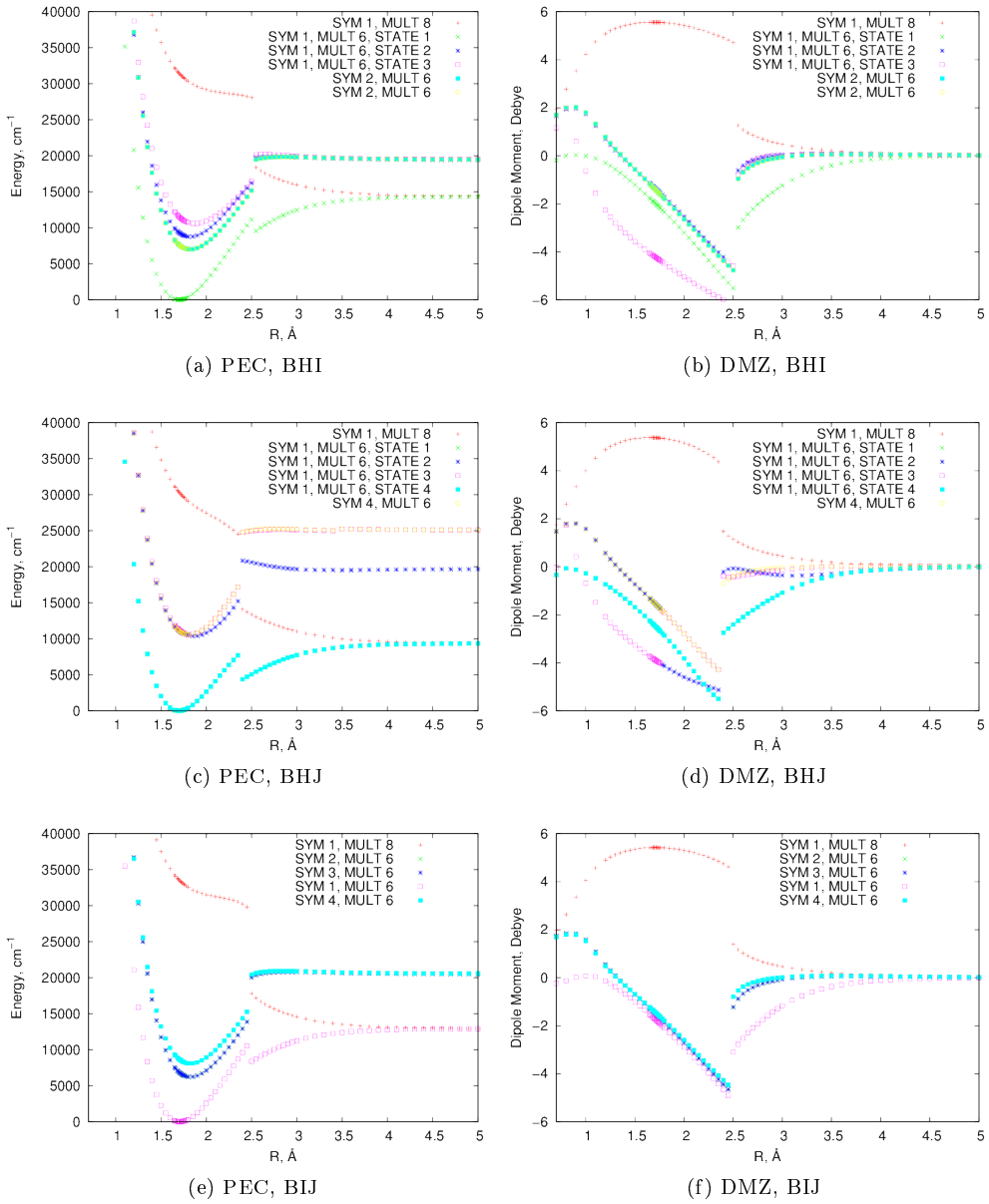

(a) PEC, BHI

(b) DMZ, BHI

(c) PEC, BHJ

(d) DMZ, BHJ

(e) PEC, BIJ

(f) DMZ, BIJ

Figure B.13: CASSCF calculations using a cc-pVDZ basis set that combine a single $^8\Sigma^+$ state (B) and a single $^6\Pi$ state (I) with one other component as defined in table 4.3.

CASSCF results (continued)

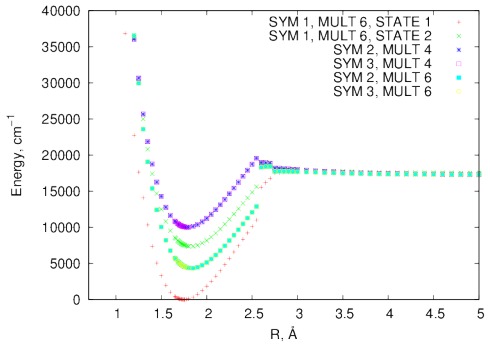

(a) PEC, DFI

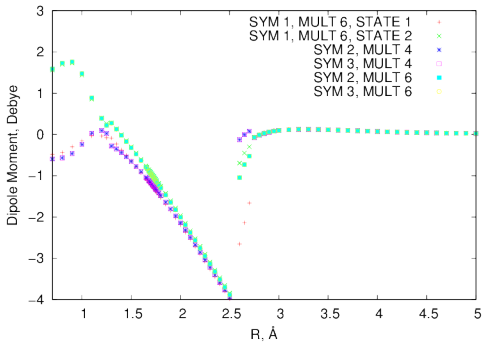

(b) DMZ, DFI

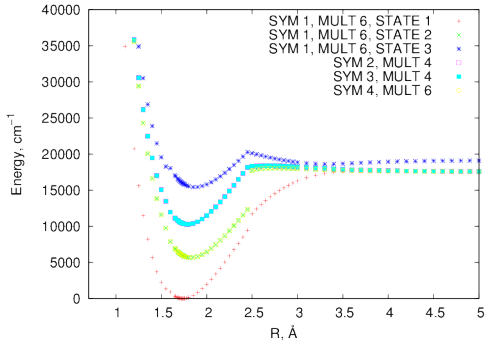

(c) PEC, DFJ

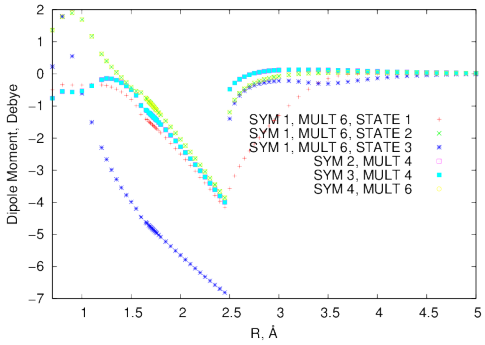

(d) DMZ, DFJ

Figure B.14: CASSCF calculations using a cc-pVDZ basis set that combine a two $^6\Sigma^+$ states (D) and a single $^4\Pi$ state (F) with one other component as defined in table 4.3.

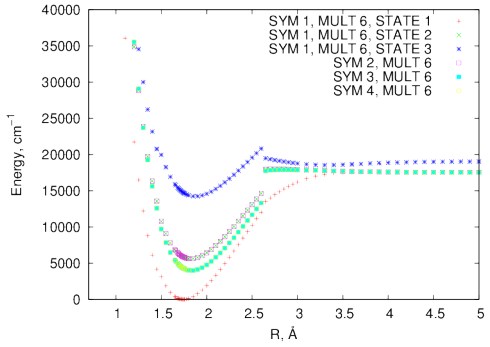

(a) PEC, DIJ

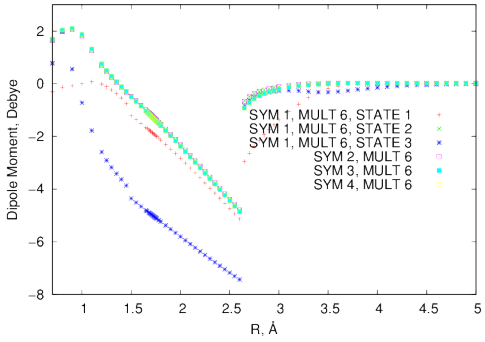

(b) DMZ, DIJ

Figure B.15: CASSCF calculations using a cc-pVDZ basis set that combine a two $^6\Sigma^+$ states (D) and a single $^6\Pi$ state (F) with one other component as defined in table 4.3.

CASSCF results (continued)

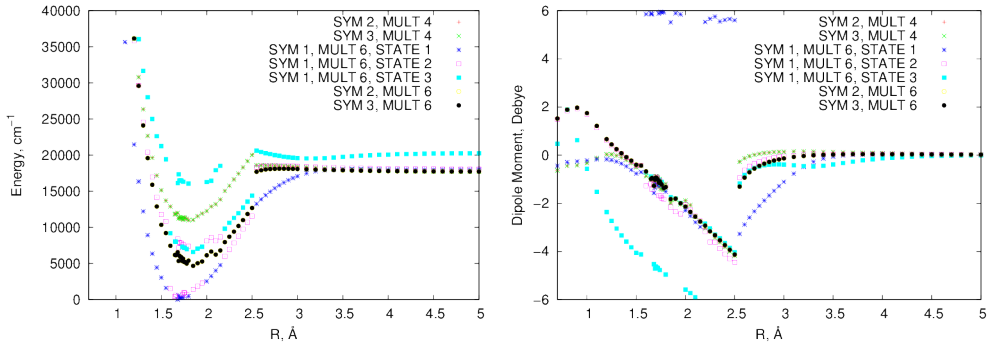

(a) PEC, FHI (b) DMZ, FHI

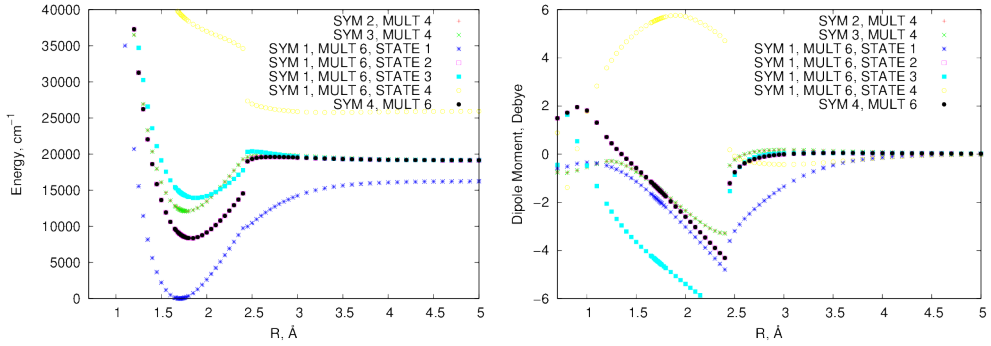

(c) PEC, FHJ (d) DMZ, FHJ

Figure B.16: CASSCF calculations using a cc-pVDZ basis set that single $^4\Pi$ state (F) and three $^6\Sigma^+$ states (H) with one other component as defined in table 4.3.

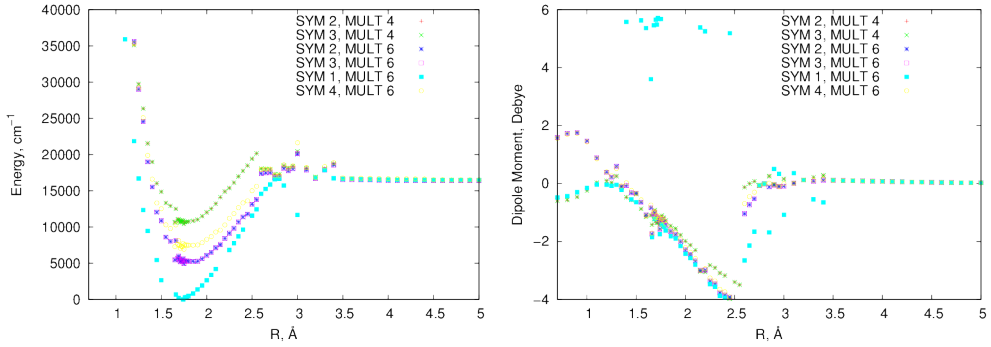

(a) PEC, FIJ (b) DMZ, FIJ

Figure B.17: CASSCF calculations using a cc-pVDZ basis set that single $^4\Pi$ state (F) and a single $^6\Pi$ state with one other component as defined in table 4.3.

CASSCF results (continued)

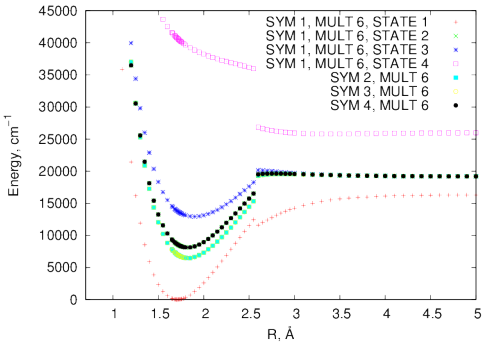

(a) PEC, HIJ

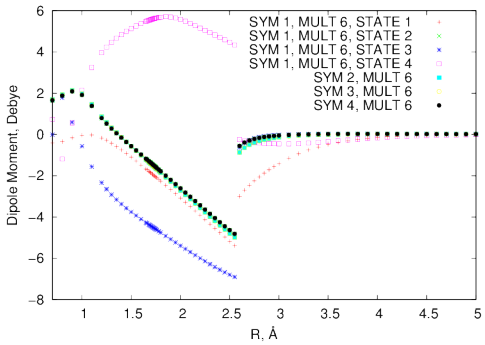

(b) DMZ, HIJ

Figure B.18: CASSCF calculations using a cc-pVDZ basis set that combine three $^6\Sigma^+$ states (H), a single $^6\Pi$ state (I) and a single $^6\Delta$ state as defined in table 4.3.

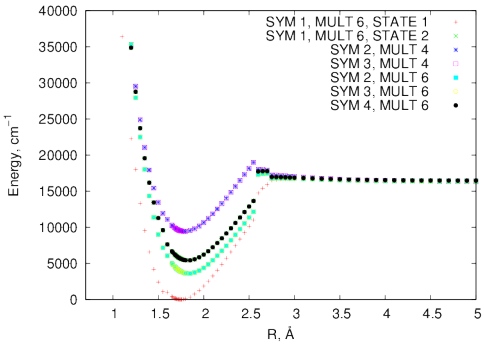

(a) PEC, AFIJ

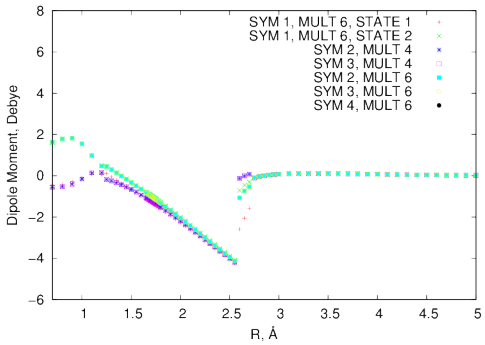

(b) DMZ, AFIJ

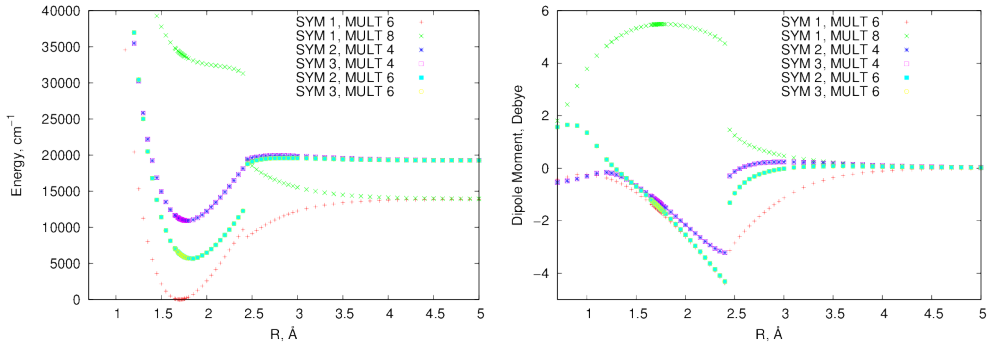

(a) PEC, ABFI

(b) DMZ, ABFI

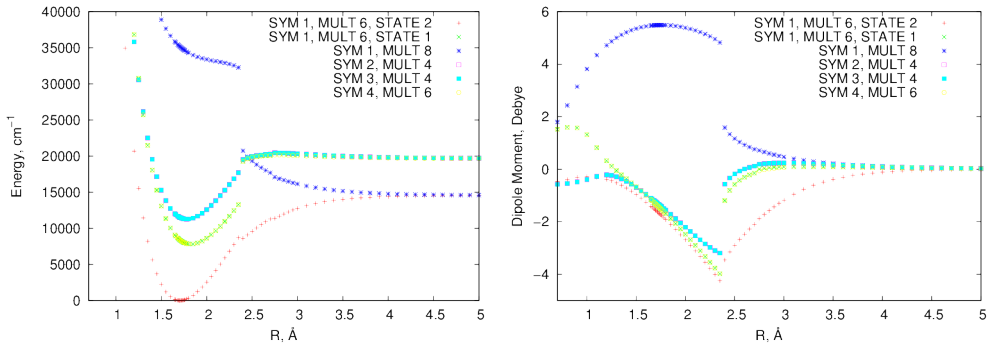

(c) PEC, ABFJ

(d) DMZ, ABFJ

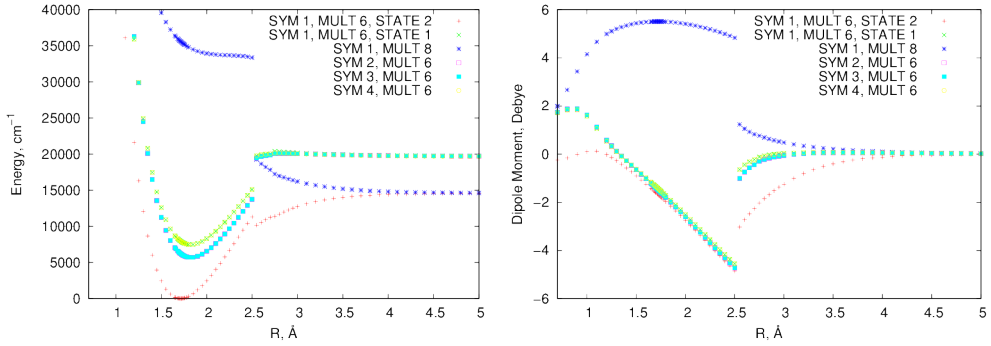

(e) PEC, ABIJ

(f) DMZ, ABIJ

Figure B.19: CASSCF calculations using a cc-pVDZ basis set that combine a single $^6\Sigma^+$ state (A), a single $^8\Sigma^+$ state (B) and two other componenets as defined in table 4.3.

CASSCF results (continued)

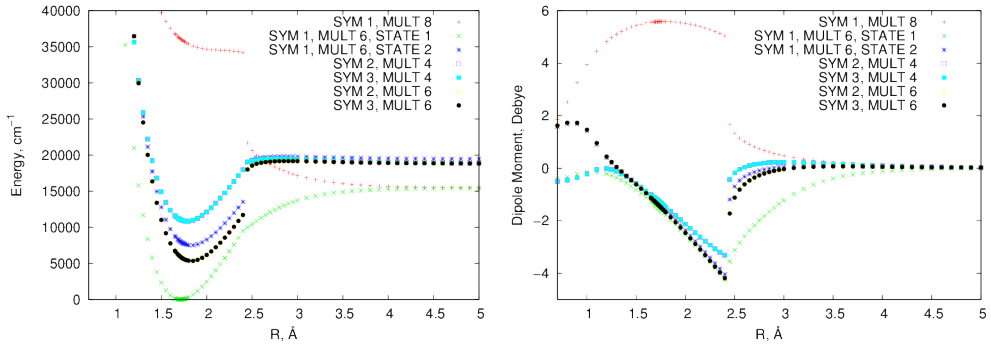

(a) PEC, BDFI

(b) DMZ, BDFI

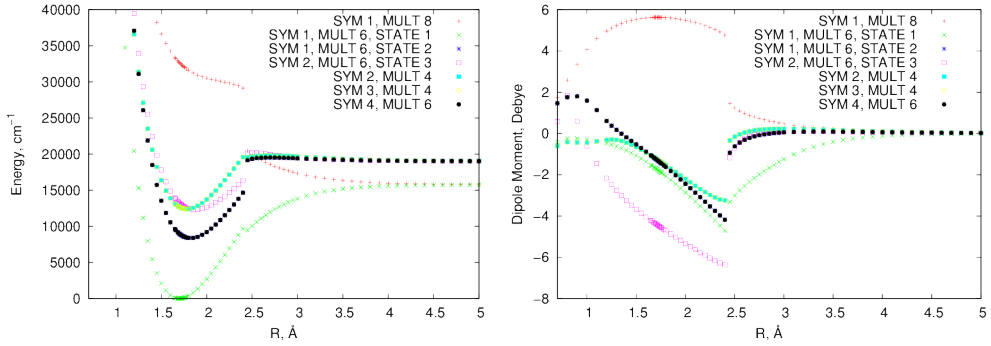

(c) PEC, BDFJ

(d) DMZ, BDFJ

Figure B.20: CASSCF calculations using a cc-pVDZ basis set that combine a single $^8\Sigma^+$ state (B), two $^6\Sigma^+$ state (D), a single $^8\Sigma^+$ state (B) and two other componenets as defined in table 4.3.

CASSCF results (continued)

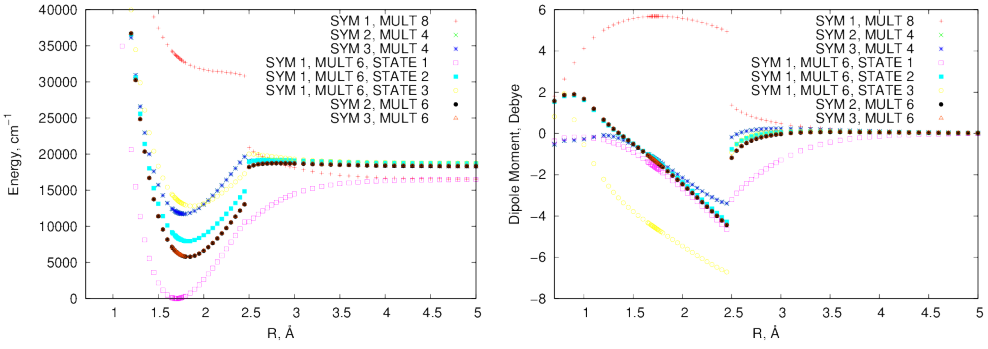

(a) PEC, BFHI

(b) DMZ, BFHI

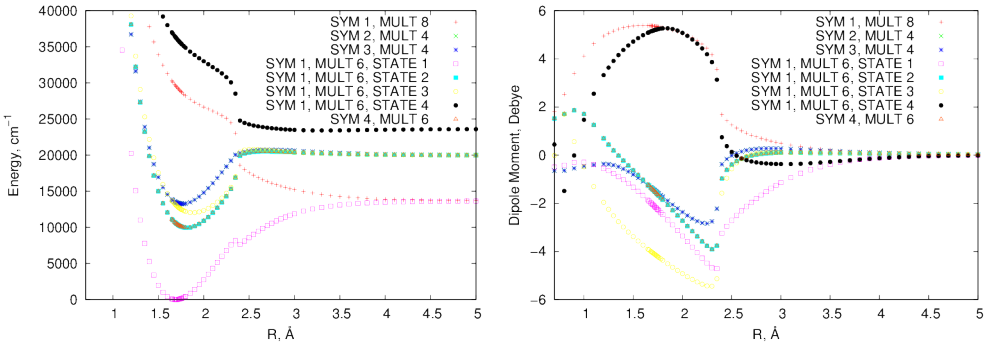

(c) PEC, BFHJ

(d) DMZ, BFHJ

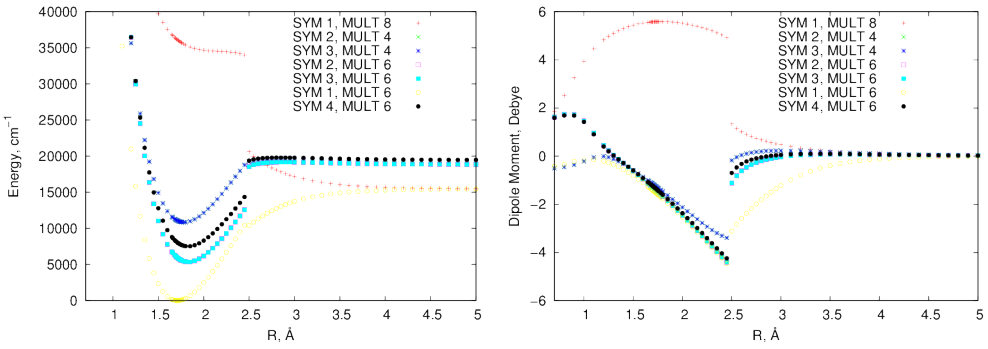

(e) PEC, BFIJ

(f) DMZ, BFIJ

Figure B.21: CASSCF calculations using a cc-pVDZ basis set that combine a single $^8\Sigma^+$ state (B), a single $^4\Pi$ state and two other componenets as defined in table 4.3.

CASSCF results (continued)

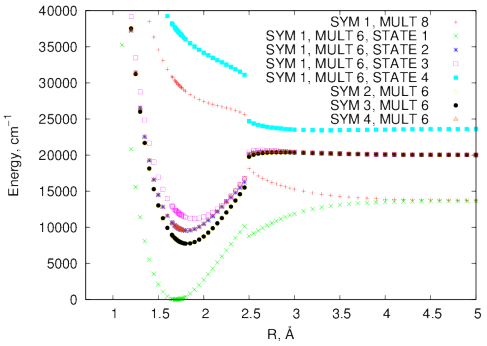

(a) PEC, BHIJ

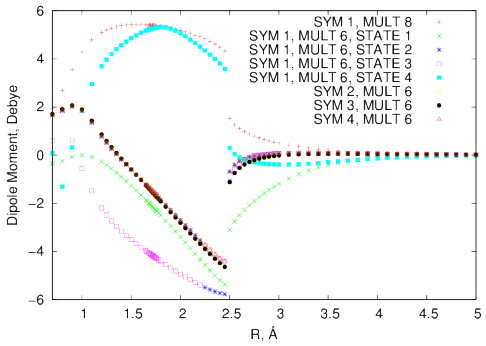

(b) DMZ, BHIJ

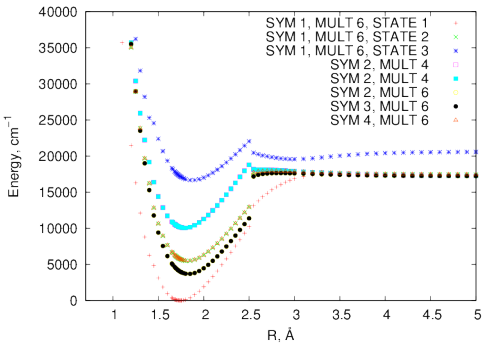

(c) PEC, DFIJ

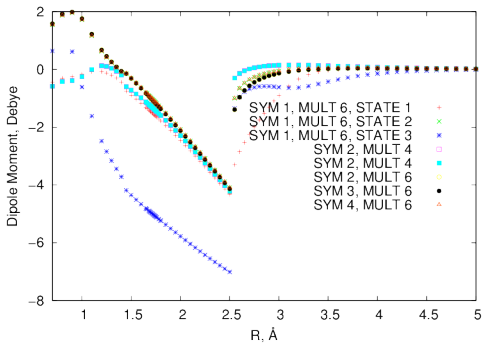

(d) DMZ, DFIJ

Figure B.22: CASSCF calculations using a cc-pVDZ basis set that combine two $^6\Sigma^+$ states (D), a single $^4\Pi$ state (F) and two other componenets as defined in table 4.3.

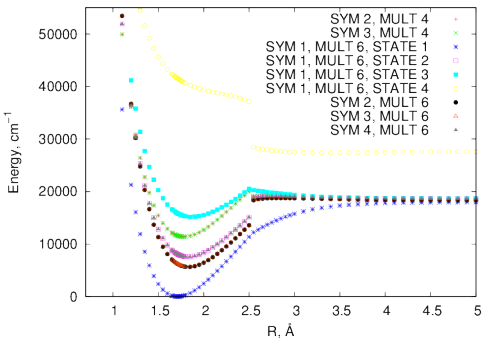

(a) PEC, FHIJ

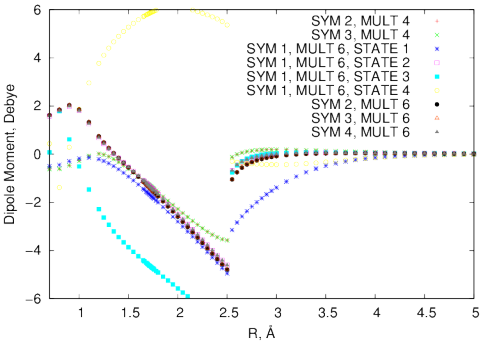

(b) DMZ, FHIJ

Figure B.23: CASSCF calculations using a cc-pVDZ basis set that combine a single $^4\Pi$ state (F), three $^6\Sigma^+$ states (H), and two other componenets as defined in table 4.3.

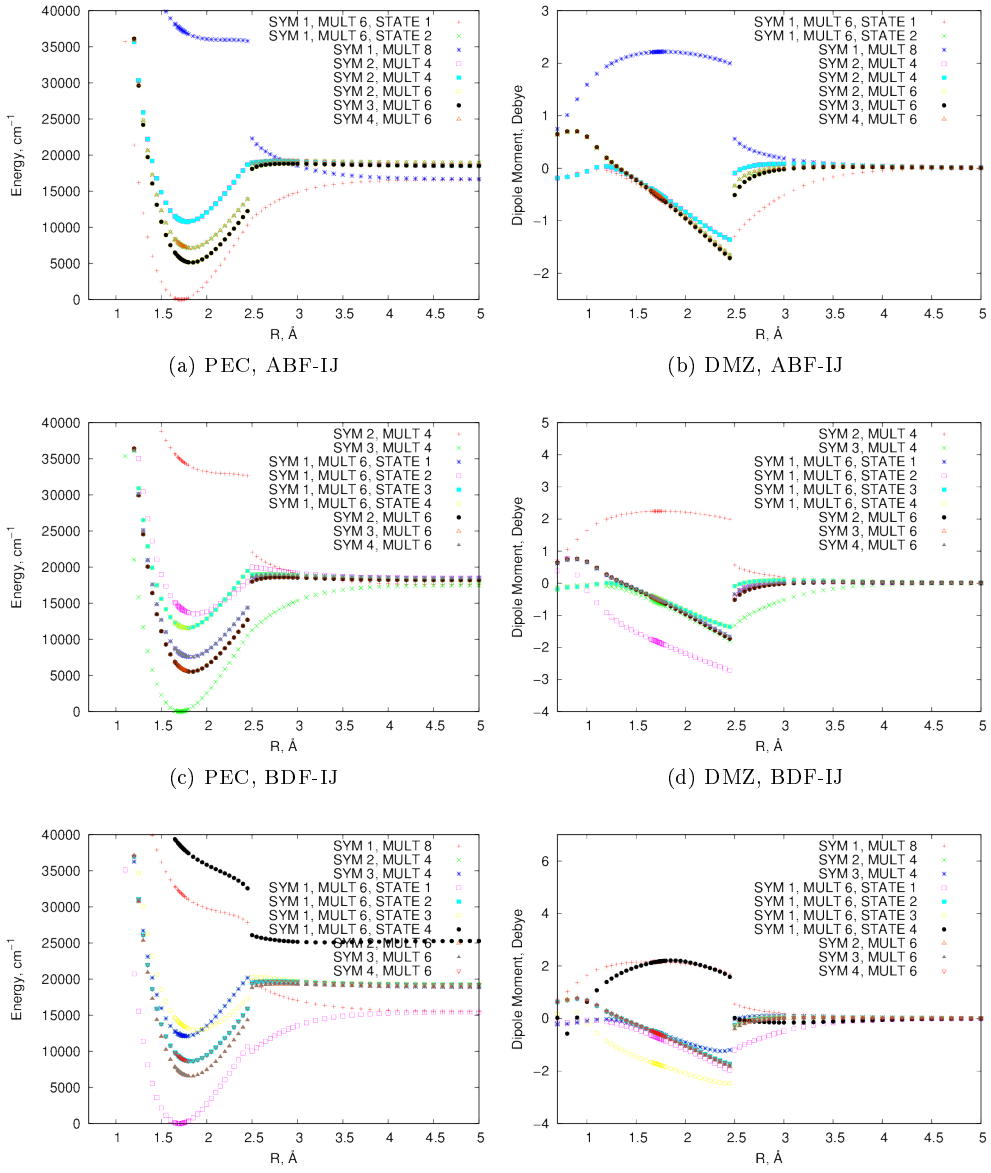

(a) PEC, ABF-IJ

(b) DMZ, ABF-IJ

(c) PEC, BDF-IJ

(d) DMZ, BDF-IJ

(e) PEC, BFH-IJ

(f) DMZ, BFH-IJ

Figure B.24: CASSCF calculations using a cc-pVDZ basis set that combine five components as defined in table 4.3.

Appendix C

MnH CASSCF Testing Results

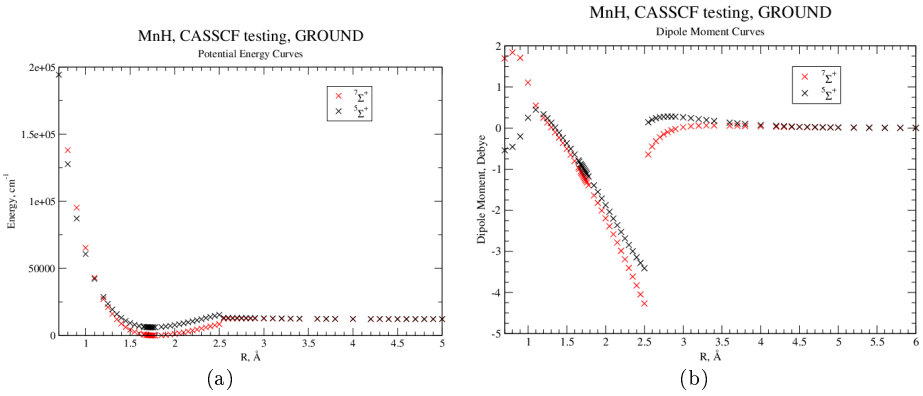

(a) (b)

Figure C.1: CASSCF calculations using a cc-pVQZ basis set that combine a single $^7\Sigma^+$ and a single $^5\Sigma^+$ state. See section 7.1 for guidance.

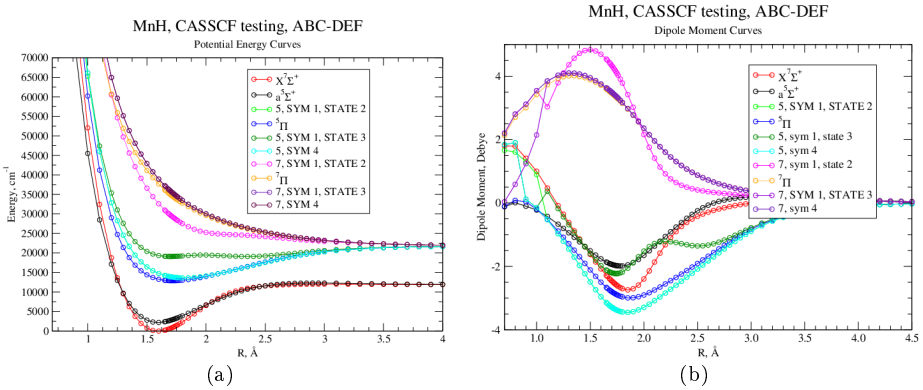

(a) (b)

Figure C.2: CASSCF calculations using a cc-pVQZ basis set that combine a single $^7\Sigma^+$ state, a single $^5\Sigma^+$ state and all six other components (i.e. "A", "B", "C", "D", "E" and "F") as defined in table 7.1.

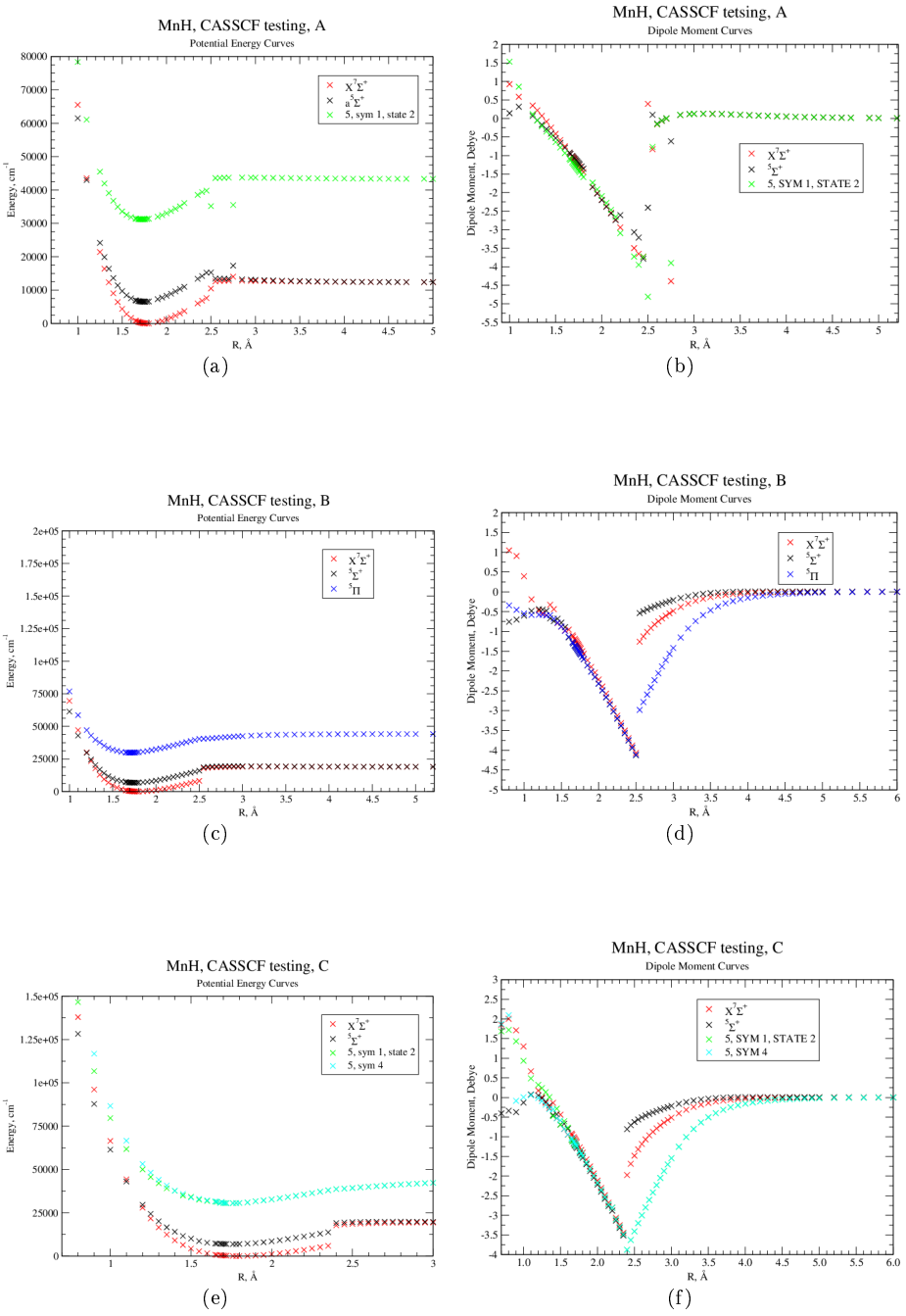

Figure C.3: CASSCF calculations using a cc-pVQZ basis set that combine a single $^7\Sigma^+$ and $^5\Sigma^+$ state with a single other component as defined in table 7.1.

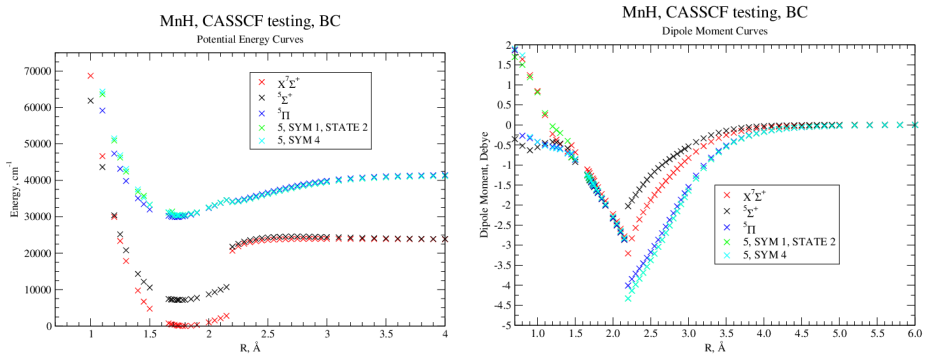

(a) (b)

Figure C.4: CASSCF calculations using a cc-pVQZ basis set that combine a single $^7\Sigma^+$, a single $^5\Sigma^+$ state, a single $^5\Pi$ state (i.e. "B") with a single other component as defined in table 7.1.

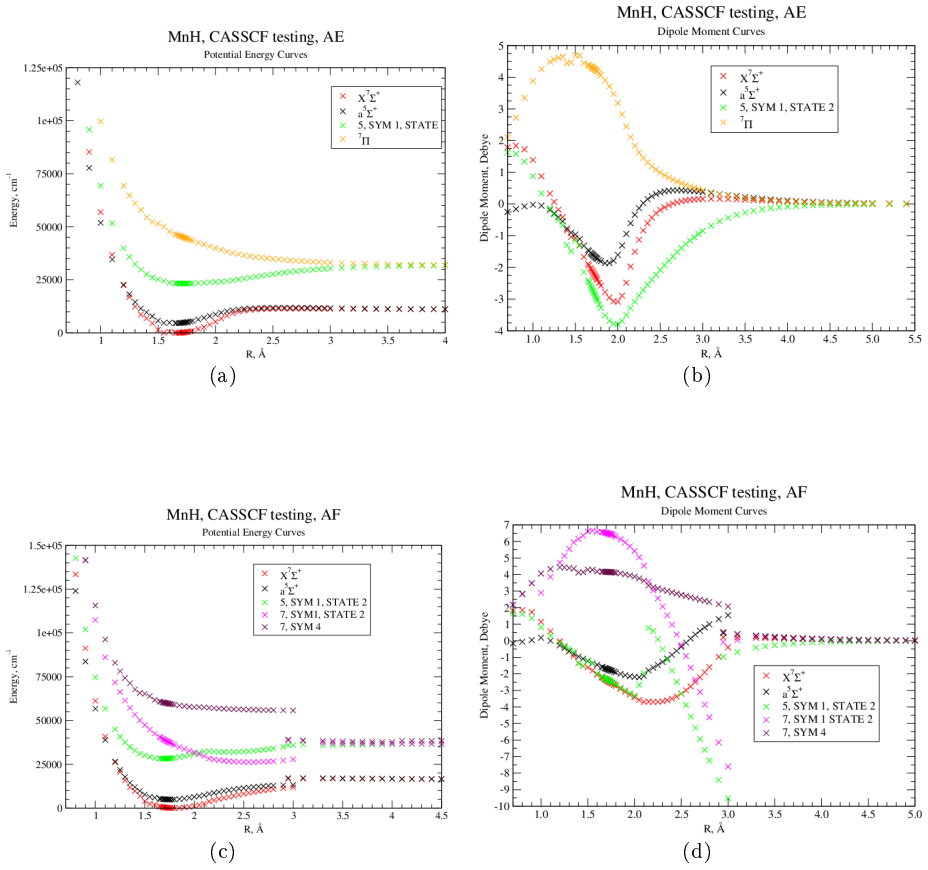

(a) (b)

(c) (d)

Figure C.5: CASSCF calculations using a cc-pVQZ basis set that combine a single $^7\Sigma^+$, two $^5\Sigma^+$ states (i.e. "A") with a single other component as defined in table 7.1.

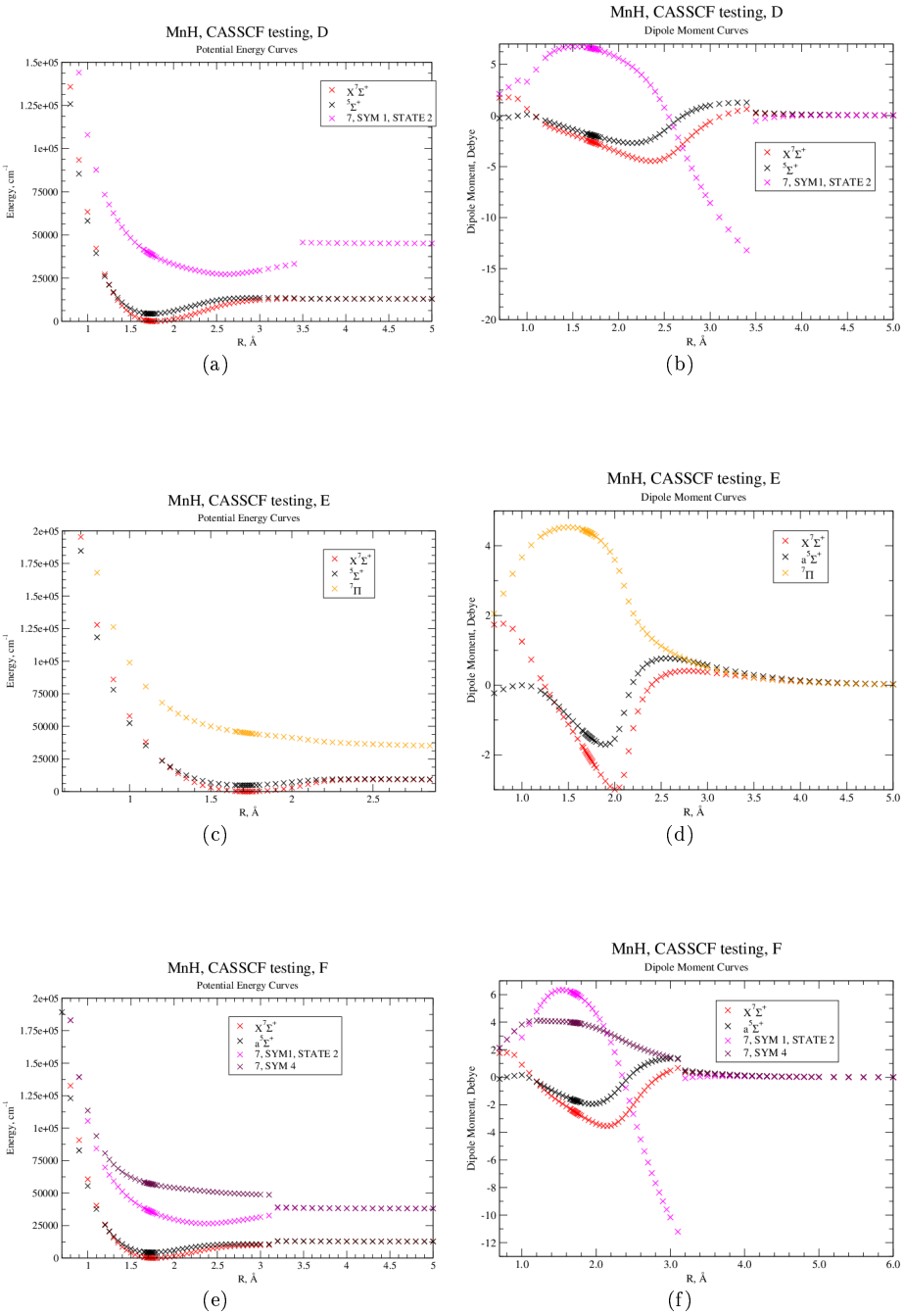

Figure C.6: CASSCF calculations using a cc-pVQZ basis set that combine a single $^7\Sigma^+$ and $^5\Sigma^+$ state with a single other component as defined in table 7.1.

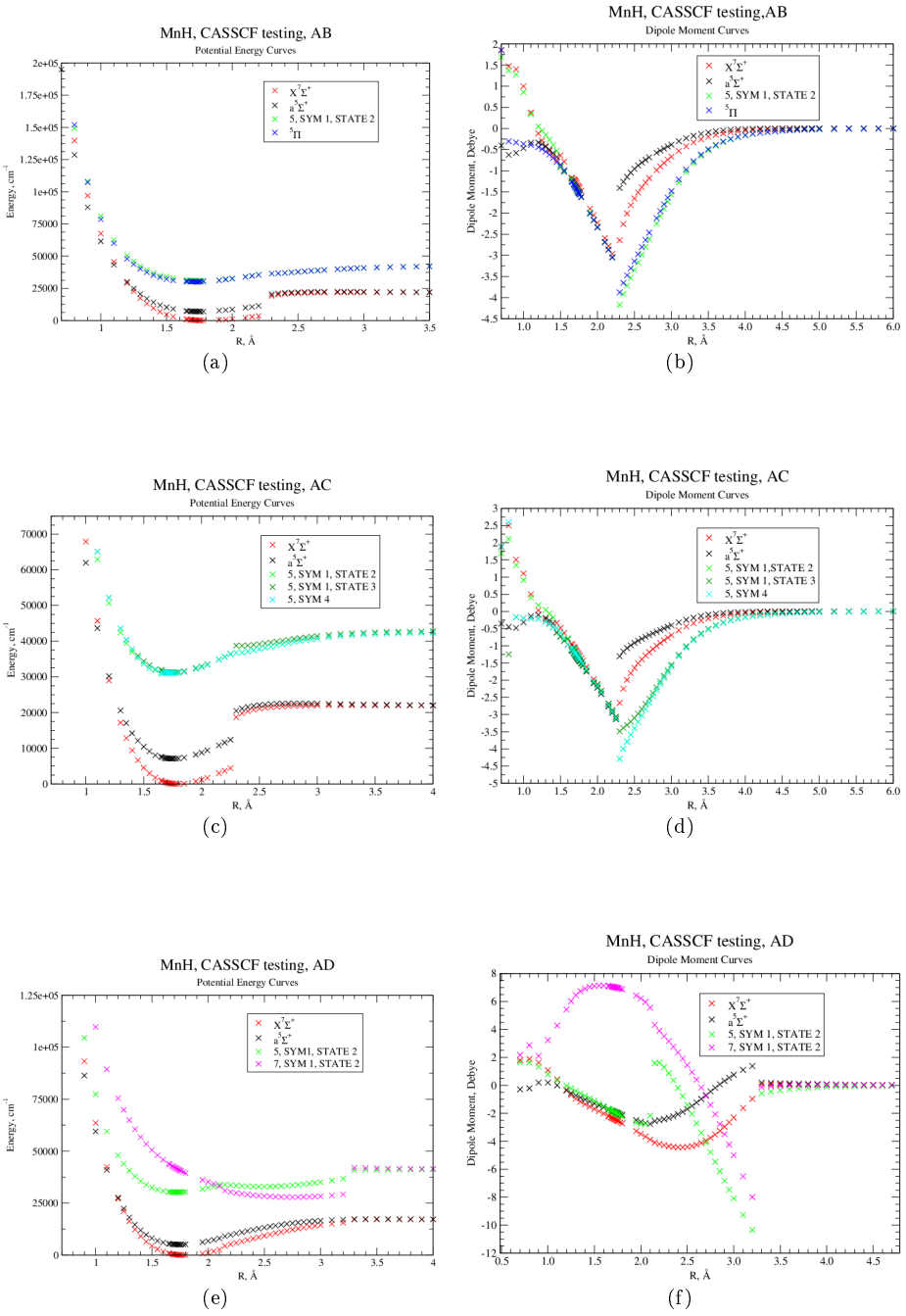

Figure C.7: CASSCF calculations using a cc-pVQZ basis set that combine a single $^7\Sigma^+$, two $^5\Sigma^+$ states (i.e. "A") with a single other component as defined in table 7.1.

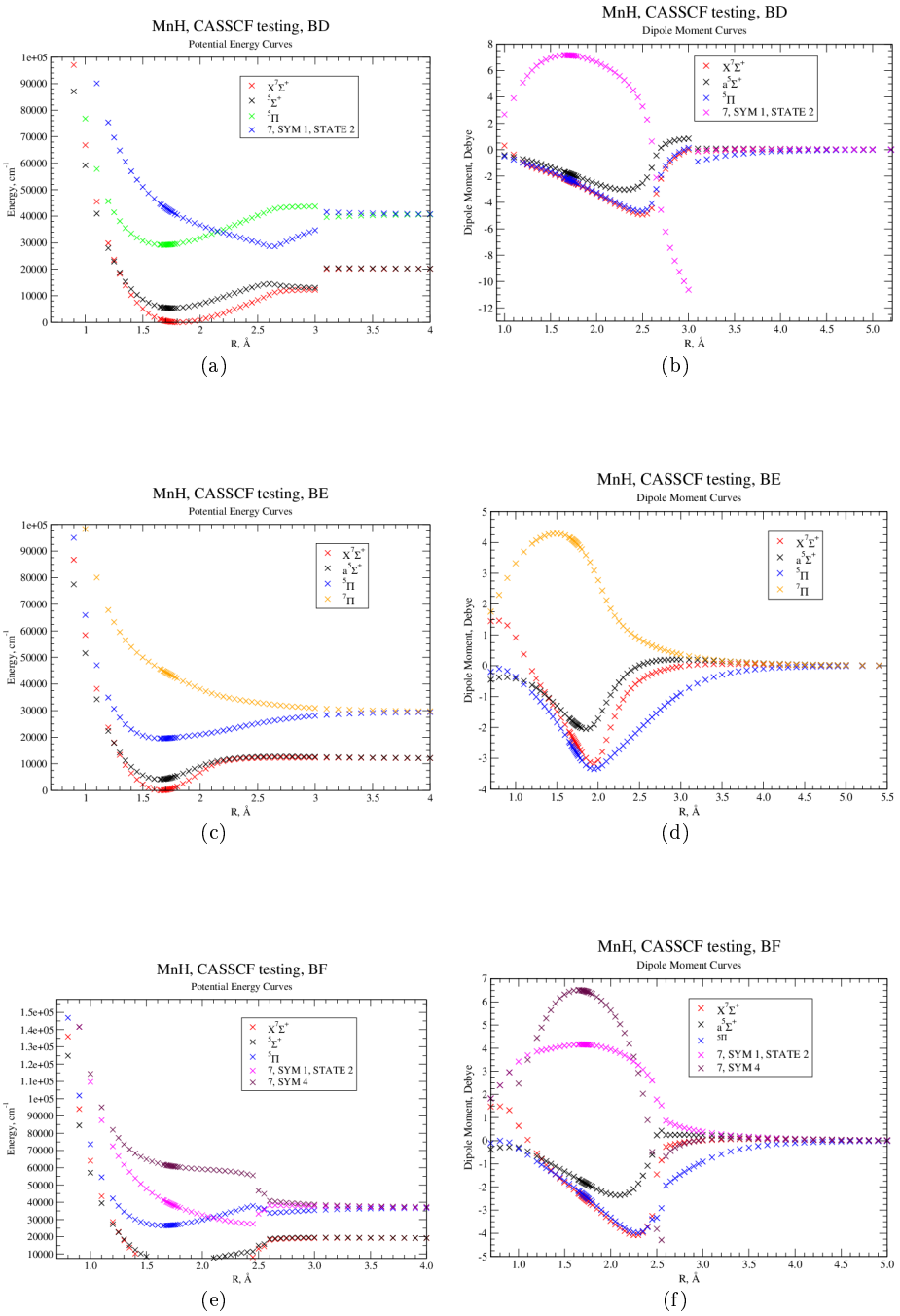

Figure C.8: CASSCF calculations using a cc-pVQZ basis set that combine a single $^7\Sigma^+$, a single $^5\Sigma^+$ state, a single $^5\Pi$ state (i.e. "B") with a single other component as defined in table 7.1.

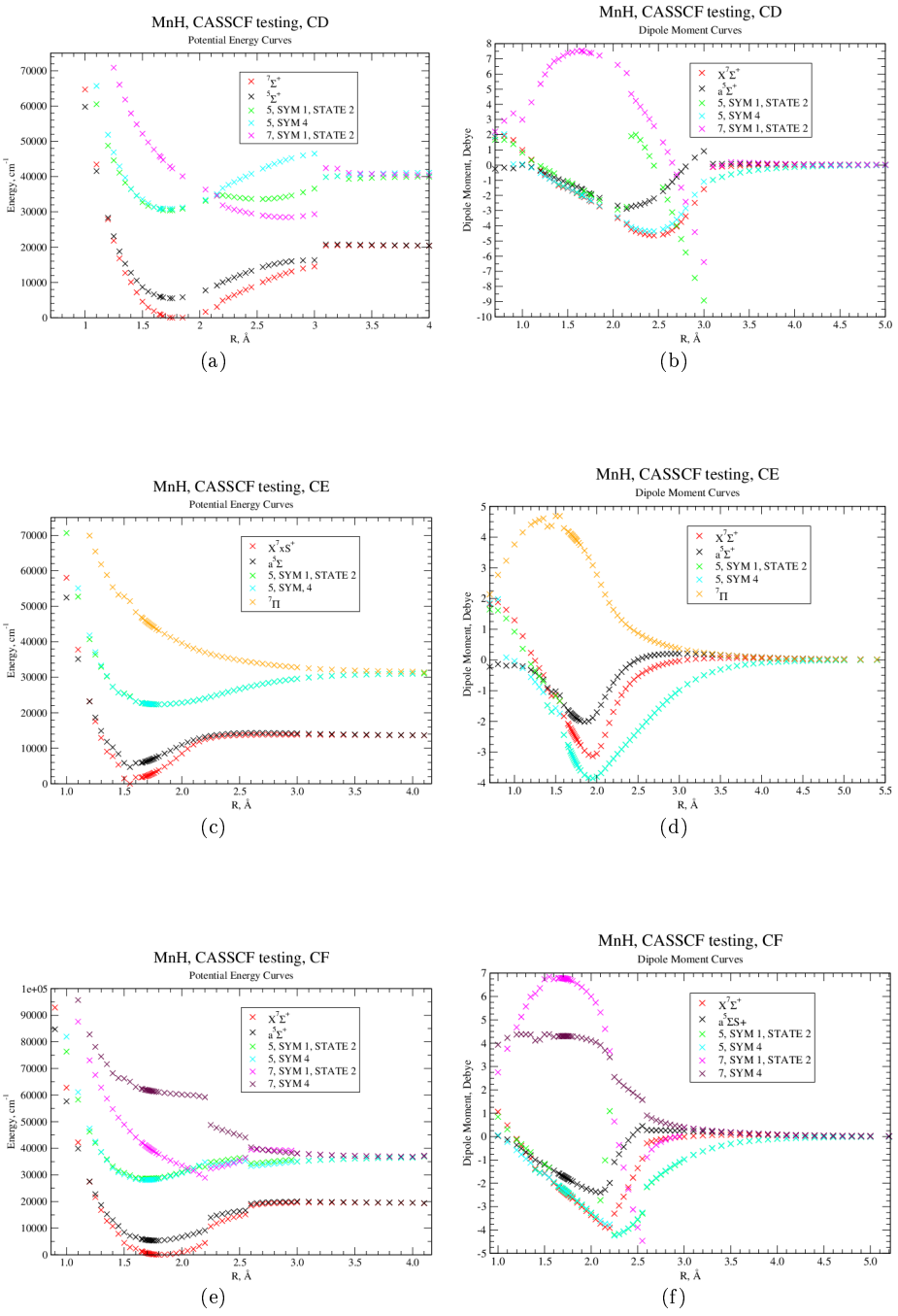

Figure C.9: CASSCF calculations using a cc-pVQZ basis set that combine a single $^7\Sigma^+$ state, two symmetry 1 components of quintet multiplicity, a single symmetry 4 component of quintet multiplicity (i.e. "C") and a single other component as defined in table 7.1.

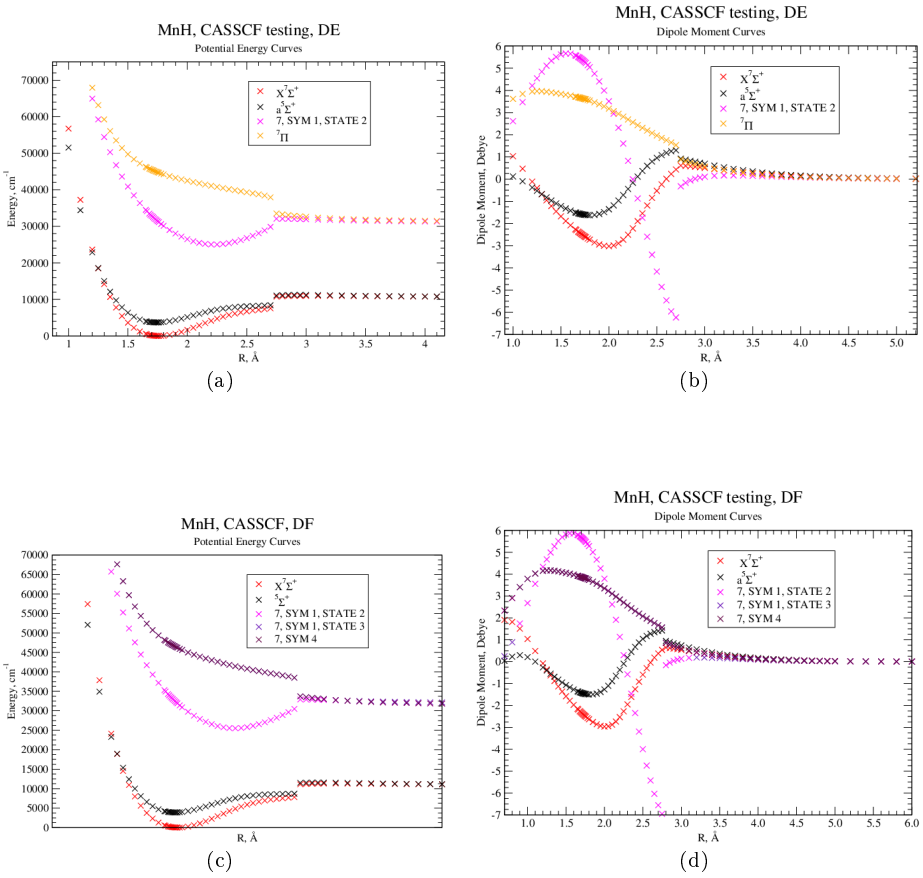

Figure C.10: CASSCF calculations using a cc-pVQZ basis set that combine a two $^7\Sigma^+$ states (i.e. "D), a single $^5\Sigma^+$ state and a single other component as defined in table 7.1.

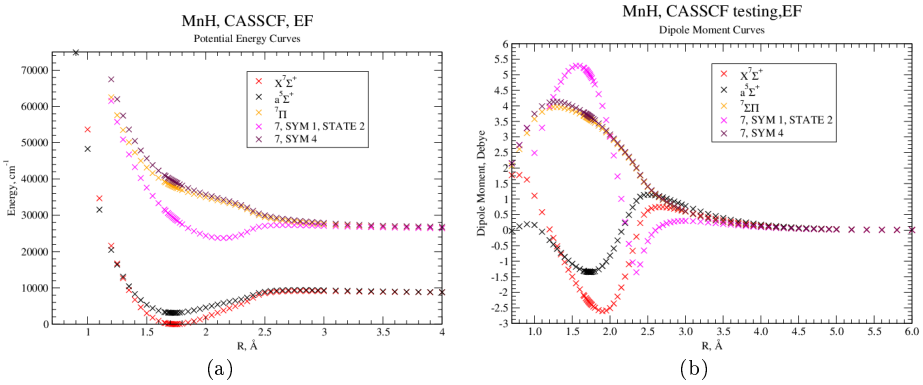

Figure C.11: CASSCF calculations using a cc-pVQZ basis set that combine a single $^5\Sigma^+$ state, two symmetry 1 components of septuplet multiplicity, a single symmetry 4 component of septuplet multiplicity (i.e. "F") and a $^7\Pi$ (i.e. "E") as defined in table 7.1.

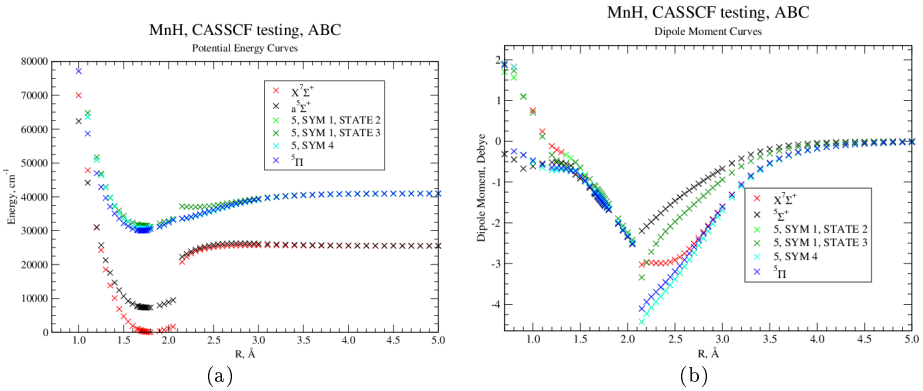

Figure C.12: CASSCF calculations using a cc-pVQZ basis set that combine a single $^7\Sigma^+$ state, three $^5\Sigma^+$ states, a $^5\Pi$ state and a $^5\Delta$ state as defined in table 7.1, two of which are "A" and "B".

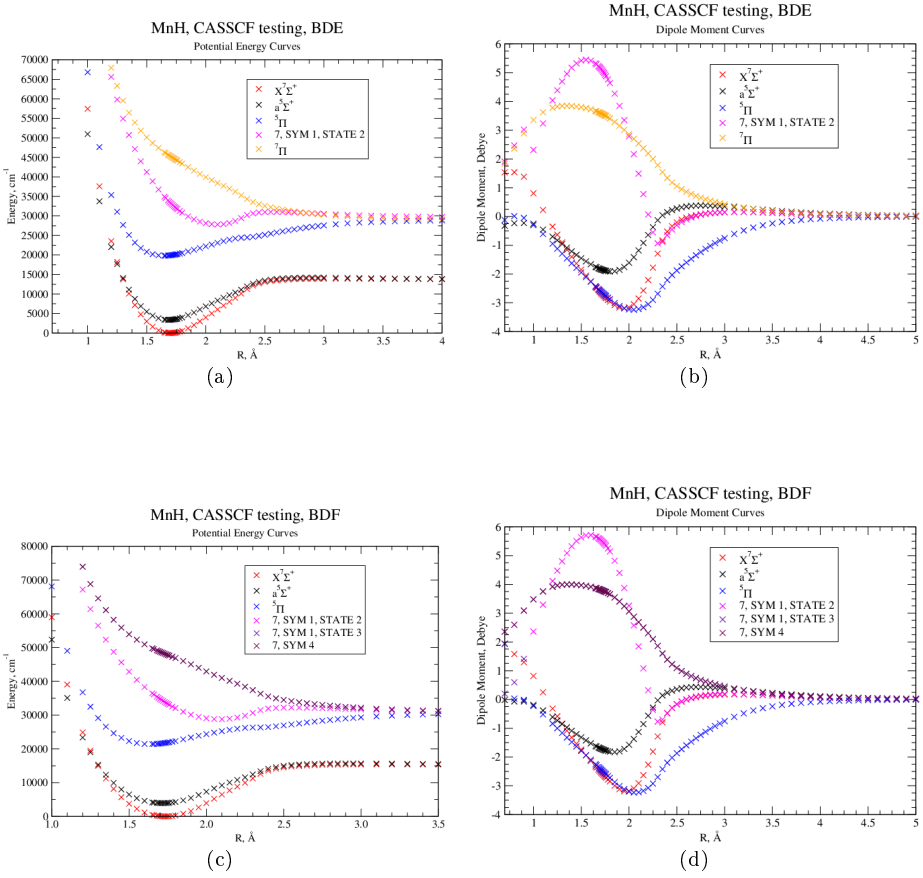

Figure C.13: CASSCF calculations using a cc-pVQZ basis set that combine a single $^7\Sigma^+$ state, a single $^5\Sigma^+$ state and three other components defined in table 7.1, two of which are "B" and "D".

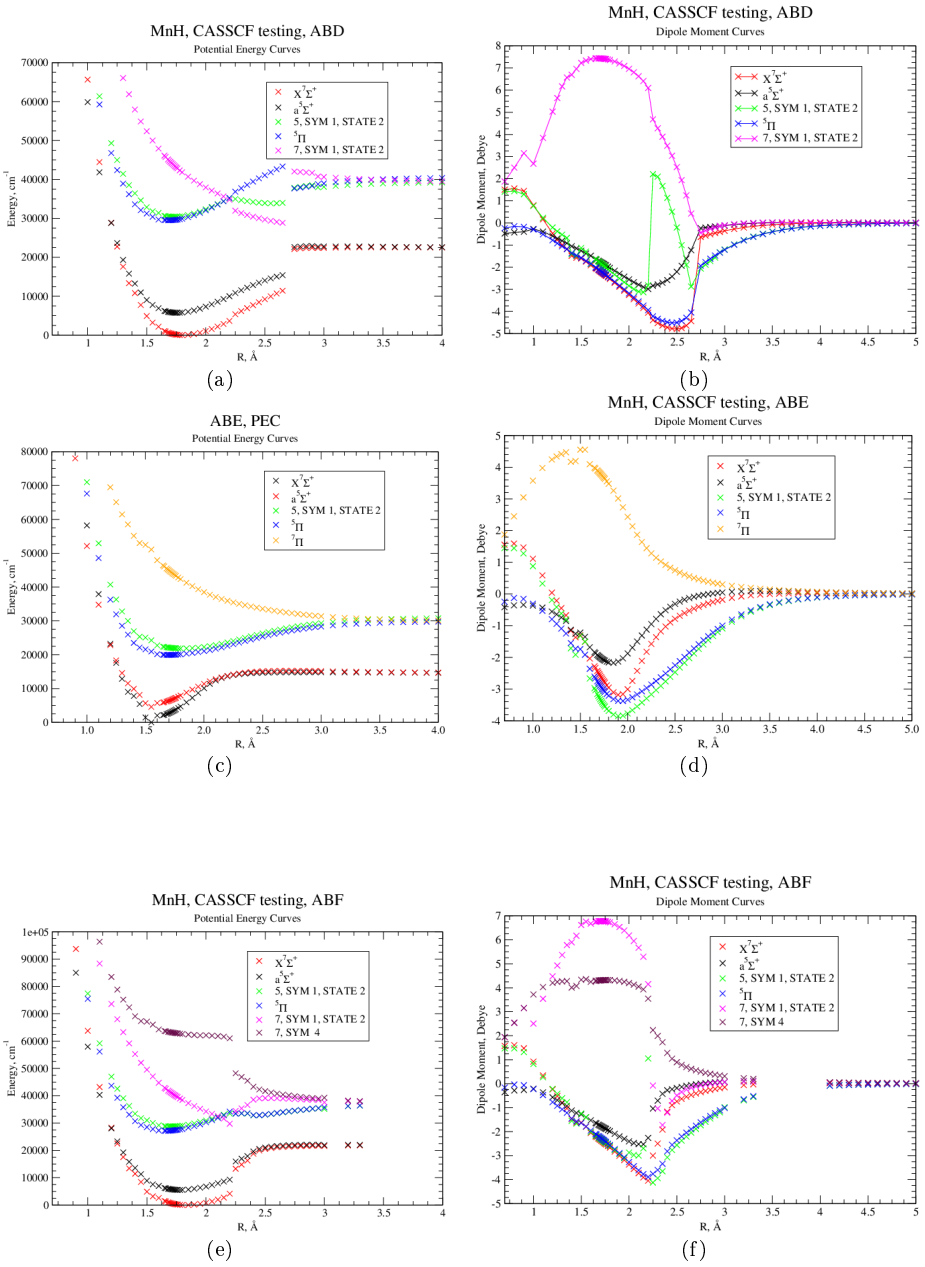

Figure C.14: CASSCF calculations using a cc-pVQZ basis set that combine a single $^7\Sigma^+$ state, two $^5\Sigma^+$ states ("A"), a $^5\Pi$ ("B") and one other component as defined in table 7.1, two of which are "A" and "B".

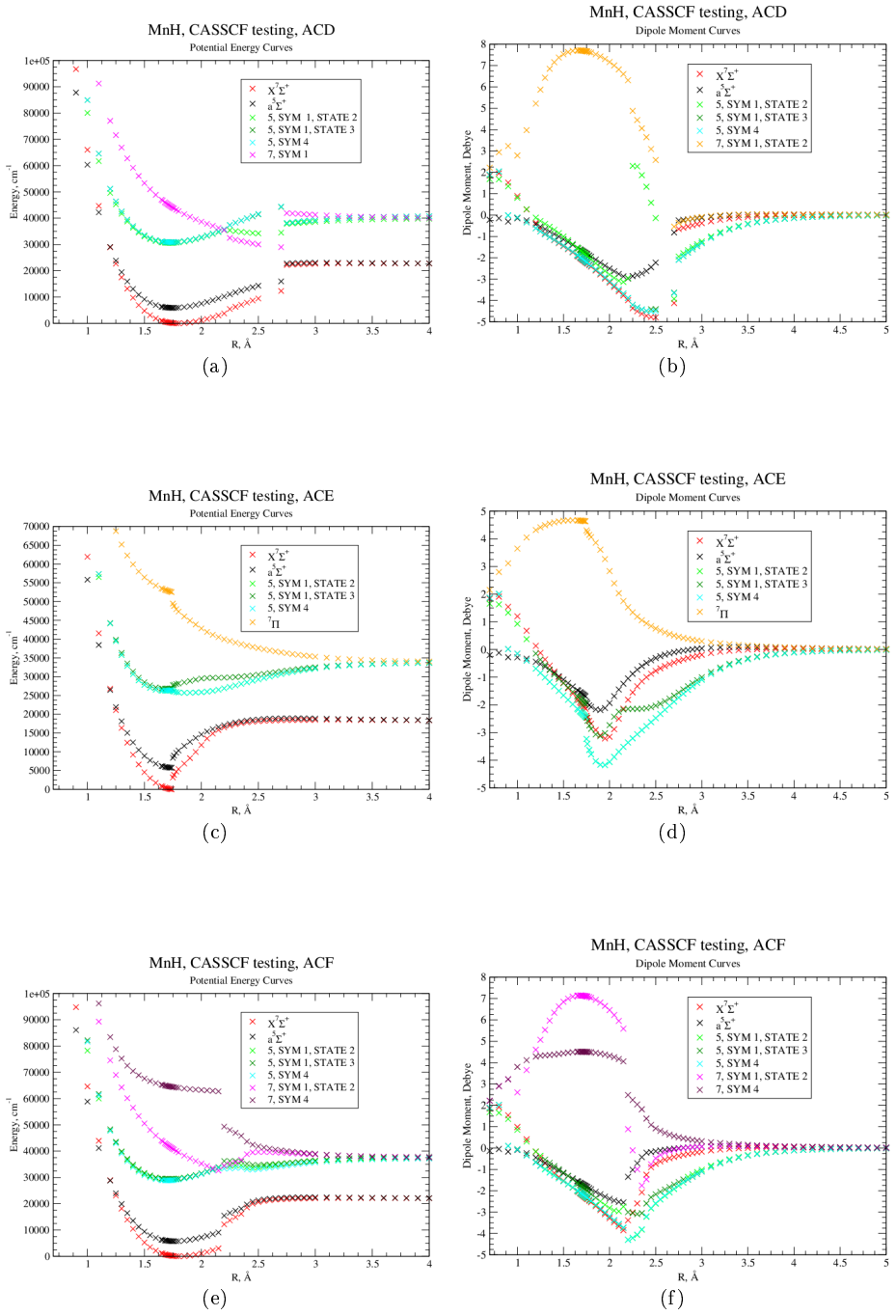

Figure C.15: CASSCF calculations using a cc-pVQZ basis set that combine a single $^7\Sigma^+$ state, a single $^5\Sigma^+$ state and three other components defined in table 7.1, two of which are "A" and "C".

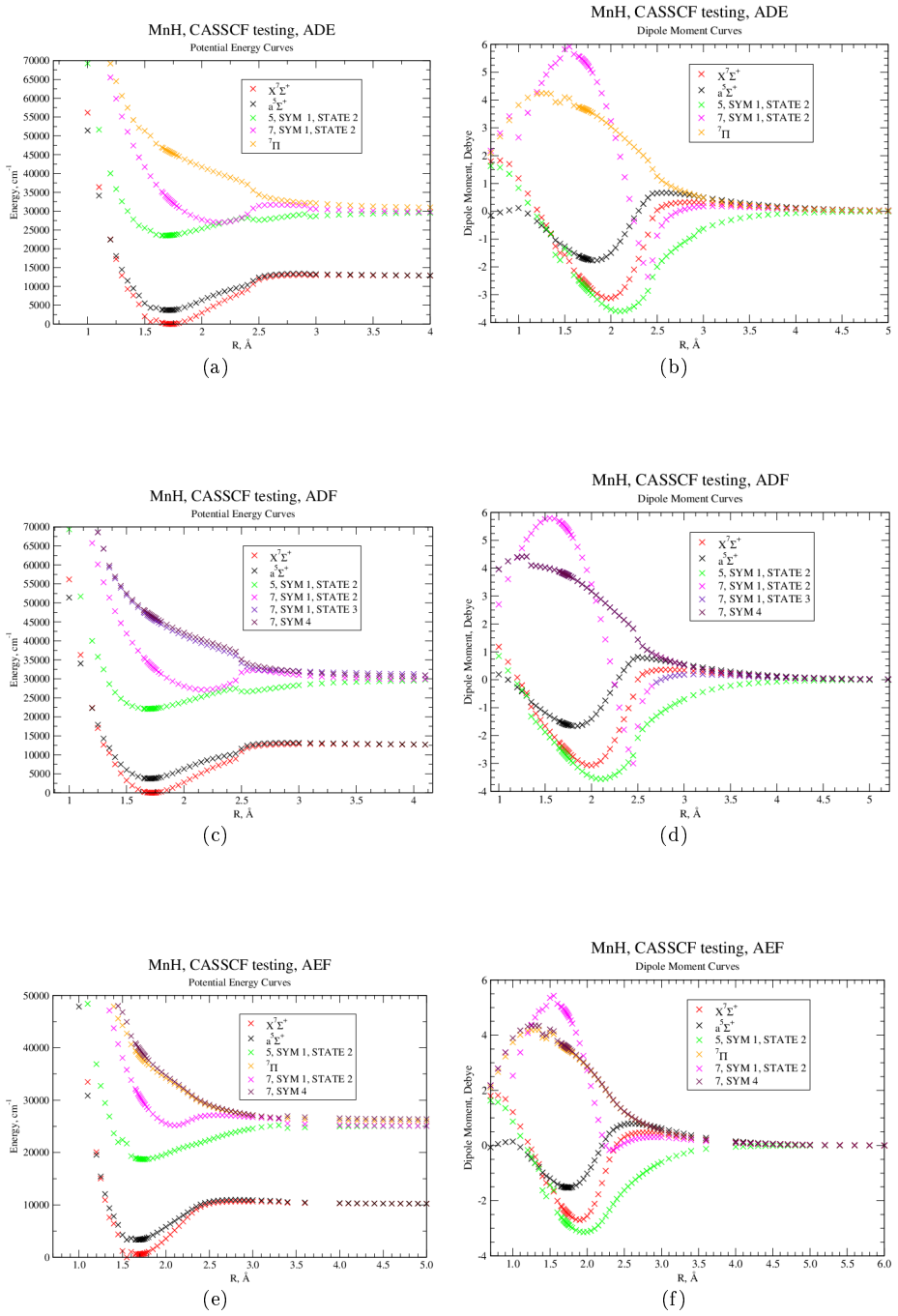

Figure C.16: CASSCF calculations using a cc-pVQZ basis set that combine a single $^7\Sigma^+$ state, a single $^5\Sigma^+$ state and three other components defined in table 7.1, one of which is "A" and the other two selected from "D", "E" and "F".

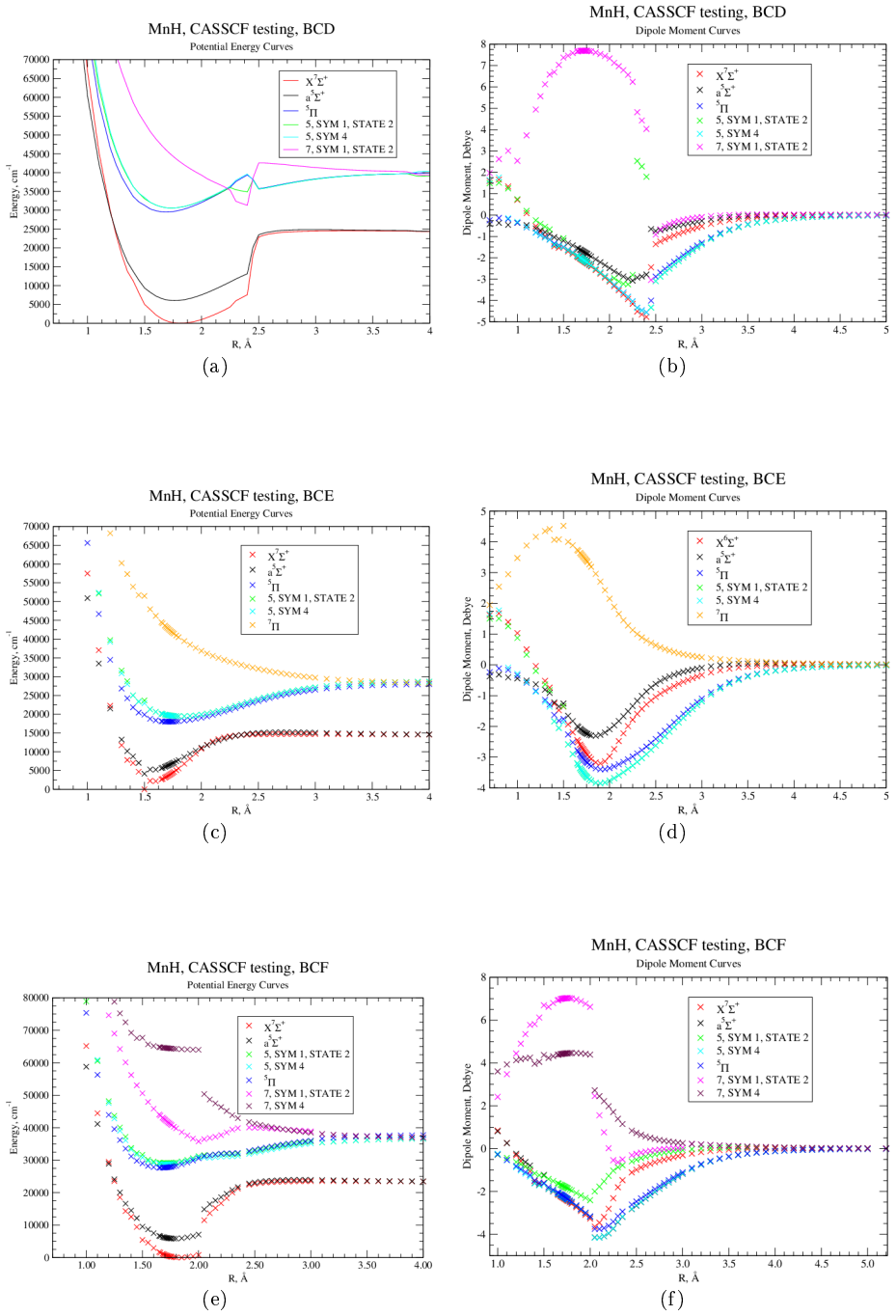

Figure C.17: CASSCF calculations using a cc-pVQZ basis set that combine a single $^7\Sigma^+$ state, a single $^5\Sigma^+$ state and three other components defined in table 7.1, two of which are "B" and "C".

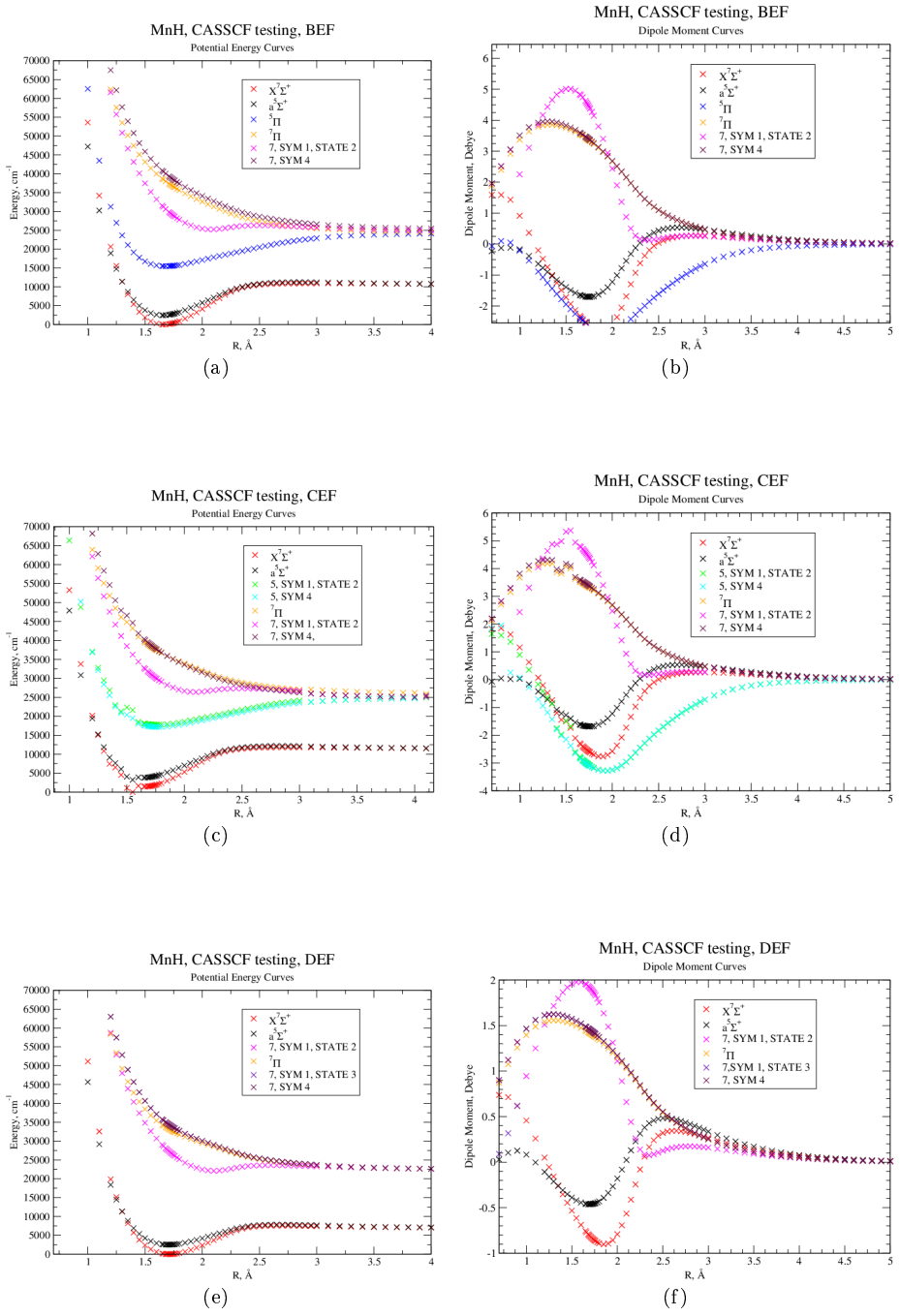

Figure C.18: CASSCF calculations using a cc-pVQZ basis set that combine a single $^7\Sigma^+$ state, a single $^5\Sigma^+$ state and three other components defined in table 7.1, two of which are "E" and "F".

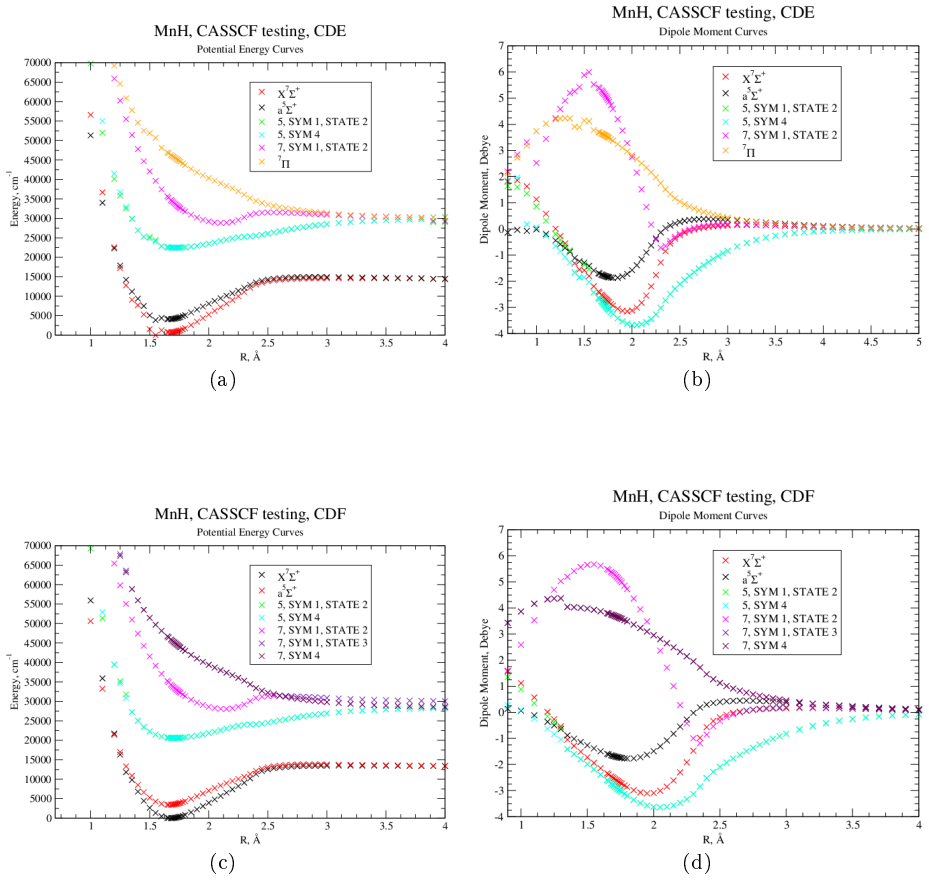

Figure C.19: CASSCF calculations using a cc-pVQZ basis set that combine a single $^7\Sigma^+$ state, a single $^5\Sigma^+$ state and three other components defined in table 7.1, two of which are "C" and "D".

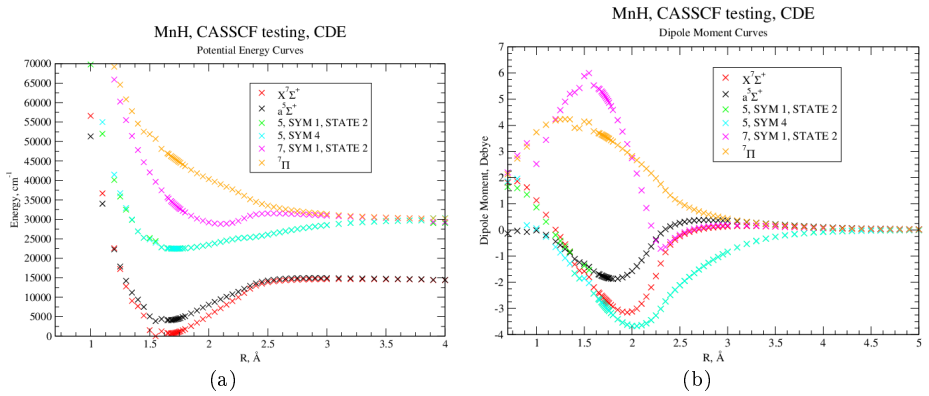

Figure C.20: CASSCF calculations using a cc-pVQZ basis set that combine a single $^7\Sigma^+$ state, a single $^5\Sigma^+$ state and the three other components of "C", "D" and "E' as defined in table 7.1.

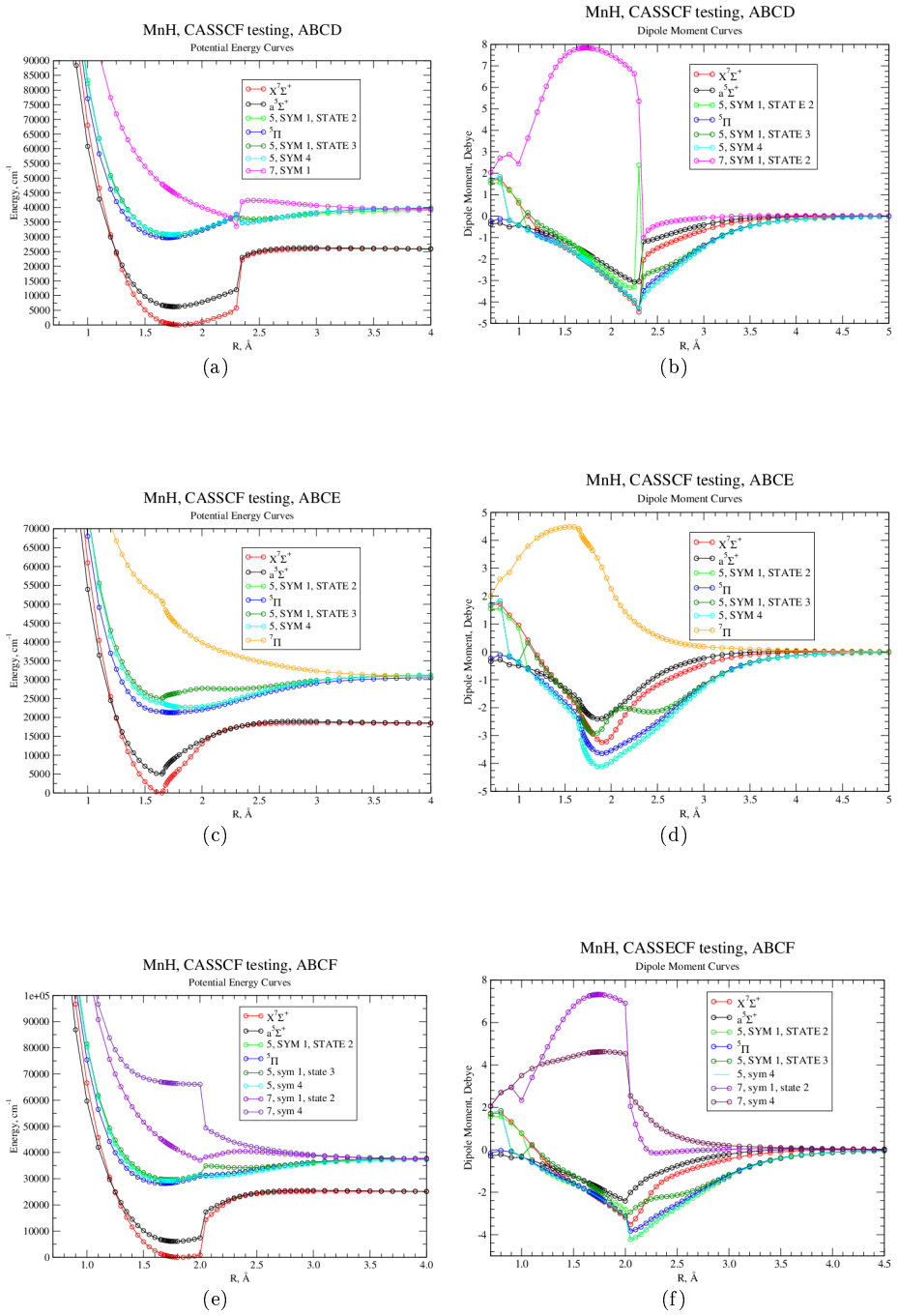

Figure C.21: CASSCF calculations using a cc-pVQZ basis set that combine a single $^7\Sigma^+$ state, a single $^5\Sigma^+$ state and four other components defined in table 7.1, three of which are "A", "B" and "C".

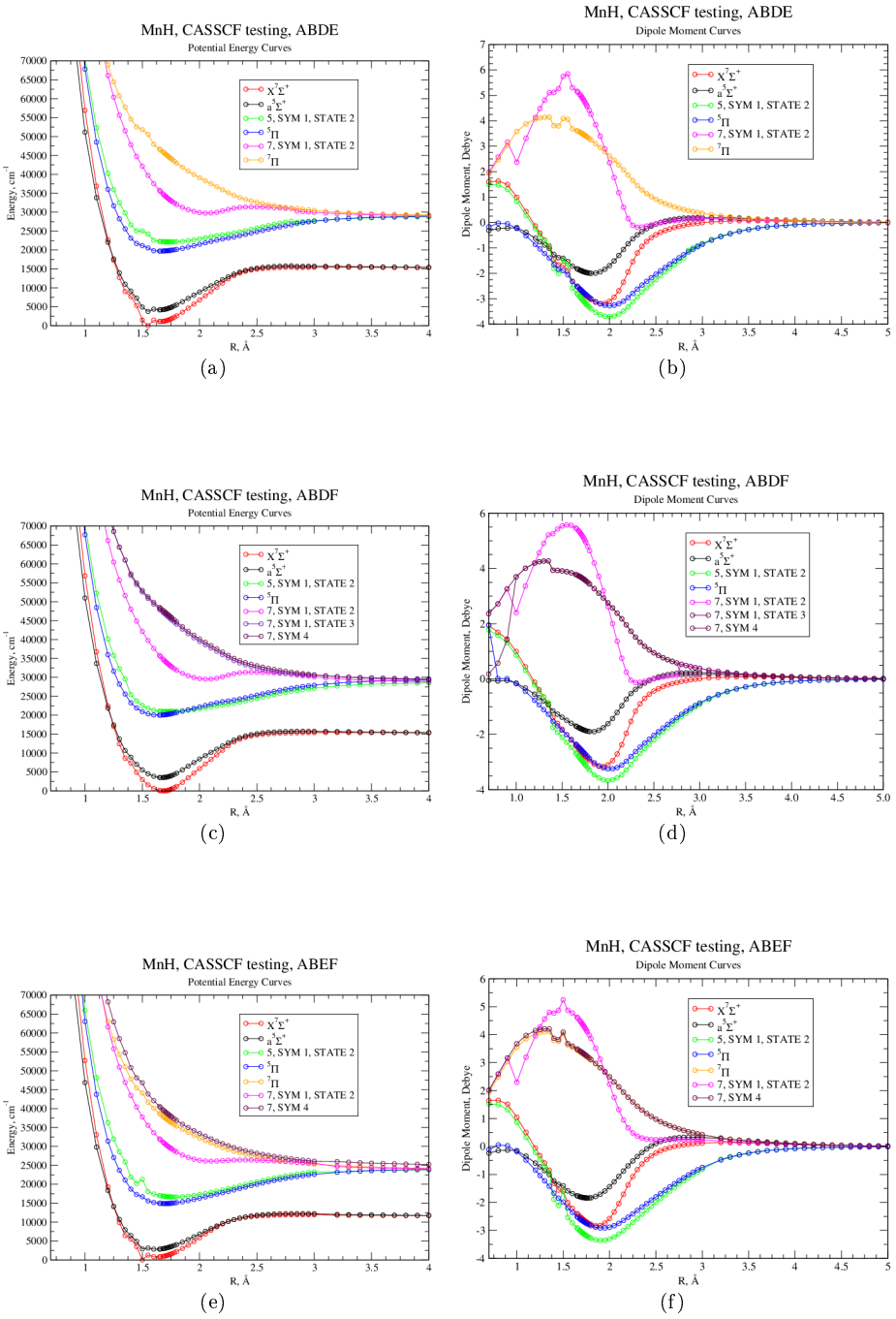

Figure C.22: CASSCF calculations using a cc-pVQZ basis set that combine a single $^7\Sigma^+$ state, a single $^5\Sigma^+$ state and four other components defined in table 7.1, two of which are "A" and "B" and the other two selected from "D", "E" and "F".

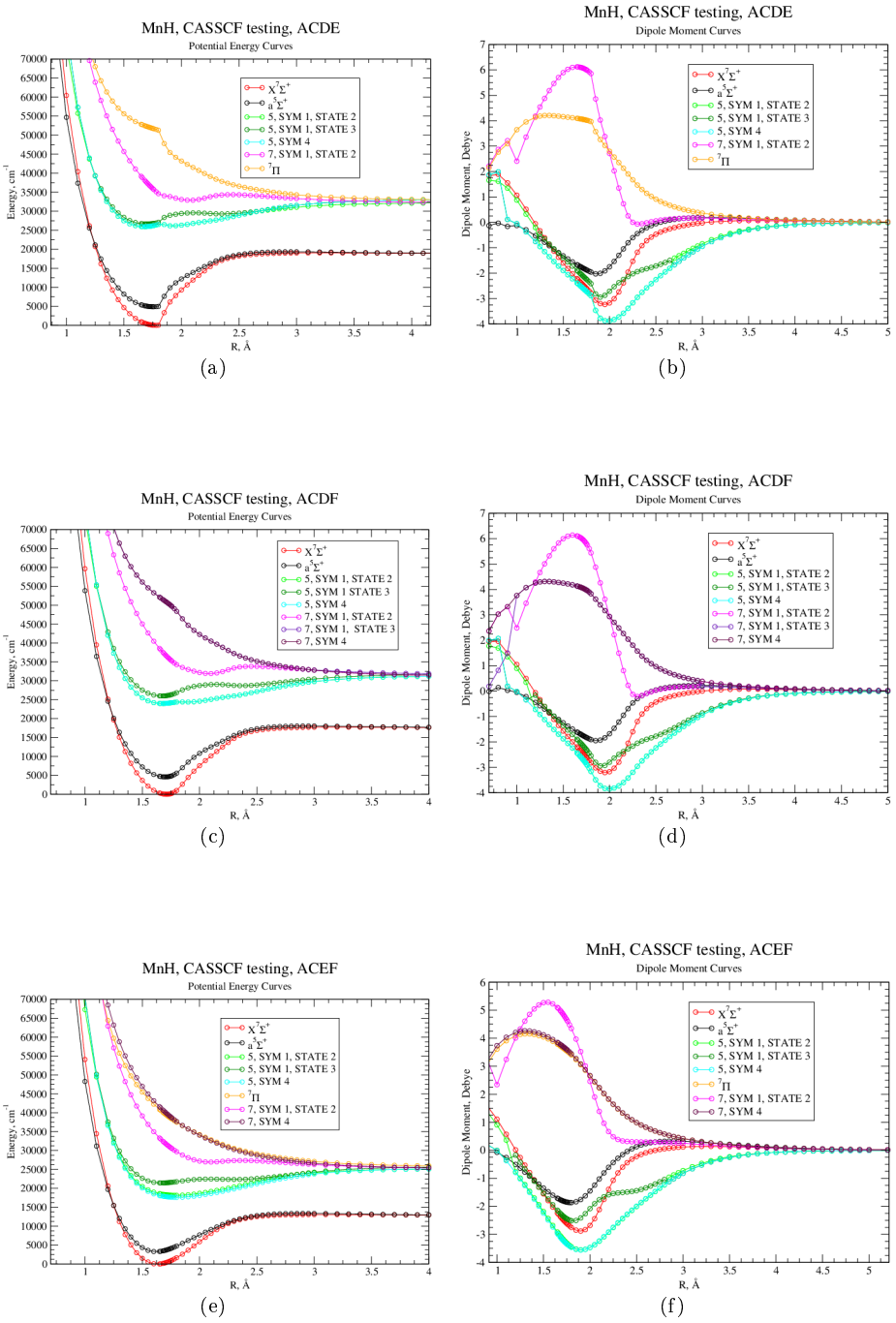

Figure C.23: CASSCF calculations using a cc-pVQZ basis set that combine a single $^7\Sigma^+$ state, a single $^5\Sigma^+$ state and four other components defined in table 7.1, two of which are "A" and "C" and the other two selected from "D", "E" and "F".

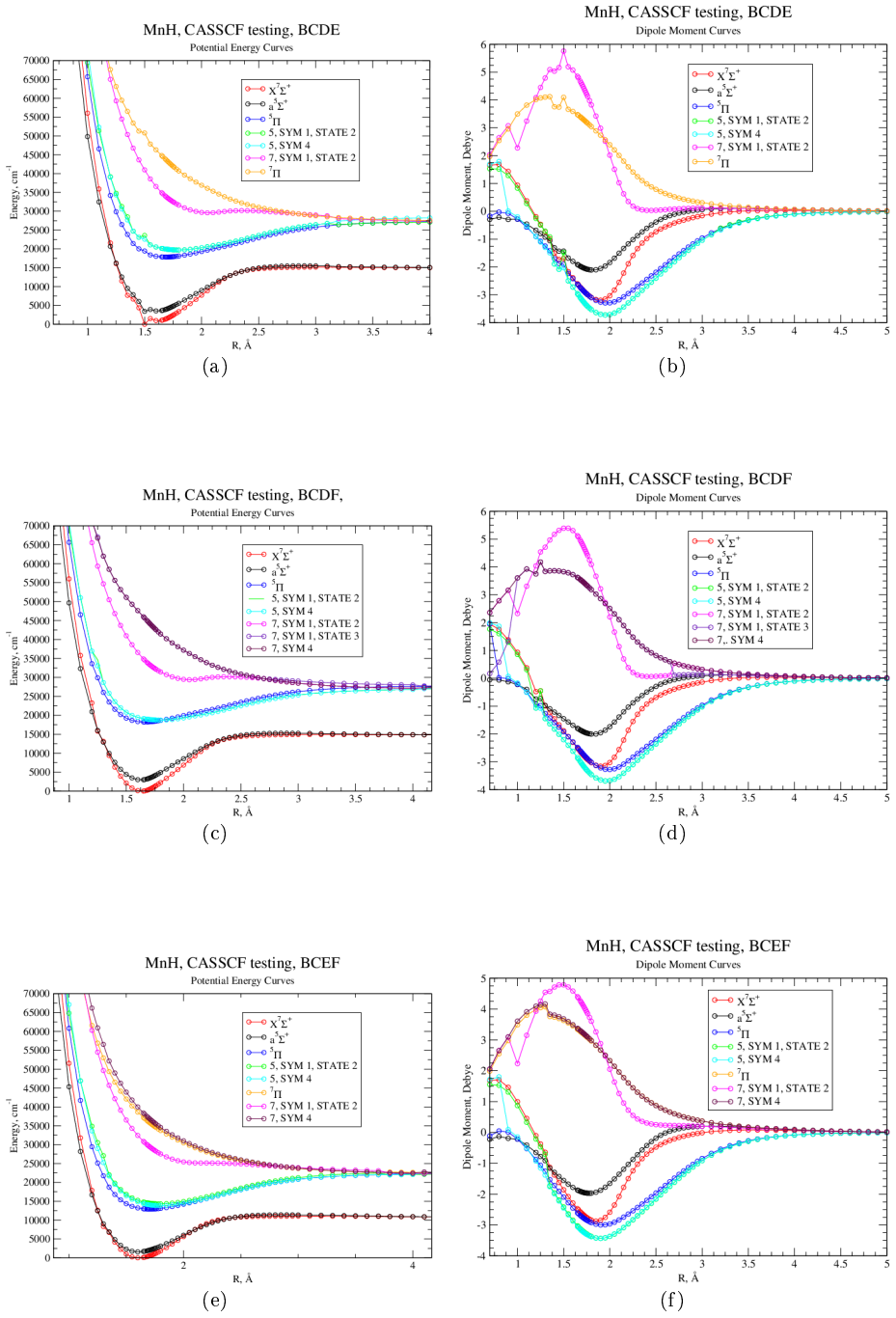

Figure C.24: CASSCF calculations using a cc-pVQZ basis set that combine a single $^7\Sigma^+$ state, a single $^5\Sigma^+$ state and four other components defined in table 7.1, two of which are "B" and "C" and the other two selected from "D", "E" and "F".

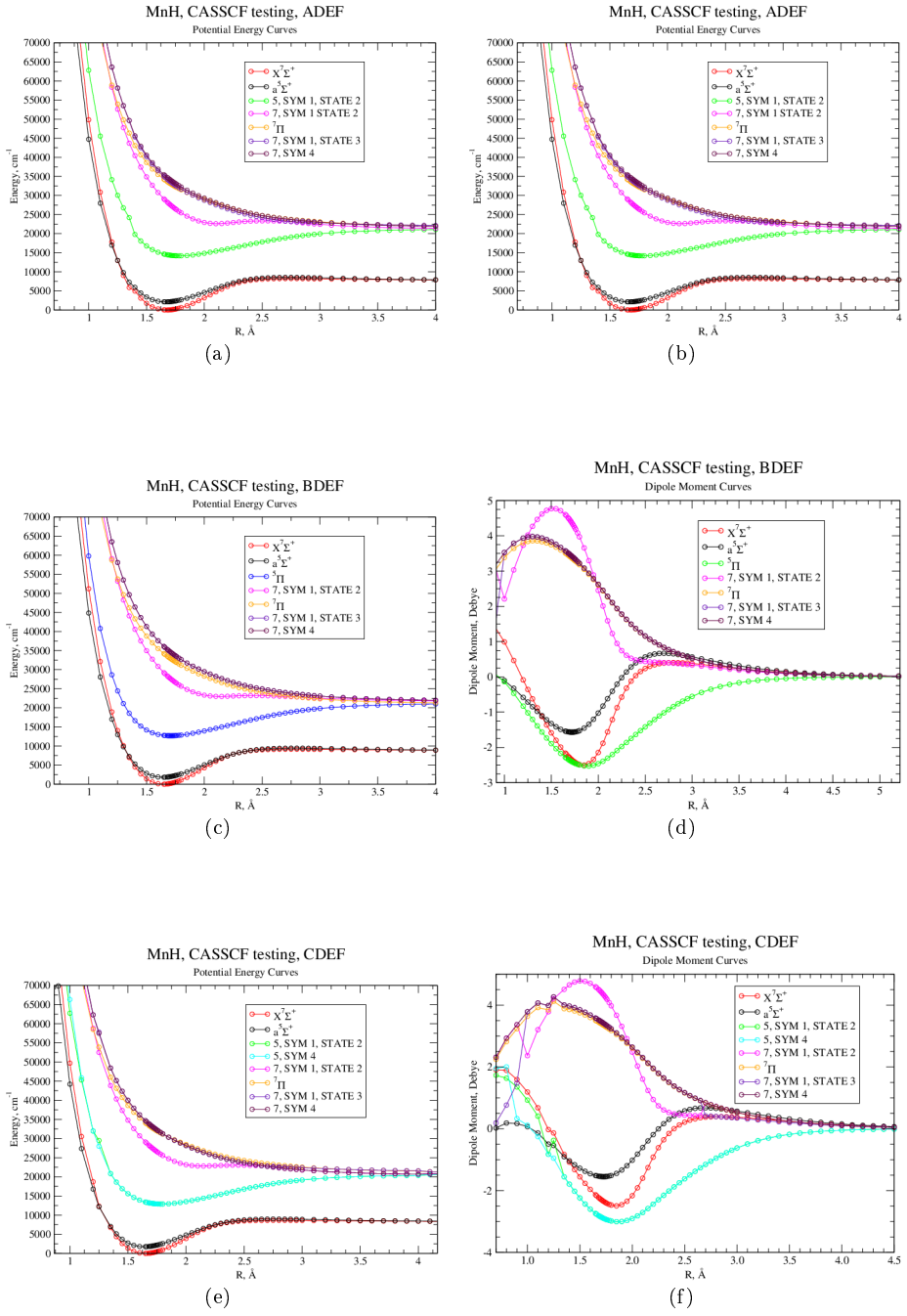

Figure C.25: CASSCF calculations using a cc-pVQZ basis set that combine a single $^7\Sigma^+$ state, a single $^5\Sigma^+$ state and four other components defined in table 7.1, three of which are "D", "E" and "F" and the other selected from "A", "B" and "C".

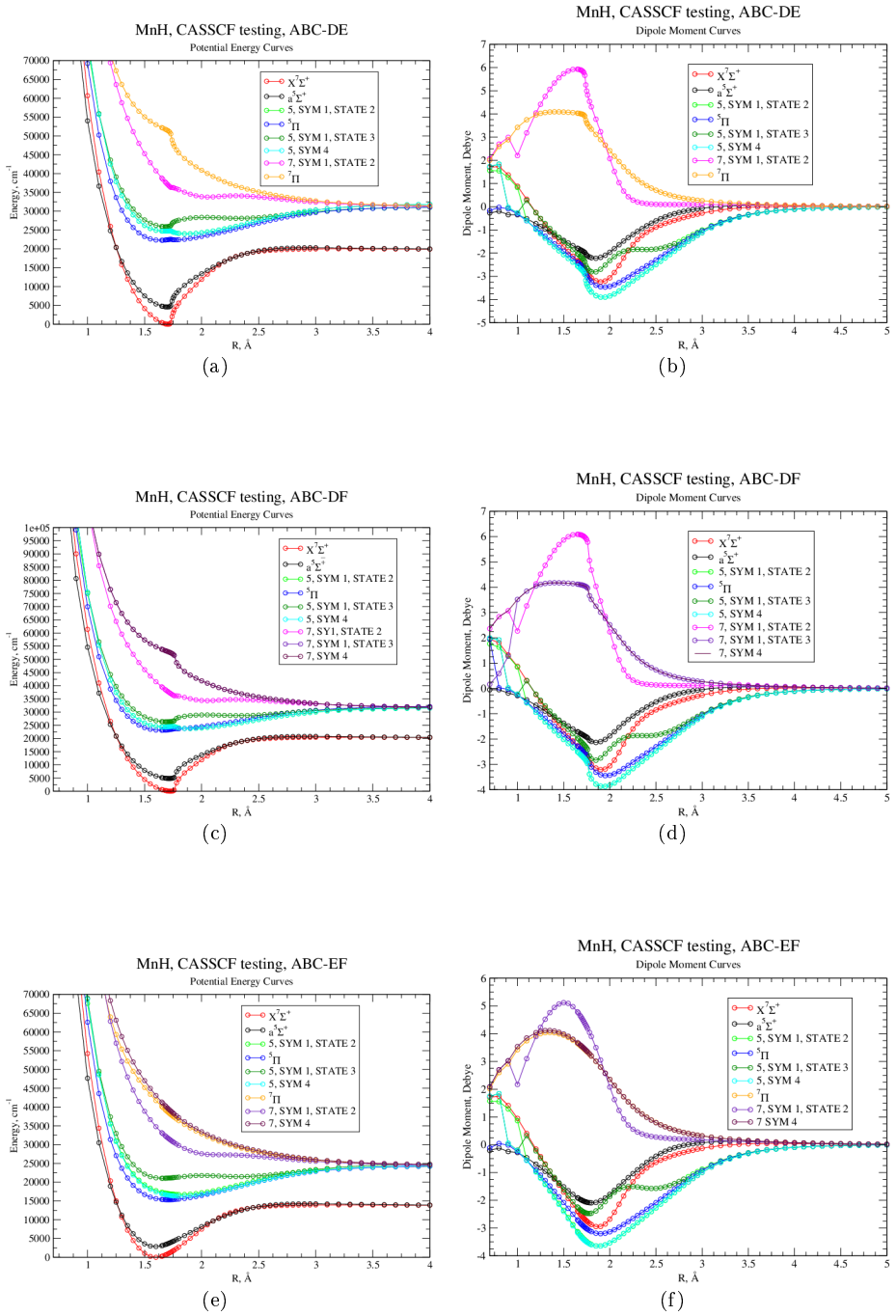

Figure C.26: CASSCF calculations using a cc-pVQZ basis set that combine a single $^7\Sigma^+$ state, a single $^5\Sigma^+$ state and five other components defined in table 7.1, three of which are "A", "B" and "C" and the other two selected from "D", "E" and "F".

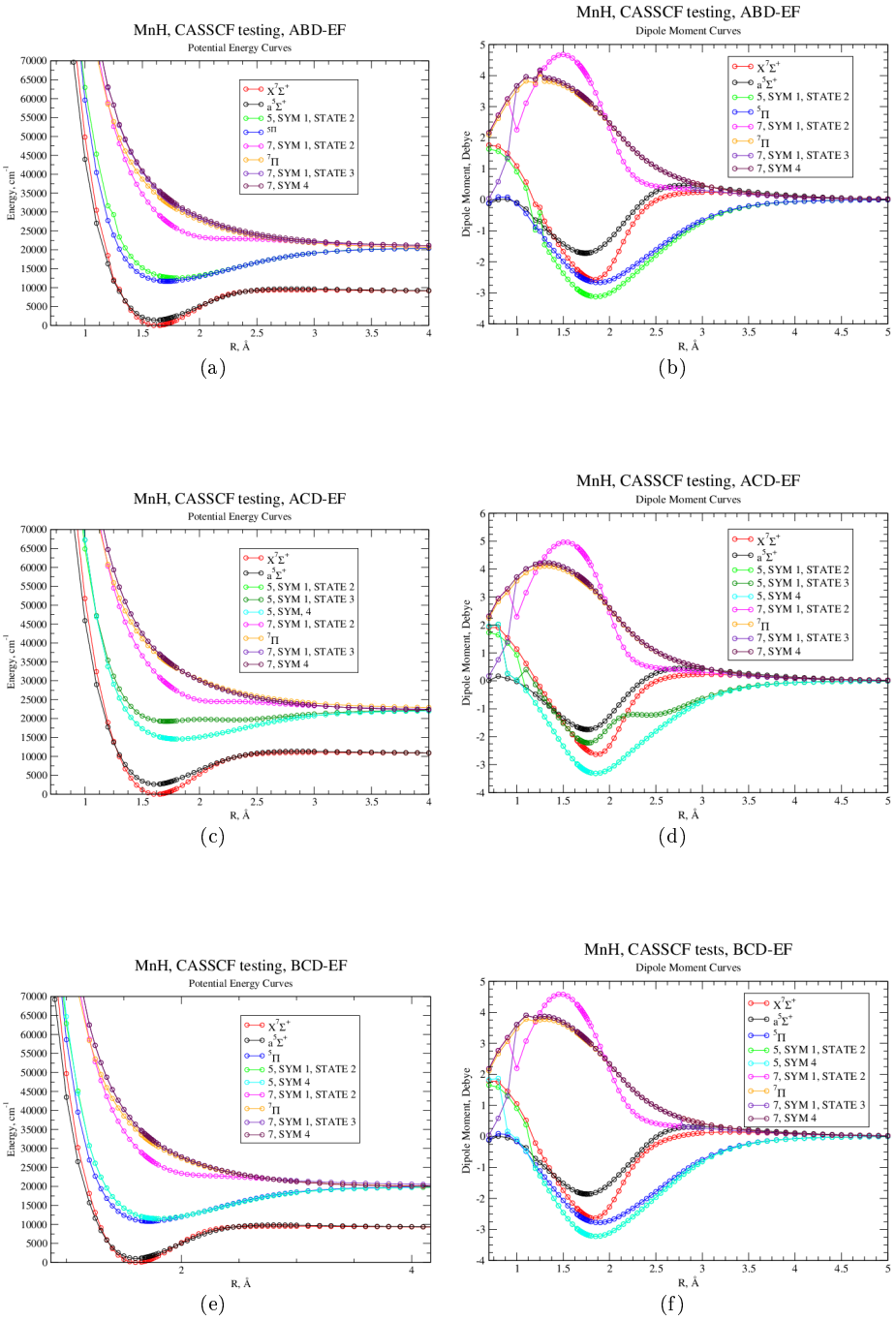

Figure C.27: CASSCF calculations using a cc-pVQZ basis set that combine a single $^7\Sigma^+$ state, a single $^5\Sigma^+$ state and five other components defined in table 7.1, three of which are "D", "E" and "F" and the other two selected from "A", "B" and "C".

Appendix D

Preliminary Calculations for Group II diatomic Hydrides

As was the case for CrH and MnH, before any *ab initio* calculations were undertaken, the lowest lying electronic states needed to be determined by consideration of the atomic dissociation limits for the H, Be, Mg and Ca atoms. These are shown in tables D.1, D.2, D.3 and D.4 respectively.

Config	Term	J	Level(cm^{-1})
$1s$	^2S	1/2	0.00000 00000
$2p$	$^2P^0$	1/2	82 259.9191133
		3/2	92 259.2850014

Table D.1: H atom dissociation energy limits up to approximately 92 000 cm^{-1}.

Configuration	Term	J	Level(cm^{-1})
$1s^22s^2$	^1S	0	0.000
$1s^22s2p$	$^3P^o$	0	21 978.28
		1	21 978.925
		2	21 981.27
$1s^22s2p$	$^1P^o$	1	42 565.35

Table D.2: Be atom dissociation energy limits up to approximately 42 000 cm^{-1}.

Confirguation	Term	J	Level(cm^{-1})
$2p^63s^2$	^1S	0	0.000
$3s3p$	$^3P^o$	0	21 850.405
		1	21 870.464
		2	21 911.178
$3s3p$	$^1P^o$	1	35 051.264

Table D.3: Mg atom dissociation energy limits up to approximately 35 000 cm^{-1}.

Configuration	Term	J	Level(cm^{-1})
$3p^6 4s^2$	^1S	0	0.000
$3p^6 4s4p$	$^3P^o$	0	15 157.901
		1	15 210.063
		2	15 315.943
$3p^6 3d4s$	^3D	1	20 335.360
		2	20 349.260
		3	20 371.000
$3p^6 3d4s$	^1D	2	21 849.634
$3p^6 4s4p$	$^1P^o$	1	23 652.304
$3p^6 4s5s$	^3S	1	31 539.495

Table D.4: Ca atom dissociation energy limits up to approximately 32 000 cm^{-1}.

To summarise, referring to tables D.2, D.3 and D.4 for BeH, CaH, MgH respectively, it can be seen that molecular states arising from the ^1S and $^3P^0$ atomic terms are of greatest interest. For both Be and Mg, the $^1P^0$ terms are significantly higher in energy so thus we can tentatively assume that that interactions with molecular states arising from these atomic dissociation limits with the lower molecular states will be negligible. Table D.5 summarises the molecular states of interest arising from the various atomic dissociation limits for BeH, MgH and CaH. Finally, tables D.6, D.7 and D.8 show the deduction of the closed and active space required for the molecules of BeH, MgH and CaH respectively with a summary of results shown in table D.9.

Atomic Term	Energy (cm^{-1})			Molecular States	
	BeH	MgH	CaH		
^1S	0.000	0.000	0.000	$^2\Sigma^+$	
$^3P^o$	21 980.156	21 980.854	15 263.089	$^2\Sigma^+$	$^4\Sigma^+$
				$^2\Pi$	$^4\Pi$
^3D			20 356.625	$^2\Sigma^+$	$^4\Sigma^+$
				$^2\Pi$	$^4\Pi$
				$^2\Delta$	$^4\Delta$
^1D			21 849.634	$^2\Sigma^+$	
				$^2\Pi$	
				$^2\Delta$	
$^1P^o$	42 565.350	35 051.264	23 652.304	$^2\Sigma^+$	
				$^2\Pi$	
^3S			31 539.495	$^2\Sigma^+$	$^4\Sigma^+$

Table D.5: Molecular states expected for alkaline metal hydrides.

Orbitals		C_{2V} Symmetry			
		A1	B1	B2	A2
closed	$1s^2$	1	0	0	0
Total closed		1	0	0	0
Active	$2s^2$	1	0	0	0
	$1s^1$(H)	1	0	0	0
Total active		2	0	0	0
Total occupied		3	0	0	0

(a)

Orbitals		C_{2V} Symmetry			
		A1	B1	B2	A2
closed	$1s^2$	1	0	0	0
Total closed		1	0	0	0
Active	$2s^1$	1	0	0	0
	$2p^1$	1	1	1	0
	$1s^1$(H)	1	0	0	0
Total active		3	1	1	0
Total occupied		4	1	1	0

(b)

Table D.6: Electronic configurations for low-lying states of diatomic molecule BeH
(a) Closed and Occupied orbitals for the $1s^2 2s^2$ ground state configuration
(b) Closed and Occupied orbitals for the $1s^2 2s^1 2p^1$ electronic configuration

Orbitals		C_{2V} Symmetry			
		A1	B1	B2	A2
closed	$1s^2$	1	0	0	0
	$2s^2$	1	0	0	0
	$2p^6$	1	1	1	0
Total closed		3	1	1	0
Active	$3s^2$	1	0	0	0
	$1s^1$(H)	1	0	0	0
Total active		2	0	0	0
Total occupied		5	1	1	0

(a)

Orbitals		C_{2V} Symmetry			
		A1	B1	B2	A2
closed	$1s^2$	1	0	0	0
	$2s^2$	1	0	0	0
	$2p^6$	1	1	1	0
Total closed		3	1	1	0
Active	$3s^1$	1	0	0	0
	$3p^1$	1	1	1	0
	$1s^1$(H)	1	0	0	0
Total active		3	1	1	0
Total occupied		6	2	2	0

(b)

Table D.7: Electronic configurations for low-lying states of diatomic molecule MgH
(a) Closed and Occupied orbitals for the $3s^2$ ground state configuration
(b) Closed and Occupied orbitals for the $3s^1 3p^1$ electronic configuration

Orbitals		C_{2V} Symmetry			
		A1	B1	B2	A2
closed	$1s^2$	1	0	0	0
	$2s^2$	1	0	0	0
	$2p^6$	1	1	1	0
	$3s^2$	1	0	0	0
	$3p^6$	1	1	1	0
Total closed		5	2	2	0
Active	$4s^2$	1	0	0	0
	$1s^1$(H)	1	0	0	0
Total active		2	0	0	0
Total occupied		7	2	2	0

(a)

Orbitals		C_{2V} Symmetry			
		A1	B1	B2	A2
closed	$1s^2$	1	0	0	0
	$2s^2$	1	0	0	0
	$2p^6$	1	1	1	0
	$3s^2$	1	0	0	0
	$3p^6$	1	1	1	0
Total closed		5	2	2	0
Active	$4s^1$	1	0	0	0
	$4p^1$	1	1	1	0
	$1s^1$(H)	1	0	0	0
Total active		3	1	1	0
Total occupied		8	3	3	0

(b)

Table D.8: Electronic configurations for low-lying states of diatomic molecule CaH
(a) Closed and Occupied orbitals for the $3p^6 4s^2$ ground state configuration
(b) Closed and Occupied orbitals for the $3p^6 4s^1 4p^1$ electronic configuration

As was the case for MnH, for each of the three Group II diatomic hydrides, there is a "LOWER" and "UPPER" active space: the "UPPER" active space is required for the

calculation of molecular states which do not converge to the lowest lying asymptote of the group II metal atom. Table D.9 summaries these various active spaces using the information determined from tables D.6, D.7 and D.8.

Molecule	Active space		
	Closed	Occupied	
		Lower	Upper
BeH	1000	3000	4110
MgH	3110	5110	6220
CaH	5220	7220	8330

Table D.9: Summary of active spaces required for calculation of electronic states for BeH, MgH and CaH.

D.1 Preliminary MRCI calculations

Preliminary MRCI calculations were performed for the Group II diatomic hydrides of BeH, MgH and CaH. The basis set used was cc-pVDZ. For each molecule, the proceeding CASSCF calculation done before the CI calculations was that for the single $X^2\Sigma^+$ ground state using the relevant "LOWER" active space for each molecule as summarised in table D.9. Figure D.1 shows for BeH, MgH and CaH the PECs and DMCs obtained for these CASSCF calculations which generated the starting orbitals used in the subsequent CI calculations. As for CrH and MnH, the CI calculations of PECs and DMCs for the various electronic states were performed by defining "*PROCS*". These are outlines in table D.10 which also states the required active space to obtain the particular electronic states. Simply put, for all three molecules the $X^2\Sigma^+$ state only requires the "LOWER" active space: the four other electronic states require the use of the "UPPER" active space. As was a similar case for MnH,

PROC	*wf* cards	STATE	Occupied orbitals
S1	doublet, symmetry 1, 1 state	$X^2\Sigma^+$	LOWER
S2			UPPER
S6	doublet, symmetry 1, 2 states	$X^2\Sigma^+$, $A^2\Sigma^+$	UPPER
S3	doublet, symmetries 2 & 3, 1 state each	$^2\Pi$	UPPER
S4	quartet, symmetry 1, 1 state	$^4\Sigma^+$	UPPER
S5	quartet, symmetries 2 & 3, 1 state each	$^4\Pi$	UPPER

Table D.10: Summary of *PROCS* used in `MOLPRO` to calculate at CI level of theory the various low-lying electronic states of BeH, MgH and CaH.

it was found that better (i.e. lower in energy) PEC for the $X^2\Sigma^+$ state was obtained by using *PROC S6* in which two $^2\Sigma^+$ states are requested and the "UPPER" active space is used. The results of calculations for the PECs and DMCs of the states listed in table D.10 are shown in figure D.2.

As was the case for CrH & MnH, the expected couplings between the various electronic states can be deduced by consideration of the various selection rules governing changes in spin (S), orbital angular momenta (L) and total angular momenta J. A sample of couplings calculated is shown in figure D.3 which is for BeH.

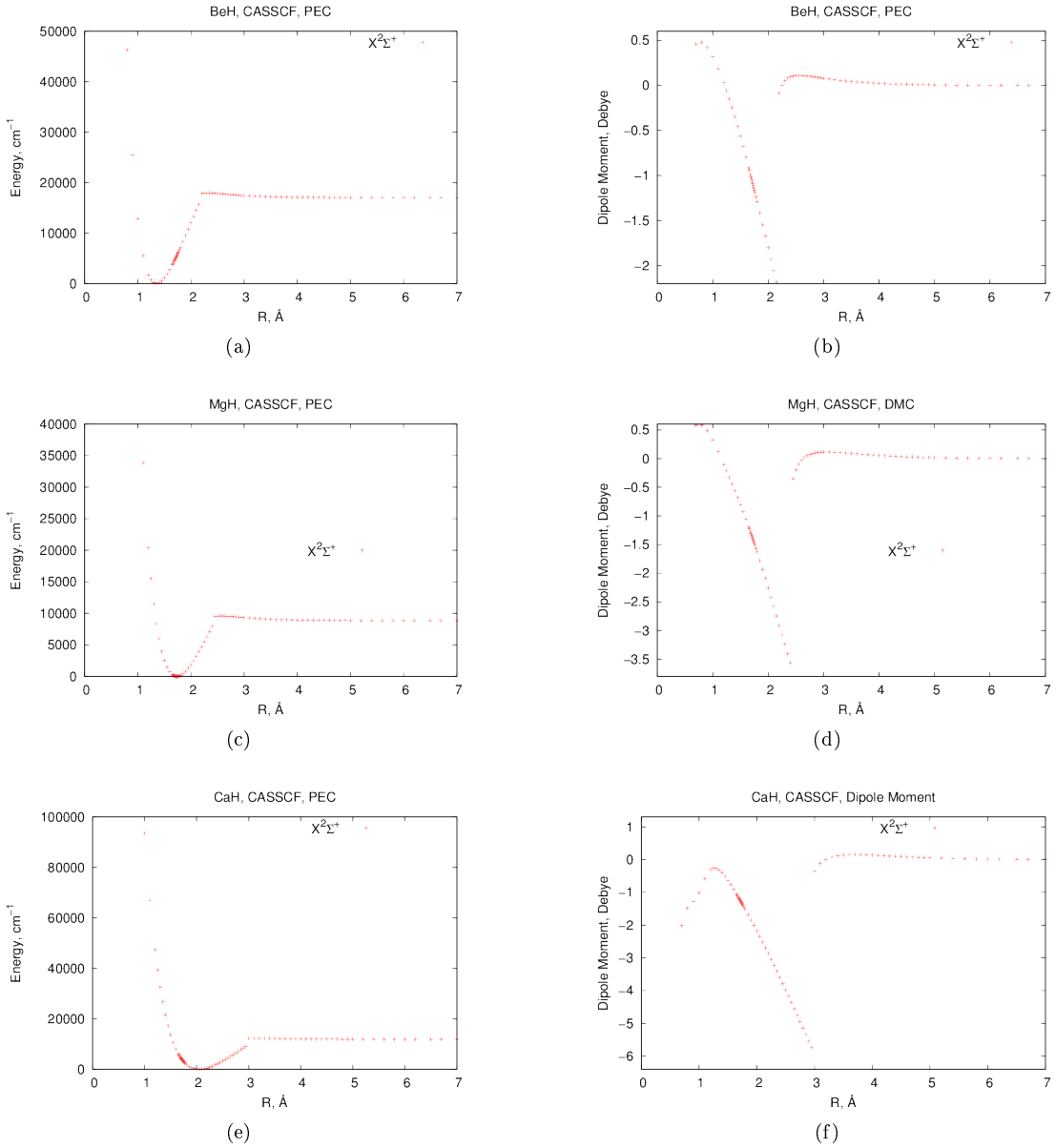

Figure D.1: PECs and DMCs calculated at CASSCF level of theory using a cc-pVDZ basis set for the ground $X^2\Sigma^+$ states of BeH, MgH and CaH. In all cases the CASSCF calculation was for this state only and used the respective "LOWER" active space for each molecule as defined in table D.9.

D.2 CASSCF state-combination testing

In addition to these preliminary calculations of PECs, DMCs and couplings, the effect of different combination of states used in the initial CASSCF has been tested out as was done in a a similar vein for CrH and MnH. More specifically the number of internuclear points (as defined on the rgeom grid, see section 2.7.1) for which a calculation converged has been summarised from this preliminary work. For all these different CASSCF "combinations" the ground $X^2\Sigma^+$ state was included. These test calculations were done using a cc-pVQZ basis set and, in contrast to the results presented in section D.1, all of these CASSCF calculations used the respective "UPPER" active

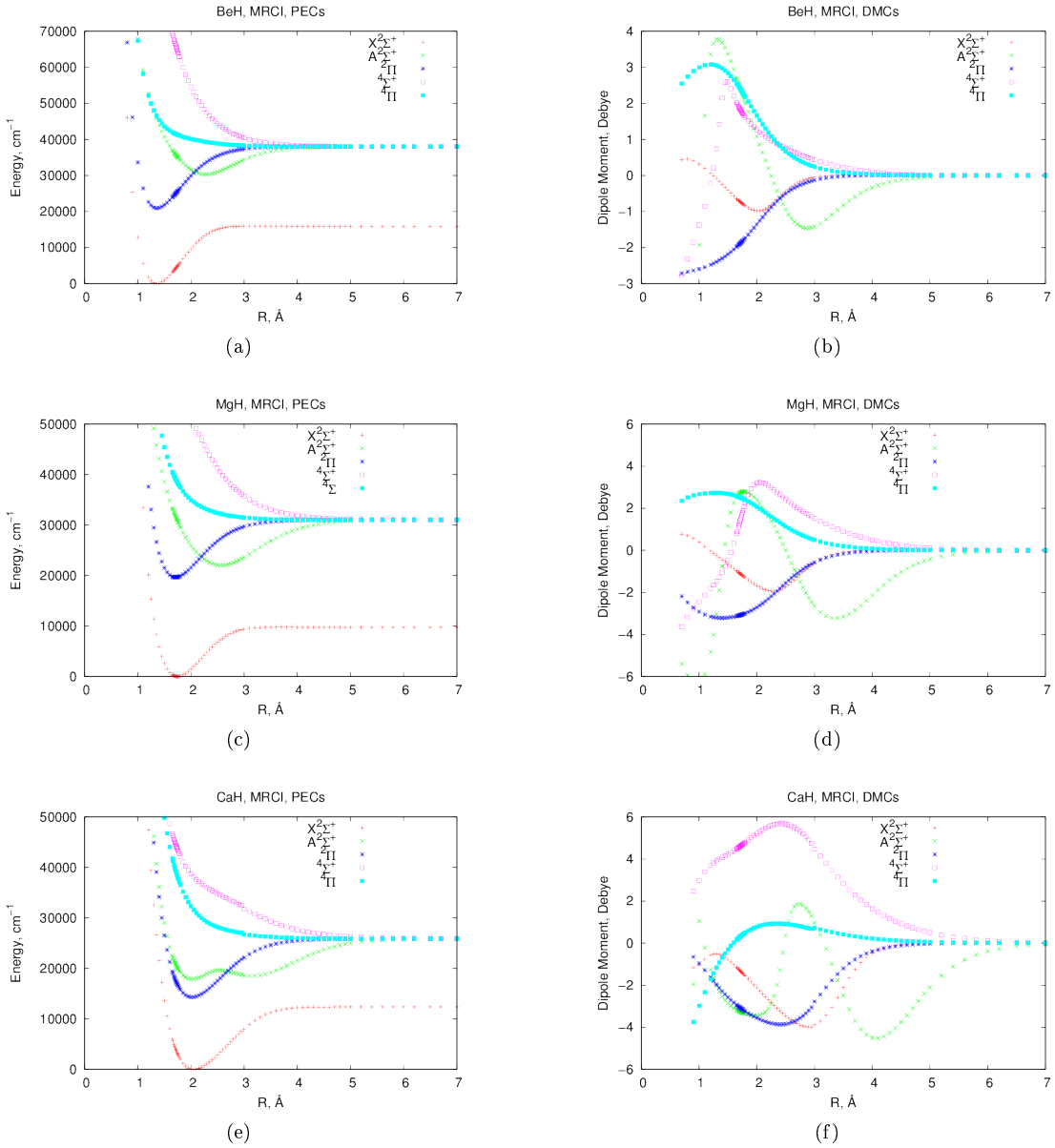

Figure D.2: PEC and DMC curves calculated at CI level for BeH, CaH and MgH using cc-pVDZ basis set and the "UPPER" active space as defined in table D.9. The proceeding CASSCF calculation for which the CI orbitals were built upon was for the ground $X^2\Sigma^+$ state using the respective "LOWER" active space.

space as defined in table D.9. As this table shows, for all three molecules, all electronic states above the $X^2\Sigma^+$ state require this. Table D.11 sets out the naming scheme (i.e. A, B, C, D) used. Referring to table D.11, combinations of these components (i.e. A, B, C, D) were then tested out by running CASSCF calculations. A summary of all the possible combinations of these "components" is shown in table D.12. Table D.12 thus shows that there are 15 possible CASSCF combinations to test out i.e. $\sum_{i=1}^{4} {}^4C_i = {}^4C_1 + {}^4C_2 + {}^4C_3 + {}^4C_4 = 4 + 6 + 4 + 1 = 15$. The PECs and DMCs produced by these different combinations of states within a CASSCF calculation are shown in sections D.2.1, D.2.2 and D.2.3 for BeH, MgH and CaH respectively.

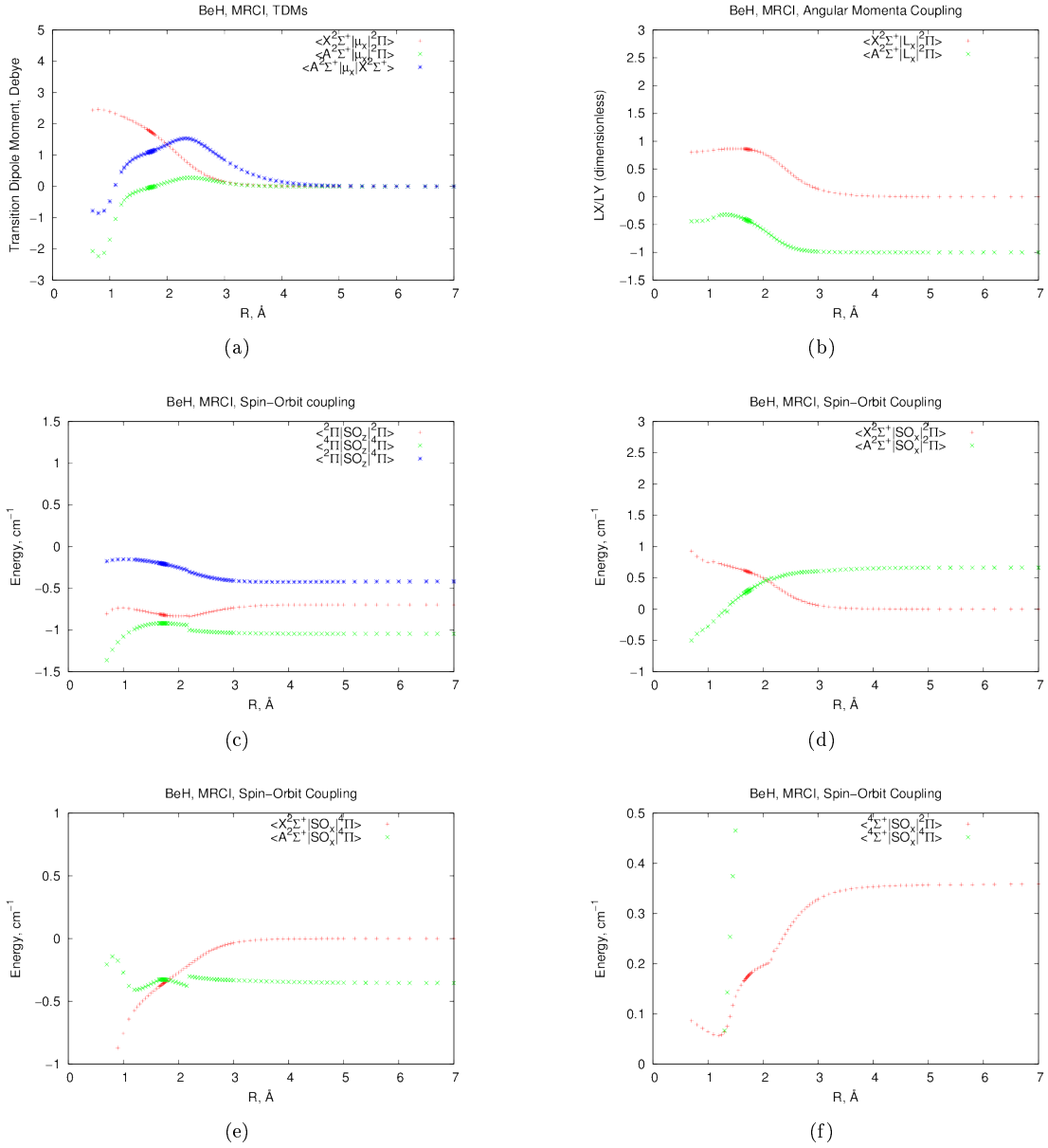

Figure D.3: Transition Dipole, anglar momenta and Spin-Orbit Couplings for BeH calculated at CI level of theory using a cc-pVDZ basis set and the "UPPER" active space as defined in table D.9. The proceeding CASSCF calculation for which the CI orbitals were built upon was for the ground $X^2\Sigma^+$ state using the "LOWER" active space for BeH.

Component	State(s)	Colour used in subsequnent figures
X	$X^2\Sigma^+$	Red
A	$^2\Sigma^+(II)$	Black
B	$^2\Pi$	Cyan
C	$^4\Sigma^+$	Magneta
D	$^4\Pi$	Orange

Table D.11: Summary of letters ("'components") assigned to the various low-lying states for testing at CASSCF level for the group 2 hydrides.

Singles	Pairs	Triplets	Quads
A	AB	ABC	ABCD
B	AC	ABD	
C	AD	ACD	
D	BC	BCD	
	BD		
	CD		

Table D.12: Summary of all the CASSCF test calculations performed for each of BeH, MgH and CaH. In this table the letters A, B, C and D have been defined in terms of what molecular electronic states they represent in table D.11.

D.2.1 BeH

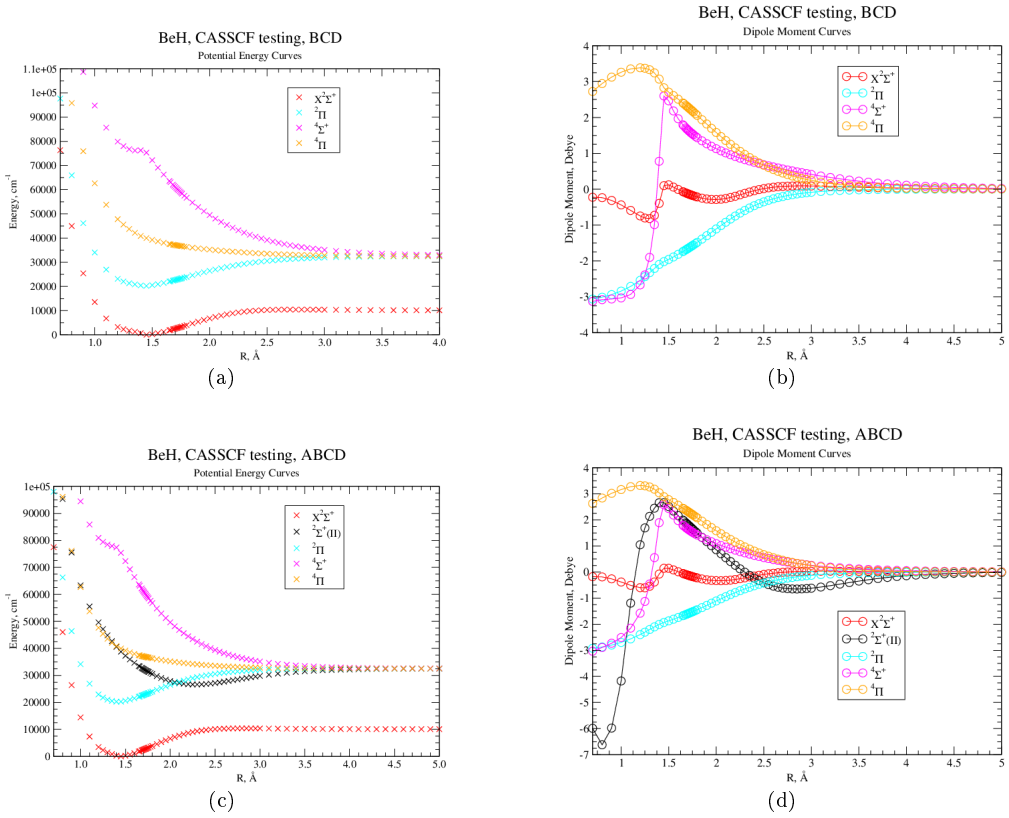

Figure D.4: CASSCF calculations of PECs and DMCs for BeH using a cc-pVQZ basis set that combine the ground $X^2\Sigma^+$ state, the $^2\Sigma^+(II)$ state ("A") and other components as defined in table D.11.

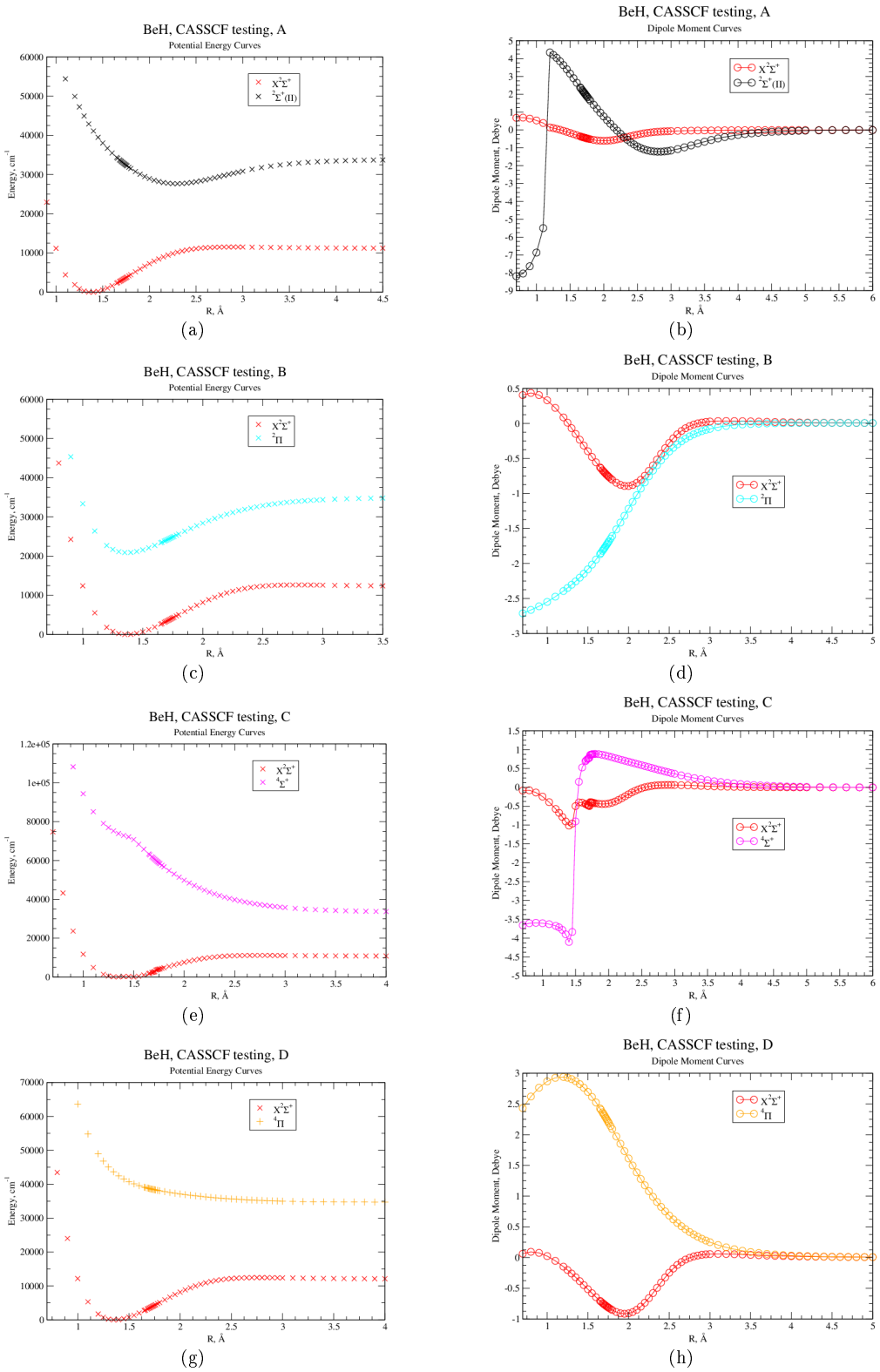

Figure D.5: CASSCF calculations of PECs and DMCs for BeH using a cc-pVQZ basis set that combine the ground $X^2\Sigma^+$ state and a single other component as defined in table D.11.

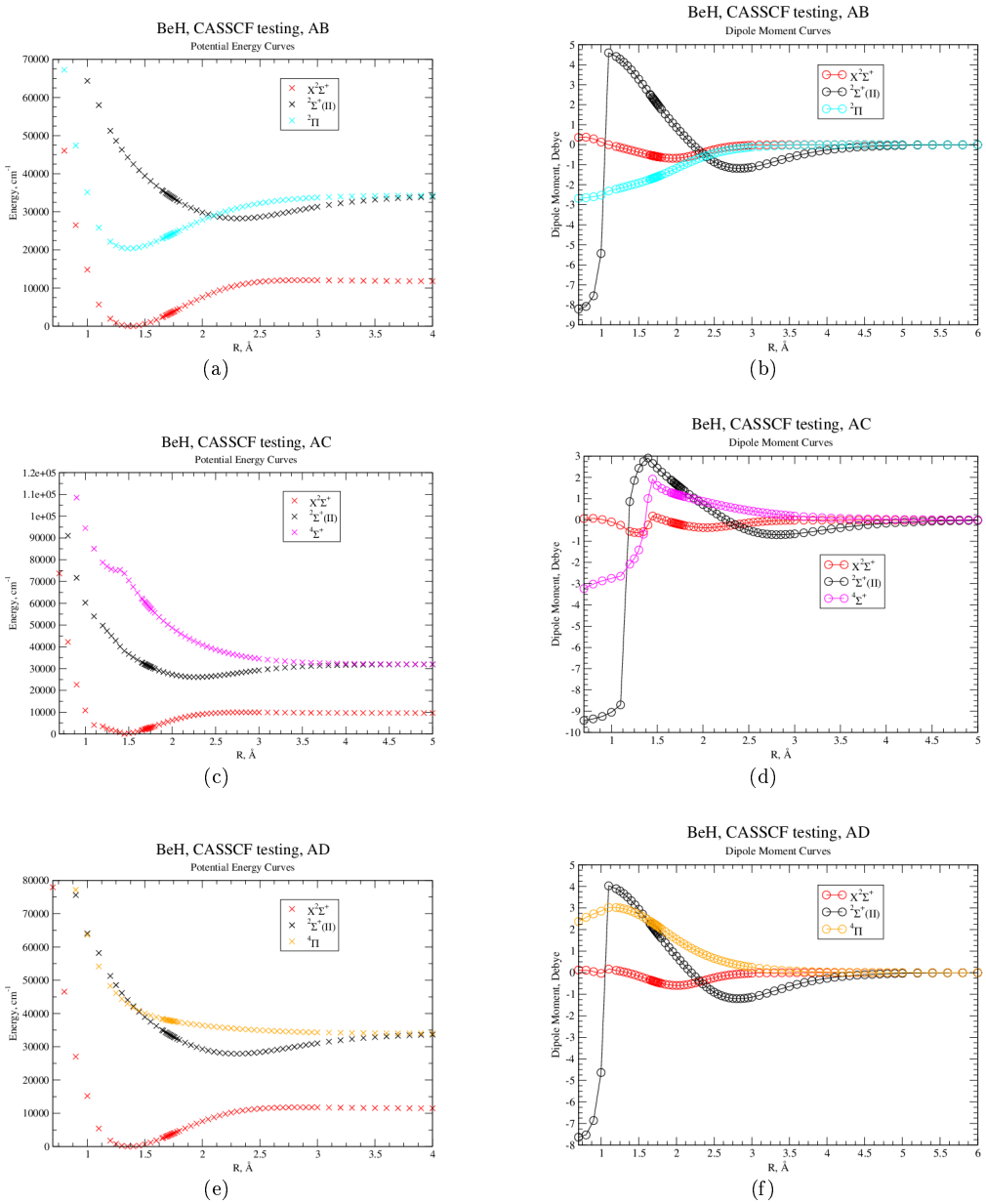

Figure D.6: CASSCF calculations of PECs and DMCs for BeH using a cc-pVQZ basis set that combine the ground $X^2\Sigma^+$ state and $^2\Sigma^+(II)$ state ("A") with and a single other component as defined in table D.11.

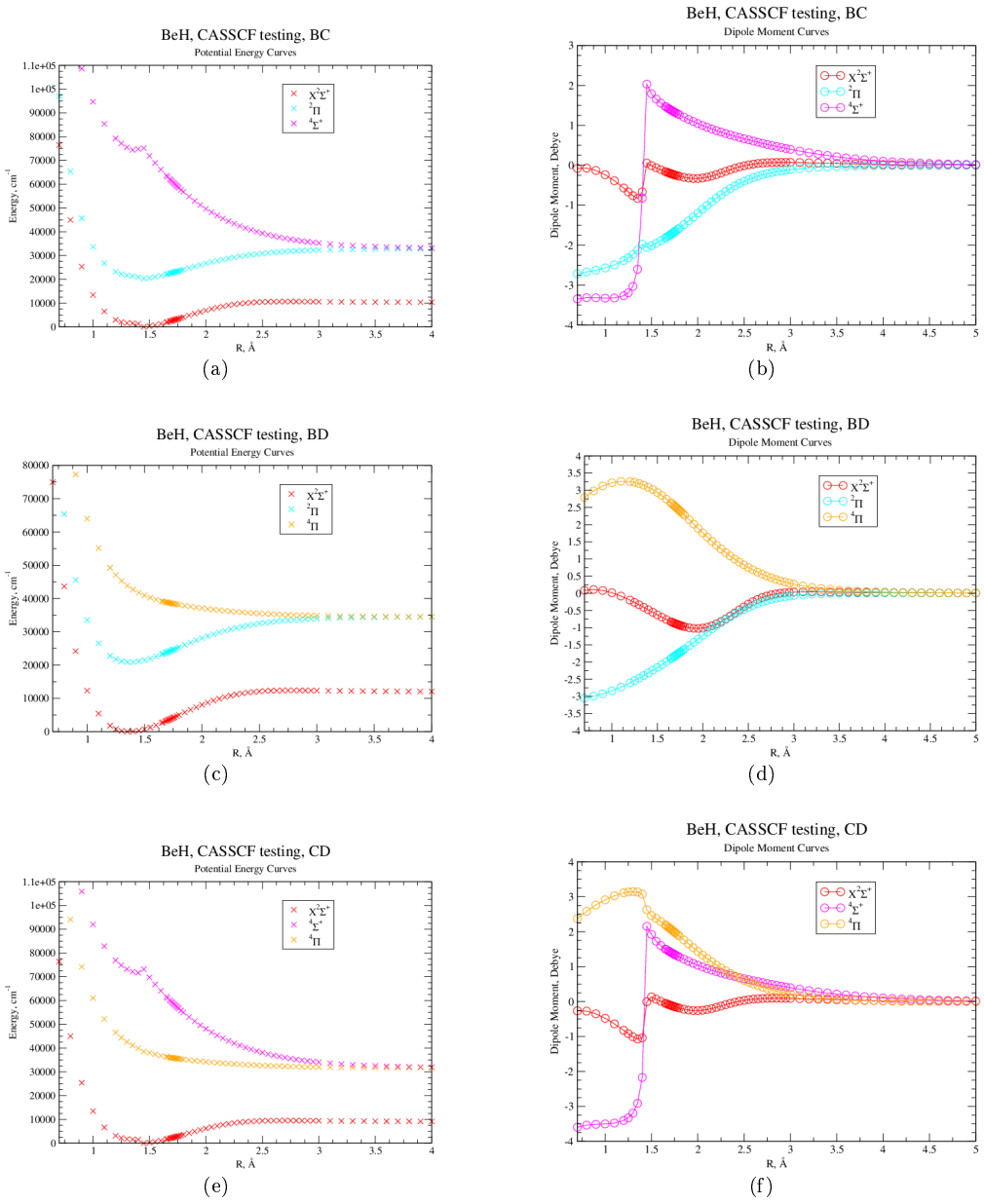

Figure D.7: CASSCF calculations of PECs and DMCs for BeH using a cc-pVQZ basis set that combine the ground $X^2\Sigma^+$ state and two other components as defined in table D.11.

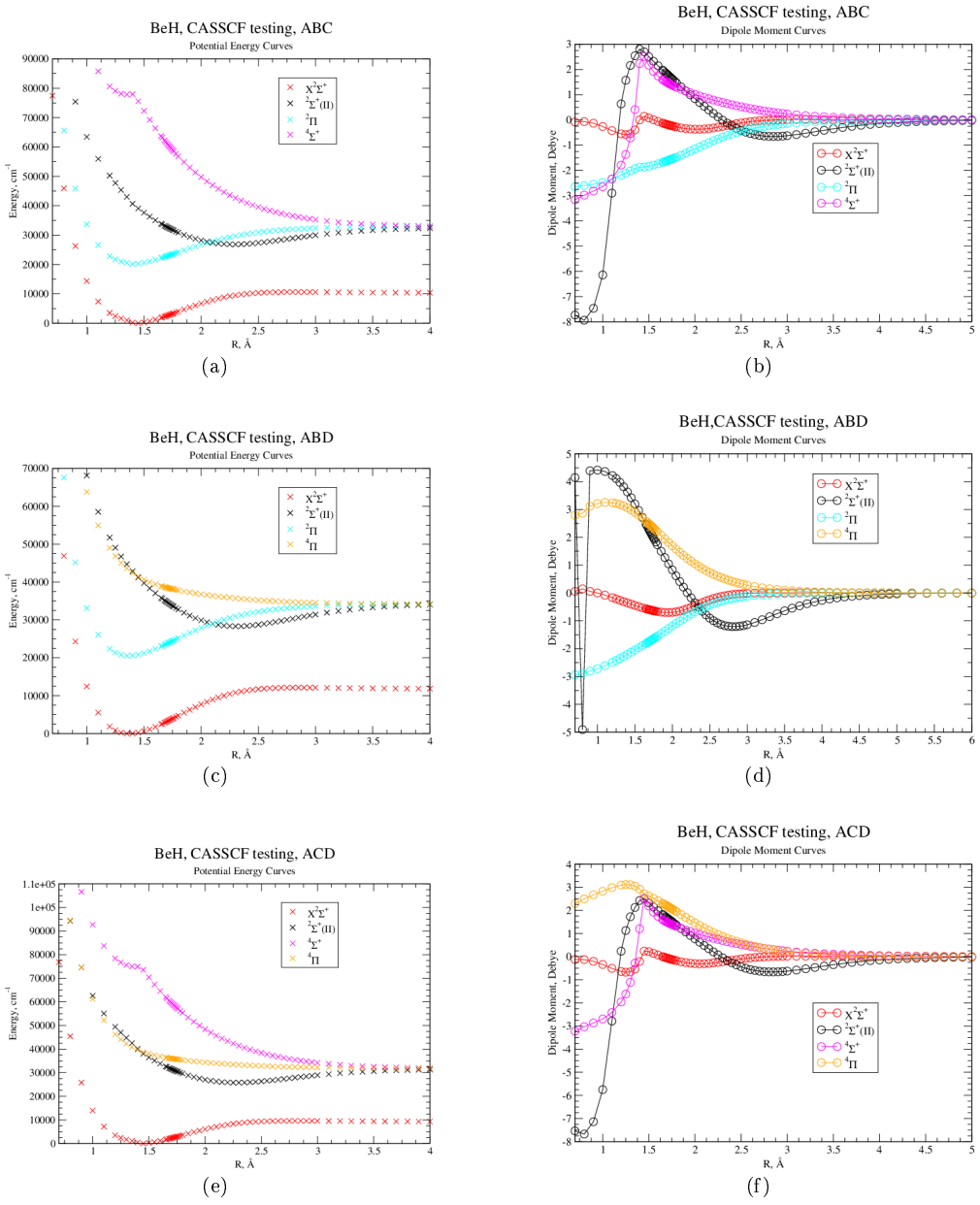

Figure D.8: CASSCF calculations of PECs and DMCs for BeH using a cc-pVQZ basis set that combine the ground $X^2\Sigma^+$ state, the $^2\Sigma^+(II)$ state ("A") and two other components as defined in table D.11.

D.2.2 MgH

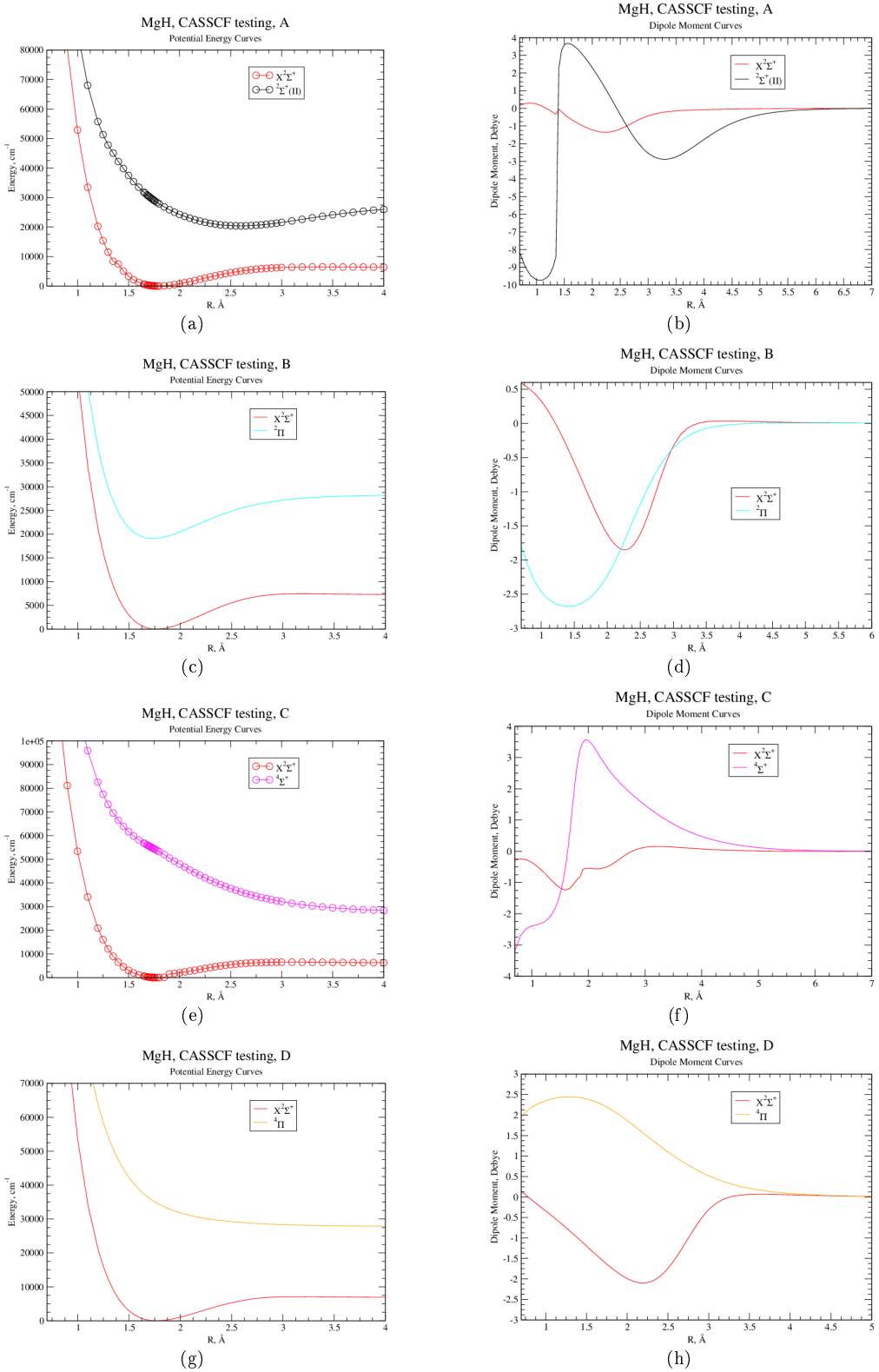

Figure D.9: CASSCF calculations of PECs and DMCs for MgH using a cc-pVQZ basis set that combine the ground $X^2\Sigma^+$ state and a single other component as defined in table D.11.

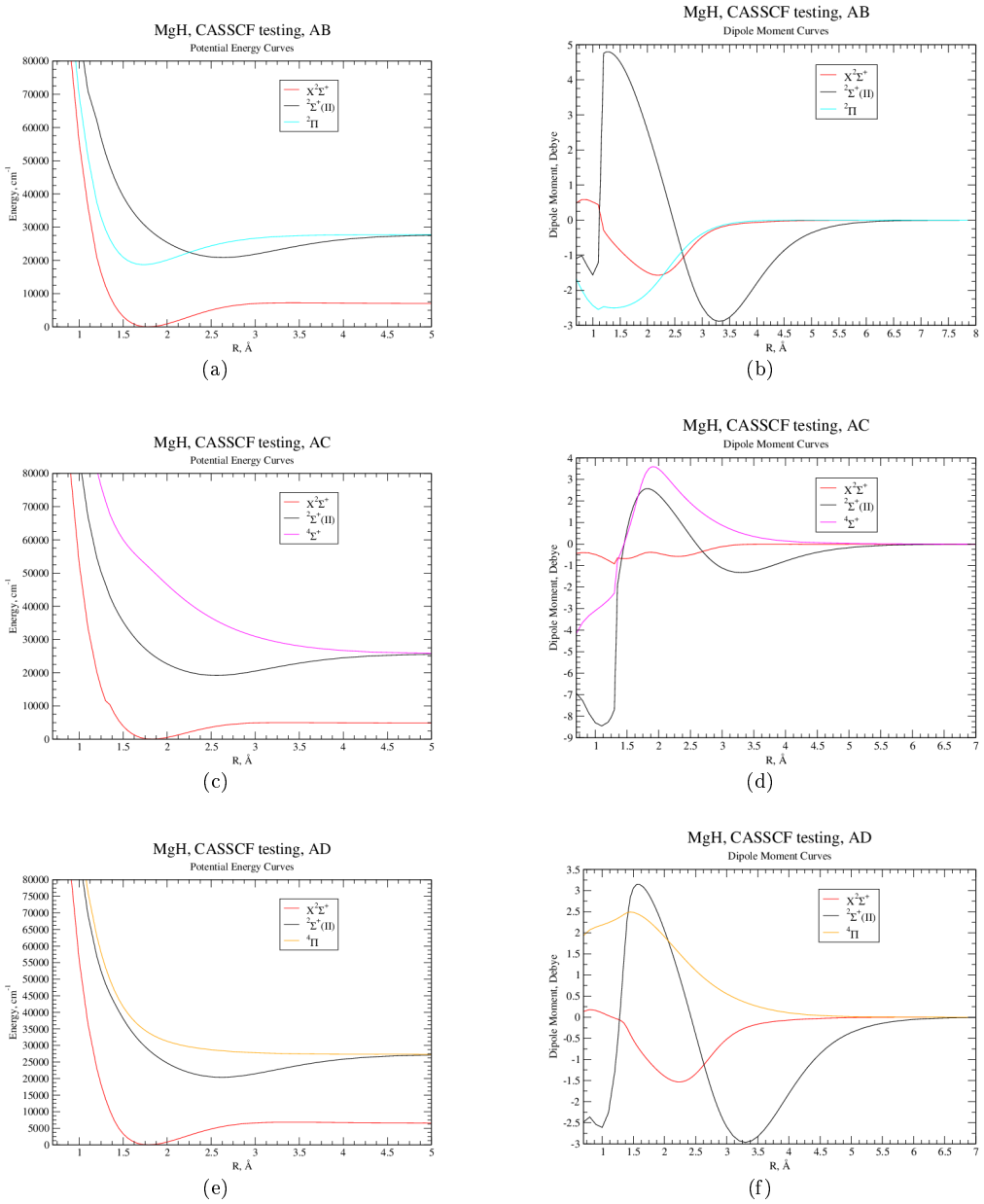

Figure D.10: CASSCF calculations of PECs and DMCs for MgH using a cc-pVQZ basis set that combine the ground $X^2\Sigma^+$ state and $^2\Sigma^+(II)$ state ("A") with and a single other component as defined in table D.11.

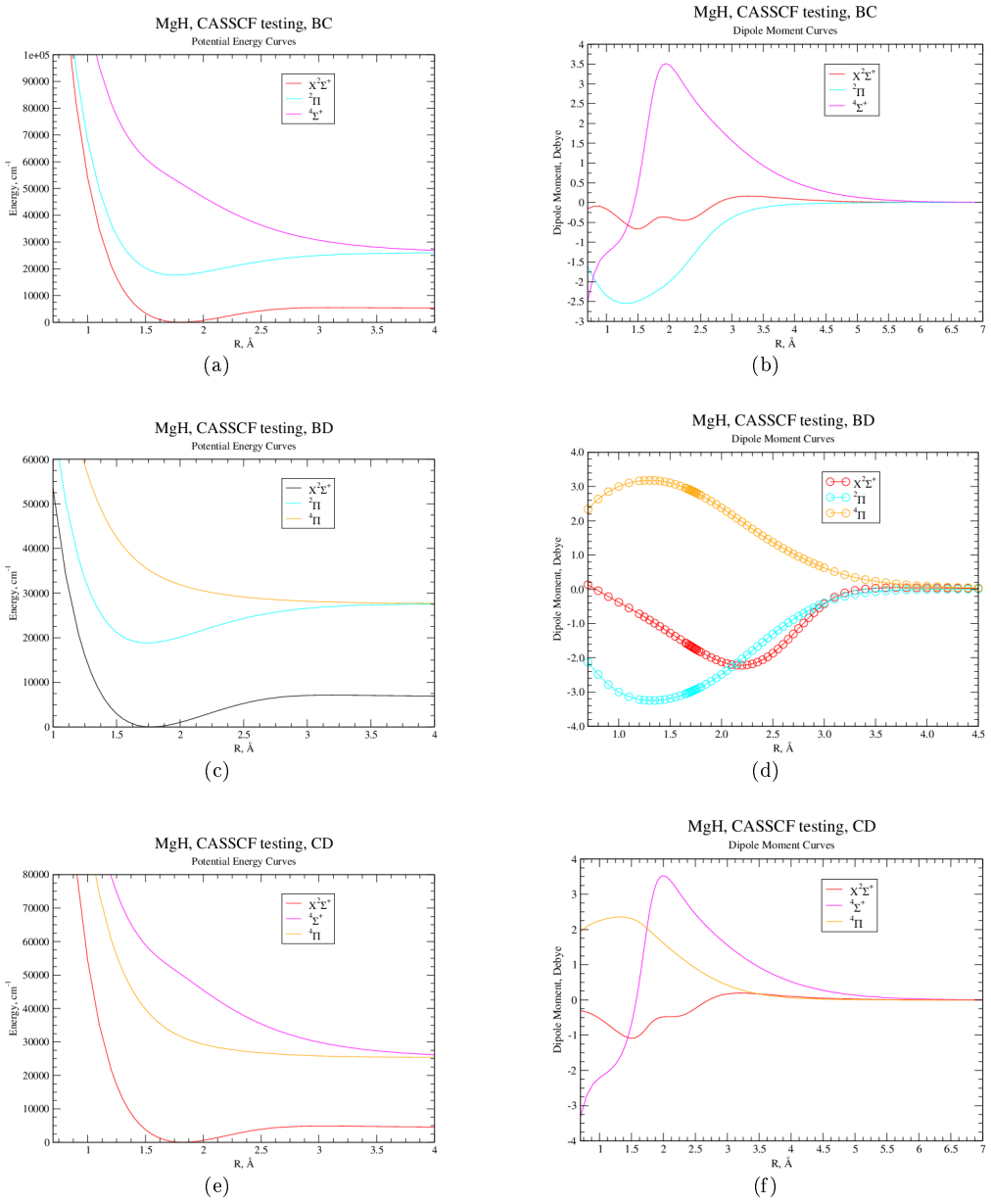

Figure D.11: CASSCF calculations of PECs and DMCs for MgH using a cc-pVQZ basis set that combine the ground $X^2\Sigma^+$ state and two other components as defined in table D.11.

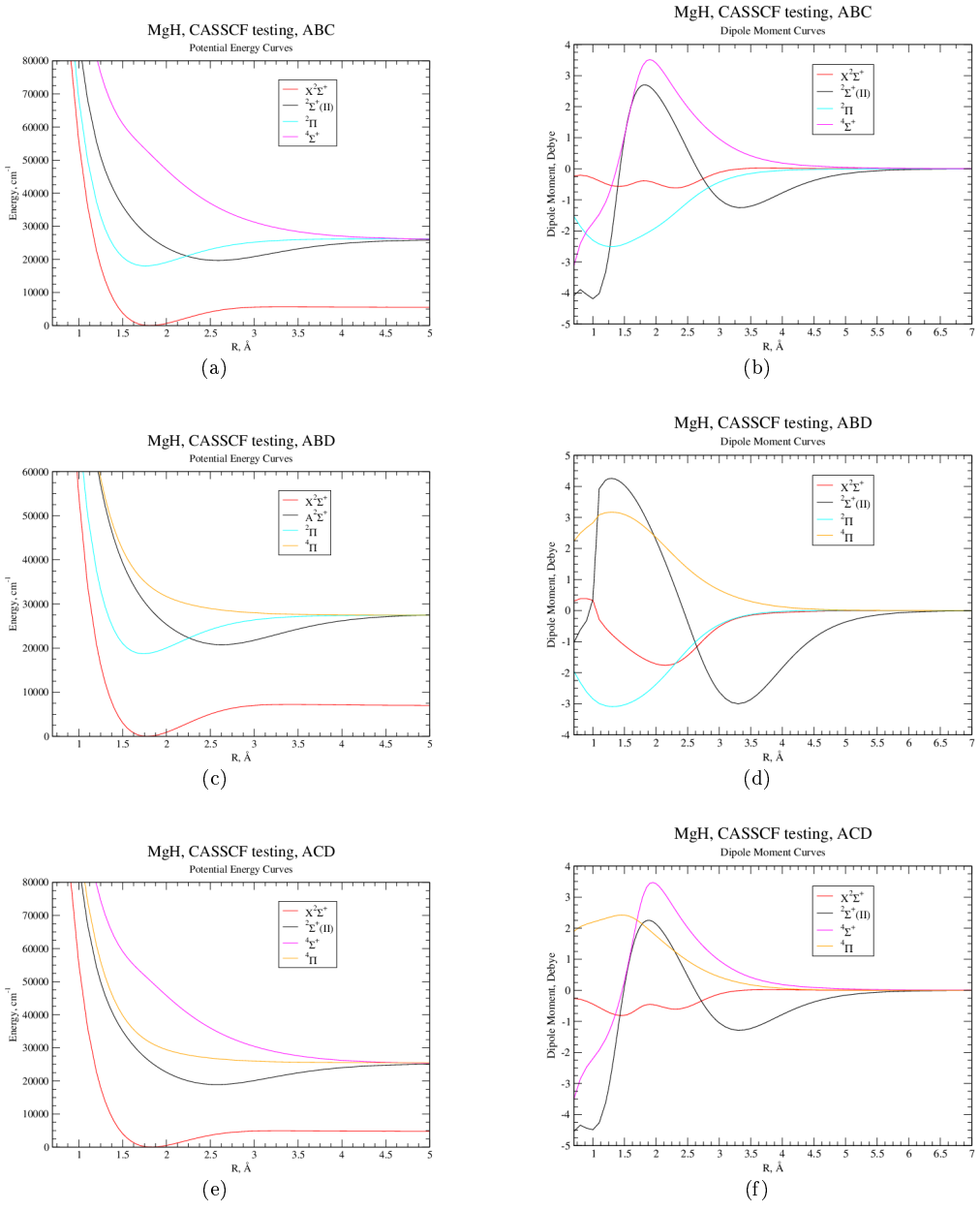

Figure D.12: CASSCF calculations of PECs and DMCs for MgH using a cc-pVQZ basis set that combine the ground $X^2\Sigma^+$ state, the $^2\Sigma^+(II)$ state ("A") and two other components as defined in table D.11.

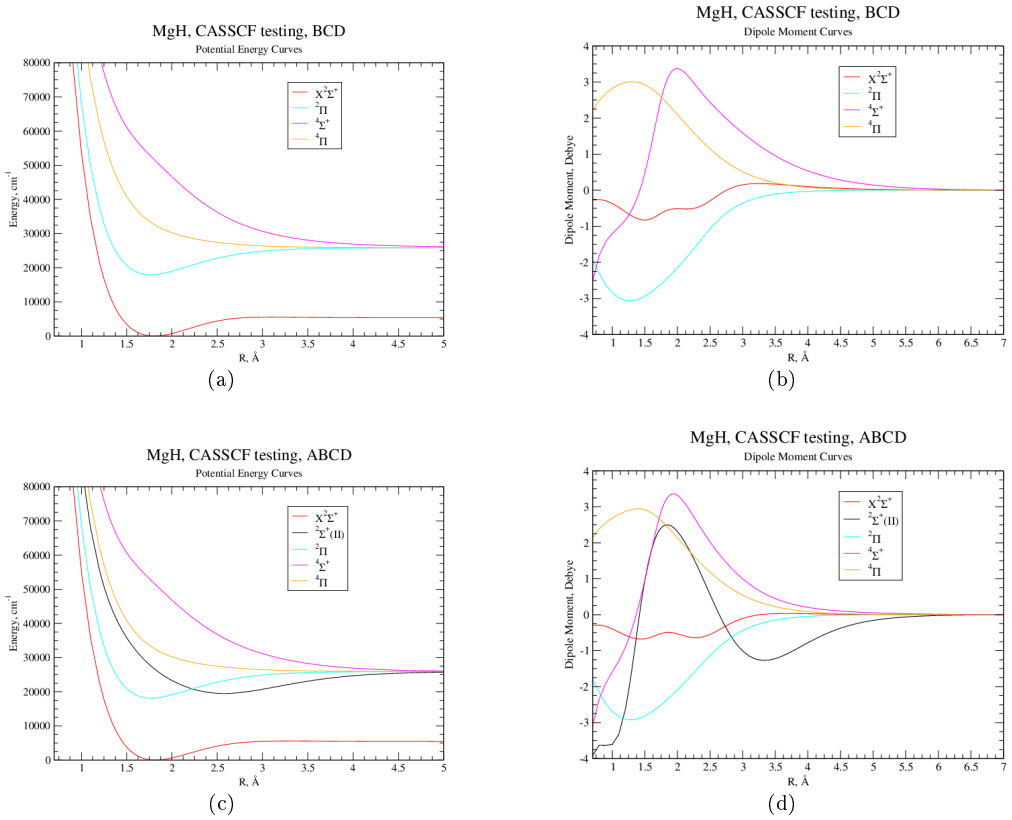

Figure D.13: CASSCF calculations of PECs and DMCs for MgH using a cc-pVQZ basis set that combine the ground $X^2\Sigma^+$ state, the $^2\Sigma^+(II)$ state ("A") and other components as defined in table D.11.

D.2.3 CaH

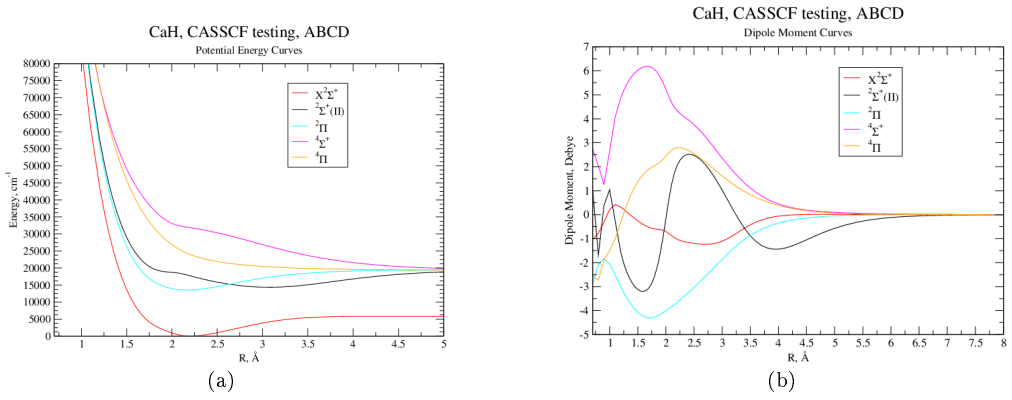

Figure D.14: CASSCF calculations of PECs and DMCs for CaH using a cc-pVQZ basis set that combine the five lowest electronic states.

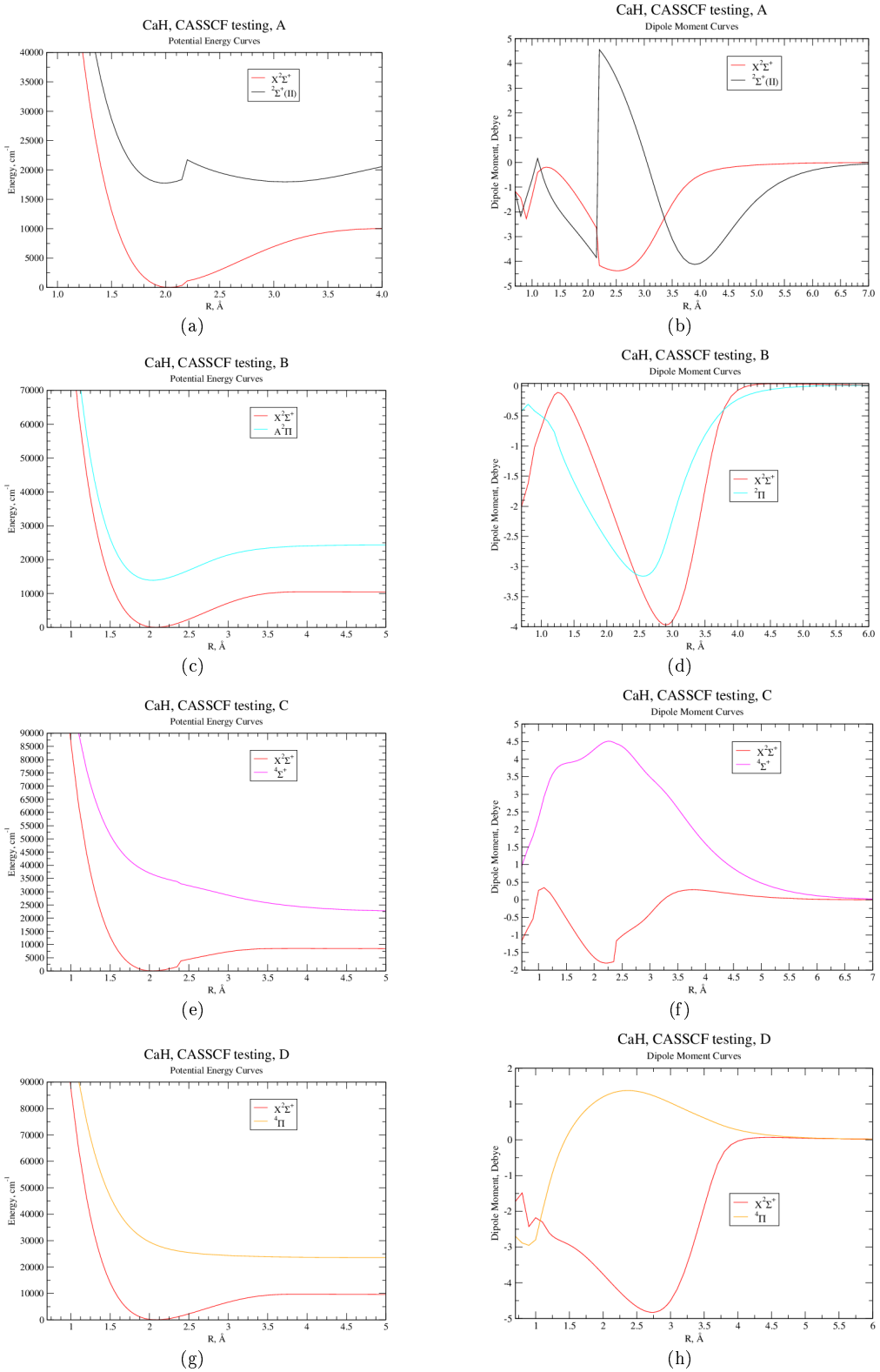

Figure D.15: CASSCF calculations of PECs and DMCs for CaH using a cc-pVQZ basis set that combine the ground $X^2\Sigma^+$ state and a single other component as defined in table D.11.

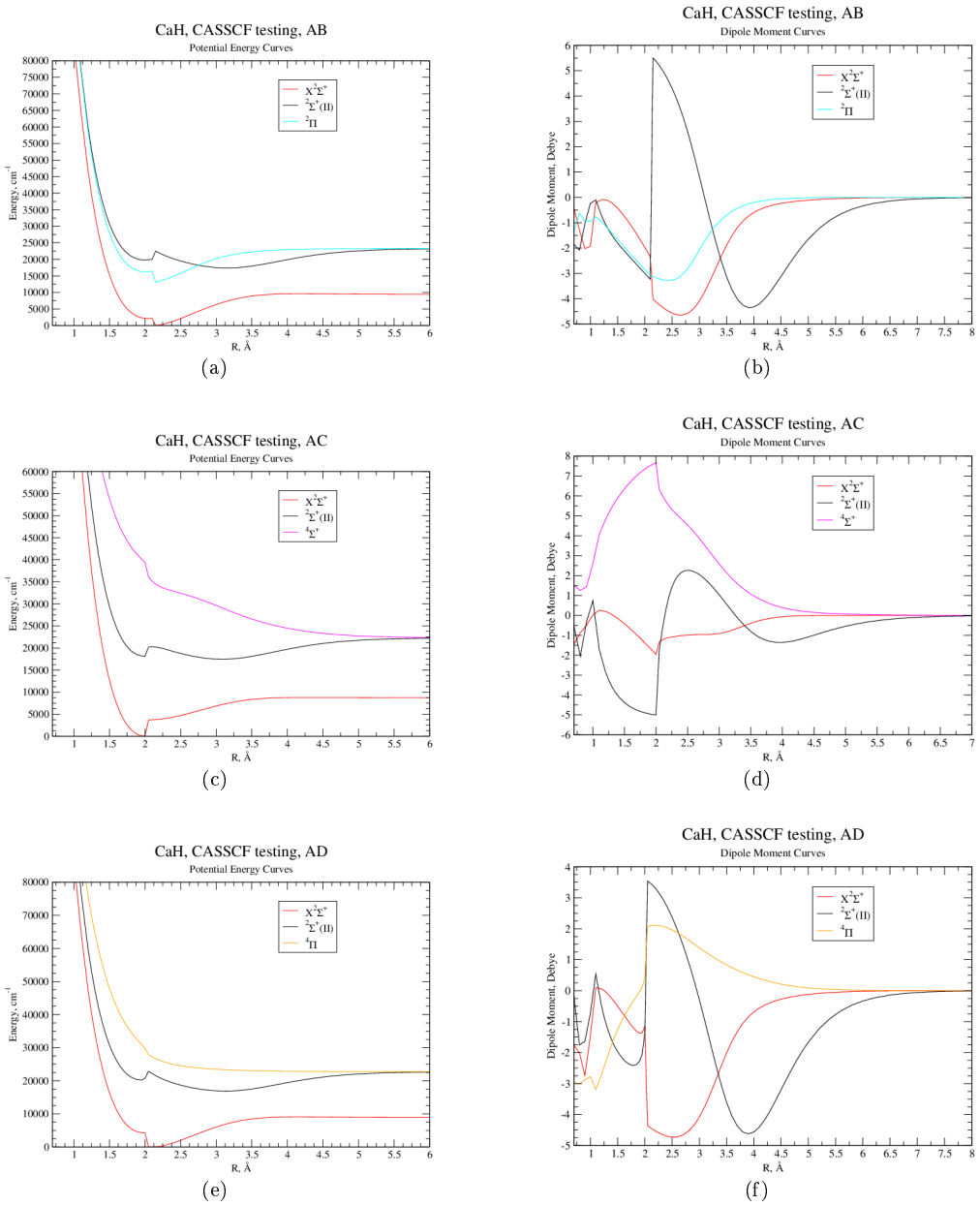

Figure D.16: CASSCF calculations of PECs and DMCs for CaH using a cc-pVQZ basis set that combine the ground $X^2\Sigma^+$ state and $^2\Sigma^+(II)$ state ("A") with and a single other component as defined in table D.11.

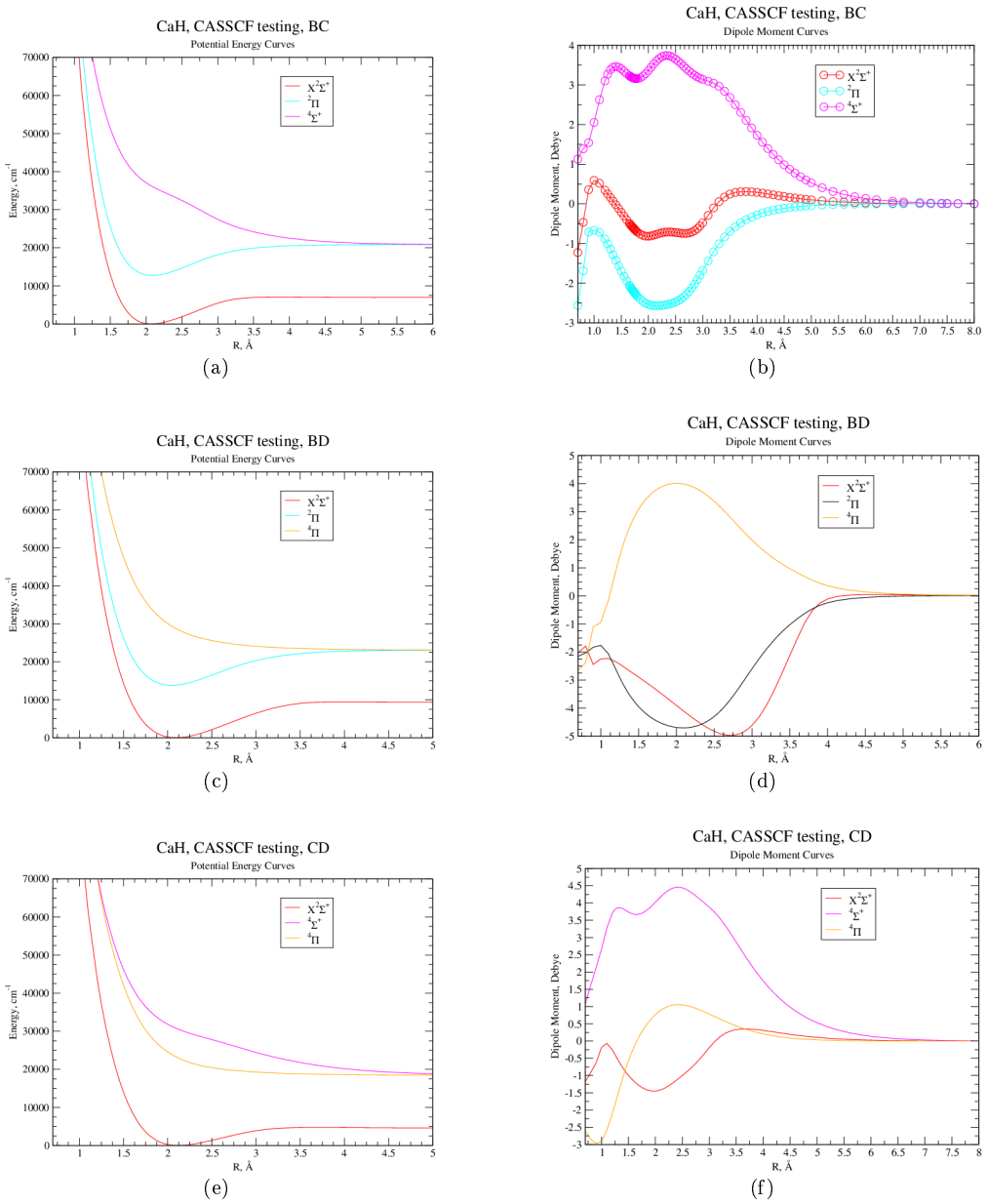

Figure D.17: CASSCF calculations of PECs and DMCs for CaH using a cc-pVQZ basis set that combine the ground $X^2\Sigma^+$ state and two other components as defined in table D.11.

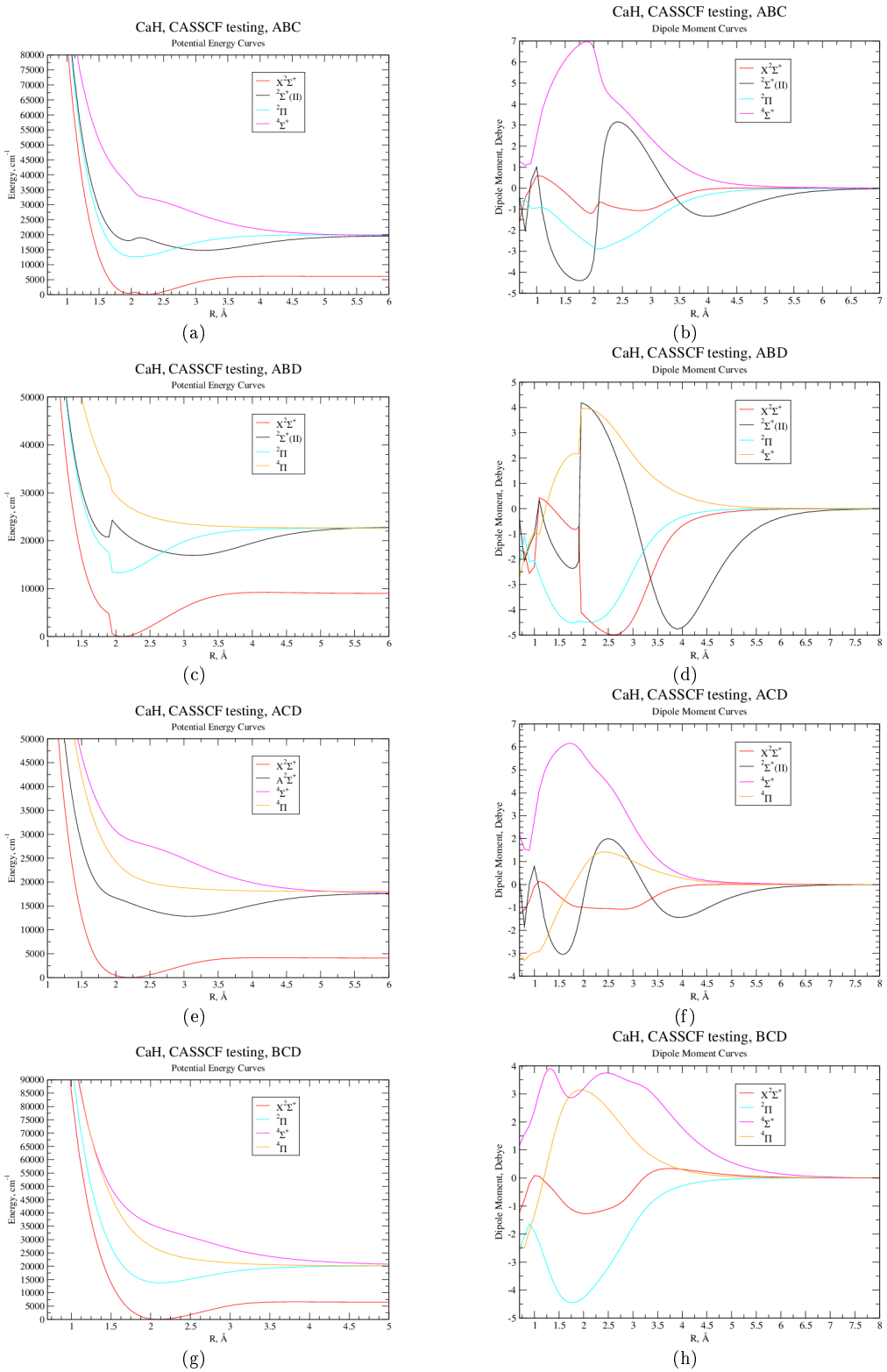

Figure D.18: CASSCF calculations of PECs and DMCs for CaH using a cc-pVQZ basis set that combine the ground $X^2\Sigma^+$ state and three other components as defined in table D.11.

These preliminary CASSCF orbital testing results can thus act as a guide to what combinations of states will give favourable convergence properties at CI level. For each set of CASSCF orbitals generated, PECs and DMCs for the five lowest-lying states

of BeH, MgH and CaH have been calculated at CI level. Maps of the inter-nuclear distances which converge for these various states at CI level for the different CASSCF calculations (i.e. different combinations of states put in a CASSCF calculation) are shown in section D.3.

D.3 Convergence at CI level as a function of CASSCF orbitals

In the following tables, a • symbol indicates that the CI calculation converged for this inter-nuclear distance using the CASSCF orbitals generated from combining various states (e.g. A, BC, ABCD etc) converged. A • symbol indicates that, according to `MOLPRO` there was insufficient overlap between the various orbitals and a • symbol indicates that there was a "Catastrophic failure in diagonalization (hsdel)". The CI calculations run are the *PROCs S6*, *S3*, *S4* and *S5* as defined in table D.10. In the following tables the inter-nuclear distances are those of the "rgeom" matrix summarised in section 2.7.1. The letters going along the horizontal are defined in table D.11; the letter X refers to the CASSCF calculation described in section D. As a reminder, it should be noted when interpreting these tables that convergence does not always guarantee that the curves plotted from these "converged" points will be devoid of discontinuities. For BeH, for the case of calculating the PEC and DMC of the $^4\Pi$ state, all points for all inter-nuclear distances and various CASSCF calculations converged. For the case of calculating the PEC and DMC of the $^4\Sigma^+$ state of MgH, all points for all inter-nuclear distances and various CASSCF calculations converged.

$R()$	X	A	B	C	D	AB	AC	AD	BC	BD	CD	ABC	ABD	ACD	BCD	ABCD
0.70		●		●		●	●	●	●		●	●		●	●	●
0.80		●		●		●	●	●	●		●	●	●	●	●	●
0.90		●		●		●	●	●	●		●	●		●	●	●
1.00		●		●		●	●	●	●		●	●		●	●	●
1.10		●		●			●		●		●	●		●	●	●
1.20	●	●	●	●	●	●	●	●	●	●	●	●	●	●	●	●
1.25	●	●	●	●	●	●	●	●	●	●	●	●	●	●	●	●
1.30	●	●	●		●	●	●	●	●	●	●	●	●	●	●	●
1.35	●	●	●		●	●	●	●	●	●	●	●	●	●	●	●
1.40	●	●	●		●	●	●	●	●	●	●	●	●	●	●	●
1.45	●	●	●	●	●	●	●	●	●	●	●	●	●	●	●	●
1.50	●	●	●	●	●	●	●	●	●	●	●	●	●	●	●	●
1.55	●	●	●	●	●	●	●	●	●	●	●	●	●	●	●	●
1.60	●	●	●	●	●	●	●	●	●	●	●	●	●	●	●	●
1.65	●	●	●	●	●	●	●	●	●	●	●	●	●	●	●	●
1.66	●	●	●	●	●	●	●	●	●	●	●	●	●	●	●	●
1.68	●	●	●	●	●	●	●	●	●	●	●	●	●	●	●	●
1.69	●	●	●	●	●	●	●	●	●	●	●	●	●	●	●	●
1.70	●	●	●	●	●	●	●	●	●	●	●	●	●	●	●	●
1.71	●	●	●	●	●	●	●	●	●	●	●	●	●	●	●	●
1.72	●	●	●	●	●	●	●	●	●	●	●	●	●	●	●	●
1.73	●	●	●	●	●	●	●	●	●	●	●	●	●	●	●	●
1.74	●	●	●	●	●	●	●	●	●	●	●	●	●	●	●	●
1.75	●	●	●	●	●	●	●	●	●	●	●	●	●	●	●	●
1.76	●	●	●	●	●	●	●	●	●	●	●	●	●	●	●	●
1.78	●	●	●	●	●	●	●	●	●	●	●	●	●	●	●	●
1.80	●	●	●	●	●	●	●	●	●	●	●	●	●	●	●	●
1.85	●	●	●	●	●	●	●	●	●	●	●	●	●	●	●	●
1.90	●	●	●	●	●	●	●	●	●	●	●	●	●	●	●	●
1.95	●	●	●	●	●	●	●	●	●	●	●	●	●	●	●	●
2.00	●	●	●	●	●	●	●	●	●	●	●	●	●	●	●	●
2.05	●	●	●	●	●	●	●	●	●	●	●	●	●	●	●	●
2.10	●	●	●	●	●	●	●	●	●	●	●	●	●	●	●	●
2.15	●	●	●	●	●	●	●	●	●	●	●	●	●	●	●	●
2.20	●	●	●	●	●	●	●	●	●	●	●	●	●	●	●	●
2.25	●	●	●	●	●	●	●	●	●	●	●		●	●	●	●
2.30	●	●	●	●	●	●	●	●	●	●	●	●	●	●	●	●
2.35	●	●	●	●	●	●	●	●		●	●	●	●			●
2.40	●	●	●	●	●	●	●	●		●	●		●			
2.45	●	●	●	●	●	●	●			●	●					
2.50	●			●	●						●					
2.55	●			●	●						●					
2.60	●			●	●						●					
2.65	●			●	●						●					
2.70	●			●	●						●					
2.75	●			●	●						●					
2.80	●	●		●	●		●				●					
2.85	●	●		●	●		●				●					
2.90	●	●		●	●		●				●					
2.95	●	●		●	●		●			●	●					
3.00	●	●	●	●	●		●	●		●	●			●		
3.10	●	●	●	●	●		●	●		●	●			●		
3.20	●	●	●	●	●		●	●		●	●			●		
3.30	●	●	●	●	●		●	●	●	●	●			●	●	
3.40	●	●	●	●	●		●	●	●	●	●			●	●	
3.50	●	●	●	●	●		●	●	●	●	●			●	●	
3.60	●	●	●	●	●	●	●	●	●	●	●	●	●	●	●	●
3.70	●	●	●	●	●	●	●	●	●	●	●	●	●	●	●	●
3.80	●	●	●	●	●	●	●	●	●	●	●	●	●	●	●	●

Table D.13: Summary of convergence for BeH for CI calculations of the $X^2\Sigma^+$ and $^2\Sigma^+$ for a range of inter-nuclear distances R. For inter-nuclear distances greated than $R = 3.8$ Å, all CI calculations converged. The grid of inter-nuclear points is defined in section 2.7.1. The CI calculations were based on the orbitals produced by proceeding CASSCF calculations which were performed for different combinations of the various low-lying electronic states indicated by the letters A, B, C, and D: this lettering scheme is defined in table D.11.

$R()$	X	A	B	C	D	AB	AC	AD	BC	BD	CD	ABC	ABD	ACD	BCD	ABCD
0.70			●		●	●		●	●	●	●	●	●	●	●	●
0.80			●		●	●		●	●	●	●	●	●	●	●	●
0.90			●		●	●		●	●	●	●	●	●	●	●	●
1.00			●		●	●		●	●	●	●	●	●	●	●	●
1.10			●		●	●		●	●	●	●	●	●	●	●	●
1.20		●	●		●	●	●	●	●	●	●	●	●	●	●	●
1.25		●	●		●	●	●	●	●	●	●	●	●	●	●	●
1.30		●	●		●	●	●	●	●	●	●	●	●	●	●	●
1.35		●	●		●	●	●	●	●	●	●	●	●	●	●	●
1.40		●	●		●	●	●	●	●	●	●	●	●	●	●	●
1.45		●	●		●	●	●	●	●	●	●	●	●	●	●	●
1.50		●	●		●	●	●	●	●	●	●	●	●	●	●	●
1.55		●	●		●	●	●	●	●	●	●	●	●	●	●	●
1.60		●	●		●	●	●	●	●	●	●	●	●	●	●	●
1.65		●	●		●	●	●	●	●	●	●	●	●	●	●	●
1.66		●	●		●	●	●	●	●	●	●	●	●	●	●	●
1.68		●	●		●	●	●	●	●	●	●	●	●	●	●	●
1.69		●	●		●	●	●	●	●	●	●	●	●	●	●	●
1.70		●	●		●	●	●	●	●	●	●	●	●	●	●	●
1.71		●	●		●	●	●	●	●	●	●	●	●	●	●	●
1.72		●	●	●	●	●	●	●	●	●	●	●	●	●	●	●
1.73		●	●	●	●	●	●	●	●	●	●	●	●	●	●	●
1.74		●	●	●	●	●	●	●	●	●	●	●	●	●	●	●
1.75	●	●	●	●	●	●	●	●	●	●	●	●	●	●	●	●
1.76	●	●	●	●	●	●	●	●	●	●	●	●	●	●	●	●
1.78	●	●	●	●	●	●	●	●	●	●	●	●	●	●	●	●
1.80	●	●	●	●	●	●	●	●	●	●	●	●	●	●	●	●

Table D.14: Summary of convergence for BeH for CI calculations of the $^2\Pi$ state for a range of inter-nuclear distances R. For inter-nuclear distances greated than $R = 1.8$ Å, all CI calculations converged. The grid of inter-nuclear points is defined in section 2.7.1. The CI calculations were based on the orbitals produced by proceeding CASSCF calculations which were performed for different combinations of the various low-lying electronic states indicated by the letters A, B, C, and D: this lettering scheme is defined in table D.11.

R (Å)	X	A	B	C	D	AB	AC	AD	BC	BD	CD	ABC	ABD	ACD	BCD	ABCD
0.70		●		●	●	●	●	●	●		●	●		●	●	●
0.80		●		●		●	●	●	●		●	●	●	●	●	●
0.90		●		●		●	●	●	●		●	●		●	●	●
1.00		●		●		●	●	●	●		●	●		●	●	●
1.10		●		●			●		●		●	●		●	●	●
1.20				●			●		●		●	●		●	●	●
1.25				●			●		●		●	●		●	●	●
1.30				●			●		●		●	●		●	●	●
1.35				●			●		●		●	●		●	●	●
1.40				●					●		●					
1.45				●												
1.50				●			●		●		●	●		●		
1.55	●	●	●	●	●	●	●	●	●		●	●	●	●	●	●
1.60	●	●	●	●	●	●	●	●	●	●	●	●	●	●	●	●
1.65	●	●	●	●	●	●	●	●	●	●	●	●	●	●	●	●
1.66	●	●	●	●	●	●	●	●	●	●	●	●	●	●	●	●
1.68	●	●	●	●	●	●	●	●	●	●	●	●	●	●	●	●
1.69	●	●	●	●	●	●	●	●	●	●	●	●	●	●	●	●
1.70	●	●	●	●	●	●	●	●	●	●	●	●	●	●	●	●

Table D.15: Summary of convergence for BeH for CI calculations of the $^4\Sigma^+$ state for a range of inter-nuclear distances R. For inter-nuclear distances greated than $R = 1.7$ Å, all CI calculations converged. The grid of inter-nuclear points is defined in section 2.7.1. The CI calculations were based on the orbitals produced by proceeding CASSCF calculations which were performed for different combinations of the various low-lying electronic states indicated by the letters A, B, C, and D: this lettering scheme is defined in table D.11.

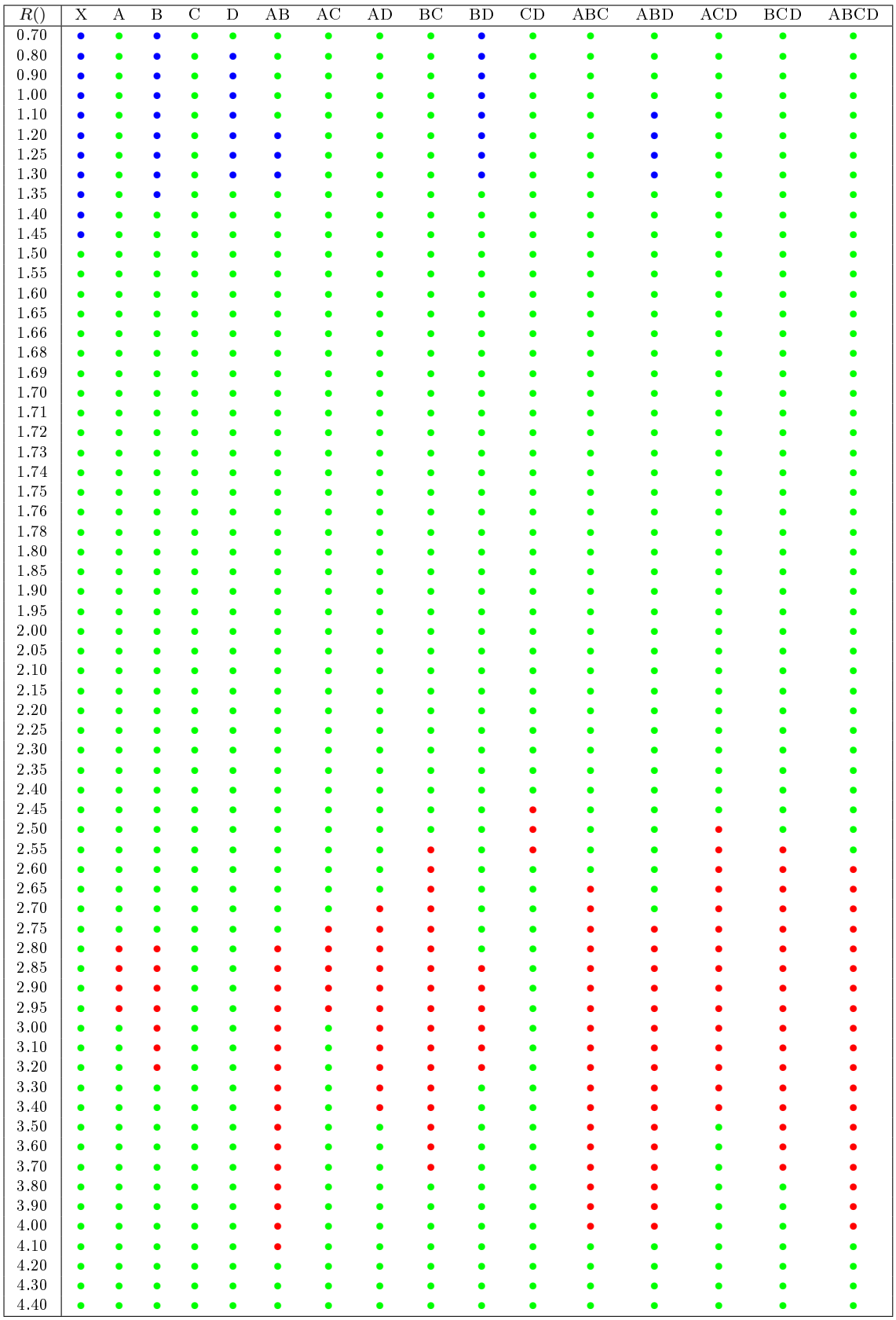

Table D.16: Summary of convergence for MgH for CI calculations of the $X^2\Sigma^+$ and $^2\Sigma^+$ state for a range of inter-nuclear distances R. For inter-nuclear distances greated than $R = 4.4$ Å, all CI calculations converged. The grid of inter-nuclear points is defined in section 2.7.1. The CI calculations were based on the orbitals produced by proceeding CASSCF calculations which were performed for different combinations of the various low-lying electronic states indicated by the letters A, B, C, and D: this lettering scheme is defined in table D.11.

$R()$	X	A	B	C	D	AB	AC	AD	BC	BD	CD	ABC	ABD	ACD	BCD	ABCD
	X	A	B	C	D	AB	AC	AD	BC	BD	CD	ABC	ABD	ACD	BCD	ABCD
0.70	●	●	●	●	●	●	●	●	●	●	●	●	●	●	●	●
0.80	●	●	●	●	●	●	●	●	●	●	●	●	●	●	●	●
0.90	●	●	●	●	●	●	●	●	●	●	●	●	●	●	●	●
1.00	●	●	●	●	●	●	●	●	●	●	●	●	●	●	●	●
1.10	●	●	●	●	●	●	●	●	●	●	●	●	●	●	●	●
1.20	●	●	●	●	●	●	●	●	●	●	●	●	●	●	●	●
1.25	●	●	●	●	●	●	●	●	●	●	●	●	●	●	●	●
1.30	●	●	●	●	●	●	●	●	●	●	●	●	●	●	●	●
1.35	●	●	●	●	●	●	●	●	●	●	●	●	●	●	●	●
1.40	●	●	●	●	●	●	●	●	●	●	●	●	●	●	●	●
1.45	●	●	●	●	●	●	●	●	●	●	●	●	●	●	●	●
1.50	●	●	●	●	●	●	●	●	●	●	●	●	●	●	●	●
1.55	●	●	●	●	●	●	●	●	●	●	●	●	●	●	●	●
1.60	●	●	●	●	●	●	●	●	●	●	●	●	●	●	●	●
1.65	●	●	●	●	●	●	●	●	●	●	●	●	●	●	●	●
1.66	●	●	●	●	●	●	●	●	●	●	●	●	●	●	●	●
1.68	●	●	●	●	●	●	●	●	●	●	●	●	●	●	●	●
1.69	●	●	●	●	●	●	●	●	●	●	●	●	●	●	●	●
1.70	●	●	●	●	●	●	●	●	●	●	●	●	●	●	●	●
1.71	●	●	●	●	●	●	●	●	●	●	●	●	●	●	●	●
1.72	●	●	●	●	●	●	●	●	●	●	●	●	●	●	●	●
1.73	●	●	●	●	●	●	●	●	●	●	●	●	●	●	●	●
1.74	●	●	●	●	●	●	●	●	●	●	●	●	●	●	●	●
1.75	●	●	●	●	●	●	●	●	●	●	●	●	●	●	●	●
1.76	●	●	●	●	●	●	●	●	●	●	●	●	●	●	●	●
1.78	●	●	●	●	●	●	●	●	●	●	●	●	●	●	●	●
1.80	●	●	●	●	●	●	●	●	●	●	●	●	●	●	●	●
1.85	●	●	●	●	●	●	●	●	●	●	●	●	●	●	●	●
1.90	●	●	●	●	●	●	●	●	●	●	●	●	●	●	●	●
1.95	●	●	●	●	●	●	●	●	●	●	●	●	●	●	●	●
2.00	●	●	●	●	●	●	●	●	●	●	●	●	●	●	●	●
2.05	●	●	●	●	●	●	●	●	●	●	●	●	●	●	●	●
2.10	●	●	●	●	●	●	●	●	●	●	●	●	●	●	●	●

Table D.17: Summary of convergence for MgH for CI calculations of the $^2\Pi$ state for a range of inter-nuclear distances R. For inter-nuclear distances greated than $R = 2.1$ Å, all CI calculations converged. The grid of inter-nuclear points is defined in section 2.7.1. The CI calculations were based on the orbitals produced by proceeding CASSCF calculations which were performed for different combinations of the various low-lying electronic states indicated by the letters A, B, C, and D: this lettering scheme is defined in table D.11.

R()	X	A	B	C	D	AB	AC	AD	BC	BD	CD	ABC	ABD	ACD	BCD	ABCD
	X	A	B	C	D	AB	AC	AD	BC	BD	CD	ABC	ABD	ACD	BCD	ABCD
0.70	●	●	●	●	●	●	●	●	●	●	●	●	●	●	●	●
0.80	●	●	●	●	●	●	●	●	●	●	●	●	●	●	●	●
0.90	●	●	●	●	●	●	●	●	●	●	●	●	●	●	●	●
1.00	●	●	●	●	●	●	●	●	●	●	●	●	●	●	●	●
1.10	●	●	●	●	●	●	●	●	●	●	●	●	●	●	●	●
1.20	●	●	●	●	●	●	●	●	●	●	●	●	●	●	●	●
1.25	●	●	●	●	●	●	●	●	●	●	●	●	●	●	●	●
1.30	●	●	●	●	●	●	●	●	●	●	●	●	●	●	●	●
1.35	●	●	●	●	●	●	●	●	●	●	●	●	●	●	●	●
1.40	●	●	●	●	●	●	●	●	●	●	●	●	●	●	●	●
1.45	●	●	●	●	●	●	●	●	●	●	●	●	●	●	●	●
1.50	●	●	●	●	●	●	●	●	●	●	●	●	●	●	●	●
1.55	●	●	●	●	●	●	●	●	●	●	●	●	●	●	●	●
1.60	●	●	●	●	●	●	●	●	●	●	●	●	●	●	●	●
1.65	●	●	●	●	●	●	●	●	●	●	●	●	●	●	●	●
1.66	●	●	●	●	●	●	●	●	●	●	●	●	●	●	●	●
1.68	●	●	●	●	●	●	●	●	●	●	●	●	●	●	●	●
1.69	●	●	●	●	●	●	●	●	●	●	●	●	●	●	●	●
1.70	●	●	●	●	●	●	●	●	●	●	●	●	●	●	●	●
1.71	●	●	●	●	●	●	●	●	●	●	●	●	●	●	●	●
1.72	●	●	●	●	●	●	●	●	●	●	●	●	●	●	●	●
1.73	●	●	●	●	●	●	●	●	●	●	●	●	●	●	●	●
1.74	●	●	●	●	●	●	●	●	●	●	●	●	●	●	●	●
1.75	●	●	●	●	●	●	●	●	●	●	●	●	●	●	●	●
1.76	●	●	●	●	●	●	●	●	●	●	●	●	●	●	●	●
1.78	●	●	●	●	●	●	●	●	●	●	●	●	●	●	●	●
1.80	●	●	●	●	●	●	●	●	●	●	●	●	●	●	●	●
1.85	●	●	●	●	●	●	●	●	●	●	●	●	●	●	●	●
1.90	●	●	●	●	●	●	●	●	●	●	●	●	●	●	●	●
1.95	●	●	●	●	●	●	●	●	●	●	●	●	●	●	●	●
2.00	●	●	●	●	●	●	●	●	●	●	●	●	●	●	●	●
2.05	●	●	●	●	●	●	●	●	●	●	●	●	●	●	●	●
2.10	●	●	●	●	●	●	●	●	●	●	●	●	●	●	●	●

Table D.18: Summary of convergence for MgH for CI calculations of the $^4\Pi$ state for a range of inter-nuclear distances R. For inter-nuclear distances greated than $R = 2.1$ Å, all CI calculations converged. The grid of inter-nuclear points is defined in section 2.7.1. The CI calculations were based on the orbitals produced by proceeding CASSCF calculations which were performed for different combinations of the various low-lying electronic states indicated by the letters A, B, C, and D: this lettering scheme is defined in table D.11.

$R()$	X	A	B	C	D	AB	AC	AD	BC	BD	CD	ABC	ABD	ACD	BCD	ABCD
0.70	●	●	●	●	●	●	●	●	●	●	●	●	●	●	●	●
0.80	●	●	●	●	●	●	●	●	●	●	●	●	●	●	●	●
0.90	●	●	●	●	●	●	●	●	●	●	●	●	●	●	●	●
1.00	●	●	●	●	●	●	●	●	●	●	●	●	●	●	●	●
1.10	●	●	●	●	●	●	●	●	●	●	●	●	●	●	●	●
1.20	●	●	●	●	●	●	●	●	●	●	●	●	●	●	●	●
1.25	●	●	●	●	●	●	●	●	●	●	●	●	●	●	●	●
1.30	●	●	●	●	●	●	●	●	●	●	●	●	●	●	●	●
1.35	●	●	●	●	●	●	●	●	●	●	●	●	●	●	●	●
1.40	●	●	●	●	●	●	●	●	●	●	●	●	●	●	●	●
1.45	●	●	●	●	●	●	●	●	●	●	●	●	●	●	●	●
1.50	●	●	●	●	●	●	●	●	●	●	●	●	●	●	●	●
1.55	●	●	●	●	●	●	●	●	●	●	●	●	●	●	●	●
1.60	●	●	●	●	●	●	●	●	●	●	●	●	●	●	●	●
1.65	●	●	●	●	●	●	●	●	●	●	●	●	●	●	●	●
1.66	●	●	●	●	●	●	●	●	●	●	●	●	●	●	●	●
1.68	●	●	●	●	●	●	●	●	●	●	●	●	●	●	●	●
1.69	●	●	●	●	●	●	●	●	●	●	●	●	●	●	●	●
1.70	●	●	●	●	●	●	●	●	●	●	●	●	●	●	●	●
1.71	●	●	●	●	●	●	●	●	●	●	●	●	●	●	●	●
1.72	●	●	●	●	●	●	●	●	●	●	●	●	●	●	●	●
1.73	●	●	●	●	●	●	●	●	●	●	●	●	●	●	●	●
1.74	●	●	●	●	●	●	●	●	●	●	●	●	●	●	●	●
1.75	●	●	●	●	●	●	●	●	●	●	●	●	●	●	●	●
1.76	●	●	●	●	●	●	●	●	●	●	●	●	●	●	●	●
1.78	●	●	●	●	●	●	●	●	●	●	●	●	●	●	●	●
1.80	●	●	●	●	●	●	●	●	●	●	●	●	●	●	●	●
1.85	●	●	●	●	●	●	●	●	●	●	●	●	●	●	●	●
1.90	●	●	●	●	●	●	●	●	●	●	●	●	●	●	●	●
1.95	●	●	●	●	●	●	●	●	●	●	●	●	●	●	●	●
2.00	●	●	●	●	●	●	●	●	●	●	●	●	●	●	●	●
2.05	●	●	●	●	●	●	●	●	●	●	●	●	●	●	●	●
2.10	●	●	●	●	●	●	●	●	●	●	●	●	●	●	●	●
2.15	●	●	●	●	●	●	●	●	●	●	●	●	●	●	●	●
2.20	●	●	●	●	●	●	●	●	●	●	●	●	●	●	●	●
2.25	●	●	●	●	●	●	●	●	●	●	●	●	●	●	●	●
2.30	●	●	●	●	●	●	●	●	●	●	●	●	●	●	●	●
2.35	●	●	●	●	●	●	●	●	●	●	●	●	●	●	●	●
2.40	●	●	●	●	●	●	●	●	●	●	●	●	●	●	●	●
2.45	●	●	●	●	●	●	●	●	●	●	●	●	●	●	●	●
2.50	●	●	●	●	●	●	●	●	●	●	●	●	●	●	●	●
2.55	●	●	●	●	●	●	●	●	●	●	●	●	●	●	●	●
2.60	●	●	●	●	●	●	●	●	●	●	●	●	●	●	●	●
2.65	●	●	●	●	●	●	●	●	●	●	●	●	●	●	●	●
2.70	●	●	●	●	●	●	●	●	●	●	●	●	●	●	●	●
2.75	●	●	●	●	●	●	●	●	●	●	●	●	●	●	●	●
2.80	●	●	●	●	●	●	●	●	●	●	●	●	●	●	●	●
2.85	●	●	●	●	●	●	●	●	●	●	●	●	●	●	●	●
2.90	●	●	●	●	●	●	●	●	●	●	●	●	●	●	●	●
2.95	●	●	●	●	●	●	●	●	●	●	●	●	●	●	●	●
3.00	●	●	●	●	●	●	●	●	●	●	●	●	●	●	●	●
3.10	●	●	●	●	●	●	●	●	●	●	●	●	●	●	●	●

Table D.19: Summary of convergence for CaH for CI calculations of the $X^2\Sigma^+$ and $^2\Sigma^+$ states for a range of inter-nuclear distances R. The grid of inter-nuclear points is defined in section 2.7.1. The CI calculations were based on the orbitals produced by proceeding CASSCF calculations which were performed for different combinations of the various low-lying electronic states indicated by the letters A, B, C, and D: this lettering scheme is defined in table D.11.

R()	X	A	B	C	D	AB	AC	AD	BC	BD	CD	ABC	ABD	ACD	BCD	ABCD
3.20	●	●	●	●	●	●	●	●	●	●	●	●	●	●	●	●
3.30	●	●	●	●	●	●	●	●	●	●	●	●	●	●	●	●
3.40	●	●	●	●	●	●	●	●	●	●	●	●	●	●	●	●
3.50	●	●	●	●	●	●	●	●	●	●	●	●	●	●	●	●
3.60	●	●	●	●	●	●	●	●	●	●	●	●	●	●	●	●
3.70	●	●	●	●	●	●	●	●	●	●	●	●	●	●	●	●
3.80	●	●	●	●	●	●	●	●	●	●	●	●	●	●	●	●
3.90	●	●	●	●	●	●	●	●	●	●	●	●	●	●	●	●
4.00	●	●	●	●	●	●	●	●	●	●	●	●	●	●	●	●
4.10	●	●	●	●	●	●	●	●	●	●	●	●	●	●	●	●
4.20	●	●	●	●	●	●	●	●	●	●	●	●	●	●	●	●
4.30	●	●	●	●	●	●	●	●	●	●	●	●	●	●	●	●
4.40	●	●	●	●	●	●	●	●	●	●	●	●	●	●	●	●
4.50	●	●	●	●	●	●	●	●	●	●	●	●	●	●	●	●
4.60	●	●	●	●	●	●	●	●	●	●	●	●	●	●	●	●
4.70	●	●	●	●	●	●	●	●	●	●	●	●	●	●	●	●
4.80	●	●	●	●	●	●	●	●	●	●	●	●	●	●	●	●
4.90	●	●	●	●	●	●	●	●	●	●	●	●	●	●	●	●
5.00	●	●	●	●	●	●	●	●	●	●	●	●	●	●	●	●
5.20	●	●	●	●	●	●	●	●	●	●	●	●	●	●	●	●
5.40	●	●	●	●	●	●	●	●	●	●	●	●	●	●	●	●
5.60	●	●	●	●	●	●	●	●	●	●	●	●	●	●	●	●

Table D.20: Summary of convergence for CaH for CI calculations of the $X^2\Sigma^+$ and $^2\Sigma^+$ states for a range of inter-nuclear distances R. For inter-nuclear distances greated than R = 5.6 Å, all CI calculations converged. The grid of inter-nuclear points is defined in section 2.7.1. The CI calculations were based on the orbitals produced by proceeding CASSCF calculations which were performed for different combinations of the various low-lying electronic states indicated by the letters A, B, C, and D: this lettering scheme is defined in table D.11.

R()	X	A	B	C	D	AB	AC	AD	BC	BD	CD	ABC	ABD	ACD	BCD	ABCD
0.70	●	●	●	●	●	●	●	●	●	●	●	●	●	●	●	●
0.80	●	●	●	●	●	●	●	●	●	●	●	●	●	●	●	●
0.90	●	●	●	●	●	●	●	●	●	●	●	●	●	●	●	●
1.00	●	●	●	●	●	●	●	●	●	●	●	●	●	●	●	●
1.10	●	●	●	●	●	●	●	●	●	●	●	●	●	●	●	●
1.20	●	●	●	●	●	●	●	●	●	●	●	●	●	●	●	●
1.25	●	●	●	●	●	●	●	●	●	●	●	●	●	●	●	●
1.30	●	●	●	●	●	●	●	●	●	●	●	●	●	●	●	●
1.35	●	●	●	●	●	●	●	●	●	●	●	●	●	●	●	●
1.40	●	●	●	●	●	●	●	●	●	●	●	●	●	●	●	●
1.45	●	●	●	●	●	●	●	●	●	●	●	●	●	●	●	●
1.50	●	●	●	●	●	●	●	●	●	●	●	●	●	●	●	●
1.55	●	●	●	●	●	●	●	●	●	●	●	●	●	●	●	●
1.60	●	●	●	●	●	●	●	●	●	●	●	●	●	●	●	●
1.65	●	●	●	●	●	●	●	●	●	●	●	●	●	●	●	●
1.66	●	●	●	●	●	●	●	●	●	●	●	●	●	●	●	●
1.68	●	●	●	●	●	●	●	●	●	●	●	●	●	●	●	●
1.69	●	●	●	●	●	●	●	●	●	●	●	●	●	●	●	●
1.70	●	●	●	●	●	●	●	●	●	●	●	●	●	●	●	●
1.71	●	●	●	●	●	●	●	●	●	●	●	●	●	●	●	●
1.72	●	●	●	●	●	●	●	●	●	●	●	●	●	●	●	●
1.73	●	●	●	●	●	●	●	●	●	●	●	●	●	●	●	●
1.74	●	●	●	●	●	●	●	●	●	●	●	●	●	●	●	●
1.75	●	●	●	●	●	●	●	●	●	●	●	●	●	●	●	●
1.76	●	●	●	●	●	●	●	●	●	●	●	●	●	●	●	●
1.78	●	●	●	●	●	●	●	●	●	●	●	●	●	●	●	●
1.80	●	●	●	●	●	●	●	●	●	●	●	●	●	●	●	●
1.85	●	●	●	●	●	●	●	●	●	●	●	●	●	●	●	●
1.90	●	●	●	●	●	●	●	●	●	●	●	●	●	●	●	●
1.95	●	●	●	●	●	●	●	●	●	●	●	●	●	●	●	●
2.00	●	●	●	●	●	●	●	●	●	●	●	●	●	●	●	●
2.05	●	●	●	●	●	●	●	●	●	●	●	●	●	●	●	●
2.10	●	●	●	●	●	●	●	●	●	●	●	●	●	●	●	●
2.15	●	●	●	●	●	●	●	●	●	●	●	●	●	●	●	●
2.20	●	●	●	●	●	●	●	●	●	●	●	●	●	●	●	●
2.25	●	●	●	●	●	●	●	●	●	●	●	●	●	●	●	●
2.30	●	●	●	●	●	●	●	●	●	●	●	●	●	●	●	●
2.35	●	●	●	●	●	●	●	●	●	●	●	●	●	●	●	●
2.40	●	●	●	●	●	●	●	●	●	●	●	●	●	●	●	●
2.45	●	●	●	●	●	●	●	●	●	●	●	●	●	●	●	●
2.50	●	●	●	●	●	●	●	●	●	●	●	●	●	●	●	●
2.55	●	●	●	●	●	●	●	●	●	●	●	●	●	●	●	●
2.60	●	●	●	●	●	●	●	●	●	●	●	●	●	●	●	●
2.65	●	●	●	●	●	●	●	●	●	●	●	●	●	●	●	●
2.70	●	●	●	●	●	●	●	●	●	●	●	●	●	●	●	●
2.75	●	●	●	●	●	●	●	●	●	●	●	●	●	●	●	●
2.80	●	●	●	●	●	●	●	●	●	●	●	●	●	●	●	●
2.85	●	●	●	●	●	●	●	●	●	●	●	●	●	●	●	●
2.90	●	●	●	●	●	●	●	●	●	●	●	●	●	●	●	●
2.95	●	●	●	●	●	●	●	●	●	●	●	●	●	●	●	●
3.00	●	●	●	●	●	●	●	●	●	●	●	●	●	●	●	●

Table D.21: Summary of convergence for CaH for CI calculations of the $^2\Pi$ states for a range of inter-nuclear distances R. For inter-nuclear distances greated than $R = 3.0$ Å, all CI calculations converged. The grid of inter-nuclear points is defined in section 2.7.1. The CI calculations were based on the orbitals produced by proceeding CASSCF calculations which were performed for different combinations of the various low-lying electronic states indicated by the letters A, B, C, and D: this lettering scheme is defined in table D.11.

R()	X	A	B	C	D	AB	AC	AD	BC	BD	CD	ABC	ABD	ACD	BCD	ABCD
	X	A	B	C	D	AB	AC	AD	BC	BD	CD	ABC	ABD	ACD	BCD	ABCD
0.70	●	●	●	●	●	●	●	●	●	●	●	●	●	●	●	●
0.80	●	●	●	●	●	●	●	●	●	●	●	●	●	●	●	●
0.90	●	●	●	●	●	●	●	●	●	●	●	●	●	●	●	●
1.00	●	●	●	●	●	●	●	●	●	●	●	●	●	●	●	●
1.10	●	●	●	●	●	●	●	●	●	●	●	●	●	●	●	●
1.20	●	●	●	●	●	●	●	●	●	●	●	●	●	●	●	●
1.25	●	●	●	●	●	●	●	●	●	●	●	●	●	●	●	●
1.30	●	●	●	●	●	●	●	●	●	●	●	●	●	●	●	●
1.35	●	●	●	●	●	●	●	●	●	●	●	●	●	●	●	●
1.40	●	●	●	●	●	●	●	●	●	●	●	●	●	●	●	●
1.45	●	●	●	●	●	●	●	●	●	●	●	●	●	●	●	●
1.50	●	●	●	●	●	●	●	●	●	●	●	●	●	●	●	●
1.55	●	●	●	●	●	●	●	●	●	●	●	●	●	●	●	●
1.60	●	●	●	●	●	●	●	●	●	●	●	●	●	●	●	●
1.65	●	●	●	●	●	●	●	●	●	●	●	●	●	●	●	●
1.66	●	●	●	●	●	●	●	●	●	●	●	●	●	●	●	●
1.68	●	●	●	●	●	●	●	●	●	●	●	●	●	●	●	●
1.69	●	●	●	●	●	●	●	●	●	●	●	●	●	●	●	●
1.70	●	●	●	●	●	●	●	●	●	●	●	●	●	●	●	●
1.71	●	●	●	●	●	●	●	●	●	●	●	●	●	●	●	●
1.72	●	●	●	●	●	●	●	●	●	●	●	●	●	●	●	●
1.73	●	●	●	●	●	●	●	●	●	●	●	●	●	●	●	●
1.74	●	●	●	●	●	●	●	●	●	●	●	●	●	●	●	●
1.75	●	●	●	●	●	●	●	●	●	●	●	●	●	●	●	●
1.76	●	●	●	●	●	●	●	●	●	●	●	●	●	●	●	●
1.78	●	●	●	●	●	●	●	●	●	●	●	●	●	●	●	●
1.80	●	●	●	●	●	●	●	●	●	●	●	●	●	●	●	●
1.85	●	●	●	●	●	●	●	●	●	●	●	●	●	●	●	●
1.90	●	●	●	●	●	●	●	●	●	●	●	●	●	●	●	●
1.95	●	●	●	●	●	●	●	●	●	●	●	●	●	●	●	●
2.00	●	●	●	●	●	●	●	●	●	●	●	●	●	●	●	●
2.05	●	●	●	●	●	●	●	●	●	●	●	●	●	●	●	●
2.10	●	●	●	●	●	●	●	●	●	●	●	●	●	●	●	●
2.15	●	●	●	●	●	●	●	●	●	●	●	●	●	●	●	●
2.20	●	●	●	●	●	●	●	●	●	●	●	●	●	●	●	●
2.25	●	●	●	●	●	●	●	●	●	●	●	●	●	●	●	●
2.30	●	●	●	●	●	●	●	●	●	●	●	●	●	●	●	●
2.35	●	●	●	●	●	●	●	●	●	●	●	●	●	●	●	●
2.40	●	●	●	●	●	●	●	●	●	●	●	●	●	●	●	●
2.45	●	●	●	●	●	●	●	●	●	●	●	●	●	●	●	●
2.50	●	●	●	●	●	●	●	●	●	●	●	●	●	●	●	●
2.55	●	●	●	●	●	●	●	●	●	●	●	●	●	●	●	●
2.60	●	●	●	●	●	●	●	●	●	●	●	●	●	●	●	●
2.65	●	●	●	●	●	●	●	●	●	●	●	●	●	●	●	●
2.70	●	●	●	●	●	●	●	●	●	●	●	●	●	●	●	●
2.75	●	●	●	●	●	●	●	●	●	●	●	●	●	●	●	●
2.80	●	●	●	●	●	●	●	●	●	●	●	●	●	●	●	●
2.85	●	●	●	●	●	●	●	●	●	●	●	●	●	●	●	●
2.90	●	●	●	●	●	●	●	●	●	●	●	●	●	●	●	●
2.95	●	●	●	●	●	●	●	●	●	●	●	●	●	●	●	●
3.00	●	●	●	●	●	●	●	●	●	●	●	●	●	●	●	●

Table D.22: Summary of convergence for CaH for CI calculations of the $^4\Sigma^+$ states for a range of inter-nuclear distances R. For inter-nuclear distances greated than $R = 3.0$ Å, all CI calculations converged. The grid of inter-nuclear points is defined in section 2.7.1. The CI calculations were based on the orbitals produced by proceeding CASSCF calculations which were performed for different combinations of the various low-lying electronic states indicated by the letters A, B, C, and D: this lettering scheme is defined in table D.11.

R()	X	A	B	C	D	AB	AC	AD	BC	BD	CD	ABC	ABD	ACD	BCD	ABCD
0.70	●	●	●	●	●	●	●	●	●	●	●	●	●	●	●	●
0.80	●	●	●	●	●	●	●	●	●	●	●	●	●	●	●	●
0.90	●	●	●	●	●	●	●	●	●	●	●	●	●	●	●	●
1.00	●	●	●	●	●	●	●	●	●	●	●	●	●	●	●	●
1.10	●	●	●	●	●	●	●	●	●	●	●	●	●	●	●	●
1.20	●	●	●	●	●	●	●	●	●	●	●	●	●	●	●	●
1.25	●	●	●	●	●	●	●	●	●	●	●	●	●	●	●	●
1.30	●	●	●	●	●	●	●	●	●	●	●	●	●	●	●	●
1.35	●	●	●	●	●	●	●	●	●	●	●	●	●	●	●	●
1.40	●	●	●	●	●	●	●	●	●	●	●	●	●	●	●	●
1.45	●	●	●	●	●	●	●	●	●	●	●	●	●	●	●	●
1.50	●	●	●	●	●	●	●	●	●	●	●	●	●	●	●	●
1.55	●	●	●	●	●	●	●	●	●	●	●	●	●	●	●	●
1.60	●	●	●	●	●	●	●	●	●	●	●	●	●	●	●	●
1.65	●	●	●	●	●	●	●	●	●	●	●	●	●	●	●	●
1.66	●	●	●	●	●	●	●	●	●	●	●	●	●	●	●	●
1.68	●	●	●	●	●	●	●	●	●	●	●	●	●	●	●	●
1.69	●	●	●	●	●	●	●	●	●	●	●	●	●	●	●	●
1.70	●	●	●	●	●	●	●	●	●	●	●	●	●	●	●	●
1.71	●	●	●	●	●	●	●	●	●	●	●	●	●	●	●	●
1.72	●	●	●	●	●	●	●	●	●	●	●	●	●	●	●	●
1.73	●	●	●	●	●	●	●	●	●	●	●	●	●	●	●	●
1.74	●	●	●	●	●	●	●	●	●	●	●	●	●	●	●	●
1.75	●	●	●	●	●	●	●	●	●	●	●	●	●	●	●	●
1.76	●	●	●	●	●	●	●	●	●	●	●	●	●	●	●	●
1.78	●	●	●	●	●	●	●	●	●	●	●	●	●	●	●	●
1.80	●	●	●	●	●	●	●	●	●	●	●	●	●	●	●	●
1.85	●	●	●	●	●	●	●	●	●	●	●	●	●	●	●	●
1.90	●	●	●	●	●	●	●	●	●	●	●	●	●	●	●	●
1.95	●	●	●	●	●	●	●	●	●	●	●	●	●	●	●	●
2.00	●	●	●	●	●	●	●	●	●	●	●	●	●	●	●	●
2.05	●	●	●	●	●	●	●	●	●	●	●	●	●	●	●	●
2.10	●	●	●	●	●	●	●	●	●	●	●	●	●	●	●	●
2.15	●	●	●	●	●	●	●	●	●	●	●	●	●	●	●	●
2.20	●	●	●	●	●	●	●	●	●	●	●	●	●	●	●	●
2.25	●	●	●	●	●	●	●	●	●	●	●	●	●	●	●	●
2.30	●	●	●	●	●	●	●	●	●	●	●	●	●	●	●	●
2.35	●	●	●	●	●	●	●	●	●	●	●	●	●	●	●	●
2.40	●	●	●	●	●	●	●	●	●	●	●	●	●	●	●	●
2.45	●	●	●	●	●	●	●	●	●	●	●	●	●	●	●	●
2.50	●	●	●	●	●	●	●	●	●	●	●	●	●	●	●	●
2.55	●	●	●	●	●	●	●	●	●	●	●	●	●	●	●	●
2.60	●	●	●	●	●	●	●	●	●	●	●	●	●	●	●	●
2.65	●	●	●	●	●	●	●	●	●	●	●	●	●	●	●	●
2.70	●	●	●	●	●	●	●	●	●	●	●	●	●	●	●	●
2.75	●	●	●	●	●	●	●	●	●	●	●	●	●	●	●	●
2.80	●	●	●	●	●	●	●	●	●	●	●	●	●	●	●	●
2.85	●	●	●	●	●	●	●	●	●	●	●	●	●	●	●	●
2.90	●	●	●	●	●	●	●	●	●	●	●	●	●	●	●	●
2.95	●	●	●	●	●	●	●	●	●	●	●	●	●	●	●	●
3.00	●	●	●	●	●	●	●	●	●	●	●	●	●	●	●	●

Table D.23: Summary of convergence for CaH for CI calculations of the $^4\Pi$ states for a range of inter-nuclear distances R. For inter-nuclear distances greated than $R = 3.0$ Å, all CI calculations converged. The grid of inter-nuclear points is defined in section 2.7.1. The CI calculations were based on the orbitals produced by proceeding CASSCF calculations which were performed for different combinations of the various low-lying electronic states indicated by the letters A, B, C, and D: this lettering scheme is defined in table D.11.

Bibliography

[1] M. Abe, M. Kajita, M. Hada, and Y. Moriwaki. Ab initio study on vibrational dipole moments of XH^+ molecular ions: X=^{24}Mg, ^{40}Ca, ^{64}Zn, ^{88}Sr, ^{114}Cd, ^{138}Ba, ^{174}Yb and ^{202}Hg. *Journal of Physics B*, 43(24), DEC 28 2010.

[2] E. Abrahamsson, T. V. Tscherbul, and R. V. Krems. Inelastic collisions of cold polar molecules in nonparallel electric and magnetic fields. *Journal of Chemical Physics*, 127(4), JUL 28 2007.

[3] S. Aldridge and A. J. Downs. Hydrides of the main-group metals: New variations on an old theme. *Chemical Reviews*, 101(11):3305–3365, NOV 2001.

[4] F. Allard, D. R. Alexander, and P. H. Hauschildt. Model Atmospheres of Very Low Mass Stars and Brown Dwarfs. In R. A. Donahue and J. A. Bookbinder, editors, *Cool Stars, Stellar Systems, and the Sun*, volume 154 of *Astronomical Society of the Pacific Conference Series*, page 63, 1998.

[5] F. Allard, P. H. Hauschildt, D. R. Alexander, and S. Starrfield. Model Atmospheres of Very Low Mass Stars and Brown Dwarfs. *Annual Review of Astronomy and Astrophysics*, 35:137–177, 1997.

[6] F. Allard, P. H. Hauschildt, D. R. Alexander, A. Tamanai, and A. Schweitzer. The limiting effects of dust in brown dwarf model atmospheres. *Astrophysical Journal*, 556(1, Part 1):357–372, JUL 20 2001.

[7] F. Allard, D. Homeier, B. Freytag, Schaffenberger, W. , and A. S. Rajpurohit. Progress in modeling very low mass stars, brown dwarfs, and planetary mass objects. *Memorie della Societa Astronomica Italiana Supplementi*, 24:128, 2013.

[8] F. Allard, D. Homeier, B. Freytag, and C. M. Sharp. Atmospheres From Very Low-Mass Stars to Extrasolar Planets. In C. Reylé, C. Charbonnel, and M. Schultheis, editors, *EAS Publications Series*, volume 57 of *EAS Publications Series*, pages 3–43, 2012.

[9] R. W. Allmendinger. Inverse and forward numerical modeling of trishear fault-propagation folds. *Tectonics*, 17:640–656, August 1998.

[10] S. V. Alyabyshev, T. V. Tscherbul, and R. V. Krems. Microwave-laser-field modification of molecular collisions at low temperatures. *Physics Review A*, 79(6), JUN 2009.

[11] E. Anders and N. Grevesse. Abundances of the elements - Meteoritic and solar. *Geochimica et Cosmochimica Acta*, 53:197, 1989. doi:10.1016/0016-7037(89)90286-X.

[12] J. Anglada, P. J. Bruna, and F. Grein. Theoretical study of low-lying electronic states of CoH^+. *The Journal of Chemical Physics*, 92(11):6732–6741, 1990. doi:10.1063/1.458258.

[13] J. Anglada, P. J. Bruna, and S. D. Peyerimhoff. Theoretical investigation of the low-lying electronic states of TiH. *Molecular Physics*, 69:281–303, 1990.

[14] S. R. Arridge and J. C. Schotland. TOPICAL REVIEW: Optical tomography: forward and inverse problems. *Inverse Problems*, 25(12):123010, December 2009.

[15] L. W. Avery, M. B. Bell, C. T. Cunningham, P. A. Feldman, R. H. Hayward, J. M. Macleod, H. E. Matthews, and J. D. Wade. Submillimeter molecular line observations of IRC +10216: Searches for MgH, SiH_2, and hco(+), and detection of hot HCN. *Astrophysical Journal*, 426(2, Part 1):737–741, MAY 10 1994.

[16] M. Aymar, R. Guerout, M. Sahlaoui, and O. Dulieu. Electronic structure of the magnesium hydride molecular ion. *Journal of Physics B*, 42(15), AUG 14 2009.

[17] M. C. Bacchus-Montabonel and D. Talbi. A theoretical treatment of the LiH and BeH formation through radiative association. *Journal of Molecular Structure*, 463(1-2):91–97, APR 23 1999. 2nd European Conference on Computational Chemistry (EUCO-CC2), LISBON, PORTUGAL, SEP 02-06, 1997.

[18] P. S. Bagus and H. F. Schaefer III. $^7\Sigma^+$ and $^7\Pi$states of manganese hydride. *Journal of Chemical Physics*, 58(5):1844, 1973.

[19] P. S. Bagus, C. M. Moser, P. Goethals, and G. Verhaege. Accurate *ab initio* calculation of BeH. 1. $X^2\Sigma^+$ and $A^2\Pi$ states. *Journal of Chemical Physics*, 58(5), 1973.

[20] P. S. Bagus and H. F. Schaefer, III. $^7\Sigma^+$ and $^7\Pi$ states of manganese hydride. *Journal of Chemical Physics*, 58:1844–1848, March 1973. doi: 10.1063/1.1679441.

[21] C. A. L. Bailer-Jones. Correlated spectral variability in brown dwarfs. *Monthly Notices of the Royal Astronomical Society*, 384(3):1145–1157, MAR 1 2008.

[22] J. Bailey. The Dawes Review 3: The Atmospheres of Extrasolar Planets and Brown Dwarfs. *Publications of the Astronomical Society of Australia*, 31:e043, 2014.

[23] N. B. Balabanov and K. A. Peterson. Systematically convergent basis sets for transition metals. I. All-electron correlation consistent basis sets for the 3d elements Sc-Zn. *Journal of Chemical Physics*, 123(6):064107, August 2005. doi: 10.1063/1.1998907.

[24] N. Balakrishnan, G. C. Groenenboom, R. V. Krems, and A. Dalgarno. The he-cah($^2\Sigma^+$) interaction. ii. collisions at cold and ultracold temperatures. *Journal of Chemical Physics*, 118(16):7386–7393, APR 22 2003.

[25] W. J. BALFOUR. The electronic spectrum of magnesium hydride and magnesium deuteride. *Journal of Physics B*, 3(12):1749, 1970.

[26] W. J. Balfour. The $A^2\Pi - X^2\Sigma^+$ systems of ^{24}MgH, ^{25}MgH and ^{26}MgH. *Astrophysical Journal*, 162:1031, December 1970.

[27] W. J Balfour. MgH and MgD spectra in the 230 - 235 nm region. *Journal of Molecular Spectroscopy*, 79(2):507–511, 1980.

[28] W. J. Balfour. The electronic spectrum of manganese hydride. *Journal of Chemical Physics*, 88:5242–5243, April 1988.

[29] W. J. Balfour and H. M. Cartwright. The $^2\Pi - X^2\Sigma^+$system and dissociation energy of magnesium hydride. *Astronomy & Astrophysics Supplement Series*, 26:389, 1976.

[30] W. J. Balfour and H. M. Cartwright. The $A^2\Pi - X^2\Sigma^+$ system and dissociation energy of magnesium hydride. *Astronomy and Astrophysics Supplement Series*, 26:389–397, December 1976.

[31] W. J. Balfour and L. Klynning. On the carrier of the band at 700 nanometers in the iron hydride spectrum of phillips and davis: Evidence favoring calcium hydride. *The Astrophysical Journal*, 424(2, Part 1):1049–1053, APR 1 1994.

[32] W. J. Balfour, O. Launila, and L. Klynning. Fourier transform spectroscopy of MnH and MnD. *Molecular Physics*, 69:443–461, 1990.

[33] W. J. Balfour, B. Lindgren, O. Launila, S. O'Connor, and E. J. Cusack. The visible spectrum of manganese hydride: Rotational analyses of the 480- and 450-nm systems. *Journal of Molecular Spectroscopy*, 154:177–200, July 1992.

[34] W. J. Balfour, B. Lindgren, and S. O'Connor. On the 1 μm system of iron hydride. *Chemical Physics Letters*, 96(2):251–252, 1983.

[35] WJ Balfour, JM Brown, and L Wallace. Electronic spectra of iron monohydride in the infrared near 1.35 and 1.58 mu m. *Journal of Chemical Physics*, 121(16):7735–7742, OCT 22 2004.

[36] A. Bar-Nun, M. Pasternak, and P. H. Barrett. Iron hydrides formation in interstellar clouds. *Astronomy & Astrophysics*, 87(3):328–329, 1980.

[37] I. Baraffe, G. Chabrier, F. Allard, and P. H. Hauschildt. Evolutionary models for solar metallicity low-mass stars: mass-magnitude relationships and color-magnitude diagrams. *Astronomy and Astrophysics*, 337:403–412, September 1998.

[38] I. Baraffe, G. Chabrier, F. Allard, and P. H. Hauschildt. Evolutionary models for low-mass stars and brown dwarfs: Uncertainties and limits at very young ages. *Astronomy and Astrophysics*, 382:563–572, February 2002.

[39] I. Baraffe, G. Chabrier, T. S. Barman, F. Allard, and P. Hauschildt. Evolutionary models for cool brown dwarfs and extrasolar giant planets. The case of HD 209458. *Astronomy & Astrophysics*, 402:701, 2003. doi:10.1051/0004-6361:20030252.

[40] I. Baraffe, G. Chabrier, T. S. Barman, F. Allard, and P. H. Hauschildt. Evolutionary models for cool brown dwarfs and extrasolar giant planets. The case of HD 209458. *Astronomy and Astrophysics*, 402:701–712, May 2003.

[41] B. Barbuy, R. P. Schiavon, J. Gregoriohetem, P. D. Singh, and C Batalha. Intensity of caH Lines in Cool Dwarfs. *Astronomy and Astrophysics Supplement*, 101(2):409–413, OCT 1993.

[42] W. L. Barclay, M. A. Anderson, and M. Ziurys, L. The millimeter-wave spectrum of CaH($X^2\Sigma^+$). *The Astrophysical Journal*, 408(1, Part 2):L65–L67, MAY 1 1993.

[43] V. Barone and C. Adamo. First-row transition-metal hydrides: A challenging playground for new theoretical approaches. *International Journal of Quantum Chemistry*, 61(3):443–451, JAN 20 1997.

[44] V. Barone and C. Adamo. First-row transition-metal hydrides: A challenging playground for new theoretical approaches. *International Journal Of Quantum Chemistry*, 61:443–451, 1997.

[45] J. K. Barstow, S. Aigrain, P. Irwin, S. Kendrew, and L. N. Fletcher. Transit spectroscopy with JWST: Systematics, starspots and stitching. In *AAS/Division for Planetary Sciences Meeting Abstracts*, volume 46 of *AAS/Division for Planetary Sciences Meeting Abstracts*, 2014.

[46] J. K. Barstow, S. Aigrain, P. G. J. Irwin, N. Bowles, L. N. Fletcher, and J.-M. Lee. On the potential of the EChO mission to characterize gas giant atmospheres. *Monthly Notices of the Royal Astronomical Society*, 430:1188–1207, April 2013.

[47] J. K. Barstow, N. E. Bowles, S. Aigrain, L. N. Fletcher, P. G. J. Irwin, R. Varley, and E. Pascale. Exoplanet atmospheres with EChO: spectral retrievals using EChOSim. *Experimental Astronomy*, June 2014.

[48] C. A. Baumann, R. J. Van Zee, and W. Jr. J. Weltner. High-spin molecules: electron spin resonance of manganese halides and sulfide at 4 K. *Journal of Physical Chemistry*, 86:5084, 1982.

[49] C. W. Bauschlicher and S. R Langhoff. Theoretical confirmation of $a^4\Delta$ ground state for FeH. *Chemical Physics Letters*, 145(3):205–210, APR 1 1988.

[50] C. W. Bauschlicher, R. S. Ram, P. F. Bernath, C. G. Parsons, and D. Galehouse. The A $^6\Sigma^+$-X $^6\Sigma^+$ transition of CrH, Einstein coefficients, and an improved description of the A state. *Journal Of Chemical Physics*, 115:1312–1318, July 2001. doi:10.1063/1.1377892.

[51] C. W. Bauschlicher and S. P. Walch. On the d bond in ScH. *Journal of Chemical Physics*, 76(9):4560, 1982.

[52] J. L. Bean, J.-M. Désert, P. Kabath, B. Stalder, S. Seager, E. Miller-Ricci Kempton, Z. K. Berta, D. Homeier, S. Walsh, and A. Seifahrt. The Optical and Near-infrared Transmission Spectrum of the Super-Earth GJ 1214b: Further Evidence for a Metal-rich Atmosphere. *Astrophysical Journal*, 743:92, December 2011.

[53] J. L. Bean, E. Miller-Ricci Kempton, and D. Homeier. A ground-based transmission spectrum of the super-Earth exoplanet GJ 1214b. *Nature*, 468:669–672, December 2010.

[54] S. P. Beaton, K. M. Evenson, T. Nelis, and J. M. Brown. Detection of the free radicals FeH, CoH, and NiH by far infrared laser magnetic resonance. *Journal of Chemical Physics*, 89(7):4446–4448, OCT 1 1988.

[55] S. P. Beaton, K. M. Evenson, T. Nelis, and J. M. Brown. Detection of the free radicals FeH, CoH, and NiH by far infrared laser magnetic resonance. *The Journal of Chemical Physics*, 89(7):4446–4448, 1988. doi:10.1063/1.454781.

[56] F. Beitia, F. Castano, M. N. S. Rayo, R. Martinez, L. Santos, and D. Husain. Kinetic investigation of the collisional quenching of ca(4^3p_J) by c_4h_10 at elevated temperatures (750âĂŞ923 k). time-resolved atomic emission and electronic energy transfer between c(4^3p_J) and cah($X^2\Sigma^+$) observed by molecular chemiluminescence. *Journal of the Chemical Society-Faraday Trancactions*, 87(10):1503–1508, MAY 21 1991.

[57] G. D. Bell, M. Herman, J. W. C. Johns, and E. R. Peck. The $D^2\Sigma^+ - X^2\Sigma^+$ Band System of CaH. *Physica Scripta*, 20(5-6):609–616, 1979.

[58] R. A. Bell, B. Edvardsson, and B. Gustafsson. The surface gravity of Arcturus from MgH lines, strong metal lines and the ionization equilibrium of iron. *Monthly Notices of the Royal Astronomical Society*, 212(3):497–515, 1985.

[59] R. A. Bell and M. J. Tripicco. Molecular equilibria and the luminosity classification of G and K stars. *Astronomical Journal*, 102(2):777–786, AUG 1991.

[60] D. Ben Abdallah, F. Najar, N. Jaidane, Z. Ben Lakhdar, N. Feautrier, A. Spielfiedel, and F. Lique. Ab initio potential energy surfaces for the $^1a'$ and $^3a'$ states of the MgH($x^2\sigma^+$) + h(^2s) system. *Chemical Physics Letters*, 473(1-3):39–42, APR 29 2009.

[61] S. V. Berdyugina, A. V. Berdyugin, D. M. Fluri, and V. Piirola. First Detection of Polarized Scattered Light from an Exoplanetary Atmosphere. *Astrophysical Journal Letters*, 673:L83–L86, January 2008.

[62] S. V. Berdyugina, D. M. Fluri, R. Ramelli, M. Bianda, D. Gisler, and J. O. Stenflo. First polarimetric measurements and modeling of the Paschen-Back effect in CaH transitions. *The Astrophysical Journal*, 649(1, Part 2):L49–L52, SEP 20 2006.

[63] S. V. Berdyugina, C. Frutiger, S. K. Solanki, and W. Livingstone. Successful spectral synthesis of Zeeman-split molecular bands in sunspot spectra. *Astronomy and Astrophysics*, 364(2):L101–L104, DEC 2000.

[64] S. V. Berdyugina and I. S. Savanov. Determination of the parameters of red giants' atmospheres - MgH as a luminosity criterion. *Astronomicheskii Zhurnal*, 69(4):829–841, JUL-AUG 1992.

[65] S. V. Berdyugina and S. K. Solanki. The molecular Zeeman effect and diagnostics of solar and stellar magnetic fields. I. Theoretical spectral patterns in the Zeeman regime. *Astronomy & Astrophysics*, 385:701–715, 2002. doi:10.1051/0004-6361:20020130.

[66] S. V. Berdyugina, S. K. Solanki, and C. Frutiger. Solar and Stellar Magnetic Fields: the Molecular Zeeman Effect as a Probe. In *ASP Conference Proceedings*, volume 248, page 99, 2001.

[67] S. V. Berdyugina, S. K. Solanki, and C. Frutiger. The molecular Zeeman effect and diagnostics of solar and stellar magnetic fields. II. Synthetic Stokes profiles in the Zeeman regime. *Astronomy & Astrophysics*, 412:513–527, 2003. doi:10.1051/0004-6361:20031473.

[68] L. E. Berg, K. Ekvall, and S. Kelly. Radiative lifetime measurement of vibronic levels of the $B^2\Sigma^+$ state of CaH by laser excitation spectroscopy. *Chemical Physics Letters*, 257(3-4):351–355, JUL 26 1996.

[69] L. E. Berg and L. Klynning. Rotational analysis of $A - X$ and $B - X$ band systems of CaH. *Physica Scripta*, 10(6):331–336, 1974.

[70] L. E. Berg, L. Klynning, and H. Martin. Laser excitation spectroscopy of the $B^2\Sigma - X^2$ transition of the CaH molecule. *Optics Communications*, 17(3):320–324, 1976.

[71] P. F. Bernath. 6 infrared emission spectroscopy. *Annu. Rep. Prog. Chem., Sect. C: Phys. Chem.*, 96:177–224, 2000.

[72] P. F. Bernath. Molecular astronomy of cool stars and sub-stellar objects. *International Reviews in Physical Chemistry*, 28(4):681–709, 2009.

[73] P. F. Bernath. Molecular astronomy of cool stars and sub-stellar objects. *International Reviews in Physical Chemistry*, 28(4):681–709, 2009. doi:10.1080/01442350903292442.

[74] P. F. Bernath, J. H. Black, and J. W. Brault. The spectrum of magnesium hydride. *Astrophysical Journal*, 298(1):375–381, 1985.

[75] S. S. Bhattacjaryya and D. Basu. Shape resonances and the photodissociation cross sectionof mgh near threshold. *Chemical Physics*, 79(1):129–135, 1983.

[76] S. Bird and T. A. Claxton. Orbitally ordered configuration-interaction calculations on small radicals. NH_2 and BeH. *Journal of the Chemical Society, Faraday Transactions II*, 80(Part 7):851–860, 1984.

[77] D. M. Bishop, J. Pipin, and B. Lam. Field and field-gradient polarizabilities of BeH, BH and CH^+. *Chemical Physics Letters*, 127(4):377–380, JUN 20 1986.

[78] M. R. A. Blomberg and P. E. M. Siegbahn. A theoretical study of NiH Optical spectrum and potential curves. *Molecular Physics*, 47:127, 1982.

[79] V. Bommier, E. Landi Degl'Innocenti, N. Feautrier, and G. Molodij. Collisional influence on the differential Hanle effect method applied to the second solar spectrum of the $a^2\pi - x^2\sigma^+(0,0)$ band of MgH. *Astronomy & Astrophysics*, 458(2):625–633, NOV 2006.

[80] J. T. Bonnell and R. A. Bell. Further determinations of the gravities of cool giant stars using Mg I and MgH features. *Monthly Notices of the Royal Astronomical Society*, 264(2):334–344, SEP 15 1993.

[81] W. J. Borucki and A. L. Summers. The photometric method of detecting other planetary systems. *ICARUS*, 58:121–134, April 1984.

[82] F. Bouchy, S. Udry, M. Mayor, C. Moutou, F. Pont, N. Iribarne, R. da Silva, S. Ilovaisky, D. Queloz, N. C. Santos, D. Ségransan, and S. Zucker. ELODIE metallicity-biased search for transiting Hot Jupiters. II. A very hot Jupiter transiting the bright K star HD 189733. *Astronomy and Astrophysics*, 444:L15–L19, December 2005.

[83] A. Boutalib, J. P. Daudey, and M. Elmouhtadi. Theoretical study of the lowest electronic states of CaH and CaH^+ molecules. *Chemical Physics*, 167(1-2):111–120, NOV 1 1992.

[84] B.H. Bransden and C.J. Joachain. *Physics of Atoms and Molecules*. Prentice Hall, 2000.

[85] W. H. Breckenridge and H. Umemoto. Bimodal rotational quantum state distribution of MgH ($x^2\sigma^+, \nu = 0$) in the reaction of mg($3s3p^1p_1$) with H_2: Evidence for microscopic branching. *Journal of Chemical Physics*, 75(8):4153–4155, 1981.

[86] W. H. Breckenridge and H. Umemoto. Nascent internal energy distributions of mgh produced in the reaction of Mg($3s3p\ ^1p_1$) with a variety of polyatomic molecules. *Journal of Chemical Physics*, 81(9):3852–3865, 1984.

[87] W. H. Breckenridge and H. Umemoto. Nascent internal energy distributions of mgh(mgd) produced in the reaction of Mg($3s3p\ ^1p_1$) with $h_2(d_2)$. *Journal of Chemical Physics*, 80(9):4168–4176, 1984.

[88] W. H. Breckenridge and J. H Wang. Dynamics of the reactions of mg($3s3p^1p_1$) with h_2, hd, and d_2: Rotational quantum state distributions of MgH (MgD) products. *Chemical Physics Letters*, 137(3):195–200, JUN 12 1987.

[89] WH BRECKENRIDGE and H UMEMOTO. Reaction of mg($3s3p^1p_1$) with a variety of alkyl câĂŞh bonds: Identical initial MgH($x^2\sigma^+, \nu = 0$) rotational quantum state distributions. *Journal of Chemical Physics*, 77(9):4464–4468, 1982.

[90] J. M. Brown. *Molecular Spectroscopy*. Oxford University Press, 1998.

[91] J. M. Brown, S. P. Beaton, and K. M. Evenson. Rotational frequencies of transition metal hydrides for astrophysical searches in the far-infrared. *Astrophysical Journal*, 414(2, Part 2):L125–L127, SEP 10 1993.

[92] J. M. Brown, S. P. Beaton, and K. M. Evenson. Rotational frequencies of transition metal hydrides for astrophysical searches in the far-infrared. *Astrophysical Journal, Letters*, 414:L125–L127, September 1993. doi:10.1086/187012.

[93] J. M. Brown, H. Korsgen, S. P. Beaton, and K. M. Evenson. The rotational and fine-structure spectrum of FeH, studied by far-infrared laser magnetic resonance. *Journal of Chemical Physics*, 124(23), JUN 21 2006.

[94] P. J. Bruna and F. Grein. Hyperfine coupling constants, electron-spin g-factors and vertical spectra of the $x^2\sigma^+$ radicals BeH, MgH, CaH and $BZ^+(+)$ AlZ^+, GaZ^+ (Z = H, Li, Na, K). A theoretical study. *Physical Chemistry Chemical Physics*, 5(15):3140–3153, 2003.

[95] P. J. Bruna and F. Grein. Hyperfine coupling constants, electron-spin g-factors and vertical spectra of the $X^2\Sigma^+$ radicals BeH, MgH, CaH and BZ^+, AlZ^+, GaZ^+ (Z = H, Li, Na, K). a theoretical study. *PCCP*, 5(15):3140–3153, 2003.

[96] PJ Bruna and F Grein. Hyperfine coupling constants, electron-spin g-factors and vertical spectra of the $X^2\Sigma^+$ radicals BeH, MgH, CaH and BZ^+, AlZ^+, GaZ^+ (Z = H, Li, Na, K). a theoretical study. *Physical Chemistry Chemical Physics*, 5(15):3140–3153, 2003.

[97] Sergiy Bubin and Ludwik Adamowicz. Calculations of the ground states of BeH and BeH^+ without the Born-Oppenheimer approximation. *Journal of Chemical Physics*, 126(21), JUN 7 2007.

[98] A. J. Burgasser. Binaries and the L Dwarf/T Dwarf Transition. *Astrophysical Journal*, 659:655–674, April 2007.

[99] A. J. Burgasser. The L dwarf/T dwarf transition: Multiplicity, magnetic activity and mineral meteorology across the hydrogen burning limit. *Astronomische Nachrichten*, 334:32, February 2013.

[100] A. J. Burgasser, J. D. Kirkpatrick, and S. Lépine. Ultracool subdwarfs: metal-poor stars and brown dwarfs extending into the late-type M, L and T dwarf regimes. In F. Favata, G. A. J. Hussain, and B. Battrick, editors, *13th Cambridge Workshop on Cool Stars, Stellar Systems and the Sun*, volume 560 of *ESA Special Publication*, page 237, March 2005.

[101] A. J. Burgasser, J. D. Kirkpatrick, J. Liebert, and A. Burrows. The spectra of T dwarfs. II. Red optical data. *The Astrophysical Journal*, 594(1, Part 1):510–524, SEP 1 2003.

[102] A. J. Burgasser, I. N. Reid, N. Siegler, L. Close, P. Allen, P. Lowrance, and J. Gizis. Not Alone: Tracing the Origins of Very-Low-Mass Stars and Brown

Dwarfs Through Multiplicity Studies. *Protostars and Planets V*, pages 427–441, 2007.

[103] A. Burrows, M. Marley, W. B. Hubbard, J. I. Lunine, T. Guillot, D. Saumon, R. Freedman, D. Sudarsky, and C. Sharp. A Nongray Theory of Extrasolar Giant Planets and Brown Dwarfs. *Astrophysical Journal*, 491:856–875, December 1997.

[104] A. Burrows, R. S. Ram, P. Bernath, C. M. Sharp, and J. A. Milsom. New CrH Opacities for the Study of L and Brown Dwarf Atmospheres. *Astrophysical Journal*, 577:986–992, October 2002. doi:10.1086/342242.

[105] A. S. Burrows. Highlights in the study of exoplanet atmospheres. *Nature*, 513:345–352, September 2014.

[106] A. S. Burrows. Spectra as windows into exoplanet atmospheres. *Proceedings of the National Academy of Science*, 111:12601–12609, September 2014.

[107] A. J. Cannon and E. C. Pickering. The Henry Draper catalogue : 21h, 22h, and 23h. *Annals of Harvard College Observatory*, 99, 1924.

[108] E. Cantarella, F. Culot, and J. Lievin. *Ab initio* calculation of vibrational dipole moment matrix elements. I. methods of calculation and diatomic test systems. *Physica Scripta*, 46(6):489–501, DEC 1992.

[109] C. Carlsund-Levin, N. Elander, A. Nunez, and A. Scrinzi. An exterior complex rotated coupled channel description of predissociation in diatomic molecules applied to a model of the four lowest $^2\Sigma^+$ states in CaH. *Physica Scripta*, 65(4):306–322, APR 2002.

[110] PK CARROLL, P MCCORMACK, and S OCONNOR. IRON HYDRIDE - LABORATORY STUDIES AND SOLAR IDENTIFICATION. *Astrophysical Journal*, 208(3):903–&, 1976.

[111] R. T. Carter and J. M. Brown. Observation and identification of the $g^6\Delta - a^6\Delta$ transition in the blue system of FeH at 493 nm. *Journal of Chemical Physics*, 101(4):2699–2709, AUG 15 1994.

[112] R. T. Carter and J. M. Brown. Observation of the $g^6\Phi_{11/12} - X^4\Delta_{7/2,\Delta\omega=2}$ Subband in FeH. *Journal of Molecular Spectroscopy*, 166(1):249–250, JUL 1994.

[113] R. T. Carter, T. C. Steimle, and J. M. Brown. The identification of a $^6\Phi - X^4\Delta$ intercombination system in the FeH radical at 448 nm. *Journal of Chemical Physics*, 99(5):3166–3173, SEP 1993.

[114] G. Chabrier and I. Baraffe. Structure and evolution of low-mass stars. *Astronomy and Astrophysics*, 327:1039–1053, 1997.

[115] G. Chabrier, I. Baraffe, F. Allard, and P. Hauschildt. Deuterium Burning in Substellar Objects. *The Astrophysical Journal*, 542(2):L119–L122, 2000. doi:10.1086/312941.

[116] G. Chabrier, I. Baraffe, F. Allard, and P. Hauschildt. Evolutionary Models for Very Low-Mass Stars and Brown Dwarfs with Dusty Atmospheres. *Astrophysical Journal*, 542:464–472, October 2000.

[117] G. Chabrier, I. Baraffe, F. Allard, and P. H. Hauschildt. Review on low-mass stars and brown dwarfs. *ArXiv Astrophysics e-prints*, September 2005.

[118] G. Chambaud and B Levy. CaH* potential curves: a simple theoretical treatment of intershell effects. *Journal of Physics B*, 22(20):3155–3165, OCT 28 1989.

[119] A. C. H. Chan and E. R. Davidson. Theoretical Study of the BeH Molecule. *Journal of Chemical Physics*, 49, 1968.

[120] W. T. Chan and I. P. Hamilton. Geometries and vibrational frequencies for calcium and strontium radical salts of H, F, Cl, Br, I, OH, SH, CN, NC, CCH, NNN, NCO, NCS, NH_2, CH_3, OCH_3, SCH_3, HCOO, CH_3COO, HCONH and $HCONCH_3$. *Chemical Physics Letters*, 297(3-4):217–224, NOV 27 1998.

[121] T. C. Chang. Pauli repulsion in the open shell species BeH and Co^+. *Journal of Computational Chemistry*, 13(3):268–274, APR 1992.

[122] Y. L. Chang, L Chen, M. K. Hsiao, J. J. Chen, and K. C. Lin. Reaction pathway for the nonadiabatic reaction of ca($4s3d^1D$) + H_2 → CaH($X^2\Sigma^+$) + H. *Journal of Chemical Physics*, 122(8), FEB 22 2005.

[123] Y. W. Chang and H. Sun. Spin-orbit splittings in the valence states of XH (X = K, Ca, Ga, Ge, As, Se, and Br) by the effective Hamiltonian approach. *Chemical Physics Letters*, 493(4-6):371–375, JUN 25 2010.

[124] D. Charbonneau, Z. K. Berta, J. Irwin, C. J. Burke, P. Nutzman, L. A. Buchhave, C. Lovis, X. Bonfils, D. W. Latham, S. Udry, R. A. Murray-Clay, M. J. Holman, E. E. Falco, J. N. Winn, D. Queloz, F. Pepe, M. Mayor, X. Delfosse, and T. Forveille. A super-Earth transiting a nearby low-mass star. *Nature*, 462:891–894, December 2009.

[125] J. Chen, T. C. Steimle, and A. J. Merer. The permanent electric dipole moment of chromium monodeuteride, CrD. *Journal Of Chemical Physics*, 127(20):204307, 2007.

[126] J. H. Chen, J. Gengler, T. C. Steimle, and J. M. Brown. Optical Zeeman spectroscopy of calcium monohydride. *Physics Review A*, 73(1), JAN 2006.

[127] J. J. Chen, Y. W. Song, K. C. Lin, and Y. M. Hung. Reaction pathway and energy disposal of the cah product in the reaction of ca($4s4p^1P_1$)+CH_4 → CaH($X^2\Sigma^+$) + CH_3. *Journal of Chemical Physics*, 118(11):4938–4944, MAR 15 2003.

[128] Jinhai Chen and T.C. Steimle. The permanent electric dipole moment of calcium monodeuteride. *Journal of Chemical Physics*, 128(14), APR 14 2008.

[129] L. Chen, M. K. Hsiao, Y. L. Chang, and K. C. Lin. Reaction dynamics of ca($4s3d^1D_{(2)}$)+ CH_4 $\rightarrow$ CaH($X^2\Sigma^+$) + CH_3: Reaction pathway and energy disposal for the CaH product. *Journal of Chemical Physics*, 124(2), JAN 14 2006.

[130] Y. M. Chen, D. E. Clemmer, and P. B. Armentrout. Gas-phase thermochemistry of VH and CrH. *Journal Of Chemical Physics*, 98:4929–4936, March 1993. doi:10.1063/1.464948.

[131] G. V. Chertihin and L. Andrews. Infrared Spectra of FeH, FeH_2, and FeH_3 in Solid Argon. *Journal of Physical Chemistry*, 99(32):12131–12134, AUG 1995.

[132] A. Chiavassa, R. Collet, L. Casagrande, and M. Asplund. Three-dimensional hydrodynamical simulations of red giant stars: semi-global models for interpreting interferometric observations. *Astronomy & Astrophysics*, 524, DEC 2010.

[133] D. P. Chong, S. R. Langhoff, C. W. Bauschlicher, and S. P. Walch. Theoretical dipole moments for the first-row transition metal hydrides. *Journal of Chemical Physics*, 85(5):2850–2860, SEP 1 1986.

[134] D. P. Chong, S. R. Langhoff, C. W. Bauschlicher, S. P. Walch, and H. Partridge. Theoretical dipole moments for the first-row transition metal hydrides. *Journal Of Chemical Physics*, 85:2850–2860, September 1986. doi:10.1063/1.451044.

[135] P. K. Chowdhury, A. J. Merer, S. J. Rixon, P. F. Bernath, and R. S. Ram. Low-N lines of the A6Σ+ X6Σ+ (1,0) band of CrH. *Physical Chemistry Chemical Physics (Incorporating Faraday Transactions)*, 8:822, 2006.

[136] T. A. Claxton, J. Tino, B. Burtons, and V. Klimo. Further study of the BeH radical by UHF-type and configuration interaction methods. *Journal of the Chemical Society, Faraday Transactions II*, 76(Part 12):1655–1663, 1980.

[137] R. E. S. Clegg and D. L. Lembert. On the identification of FeH and CeO in S stars. *Astrophysical Journal*, 226(3):931–936, 1978.

[138] C. Clerbaux and R. Colin. The 3d Rydberg state of the beh molecule. *Molecular Physics*, 72(2):471–486, FEB 10 1991.

[139] P. Coelho, B. Barbuy, J. Melendez, R. P. Schiavon, and B. V. Castilho. A library of high resolution synthetic stellar spectra from 300 nm to 1.8 μm with solar and alpha-enhanced composition. *Astronomy & Astrophysics*, 443(2):735–U183, NOV 2005.

[140] R. Colin, D. Degreef, P. Goethals, and Verhaege G. The ionization-potential of the BeH molecule. *Chemical Physics Letters*, 25(1):70–73, 1974.

[141] R. Colin and M. Steinhauer. The $3d - 4s$ Molecular Complex of Beryllium Monohydride. *Bulletin Des Societes Chimiques Belges*, 92(6-7):507, 1983.

[142] D. L Cooper. Spin splitting in the $x^2\sigma^+$ state of MgH. *Journal of Chemical Physics*, 76(7):3692–3693, 1982.

[143] D. L. Cooper. Theoretical investigation of the $X^2\Sigma^+$ and $C^2\Sigma^+$ states of BeH. *Journal of Chemical Physics*, 80(5):1961–1963, 1984.

[144] D. L. Cooper, R. Ponec, T. Thorsteinsson, and G. Raos. Pair populations and effective valencies from ab initio scf and spin-coupled wave functions. *International Journal of Quantum Chemistry*, 57(3):501–518, FEB 5 1996. 8th International Congress of Quantum Chemistry, PRAGUE, CZECH REPUBLIC, JUN 19-23, 1994.

[145] D. L. Cooper and W. G. Richards. Spin doubling in CaH. *Journal of Chemical Physics*, 73(2):991–992, 1980.

[146] S. M. Corkery, J. M. Brown, S. P. Beaton, and K. M. Evenson. Molecular parameters of chromium hydride in its $X^6\Sigma^+$ state determined by far-infrared laser magnetic resonance spectroscopy. *Journal of Molecular Spectroscopy*, 149:257–273, September 1991. doi:10.1016/0022-2852(91)90158-7.

[147] A. Corney. *Atomic and laser spectroscopy*. Oxford: Clarendon Press, 1977.

[148] Giorgina Corongiu. Hartree-Fock-Heitler-London method. 2. First and second row diatomic hydrides. *Journal of Physical Chemistry A*, 110(40):11584–11598, OCT 12 2006.

[149] P. L Cottrell. Extreme subdwarfs. I - Molecular band strengths - A theoretical approach. *Astrophysical Journal*, 223(2):544–551, 1978.

[150] MC Cushing, JT Rayner, SP Davis, and WD Vacca. FeH absorption in the near-infrared spectra of late M and L dwarfs. *Astrophysical Journal*, 582(2, Part 1):1066–1072, JAN 10 2003.

[151] J. Czarny, P. Felenbok, and E. Roueff. A search for interstellar NaH and MgH in diffuse clouds. *Astronomy and Astrophysics*, 188(1):155–158, DEC 1987.

[152] D. G. Dai and K. Balasubramanian. Spectroscopic Properties and Potential Energy Curves for 21 Electronic States of CrH. *Journal of Molecular Spectroscopy*, 161(2):455–465, October 1993. doi:10.1006/jmsp.1993.1251.

[153] G DAS. A pseudopotential study of the iron-series transition metal hydrides. *Journal of Chemical Physics*, 74(10):5766–5774, 1981.

[154] G. Das. A pseudopotential study of the ironseries transition metal hydrides. *Journal of Chemical Physics*, 74:5766, 1981. http://dx.doi.org/10.1063/1.440888.

[155] K. K. Datta, D. Basu, S. Saha, and A. K. Barua. Photodissociation of mgh in the solar atmosphere. *Journal of Physics B*, 16(13):2377–2384, 1983.

[156] P. de Bievre and I. L. Barnes. Table of the isotopic composition of the elements as determined by mass spectrometry. *International Journal of Mass Spectrometry and Ion Processes*, 65(1-2):211–230, 1985.

[157] D. Degreef and R. Colin. The electronic isotope-shift in $A^2\Sigma^+X^2\Sigma^+$ bands of BeH, BeD and BeT. *Journal of Molecular Structure*, 53(3):455–465, 1974.

[158] C. del Burgo, E. L. Martin, M. R. Zapatero Osorio, and P. H. Hauschildt. Physical parameters of T dwarfs derived from high-resolution near-infrared spectra. *Astronomy & Astrophysics*, 501(3):1059–1071, JUL 2009.

[159] X. Delfosse, C. G. Tinney, T. Forveille, N. Epchtein, E. Bertin, J. Borsenberger, E. Copet, B. de Batz, P. Fouque, S. Kimeswenger, T. Le Bertre, F. Lacombe, D. Rouan, and D. Tiphene. Field brown dwarfs found by DENIS. *Astronomy & Astrophysics*, 327:L25–L28, 1997.

[160] A. Dendramis, R. J. van Zee, and W. Weltner, Jr. The feh molecule at 4 k. *Astronomy & Astrophysics*, 231:632–636, July 1979.

[161] A. Dendramis, RJ VANZEE, and W WELTNER. The FeH molecule at 4 . *Astrophysical Journal*, 231(2):632–636, 1979.

[162] M. D. Di Rosa. Laser-cooling molecules - concept, candidates, and supporting hyperfine-resolved measurements of rotational lines in the $a - x(0,0)$ band of CaH. *European Physical Journal D*, 31(2):395–402, NOV 2004.

[163] M. Dolg, U. Wedig, H. Stoll, and H. Preuss. *A b i n i t i o* pseudopotential study of the first row transition metal monoxides and iron monohydride. *Journal of Chemical Physics*, 86(4):2123–2131, FEB 15 1987.

[164] M. Dulick, C. W. Bauschlicher, A. Burrows, C. M. Sharp, R. S. Ram, and P. Bernath. Line Intensities and Molecular Opacities of the FeH $F^4\Delta - X^4\Delta$ Transition. *The Astrophysical Journal*, 594(1):651–663, 2003. doi:10.1086/376791.

[165] M. Dulick, C. W. Bauschlicher, A. Burrows, C. M. Sharp, R. S. Ram, and P. Bernath. Line intensities and molecular opacities of the FeH $F^4\Delta_i - X^4\Delta_i$ transition. *Astrophysical Journal*, 594(1, Part 1):651–663, SEP 1 2003.

[166] C. M. Dutta, C. Oubre, P. Nordlander, M. Kimura, and A. Dalgarno. Charge-transfer cross sections in collisions of ground-state Ca and H^+. *Physics Review A*, 73(3), MAR 2006.

[167] G. Duxbury, M. F. Stamp, and H. P. Summers. Observations and modelling of diatomic molecular spectra from JET. *Plasma Physics AND Controlled Fusion*, 40(3):361–370, MAR 1998.

[168] J. L Elkind and P. B. Armentrout. Transition-metal hydride bond energies: first and second row. *Inorganic Chemistry*, 25(8):1078–1080, APR 9 1986.

[169] F. O. Ellison and C. Chen. Generalization of atoms in molecules theory to include independent scaling of inner and outer shells. *Journal of Chemical Physics*, 81(12):5855–5863, 1984.

[170] S. Elser, B. Moore, J. Stadel, and R. Morishima. How common are Earth-Moon planetary systems? *Icarus*, 214:357–365, August 2011.

[171] O. Engvold, H. Woehl, and J. W. Brault. Identification of the CrH molecule in a sunspot spectrum. *Astronomy & Astrophysics Supplement Series*, 42:209–213, 1980.

[172] K. M. Evenson and R. J. Saykally. *Far Infrared Laser Magnetic Resonance Spectroscopy.* Interstellar Molecules, Proceedings of the IAU Symposium No. 87 held 6-10 August 1979 in Mont Tremblant, Quebec, Canada. Edited by B.H. Andrews. Dordrecht: D. Reidel Publishing Co, 1980.

[173] G. Fabre, M. Elajli, R. Stringat, C. Effantin, J. Dincan, and A. Bernard. Cah emission from Ca excited in its metastable state $4s4p\ ^3p$. *Chemical Physics Letters*, 259(1-2):237–240, AUG 30 1996.

[174] P. L. Fast, M. L. Sanchez, J. C. Corchado, and D. G. Truhlar. The Gaussian-2 method with proper dissociation, improved accuracy, and less cost. *Journal of Chemical Physics*, 110(24):11679–11681, JUN 22 1999.

[175] D. Fawzy. The rotational temperature of the FeH molecules in a large sunspot. *NEW ASTRONOMY*, 14(8):708–710, NOV 2009.

[176] D. E. Fawzy, N. H. Youssef, and O. Engvold. Identification of FeH molecular lines in the spectrum of a sunspot umbra. *Astronomy & Astrophysics Supplement Series*, 129(3):435–443, MAY 1998.

[177] B Fernandez and P Jorgensen. Evaluation of hyperfine coupling tensors of the BeH and BeF radicals. *Chemical Physics Letters*, 232(5-6):463–471, JAN 27 1995.

[178] J. Fiser and J. Vojtik. Nuclear quadrupole coupling constants of BeH, BeH^+ and BeH: *Ab initio* study of their rovibrational dependence. *Chemical Physics*, 205(3):351–358, MAY 1 1996.

[179] D. A. Fletcher, R. T. Carter, J. M. Brown, and T. C. Steimle. The green system of FeH recorded at ambient temperatures. *Journal of Chemical Physics*, 93(12):9192–9193, DEC 15 1990.

[180] C Focsa, PF Bernath, R Mitzner, and R Colin. Fourier transform emission spectroscopy of the $A^2\Pi - X^2\Sigma^+$ transition of BeD. *Journal of Molecular Structure*, 192(2):348–358, DEC 1998.

[181] C. Focsa, S. Firth, P. F. Bernath, and R. Colin. Fourier transform emission spectroscopy of the $A^2\Pi - X^2\Sigma^+$ system of BeH. *Journal of Chemical Physics*, 109(14):5795–5802, OCT 8 1998.

[182] A. Frank, R. Lemus, and F. Iachello. Algebraic approach to molecular electronic spectra. I. Energy levels. *Journal of Chemical Physics*, 91(1):29–41, JUL 1 1989.

[183] B. Friedrich, J. D. Weinstein, R. Decarvalho, and J. M. Doyle. Zeeman spectroscopy of CaH molecules in a magnetic trap. *Journal of Chemical Physics*, 110(5):2376–2383, FEB 1 1999.

[184] C. I. Frum, J. J. Oh, E. A. Cohen, and H. M. Pickett. Rotational spectra of the $X^2\Sigma^+$ states of CaH and CaD. *The Astrophysical Journal*, 408(1):L61–L64, MAY 1 1993.

[185] C. I. Frum and H. M. Pickett. High-Resolution Infrared Fourier Transform Emission Spectroscopy of Metal Hydrides: $X^2\Sigma^+$ state of CaH. *Journal of Molecular Spectroscopy*, 159(2):329–336, JUN 1993.

[186] P. Fuentealba, O. Reyes, H. Stoll, and H. Preuss. Ground state properties of alkali and alkalineâĂŞearth hydrides. *Journal of Chemical Physics*, 87(9):5338–5345, NOV 1 1987.

[187] P. Fuentealba, O. Reyes, H. Stoll, and H. Preuss. Ground state properties of alkali and alkalineâĂŞearth hydrides. *Journal of Chemical Physics*, 87(9):5338–5345, NOV 1 1987.

[188] P. Fuentealba, O. Reyes, H. Stoll, and H. Preuss. Ground state properties of alkali and alkalineâĂŞearth hydrides. *Journal of Chemical Physics*, 87(9):5338–5345, NOV 1 1987.

[189] MP Fulscher and L Serrano-Andres. Quasi diabatic CASSCF state functions. *Molecular Physics*, 100(6):903–909, MAR 2002.

[190] T. Furtenbacher, A. G. Császár, and J. Tennyson. MARVEL: measured active rotational vibrational energy levels. *Journal of Molecular Spectroscopy*, 245(2):115–125, 2007. doi:10.1016/j.jms.2007.07.005.

[191] F. X. Gadea and A. V. Zaitsevskii. Variational Ansatz for effective Hamiltonians: solution of convergence problem via the intermediate Hamiltonian approach. *Chemical Physics Letters*, 191(1-2):77–81, MAR 27 1992.

[192] K. Gasmi, R. M. Al-Tuwirqi, S. Skowronek, H. H. Telle, and A. G. Urena. Rotationally resolved (1+1‘) resonance-enhanced multiphoton ionization (REMPI) of CaR (r = H, D) in supersonic beams: CaR $X^2\Sigma^+(\nu''=0) \rightarrow \mathrm{CaR}^* B^2\Sigma^+(\nu'=0,1) \rightarrow \mathrm{CaR}^+ X^1\Sigma^+$. *Journal of Physical Chemistry A*, 107(50):10960–10968, DEC 18 2003.

[193] P. L. Gay and D. L. Lambert. The isotopic abundances of magnesium in stars. *Astrophysical Journal*, 533(1, Part 1):260–270, APR 10 2000.

[194] P. L. Gay and D. L. Lambert. The isotopic abundances of magnesium in stars. *Astrophysical Journal*, 533(1, Part 1):260–270, APR 10 2000.

[195] A. G. Gaydon. *Dissociation Energies and Spectra of Diatomic Molecules*. Chapman and Hall, Ltd., London, 3 edition, 1968.

[196] A. G. Gaydon and R. W. B. Pearse. Band Spectrum of Chromium Hydride, CrH. *Nature(London)*, 140:110, 1937. doi:10.1038/140110a0.

[197] J. J. Gengler, T. C. Steimle, J. J. Harrison, and J. M. Brown. An analysis of the rotational, fine and hyperfine effects in the (0, 0) band of the $A^7\Pi$- $X^7\Sigma^+$ transition of manganese monohydride, MnH. *Journal of Molecular Spectroscopy*, 241:192–199, February 2007. doi: 10.1016/j.jms.2006.12.010.

[198] J. Gerratt and M. Raimondi. The Spin-Coupled Valence Bond Theory of Molecular Electronic Structure. i. Basic Theory and Application to the $^2\Sigma^+$ States of BeH. *Proceedings of the Royal Society of London Series A*, 371(1747):525–552, 1980.

[199] G. Ghigo, B. O. Roos, P. C. Stancil, and P. F. Weck. A theoretical study of the excited states of CrH: Potential energies, transition moments, and lifetimes. *Journal Of Chemical Physics*, 121:8194–8200, November 2004. doi:10.1063/1.1794631.

[200] V. N. Glushkov. On a choice of multireference space in many-body perturbation theory. *Chemical Physics Letters*, 244(1-2):1–9, SEP 29 1995.

[201] V. N. Glushkov. Asymptotic method of building restricted open-shell wavefunctions satisfying the generalized Brillouin's theorem. *Chemical Physics Letters*, 273(3-4):122–128, JUL 18 1997.

[202] VN Glushkov and S Wilson. Distributed gaussian basis sets: Variationally optimized s-type sets for the open-shell systems HeH and BeH. *International Journal of Quantum Chemistry*, 99(6, SI):903–913, SEP 20 2004. 7th European Workshop on Quantum Systems in Chemistry and Physics (QSCP 7), Bratislava, SLOVAKIA, SEP 10-15, 2002.

[203] S. Goel and A. E. Masunov. Potential energy curves and electronic structure of 3d transition metal hydrides and their cations. *Journal of Chemical Physics*, 129(21), DEC 7 2008.

[204] B. Goldman, M. C. Cushing, M. S. Marley, E. Artigau, K. S. Baliyan, V. J. S. Bejar, J. A. Caballero, N. Chanover, M. Connelley, R. Doyon, T. Forveille, S. Ganesh, C. R. Gelino, H. B. Hammel, J. Holtzman, S. Joshi, U. C. Joshi, S. K. Leggett, M. C. Liu, E. L. Martin, V. Mohan, D. Nadeau, R. Sagar, and D. Stephens. CLOUDS search for variability in brown dwarf atmospheres - Infrared spectroscopic time series of L/T transition brown dwarfs. *Astronomy & Astrophysics*, 487(1):277–292, AUG 2008.

[205] L. Gonzalez-Sanchez, E. Bodo, E. Yurtsever, and F. A. Gianturco. Quenching efficiency of "hot" polar molecules by He buffer gas at ultralow energies: quantum results for MgH and LiH rotations. *European Physical Journal D*, 48(1):75–82, JUN 2008.

[206] D. M. Goodridge, R. T. Carter, J. M. Brown, and T. C. Steimle. Rotational analysis and assignment of the green band system of FeH to the $e^6\Pi - a^6\Delta$ transition. *Journal of Chemical Physics*, 106(12):4823–4831, MAR 22 1997.

[207] D. M. Goodridge, D. F. Hullah, and J. M. Brown. Rotational analysis and assignment of the 630 nm band system of FeH to the $e^6\Pi - c^6\Sigma^+$ transition. *Journal of Chemical Physics*, 108(2):428–435, JAN 1998.

[208] I. E. Gordon, D. R. T. Appadoo, A. Shayesteh, K. A. Walker, and P. F. Bernath. Fourier transform infrared emission spectra of MnH and MnD. *Journal of Molecular Spectroscopy*, 229:145–149, January 2005. doi: 10.1016/j.jms.2004.08.010.

[209] R. O. Gray and C. J. Corbally. *Stellar Spectral Classification*. Princeton University Press, 2009.

[210] N. Grevesse and A. J. Sauval. Standard Solar Composition. *Space Science Reviews*, 85:161–174, May 1998.

[211] G. C. Groenenboom and N. Balakrishnan. The He-CaH ($^2\Sigma^+$) interaction. I. Three-dimensional ab initio potential energy surface. *Journal of Chemical Physics*, 118(16):7380–7385, APR 22 2003.

[212] O. Gropen, U. Wahlgren, and L. Pettersson. Effective core potential calculations on small molecules containing transition metal atoms. *Chemical Physics*, 66:459–464, April 1982. doi:10.1016/0301-0104(82)88047-6.

[213] J. Guan, M. E. Casida, and D. R. Salahub. Time-dependent density-functional theory investigation of excitation spectra of open-shell molecules. *Journal of Molecular Structure*, 527(SI):229–244, AUG 4 2000.

[214] M. Guitou, A. Spielfiedel, and N. Feautrier. Accurate potential energy functions and non-adiabatic couplings in th Mg + H system. *Chemical Physics Letters*, 488(4-6):145–152, MAR 22 2010.

[215] T. R. Gull, G. V. Kober, and K. E. Nielsen. Eta Carinae across the 2003.5 Minimum: The Character and Variability of the Ejecta Absorption in the Near-Ultraviolet. *The Astrophysical Journal Supplement Series*, 163:173–183, March 2006. doi: 10.1086/500113.

[216] T. Gustavsson, L. Klynning, and B. Lindgren. Absorption and Emission Spectrum of the $D^2\Sigma - X^2\Sigma$ Transition of the CaD Molecule. *Physica Scripta*, 31(4):269–274, 1985.

[217] H. C. Wolf H. Haken. *Molecular Physics and Elements of Quantum Chemistry*. Springer-Verlag Berlin Heidelberg, 2004.

[218] E. A. Reinsch H. J. Werner. The self-consistent electron pairs method for multiconfiguration reference state functions. *Journal of Chemical Physics*, 76:3144, 1982.

[219] P. J. Knowles H. J. Werner. A second order multiconfiguration SCF procedure with optimum convergence. *Journal of Chemical Physics*, 82:5053, 1985.

[220] W. Meyer H. J. Werner. A quadratically convergent multiconfiguration-self-consistent field method with simultaneous optimization of orbitals and CI coefficients. *Journal of Chemical Physics*, 73:2342, 1980.

[221] W. Meyer H. J. Werner. A quadratically convergent MCSCF method for the simultaneous optimization of several states. *Journal of Chemical Physics*, 74:5794, 1981.

[222] D. Halfen and L. Ziurys. Laboratory Rotational Spectroscopy of Astrophysical Interesting Diatomic Hydrides. In *American Astronomical Society Meeting Abstracts #212*, volume 40 of *Bulletin of the American Astronomical Society*, page 189, May 2008.

[223] D. T. Halfen, A. J. Apponi, and L. M. Ziurys. Astronomical Searches for Organic Molecules. In *IAU Symposium*, volume 235 of *IAU Symposium*, page 269P, 2005.

[224] D. T. Halfen, C. S. Savage, A. J. Apponi, and L. M. Ziurys. Sub-millimeter Spectroscopy of Diatomic Hydrides of Astrophysical Interest. In *American Astronomical Society Meeting Abstracts #206*, volume 37 of *Bulletin of the American Astronomical Society*, page 482, May 2005.

[225] D. T. Halfen and L. M. Ziurys. The Submillimeter Spectrum of CrH and CrD ($X^6\Sigma^+$). *The Astrophysical Journal*, 611(1):L65–L68, 2004. doi:10.1086/423426.

[226] D. T. Halfen and L. M. Ziurys. The Submillimeter Spectrum of MnH and MnD ($X^7\Sigma^+$). *The Astrophysical Journal*, 672:L77–L80, January 2008. doi:10.1086/526399.

[227] G. Hallinan, A. Antonova, J. G. Doyle, S. Bourke, W. F. Brisken, and A. Golden. Rotational Modulation of the Radio Emission from the M9 Dwarf TVLM 513-46546: Broadband Coherent Emission at the Substellar Boundary? *The Astrophysical Journal, Volume*, 653:690, 2006. doi:10.1086/508678.

[228] G. Hallinan, S. Bourke, C. Lane, A. Antonova, R. T. Zavala, W. F. Brisken, R. P. Boyle, F. J. Vrba, J. G. Doyle, and A. Golden. Periodic Bursts of Coherent Radio Emission from an Ultracool Dwarf. *The Astrophysical Journal*, 663(1):L25–L28, 2007. doi:10.1086/519790.

[229] K. Hammami, N. Jaidane, N. Feautrier, A. Spielfiedel, and F. Lique. Tensor cross sections and collisional depolarization of MgH by He atoms. *Chemical Physics Letters*, 484(4-6):148–153, JAN 7 2010.

[230] J. Haqq-Misra. Funding the Search for Extraterrestrial Intelligence with a Lottery Bond. *ArXiv e-prints*, 2013.

[231] R. J. Hargreaves, K. H. Hinkle, C. W. Bauschlicher, Jr., S. Wende, A. Seifahrt, and P. F. Bernath. High-resolution 1.6 μm Spectra of FeH in M and L Dwarfs. *Astronomical Journal*, 140(4):919–924, OCT 2010.

[232] J. F. Harrison. Electronic structure of diatomic molecules composed of a first-row transition metal and main-group element (H-F). *Chemical Reviews*, 100(2):679–716, FEB 2000.

[233] J. J. Harrison and J. M. Brown. Measurement of the Magnetic Properties of FeH in its $X^4\Delta$ and $F^4\Delta$ States from Sunspot Spectra. *Astrophysical Journal*, 686(2):1426–1431, OCT 20 2008.

[234] J. D. Hartman, G. Á. Bakos, G. Torres, D. W. Latham, G. Kovács, B. Béky, S. N. Quinn, T. Mazeh, A. Shporer, G. W. Marcy, A. W. Howard, D. A. Fischer, J. A. Johnson, G. A. Esquerdo, R. W. Noyes, D. D. Sasselov, R. P. Stefanik, J. M. Fernandez, T. Szklenár, J. Lázár, I. Papp, and P. Sári. HAT-P-32b and HAT-P-33b: Two Highly Inflated Hot Jupiters Transiting High-jitter Stars. *Astrophysical Journal*, 742:59, 2011.

[235] P. H. Hauschildt, F. Allard, and E. Baron. The NextGen Model Atmosphere Grid for 3000<=Teff<=10,000 K. *The Astrophysical Journal*, 512:377, 1999. doi:10.1086/306745.

[236] N. L. Haworth, M. B. Sullivan, A. K. Wilson, J. M. L. Martin, and L. Radom. Structures and thermochemistry of calcium-containing molecules. *Journal of Physical Chemistry A*, 109(40):9156–9168, OCT 13 2005.

[237] W. Hayes, P. D. McCarvill, and T. E. Nevin. RESEARCH NOTES: The Structure of the $X^7\Sigma$ State of MnH and MnD. *Proceedings of the Physical Society A*, 70:904–905, December 1957. doi: 10.1088/0370-1298/70/12/409.

[238] K. Haynes, A. M. Mandell, N. Madhusudhan, D. Deming, and H. Knutson. Spectroscopic Evidence for a Temperature Inversion in the Dayside Atmosphere of Hot Jupiter WASP-33b. *Astrophysical Journal*, 806:146, June 2015.

[239] R. Hefferlin and L. A. Kuznetsova. Systematics of diatomic molecular transition moments. *Journal of Quantitative Spectroscopy & Radiative Transfer*, 62(6):765–774, AUG 1999.

[240] T. Heimer. Das Bandenspektrum von MnH. *Naturwissenschaften*, 24:521–522, August 1936. doi: 10.1007/BF01473820.

[241] A. Henderson, G. Das, and A. C. Wahl. Multiconfiguration studies of some low lying bound states of VH. *Journal of Chemical Physics*, 63(7):2805, 1975. http://dx.doi.org/10.1063/1.431712.

[242] K. Heng and A. P. Showman. Atmospheric Dynamics of Hot Exoplanets. *Annual Review of Earth and Planetary Sciences*, 43:509–540, May 2015.

[243] C. Henriet and G. Verhaegen. Valence and Rydberg states of the BeH molecule. *Journal of Molecular Structure*, 16(FEB):63–73, 1984.

[244] C. Henriet and G. Verhaegen. Accurate Calculation of the Excited States of the Molecule BeH. *Physica Scripta*, 33(4):299–309, APR 1986.

[245] T. J. Henry and D. W. McCarthy, Jr. The mass-luminosity relation for stars of mass 1.0 to 0.08 solar mass. *Astronomical Journal*, 106:773–789, August 1993.

[246] T. J. Henry, J. P. Subasavage, M. A. Brown, T. D. Beaulieu, W. Jao, and N. C. Hambly. The Solar Neighborhood. X. New Nearby Stars in the Southern Sky and Accurate Photometric Distance Estimates for Red Dwarfs. *The Astronomical Journal*, 128(5):2460–2473, 2004. doi:10.1086/425052.

[247] C. Hill, S. N. Yurchenko, and J. Tennyson. Temperature-dependent molecular absorption cross sections for exoplanets and other atmospheres. *Icarus*, 226:1673–1677, 2013.

[248] M. Hirai and K. Chinami. Identification of FeH Lines in M, S and C Stars. *Proceedings of the Japan Academy, Series B*, 68(1):4–8, JAN 1992.

[249] S. Hirata and M. Head-Gordon. Time-dependent density functional theory for radicals - an improved description of excited states with substantial double excitation character. *Chemical Physics Letters*, 302(5-6):375–382, MAR 26 1999.

[250] F. Holka and M. Urban. The dipole moment and molecular properties of CaH: A theoretical study. *Chemical Physics Letters*, 426(4-6):252–256, AUG 4 2006.

[251] N. Honjou, T. Noro, M. Takagi, K. Ohno, and M. Makita. Ab Initio Configuration Interaction Calculation of the Low-Lying Electronic States of CaH Molecule. *Journal of the Physical Society of Japan*, 48(2):586–590, 1980.

[252] N. Honjou, M. Takagi, M. Makita, and K. Ohno. Theoretical Study of the Low-Lying Electronic States of CaH. *Journal of the Physical Society of Japan*, 50(6):2095–2100, 1981.

[253] J. Horner, J. B. Gilmore, and D. Waltham. The role of Jupiter in driving Earth's orbital evolution: an update. *ArXiv e-prints*, November 2015.

[254] H. P. Huber and G. Herzberg. *Molecular Spectra and Molecular Structure. IV. Constants of Diatomic Molecules*. Van Nostrand Reinhold Company, New York, 1979.

[255] D. F. Hullah, R. F. Barrow, and J. M. Brown. Low-lying energy levels of the FeH molecule. *Molecular Physics*, 97(1-2):93–103, JUL 10 1999.

[256] D. F. Hullah, C. Wilson, R. F. Barrow, and J. M. Brown. New assignments in the green and red band systems of the FeH radical. *Journal of Molecular Spectroscopy*, 192(1):191–197, NOV 1998.

[257] Y. M. Hung and K. C. Lin. Quasiclassical Trajectory Calculations of $Mg(3s3p^1p_1)$ + h_2 ($\nu = 0, n = 1$) $\rightarrow$ MgH (ν, n) + h: Trajectory and Angular Momentum Analysis on Improved ab Initio Potential Energy Surfaces. *Journal of Physical Chemistry A*, 105(1):41–47, JAN 11 2001.

[258] Karl K. Irikura. Experimental vibrational zero-point energies: Diatomic molecules. *Journal of Physical and Chemical Reference Data*, 36(2):389–397, JUN 2007.

[259] P. G. J. Irwin, N. A. Teanby, R. de Kok, L. N. Fletcher, C. J. A. Howett, C. C. C. Tsang, C. F. Wilson, S. B. Calcutt, C. A. Nixon, and P. D. Parrish. The NEMESIS planetary atmosphere radiative transfer and retrieval tool. *Journal of Quantitative Spectroscopy & Radiative Transfer*, 109:1136–1150, April 2008.

[260] K. Ishida. Spin and charge densities from the Hiller-Sucher-Feinberg identity: H_2 and BeH. *Chemical Physics Letters*, 158(3-4):217–221, JUN 9 1989.

[261] K. Ishida. Spin and charge densities from the Hiller-Sucher-Feinberg identity: double-perturbation calculations for BeH. *Chemical Physics Letters*, 175(1-2):133–137, NOV 30 1990.

[262] K. Iwamoto, F. Brachwitz, K. Nomoto, N. Kishimoto, H. Umeda, W. R. Hix, and F.-K. Thielemann. Nucleosynthesis in Chandrasekhar Mass Models for Type IA Supernovae and Constraints on Progenitor Systems and Burning-Front Propagation. *The Astrophysical Journal Supplement Series*, 125:439–462, December 1999.

[263] J. M. Brown and A. Carrington. *Rotational Spectroscopy of Diatomic Molecules*. Cambridge University Press, 2003.

[264] M. Jackson, L. R. Zink, J. P. Towle, N. Riley, and J. M. Brown. The rotational spectrum of the FeD radical in its $X^4\Delta$ state measured by far-infrared laser magnetic resonance. *Journal of Chemical Physics*, 130(15), APR 21 2009.

[265] Michael Jackson, Lyndon R. Zink, Jonathan P. Towle, Neil Riley, and John M. Brown. The rotational spectrum of the FeD radical in its X (4)Delta state, measured by far-infrared laser magnetic resonance. *Journal of Chemical Physics*, 130(15), APR 21 2009.

[266] M. E. Jacok. Comparison of the electronic energy levels of diatomic molecules in the gas phase and in inert solid matrices. *Journal Of Molecular Structure*, 157:43–59, 1987. doi:10.1016/0022-2860(87)87081-3.

[267] T. Jayasekharan and Tapan K. Ghanty. Significant increase in the stability of rare gas hydrides on insertion of beryllium atom. *Journal of Chemical Physics*, 127:114314, 2007.

[268] F. Jenc and B. A. Brandt. The ground state reduced potential curves (RPC) of the metal hydrides CuH and MgH. *Spectrochimica Acta Part A*, 41(10):1211–1214, 1985.

[269] G. Jeung, J. P. Daudey, and J. P. Malrieu. Theoretical study of the electronic states of calcium and calcium hydride. *Chemical Physics Letters*, 98(5):433–438, 1983.

[270] Masatoshi Kajita. Prospects of detecting m_e/m_p variance using vibrational transition frequencies of $^2\Sigma$ state molecules. *Physics Review A*, 77(1), JAN 2008.

[271] Masatoshi Kajita. Sensitive measurement of m_p/m_e variance using vibrational transition frequencies of cold molecules. *New Journal of Physics*, 11, MAY 14 2009.

[272] M. Kaupp, P. V. Schleyer, H. Stoll, and H. Preuss. Pseudopotential approaches to Ca, Sr, and Ba hydrides. why are some alkaline earth mx_2 compounds bent? *Journal of Chemical Physics*, 94(2):1360–1366, JAN 15 1991.

[273] B. Kaving and B. Lindgren. Ultraviolet Absorption Spectrum of the CaH Molecule II. the structure of the d-complex around 2 850 å. *Physica Scripta*, 10(1-2):81–85, 1974.

[274] B. Kaving and B. Lindgren. Ultraviolet Absorption Spectrum of the CaH Molecule III. A comparison between CaH and CaD spectra in the region $2800 - 3200$ å. *Physica Scripta*, 13(1):39–46, 1976.

[275] B. Kaving and B. Lindgren. Ultraviolet Absorption Spectrum of the CaH Molecule. IV. on the $c - x$ System. *Physica Scripta*, 24(4):752–754, 1981.

[276] B. Kaving, B. Lindgren, and D. A. Ramsay. Ultraviolet Absorption Spectrum of the CaH Molecule I. Rotational analysis of the 3 060 åband system. *Physica Scripta*, 10(1-2):73–79, 1974.

[277] P. C. Keenan. Bands in the photographic infra-red spectra of S-type stars. *Astronomical Journal*, 55:74, 1950. doi:10.1086/106346.

[278] P. C. Keenan. Stellar Spectra in the Red and Near Infrared. *Publications of the Astronomical Society of the Pacific*, 69(406):5, 1957. doi:10.1086/127007.

[279] B. Kerkeni. Depolarization rates of resonance lines of Mg, Ca, Sr and Na atoms by collisions with neutral hydrogen. *Astronomy & Astrophysics*, 390(2):783–791, AUG 2002.

[280] B. Kerkeni, P. S. Barklem, A. Spielfiedel, and N. Feautrier. Collisional broadening of Mg, Sr, Ca and Na resonance lines by atomic hydrogen. *Journal of Physics B*, 37(3):677–688, FEB 14 2004.

[281] I. S. K. Kerkines and A. Mavridis. A theoretical study of calcium monohydride, CaH: Low-lying states and their permanent electric dipole moments. *Journal of Physical Chemistry A*, 111(2):371–374, JAN 18 2007.

[282] I. A. Khan, S. J. A. Hussainee, M. Rafi, and M. A. Khan. Studies of CaH spectra around 2535 å. *Il Nuovo Cimento B*, 49(2):298–306, 1979.

[283] K. H. Kim, H. S. Lee, Y. S. Lee, and G. H. Jeung. Potential energy surfaces for the photochemical reactions $ca^* + h_2 \rightarrow CaH + h$. *Journal of Chemical Physics*, 116(2):589–593, JAN 8 2002.

[284] D. M. Kipping. LUNA: an algorithm for generating dynamic planet-moon transits. *Monthly Notices of the Royal Astronomical Society*, 416:689–709, September 2011.

[285] D. M. Kipping, G. Á. Bakos, L. Buchhave, D. Nesvorný, and A. Schmitt. The Hunt for Exomoons with Kepler (HEK). I. Description of a New Observational project. *Astrophysical Journal*, 750:115, May 2012.

[286] D. M. Kipping, D. Forgan, J. Hartman, D. Nesvorný, G. Á. Bakos, A. Schmitt, and L. Buchhave. The Hunt for Exomoons with Kepler (HEK). III. The First Search for an Exomoon around a Habitable-zone Planet. *Astrophysical Journal*, 777:134, 2013.

[287] D. M. Kipping, S. J. Fossey, and G. Campanella. On the detectability of habitable exomoons with Kepler-class photometry. *Monthly Notices of the Royal Astronomical Society*, 400:398–405, November 2009.

[288] D. M. Kipping, J. Hartman, L. A. Buchhave, A. R. Schmitt, G. Á. Bakos, and D. Nesvorný. The Hunt for Exomoons with Kepler (HEK). II. Analysis of Seven Viable Satellite-hosting Planet Candidates. *Astrophysical Journal*, 770:101, June 2013.

[289] D. M. Kipping, D. Nesvorný, L. A. Buchhave, J. Hartman, G. Á. Bakos, and A. R. Schmitt. The Hunt for Exomoons with Kepler (HEK). IV. A Search for Moons around Eight M Dwarfs. *Astrophysical Journal*, 784:28, March 2014.

[290] D. M. Kipping, A. R. Schmitt, X. Huang, G. Torres, D. Nesvorný, L. A. Buchhave, J. Hartman, and G. Á. Bakos. The Hunt for Exomoons with Kepler (HEK): V. A Survey of 41 Planetary Candidates for Exomoons. *Astrophysical Journal*, 813:14, 2015.

[291] K KIRBY, RP SAXON, and B LIU. Oscillator Strengths and Photodissociation Cross Sections in the x→a and x→b' Band Systems in MgH. *Astrophysical Journal*, 231(2):637–641, 1979.

[292] J. D. Kirkpatrick, C. A. Beichman, and M. F. Skrutskie. The Coolest Isolated M Dwarf and Other 2MASS Discoveries. *The Astrophysical Journal*, 476(1):311–318, 1997.

[293] J. D. Kirkpatrick, M. C. Cushing, C. R. Gelino, R. L. Griffith, M. F. Skrutskie, K. A. Marsh, E. L. Wright, A. Mainzer, P. R. Eisenhardt, I. S. McLean, M. A. Thompson, J. M. Bauer, D. J. Benford, C. R. Bridge, S. E. Lake, S. M. Petty, S. A. Stanford, C.-W. Tsai, V. Bailey, C. A. Beichman, J. S. Bloom, J. J. Bochanski, A. J. Burgasser, P. L. Capak, K. L. Cruz, P. M. Hinz, J. S. Kartaltepe, R. P. Knox, S. Manohar, D. Masters, M. Morales-Calderón, L. A. Prato, T. J. Rodigas, M. Salvato, S. D. Schurr, N. Z. Scoville, R. A. Simcoe, K. R. Stapelfeldt, D. Stern, N. D. Stock, and W. D. Vacca. The First Hundred Brown Dwarfs Discovered by the Wide-field Infrared Survey Explorer (WISE). *Astrophysical Journal*, 197:19, December 2011.

[294] J. D. Kirkpatrick, T. J. Henry, and D. W.Jr. McCarthy. A standard stellar spectral sequence in the red/near-infrared - Classes K5 to M9. *Astrophysical Journal Supplement Series*, 77:417–400, 1991. doi:10.1086/191611.

[295] J. D. Kirkpatrick, I. N. Reid, J. Liebert, R. M. Cutri, B. Nelson, C. A. Beichman, C. C. Dahn, D. G. Monet, J. E. Gizis, and M. F. Skrutskie. Dwarfs Cooler than "M": The Definition of Spectral Type "L" Using Discoveries from the 2 Micron All-Sky Survey (2MASS). *The Astrophysical Journal*, 519(2):802–833, 1999. doi:10.1086/307414.

[296] R. A. Klein and M. A Zottola. Corrigendum and Addendum to Pople versus dunning basis-sets for group IA metal hydrides and some other second row hydrides. BeH and BeH_2. *Chemical Physics Letters*, 421(4-6):595–596, APR 15 2006.

[297] RA Klein and MA Zottola. Pople versus Dunning basis-sets for group IA metal hydrides and some other second row hydrides: The case against a de Facto standard. *Chemical Physics Letters*, 419:254–258, 2006.

[298] B. Kleman and B. Liljeqvist. On the band spectrum of CrH. *Arkiv foer Physik*, 9:345, 1955.

[299] B. Kleman and U. Uhler. A $^6\Sigma - ^6\Sigma$ transition in CrH. *Canadian Journal of Physics*, 37:537, 1959. doi:10.1139/p59-061.

[300] L Klynning and H. Martin. Ionic Bonds in the Group-IIA Hydrides. *Physia Scripta*, 20(5-6):594–598, 1979.

[301] L. Klynning and H. Martin. Ionic Bonds in the Group IIA Hydrides. *Physica Scripta*, 20(5-6):594–598, 1979.

[302] L. Klynning and H. Martin. A doublet state perturbing the a state of CaH. *Journal of Physics B*, 14(11):L365–L366, 1981.

[303] L. Klynning, H. Martin, P. Nylen, and P. Royen. Radiative Lifetime Measurements of the Low Lying Electronic $B^2\Sigma$ State of CaH. *Physica Scripta*, 25(2):362–364, 1982.

[304] G. R. Knapp, S. K Leggett, X Fan, MS Marley, TR Geballe, D. A. Golimowski, D. Finkbeiner, J. E. Gunn, J. Hennawi, Z. Ivezic, R. H. Lupton, D. J. Schlegel, M. A. Strauss, Z. I. Tsvetanov, K. Chiu, E. A. Hoversten, K. Glazebrook, W. Zheng, M. Hendrickson, C. C. Williams, A. Uomoto, F. J. Vrba, A. A. Henden, C. B. Luginbuhl, H. H. Guetter, J. A. Munn, B. Canzian, D. P. Schneider, and J. Brinkmann. Near-infrared photometry and spectroscopy of L and T dwarfs: The effects of temperature, clouds, and gravity. *Astronomical Journal*, 127(6):3553–3578, JUN 2004.

[305] P. J. Knowles and H.-J. Werner. An efficient method for the evaluation of coupling coefficients in configuration interaction calculations. *Chemical Physics Letters, Volume 145, Issue 6, p. 514-522.*, 145(6):514–552, April 1988. doi:10.1016/0009-2614(88)87412-8.

[306] H. A. Knutson, D. Charbonneau, L. E. Allen, J. J. Fortney, E. Agol, N. B. Cowan, A. P. Showman, C. S. Cooper, and S. T. Megeath. A map of the day-night contrast of the extrasolar planet HD 189733b. *Nature*, 447:183–186, May 2007.

[307] T Kobayashi, K Sasagane, and K Yamaguchi. Calculation of frequency-dependent polarizabilities for open-shell systems at the second-order Moller-Plesset perturbation theory level based on the quasi-energy derivative method. *International Journal of Quantum Chemistry*, 65(5):665–677, DEC 5 1997.

[308] T. Kobayashi, K. Sasagane, and K. Yamaguchi. Calculation of frequency-dependent polarizabilities for open-shell systems at the second-order Moller-Plesset perturbation theory level based on the quasi-energy derivative method. *International Journal of Quantum Chemistry*, 65(5):665–677, DEC 5 1997.

37th Annual Sanibel Symposium, UNIV FLORIDA, PONCE DE LEON CONF CTR, ST AUGUSTINE, FL, MAR 01-07, 1997.

[309] T. Kobayashi, K. Sasagane, and K. Yamaguchi. Calculation of frequency-dependent polarizabilities for open-shell systems at the second-order MollerâĂŞPlesset perturbation theory level based on the quasi-energy derivative method. *International Journal of Quantum Chemistry*, 65(5):665–677, DEC 5 1997. 37th Annual Sanibel Symposium, UNIV FLORIDA, PONCE DE LEON CONF CTR, ST AUGUSTINE, FL, MAR 01-07, 1997.

[310] Jacek Koput. The *ab initio* ground-state potential energy function of beryllium monohydride, BeH. *Journal of Chemical Physics*, 135(24, Part 2011), DEC 28 2011.

[311] S. Koseki, T. Matsushita, and M. S. Gordon. Dissociation Potential Curves of Low-Lying States in Transition Metal Hydrides. 3. Hydrides of Groups 6 and 7. *Journal of Physical Chemistry A*, 110:2560–2570, February 2006. doi:10.1021/jp056258z.

[312] I. Kovacs. *Rotational structure in the spectra of diatomic molecules.* Cambridge University Press, 1969.

[313] I. Kovacs and P. Pacher. Fine structure of $^7\Pi$ and $^7\Sigma$ states in diatomic molecules. *Journal of Physics B Atomic Molecular Physics*, 8:796–803, April 1975. doi: 10.1088/0022-3700/8/5/014.

[314] A. Kramida, Y. Ralchenko, J. Reader, and NIST ASD team. *NIST Atomic Spectra Database (version 5.0)*, 2014.

[315] A. E. Kramida. A Critical Compilation of Experimental Data on Spectral Lines and Energy Levels of Hydrogen, Deuterium, and Tritium. *Atomic Data and Nuclear Data Tables*, 96(6):586–644, November 2010. doi:10.1016/j.adt.2010.05.001.

[316] L. Kreidberg. BATMAN: BAsic Transit Model cAlculatioN in Python. *Publications of the Astronomical Society of the Pacific*, 127:1161–1165, December 2015.

[317] R. V. Krems and A. Dalgarno. Quantum-mechanical theory of atom-molecule and molecular collisions in a magnetic field: Spin depolarization. *Journal of Chemical Physics*, 120(5):2296–2307, FEB 1 2004.

[318] R. V. Krems, A. Dalgarno, N. Balakrishnan, and G. C. Groenenboom. Spin-flipping transitions in $^2\Sigma$ molecules induced by collisions with structureless atoms. *Physics Review A*, 67(6), JUN 2003.

[319] N. Krstulović, I. Labazan, and S. Milošević. Study of Mn laser ablation in methane atmosphere. *European Physical Journal D*, 37:209–215, February 2006. doi: 10.1140/epjd/e2005-00285-3.

[320] J. Kulaczewski, D. Degenhardt, and F. Kneer. MgH as a diagnostic tool for fluctuations in the solar photosphere. *Astronomy and Astrophysics*, 234:530–534, August 1990.

[321] H. J. Kulik and N. Marzari. Systematic study of first-row transition-metal diatomic molecules: A self-consistent DFT + U approach. *Journal of Chemical Physics*, 133(11), SEP 21 2010.

[322] H. J. Kulik and N. Marzari. Systematic study of first-row transition-metal diatomic molecules: A self-consistent DFT + U approach. *Journal of Chemical Physics*, 133(11), SEP 21 2010.

[323] R. L. Kurucz. Atomic and molecular data for opacity calculations. *Revista Mexicana de Astronomia y Astrofisica*, 23(SI):45–48, MAR 1992.

[324] O. Kuzmychov and S. V. Berdyugina. CrH molecule: New diagnostic tool for measuring magnetic fields of cool dwarfs. In *Proceedings of the International Astronomical Union*, volume 294, pages 477–478, 2013. doi:10.1017/S1743921313002949.

[325] O. Kuzmychov and S. V. Berdyugina. Paschen-Back effect in the CrH molecule and its application for magnetic field measurements on stars, brown dwarfs, and hot exoplanets. *Astronomy & Astrophysics*, 558, 2013. doi:10.1051/0004-6361/201220041.

[326] O. Kuzmychov, S. V. Berdyugina, D. Harrington, and J. Kuhn. Investigating the magnetism of brown dwarfs. *Memorie della Societa Astronomica Italiana*, 84(4):1127, 2013.

[327] L. Laaksonen, F. Mullerplathe, and G. H. F. Diercksen. Fully numerical restricted hartree-fock calculations on openâĂŘshell hydrides: On the basis-set truncation error. *Journal of Chemical Physics*, 89(8):4903–4908, OCT 15 1988.

[328] L. Laaksonen, F. Mullerplathe, and Diercksenm G. H. F. Fully numerical restricted Hartree-Fock calculations on open-shell hydrides: On the basis-set truncation error. *Journal of Chemical Physics*, 89(8):4903–4908, OCT 15 1988.

[329] D. L. Lambert, E. A. Mallia, and A. D. Petford. Magnesium hydride in the sun. *Monthly Notices of the Royal Astronomical Society*, 154(3):265, 1971.

[330] D. L Lambert and A. McWilliam. Isotopic abundances of magnesium in the metal-poor subgiant V INDI. *Astrophysical Journal*, 304(1, Part 1):436–442, MAY 1 1986.

[331] S. R. Langhoff and C. W. Bauschlicher. Theoretical study of the spectroscopy of FeH. *Journal of Molecular Spectroscopy*, 141(2):243–257, JUN 1990.

[332] S. R. Langhoff, C. W. Bauschlicher, and A. P. Rendell. The spectroscopy of MnH. *Journal of Molecular Spectroscopy*, 138:108–122, November 1989. doi: 10.1016/0022-2852(89)90104-5.

[333] M. Larsson. On the possibility of a potential barrier in the ground state of BeH. *Journal of Chemical Physics*, 81(12):6409–6410, 1984.

[334] M. Larsson. *Ab-initio* Calculated Infrared Transition Probabilities, Dipole Moments and Spectroscopic constants for the $X^2\Sigma^+$ State of BeH. *Physica Scripta*, 32(2):97–102, 1985.

[335] G. Laughlin and J. J. Lissauer. Exoplanetary Geophysics – An Emerging Discipline. *ArXiv e-prints*, January 2015.

[336] O. Launila. Spectroscopy of MnCl: vibrational analysis of a band system near 877 nm and observation of a new band system near 1001 nm. *Molecular Physics*, 76:319–325, June 1992. doi: 10.1080/00268979200101351.

[337] B. J. Laurenzi and C. Litto. Isoelectronic molecules: The 13 and 22 electron sequences of diatomics. *Journal of Chemical Physics*, 78(11):6808–6823, 1983.

[338] R. J. Le Roy, D. R. T. Appadoo, R. Colin, and P. F. Bernath. On the $X^2\Sigma^+$, $A^2\Pi$ and $C^2\Sigma^+$ states of BeH, BeD, and BeT. *Journal of Molecular Structure*, 236(2):178–188, APR 2006.

[339] H. Lefebvrebrion and R. Colin. Anomalous isotope effects in indirect predissociations: An example in the spectrum of beh. *Journal of Molecular Structure*, 65(1):33–45, 1977.

[340] T. Leininger and G. H. Jeung. Ab initio calculation of rovibronic transition spectra of CaH. *Journal of Chemical Physics*, 103(10):3942–3949, SEP 8 1995.

[341] M. Lemeshko and B. Friedrich. Collisions of paramagnetic molecules in magnetic fields: An analytic model based on Fraunhofer diffraction of matter waves. *Physics Review A*, 79(1), JAN 2009.

[342] B. Lemine, C. Demuynck, J. L Destombes, and P. B. Davies. Infrared diode laser spectra of MgH and MgD ($x^2\sigma^+$). *Journal of Chemical Physics*, 89(2):673–677, JUL 15 1988.

[343] B. Lemoine, C. Demuynck, J. L. Destombes, and P. B. Davies. Infrared diode laser spectra of MgH and MgD ($X^2\Sigma^+$). *Journal of Chemical Physics*, 89:673–677, July 1988. doi:10.1063/1.455188.

[344] K. R. Leopold, L. R. Zink, K. M. Evenson, D. A Jennings, and M. Mizushima. The far infrared spectrum of magnesium hydride. *Journal of Chemical Physics*, 84(3):1935–1937, FEB 1 1986.

[345] G. Li, J. J. Harrison, R. S. Ram, C. M. Western, and P. F. Bernath. Einstein A coefficients and absolute line intensities for the $E^2\Pi - X^2\Sigma^+$ transition of CaH. *Journal of quantitative spectroscopy & radiative transfer*, 113:67–74, January 2012.

[346] X. Z. Li and J. Paldus. Spin-adapted open-shell stateâĂŘselective coupled cluster approach and doublet stability of its HartreeâĂŞFock reference. *Journal of Chemical Physics*, 102(5):2013–2023, FEB 1 1995.

[347] J. S. Lin and J. V. Ortiz. Electron propagator calculations on the ionization energies of CrH^-, MnH^- and FeH^-. *Chemical Physics Letters*, 171(3):197–200, 1990. doi:10.1016/0009-2614(90)85226-3.

[348] B. Lindgren and G. Olofsson. On the identification problem of the infrared 'Keenan bands' in S stars. *Astronomy & Astrophysics*, 84:300–303, April 1980.

[349] K. Lipus, E. Bachem, and W. Urban. Vibration-rotation spectroscopy of the CrH radical in its X6Σ ground state by CO-Faraday laser magnetic resonance. *Molecular Physics*, 73:1041–1050, 1991. doi:10.1080/00268979100101751.

[350] D. K. Liu, J. J. Chen, C. F. Nien, and K. C. Lin. Nascent rotational distribution and energy disposal of the cah product in the reaction of $Ca(4s4p^1P_1) + H_2 \rightarrow CaH(X^2\Sigma^+) + H$. *Journal of Chemical Physics*, 111(11):5277–5278, SEP 15 1999.

[351] D. K. Liu, T. L. Chin, and K. C. Lin. Vibrational and rotational population distributions of MgH($\nu'' = 0$ and 1) produced in the reaction of $Mg(3s3p^1p_1)$ with h_2. *Physical Review A*, 50(6, Part a):4891–4898, DEC 1994.

[352] M. Liu, T. Pauchard, M. Sjodin, O. Launila, P. Van Der Meulen, and L. E. Berg. Time-resolved study of the $A^2\Pi$ state of CaH by laser spectroscopy. *Journal of Molecular Spectroscopy*, 257(1):105–107, SEP 2009.

[353] L. Lodi and J. Tennyson. PhD TUTORIAL: Theoretical methods for small-molecule ro-vibrational spectroscopy. *Journal of Physics B: Atomic, Molecular, and Optical Physics*, 43(13), jul 2010. doi:10.1088/0953-4075/43/13/133001.

[354] L. Lodi, R. N. Tolchenov, J. Tennyson, A. E. Lynas-Gray, S. V. Shirin, N. F. Zobov, O. L. Polyansky, A. G. Császár, J. N. P. van Stralen, and L. Visscher. A new ab initio ground-state dipole moment surface for the water molecule. *Journal of Chemical Physics*, 128(4):044304–044304, January 2008.

[355] L. Lodi, S.N. Yurchenko, and J. Tennyson. The calculated rovibronic spectrum of scandium hydride, ScH. *Journal of Molecular Physics*, 113:1998–2011, 2015.

[356] A. Luchow and J. B. Anderson. First-row hydrides: Dissociation and ground state energies using quantum Monte Carlo. *Journal of Chemical Physics*, 105(17):7573–7578, NOV 1 1996.

[357] G. W. Lugmair and A. Shukolyukov. Early solar system timescales according to ^{53}Mn- ^{53}Cr systematics. *Geochimica et Cosmochimica Acta*, 62:2863–2886, August 1998.

[358] G. H. Lushington, P. J. Bruna, and F. Grein. *Ab initio* calculations of electron-spin magnetic moments for Li, Be and B hydrides in $X^2\Sigma^+$ states. *Zeitschrift für Physik D Atoms, Molecules and Clusters*, 36(3-4):301–309, 1996.

[359] Y. Lyubchik, H. R. A. Jones, Y. V. Pavlenko, E. Martin, I. S. McLean, L. Prato, R. J. Barber, and J. Tennyson. Spectral analysis of high resolution near-infrared spectra of ultra cool dwarfs. *Astronomy & Astrophysics*, 473(1):257–264, OCT 2007.

[360] Y. Lyubchik, H. R. A. Jones, Ya. V. Pavlenko, E. Martin, I. S. McLean, L. Prato, R. J. Barber, and J. Tennyson. Spectral analysis of high resolution near-infrared spectra of ultra cool dwarfs. *Astronomy & Astrophysics*, 473(1):257–264, 2007. doi:10.1051/0004-6361:20065386.

[361] Pettersson L. G. M., U. Wahlgreen, and O. Gropen. Effective core potential calculations using frozen orbitals. Applications to transition metals. *Chemical Physics*, 80(1-2):7–16, 1983.

[362] M. Pasternak and M. Van Der Heyden and G. Langouche. The characterization of FeH molecules by mössbauer spectroscopy. *Chemical Physics Letters*, 104(4):398 – 400, 1984.

[363] A. Maatouk, A. Ben Houria, O. Yazidi, N. Jaidane, and M. Hochlaf. Electronic states of MgO: Spectroscopy, predissociation, and cold atomic Mg and O production. *Journal of Chemical Physics*, 133:144302, 2010. http://dx.doi.org/10.1063/1.3498900.

[364] F. B. C. Machado, O. Roberto-Neto, and F. R. Ornellas. On the assignment of transitions involving some $^2\Pi$ Rydberg states of the BeH molecule. *Chemical Physics Letters*, 284(3-4):293–299, FEB 27 1998.

[365] F. B. C. Machado, O. Roberto-Neto, and F. R. Ornellas. Radiative transition probabilities and lifetimes for the band systems $A^2\Pi - X^2\Sigma^+$ and $C^2\Sigma^+ - X^2\Sigma^+$ of the BeH molecule. *Chemical Physics Letters*, 305(1-2):156–162, MAY 14 1999.

[366] W. J Maciel and P. D Singh. The ^{24}MgH Molecule in the Atmospheres of Late Type Stars - Transition Probabilities, Oscillator Strengths and Fine Structures of Rotation-vibration bands. *Astronomy and Astrophysics*, 54(2):417–424, 1977.

[367] N. Madhusudhan, H. Knutson, J. J. Fortney, and T. Barman. Exoplanetary Atmospheres. *Protostars and Planets VI*, pages 739–762, 2014.

[368] L. Magnani, S. Lugo, and T. M. Dame. CH 3 GHz Observations of Molecular Clouds along the Galactic Plane. *The Astronomical Journal*, 130:2725–2731, December 2005. doi: 10.1086/497538.

[369] E. Magnusson and S. Petrie. Classical versus nonclassical covalent bonding between the metal hydride radicals MH and M'H_j (MH = HBe, HMg, HCa; M'H_j = Li, BeH, BH_2, Na, MgH, AlH_2, K, CaH, GaH_2). *Journal of Physical Chemistry A*, 107(35):6882–6890, SEP 4 2003.

[370] M. S. Marley, A. S. Ackerman, J. N. Cuzzi, and D. Kitzmann. *Clouds and Hazes in Exoplanet Atmospheres*, pages 367–391. University of Arizona Press, 2013.

[371] M. S. Marley, M. C. Cushing, and D. Saumon. The L to T dwarf transition. In F. Favata, G. A. J. Hussain, and B. Battrick, editors, *13th Cambridge Workshop on Cool Stars, Stellar Systems and the Sun*, volume 560 of *ESA Special Publication*, page 791, March 2005.

[372] E. L. Martin, N. Phan-Bao, M. Bessell, X. Delfosse, T. Forveille, A. Magazzu, C. Reyle, H. Bouy, and R. Tata. Spectroscopic characterization of 78 DENIS ultracool dwarf candidates in the solar neighborhood and the Upper Scorpii OB association. *Astronomy & Astrophysics*, 517, JUL 2010.

[373] H. Martin. Laser spectroscopic investigations of the red band systems of CaH. *Journal of Molecular Spectroscopy*, 108(1):66–81, 1984.

[374] H. MARTIN. Empirically fitting the potential energy curves for the x, b, and b double minimum and the $D^2\Sigma^+$ states in CaH using united knowledge of CaH and CaD. *Journal of Chemical Physics*, 88(3):1797–1806, FEB 1 1988.

[375] J. M. L. Martin. Benchmark *ab initio* calculations of the total atomization energies of the first-row hydrides AH(n) (A=Li-F). *Chemical Physics Letters*, 273(1-2):98–106, JUL 11 1997.

[376] J. M. L. Martin. Benchmark *ab initio* potential curves for the light diatomic hydrides. Unusually large nonadiabatic effects in BeH and BH. *Chemical Physics Letters*, 283(5-6):283–293, FEB 13 1998.

[377] J. M. L. Martin, J. P. Francois, and R. Gijbels. Accurate ab initio predictions of the dissociation energy and heat of formation of first-row hydrides. *Chemical Physics Letters*, 163(4-5):387–391, NOV 17 1989.

[378] R. Martinazzo, A. Famulari, M. Raimondi, E. Bodo, and F. A. Gianturco. A multireference valence bond approach to electronic excited states. *Journal of Chemical Physics*, 115(7):2917–2925, AUG 15 2001.

[379] M. Mayor and D. Queloz. A Jupiter-mass companion to a solar-type star. *Nature*, 378:355–359, November 1995.

[380] P. McCormack and S. Oconnor. Wavelengths and line intensities for the 4920 å, 5320 åand 8690 åbands of feh. *Astronomy & Astrophysics Supplement Series*, 26:373–380, December 1976.

[381] A. McDougall and M. D. Albrow. Microlensing observations rapid search for exoplanets: MORSE code for GPUs. *Monthly Notices of the Royal Astronomical Society*, 456:565–570, February 2016.

[382] R. H. McFarland, A. S. Schlachter, J. W. Stearns, B. Liu, and R. E. Olson. D^- production by charge transfer of (0.3 -3) keV D^+ in thick alkaline-earth vapor targets: Interaction energies for CaH^+, CaH, and CaH^-. *Physics Review A*, 26(2):775–785, 1982.

[383] M. R. McGovern, J. D. Kirkpatrick, I. S. McLean, A. J. Burgasser, L. Prato, and P. J. Lowrance. Identifying young brown dwarfs using gravity-sensitive spectral features. *The Astrophysical Journal*, 600(2, Part 1):1020–1024, JAN 10 2004.

[384] I. S. McLean, L. Prato, M. R. McGovern, A. J. Burgasser, J. D. Kirkpatrick, E. L. Rice, and S. S. Kim. The nirspec brown dwarf spectroscopic survey. II.

High-resolution J-band spectra of M, L, and T dwarfs. *Astrophysical Journal*, 658(2, Part 1):1217–1235, APR 1 2007.

[385] H. Meissner and J. Paldus. Direct iterative solution of the generalized bloch equation. iv. Application to h_2, LiH, BeH, and CH_2. *Journal of Chemical Physics*, 113(7):2622–2637, AUG 15 2000.

[386] A. J. Merer. Spectroscopy of the Diatomic 3d Transition Metal Oxides. *Annual Review of Physical Chemistry*, 40:407–438, October 1989. doi: 10.1146/annurev.pc.40.100189.002203.

[387] J. M. Mestdagh, P. de Pujo, B. Soep, and F. Spiegelman. Ab-initio calculation of the ground and excited states of MgH using a pseudopotential approach. *CHEMICAL PHYSICS LETTERS*, 471(1-3):22–28, MAR 16 2009.

[388] W. Meyer and P. Rosmus. PnoâĂŞci and cepa studies of electron correlation effects. iii. spectroscopic constants and dipole moment functions for the ground states of the first-row and second-row diatomic hydrides. *Journal of Chemical Physics*, 63(6):2356–2375, 1975.

[389] W. Meyer and P. Rosmus. PnoâĂŞci and CEPA studies of electron correlation effects. III. Spectroscopic constants and dipole moment functions for the ground states of the first-row and second-row diatomic hydrides. *Journal of Chemical Physics*, 63(6):2356–2375, 1975.

[390] A. E. S. Miller, C. S. Feigerle, and W. C. Lineberger. Laser photoelectron spectroscopy of CrH^-, CoH^-, and NiH^-: Periodic trends in the electronic structure of the transition-metal hydrides. *Journal Of Chemical Physics*, 87:1549–1556, August 1987. doi:10.1063/1.453214.

[391] J. Mitroy and J. Y. Zhang. Long range dispersion interactions of the low lying states of mg with H, He, Ne, Ar, Kr and Xe. *Molecular Physics*, 106(1):127–132, 2008.

[392] J. Mitroya and J. Y. Zhang. Properties and long range interactions of the calcium atom. *Journal of Chemical Physics*, 128(13), APR 7 2008.

[393] S. Mohanty, G. Basri, Allard. F Javardhana, R., P. Hauschildt, and D. Ardila. Measuring Fundamental Parameters of Substellar Objects. I. Surface Gravities. *The Astrophysical Journal*, 609(2):854, 2004. doi:10.1086/420923.

[394] R. Mohlenkamp and H. J. Korsch. Semiclassical complex-energy quantization for coupled equations: Feshbach resonances and predissociation. *Physical Review A*, 34(6):4716–4721, DEC 1986.

[395] W. W. Morgan, P. C. Keenan, and E. Kellman. *An atlas of stellar spectra, with an outline of spectral classification*. The University of Chicago press, 1943.

[396] C. V. Morley, J. J. Fortney, E. M.-R. Kempton, M. S. Marley, C. Visscher, and K. Zahnle. Quantitatively Assessing the Role of Clouds in the Transmission Spectrum of GJ 1214b. *Astrophysical Journal*, 775:33, September 2013.

[397] J. R. Mould and S. Wycjoff. Iron hydride in stellar atmospheres. *Monthly Notices of the Royal Astronomical Society*, 182(1):63–&, 1978.

[398] J. S. Mulchaey. The rotational temperature of the FeH molecule in a sunspot. *Publications of the Astronomical Society of the Pacific*, 101(636):211–214, FEB 1989.

[399] M. Munzarová and M. Kaupp. A Critical Validation of Density Functional and Coupled-Cluster Approaches for the Calculation of EPR Hyperfine Coupling Constants in Transition Metal Complexes. *Journal of Physical Chemistry A*, 103:9966–9983, December 1999. doi: 10.1021/jp992303p.

[400] M. L. Munzarová, P. Kubáček, and M. Kaupp. Mechanisms of EPR Hyperfine Coupling in Transition Metal Complexes. *Journal of the American Chemical Society*, 122:11900–11913, 2000.

[401] T. Nakajima and H. Nakatsuji. Energy gradient method for the ground, excited, ionized, and electron-attached states calculated by the SAC (symmetry-adapted cluster)/SAC-CI (configuration interaction) method. *Chemical Physics*, 242(2):177–193, APR 1 1999.

[402] T. Nakajima and H. Nakatsuji. Second-order perturbative approximation to the SAC/SAC-CI method. *Chemical Physics Letters*, 300(1-2):1–8, JAN 29 1999.

[403] K.-i. Namiki and S. Saito. Microwave spectrum of the MnO radical in the $X^6\Sigma^+$ state. *Journal of Chemical Physics*, 107:8848–8853, December 1997. doi: 10.1063/1.475176.

[404] O. Nedelec and Dufayard J. Lifetimes of the mgh (mgd) and hgh (hgd) a $^2\pi$ states excited by a pulsed dye laser. *Journal of Chemical Physics*, 69(5):1833–1835, 1978.

[405] T. Nelis, S. P. Beaton, K. M. Evenson, and J. M. Brown. A determination of the molecular parameters for NiH in its $^2\Delta$ ground state by laser magnetic resonance. *Journal of Molecular Spectroscopy*, 148(2):462–478, 1991. doi:10.1016/0022-2852(91)90402-V.

[406] D. A. Neufeld, J. Zmuidzinas, P. Schilke, and T. G. Phillips. Discovery of Interstellar Hydrogen Fluoride 1. *Astrophysical Journal*, 488:L141–L144, October 1997. doi: 10.1086/310942.

[407] T. E. Nevin. *Proceedings of the Royal Irish Academy*, 1, 1942.

[408] T. E. Nevin. *Proceedings of the Royal Irish Academy*, 50:123, 1945.

[409] T. E. Nevin and D. V. Stephens.

[410] T. E. Nevin and P. G. Doyle. The band spectrum of manganese hydride, mn h. iii - the structure of the a 5207 band. *Proceedings of the Royal Irish Academy*, 52:123, 1948.

[411] T.E. Nevin, M. Conway, and M. Cranley. The Rotational Analysis of the (0,O) and (0,1) Bands of the $^7\Pi - ^7\Sigma$ System of Manganese Deuteride. *Proceedings of the Physical Society*, 65:115–124, 1952.

[412] H. L. Nordh, B. Lindgren, and R. F. Wing. A proposed identification of FeH in the spectra of M dwarfs and S stars. *Astronomy & Astrophysics*, 56(1-2):1–6, 1977.

[413] .S O'Connor. The Infrared Spectrum of CrH and CrD. *Proceedings of the Royal Irish Academy. Section A: Mathematical and Physical Sciences*, 65:95–111, 1966/1967. ISSN:00358975.

[414] S. O'Connor. A predissociation in the chromium hydride molecule. *Journal of Physics B: Atomic and Molecular Physics*, 2(5):541, 1969. doi:10.1088/0022-3700/2/5/306.

[415] B. R. Oppenheimer, S. R. Kulkarni, K. Matthews, and T. Nakajima. Infrared Spectrum of the Cool Brown Dwarf Gl 229B. *Science*, 270:1478–1479, December 1995.

[416] Y. R. Ou, Y. H. Hung, and K. C. Lin. Quasiclassical Trajectory Study of $Mg(3s3p^1p_1)$ + h_2 Reaction on Fitted *ab Initio* Surfaces. *Journal of Physical Chemistry A*, 103(40):7938–7948, OCT 7 1999.

[417] H. J. Werner P. J. Knowles. An efficient second-order MCSCF method for long configuration expansions. *Chemical Physics Letters*, page 259, 115 1985.

[418] H. J. Werner P. J. Knowles. An efficient method for the evaluation of coupling coefficients in configuration interaction calculations. *Chemical Physics Letters*, 145:514, 1988.

[419] P. Pacher. Fine structure of septet states in diatomic molecules, the $X^7\Sigma^+$ state of MnH. *Acta Physica Academiae Scientiarum Hungaricae*, 35:73–78, March 1974.

[420] S. Patchkovskii, R. T. Strong, C. J. Pickard, and S. Un. Gauge invariance of the spin-other-orbit contribution to the g-tensors of electron paramagnetic resonance. *Journal of Chemical Physics*, 122(21):214101, June 2005. doi: 10.1063/1.1917840.

[421] S. Patchkovskii and T. Ziegler. Calculation of the EPR g-Tensors of High-Spin Radicals with Density Functional Theory. *Journal of Physical Chemistry A*, 105:5490–5497, June 2001. doi: 10.1021/jp010457a.

[422] I. Pater and J. J. Lissauer. *Planetary Sciences 3rd Edition*. Cambridge University Press, 2010.

[423] A. T. Patrascu, C. Hill, J. Tennyson, and S. N. Yurchenko. Study of the electronic and rovibronic structure of the $X^2\Sigma^+$, $A^2\Pi$ and $B^2\Sigma^+$ states of AlO. *The Journal of Chemical Physics*, 141(14), 2014.

[424] A.T. Patrascu, S. N. Yurchenko, and J. Tennyson. The spectrum of AlO. *Monthly Notices of the Royal Astronomical Society*, 449:3613–3619, 2015.

[425] Ya. V. Pavlenko. Lithium Lines in the Spectra of M Dwarfs: UX Tau C. *Astronomy Reports*, 44(4):219–226, 2000. doi:10.1134/1.163844.

[426] Ya. V. Pavlenko. H_2O and HDO Bands in the Spectra of Late-Type Dwarfs. *Astronomy Reports*, 46(7):567–578, 2002. doi:10.1134/1.1495033.

[427] Ya. V. Pavlenko, G. J. Harris, J. Tennyson, H. R. A. Jones, J. M. Brown, C. Hill, and L. A. Yakovina. The electronic bands of CrD, CrH, MgD and MgH: application to the 'deuterium test'. *Monthly Notices of the Royal Astronomical Society*, 386(3):1338–1346, 2008. doi:10.1111/j.1365-2966.2008.12522.x.

[428] Ya. V. Pavlenko, H. R. A. Jones, Yu. Lyubchik, J. Tennyson, and D. J. Pinfield. Spectral energy distribution for GJ406. *Astronomy & Astrophysics*, 447(2):709–717, 2006. doi:10.1051/0004-6361:20052979.

[429] Ya. V. Pavlenko, M. R. Zapatero Osorio, and R. Rebolo. On the interpretation of the optical spectra of L-type dwarfs. *Astronomy & Astrophysics*, 355:245–255, 2000.

[430] R. W. B. Pearse and A. G. Gaydon. Band Spectrum of Manganese Hydride, MnH. *Nature*, 139:590, April 1937. doi: 10.1038/139590a0.

[431] R. W. B. Pearse and A. G. Gaydon. The spectrum of manganese hydride, MnH. *Proceedings of the Physical Society*, 50:201–206, March 1938. doi: 10.1088/0959-5309/50/2/305.

[432] R. Pereira, S. Skowronek, A. G. Urena, A. Pardo, J. M. L. Poyato, and A. H. Pardo. Rotationally resolved REMPI spectra of CaH in a molecular beam. *Journal of Molecular Spectroscopy*, 212(1):17–21, MAR 2002.

[433] M. A. C. Perryman. Extra-solar planets. *Reports on Progress in Physics*, 63:1209–1272, August 2000.

[434] D. Petitprez, B. Lemoine, C. Demuynck, J. L. Destombes, and B. Macke. Infrared diode laser spectroscopy of CaH and CaD($X^2\Sigma^+$). Determination of mass-independent parameters. *Journal of Chemical Physics*, 91(8):4462–4467, OCT 15 1989.

[435] I. D. Petsalakis, R. J. Buenker, G. Hirsch, and G. Theodorakopoulos. Predissociation widths and lifetimes of the $n = 3^2\Sigma^+$ states of BeH and BeD. *Journal of Physics B*, 30(21):4935–4941, NOV 14 1997.

[436] I. D. Petsalakis, D. Papadopoulos, G. Theodorakopoulos, and R. J. Buenker. Theoretical calculations on the linewidths of rovibrational levels of the 3d Rydberg states of BeH and BeD. *Journal of Physics B*, 32(13):3225–3237, JUL 14 1999.

[437] I. D. Petsalakis, G. Theodorakopoulos, and C. A. Nicolaides. Adiabatic and quasidiabatic $^2\Sigma^+$ States of BeH. *Journal of Chemical Physics*, 97(10):7623–7628, NOV 15 1992.

[438] L. G. M Pettersson, P. E. M. Siegbahn, and S. Ismail. Core-valence correlation effects in calcium hydride. *Chemical Physics*, 82(3):355–368, 1983.

[439] A. C. Philips. *The Physics of Stars*. John Wiley and Sons Ltd, England, 1999.

[440] J. G. Phillips and S. P. Davis. On the rotation and vibration-rotation spectrum of FeH. *Astrophysical Journal Supplement Series*, 66(2):227–232, FEB 1988.

[441] J. G. Phillips and S. P. Davis. On the carrier of the band at 700 nanometers in the iron hydride spectrum. *Astrophysical Journal*, 409(2, Part 1):860–868, JUN 1 1993.

[442] J. G. Phillips, S. P. Davis, B. Lindgren, and W. J. Balfour. The near-infrared spectrum of the FeH molecule. *Astrophysical Journal Supplement Series*, 65(4):721–778, DEC 1987.

[443] J. Pitarch-Ruiz, J. Sanchez-Marin, A. M. Velasco, and I. Martin. Full configuration interaction calculation of BeH adiabatic states. *Journal of Chemical Physics*, 129(5), AUG 7 2008.

[444] M. Polasek and R. Zahradnik. A quantum chemical study of small beryllium hydrides and their radical anions. *International Journal of Quantum Chemistry*, 54(2):93–98, APR 15 1995.

[445] R. Pollet, A. Savin, T. Leininger, and H. Stoll. Combining multideterminantal wave functions with density functionals to handle near-degeneracy in atoms and molecules. *Journal of Chemical Physics*, 116(4):1250–1258, JAN 22 2002.

[446] HE Popkie. Theoretical Electronic Transition Probabilities in Diatomic Molecules. III BeH and MgH ($a^2\pi - x^2\sigma^+$) systems. *Journal of Chemical Physics*, 54(11):4597, 1971.

[447] K. Poppenhaeger. Stellar magnetic activity and Star-Planet Interactions (invited review). *ArXiv e-prints*, 2014.

[448] W. Qin, D. G. McCoy, L. Torop, and A. J. Blake. Intermediate coupling strength pre-dissociation of diatomic molecules: transition from diabatic to adiabatic case. *Chemical Physics*, 221(1-2):77–84, AUG 15 1997.

[449] Li Qui-Xia, Gao Tao, and Zhang Yun-Guang. The splitting of low-lying or low excited states for hydride molecules(cations) of the third period under spin-orbit coupling. *CHINESE PHYSICS B*, 17(6):2040–2047, JUN 2008.

[450] H. M. Quiney, V. N. Glushkov, and S. Wilson. The dirac equation in the algebraic approximation. IX. Matrix Dirac-Hartree-Fock calculations for the Heh and Beh ground states using distributed Gaussian basis sets. *International Journal of Quantum Chemistry*, 99(6, SI):950–962, SEP 20 2004. 7th European Workshop on Quantum Systems in Chemistry and Physics (QSCP 7)*, Bratislava, SLOVAKIA, SEP 10-15, 2002.

[451] P. Raghavan. Table of Nuclear Moments. *Atomic Data and Nuclear Data Tables*, 42:189, 1989. doi: 10.1016/0092-640X(89)90008-9.

[452] R. S. Ram, C. N. Jarman, and P. F. Bernath. Fourier Transform Emission Spectroscopy of the $A^6\Sigma - X^6\Sigma$ System of CrH: Evidence for a $^4\Sigma^+$ Lowest Excited State. *Journal of Molecular Spectroscopy*, 161:445–454, October 1993. doi:10.1006/jmsp.1993.1250.

[453] R. S. Ram, K. Tereszchuk, I. E. Gordon, K. A. Walker, and P. F. Bernath. Fourier transform emission spectroscopy of the $E^2\Pi - X^2\Sigma^+$ transition of CaH and CaD. *Journal of Molecular Spectroscopy*, 266(2):86–91, APR 2011.

[454] A. A. Ramos and J. T. Bueno. Evidence for collisional depolarization in the mgh lines of the second solar spectrum. *Astrophysical Journal*, 635(1, Part 2):L109–L112, DEC 10 2005.

[455] A. A. Ramos, J. T. Bueno, and M. Collados. Detection of polarization from the $E^4\Pi - A^4\Pi$ system of FeH in sunspot spectra. *Astrophysical Journal*, 603(2):L125–L128, MAR 10 2004.

[456] D. M. Rao and K. E. Rangarajan. Molecular line polarization in the solar atmosphere: MgH lines. *Astrophysical Journal*, 524(2, Part 2):L139–L142, OCT 20 1999.

[457] T. V. R. Rao, R. R. Reddy, and A. S. Reddy. Potential energy curves and bond dissociation energies of CaF, CaCl, CaI and CaH. *Journal of Molecular Structure*, 14(3-4):249–257, 1983.

[458] H. Rauer, C. Catala, C. Aerts, T. Appourchaux, W. Benz, A. Brandeker, J. Christensen-Dalsgaard, M. Deleuil, L. Gizon, M.-J. Goupil, M. Güdel, E. Janot-Pacheco, M. Mas-Hesse, I. Pagano, G. Piotto, D. Pollacco, Ċ. Santos, A. Smith, J.-C. Suárez, R. Szabó, S. Udry, V. Adibekyan, Y. Alibert, J.-M. Almenara, P. Amaro-Seoane, M. A.-v. Eiff, M. Asplund, E. Antonello, S. Barnes, F. Baudin, K. Belkacem, M. Bergemann, G. Bihain, A. C. Birch, X. Bonfils, I. Boisse, A. S. Bonomo, F. Borsa, I. M. Brandão, E. Brocato, S. Brun, M. Burleigh, R. Burston, J. Cabrera, S. Cassisi, W. Chaplin, S. Charpinet, C. Chiappini, R. P. Church, S. Csizmadia, M. Cunha, M. Damasso, M. B. Davies, H. J. Deeg, R. F. Díaz, S. Dreizler, C. Dreyer, P. Eggenberger, D. Ehrenreich, P. Eigmüller, A. Erikson, R. Farmer, S. Feltzing, F. de Oliveira Fialho, P. Figueira, T. Forveille, M. Fridlund, R. A. García, P. Giommi, G. Giuffrida, M. Godolt, J. Gomes da Silva, T. Granzer, J. L. Grenfell, A. Grotsch-Noels, E. Günther, C. A. Haswell, A. P. Hatzes, G. Hébrard, S. Hekker, R. Helled, K. Heng, J. M. Jenkins, A. Johansen, M. L. Khodachenko, K. G. Kislyakova, W. Kley, U. Kolb, N. Krivova, F. Kupka, H. Lammer, A. F. Lanza, Y. Lebreton, D. Magrin, P. Marcos-Arenal, P. M. Marrese, J. P. Marques, J. Martins, S. Mathis, S. Mathur, S. Messina, A. Miglio, J. Montalban, M. Montalto, M. J. P. F. G. Monteiro, H. Moradi, E. Moravveji, C. Mordasini, T. Morel, A. Mortier, V. Nascimbeni, R. P. Nelson, M. B. Nielsen, L. Noack, A. J. Norton, A. Ofir, M. Oshagh, R.-M. Ouazzani, P. Pápics, V. C. Parro, P. Petit,

B. Plez, E. Poretti, A. Quirrenbach, R. Ragazzoni, G. Raimondo, M. Rainer, D. R. Reese, R. Redmer, S. Reffert, B. Rojas-Ayala, I. W. Roxburgh, S. Salmon, A. Santerne, J. Schneider, J. Schou, S. Schuh, H. Schunker, A. Silva-Valio, R. Silvotti, I. Skillen, I. Snellen, F. Sohl, S. G. Sousa, A. Sozzetti, D. Stello, K. G. Strassmeier, M. Švanda, G. M. Szabó, A. Tkachenko, D. Valencia, V. Van Grootel, S. D. Vauclair, P. Ventura, F. W. Wagner, N. A. Walton, J. Weingrill, S. C. Werner, P. J. Wheatley, and K. Zwintz. The PLATO 2.0 mission. *Experimental Astronomy*, 38:249–330, November 2014.

[459] J. T. Rayner, M. C. Cushing, and W. D. Vacca. The Infrared Telescope Facility (IRTF) Spectral Library: Cool Stars. *Astrophysical Journal Supplement Series*, 185(2):289–432, DEC 2009.

[460] John T. Rayner, Michael C. Cushing, and William D. Vacca. The infrared telescope facility (IRTF) spectral library: Cool stars. *Astrophysical Journal*, 185(2):289–432, DEC 2009.

[461] I. N. Reid, J. E. Gizis, J. G. Cohen, M. A. Pahre, D. W. Hogg, L. Cowie, E. Hu, and A. Songaila. Faint M dwarfs and the structure of the galactic disk. *Publications Of The Astronomical Society Of The Pacific*, 109(735):559–565, MAY 1997.

[462] I. N. Reid and S. L. Hawley. *New Light on Dark Stars*. Praxis Publishing Ltd, 2005.

[463] A. Reiners. The narrowest M-dwarf line profiles and the rotation-activity connection at very slow rotation. *Astronomy & Astrophysics*, 467(1):259–268, MAY 2007.

[464] A. Reiners and G. Basri. Measuring magnetic fields in ultracool stars and brown dwarfs. *Astrophysical Journal*, 644(1, Part 1):497–509, JUN 10 2006.

[465] A. Reiners, D. Homeier, P. H. Hauschildt, and F. Allard. A high resolution spectral atlas of brown dwarfs. *Astronomy & Astrophysics*, 473(1):245–255, OCT 2007.

[466] A. Reiners, J. H. M. M. Schmitt, and C. Liefke. Rapid magnetic flux variability on the flare star CN Leonis. *Astronomy & Astrophysics*, 466(2):L13–L16, MAY 2007.

[467] K. W. Richman, Z. G. Shi, and E. A. McCullough. Calculation of the hyperfine splitting constants for diatomic molecules using numerical wave-functions. *Chemical Physics Letters*, 141(3):186–192, NOV 6 1987.

[468] K. W. Richman, Z. G. Shi, and E. A. McCullough. Calculation of the hyperfine splitting constants for diatomic molecules using numerical wavefunctions. *Chemical Physics Letters*, 141(3):186–192, NOV 6 1987.

[469] Z. Rinkevicius, L. Telyatnyk, O. Vahtras, and H. Ågren. Density functional theory for hyperfine coupling constants with the restricted-unrestricted approach. *The Journal of Chemical Physics*, 121:7614, 2004. doi: 10.1063/1.1799013.

[470] M. H. Ritzwoller and E. M. Lavely. A unified approach to the helioseismic forward and inverse problems of differential rotation. *Astrophysical Journal*, 369:557–566, March 1991.

[471] R.D. Robinson Jr. Magnetic field measurements on stellar sources - A new method. *Astrophysical Journal*, 239:961, 1980. doi:10.1086/158184.

[472] B. 0. Roos. A theoretical study of the $X^6\Sigma^+$, $A^6\Sigma^+$, and $^6\Delta$ states of CrH. *Molecular Physics*, 101:87–91, 2003. doi:10.1080/00268970210158731.

[473] P. Rosmus and H. J. Werner. Einstein transition-probability coefficients in the electronic ground states of the diatomic hydrides. *Journal of Molecular Structure*, 60(JAN):405–408, 1980.

[474] P. Rosmus and H. J Werner. Einstein transition-probability coefficients in the electronic ground states of the diatomic hydrides. *Journal of Molecular Structure*, 60(JAN):405–408, 1980.

[475] R. J. Le Roy. *LEVEL 8.0: A Computer Program for Solving the Radial Schróodinger Equation for Bound and Quasibound Levels.* Guelph-Waterloo Centre for Graduate Work in Chemistry University of Waterloo, Waterloo, Ontario N2L 3G1, Canada, 2007. see http://leroy.uwaterloo.ca/programs/.

[476] S. N. Yurchenko and A. Blissett and U. Asari and M. Vasilios and C. Hill and J. Tennyson. ExoMol molecular line lists - XIII: The spectrum of CaO. *Monthly Notices of the Royal Astronomical Society*, 456:4524, 2016.

[477] S.H. Saar. Improved methods for the measurement and analysis of stellar magnetic fields. *Astrophysical Journal*, 324:441, 1988. doi:10.1086/165907.

[478] S. Sakamoto, G. J. White, K. Kawaguchi, M. Ohishi, K. S. Usuda, and T. Hasegawa. A search for absorption of Mg and Ca compounds in molecular clouds towards galactic continuum sources. *Monthly Notices of the Royal Astronomical Society*, 301(3):872–880, DEC 11 1998.

[479] C. J. Sansonetti and G. Nave. Extended Analysis of the Spectrum of Singly Ionized Chromium (Cr II). *The Astrophysical Journal Supplement*, 213, August 2014. doi:10.1088/0067-0049/213/2/28.

[480] D. Saumon and M. S. Marley. The Evolution of L and T Dwarfs in Color-Magnitude Diagrams. *Astrophysical Journal*, 689:1327–1344, December 2008.

[481] A. J. Sauval and J. B. Tatum. A set of partition functions and equilibrium constants for 300 diatomic molecules of astrophysical interest. *Astrophysical Journal Supplement Series*, 56(2):193–209, 1984.

[482] R. P. Saxon, K. Kirby, and B. Liu. Erratum: Ab initio configuration interaction study of the low-lying electronic states of mgh [j. chem. phys. [bold 69], 5301 (1978)]. *The Journal of Chemical Physics*, 78(12):7507–7507, 1983.

[483] R. P. Saxon, K. Kirkby, and B. Liu. *Ab initio* configuration interaction study of the low-lying electronic states of MgH. *Journal of Chemical Physics*, 69(12):5301–5309, 1978.

[484] R. P. Schiavon, B. Barbuy, and P. D. Singh. The FeH Wing-Ford band in spectra of M stars. *Astrophysical Journal*, 484(1, Part 1):499–510, JUL 20 1997.

[485] A. B. Schultz, F. Allard, M. Clampin, M. McGrath, F. C. Bruhweiler, J. A. Valenti, P. Plait, S. Hulbert, S. Baum, B. E. Woodgate, C. W. Bowers, R. A. Kimble, S. P. Maran, H. W. Moos, and F. Roesler. First results from the Space Telescope Imaging Spectrograph: Optical spectra of Gliese 229B. *Astrophysical Journal*, 492(2, Part 2):L181–L184, JAN 10 1998.

[486] R. H. Schultz and P. B. Armentrout. The gas-phase thermochemistry of FeH. *Journal of Chemical Physics*, 94(3):2262–2268, FEB 1 1991.

[487] P. R. Scott and W. G. Richards. On the low-lying electronic states of ScH. *Journal of Physics B*, 7:1679, 1974.

[488] P. R. Scott and W. G. Richards. On the low-lying electronic states of TiH. *Journal of Physics B*, 7:500, 1974.

[489] P. R. Scott and W. G. Richards. Electronic structure of FeH. *Journal of Chemical Physics*, 63(4):1690–1691, 1975.

[490] P. R. Scott and W. G. Richards. Electronic structure of FeH. *Journal of Chemical Physics*, 83(4):1690, 1975.

[491] S. Seager. Exoplanet Habitability. *Science*, 340:577–581, May 2013.

[492] S. Seager, W. Bains, and R. Hu. A Biomass-based Model to Estimate the Plausibility of Exoplanet Biosignature Gases. *Astrophysical Journal*, 775:104, October 2013.

[493] S. Seager and D. Deming. Exoplanet Atmospheres. *Annual Review of Astronomy and Astrophysics*, 48:631–672, September 2010.

[494] S. Seager, M. Kuchner, C. A. Hier-Majumder, and B. Militzer. Mass-Radius Relationships for Solid Exoplanets. *Astrophysical Journal*, 669:1279–1297, November 2007.

[495] S. Seager, E. L. Turner, J. Schafer, and E. B. Ford. Vegetation's Red Edge: A Possible Spectroscopic Biosignature of Extraterrestrial Plants. *Astrobiology*, 5:372–390, June 2005.

[496] H. Sekino and R. J. Bartlett. Spin density of radicals by finite field manybody methods. *Journal of Chemical Physics*, 82(9):4225–4229, 1985.

[497] A. Serrano and S. Canuto. Calculated polarizabilities and gradients: Rayleigh and Raman scattering activities for the MgH molecule. *Journal of Molecular Structure*, 432(1):69–74, MAY 2 1998.

[498] K. R. Shamasundar, G. Knizia, and H.-J. Werner. A new internally contracted multi-reference configuration interaction method. *Journal of Chemical Physics*, 135(5):054101–054101–17, August 2011. doi;10.1063/1.3609809.

[499] R. Shanmugavel, S. P. Bagare, and N. Rajamanickam. Astrophysically Useful Parameters for Certain Band Systems of BeH, BeD and BeT Molecules. *Serbian Astronomical Journal*, 173:83, December 2006.

[500] R. Shanmugavel, S. P. Bagare, N. Rajamanickam, and K. Balachandra Kumar. Identification of Beryllium Hydride Isotopomer Lines in Sunspot Umbral Spectra. *Serbian Astronomical Journal*, 176:51–58, June 2008.

[501] A. Shayesteh, D. R. T. Appadoo, I. Gordon, R. J. Le Roy, and P. F. Bernath. Fourier transform infrared emission spectra of MgH and MgD. *Journal of Chemical Physics*, 120(21):10002–10008, JUN 1 2004.

[502] A. Shayesteh and Peter F. Bernath. Rotational analysis and deperturbation of the $a^2\pi \rightarrow x^2\sigma^+$ and $b'^2\sigma^+ \rightarrow x^2\sigma^+$ emission spectra of MgH. *Journal OF Chemical Physics*, 135(9), SEP 7 2011.

[503] A. Shayesteh, K. Tereszchuk, P. F. Bernath, and R. Colin. Infrared emission spectra of BeH and BeD. *Journal of Chemical Physics*, 118(3):1158–1161, JAN 15 2003.

[504] A. Shayesteh, K. A. Walker, I. Gordon, D. R. T. Appadoo, and P. F. Bernath. New fourier transform infrared emission spectra of CaH and SrH: combined isotopomer analyses with CaD and SrD. *Journal of Molecular Structure*, 695(SI):23–37, JUN 30 2004.

[505] P. M. Sheridan and L. M. Ziurys. Molecules in high spin states II: the pure rotational spectrum of MnF ($X\ ^7\Sigma^+$). *Chemical Physics Letters*, 380:632–646, October 2003. doi: 10.1016/j.cplett.2003.08.106.

[506] N. Shida, K. Tanaka, and K. Ohno. A theoretical study of rotational-vibrational levels of the lower two $^2\Sigma^+$ states of the CaH molecule. *Journal of Molecular Spectroscopy*, 121(2):283–293, FEB 1987.

[507] S. Shin, D. J. Brugh, and M. D. Morse. Radiative Lifetime of the v=0, 1 Levels of the $A^6\Sigma^+$ State of CrH. *Astrophysical Journal*, 619:407–411, January 2005. doi:10.1086/426468.

[508] A. P. Showman, J. Y.-K. Cho, and K. Menou. *Atmospheric Circulation of Exoplanets*, pages 471–516. University of Arizona Press", December 2010.

[509] D. Shulyak, A. Reiners, S. Wende, O. Kochukhov, N. Piskunov, and A. Seifahrt. Modelling the molecular Zeeman-effect in M-dwarfs: methods and first results. *Astronomy & Astrophysics*, 523, NOV-DEC 2010.

[510] M. Singh and J. P. Chaturvedi. One hundred and fifty-three diatomic molecules, molecular ions, and radicals of astrophysical interest. *Astrophysics & Space Science*, 135(1):1–74, JUL 1987.

[511] M. L. Sink, A. D. Bandraux, W. H. Henneker, H. Lefbvrebriton, and G. Raseev. Theoretical study of the low-lying electronic states of MgH. *Chemical Physics Letters*, 39(3):505–510, 1976.

[512] S. Skory, P. F. Weck, P. C. Stancil, and K. Kirby. New Theoretical Line List for the $b'^2\sigma^+ \leftarrow x^2\sigma^+$ System of ^{24}MgH. *Astrophysical Journal Supplement Series*, 148(2):599–606, OCT 2003.

[513] A. M. S. Smith, D. R. Anderson, I. Skillen, A. Collier Cameron, and B. Smalley. Thermal emission from WASP-33b, the hottest known planet. *Monthly Notices of the Royal Astronomical Society*, 416:2096–2101, September 2011.

[514] R. E. Smith. Diatomic Hydride and Deuteride Spectra of the Second Row Transition Metals. *Proceedings of the Royal Society of London. Series A, Mathematical and Physical Sciences*, 332(1588):113–127, February 1973.

[515] M Sodupe, J. M. Lluch, A. Oliva, F. Illas, and J. Rubio. *Abinitio* study of the ground and low-lying states of FeH. *Journal of Chemical Physics*, 92(4):2478–2480, FEB 15 1990.

[516] Y. W. Song, J. J. Chen, M. K. Hsiao, K. C. Lin, and Y. M. Hung. Reaction pathway and potential barrier for the cah product in the reaction of ca($4s4p^1P_1$)+ $H_2 \rightarrow$ CaH($X^2\Sigma^+$) + H. *Journal of Chemical Physics*, 120(6):2774–2779, FEB 8 2004.

[517] H. Spinrad and D. B. Wood. Magnesium hydride in cool stars and galaxies. *Astrophysical Journal*, 141(1):109–&, 1965.

[518] J. M. Standard and P. R. Certain. Bounds to two- and three-body longâĂŘrange interaction coefficients for s-state atoms. *Journal of Chemical Physics*, 83:3002, 1985.

[519] T. C. Steimle, T. P. Meyer, Y. Alramadin, and P. Bernath. Excited state magnetic hyperfine interactions in gas phase strontium and calcium monohydrides. *Journal of Molecular Spectroscopy*, 125(1):225–232, SEP 1987.

[520] TC Steimle, JH Chen, and J Gengler. The permanent electric dipole moments of calcium monohydride, CaH. *Journal of Chemical Physics*, 121(2):829–834, JUL 8 2004.

[521] Steimle, T. C. and Chen, J. H. and Harrison, J. J. and Brown, J. M. A molecular-beam optical Stark study of lines in the (1,0) band of the $F^4\Delta_{7/2} - X^4\Delta_{7/2}$ transition of iron monohydride, FeH. *Journal of Chemical Physics*, 124(18), MAY 2006.

[522] A. E. Stevens, C. S. Feigerle, and W. C. Lineberger. Laser photoelectron spectroscopy of MnH^- and FeH^-: Electronic structures of the metal hydrides, identification of a low-spin excited state of MnH, and evidence for a low-spin ground state of FeH. *Journal of Chemical Physics*, 78:5420–5431, May 1983. doi: 10.1063/1.445470.

[523] A. E. Stevens, C. S. Feigerle, and W. C. Lineberger. Laser photoelectron spectroscopy of mnh^- and feh^-: Electronic structures of the metal hydrides, identification of a low-spin excited state of mnh, and evidence for a low-spin ground state of feh. *Journal of Chemical Physics*, 78, 1983.

[524] A. E. Stevens Miller, C. S. Feigerle, and W. C. Lineberger. Laser photoelectron spectroscopy of CrH^-, CoH^-, and NiH^-: Periodic trends in the electronic structure of the transition-metal hydrides. *Journal of Chemical Physics*, 87:1549–1556, August 1987. doi:10.1063/1.453214.

[525] J. Sugar and C. Corliss. *Atomic energy levels of the iron-period elements: Potassium through Nickel*. Washington: American Chemical Society, 1985. http://adsabs.harvard.edu/abs/1985aeli.book.....S.

[526] M. R. Swain, G. Vasisht, and G. Tinetti. The presence of methane in the atmosphere of an extrasolar planet. *Nature*, 452:329–331, March 2008.

[527] P. G. Szalay and J. Gauss. Spin-restricted open-shell coupled-cluster theory for excited states. *Journal of Chemical Physics*, 112(9):4027–4036, MAR 1 2000.

[528] M. Tacconi, F. A. Gianturco, E. Yurtsever, and D. Caruso. Cooling and quenching of $^{24}MgH(x^1\sigma^+)$ by $^4He(^1s)$ in a Coulomb trap: A quantum study of the dynamics. *Physical Review A*, 84(1), JUL 13 2011.

[529] T. J. Tague and L. Andrews. Pulsed Laser Evaporated Magnesium Atom Reactions with Hydrogen: Infrared Spectra of Five Magnesium Hydride Molecules. *Journal of Physical Chemistry*, 98(35):8611–8616, SEP 1 1994.

[530] TJ Tague and L Andrews. Reactions of beryllium atoms with hydrogen. Matrix infrared spectra of novel product molecules. *Journal of the American Chemical Society*, 115(25):12111–12116, DEC 15 1993.

[531] K. Tanaka, M. Sekiya, and M Yoshimine. Ab initio study of the lower few states of FeH: Application of the multireference coupled pair approximation. *Journal of Chemical Physics*, 115(10):4558–4564, SEP 8 2001.

[532] J. Tennyson. Vibration-rotation transition dipoles from first principles. *Journal of Molecular Spectroscopy*, 298:1–6, April 2014. doi:10.1016/j.jms.2014.01.012.

[533] J. Tennyson, C. Hill, and S. N. Yurchenko. Data structures for ExoMol: Molecular line lists for exoplanet and other atmospheres. *AIP Conference Proceedings*, 1545:186, 2013.

[534] J. Tennyson and S. N. Yurchenko. ExoMol: molecular line lists for exoplanet and other atmospheres. *Monthly Notices of the Royal Astronomical Society*, 425(1):21–33, September 2012. doi:10.1111/j.1365-2966.2012.21440.x.

[535] J. Tennyson and S. N. Yurchenko. ExoMol: molecular line lists for exoplanet and other atmospheres. *Monthly Notices of the Royal Astronomical Society*, 425:21–33, 2012.

[536] J. Tennyson, S. N. Yurchenko, A. F. Al-Refaie, E. J. Barton, K. L. Chubb, P. A. Coles, S. Diamantopoulou, M. N. Gorman, C. Hill, A. Z. Lam, L. Lodi, L. K. McKemmish, Y. Na, A. Owens, O. L. Polyansky, C. Sousa-Silva, D. S. Underwood, A. Yachmenev, and E. Zak. The ExoMol database: molecular line lists for exoplanet and other hot atmospheres. *ArXiv e-prints*, March 2016.

[537] J. M. Thompsen, M. A. Brewster, and L. M. Ziurys. Molecules in high spin states: The millimeter and submillimeter spectrum of the MnS radical ($X^6\Sigma^{+)}$. *Journal of Chemical Physics*, 116:10212–10220, June 2002. doi: 10.1063/1.1476931.

[538] C. Thomson. *Ab initio* calculations on small molecules, and potential energy surfaces . *Annual Reports on the Progress of Chemistry, Section A*, 71:5–28, 1974.

[539] G. Tinetti, T. Encrenaz, and A. Coustenis. Spectroscopy of planetary atmospheres in our Galaxy. *The Astronomy and Astrophysics Review*, 21:63, October 2013.

[540] G. Tinetti, A. Vidal-Madjar, M.-C. Liang, J.-P. Beaulieu, Y. Yung, S. Carey, R. J. Barber, J. Tennyson, I. Ribas, N. Allard, G. E. Ballester, D. K. Sing, and F. Selsis. Water vapour in the atmosphere of a transiting extrasolar planet. *Nature*, 448:169–171, July 2007.

[541] J. Tino, V. Klimo, T. A. Claxton, and B. Burton. Study of the BeH radical by UHF-type and complete configuration interaction methods. *Journal of the Chemical Society, Faraday Transactions II*, 75(Part 9):1307–1312, 1979.

[542] J. Tomkin and D. L Lambert. Isotopic abundances of magnesium in five G and K dwarfs. *Astrophysical Journal*, 235(3):925–938, 1980.

[543] M. Tomonari, U. Nagashima, and T. Hirano. Ab initio calculation of the electronic structures of the $^7\Sigma^+$ ground and A $^7\Pi$ and a $^5\Sigma^+$ excited states of MnH. *Journal of Chemical Physics*, 130(15):154105, April 2009. doi: 10.1063/1.3098917.

[544] J. P. Towle, J. M. Brown, K. Lipus, E. Bachem, and W. Urban. The infrared spectrum of the FeH radical by laser magnetic resonance. *Molecular Physics*, 79(4):835–845, JUL 1993.

[545] B. M. Tripahi and V. P. Gaur. Partition functions and dissociation constants for MgH. *Journal of Quantitative Spectroscopy & Radiative Transfer*, 22(4):407–409, 1979.

[546] H. Uehara. Dunham treatment including effects of the Born-Oppenheimer breakdown for open-shell diatomic molecules in $^2\Sigma$ states. *Journal of Molecular Spectroscopy*, 192(2):417–423, DEC 1998.

[547] R.-D. Urban and H. Jones. The ground state infrared spectrum of the MnH radical ($^7\Sigma$) from diode laser spectroscopy. *Chemical Physics Letters*, 163:34–40, November 1989. doi: 10.1016/0009-2614(89)80007-7.

[548] R.-D. Urban and H. Jones. Diode laser spectroscopy of the MnD radical ($^7\Sigma$) and the determination of mass-independent parameters. *Chemical Physics Letters*, 178:295–300, March 1991. doi: 10.1016/0009-2614(91)87072-J.

[549] F. P. Urena, M. F. Gomez, J. J. L. Gonzalez, and N. Rajamanickam. Astrophysical molecules AlD and CaH: Transition probabilities and dissociation energy. *Astrophysics and Space Science*, 272(4):345–352, 2000.

[550] J.A. Valenti and C.M. Johns-Krull. Magnetic Field Measurements for Cool Stars. In *ASP Conference Proceedings*, volume 248, page 179, 2001.

[551] J.A. Valenti, C.M. Johns-Krull, and N. E. Piskunov. Using FeH to Measure Magnetic Fields on Cool Stars and Brown Dwarfs. In *ASP Conference Proceedings*, volume 223, page 1579, 2001.

[552] R. Vallon, S. H. Ashworth, P. Crozet, R. W. Field, D. Forthomme, H. Harker, C. Richard, and A. J. Ross. Room-Temperature Metal-Hydride Discharge Source, with Observations on NiH and FeH. *Journal of Physical Chemistry A*, 113(47):13159–13166, NOV 26 2009.

[553] R. J. van Zee, C. A. Baumann, and W. Weltner, Jr. HCr, LiCr, and NaCr molecules: ESR and ground state properties. *Chemical Physics Letters*, 113:524–529, February 1985. doi:10.1016/0009-2614(85)85025-9.

[554] R. J. van Zee, T. C. Devore, J. L. Wilkerson, and W. Weltner, Jr. High spin molecules: ESR and optical spectroscopy of MnH ($^7\Sigma$) and MnH_2 ($^6A_1$) at 4 °K. *Journal of Chemical Physics*, 69:1869–1875, September 1978. doi: 10.1063/1.436823.

[555] R. J. van Zee, D. A. Garland, and W. Weltner, Jr. ENDOR of the MnH molecule. *Journal of Chemical Physics*, 84:5968–5970, May 1986. doi: 10.1063/1.450784.

[556] R. J. van Zee, D. A. Garland, and W. Weltner, Jr. ENDOR/ESR of Mn atoms and MnH molecules in solid argon. *Journal of Chemical Physics*, 85:3237–3242, September 1986. doi: 10.1063/1.450993.

[557] T. D. Varberg, R. W. Field, and A. J. Merer. Hyperfine structure of the MnH X^7Sigma^+ state: A large gas-to-matrix shift in the Fermi contact interaction. *Journal of Chemical Physics*, 92:7123–7127, June 1990. doi: 10.1063/1.458252.

[558] T. D. Varberg, R. W. Field, and A. J. Merer. Elucidation of electronic structure by the analysis of hyperfine interactions: The MnH $A7\Pi - X^7Sigma^+$ $(0,0)$ band. *Journal of Chemical Physics*, 95:1563–1576, August 1991. doi: 10.1063/1.461071.

[559] T. D. Varberg, J. A. Gray, R. W. Field, and A. J. Merer. Reanalysis and extension of the MnH $A^7\Pi - X^7\Sigma^+$ $(0,0)$ band: Fine structure and hyperfine-induced rotational branches. *Journal of Molecular Spectroscopy*, 156:296–318, December 1992. doi: 10.1016/0022-2852(92)90233-E.

[560] A. M. Velasco, C. Lavin, I. Martin, J. Pitarch-Ruiz, and J. Sanchez-Marin. Theoretical study of the discrete and continuum spectrum of BeH. *Chemical Physics Letters*, 462(4-6):344–347, SEP 10 2008.

[561] C. Visscher, K. Lodders, and B. Fegley, Jr. Atmospheric Chemistry in Giant Planets, Brown Dwarfs, and Low-Mass Dwarf Stars III. Iron, Magnesium, and Silicon. *Astrophysical Journal*, 716(2):1060–1075, JUN 20 2010.

[562] A. A. Šurkus, R.J. Rakauskas, and A.B. Bolotin. The generalized potential energy function for diatomic molecules. *Chemical Physics Letters*, 105:291, 1984.

[563] S. P. Walch, , and C. W. Bauschlicher. CASSCF/CI Calculations for First Row Transition Metal Hydrides - the TiH($^4\Phi$), VH($^5\Delta$), CrH($^6\Sigma^+$), MnH($^7\Sigma^+$), FeH($^4\Delta$, $^6\Delta$) and NiH($^2\Delta$) States. *Journal Of Chemical Physics*, 78:4597–4605, April 1983. doi:10.1063/1.445301.

[564] S. P. Walch. Model studies of the interaction of h atoms with bcc iron. *Surface Science*, 143:188, 1984.

[565] S. P. Walch. Theoretical evidence supporting the $^4\Delta$ ground-state assignment for FeH. *Chemical Physics Letters*, 105(1):54–57, 1984.

[566] S. P. Walch and C. W. Bauschlicher. CASSCF/CI calculations for first row transition metal hydrides: The TiH ($^4\Phi$), VH ($^5\Delta$), CrH ($^6\Sigma^+$), MnH ($^7\Sigma^+$), FeH ($^{4,6}\Delta$), and NiH ($^2\Delta$) states. *Journal of Chemical Physics*, 78(7):4597–4605, 1983.

[567] I. P. Waldmann, M. Rocchetto, G. Tinetti, E. J. Barton, S. N. Yurchenko, and J. Tennyson. Tau-REx II: Retrieval of Emission Spectra. *Astrophysical Journal*, 813:13, 2015.

[568] I. P. Waldmann, G. Tinetti, M. Rocchetto, E. J. Barton, S. N. Yurchenko, and J. Tennyson. Tau-REx I: A Next Generation Retrieval Code for Exoplanetary Atmospheres. *Astrophysical Journal*, 802:107, April 2015.

[569] L. Wallace and K. Hinkle. Detection of the 1.6 μm $E^4\Pi - A^4\Pi$ FeH system in sunspot and cool star spectra. *Astrophysical Journal*, 559(1, Part 1):424–427, SEP 20 2001.

[570] L. Wallace, K. Hinkle, G. Li, and P. Bernath. The MgH $b'^2\sigma^+ - x^2\sigma^+$ transition: A new tool for studying magnesium isotope abundances. *Astrophysical Journal*, 524(1, Part 1):454–461, OCT 10 1999.

[571] X. Wang and L. Andrews. Matrix Infrared Spectra and Density Functional Theory Calculations of Manganese and Rhenium Hydrides. *Journal of Physical Chemistry A*, 107:4081–4091, May 2003. doi: 10.1021/jp034392i.

[572] X. Wang and L. Andrews. Infrared Spectra and Theoretical Calculations for Fe, Ru, and Os Metal Hydrides and Dihydrogen Complexes. *Journal of Physical Chemistry A*, 113(3):551–563, JAN 2009.

[573] X. F. Wang and L. Andrews. Infrared spectra of magnesium hydride molecules, complexes, and solid magnesium dihydride. *Journal of Physical Chemistry A*, 108(52):11511–11520, DEC 30 2004.

[574] P. F. Weck, A. Schweitzer, P. C. Stancil, P. H. Hauschildt, and K. Kirby. The molecular continuum opacity of ^{24}MgH in cool stellar atmospheres. *Astrophysical Journal*, 584(1, Part 1):459–464, FEB 10 2003.

[575] P. F. Weck, A. Schweitzer, P. C. Stancil, P. H. Hauschildt, and K. Kirby. The molecular line opacity of MgH in cool stellar atmospheres. *ASTROPHYSICAL JOURNAL*, 582(2, Part 1):1059–1065, JAN 10 2003.

[576] P. F. Weck, P. C. Stancil, and K. Kirby. $B' \leftarrow X$ rovibrationally resolved photodissociation of ^{24}(MgH). *ASTROPHYSICAL JOURNAL*, 582(2, Part 1):1263–1268, JAN 10 2003.

[577] P. F. Weck, P. C. Stancil, and K. Kirby. Theoretical study of the rovibrationally resolved transitions of CaH. *Journal of Chemical Physics*, 118(22):9997–10005, JUN 8 2003.

[578] J. D. Weinstein, R. Decarvalho, T. Guillet, B. Friedrich, and J. M. Doyle. Magnetic trapping of calcium monohydride molecules at millikelvin temperatures. *Nature*, 395(6698):148–150, SEP 10 1998.

[579] S. Wende, A. Reiners, and H-G. Ludwig. 3D simulations of M star atmosphere velocities and their influence on molecular FeH lines. *Astronomy & Astrophysics*, 508(3):1429–1442, DEC 2009.

[580] S. Wende, A. Reiners, A. Seifahrt, and P. F. Bernath. CRIRES spectroscopy and empirical line-by-line identification of FeH molecular absorption in an M dwarf. *Astronomy & Astrophysics*, 523, NOV-DEC 2010.

[581] PG Wenthold. A computational study of the hydride affinities of group I and group II metals. *International Journal of Mass Spectrometry*, 195(SI):319–325, JAN 21 2000.

[582] PG Wenthold. A computational study of the hydride affinities of group I and group II metals. *International Journal of Mass Spectrometry*, 195(SI):319–325, JAN 21 2000.

[583] H.-J. Werner. Ab Initio Methods in Quantum Chemistry. *Advances in Chemical Physics*, (LXIX,1), 1987.

[584] H.-J. Werner and P. J. Knowles. An efficient internally contracted multiconfiguration-reference configuration interaction method. *Journal of Chemical Physics*, 89(9):5803, November 1988. doi:10.1063/1.455556.

[585] H. J. Werner and P. J. Knowles. An efficient internally contracted multiconfigurationâĂŞreference configuration interaction method. *Journal of Chemical Physics*, 89:5803, 1988.

[586] H.-J. Werner, P. J. Knowles, G. Knizia, F. R. Manby, and M. Schütz. MOLPRO: a general purpose quantum chemistry program package. *Wiley Interdisciplinary Reviews: Computational Molecular Science*, 2012.

[587] H.-J. Werner, P. J. Knowles, G. Knizia, F. R. Manby, M. Schütz, P. Celani, T. Korona, R. Lindh, A. Mitrushenkov, G. Rauhut, K. R. Shamasundar, T. B. Adler, R. D. Amos, A. Bernhardsson, A. Berning, D. L. Cooper, M. J. O. Deegan, A. J. Dobbyn, F. Eckert, E. Goll, C. Hampel, A. Hesselmann, G. Hetzer, T. Hrenar, G. Jansen, C. KÃűppl, Y. Liu, A. W. Lloyd, R. A. Mata, A. J. May, S. J. McNicholas, W. Meyer, M. E. Mura, A. Nicklass, D. P. O'Neill, P. Palmieri, D. Peng, K. PflÃijger, R. Pitzer, M. Reiher, T. Shiozaki, H. Stoll, A. J. Stone, R. Tarroni, T. Thorsteinsson, and M. Wang. MOLPRO, version 2012.1, a package of ab initio programs, 2012. see http://www.molpro.net.

[588] H.-J. Werner and E. A. Reinsch. The self-consistent electron pairs method for multiconfiguration reference state functions. *Journal of Chemical Physics*, 76(6):3144–3156, mar 1982. doi:10.1063/1.443357.

[589] C. Western. Recent Changes in Pgopher: a General Purpose Program for Simulating Rotational Structure. In *65th International Symposium On Molecular Spectroscopy*, June 2010.

[590] C. Western. PGOPHER in the Classroom and the Laboratory. In *70th International Symposium on Molecular Spectroscopy*, June 2015.

[591] D. M. Williams, J. F. Kasting, and R. A. Wade. Habitable moons around extrasolar giant planets. *Nature*, 385:234–236, January 1997.

[592] D. Willock. *Molecular Symmetry*. Wiley & Sons, 2009.

[593] C. Wilson and J. M. Brown. Identification of new hot bands in the blue and green band systems of FeH. *Journal of Molecular Spectroscopy*, 197(2):188–198, OCT 1999.

[594] C. Wilson and J. M. Brown. The FeH radical: rotational assignment of the $a^6\Delta(\nu = 2)$ and $b^6\Pi(\nu = 1)$ levels. *Molecular Physics*, 99(18):1549–1561, SEP 2001.

[595] C Wilson, HM Cook, and JM Brown. Complete characterization of the $a^6\Delta$ state of the FeH radical. *Journal of Chemical Physics*, 115(13):5943–5956, OCT 1 2001.

[596] R. F. Wing, J. Cohen, and J. W. Brault. Confirmation of the presence of iron hydride in sunspots and cool stars. *Astrophysical Journal*, 216(2):659–664, 1977.

[597] H. Wöhl. On Molecules in Sunspots. *Solar Physics*, 16(2):362–372, 1971.

[598] A. A. Wyller. Rotational temperatures of C_2, CH, AlH, MgH and SiH in Beta Pegasi. *Astrophysical Journal*, 134(3):805–808, 1961.

[599] B. Yadin, T. Veness, P. Conti, C. Hill, S. N. Yurchenko, and J. Tennyson. ExoMol line lists I. The rovibrational spectrum of BeH, MgH and CaH in the $X^2\Sigma^+$ state. *Monthly Notices of the Royal Astronomical Society*, 425:34–43, Sep 2012.

[600] B. Yadin, T. Veness, P. Conti, C. Hill, S. N. Yurchenko, and J. Tennyson. ExoMol line lists âĂŞ I. The rovibrational spectrum of BeH, MgH and CaH in the $X^2\Sigma^+$ state. *Monthly Notices of the Royal Astronomical Society*, 425:34–43, September 2012.

[601] D. Yong, D. L. Lambert, and I. I. Ivans. Magnesium isotopic abundance ratios in cool stars. *Astrophysical Journal*, 599(2, Part 1):1357–1371, DEC 20 2003.

[602] S. N. Yurchenko, L. Lodi, J. Tennyson, and A. V. Stolyarov. DUO: A general program for calculating spectra of diatomic molecules. *Computer Physics Communications*, 202:262–275, May 2016.

[603] S. N. Yurchenko, L. Lodi, J. Tennyson, and A. V. Stolyarov. Duo: A general program for calculating spectra of diatomic molecules. *Computer Physics Communications*, 2016.

[604] S. N. Yurchenko, J. Tennyson, J. Bailey, M. D. J. Hollis, and G. Tinetti. Spectrum of hot methane in astronomical objects using a comprehensive computed line list. *Proceedings of the National Academy of Science*, 111:9379–9383, July 2014.

[605] S. N. Yurchenko, W. Thiel, and P. Jensen. Theoretical ROVibrational Energies (TROVE): A robust numerical approach to the calculation of rovibrational energies for polyatomic molecules. *Journal of Molecular Spectroscopy*, 245(2):126–140, October 2007. doi:10.1016/j.jms.2007.07.009.

[606] R.N. Zare. *Angular Momentum: Understanding Spatial Aspects in Chemistry and Physics*. Dover Publications, Incorporated, 2007.

[607] L. R. Zink, D. A. Jennings, K. M. Evenson, and K. R. Leopold. Laboratory measurements for the astrophysical identification of MgH. *Astrophysical Journal*, 359(2, Part 2):L65–L66, AUG 20 1990.

[608] L. Ziurys. Millimeter/Sub-millimeter Spectroscopy: Revealing the Building Blocks of Complex Molecules in Space. In *APS Division of Atomic, Molecular and Optical Physics Meeting Abstracts*, page C2001, May 2006.

[609] L. M. Ziurys. Interstellar Chemistry Special Feature: The chemistry in circumstellar envelopes of evolved stars: Following the origin of the elements to the origin of life. *Proceedings of the National Academy of Science*, 103:12274–12279, August 2006.

[610] L. M. Ziurys. Millimeter-Wave Spectroscopy of Metal-Bearing Molecules in the ISM. In R. I. Kaiser, P. Bernath, Y. Osamura, S. Petrie, and A. M. Mebel, editors, *Astrochemistry - From Laboratory Studies to Astronomical Observations*,

volume 855 of *American Institute of Physics Conference Series*, pages 231–242, September 2006.

[611] L. M Ziurys, W. L. Barclay, and M. A. Anderson. The millimeter-wave spectrum of the MgH and MgD radicals. *Astrophysical Journal*, 402(1, Part 2):L21–L24, JAN 1 1993.

[612] L. M. Ziurys, W. L. Barclay, Jr., M. A. Anderson, D. A. Fletcher, and J. W. Lamb. A millimeter/submillimeter spectrometer for high resolution studies of transient molecules. *Review of Scientific Instruments*, 65:1517–1522, May 1994. doi: 10.1063/1.1144885.

[613] L. M. Ziurys, M. A. Flory, and D. T. Halfen. Sub-millimeter Spectroscopy of Astrophysically Important Molecules and Ions: Metal Hydrides, Halides, and Cyanides. In P. F. Weck, V. H. S. Kwong, and F. Salama, editors, *NASA LAW 2006*, page 292, 2006.